Published in Journals: Applied Sciences, Minerals, Mining and Sustainability

Topic Reprint

Mining Innovation

Edited by
Krzysztof Skrzypkowski, René Gómez, Fhatuwani Sengani, Derek B. Apel, Faham Tahmasebinia and Jianhang Chen

mdpi.com/topics

Mining Innovation

Mining Innovation

Topic Editors

Krzysztof Skrzypkowski
René Gómez
Fhatuwani Sengani
Derek B. Apel
Faham Tahmasebinia
Jianhang Chen

MDPI

Basel • Beijing • Wuhan • Barcelona • Belgrade • Novi Sad • Cluj • Manchester

Topic Editors

Krzysztof Skrzypkowski
Faculty of Civil Engineering and Resource Management
AGH University of Krakow
Kraków
Poland

René Gómez
Departamento de Ingeniería Metalúrgica
Universidad de Concepción
Concepción
Chile

Fhatuwani Sengani
Department of Geology and Mining
University of Limpopo
Sovega
South Africa

Derek B. Apel
Faculty of Engineering, Civil and Environmental Engineering Dept
University of Alberta
Edmonton, AB
Canada

Faham Tahmasebinia
School of Civil Engineering
The University of Sydney
Sydney
Australia

Jianhang Chen
School of Energy and Mining Engineering
China University of Mining and Technology (Beijing)
Beijing
China

Editorial Office

MDPI AG
Grosspeteranlage 5
4052 Basel, Switzerland

This is a reprint of the Topic, published open access by the journals *Applied Sciences* (ISSN 2076-3417), *Minerals* (ISSN 2075-163X), *Mining* (ISSN 2673-6489) and *Sustainability* (ISSN 2071-1050), freely accessible at: https://www.mdpi.com/topics/V3W8O5TWEY.

For citation purposes, cite each article independently as indicated on the article page online and as indicated below:

Lastname, A.A.; Lastname, B.B. Article Title. *Journal Name* **Year**, *Volume Number*, Page Range.

ISBN 978-3-7258-3479-2 (Hbk)
ISBN 978-3-7258-3480-8 (PDF)
https://doi.org/10.3390/books978-3-7258-3480-8

Contents

mining

MDPI

Article

Physical and Numerical Modeling of a Flow Control Layer Made with a Sludge and Slag Mixture for Use in Waste Rock Pile Reclamation

Nelcy Carolina Otalora Vasquez, Abdelkabir Maqsoud * and Tikou Belem

Research Institut on Mines and Environment, Université du Québec en Abitibi-Témiscamingue, Rouyn-Noranda, QC J9X 5E4, Canada; nelcycarolina.otaloravasquez@uqat.ca (N.C.O.V.); tikou.belem@uqat.ca (T.B.)
* Correspondence: abdelkabir.maqsoud@uqat.ca

Abstract: The reclamation of waste rock piles (WRPs) is complex, requiring adaptation of existing mine site reclamation techniques. An alternative approach has been developed for waste rock piles reclamation which involves installing finer materials on the top of waste rock piles. These finer layers (flow control layers—FCLs) redirect water flowing inside the pile toward its slope and limits water infiltration into reactive waste rocks. In the context of sustainable development, a mixture material made with sludge and slag can be used as an FCL in the reclamation of a waste rock pile. To assess the effectiveness of this material, a physical model was used and instrumented with sensors for monitoring volumetric water content and suction and equipped with the following components: (1) a rain simulator; and (2) drains that allow the recovery of water that infiltrates through the system. The physical model was tested with various cover layer thicknesses, inclinations, and precipitation rates. Investigation results showed that the water infiltration across the system was very low, leading to the conclusion that the sludge and slug mixture performed well as a flow control layer in the reclamation of waste rock piles.

Keywords: acid mine drainage; waste rock piles; reclamation; flow control layers

Citation: Otalora Vasquez, N.C.; Maqsoud, A.; Belem, T. Physical and Numerical Modeling of a Flow Control Layer Made with a Sludge and Slag Mixture for Use in Waste Rock Pile Reclamation. *Mining* **2024**, *4*, 841–862. https://doi.org/10.3390/mining4040047

Academic Editors: Krzysztof Skrzypkowski, René Gómez, Fhatuwani Sengani, Derek B. Apel, Faham Tahmasebinia and Jianhang Chen

Received: 12 July 2024
Revised: 18 September 2024
Accepted: 22 September 2024
Published: 16 October 2024

1. Introduction

Quémont 2 tailings storage facility (TSF) is an active site located approximately 2.5 km northeast of the Horne smelter plant, positioned between Osisko and Dufault Lakes, as illustrated in Figure 1. Its area is estimated to be 105 hectares. Deposition of tailings at this TSF began in 1949. Initially, sulfide tailings, which contributed to acidity, were deposited at this site. Subsequently, they were overlaid with a mixture of slag tailings and treatment sludge (UTAF sludge), which did not produce acidity. Between 1949 and 2018, approximately 7.6 Mt of sulfide tailings, 14.2 Mt of slag, and 1.1 Mt of UTAF sludge were deposited. These materials originated from the Quémont mine, the Gallen mine, and the slag and hydrometallurgical treatment (UTAF) circuit [1]. It is important to note that some of these materials may contribute to acid mine drainage.

Acid mine drainage (AMD) is widely acknowledged as one of the foremost environmental challenges linked with the mining industry. To limit the generation of AMD, numerous waste management options and site reclamation strategies are available. Among these approaches, one can find oxygen barrier and hydraulic barrier covers [2].

Indeed, store and release covers (SRCs) represent another approach used to control water infiltration into reactive tailings, particularly in arid environments [3–6].

In the context of sustainable development, the aim is to utilize sludge and slag materials derived from metallurgical treatment by integrating them into construction materials for engineering covers, especially as flow control layers (FCLs). To achieve this objective, this study intends to test sludge and slag materials as FCLs using a physical model. The study will involve varying the layer thickness, the slope, and the intensity of precipitation to assess their effects on cover performance. It is important to recall that the sludge and slag materials were tested to evaluate their geochemistry using humidity cells kinetic tests, and results showed that these materials can be considered as not AMD generating with the pH close to the neutrality [7].

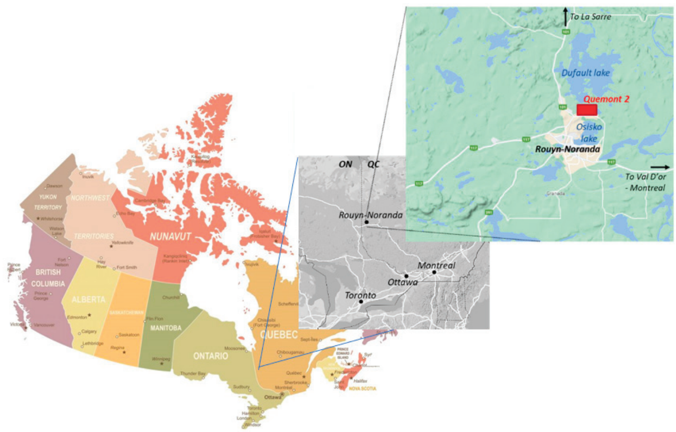

Figure 1. Quémont 2 mine site location (https://mapamundi.online maps images, accessed on 11 July 2024).

In this paper, we begin with an overview of mine site reclamation techniques followed by the sludge and slag material characterizations, along with descriptions of the physical model configurations used in our study. Subsequently, investigation results obtained from physical and numerical modeling are presented. Finally, this paper ends by a conclusion.

1.1. Mine Site Reclamation

The reclamation of mine sites is indeed a crucial aspect of mining practices, with the primary goal of minimizing the environmental impact caused by mining activities. The reclamation of mine sites is indeed a crucial aspect of mining practices, with the primary goal of minimizing the environmental impact caused by mining activities.

One of the principal purposes of reclamation methods is to mitigate AMD by eliminating or reducing the presence of reactive elements involved in the acidification process, as presented in Equation (1):

$$FeS_2 + 15/4\ O_2 + 7/2\ H_2O \rightarrow Fe(OH)_3 + 2SO_4{}^{2-} + 4H^+ \tag{1}$$

Various methods of the prevention and control of AMD are available, and the selection of the most suitable method depends on the specific characteristics of each mine site. Below is a summary of the major methods used for the prevention and control of AMD.

1.1.1. Oxygen Barrier

The objective of this method is to minimize or prevent the oxygen flow towards sulfide tailings. There are several techniques commonly used to exclude oxygen to achieve this objective, including the following ones [2]:

1. Water covers can effectively act as an oxygen barrier due to the lower concentration of oxygen and the lower diffusion coefficient in water compared to in air [8,9];
2. The elevated water table combined with a monolayer cover technique aims to maintain reactive tailings saturated or close to saturation (Sr = 1) by keeping the water table at a higher level and close to interface cover-reactive tailings. This technique is similar to water covers in that it provides a barrier to oxygen migration [10–12];

3. Covers with a capillary barrier effect (CCBEs) are multilayer covers whose aim is to maintain at least one of the layers at a high degree of saturation (Sr > 85%) to control the migration of gases to reactive waste and limit water infiltration [13–15];
4. Oxygen-consuming materials (wood chips water, treatment sludge, etc.) can also control oxygen migration by placing them on reactive tailings. Oxygen-consuming materials limit the availability of oxygen that can reach underlying materials [16,17].

1.1.2. Hydraulic Barrier

In contrast, hydraulic barriers are specifically designed to prevent water infiltration. In regions with humid climates, these barriers can be constructed using a combination of natural and/or synthetic materials. Examples of such materials include clay, geosynthetic clay liners, and geomembranes.

This method relies on the installation of covers composed of materials with a saturated hydraulic conductivity (k_{sat}) lower than 1×10^{-9} m/s. These covers typically made from natural soils such as clays or compacted tills, as well as synthetic materials (geotextiles, geomembranes, or geosynthetic clay liners), act as physical barriers to control water infiltration into mine waste [2,18–20].

1.1.3. Flow Control Layer

This method aims to limit water infiltration into waste rocks by redirecting precipitation water along inclined layers. Precipitation is temporarily stored in a flow control layer (FCL) and then evacuated by evaporation or lateral drainage, thereby preventing the contact with waste rock materials [21–25].

Various laboratory work and numerical modeling have validated the effectiveness of this method, including experiments conducted on waste rock piles of Lake Tio Mine. Factors such climatic conditions, the thickness of the FCL, inclination, and cover material properties influence the FCL performance [26–30].

The FCL will be tested in a laboratory by using a mixture material made from sludge and slag.

In the following sections, materials and methods used in this evaluation are presented.

2. Materials and Methods

The material was both physically and hydrogeologically tested in a laboratory. Physical characterization included assessing particle size distribution and specific gravity, while hydrogeological characterization involved determining parameters such as saturated hydraulic conductivity (k_{sat}) and the water retention curve (WRC).

2.1. Physical Characterization

The purpose of particle size analysis was to quantitatively determine the distribution of soil particles based on their diameter classes. For the sludge and slag mixture, particle size distribution testing was conducted using *a* Malvern analytical Mastersizer 3000 laser particle sizer. The results of the grain size distribution (GSD) are illustrated in Figure 2, which displays the size distribution of particles in the mixture. The results of the GSD analyses indicated very low percentages of the clay fraction (lower than 2 μm) in both materials. The sludge–slag mixture had a silt fraction of 82% (fraction included between 2 and 80 μm). Additionally, the gravel material comprised a sand fraction of 49% and a gravel fraction of 40%.

According to [31], the sludge and slag mixture and gravel materials can be categorized as low plasticity silt (ML) and well-graded sand with silt (SW-SM), respectively.

Key parameters were extracted from the GSD curves and are listed in Table 1. D_{10}, D_{30}, and D_{60} represent the diameters corresponding to 10%, 30%, and 60% passing on the cumulative GSD curve, respectively (see Table 1). The coefficient of uniformity was calculated as $C_U = D_{60}/D_{10}$. The C_U values of the sludge–slag mixture and the gravel materials were 7.6 and 45.4, respectively. According to [31], these values (between 5 and 20) led to a classified sludge and slug materials as having a poorly graded GSD. In contrast, the gravel was classified as having a well graded GSD.

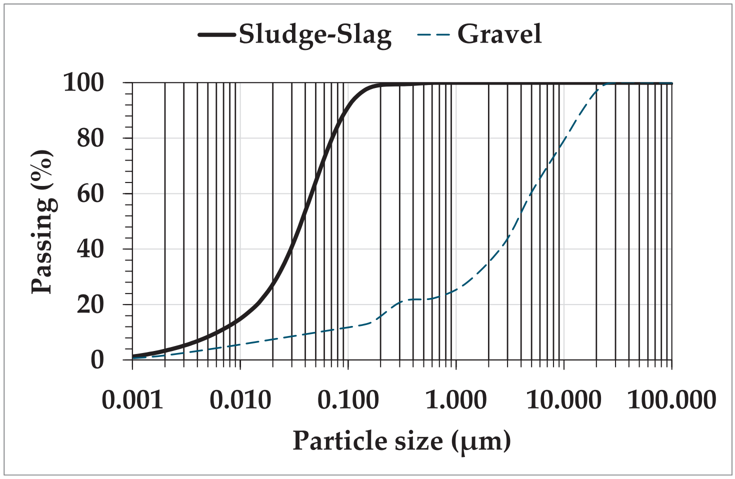

Figure 2. Particle size distribution of materials.

Table 1. Grain size distribution parameters of the used materials.

Material	% Clay	% Silt	% Sand	D_{10} (mm)	D_{30} (mm)	D_{60} (mm)	C_U	C_C
Sludge and slag	3	82	15	0.006	0.02	0.04	7.6	1.7
Gravel	2	9	49	0.11	1.5	5	45.4	4.1

The liquid limit (W_L) corresponds to the water content at which the behavior of a material changes from the plastic state to the liquid state. The W_L was determined using the Casagrande method, following ASTM D4318-17e1 [30]. The plastic limit (W_P) is the water content at which a material sample begins to disintegrate into pieces that are 3 to 10 mm long when rolled into a cylinder with a diameter of 3 mm. The W_P was determined using the rolling method [32].

For the sludge–slag mixture, the W_L was 22%, and the W_P was about 17%. These values were used to calculate the plasticity index (PI). This index showed the difference between the W_L and the W_P. The calculated PI was 5%, allowing concluding that this material can be considered as a low plastic material.

The proctor tests is a method allowing evaluating the optimal water content at which a given soil type becomes most dense and achieves its maximum dry density [33]. Protector test results showed that from the compaction curves the maximum dry unit weight (γ_{dopt}), the optimum water content (w_{opt} (%)), the optimum void ration ($e_{\gamma opt}$), and the optimum porosity ($n_{\gamma opt}$) were 2.5 g/cm^3, 10 %, 0.80, and 0.44 respectively.

In this case, the sludge and slag mixture can be categorized as silt ML.

2.2. Hydrogeological Characterization

For the sludge and slag mixture, the water retention curve (WRC) was measured in a laboratory using the Tempe cell. Laboratory testing using the "Tempe cell" method was conducted at 20 °C on a single sample in a ceramic cylinder with a diameter of 85 mm and a height of 60 mm. The Tempe cell is an instrument for assessing the volumetric water content of a saturated sample, which desaturates after the application of suction. Desaturation occurs when the applied suction pressures begin to force the water present in the pores of the sample to move and, consequently, to be extracted downwards from the cylinder [34,35].

Measurement results are presented in Figure 3 and were fitted using the van Genuchten model [36]. The fitting parameters for the sludge–slag mixture included volumetric water content at saturation θs (0.53), residual volumetric water content θ_r (0.10), α_{vG} (0.029 cm^{-1}), and n_{vG} (2.911). The AEV calculated using the tangent method (see [37]) was about 22 kPa.

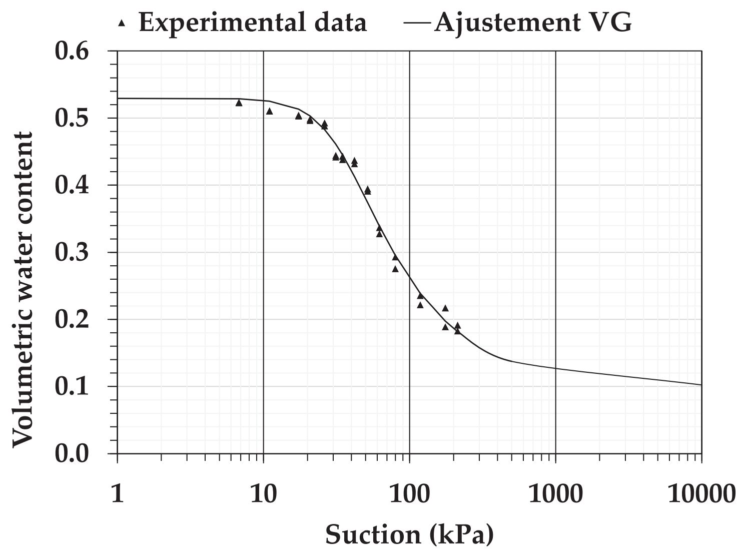

Figure 3. Measured and fitted water retention curves of the sludge and slag mixture.

The saturated hydraulic conductivity (k_{sat}) for the sludge–slag mixture was measured in the laboratory using a constant-load rigid-wall permeameter [31]. The permeameter used had a diameter of 11.4 cm and a height of 24 cm. It consisted of a Plexiglas cylinder, two perforated plates, seals, a base, and a plastic cap fitted with a drainage valve. The sludge–slag material was placed in the permeameter, and by applying a hydraulic load difference across the sample, water could pass through the sample in a given time interval. The saturated k_{sat} of the sludge–slag mixture was calculated using the following Equation (2):

$$k_{sat} = \frac{QL}{\Delta h \ A \ t} \tag{2}$$

where Q is the quantity of water that flows (L^3), L is the height of the material (L), Δh is the hydraulic head difference (L), A is the flow area (L), and t is the time (T).

The average measured values of k_{sat} of the sludge–slag material was about 1.00×10^{-4} cm/s.

For the gravel, the k_{sat} was estimated using the predictive modified Kozeny–Carman model (see Equation (3) [38]). In this model, only basic geotechnical properties are used (see Table 1):

$$k_{sat} = C_G \frac{\gamma_w}{\mu_w} \frac{e^{3+x}}{(1+e)} C_U^{1/3} D_{10}^2 \tag{3}$$

where e is the void ratio, C_U is the coefficient of uniformity, D_{10} represents the diameter corresponding to 10% (in cm), C_G is the porous space geometry constant equal to 0.1, γ_w is the unit weight of the water (N/m^3), μ_w is the dynamic viscosity of water, and x ≈ 2.

The estimated k_{sat} corresponded to 2.18×10^{-1} cm/s.

2.3. Experimental Setup and Physical Modeling

To assess the effectiveness of the FCL method in the waste rock pile reclamation, a laboratory physical model was utilized. This model had dimensions of 2.5 m in length, 0.6 m in width, and 1.5 m in height (see Figure 4). Equipped with a rotation axis, the physical model allowed for adjustment and variation of inclination with angles ranging up to 20 degrees [39]. Specific perforation in the lower part of the model along with drains enabled the separate recovery of infiltration and runoff water. Drainpipes were used to strain and collect infiltration water and runoff water separately.

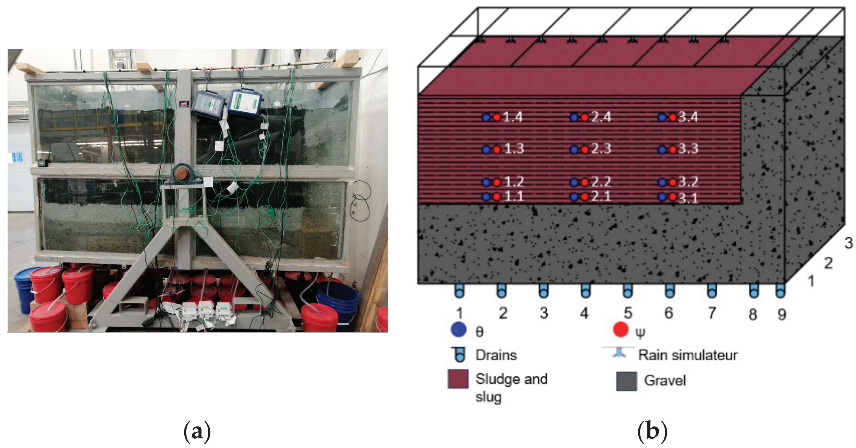

Figure 4. Experimental setup: (**a**) laboratory physical model; (**b**) locations of different devices used for volumetric water content (θ), suction (ψ) measurements, and drains used to recover infiltration and runoff.

The experimental setup was equipped with sensors for volumetric water content (θ) and suction (ψ) measurements (see Figure 4 for sensor locations).

A water dispersion device served as a rain simulator, ensuring a homogeneous distribution of precipitation and preventing the formation of preferential infiltration paths. Additionally, a flow meter was installed to maintain the specific flow rate. In the tests, precipitation rates for return periods of 25 and 100 years for the Abitibi region (Québec, Canada) were used.

The FCL physical model was constructed in three 25 cm layers of the slag–sludge mixture to evaluate the impact of the FCL thicknesses on the cover performance (25 cm, 50 cm, and 75 cm). A non-reactive gravel layer with a draining function was installed at the bottom of the device; this layer had a thickness of 50 cm; another layer was also installed in the front of the FCL to facilitate water drainage from the FCL (see Figure 2).

In the first 25 cm layer, 6 volumetric water content probes (5TM) and 6 suction probes (Watermark) were installed to monitor the sludge–slag layer near the top and near the gravel–sludge–slag interface (see Figure 4). For the other layers (when the FCL thicknesses were about 50 cm and 75 cm), only one level of instrumentation was installed (see Figure 4).

Two slope values were used: 2.5° and 5°; the 2.5° slope represents the average slope of various tailings storage facilities measured using satellite images. Conversely, the 5° slope was utilized in an experimental cell constructed at the Lac Tio mine in 2014 to investigate the hydrogeological behavior of an FCL under field conditions [23,25].

The proposed modeling aimed to assessing the impact of certain parameters on the hydrogeological behavior of an FCL composed of a sludge–slag mixture. The elements tested using the physical model were as follows: (i) the FCL thickness; (ii) the model slope; and (iii) the intensity of precipitations.

Considering the different variables to test (the thickness of the layer, the slope, and the intensity of precipitation), a total of 12 scenarios were performed as shown in Table 2.

Table 2. Simulated scenarios conditions.

Thickness Layers	Slope Used	Precipitation Rate (mm/h)
25 cm 50 cm 75 cm	2.5° 5°	60.6 (100 years) 46.8 (25 years)

In each tested scenario, all parameters were kept constant, except for one which was varied to highlight its influence. In the first series of tests, a 25 cm layer of the sludge–slag mixture was used as an FCL. Two inclinations were tested: 2.5° and 5°. For each inclination of the physical model, two different rates of precipitation were applied: 46.8 mm/h and 60.6 mm/h.

In the second series of tests, the thickness of the slag–sludge layer was increased to 50 cm by adding an additional 25 cm layer. For this configuration, the same scenarios were tested with the same slopes and precipitation rates as for the 25 cm layer. In the third series of tests, the thickness of the sludge–slag layer was further increased by adding another 25 cm layer, resulting in a total thickness of 75 cm. For this new thickness, the same scenarios as in the previous cases were tested. Each series of tests lasted approximately three weeks, with precipitation conducted for 1 h and a drainage period of about 21 days. This period was left between successive tests to allow the system to equilibrate.

2.4. Numerical Simulation Modeling

Simulations were conducted using SEEP/W 2021. This software employs the finite element method (FEM) to simulate the movement of liquid water or water vapor through both saturated and unsaturated porous media. Water flow modeling with SEEP/W is based on the Richards equation, and simulations can be performed in either the steady state or the transient mode, considering hydrogeological conditions [40].

Two-dimensional (2D) model was constructed. The model simulates FCLs was built with the same dimensions as the laboratory physical model and include hydrogeological properties of the materials measured in a laboratory (see Figure 5). These models represent various scenarios and include different thicknesses of sludge–sludge layers (25 cm, 50 cm, and 75 cm) and gravel drainage layers (highlighted in yellow in Figure 5). Regarding the mesh sizes of the models, the 25 cm FCL model comprises 816 nodes and 750 quadrilateral elements, the 50 cm FCL model comprises 1071 nodes and 1000 quadrilateral elements, and the 75 cm FCL model comprises 1326 nodes and 1250 quadrilateral elements.

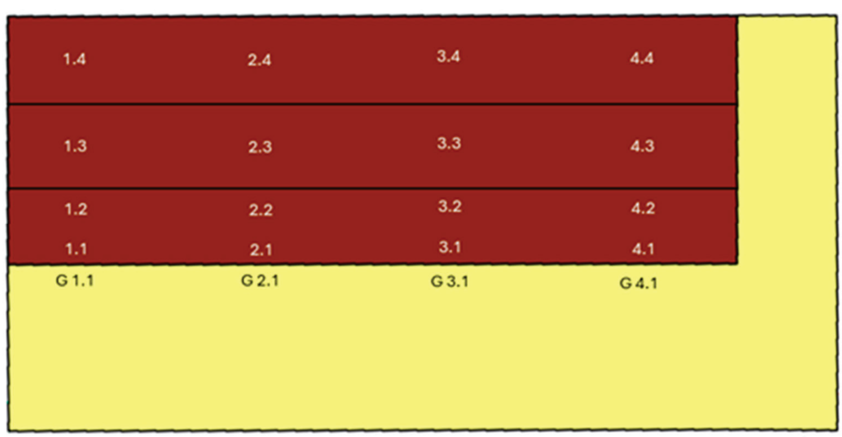

Figure 5. Numerical model and location of simulated sensors in SEEP/W.

The van Genuchten (1980) model was chosen to describe the WRC and Mualem (1976) model to predict the unsaturated hydraulic conductivity function.

The used functions (WRC and permeability functions) are presented in Figures 6 and 7 clearly shows the contrast in hydraulic properties between the used materials, allowing creating the capillary barrier effects.

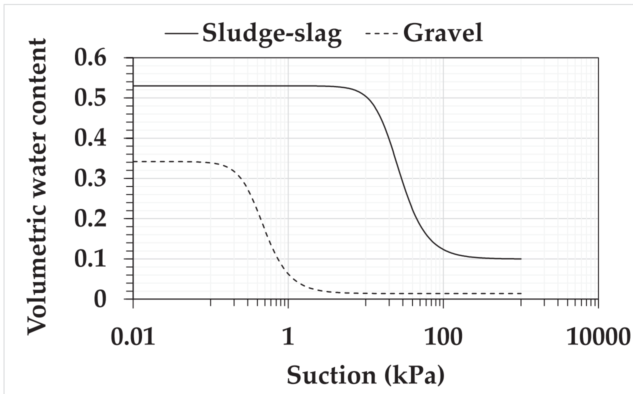

Figure 6. Volumetric water content of the gravel and the sludge–slag materials.

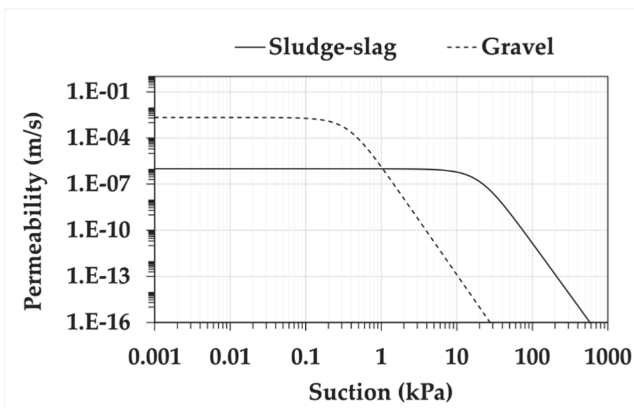

Figure 7. Permeability function of the gravel and the sludge–slag materials.

3. Results

3.1. Infiltration and Runoff

After each test, seepage and runoff water were collected, measured and compared with the volume of water injected. Results expressed as a percentage of injected water are presented in Figure 8. Figure 8 presents the average ratios of the infiltration percentage (drains 1–7) and the runoff (drains 8 and 9) for the different drains across various tested scenarios, encompassing variations in precipitation, slope, and FCL thickness.

The yellow columns in Figure 8 represent the results of the initial infiltration tests, conducted solely on the gravel layer, aiming to demonstrate that the infiltration system did not impact drains 8 and 9, which captured runoff water. The green columns depict precipitation at a rate of 60.6 mm/h, while the blue columns represent precipitation at 46.8 mm/h. Generally, the results indicated that runoff (drains 8 and 9) was higher with a 5° slope. Similarly, the 2.5° slope showed a higher infiltration rate on drain 7 by comparison to on the other drains (1 to 6).

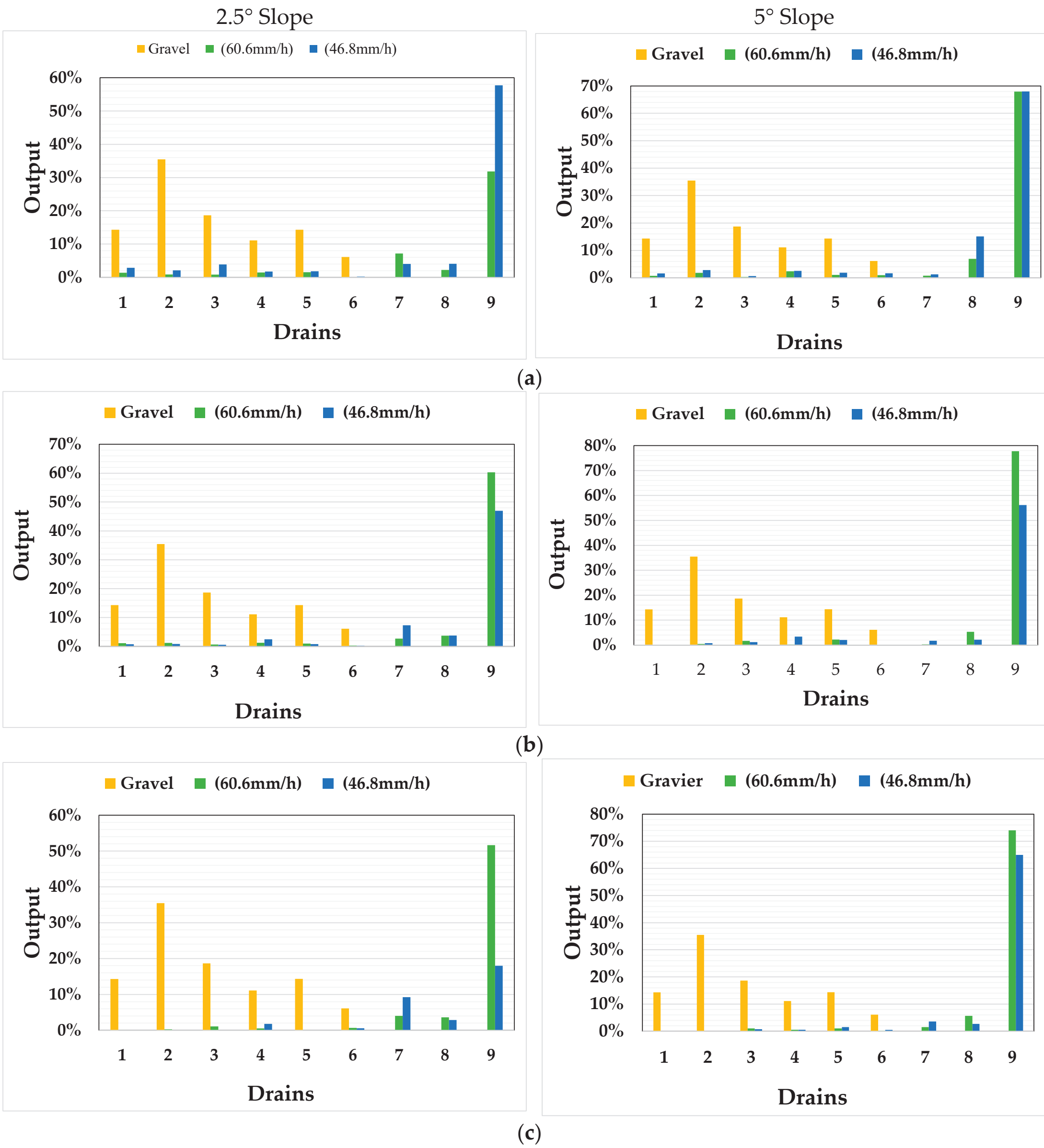

Figure 8. Infiltration and runoff rates for different drains and for different slope and thickness scenarios: (**a**) thickness of 25 cm; (**b**) thickness of 50 cm; and (**c**) thickness of 75 cm.

For the various scenarios tested, total infiltration and total runoff were calculated. Results of these calculations are presented in Figure 9. Figure 9 indicates that the lowest infiltration rates were 8%, 5%, and 4% for the FCL thicknesses of 25, 50, and 75 cm, respectively, when the inclination was 5° and the precipitation rate was 60.6 mm/h. In the same way, we can observe that the infiltration values were lower for the 75 cm layer compared to the 25 cm layer infiltration values.

For the runoff, one can observe that this parameter increased with an increase in inclination. The higher values were observed with the precipitation rate of 60.6 mm/h.

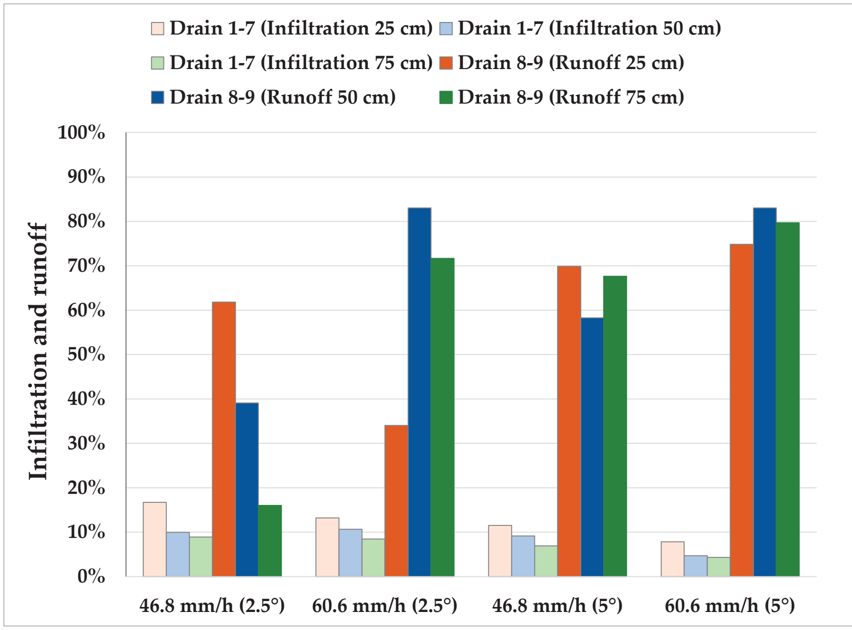

Figure 9. Infiltration and runoff rates for different slope and thickness scenarios.

3.2. *Volumetric Water Content and Suction*

Figures 10 and 11 show the follow-up of the saturation degree and suction data measured in the physical model. After the infiltration test, a drying process occurred over 20 days. The scenario presented here corresponded to the FCL with a 25 cm thickness, a 2.5° slope, and a precipitation rate of 60.6 mm/h. Figure 10 shows that during the infiltration test, the saturation degree increased rapidly. During the drainage period, a decrease in saturation degree (S_r) was observed at different levels.

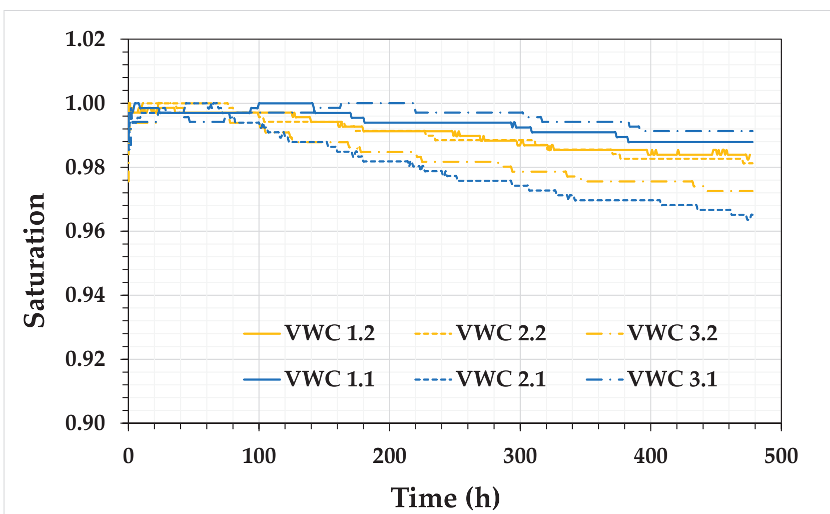

Figure 10. Saturation profiles for the scenario with an FCL thickness of 25 cm and a slope of 2.5°.

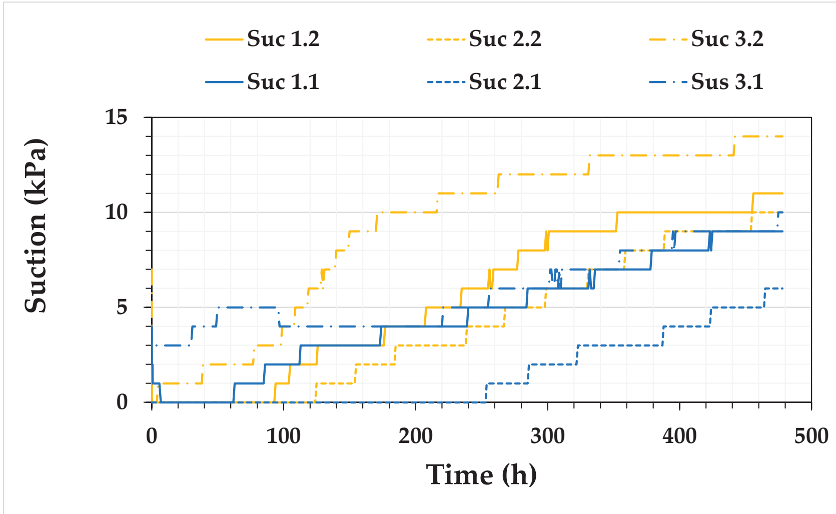

Figure 11. Suction profiles for the scenario with an FCL thickness of 25 cm and slope 2.5.

A significant decrease was observed at location 2.1 (near the middle of the model; see Figure 4 for sensor locations). However, for all the sensors, the saturation degree remained higher than 90%, indicating that this layer was maintained at a high degree of saturation. This saturation was favorized by the capillary barrier effect created between a gravel layer and an FCL.

In addition, this effect of capillary barrier effect was created near the front of the model due to the presence of the gravel material.

Figure 11 illustrates the evolution of suctions where one can observe after the drop in suction following the wetting test, an increase in suction was observed at various sensors. The highest suction, 14 kPa, was measured at sensor 3.2. The lowest suctions, not exceeding 6 kPa, were measured at sensor 2.1. It is worth mentioning that all measured suctions remained below the Air Entry Value (AEV) of 22 kPa. These results agreed with measurements of volumetric water content.

Results for the scenario with an FCL that was 50 cm thick with a 5° slope and a precipitation rate of 60.6 mm/h are presented in Figures 12 and 13, showing saturation degrees and suctions respectively. The saturation degrees for a drainage period of 31 days indicated that desaturation was not significative. The sensor 1.3, located near the surface layer, showed the lowest degree of saturation which was close to 97%. The other sensors displayed saturation degrees equal to or greater than 98%. These saturation values showed a good retention capacity of the sludge–slag mixture, similarly to the previous case. The saturation of the FCL was favorized by the capillary barrier effect created between an FCL and a gravel layer due to the contrast in the hydraulic properties of used materials. It is worth mentioning that the FCL had some saturation at the start of this test, which contributed to explaining the high saturation measured during this period.

At the end of the drainage period, the highest suction, 11 kPa, was measured at sensor 3.2. The lowest suctions, not exceeding 2 kPa, were measured at sensor 2.1. It is worth mentioning that all measured suctions remained below the AEV of 22 kPa (calculated using the tangent method in the water retention curve). These results agreed with measurements of volumetric water content.

Measurement results showed that infiltration rates through the model were lower than runoff rates and the FCL layer remained highly saturated. It is important to note that the drain layer positioned at the model's end enhanced water retention, potentially affecting diversion capacity. This hypothesis will be further evaluated using numerical modeling.

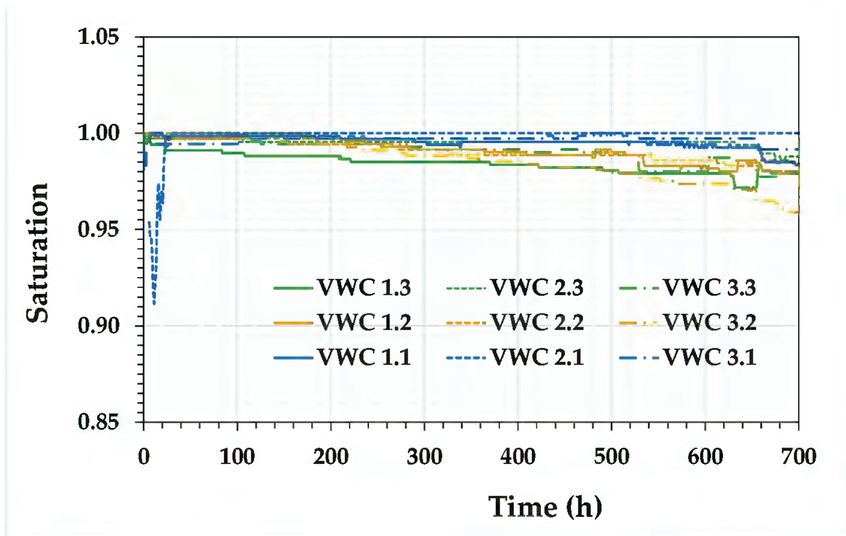

Figure 12. Saturation profiles for the scenario with an FCL thickness of 50 cm and a slope of 5°.

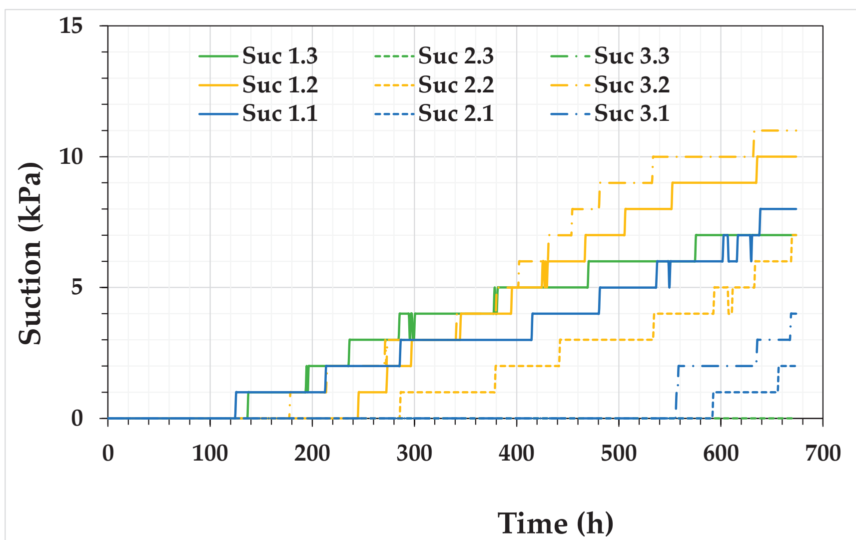

Figure 13. Suction profiles for the scenario with an FCL thickness of 50 cm and a slope of 5°.

3.3. Numerical Simulation Results

Figures 14–25 show the results of volumetric water content simulations for a precipitation of 46.8 mm/h. The evolution of volumetric water content showed that it increased only during the first hour (period of a precipitation event) and then it began to decrease. The time in which the volumetric water content began to decrease was less for the 5° slope, compared to for the slope of 2.5°.

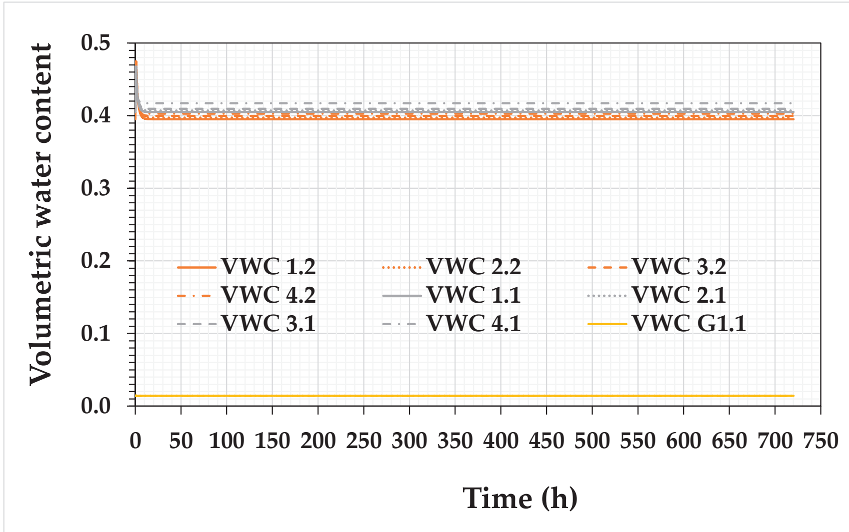

Figure 14. Volumetric water content results for a precipitation of 46.8 mm/h, a slope of 2.5°, a layer thickness of 25 cm, and a period of 720 h (30 days).

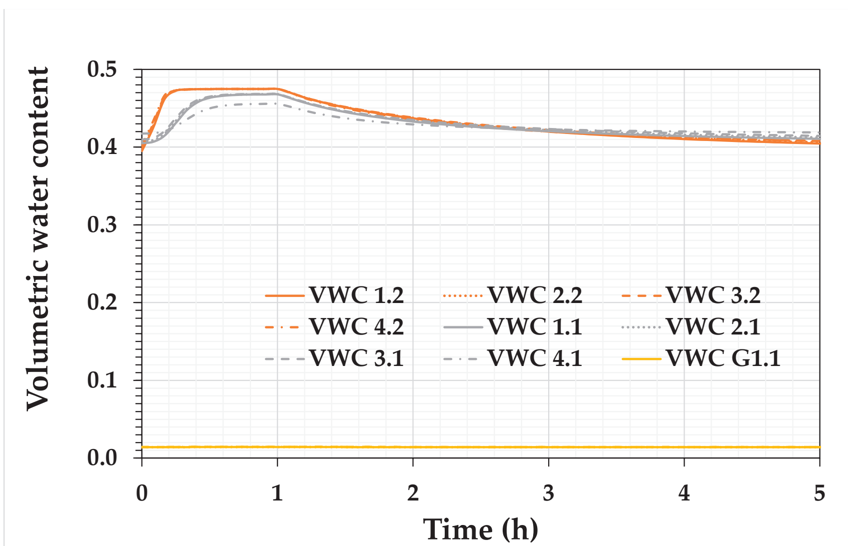

Figure 15. Volumetric water content results at a precipitation rate of 46.8 mm/h, a slope of 2.5°, a layer thickness of 25 cm, and a period of 5 h.

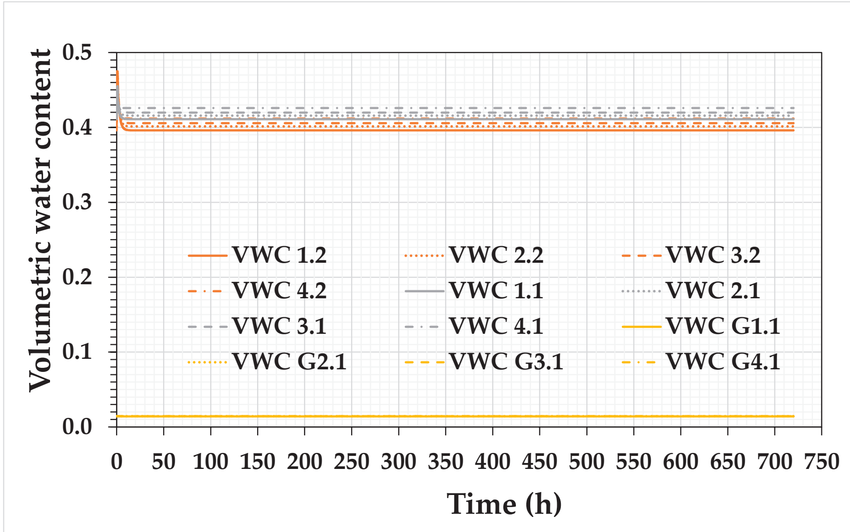

Figure 16. Volumetric water content results for a precipitation of 46.8 mm/h, a slope of 5°, a layer thickness of 25 cm, and a period of 720 h (30 days).

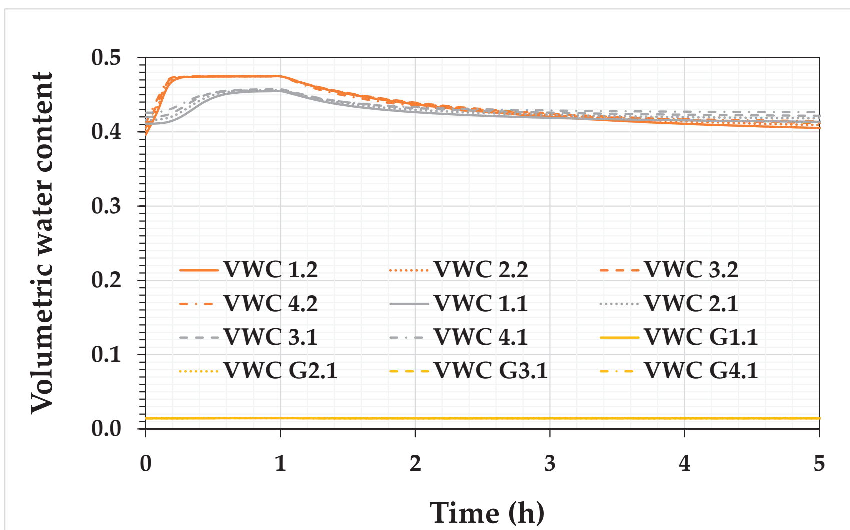

Figure 17. Volumetric water content results for a precipitation of 46.8 mm/h, a slope of 5°, a layer thickness of 25 cm, and a period of 5 h.

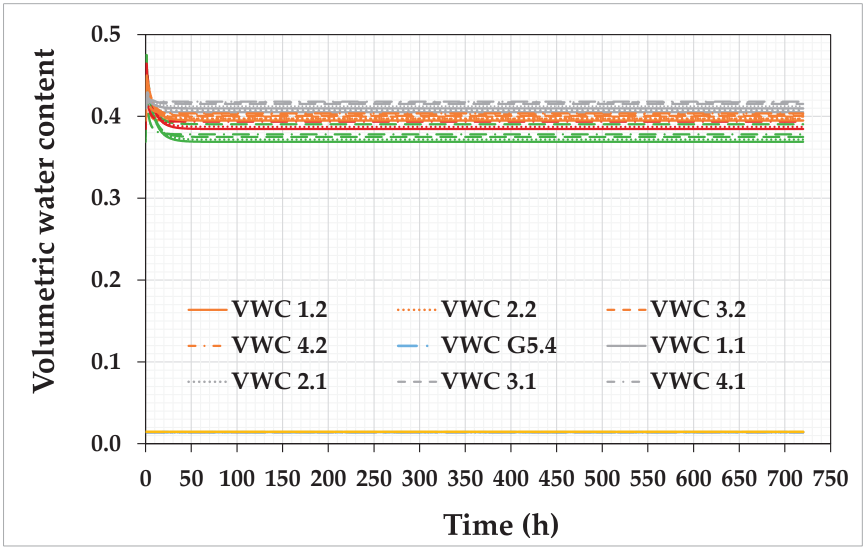

Figure 18. Volumetric water content results for a precipitation of 46.8 mm/h, a slope of 2.5°, a layer thickness of 50 cm, and a period of 720 h (30 days).

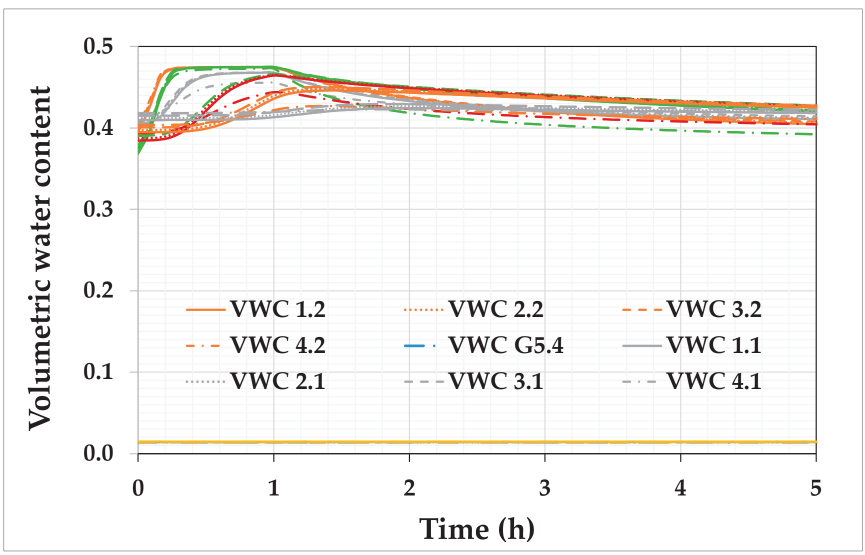

Figure 19. Volumetric water content results for a precipitation of 46.8 mm/h, a slope of 2.5°, a layer thickness of 50 cm, and a period of 5 h.

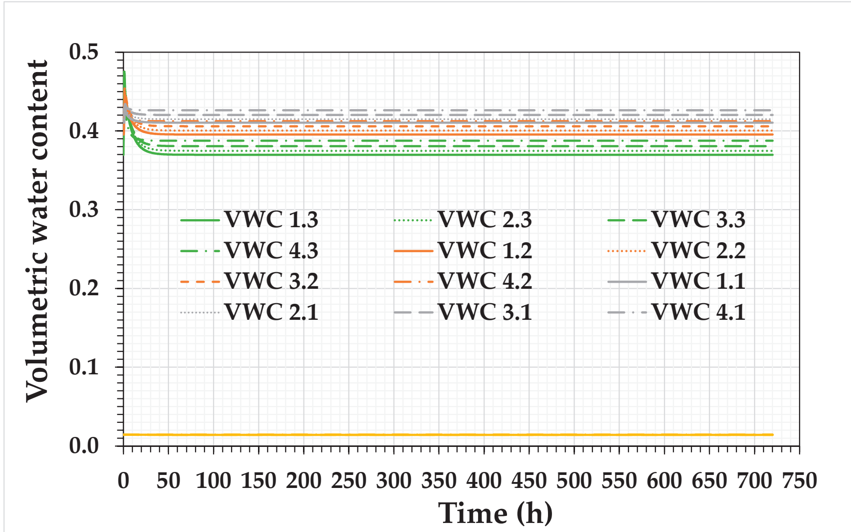

Figure 20. Volumetric water content results for a precipitation of 46.8 mm/h, a slope of 5°, a layer thickness of 50 cm, and a period of 720 h (30 days).

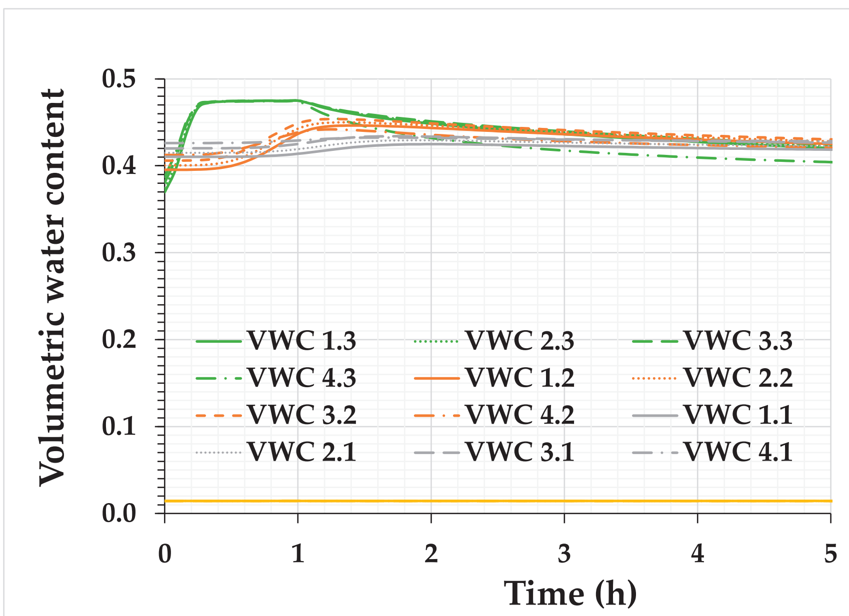

Figure 21. Volumetric water content results for a precipitation of 46.8 mm/h, a slope of 5°, a layer thickness of 50 cm, and a period of 5 h.

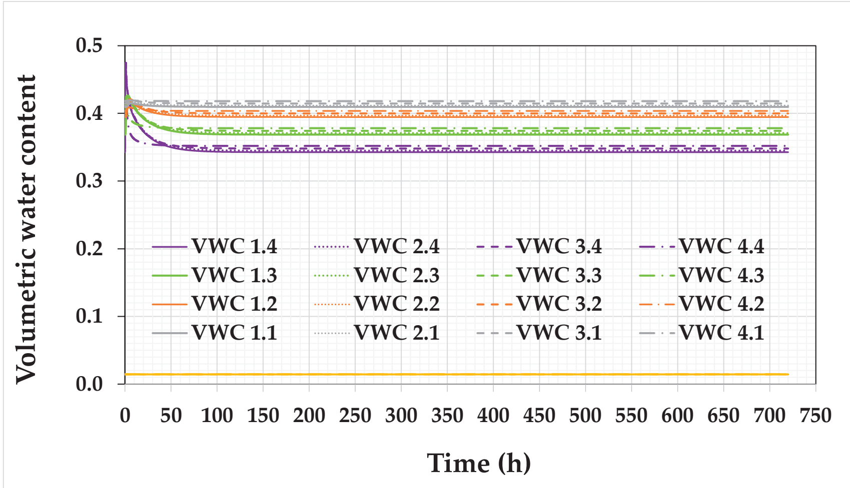

Figure 22. Volumetric water content results for a precipitation of 46.8 mm/h, a slope of 2.5°, a layer thickness of 75 cm, and a period of 720 h (30 days).

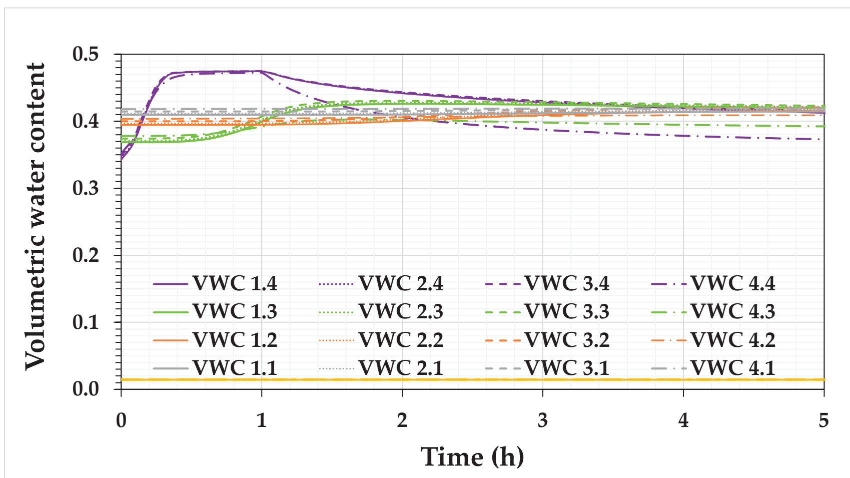

Figure 23. Volumetric water content results for a precipitation of 46.8 mm/h, a slope of 2.5°, a layer thickness of 75 cm, and a period of 5 h.

For the layer thickness of 25 cm (see Figures 14–17), both sensors were affected by precipitation. However, for the thickness of 50 cm (see Figures 18–21), it was observed that the most superficial sensors were affected by precipitation, while the sensors near the bottom of the FCL showed no variation in volumetric water content.

For the layer thickness of 75 cm (see Figures 22–25), it was observed that the sensors most affected by precipitation were the ones closest to the superficial. Additionally, it was evidenced that the deeper sensors showed little, or no variation induced by precipitation.

In the gravel layer and near the interface (G1-1, G2-1, G3-1, and G4-1), volumetric water content showed no variation in any of the performed tests (different precipitation rates, thicknesses, and slopes). This numerical simulation results indicated that water infiltration did not reach the gravel layer. These results obtained at the gravel layer level contradicted those from physical modeling. However, the infiltration water collected at the base of the model could be explained by the presence of a preferential flow along the walls of the physical model.

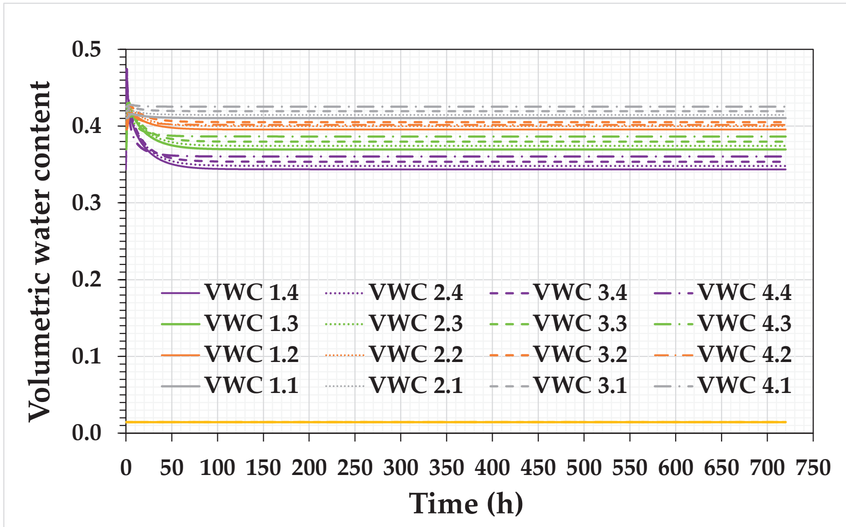

Figure 24. Volumetric water content results for a precipitation of 46.8 mm/h, a slope of 5°, a layer thickness of 75 cm, and a period of 720 h (30 days).

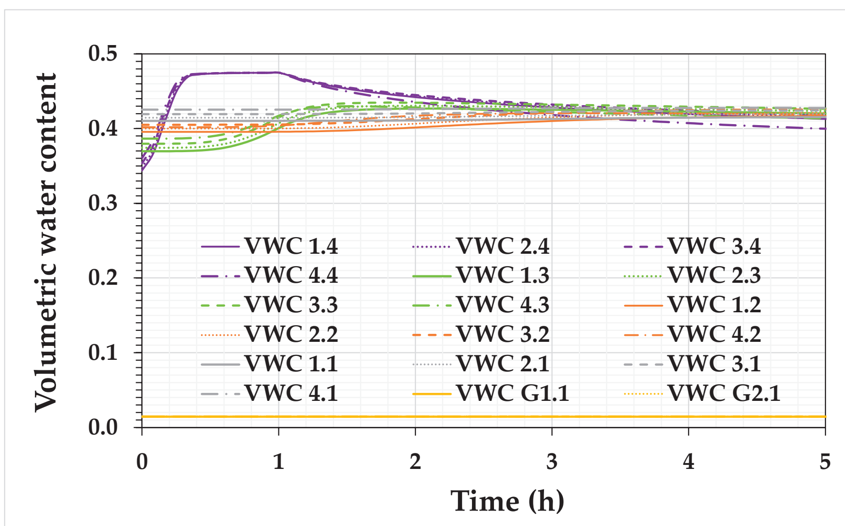

Figure 25. Volumetric water content results for a precipitation of 46.8 mm/h, a slope of 5°, a layer thickness of 75 cm, and a period of 5 h.

This hypothesis could be verified by numerical simulation or artificial chemical tracing. For numerical simulations, an additional boundary condition corresponding to vertical flow along the wall could be included. For chemical tracing, a tracer could be placed along the walls, and its presence at the bottom of the model could be monitored to confirm the preferential flow.

4. Final Remark

During laboratory tests, slopes of 2.5° and 5° showed no visible superficial erosion (see Figure 26). However, additional tests conducted with a 10° slope demonstrated a significant increase in water velocity and visible superficial erosion (see Figure 27). These findings suggest that high slopes are unsuitable for FCLs unless protective measures are implemented to safeguard the FCLs.

Figure 26. Photos showing FCLs at 2.5° and 5° slopes which were not affected by superficial erosion.

Figure 27. Visible superficial erosion for an FCL with a 10° slope.

Due to the erosion observed with the 10° slope (see Figure 27), an additional test was conducted with a 10 cm gravel layer for protection of an FCL. This measure successfully prevented superficial erosion. Subsequently, in this test involving an FCL with a thickness of 75 cm, the measured infiltration rate was 2%.

As a final remark, the FCL remained saturated after the various tests, aided by the capillary barrier effects created at the interface between the gravel layer and the FCL. This capillary barrier effect was also present along the front of the FCL. This concept can be applied to the inclined CEBC where the retention layer shows significant desaturation, thereby reducing their performance.

5. Conclusions

The sludge and slag mixture has been classified as an ML, indicating a texture that suggests low permeability behavior, as confirmed by the hydraulic conductivity test (k_{sat} = 1.00 × 10^{-4} cm/s). This characterization leads to the expectation of a low infiltration rate.

Investigation results demonstrated that a steeper slope correlated with lower infiltration rates. For instance, in the scenario with a rainfall intensity of 46.8 mm/h and an FCL thickness of 25 cm, the infiltration rates were 17% for a 2.5° slope and 12% for a 5°

slope. With a thicker FCL layer of 75 cm in thickness and the same rainfall intensity, the infiltration rates were reduced to 9% and 7% for 2.5° and 5° slopes, respectively.

Similarly, when considering a rainfall intensity of 60.6 mm/h and a soil thickness of 0.25 m, the infiltration rates were 13% and 8% for 2.5° and 5° slopes, respectively. For a scenario with an FCL thickness of 0.75 m, the rate decreased to 8% and 4% for 2.5° and 5° slopes, respectively.

Furthermore, the results indicated that a greater FCL thickness led to a lower infiltration rate. For instance, with a 2.5° slope and a rainfall intensity of 60.6 mm/h, the infiltration rates were 13%, 9%, and 7% for FCL thicknesses of 0.25 m, 0.5 m, and 0.75 m, respectively. Similarly, with a 5° slope and a rainfall intensity of 46.8 mm/h, the infiltration rates were 12%, 9%, and 7% for the respective FCL thicknesses of 0.25 m, 0.5 m, and 0.75 m.

In terms of rainfall intensity, the lowest infiltration rates occurred during heavier precipitation. For instance, for a 2.5° slope and a FCL thickness of 0.25 m, the infiltration rate decreased from 17% at a rain intensity of 46.8 mm/h to 13% at a rain intensity of 60.6 mm/h. Similarly, for a 5° slope, infiltration rates dropped from 12% to 8% when rainfall intensity increased from 46.8 mm/h to 60.6 mm/h.

For the runoff, one can observe that this parameter increased with an increase in inclination. The higher values were observed with the precipitation rate of 60.6 mm/h.

The monitoring data indicated that sludge and slag possessed a higher water retention capacity. Even after three weeks without rainfall under laboratory conditions, the minimum observed volumetric water content corresponded to 96% of saturation. This high saturation degree effectively restricted oxygen migration to reactive tailings.

The different results of simulated infiltration test indicated that precipitation rates significantly influenced outcomes. For instance, during a 100-year return period rain event, infiltration rates were 13% and 8% for slopes of 2.5° and 5°, respectively. Conversely, during a 25-year return period rain event, infiltration rates were 17% and 14% for slopes of 2.5° and 5°, respectively, with an FCL thickness of 25 cm.

The sludge and slag mixture presented a good performance as an FCL. Once saturated, the mixture demonstrated effective water diversion at a laboratory scale. Measurements performed during different tests indicated strong water retention capabilities in this material under controlled laboratory conditions (constant temperature and humidity and no wind).

The numerical simulations confirmed the experimental results, allowing concluding that this material can be used as an FCC layer or can be used as a component in a cover with a capillary barrier effect.

Author Contributions: Conceptualization, A.M. and N.C.O.V.; methodology, A.M. and N.C.O.V.; validation, A.M. and T.B.; formal analysis, A.M. and N.C.O.V.; investigation, N.C.O.V., A.M. and T.B.; resources, A.M. and T.B.; data curation, A.M.; writing—original draft preparation, N.C.O.V. and A.M.; writing—review and editing, A.M. and T.B.; visualization, N.C.O.V. and A.M; supervision, A.M. and T.B.; project administration, A.M. and T.B.; funding acquisition, A.M. and T.B. All authors have read and agreed to the published version of the manuscript.

Funding: This research was funded by the Fonds de Recherche du Québec sur la Nature et les Technologies (FRQNT): sustainable development of the mining sector program and the industrial partner Fonderie Horne.

Data Availability Statement: Data are contained within the article.

Conflicts of Interest: The author declares no conflicts of interest.

References

1. Kahlaoui, S. Évaluation des Échanges Hydrogéochimiques Entre un parc à Résidus Miniers et les Aquifères Périphériques. Ph.D. Thesis, Polytechnique Montréal, Montréal, QC, Canada, 2022.
2. Aubertin, M.; Pabst, T.; Bussière, B.; James, M.; Mbonimpa, M.; Benzaazoua, M.; Maqsoud, A. Revue des meilleures pratiques de restauration des sites d'entreposage de rejets miniers générateurs de DMA. In Proceedings of the Symposium 2015 Sur L'environnement et les Mines, Rouyn-Noranda, QC, Canada, 14–17 June 2015.

3. Bossé, B.; Bussière, B.; Hakkou, R.; Maqsoud, A.; Benzaazoua, M. Field experimental cells to assess hydrogeological behaviour of store-and-release covers made with phosphate mine waste. *Can. Geotech. J.* **2015**, *52*, 1255–1269. [CrossRef]
4. Knidiri, J.; Bussière, B.; Hakkou, R.; Bossé, B.; Maqsoud, A.; Benzaazoua, M. Hydrogeological behaviour of an inclined store-and-release cover experimental cell made with phosphate mine wastes. *Can. Geotech. J.* **2017**, *54*, 102–116. [CrossRef]
5. Wilson, G.W.; Williams, D.J.; Rykaart, E.M. The integrity of cover systems—An update. In *Proceedings of the 6th International Conference for Acid Rock Drainage, Cairns, QLD, Australia, 14–17 July 2003*; Australian Institute of Mining & Metallurgy: Carlton, VIC, Australia, 2003; pp. 445–451.
6. Zhan, G.; Mayer, A.; McMullen, J.; Aubertin, M. Capillary cover design for a spent leach pad. In Proceedings of the International Symposium on Hydrogeology and the Environment, Wuhan, China, 17 October 2000; pp. 17–21.
7. El Hamidi, M.-J.; Maqsoud, A.; Belem, T.; Viger, M.-E.; Çiner, A.; Khari, M.F.; Kallel, M.; Rodrigo-Comino, J.; Parise, M.; Barzagar, R.; et al. A Kinetic test method to assess the long-term acid generation behavior of sludge/slag and mine tailings of Quemont 2 (Quebec, Canada). In *Recent Research on Sedimentology, Stratigraphy, Paleontology, Geochemistry, Volcanology, Tectonics, and Petroleum Geology, Advances in Science, Technology & Innovation*; Springer: Cham, Switzerland, 2022. [CrossRef]
8. Amyot, G.; Vézina, S. Flooding as a reclamation solution to an acidic tailings pond-the Solbec case. In Proceedings of the 4th International Conference on Acid Rock Drainage, Vancouver, BC, Canada, 31 May–6 June 1997; Volume 31, pp. 681–696.
9. Awoh, A.S. *Étude Expérimentale du Comportement Géochimique de Résidus Miniers Hautement Sulfureux Sous un Recouvrement en Eau*; Universite du Quebec en Abitibi-Temiscamingue (Canada): Rouyn-Noranda, QC, Canada, 2012.
10. Demers, I. *Performance d'une Barrière à L'oxygène Constituée de Résidus Miniers Faiblement Sulfureux Pour Contrôler la Production de Drainage Minier Acide*; Université du Québec en Abitibi-Témiscamingue: Rouyn-Noranda, QC, Canada, 2008.
11. Ethier, M.-P. *Évaluation de la Performance d'un Système de Recouvrement Monocouche Avec Nappe Surélevée Pour la Restauration d'un parc à Résidus Miniers Abandonné*; Université du Québec en Abitibi-Témiscamingue: Rouyn-Noranda, QC, Canada, 2018.
12. Ouangrawa, M.; Aubertin, M.; Molson, J.; Zagury, G.; Bussière, B. An evaluation of the elevated water table concept using laboratory columns with sulphidic tailings. In Proceedings of the Geosask2005, 58th Canadian Geotechnical Conference and 6th Joint IAHC-NC, Saskatoon, SK, Canada, 18–21 September 2005.
13. Aubertin, M.; Chapuis, R. Considérations hydro-géotechniques pour l'entreposage des résidus miniers dans le nord-ouest du Québec. In Proceedings of the Second International Conference on the Abatement of Acidic Drainage, Montreal, QC, Canada, 16–18 September 1991; MEND/Canmet. Volume 3, pp. 1–22.
14. Nicholson, R.V.; Gillham, R.W.; Cherry, J.A.; Reardon, E.J. Reduction of acid generation in mine tailings through the use of moisture-retaining cover layers as oxygen barriers. *Can. Geotech. J.* **1989**, *26*, 1–8. [CrossRef]
15. Ricard, J.; Aubertin, M.; Firlotte, F.; Knapp, R.; McMullen, J.; Julien, M. Design and construction of a dry cover made of tailings for the closure of Les Terrains Aurifères site, Malartic, Québec, Canada. In Proceedings of the 4th International Conference on Acid Rock Drainage, Vancouver, BC, Canada, 31 May–6 June 1997; Volume 31, pp. 1515–1530.
16. Rakotonimaro, T.V.; Neculita, C.M.; Bussière, B.; Benzaazoua, M.; Zagury, G.J. Recovery and reuse of sludge from active and passive treatment of mine drainage-impacted waters: A review. *Environ. Sci. Pollut. Res.* **2017**, *24*, 73–91. [CrossRef] [PubMed]
17. Tassé, N.; Germain, D.; Dufour, C.; Tremblay, R. Le recouvrement de résidus organiques au parc East Suillivan: Au delà de la barrière d'oxygène. In *Proceedings of the Colloque sur le Programme de Neutralisation des Eaux de Drainage dans l'Environnement Minier, Rouyn-Noranda, QC, Canada, 29–30 October 1996*; Ministère des Ressources Naturelles Quebec: Québec, QC, USA, 1996; pp. 106–128.
18. Albright, W.H.; Benson, C.H.; Gee, G.W.; Abichou, T.; McDonald, E.V.; Tyler, S.W.; Rock, S.A. Field performance of a compacted clay landfill final cover at a humid site. *J. Geotech. Geoenviron. Eng.* **2006**, *132*, 1393–1403. [CrossRef]
19. Maqsoud, A.; Bussière, B.; Mbonimpa, M. Low saturated hydraulic conductivity covers. In *Hard Rock Mine Reclamation: From Prediction to Management of Acid Mine Drainage*; Bussière, B., Guittonny, M., Eds.; CRC Press: Boca Raton, FL, USA, 2021.
20. Rarison, R.F. *Évaluation des Propriétés Chimiques, Mécaniques et Hydrogéologiques de Géomembranes Utilisées Comme Matériaux de Recouvrement Pour Restaurer des Sites Miniers en Milieu Froid et Acide*; Polytechnique Montréal: Montréal, QC, Canada, 2021.
21. Aubertin, M.; Cifuentes, E.; Apithy, S.; Bussière, B.; Molson, J.; Chapuis, R. Analyses of water diversion along inclined covers with capillary barrier effects. *Can. Geotech. J.* **2009**, *46*, 1146–1164. [CrossRef]
22. Bussière, B.; Plante, B.; Broda, S.; Aubertin, M.; Chen, D.; Medina, F. Contrôle des infiltrations d'eau dans les haldes à stériles à l'aide des effets de barrière capillaire: Design, construction et instrumentation de la halde expérimentale de la mine Tio. In Proceedings of the Symposium sur L'environnement et Les Mines, Rouyn-Noranda, QC, Canada, 14–17 June 2015; pp. 14–17.
23. Dimech, A.; Chouteau, M.; Aubertin, M.; Bussière, B.; Martin, V.; Plante, B. Three-dimensional time-lapse geoelectrical monitoring of water infiltration in an experimental mine waste rock pile. *Vadose Zone J.* **2019**, *18*, 1–19. [CrossRef]
24. Ait Khouia, A. *Évaluation de la Capacité de Déviation Latérale de la Couche de Contrôle des Écoulements d'eau Dans un Modèle physique au Laboratoire*; Ecole Polytechnique: Montreal, QC, Canada, 2018.
25. Martin, V.; Bussière, B.; Plante, B.; Pabst, T.; Aubertin, M.; Medina, F.; Bréard-Lanoix, M.L.; Dimech, A.; Dubuc, J.; Poaty, B.; et al. Controlling water infiltration in waste rock piles: Design, construction, and monitoring of a large-scale in-situ pilot test pile. In Proceedings of the 70th Canadian Geotechnical Society Conference, Ottawa, ON, Canada, 1–4 October 2017; Volume 70.
26. Crouzal, T.; Pabst, T. A black-box automated approach to calibrate numerical simulations and optimize cover design: Application to a flow control layer constructed on an experimental waste rock pile. *Vadose Zone J.* **2021**, *20*, e20130. [CrossRef]

27. Dubuc, J. *Étude du Comportement Hydrogéologique d'une Couche de Contrôle des Écoulements Placée à la Surface d'une Halde à Stériles Expérimentale*; Ecole Polytechnique: Montreal, QC, Canada, 2018.
28. Poaty, B.; Plante, B.; Bussière, B.; Benzaazoua, M. Assessment of hydrogeochemical behavior of layered waste rock stockpiles: A meso-scale laboratory experiment. *Appl. Geochem.* **2022**, *136*, 105154. [CrossRef]
29. Raymond, K.E.; Seigneur, N.; Su, D.; Poaty, B.; Plante, B.; Bussière, B.; Mayer, K.U. Numerical modeling of a laboratory-scale waste rock pile featuring an engineered cover system. *Minerals* **2020**, *10*, 652. [CrossRef]
30. Rossit, M. *Utilisation des Stériles Miniers Concassés et Compactés Comme Couche de Contrôle des Écoulements Pour Contrôler le DMA*; Ecole Polytechnique: Montreal, QC, Canada, 2020.
31. Tremblay, D.; Robitaille, V. *Mécanique des Sols: Théorie et Pratique*, 2nd ed.; Groupe Modulo: Quebec, QC, Canada, 2014; ISBN 978-2-89650-627-9.
32. *ASTM D4318-17e1*; Standard Test Methods for Liquid Limit, Plastic Limit, and Plasticity Index of Soils. American Society for Testing of Materials (ASTM): West Conshohocken, PA, USA, 2017.
33. *ASTM D1557-12(2021)*; Standard Test Methods for Laboratory Compaction Characteristics of Soil Using Modified Effort (56,000 ft-lbf/ft3 (2,700 kN-m/m3)). American Society for Testing of Materials (ASTM): West Conshohocken, PA, USA, 2021.
34. Delage, P.; Cui, Y.-J. *L'eau Dans les Sols*; Edition Technique de l'ingénieur: Paris, France, 2000; Volume C2.
35. *ASTM D2434-22*; Standard Test Methods for Measurement of Hydraulic Conductivity of Coarse-Grained Soils. American Society for Testing of Materials (ASTM): West Conshohocken, PA, USA, 2022.
36. Van Genuchten, M.T. A closed-form equation for predicting the hydraulic conductivity of unsaturated soils. *Soil Sci. Soc. Am. J.* **1980**, *44*, 892–898. [CrossRef]
37. Aubertin, M.; Mbonimpa, M.; Bussière, B.; Chapuis, R.-P. A model to predict the water retention curve from basic geotechnical properties. *Can. Geotech. J.* **2003**, *40*, 1104–1122. [CrossRef]
38. Mbonimpa, M.; Aubertin, M.; Bussière, B. Predicting the unsaturated hydraulic conductivity of granular soils from basic geotechnical properties using the modified Kovacs (MK) model and statistical models. *Can. Geotech. J.* **2006**, *43*, 773–787. [CrossRef]
39. Otalora, C.; Maqsoud, A.; Belem, T. *Evaluation of the Sludge and Slag Mixture to Act Flow Control Layer in the Waste Rock Pile Reclamation*; A Springer Book Series Advances in Science, Technology & Innovation; Springer: Berlin/Heidelberg, Germany, 2024.
40. GEOSLOPE International Ltd. *Heat and Mass Transfer Modeling with GeoStudio 2020*, 1st ed.; GEOSLOPE International Ltd.: Calgary, AB, Canada, 2020.

mining

MDPI

Article

An AI-Based Approach for Developing a Recommendation System for Underground Mining Methods Pre-Selection

Elsa Pansilvania Andre Manjate [1,2,*], Natsuo Okada [1], Yoko Ohtomo [3], Tsuyoshi Adachi [4], Bernardo Miguel Bene [2], Takahiko Arima [3] and Youhei Kawamura [3]

[1] Division of Sustainable Resources Engineering, Graduate School of Engineering, Hokkaido University, Sapporo 060-8628, Japan; natsu0807chi@gmail.com
[2] Instituto Superior Politécnico de Tete, Tete 2300, Mozambique; bbene@ispt.ac.mz
[3] Division of Sustainable Resources Engineering, Faculty of Engineering, Hokkaido University, Sapporo 060-8628, Japan; ohtomoy@eng.hokudai.ac.jp (Y.O.); takahiko_arima@eng.hokudai.ac.jp (T.A.); kawamura@eng.hokudai.ac.jp (Y.K.)
[4] Graduate School of International Resource Sciences, Akita University, Akita 010-8502, Japan; adachi.t@gipc.akita-u.ac.jp
* Correspondence: manjateelsapansilvania@gmail.com

Abstract: Selecting the most appropriate mining method to recover mineral resources is a critical decision-making task in mining project development. This study introduces an artificial intelligence-based mining methods recommendation system (AI-MMRS) for the pre-selection of underground mining methods. The study integrates and evaluates the capability of two approaches for mining methods selection (MMS): the memory-based collaborative filtering (CF) approach aided by the UBC-MMS system to predict the top-3 relevant mining methods and supervised machine learning (ML) classification algorithms to enhance the effectiveness and novelty of the AI-MMRS, addressing the limitations of the CF approach. The results reveal that the memory-based CF approach achieves an accuracy ranging from 81.8% to 87.9%. Among the classification algorithms, artificial neural network (ANN) and k-nearest neighbors (KNN) classifiers perform the best, with accuracy levels of 66.7% and 63.6%, respectively. These findings demonstrate the effectiveness and viability of both approaches in MMS, acknowledging their limitations and the need for continuous training and optimization. The proposed AI-MMRS for the pre-selection stage supplemented by the direct involvement of mining professionals in later stages of MMS, has the potential to significantly aid in the MMS decision-making, providing data-driven and experience-based recommendations following the ongoing evolution of mining practices.

Keywords: mining methods selection; underground mining; decision-making; recommendation system; memory-based collaborative filtering; classification machine learning

Citation: Manjate, E.P.A.; Okada, N.; Ohtomo, Y.; Adachi, T.; Bene, B.M.; Arima, T.; Kawamura, Y. An AI-Based Approach for Developing a Recommendation System for Underground Mining Methods Pre-Selection. *Mining* **2024**, *4*, 747–765. https://doi.org/10.3390/mining4040042

Academic Editors: Krzysztof Skrzypkowski, René Gómez, Fhatuwani Sengani, Derek B. Apel, Faham Tahmasebinia and Jianhang Chen

Received: 8 July 2024
Revised: 21 September 2024
Accepted: 26 September 2024
Published: 2 October 2024

1. Introduction

The mining industry plays a crucial role in human civilization, providing raw materials, critical minerals, and metals vital for development, technological advancements, and economic growth. Central to the success of any mining project is the careful selection of the most feasible mining methods to extract mineral resources from the earth. These methods typically fall into two most common categories: surface and underground mining. Underground mining methods are more complex; they are applied to recover deposits that are not economically (socially or politically, technically, and economically) feasible to be recovered using surface methods. Underground mining methods are usually classified into three groups based on a geotechnical viewpoint depending on the extent of support required to sustain underground infrastructure and ensure the stability of the openings: unsupported, supported, and caving [1]. Each mining method presents its own set of advantages and drawbacks, and the selection of the most appropriate method(s) is influenced by multiple interconnected influencing factors. Key factors in selecting surface and underground mining methods include the orebody geometry, geology and hydrology, geotechnical properties, technological factors, economic factors, and environmental considerations [1,2]. The primary objective of mining methods selection (MMS) is to select method(s) that maximize profitability, operational efficiency, safety, and cost-effectiveness while minimizing negative environmental impacts. Typically, the task of MMS is performed by experienced mining professionals (or decision-makers) who usually conduct comprehensive evaluations of the various influencing factors to achieve the primary goal of MMS. Over the years, the subject of MMS has undergone extensive study, leading to the development of different methodologies aimed at addressing this complex decision-making process.

1.1. Previous Work on Mining Methods Selection

Research on mining methods selection (MMS) has been ongoing for several years, yielding various methodologies/systems aimed at aiding decision-makers in this complex decision-making process. This study categorizes MMS systems into four groups: qualitative, quantitative, MCDM-based, and machine-learning-based.

Qualitative and quantitative systems were introduced in the 1970s, 1980s and 1990s. Qualitative systems were flowcharts used to evaluate the suitability of mining methods for particular deposits, mostly based on orebody geometry, geology, and geotechnical properties [1,3]. The need for improvement and numerical methods led to the introduction of the first quantitative system in 1981: the Nicholas approach [4]. In 1995, the University of British Columbia (UBC) developed the UBC-MMS system [5]: a modified version of the Nicholas approach to adjust the Nicholas approach to Canadian mining operations. Quantitative systems are based on a numerical decision matrix with ranks/weights assigned to evaluate the feasibility of the mining methods based on orebody characteristics, including orebody geometry, geology, and geotechnical properties. The advantage of the quantitative system is providing solutions for the first phase of MMS or preliminary selection providing a set of safe or suitable mining methods that will be submitted for further detailed evaluation by the decision-making team. Perhaps that is one of the reasons quantitative systems are still the most practically implemented in industries and studies/research. However, in these systems, the relative importance of the influencing factors is not considered, implying that all factors have the same weight (i.e., level of importance) during the evaluation and selection process; plus, the systems may offer obsolete solutions for the current situation in the mining practices. Since the 2000s, attention to multi-criteria decision-making (MCDM) techniques has gained traction in addressing the shortcomings of quantitative systems, introducing MCDM-based systems. Over the years, crisp and fuzzy MCDM techniques, commonly the analytical hierarchy process (AHP), order of preference by similarity to ideal solution (TOPSIS), and preference-ranking organization method for enrichment evaluations (PROMETHEE), have been implemented for evaluating and selecting mining methods for different case studies [6–9]. The advantage of the MCDM-based systems is the consideration of the weights or the relative importance of the influencing factors and the possibility of including a wide range of factors and methods customized to a case study. In most MCDM-based systems, decision-makers (mining professionals) are directly involved in the task, which can be of great advantage since the team can customize the evaluations according to the objectives of a particular case study. Usually, the decision-making team is assigned to select relevant methods and factors to consider in the evaluations and to determine the weights or the relative importance of the factors based on their subjective judgment or opinions, which reflect their experience in the field. However, using subjective judgment may introduce a certain level of bias, which can inherently affect the eligibility and accuracy of the evaluations [10,11]. Plus, the subjective judgment from the decision-makers is mostly customized to a particular case study or mining project; that is, a decision made for a particular case study/project may not be transferrable to another case study/project [11]. In a study by Manjate et al. [10], the Entropy method (Shannon's

Entropy) was proposed as a method to determine the weights of the factors objectively without the direct involvement of decision-makers in an attempt to avoid bias and the customization of the decision-making process and enable the implementation of the results when the direct judgment of the decision-makers is unavailable (totally or partially) or not required.

In recent years, data-driven decision-making powered by artificial intelligence (AI) systems has been heavily studied and gradually implemented for solving complex problems in different fields of science and engineering. The concept of Smart Mining or Mining 4.0 has emerged in the mining industry, which involves integrating digital technologies, AI, and advanced data analytics to address challenges in the mining value chain to optimize mining activities. Machine learning (ML) is a popular field of study in AI aimed at training predictive models for AI systems; ML-based systems usually rely on algorithms trained based on extensive historical data to learn the data pattern and predict future outcomes. Recently, a few studies [12–16] have investigated the applicability of artificial neural networks (ANN) in MMS introducing ML-based MMS systems. Lv and Zhihui [13] and Chen and Shixiang [14] investigated and showed the effectiveness of ANN in evaluating and selecting underground mining methods for thin and thick coal seams. In 2020, Ozyurt and Karadogan [12] further investigated the applicability of ANNs and game theory to develop a model for underground MMS for different ore types. Their study further demonstrated the effectiveness of ANNs in developing a robust system for detailed evaluations of underground mining conditions to select the most feasible mining method. According to the authors, their model can be applied even when there is a lack of information regarding the relevant factors, thereby addressing one of the shortcomings of MCDM-based systems. In 2022, Shohda et al. [16] developed a model for MMS by modifying the UBC-MMS system and integrating ANN. Their study compared the results of the ANN model with a commonly used MCDM TOPSIS technique, showing that the ANN model provided similar results to the TOPSIS more easily and accurately. The above study demonstrated ANN's effectiveness in solving the complexity of the MMS process. Manjate et al. [11] introduced the recommendation system concept in MMS through one of the collaborative filtering algorithms: the nonnegative matrix factorization (NMF) algorithm. The authors investigated the applicability of NMF to predicting underground mining methods, which was shown to be effective with reasonable performance. Their NMF model was also proposed for predicting missing information about the required input variables for MMS to enable the implementation of the model even when information about some input variables is not accessible. The advantage of ML-based systems is the provision of data-driven decision-making insights and the possibility to continuously train and optimize the models with up-to-date information. Moreover, ML-based systems may enable the possible use of the system with or without the direct involvement of decision-makers, even with missing variables.

1.2. Purpose of the Study

Considering improving and expanding the application of AI in MMS, this study proposes an AI-based approach to develop a system to recommend underground mining methods in the preliminary stage of MMS (i.e., pre-selection). The proposed MMS system is termed the AI-based mining methods recommendation system (AI-MMRS). The proposed approach is to explore available databases of mining projects to develop a decision-making support system during mine planning mainly based on the recommendation systems approach. Recommendation systems are AI systems aimed at helping users deal with information overload by filtering information to make customized recommendations (of items that users might like), thus improving users' decision-making capability [17]. The study's main objective is to investigate effective approaches for developing the AI-MMRS integrating the memory-based collaborative filtering approach and classification machine learning algorithms for MMS. This study also integrates the results from previous studies where the Entropy method [10] and nonnegative matrix factorization (NMF) [11] were proposed as strategies to address challenges and gaps in the MMS, therefore, enhancing the effectiveness of the AI-MMRS. The integrated AI-MMRS is intended to recommend underground mining methods by evaluating the similarities among the projects regarding orebody characteristics, including ore strength, host-rock strength, orebody thickness, shape, and dip. By acknowledging the critical importance of MMS in mine planning and the limitations of AI-based approaches in such a decision-making task, this study emphasizes the need for the direct involvement of the decision-making team (i.e., mining professionals) to perform detailed evaluations and selection of the most feasible methods in the MMS process. As such, the proposed AI-MMRS is intended to serve as a decision-making support tool for the preliminary selection of underground mining methods (i.e., based on orebody characteristics), thereby recommending a set of methods that are suitable to the orebody characteristics, which must then be submitted for further detailed evaluations (i.e., environmental, economic, technological, and other relevant aspects for evaluations) by the decision-making team. The proposed AI-MMRS has the potential to enhance the efficiency and effectiveness of the decision-making process by providing data-driven and experience-based recommendations based on past or existing mining projects' procedures, practices, and experiences. Furthermore, by leveraging the power of AI aided by the direct involvement of decision-makers (in later stages of MMS), this approach can help to identify and address key challenges in mining project development and support the ongoing evolution of mining practices, especially the MMS discipline.

The remainder of this paper is organized into four main sections. Section 2 describes and explains the methodology for developing the AI-MMRS. Section 3 presents the experimental results. Section 4 presents a discussion of the results. Finally, the concluding remarks are presented in Section 5.

2. Materials and Methods

The process of evaluating and selecting mining methods typically involves two or three main stages, with the initial stage focusing on the preliminary selection of methods suited to the deposit's characteristics, which is the outcome given in most qualitative and quantitative mining methods selection (MMS) systems [1,3–5]. This preliminary selection phase usually assesses factors such as orebody geometry, geology, and geotechnical properties to identify a set of suitable mining methods and eliminate less suitable ones. Subsequently, the methods deemed most suitable undergo further feasibility evaluations in later stages, considering technological, economic, environmental, and other relevant factors to select the most sustainable method(s) to recover the ore deposit. This study emphasizes the need for the direct involvement of the decision-making team (i.e., mining professionals) to perform detailed evaluations and selection of the most sustainable mining methods in the MMS process, thereby proposing an AI-based mining methods recommendation system (AI-MMRS) for the preliminary selection of underground mining methods.

The methodology for developing the AI-MMRS integrates artificial intelligence (AI) techniques to leverage available mining project databases and facilitate the decision-making process in mine planning, particularly in the mining methods selection (MMS) task. Specifically, the study explores the effectiveness of the memory-based collaborative filtering (CF) approach [18] and classification machine learning (ML) algorithms [19] for predicting underground mining methods based on orebody characteristics (i.e., ore strength, host-rock strength, thickness, shape, and dip). Figure 1 illustrates the methodological strategy for developing the AI-MMRS, encompassing data preparation and ML model evaluation as the main phases. In the data preparation phase, this study incorporates findings from a previous study to determine the relative importance of factors influencing the MMS process [10]. Additionally, insights from a prior study where the nonnegative matrix factorization (NMF) algorithm was proposed to predict mining methods and address missing variables in sparse input data are integrated into the AI-MMRS [11].

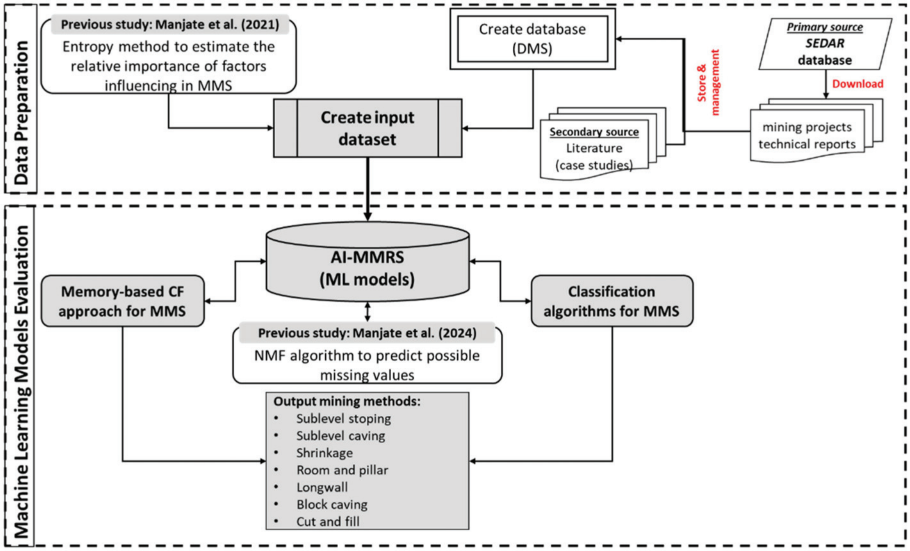

Figure 1. Methodology for developing the AI-MMRS (DMS: document management software: LogicalDOC Business version 8.7.3; ML: machine learning, CF: collaborative filtering, NMF: nonnegative matrix factorization) [10,11].

2.1. Estimating the Relative Importance of Factors Influencing MMS

Naturally, mining methods selection (MMS) is a complex task given the need to consider many conflicting (and interconnected) factors to evaluate the performance of different mining methods and select the most feasible method(s). In this study, the Entropy method is adopted in the data preparation phase to address the complexity of the MMS caused by many influencing factors. As such, the Entropy method is proposed as a feature selection technique to assess the relative importance of factors influencing the MMS process and identify the most relevant factors to be used as main input variables in the input dataset. In ML, feature selection [20] is an essential step to improve the performance of the prediction models (and reduce computation time) and the quality of the outcomes by reducing the number of irrelevant (and redundant) features and selecting the most relevant ones for building prediction models.

The Entropy method is used in a multi-criteria decision-making (MCDM) problem to assess the relative importance of influencing factors in the MMS process [10]. In most MCDM-based studies, the relative importance of the influencing factors is determined based on the direct subjective opinions or judgment of the decision-makers involved in the evaluation process for particular projects or case studies [6–9]. While the use of a subjective approach offers the benefits of providing customized solutions to a specific case study, it also means that the decisions made may not be generalized, i.e., the decisions may not be easily applicable or transferable to different case studies. The proposed AI-based mining methods recommendation system (AI-MMRS) seeks to leverage data-driven decision-making drawn from diverse case studies, enabling its implementation across different case studies (or project types). Subjective decision-making methods, while effective in certain contexts, would introduce bias into the outputs of the AI-MMRS, potentially compromising their eligibility and accuracy. Recognizing the limitation of subjective methods and considering the primary aim of the study, which is to develop a system capable of supporting the decision-making process across various case studies, the Entropy method was found suitable due to its advantage of estimating the weights of the factors objectively. Unlike subjective decision-making, the Entropy method determines the weights of the factors objectively without the need for the direct involvement of decision-makers, thus, providing less biased and generalized outcomes suitable for diverse case studies. In this case, the use of the Entropy method enhances the effectiveness and applicability of the AI-MMRS across diverse mining projects.

In our previous study [10], the Entropy method, which is rooted in information theory by Shannon [21], was applied to assess the relative importance of the factors categorized into orebody geometry, geology and geotechnical properties, technological, economic, and environmental factors. The Entropy method estimated the objective weights of the factors based on a decision matrix created from literature sources, particularly methodologies proposed by Miller et al. [5] and Hartman and Mutmansky [1], renowned for their contributions to the MMS discipline. This decision matrix encompassed twenty influencing factors which are used to evaluate twelve mining methods (comprising both surface and underground methods). Using the decision matrix as input, the Entropy method determined the objective weights of the factors based on the following steps:

1. Normalization of values in the decision matrix using Equation (1) to ensure uniform scaling across factors (or criteria) and mining methods (or alternatives):

$$r_{ij} = \frac{x_{ij}}{\sum_{j=1}^{n} x_{ij}},\ i = 1, 2 \ldots, m;\ j = 1, 2 \ldots n \tag{1}$$

where x_{ij} is the criteria rate; r_{ij} is the normalized criteria rate; n is the number of criteria (or factors), and m is the number of alternatives (mining methods).

2. Computation of Entropy (Ej) values in the matrix using Equation (2), measuring the uncertainty among mining methods in the absence of factor preference:

$$E_j = -h\sum_{i=1}^{m} r_{ij}\ln\left(r_{ij}\right), j = 1, 2, \ldots, n;\ h = \frac{1}{ln(m)} \tag{2}$$

where $r_{ij}ln(r_{ij}) = 0$ if $r_{ij} = 0$ and h is the Entropy constant.

3. Determination of diversity (Dj) or the degree of diversification using Equation (3), which indicates the dispersion between rates of different mining methods for each factor:

$$D_j = 1 - E_j \tag{3}$$

4. Calculation of objective weights of criteria based on Equation (4), which represents the relative importance of factors in the evaluation and selection process:

$$w_j = \frac{D_j}{\sum_{j=1}^{n} D_j}, j = 1, 2, \ldots, n \tag{4}$$

where w_j is the degree of importance or the objective weight of criterion j.

The results of the Entropy method, as shown in Table 1, provide entropy, diversity, and objective weight values for the evaluated factors. These objective weights indicate the relative importance of each factor in the mining methods selection (MMS) process. Notably, geotechnical properties such as ore strength and host-rock strength, along with orebody geometry factors like thickness, shape, and dip, were assigned the highest objective weights. This underscores their critical role in the MMS process, especially during the preliminary selection phase. On the other hand, environmental factors such as health and safety and the stability of openings were attributed to comparatively lower objective weights. This suggests their relatively lower impact on the decision-making process during the preliminary selection stage. Based on the objective weights obtained, the study identified the first five factors, ore strength, host-rock strength, orebody thickness, shape, and dip, as the most critical in the preliminary selection stage with objective weights of 0.132, 0.115, 0.104, 0.100 and 0.072, respectively. The identified factors are then used as the main variables in the input dataset used to train and evaluate the machine learning (ML) models for the AI-MMRS. The high objective of the five factors weights signifies their substantial influence on the MMS process, particularly in the preliminary evaluation stage. These results emphasize the critical role of the orebody characteristics, including the geotechnical properties, orebody geometry, and geology, in the preliminary evaluation and selection of mining methods, as is already shown in other MMS systems [1,3–5].

Table 1. Results of the Entropy method: highlighting the five most relevant factors.

Influential Factor	Entropy	Diversity	Weights
Ore strength	0.895	0.105	0.132
Host-rock strength	0.909	0.091	0.115
Thickness	0.917	0.083	0.104
Shape	0.920	0.080	0.100
Dip	0.943	0.057	0.072
Ore uniformity	0.946	0.054	0.068
Mining cost	0.952	0.048	0.061
Dilution	0.955	0.045	0.057
Ore grade	0.961	0.039	0.048
Selectivity	0.968	0.032	0.040
Recovery	0.976	0.024	0.030
Productivity	0.977	0.023	0.029
Capital investment	0.981	0.019	0.024
Depth capacity	0.982	0.018	0.023
Flexibility	0.982	0.018	0.022
Depth	0.985	0.015	0.019
Production rate	0.985	0.015	0.019
Development rate	0.985	0.015	0.019
Health and Safety	0.991	0.009	0.011
Stability of openings	0.995	0.005	0.007

2.2. Study's Database and Input Dataset

The proposed AI-based mining methods recommendation system (AI-MMRS) relies on a comprehensive database comprising historical data extracted from mining projects' technical reports (and literature-based data). The primary data source for this study is the SEDAR database (The System for Electronic Document Analysis and Retrieval (SEDAR): https://www.sedar.com/homepage_en.htm: accessed on 11 July 2022), a publicly accessible repository of documents filed by Canadian public companies. Although there are other platforms like Mining Data Online (MDO) (https://miningdataonline.com/##, accessed on 11 July 2022) offering mining projects' data, SEDAR's open nature and global coverage make it a suitable choice for this study. The study's database encompasses technical reports dating from 2000 to 2022, representing mining projects across various continents and regions (in Africa, Asia, Europe, Oceania, and Central, North and South America), all owned by Canadian companies. Around 1315 mining projects' technical reports were collected from SEDAR and managed within a document management software (DMS). The database built into the DMS serves as a vital complementary resource for the AI-MMRS, providing additional relevant insights for mine project planning, such as local and regional geological, geotechnical conditions, labor costs, sociopolitical, environmental considerations, and infrastructure availability, among others. In instances where data from SEDAR was insufficient, literature sources such as papers and theses were utilized as secondary data sources. The study data from the secondary source were cross-checked with other literature, and the entire data (from primary and secondary sources) underwent a validation process using the UBC-MMS system [5], to ensure data integrity and reliability. Additionally, a thorough background check was conducted on the mining projects included in the database, thereby excluding projects with a history of failure or negative practices.

The process of data cleaning and validation plays a crucial role in enhancing the quality and reliability of the dataset used in this study. However, it is essential to acknowledge that this rigorous process has also resulted in a reduction in the size of the input dataset, which occurs as unreliable or inconsistent datapoints are filtered out to ensure that only high-quality and relevant information is retained for subsequent use. The limited number of datapoints (or samples) in the input dataset stands as one of the biggest limitations of this study, which can potentially affect the performance of the machine learning (ML) models because usually, ML models require large input datasets in order to have a good performance in the training and evaluation processes.

The input dataset for this study comprises historical information from thirty-three mining projects, characterized by the five input variables selected using the Entropy method [10] (i.e., ore strength, host-rock strength, orebody thickness, shape, and dip) along with the underground mining methods selected or considered for each deposit. The seven underground mining methods considered in this study are categorized into unsupported, supported, and caving methods [1], with sublevel stoping, shrinkage, and room and pillar representing the unsupported methods. Cut and fill is the only commonly applied supported mining method, while longwall, block caving, and sublevel caving represent the caving methods. While variations exist within these methods, this study focuses on the seven main underground mining methods mentioned earlier for the preliminary evaluation and selection. The proposed AI-MMRS aims to provide recommendations for the preliminary evaluation and selection of underground mining methods, thus recommending a set of the most suitable main underground methods, which can be submitted to further detailed evaluations by the decision-making team in subsequent stages to select the most sustainable methods (including different variants of the main methods) considering variety of factors like technical, economic, sociopolitical, and environmental, among other factors.

The study's assessment of ore and host-rock strength factors is based on the widely used and most available in the mining project historical data, the rock mass rating (RMR) system, while the thickness, shape, and dip factors are described using the Nicholas approach [11] and the UBC MMS system [12]. Table 2 shows the characteristics of the input dataset utilized to evaluate machine learning algorithms for the AI-MMRS in subsequent sections, including the classification of variables and the distribution of the projects (or samples) in each mining method.

Table 2. Characteristics and classification of the variables in the input dataset.

Variables	Description
Ore strength	Very weak, weak, moderate, strong, and very strong
Host rock-strength	Very weak, weak, moderate, strong, and very strong
Thickness	Very narrow, narrow, intermediate, thick, and very thick
Shape	Irregular, tabular, and massive
Dip	Flat, intermediate, and steep
Underground mining methods	Sublevel stoping: 16 projects Cut and fill: 10 projects Longwall: 2 projects Shrinkage: 2 projects Room and pillar: 1 project Block caving: 1 project Sublevel caving: 1 project

2.3. Memory-Based Collaborative Filtering Approach for Mining Methods Selection

Memory-based collaborative filtering (CF), also known as the neighborhood-based approach [22], is one of the earliest and simplest approaches for building recommendation systems. It relies on the principle of similarity, which predicts unknown ratings for an active user based on the ratings of its nearest neighbors or the most similar users. To illustrate the CF recommendation system framework, let us consider a scenario where we have a typical user—item rating dataset X shown in Figure 2, where each row represents a user U, each column represents an item I, and the entries in the matrix represent the ratings given by users for each item. The task is to generate recommendations for the active user $U5$ who has watched movies 2, 3, and 6 (I2, I3, and I6) but has not yet watched movies 1, 4, and 5 (I1, I4, and I5).

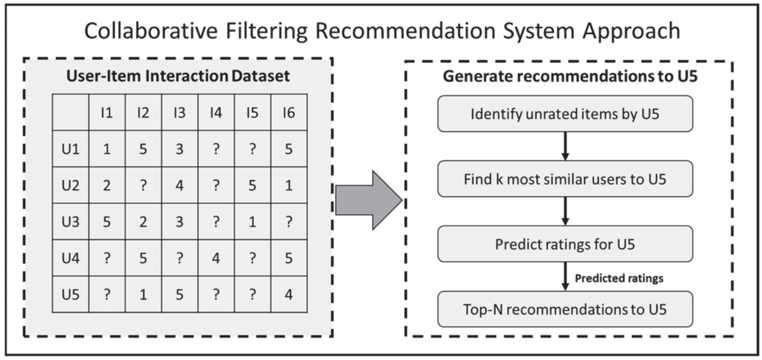

Figure 2. Collaborative filtering recommendation system framework based on the user–item interaction dataset X composed of u-users and i-items with ratings ranging from 1 to 5, "?" unknown or missing rating.

There are two main steps to building a memory-based CF recommendation system: (1) measure similarity and (2) generate predictions and recommendations [23]:

Step 1: Measuring similarity

The first step in building a memory-based CF recommendation system is to measure the similarity between users or items. For example, we can use the cosine similarity Equation (5) to compute the similarity between users. In this case, we need to find users who are similar to *U5* based on their ratings for movies 2, 3, and 6.

$$sim(a,b) = \cos(\theta) = \frac{r_a . r_b}{\|r_a\| \|r_b\|} = \sum\nolimits_I \frac{r_{aI} . r_{bI}}{\sqrt{\sum_I {r_{aI}}^2}\sqrt{\sum_I {r_{bI}}^2}} \quad (5)$$

where, r_{aI} is the rating of user a to an item I, and $sim(a,b)$ is the similarity between users a and b.

Step 2: Generate Predictions and Recommendations:

Once similarities are computed, we use the ratings from the most similar users to predict unknown ratings for the active user *U5*. The weighted sum method shown in Equation (6) is commonly used for prediction, where we compute the weighted average of the ratings given by the most similar users.

$$r_{uI} = \frac{\sum_{i \in users} sim(u,I) * r_{uI}}{\sum_{v \in users} |sim(u,I)|} \quad (6)$$

Finally, based on the predicted ratings, we can recommend the top-N movies with the highest predicted ratings to user *U5*.

The k-nearest neighbors (KNN) algorithm is often employed to implement the memory-based CF approach. The KNN algorithm is a non-parametric supervised machine learning (ML) algorithm used as an unsupervised learner in the memory-based CF approach to search for nearest neighbors and compute similarities among users and items [24]. In this study, the KNN-cosine similarity algorithm is used to compute similarities among mining projects. Thereafter, the weighted sum method is used to predict the ratings of the mining methods for generating recommendations. The approach aims to build a model that predicts and recommends the top-N relevant underground mining methods by analyzing the similarities among the projects based on the orebody characteristics.

Data Pre-Processing for Memory-Based CF Approach

To incorporate the memory-based collaborative filtering (CF) approach for predicting and recommending the top-N underground mining methods, the input dataset (described in Section 2.2) needs to be prepared accordingly. The first step involves transforming the qualitative of the input variables into numerical values: the qualitative values of ore strength (OS), host-rock strength (RS), thickness (TH), shape (SH), and dip (DP) are transformed into numerical values based on their objective weights (shown in Table 1) obtained from the previous study [10]. Then, transform the mining methods (which are classes) into items to be recommended: the mining methods such as sublevel stoping (SS), room and pillar (RP), shrinkage (SH), cut and fill (CF), longwall (LW), block caving (BC), and sublevel caving (SC) are transformed from classes (or dependent variable) to items to be recommended to the projects/users according to their similarity across the input variables. Thereafter, assign relevant mining methods to each project: each project is assigned three relevant mining methods, one primary and two secondary methods. The project's primary mining methods are obtained from the database (i.e., technical reports and literature sources), and the two secondary mining methods are obtained using the UBC-MMS tool [5]. Finally, ratings are assigned to the mining methods for each project using a 9-point rating scale: a rating of 9 is assigned to the primary methods of the projects, a rating of 5 is assigned to the two secondary methods, and the remaining methods are assigned a rating of 1 (indicating they are not in the top 3 most relevant methods). In this case, the task of the memory-based model is to provide an output of the top-3 most relevant mining methods for each project. The employed 9-point rating system ensures the diversity of the proposed AI-MMRS to recommend a set of top-N most relevant mining methods for a particular active project according to the orebody characteristics.

Figure 3 illustrates the data pre-processing steps, showing the transformation of the input dataset for experiments to evaluate the proposed memory-based collaborative filtering approach. The transformed input dataset consists of thirty-three mining projects (project IDs: PJ001, PJ002, . . . PJ033) characterized by the five input variables (OS, RS, TH, SH, and DP) and the corresponding mining methods (SS, RP, SH, Cf, LW, BC and SC) with the respective ratings. In the experiments, the transformed dataset is used to evaluate the effectiveness of the proposed memory-based CF model in predicting and recommending the top-3 most relevant mining methods.

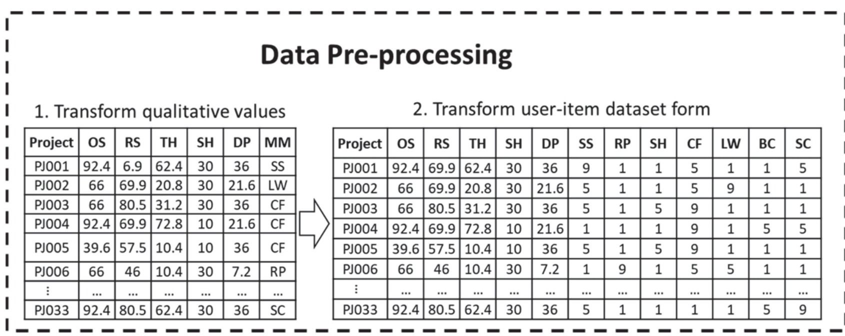

Project	OS	RS	TH	SH	DP	MM
PJ001	92.4	6.9	62.4	30	36	SS
PJ002	66	69.9	20.8	30	21.6	LW
PJ003	66	80.5	31.2	30	36	CF
PJ004	92.4	69.9	72.8	10	21.6	CF
PJ005	39.6	57.5	10.4	10	36	CF
PJ006	66	46	10.4	30	7.2	RP
⋮	...	...	...	...	...	...
PJ033	92.4	80.5	62.4	30	36	SC

Project	OS	RS	TH	SH	DP	SS	RP	SH	CF	LW	BC	SC
PJ001	92.4	69.9	62.4	30	36	9	1	1	5	1	1	5
PJ002	66	69.9	20.8	30	21.6	5	1	1	5	9	1	1
PJ003	66	80.5	31.2	30	36	5	1	5	9	1	1	1
PJ004	92.4	69.9	72.8	10	21.6	1	1	1	9	1	5	5
PJ005	39.6	57.5	10.4	10	36	5	1	5	9	1	1	1
PJ006	66	46	10.4	30	7.2	1	9	1	5	5	1	1
⋮	...	...	...	...	...	...	...	...	...	...	...	...
PJ033	92.4	80.5	62.4	30	36	5	1	1	1	1	5	9

Figure 3. Showing the data pre-processing: transformation of the input dataset for experiments to evaluate the proposed memory-based collaborative filtering approach.

2.4. The Need for Supervised Classification Machine Learning Algorithms

In this study, supervised machine learning (ML) algorithms are a useful addition to the memory-based collaborative filtering (CF) approach in addressing its limitations associated with the dependence of the approach on the UBC-MMS tool, thus enhancing the effectiveness of the proposed AI-MMRS for mining methods selection (MMS). Supervised ML algorithms are trained using labeled datasets and are capable of predicting labels or responses based on the learned relationship between input variables and labels of datapoints or samples [25]. Classification ML models are particularly relevant for MMS problems as they are trained to predict class labels of datapoints based on input variables [19]. In this study, five classifiers were selected for evaluation to identify the best models for MMS problems: decision trees, K-nearest neighbors (KNN) with cosine similarity, support vector machines (linear SVM), kernel approximation (kernel SVM) and artificial neural networks (ANN). The KNN algorithm is similar to the one implemented in the memory-based CF approach; however, this section implements it as a supervised classification algorithm [26]. Like KNN, the decision tree is a non-parametric algorithm that learns the relationship between input variables and class labels as a hierarchical tree structure. SVM finds a hyperplane that classifies datapoints in N-dimensional linear space, while the kernel version solves the problem in non-linear space. Lastly, ANN is a powerful algorithm inspired by the biological neural network of humans or animals [27], consisting of interconnected nodes that mimic the neurons in the biological brain, enabling it to solve complex tasks like classification and regression problems.

These algorithms have been extensively investigated in mining studies, including MMS studies [12–15,28–31], and their implementation can enhance the effectiveness and novelty of the proposed AI-MMRS. By leveraging these supervised ML algorithms, the AI-MMRS can overcome the limitations of the memory-based CF approach and generate more accurate, diverse, and novel recommendations.

3. Results

3.1. Memory-Based Collaborative Filtering Approach for Predicting and Recommending Mining Methods

The memory-based collaborative filtering (CF) evaluation strategy for predicting and recommending the top-N relevant mining methods is similar to the strategy used for the offline evaluation of recommendation systems [18]. The strategy involves simulating the practical implementation or real-world scenario of the AI-based mining methods recommendation system (AI-MMRS). The first step in the experiments involves creating sparse datasets from a dense input dataset by masking/hiding the known ratings of all seven mining methods for a target project (e.g., Figure 4: in step 1, PJ001 masked rating). Then, the proposed memory-based CF model is used to predict the masked ratings of the mining methods for the target project (i.e., step 2 in Figure 4: predicted ratings highlighted by thesquare). A list of the top-3 most relevant mining methods is extracted based on the predicted ratings (i.e., step 3: extract the list based on ratings predicted in step 2); priority is given to mining methods with higher predicted ratings. The hidden/masked ratings are kept as ground truth data and used for evaluating the accuracy and quality of the predictions and top-3 recommendations by comparing the predictions and the actual relevant mining methods for the project. In other words, the performance of the memory-based CF model in predicting the missing ratings and recommending the top-3 relevant mining methods is evaluated based on how well it matches the target project's three relevant mining methods (one primary and two secondary methods).

Prediction Accuracy and Quality of Recommendations

The memory-based CF model is tasked with predicting and outputting a list of top-3 most relevant mining methods for the projects. The performance of the memory-based model is evaluated in two ways:

Evaluation 1: Evaluate the model's capabilities to predict the primary mining methods as the top-1 most relevant method for each project because the primary mining methods' prediction defines the overall model's quality. In this case, the global accuracy rate (GAR) in Equation (7) is used as the performance evaluation metric:

$$GAR(\%) = \frac{number\ of\ correct\ classifications}{total\ number\ of\ classification} \times 100, \quad (7)$$

Evaluation 2: Evaluate the quality of the top-3 predicted and recommended mining methods for each project. The evaluation is performed using decision support metrics such as F1-score for a fixed N (number of items in the list) based on the Precision (@N), Recall (@N) and, which can be computed as shown in Equations (8)–(10) [32].

$$Precision(@N) = \frac{TP}{TP + FP}, \tag{8}$$

$$Recall(@N) = \frac{TP}{TP + FN}, \tag{9}$$

$$F1 - score = 2 \times \frac{Recall \times Precision}{Recall + Precision}, \tag{10}$$

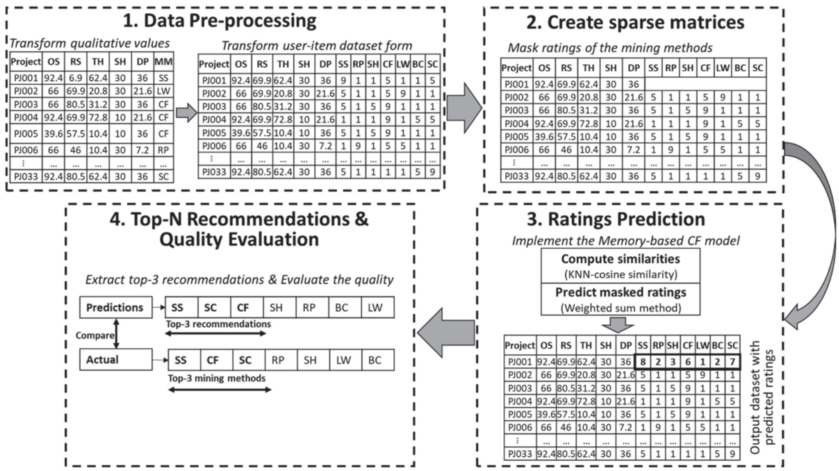

Figure 4. Workflow of the proposed methodology for practical experiments: the memory-based collaborative filtering approach for predicting and recommending top-N mining methods.

Figure 5 shows the model's performance results regarding the global accuracy rate (GAR) and the F1-score. Using the KNN-cosine similarity algorithm to find the nearest projects, it is required to set the parameter k, which is the number of neighbors or projects used for predictions [33]. In the experiments, the model's accuracy is evaluated for the number of projects (neighborhood size) ranging from 2 to 10. The results show that the model's performance depends on the number of projects used for predictions (neighborhood size), where the highest accuracy is achieved when using the two nearest projects.

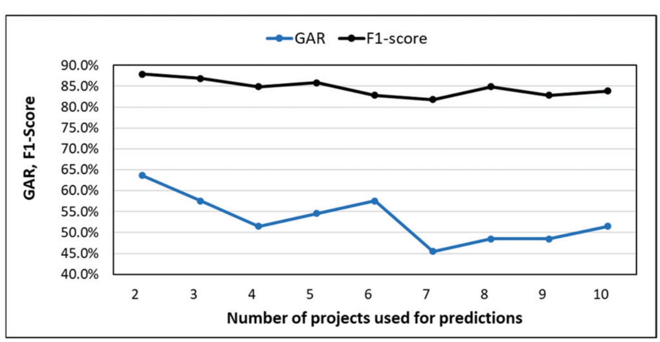

Figure 5. Performance of the proposed model in predicting primary and top-3 most relevant mining methods in terms of GAR and F1-score.

The GAR measures the model's overall accuracy for predicting the primary methods as the top-1 within the top-3 list of recommendations. The GAR ranges from 45.5% to 63.6%, indicating that the model can correctly predict the primary mining method as a top-1 method between 45.5% and 63.6% of the time, depending on the number of projects used for predictions. The F1-score is used to further evaluate the accuracy and precision of a recommendation system in predicting the top-3 relevant mining methods for a given project, regardless of their exact rank position. The results in Figure 5 show the F1-score ranging from 81.2% to 87.9%; the highest accuracy of 87.9% was achieved when using the two nearest projects for prediction. These results suggest that the memory-based CF model performs better when using a smaller neighborhood size.

In summary, the results show that the memory-based CF model provides the best results when using a smaller neighborhood size (number of nearest projects for predictions) for predictions and recommendations, which may be directly related to the intrinsic characteristics of the input dataset (i.e., the size and class distribution of the datapoints). The model performs reasonably well in predicting the primary mining methods as top-1 and performs even better in predicting the top-3 relevant mining methods. Despite the limitations of the dataset size (dataset with thirty-three projects), the proposed memory-based CF approach performs quite well in generating recommendations of the top-3 most relevant underground mining methods with about 87.9% prediction accuracy.

3.2. Classification Machine Learning for Predicting (Classifying) Underground Mining Methods

This section presents the experimental results of classification machine learning for predicting (classifying) underground mining methods. The experiments were conducted in MATLAB R2022a, using the Statistics and Machine Learning Toolbox, with the classification learner application [34]. Five classifiers were evaluated on the same dataset: decision trees, linear support vector machine (SVM), k-nearest neighbors (KNN) with cosine similarity, kernel approximation (SVM kernel), and artificial neural networks (ANN). The 10-fold cross-validation method was used to evaluate and validate the five classifiers. The k-fold cross-validation method is known to perform better on small datasets (datasets with a limited number of datapoints) as it ensures that every datapoint in the dataset can appear in the training and testing sets [35]. Using the k-fold cross-validation results in models that learn the underlying patterns well and evenly, creating more generalized and less biased models [36].

Prediction (Classification) of Underground Mining Methods

The global accuracy rate (GAR), F1-score, and the confusion matrix are used to evaluate the performance of the classifiers. Table 3 shows the results of the performance of the classifiers in terms of the GAR and average per class F1-score. The artificial neural network (ANN) model performed the best at 66.7% GAR, followed by k-nearest neighbors (KNN) with 63.3%. It is worth noting that while the GAR metric provides an overall evaluation of the classifier's performance, it may not always reflect the per-class performance. Therefore, the average per class F1-score is used to depict how well the classifier performs for each class label (each mining method). In the context of mining methods prediction, this means understanding how well the classifier performs for each specific mining method, as each method may have different characteristics and patterns that need to be learned by the classifier. In this case, we can observe lower values of the F1-score than the GAR which can suggest that the classifiers are not performing well in identifying or classifying individual classes.

Figure 6 further depicts the confusion matrix of the ANN model, showing each class's (mining methods) Recall or True Positive Rate (TPR) and the True Negative Rate (TNR). The TPR shows the proportion of correct predictions in each mining method. As for any other classification algorithm, the class-imbalanced dataset problem negatively affects the performance of the evaluated classifiers. Class imbalanced datasets happen when the distribution of datapoints among the classes is uneven, with majority and minority classes [37]. The study's input dataset is class imbalanced, comprising thirty-three projects (datapoints), with sixteen projects in sublevel stoping, ten in cut and fill, two in longwall and shrinkage, and one in room and pillar and sublevel caving. Imbalanced datasets can cause the classifiers to be biased towards the majority class, resulting in a model that overlearns the patterns of the majority classes and ignores the minority classes [38]. The confusion matrix shows that the ANN model accurately predicts the majority classes, sublevel stoping (100%), and cut and fill (60%). However, it performs poorly predicting the minority classes (block caving, longwall, room and pillar, and sublevel caving), all with 0% TPR. This result indicates that the class imbalance problem in the dataset negatively affected the performance of the classifiers in learning the patterns of the seven underground mining methods. This suggests the need to improve the dataset's quality to build less biased and generalized classifiers towards developing a robust AI-MMRS.

Table 3. Performance evaluation results of the classifiers in terms of global accuracy rate (GAR) and average per-class F1-score.

Classifier	GAR (%)	Average Per-Class F1-Score (%)
ANN	66.7	20.6
KNN	63.6	20.3
SVM	63.6	21.2
Decision Tree	57.6	18.2
SVM Kernel	54.5	16.0

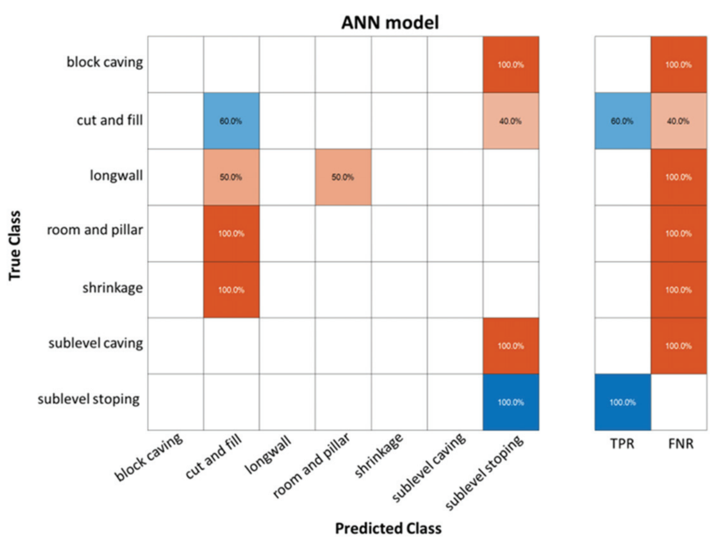

Figure 6. Confusion matrix of the artificial neural network (ANN) model showing the per-class Recall or True Positive Rate (TPR) and the True Negative Rate (TNR).

In summary, the results of evaluating the applicability of the five machine learning classification algorithms to predict underground mining methods suggest that the ANN model is more effective in solving the complexity of mining methods selection (MMS). This finding is consistent with the results of previous studies [12–14,16], which have also demonstrated the effectiveness of regression ANN in MMS. The results also show that the KNN classification model was effective for MMS. As a recap, this study used the same KNN algorithm for implementing the memory-based collaborative filtering approach for predicting and recommending top-N underground mining methods, producing reliable and effective results with good accuracy. These findings consistently demonstrate the effectiveness of classification algorithms, including ANN and KNN, in solving the complexity of MMS, which can potentially be further optimized and implemented interchangeably to provide accurate recommendations.

4. Discussion

This study incorporates artificial intelligence (AI) to explore the available database of mining projects and develop a system that can assist in mine project development decision-making, particularly in the mining methods selection (MMS) task. This study develops an integrated MMS system termed the AI-based mining methods recommendation system (AI-MMRS). The study investigated the applicability of the memory-based collaborative filtering (CF) approach and classification algorithms (i.e., KNN, ANN, SVM, decision trees, and SVM kernel) for predicting underground mining methods. The proposed models were evaluated based on an input dataset comprising data from thirty-three mining projects described by five input variables (ore strength, host-rock, thickness, shape, and dip) and seven underground mining methods (block caving, cut and fill, longwall, room and pillar, shrinkage, sublevel caving, and sublevel stoping). The input dataset is characterized as small for typical machine learning problems and imbalanced class issues, which stands as one of the limitations of the study.

The results of evaluating the performance of the proposed memory-based approach to predicting and recommending the top-3 most relevant underground mining methods have demonstrated the models' effectiveness with moderately good accuracy. On the other hand, among the five evaluated classification models, artificial neural networks (ANN) and k-nearest neighbors (KNN) performed the best in predicting (classifying) underground mining methods, showing their effectiveness in solving the complexity of underground MMS with moderate accuracy. The proposed memory-based approach generates recommendations of the top-3 relevant underground mining methods aided by the UBC-MMS system [5] in the data preprocessing step. The classification models are independent of the UBC-MMS system; they are implemented to enhance the effectiveness and novelty of the proposed AI-MMRS, as they can address the limitations of the memory-based approach and generate more accurate and diverse recommendations. Furthermore, the AI-MMRS integrates results from the previous study [11] using the NMF model to predict possible missing information about the required input variables (orebody characteristics) to enable the implementation of the AI-MMRS in situations where the information (or data) about the necessary input variables is not available/missing, especially during early stages of mine project development.

Some of the findings from this study are consistent with previous studies which have shown the effectiveness of regression ANN in MMS [12–14,16]. Similar to the ANN model by Ozyurt and Karadogan [12], this study is developed considering different ore types (or commodities), which differs from the models by Lv and Zhang [13] and Chen and Shixiang [14], which were specific to coal seams. In contrast to the model by Ozyurt and Karadogan [12] and similar to the models by Lv and Zhang [13] and Chen and Shixiang [14], the proposed AI-MMRS is fully based on data from real case studies. For the study, the proposed AI-MMRS requires minimum and fairly easily accessible input factors, especially during the early stages of mining project development where there can be limited access to information about the deposit. The weights and selection of the five input variables in the dataset were determined objectively in a previous study using the Entropy method without the need for the direct involvement of decision-makers [10], unlike most MCDM-based MMS systems [6–9], which typically require some level of subjective judgement. The advantage of AI or ML-based systems is the possibility of continuous learning; as new data becomes available and mining practices evolve, the models can be updated to reflect the changes and provide up-to-date recommendations. This may help avoid the risk of obsolete recommendations, which may be the case for quantitative and some MCDM-based systems.

Understanding the limitations of AI-based approaches in decision-making as well as the need for careful evaluations in the mining methods selection (MMS) process, this study emphasizes the need for the direct involvement of the decision-making team (i.e., mining professionals) to perform detailed evaluations and selection of most feasible methods in the MMS process. Therefore, this study proposes an AI-based approach to develop a mining methods recommendation system (AI-MMRS) for the preliminary evaluation and selection of underground mining methods. As such, the proposed AI-MMRS is intended to serve as a decision-making support system for the preliminary evaluation and selection of underground mining methods, that is, to recommend options of suitable underground mining methods based on orebody characteristics (geometry, geology, and geotechnical properties). The recommended suitable methods by the AI-MMRS can then undergo further feasibility evaluations by the decision-making team (mining experts), who will ultimately select the most sustainable method(s) based on technological, economic, environmental, and other relevant factors for the project evaluation. The proposed system is meant to aid in the pre-selection stage (for new projects or ongoing projects that may need to select mining methods for new horizons in the mine) based on historical and evolving data. The system can help professionals focus their detailed evaluations on a narrower, more relevant set of mining methods, thus enhancing the efficiency and thoroughness of the decision-making process. In practical implementation, a target project should provide five input variables (ore strength, host-rock strength, thickness, shape and dip) which will be used to search for other projects with similar orebody characteristics in the database. Thereafter, the system recommends a set of most suitable underground mining methods for the deposit characteristics, to be submitted for further evaluations by the decision-making team. The system is designed with the understanding that, due to the complexity of orebody characteristics (such as geometry and geotechnical conditions), using a single mining method is often impractical; therefore, the system provides recommendations for multiple suitable methods. The study also highlights the importance of incorporating sociopolitical and environmental risk assessments in the early stages of mine project planning, including during the MMS process, which is demonstrated in a study by Barakos and Misho [39]. The proposed integrated system can assist with these assessments, using its database of mining project historical data to provide relevant information for decision-making, including details about local or regional sociopolitical aspects, environmental concerns, common mining methods, geology, geotechnical conditions, labor costs, infrastructure, and mineral processing procedures and other project-specific factors.

In summary, this study demonstrated the effectiveness and viability of the proposed approaches to develop the integrated AI-MMRS, which has significant potential to improve the efficiency and effectiveness of decision-making in the MMS task. Despite the limitations, the findings from this study are significant and can pave the way for future studies on the MMS discipline and Smart Mining (Mining 4.0) in general, providing insights for researchers and industry interested in leveraging the power of AI and data analytics to improve efficiency and quality of the decision-making process. By leveraging the power of AI and recommendation systems, this approach can help to address key challenges in mining project development and support the ongoing evolution of mining practices. As such, the system should be continually updated and improved with new data to ensure its recommendations remain relevant and accurate.

5. Limitations and Future Works

The use of AI-based approaches in MMS is promising as it can be more efficient and provide experience-based recommendations. However, a major limitation of the study is the size and quality of the input dataset, primarily due to the limited access to reliable mining projects' historical data, which reflects on the quality and performance of the models, especially classification models. As for any ML-based system, the proposed AI-MMRS will only provide good predictions and better recommendations if continuous data collection and training are performed. Therefore, the system is designed to be flexible and open to the inclusion of new mining methods as they are developed or identified by making the model open for new additions. Future studies will focus on improving the quality of the input dataset, optimizing machine learning models, and validating the models considering various case studies. Additionally, actively include sociopolitical, environmental and other critical aspects deemed critical in mine planning in the model to enable active risk assessment analysis in decision-making, particularly in the evaluation selection of mining methods.

To address the major limitation of the study, thereby improving the quality of the training dataset, it is proposed to make the model open for new additions through an open-line platform where industry professionals, researchers, and mining experts can contribute to mining projects, which will continuously expand the training dataset. This approach not only increases the dataset but also promotes collaborative knowledge sharing within the mining community. By enriching the dataset over time, the AI model will become more robust, improving its accuracy and utility in future applications. This strategy ensures that the AI system evolves along with advancements in mining methods, emerging technologies, and changes in orebody conditions and relevant selection factors, making it a valuable tool for both current and future projects.

6. Conclusions

This study proposed an artificial intelligence (AI)-based approach to developing an AI-based mining methods recommendation system (AI-MMRS) to serve as a decision support system for the preliminary evaluation and selection of underground mining methods. The study investigated the most effective approaches to exploring the available database of mining projects to develop a decision-making system for mining project development (mine planning), the AI-MMRS. The proposed AI-MMRS was developed based on the integration of two main approaches to train the prediction models: memory-based collaborative filtering (CF) and classification models to provide efficient and diverse recommendations for underground mining methods. The study evaluated the applicability of the two approaches in predicting underground mining methods based on orebody characteristics (i.e., ore strength, host-rock strength, thickness, shape and dip). The results have demonstrated the effectiveness of the memory-based CF approach and classification models (i.e., ANN and KNN) with moderately good accuracy.

Despite the study's limitations in the size and quality of the dataset, the findings demonstrated that the integrated approaches in the AI-MMRS can be viable and practical for MMS. Understanding that the mining methods selection (MMS) process is one of the most critical decision-making tasks in mine planning, this study emphasizes the need for the direct involvement of the decision-makers (mining professionals) to perform further detailed evaluations and selection of mining methods. Therefore, the proposed AI-MMRS is intended to serve as a decision-support tool for the preliminary evaluation and selection of underground mining methods based on historical and evolving data. The system can help professionals focus their detailed evaluations on a narrower, more relevant set of mining methods, thus enhancing the efficiency and thoroughness of the decision-making process.

The proposed AI-MMRS has the potential to aid in decision-making in the mining industry by providing efficient and experience-based recommendations for the preliminary evaluation and selection of underground mining methods. However, as with any AI or ML-based systems, the proposed AI-MMRS will only provide better recommendations if continuous data collection and training are performed. Therefore, the system is designed to be flexible and open to the inclusion of new mining methods as they are developed or identified. Future studies will focus on improving the quality of the input dataset, optimizing machine learning models, and validating the models on various case studies.

The study's findings provide new insights into applying memory-based collaborative filtering and classification models in MMS, providing a valuable resource for researchers and industry professionals interested in data-driven approaches to mining project decision-making. The study thus demonstrates that the application of AI and data analytics in the mining industry has the potential to optimize the efficiency and effectiveness of decision-making, which is the concept of Smart Mining (Mining 4.0).

Author Contributions: Conceptualization, E.P.A.M., Y.K. and T.A. (Tsuyoshi Adachi), methodology, E.P.A.M. and Y.K., software, E.P.A.M. and N.O., validation, E.P.A.M., Y.K. and B.M.B., formal analysis, E.P.A.M., investigation, E.P.A.M. and N.O., resources, Y.K., Y.O. and T.A. (Takahiko Arima), data curation, E.P.A.M., writing—original draft preparation, E.P.A.M., writing—review and editing, E.P.A.M., Y.K., Y.O., T.A. (Takahiko Arima) and B.M.B., visualization, E.P.A.M., supervision, Y.K. and T.A. (Tsuyoshi Adachi); project administration, Y.K., funding acquisition, Y.K. All authors have read and agreed to the published version of the manuscript.

Funding: This study was funded by the Japan International Cooperation Agency (JICA) through the KIZUNA program.

Data Availability Statement: Data are contained within the article.

Conflicts of Interest: The authors declare no conflicts of interest.

References

1. Hartman, H.L.; Mutmansky, J.M. *Introductory Mining Engineering*, 2nd ed.; John Wiley & Sons, Inc.: Hoboken, NJ, USA, 2002.
2. Brady, B.H.G.; Brown, E.T. *Rock Mechanics for Underground Mining*, 3rd ed.; Springer Science + Business Media, Inc.; Kluwer Academic Publishers: New York, NY, USA, 2004; Volume 24. [CrossRef]
3. Carter, P.G. Selection Process for Hard-Rock Mining. In *SME Mining Engineering Handbook*, 3rd ed.; Darling, P., Ed.; Society for Mining Engineering, Metallurgy and Exploration, Inc.: New York, NY, USA, 2011; Chapter 6.3; pp. 357–376.
4. Nicholas, D.E. Method Selection—A numerical Approach. In *Design and Operation of Caving and Sublevel Stoping Mines*; Illustrated; Stewart, D.R., Ed.; Society of Mining Engineers of the American Institute of Mining, Metallurgical and Petroleum Engineers (SME-AIME): New York, NY, USA, 1981; Chapter 4; pp. 39–53. Available online: https://www.cnitucson.com/publications.html (accessed on 16 January 2023).
5. Miller-Tait, L.; Pakalnis, R.; Poulin, R. UBC Mining Method Selection. In *Mine Planning and Equipment Selection (MPES)*; Balkema: Rotterdam, The Netherlands, 1995; pp. 163–168.
6. Ataei, M.; Jamshidi, M.; Sereshki, F.; Jalali, S. Mining method selection by AHP approach Some applications of AHP in mining Engineering area. *J. S. Afr. Inst. Min. Metall.* **2008**, *108*, 741–749.
7. Bogdanovic, D.; Nikolic, D.; Ilic, I. Mining method selection by integrated AHP and PROMETHEE method. *An. Acad. Bras. De Ciências* **2012**, *84*, 219–233. [CrossRef]
8. Shariati, S.; Yazdani-chamzini, A.; Bashari, B.P. Mining method selection by using an integrated model. *Int. Res. J. Appl. Basic Sci.* **2013**, *6*, 199–214.
9. Ali, M.A.M.; Kim, J.-G. Selection mining methods via multiple criteria decision analysis using TOPSIS and modification of the UBC method. *J. Sustain. Min.* **2021**, *20*, 49–55. [CrossRef]
10. Manjate, E.P.A.; Saadat, M.; Toriya, H.; Inagaki, F.; Kawamura, Y. Application of Entropy Method for Estimating Factor Weights in Mining-Method Selection for Development of Novel Mining-Method Selection System. *J. Sustain. Min.* **2022**, *20*, 296–308. [CrossRef]
11. Manjate, E.P.A.; Ohtomo, Y.; Arima, T.; Adachi, T.; Kawamra, Y.; Bene, B.M. Applying Nonnegative Matrix Factorization for Underground Mining Method Selection Based on Mining Projects Historical Data. *Int. J. Soc. Mater. Eng. Resour.* **2024**, *26*, 1–10. [CrossRef]
12. Özyurt, M.C.; Karadogan, A. A New Model Based on Artificial Neural Networks and Game Theory for the Selection of Underground Mining Method. *J. Min. Sci.* **2020**, *56*, 66–78. [CrossRef]
13. Lv, W.Y.; Zhang, Z.H. Application of Thick Coal Seam Mining Method Prediction Model Based on Artificial Neural Network. *Adv. Mater. Res.* **2014**, *962–965*, 242–246. [CrossRef]
14. Shixiang, T.; Chen, W. Evolving neural network using genetic algorithm for mining method evaluation in thin coal seam working face. *Int. J. Min. Miner. Eng.* **2018**, *9*, 228. [CrossRef]
15. Abdelrasoul, M.E.I.; Wang, G.; Kim, J.-G.; Ren, G.; Mohamed, M.A.-E.; Ali, M.A.M.; Abdellah, W.R. Review on the Development of Mining Method Selection to Identify New Techniques Using a Cascade-Forward Backpropagation Neural Network. *Adv. Civ. Eng.* **2022**, *2022*, 6952492. [CrossRef]
16. Shohda, A.M.A.; Ali, M.A.M.; Ren, G.; Kim, J.G.; Mohamed, M.A.E.H. Application of Cascade Forward Backpropagation Neural Networks for Selecting Mining Methods. *Sustainability* **2022**, *14*, 635. [CrossRef]
17. Ricci, F.; Rokach, L.; Shapira, B.; Kantor, P.B. (Eds.) *Recommender Systems Handbook*, 1st ed.; Springer: Boston, MA, USA, 2011. [CrossRef]
18. Parra, D.; Sahebi, S. Recommender Systems: Sources of Knowledge and Evaluation Metrics. In *Advanced Techniques in Web Intelligence-2*; Velásquez, J.D., Palade, V., Jain, L.C., Eds.; Springer: Berlin/Heidelberg, Germany, 2013; Chapter 7; p. 149.
19. Soofi, A.A.; Awan, A. Classification Techniques in Machine Learning: Applications and Issues. *J. Basic Appl. Sci.* **2017**, *13*, 459–465. [CrossRef]
20. Chen, R.C.; Dewi, C.; Huang, S.W.; Caraka, R.E. Selecting critical features for data classification based on machine learning methods. *J. Big Data* **2020**, *7*, 52. [CrossRef]

21. Shannon, C.E. A Mathematical Theory of Communication. *Bell Syst. Tech. J.* **1948**, *27*, 623–656. [CrossRef]
22. Ning, X.; Desrosiers, C.; Karypis, G. A Comprehensive Survey of Neighborhood-Based Recommendation Methods. In *Recommender Systems Handbook*, 2nd ed.; Ricci, F., Rokach, L., Shapira, B., Eds.; Springer Science + Business Media LLC: New York, NY, USA, 2015; Chapter 2; pp. 37–76. [CrossRef]
23. Gong, S.; Ye, H.; Tan, H. Combining Memory-Based and Model-Based Collaborative Filtering in Recommender System. In Proceedings of the 2009 Pacific-Asia Conference on Circuits, Communications and Systems, Chengdu, China, 16–17 May 2009; IEEE: Piscataway, NJ, USA, 2009; pp. 690–693. [CrossRef]
24. Airen, S.; Agrawal, J. Movie Recommender System Using K-Nearest Neighbors Variants. *Natl. Acad. Sci. Lett.* **2022**, *45*, 75–82. [CrossRef]
25. Singh, A.; Thakur, N.; Sharma, A. A review of supervised machine learning algorithms. In Proceedings of the 2016 3rd International Conference on Computing for Sustainable Global Development (INDIACom), New Delhi, India, 16–18 March 2016; pp. 1310–1315.
26. Zhang, M.-L.; Zhou, Z.-H. ML-KNN: A lazy learning approach to multi-label learning. *Pattern Recognit.* **2007**, *40*, 2038–2048. [CrossRef]
27. Hastie, T.; Tibshirani, R.; Friedman, J. *The Elements of Statistical Learning: Data Mining, Inference, and Prediction*, 2nd ed.; Springer: New York, NY, USA, 2009. [CrossRef]
28. Mohammadi, N.M.; Hezarkhani, A. Application of support vector machine for the separation of mineralised zones in the Takht-e-Gonbad porphyry deposit, SE Iran. *J. Afr. Earth Sci.* **2018**, *143*, 301–308. [CrossRef]
29. Lee, S.; Park, I. Application of decision tree model for the ground subsidence hazard mapping near abandoned underground coal mines. *J. Environ. Manag.* **2013**, *127*, 166–176. [CrossRef]
30. Olivier, J.; Aldrich, C. Use of Decision Trees for the Development of Decision Support Systems for the Control of Grinding Circuits. *Minerals* **2021**, *11*, 595. [CrossRef]
31. Chen, Y.; Wu, W.; Zhao, Q. A Bat-Optimized One-Class Support Vector Machine for Mineral Prospectivity Mapping. *Minerals* **2019**, *9*, 317. [CrossRef]
32. Gunawardana, A.; Shani, G. A Survey of Accuracy Evaluation Metrics of Recommendation Tasks. *J. Mach. Learn. Res.* **2009**, *10*, 2935–2962.
33. Bahadorpour, M.; Neysiani, B.S.; Shahraki, M.H.N. Determining Optimal Number of Neighbors in Item-based kNN Collaborative Filtering Algorithm for Learning Preferences of New Users. *J. Telecommun. Electron. Comput. Eng.* **2017**, *9*, 163–167.
34. The MathWorks Inc. *Statistics and Machine Learning Toolbox: 12.3 (R2022a)*; The MathWorks Inc.: Natick, MA, USA, 2022; Available online: https://www.mathworks.com (accessed on 1 September 2024).
35. Raschka, S. Model Evaluation, Model Selection, and Algorithm Selection in Machine Learning. CoRR 2018. Available online: http://arxiv.org/abs/1811.12808 (accessed on 14 December 2022).
36. Hastie, T.; Tibshirani, R.; Friedman, J. Model Assessment and Selection. In *The Elements of Statistical Learning*, 2nd ed.; Springer: New York, NY, USA, 2009; Chapter 7.
37. Kumar, P.; Bhatnagar, R.; Gaur, K.; Bhatnagar, A. Classification of Imbalanced Data: Review of Methods and Applications. *IOP Conf. Ser. Mater. Sci. Eng.* **2021**, *1099*, 012077. [CrossRef]
38. Lango, M.; Napierala, K.; Stefanowski, J. Evaluating Difficulty of Multi-Class Imbalanced Data. In *Foundations of Intelligent Systems. ISMIS 2017*; Kryszkiewicz, M., Appice, A., Ślęzak, D., Rybinski, H., Skowron, A., Raś, Z.W., Eds.; Springer: Warsaw, Poland, 2017; pp. 312–322. [CrossRef]
39. Barakos, G.; Mischo, H. Insertion of the social license to operate into the early evaluation of technical and economic aspects of mining projects: Experiences from the Norra Kärr and Bokan Dotson rare earth element projects. *Extr. Ind. Soc.* **2021**, *8*, 100814. [CrossRef]

applied sciences

MDPI

Article

Design Parameters Affecting Rill Swell Events for Block Caving Applications

Raúl Castro [1], Carlos Valdés [1], René Gómez [2,*], Krzysztof Skrzypkowski [3,*] and Krzysztof Zagórski [4]

[1] Advanced Mining Technology Center, Universidad de Chile, Santiago 8331051, Chile; carlos.valdes@ug.uchile.cl (C.V.)
[2] Faculty of Engineering, Universidad de Concepción, Concepcion 4070386, Chile
[3] Faculty of Civil Engineering and Resource Management, AGH University of Krakow, Mickiewcza 30 Av., 30-059 Krakow, Poland
[4] Faculty of Mechanical Engineering and Robotics, AGH University of Krakow, Mickiewcza 30 Av., 30-059 Krakow, Poland; zagkrzys@agh.edu.pl
* Correspondence: regomez@udec.cl (R.G.); skrzypko@agh.edu.pl (K.S.)

Abstract: Rill swell (RS) events are outflows of dry, fine-grained material mainly observed at drawpoints in cave mining. These events can negatively affect production and have fatal consequences. Unfortunately, comprehensive studies analyzing these events are lacking. This paper uses the discrete element method to study RS events. With this method, a numerical model was constructed and calibrated based on an RS event recorded in Ridgeway Deeps Block Cave. Drawpoint geometries, material properties, and the initial mass of the fine material were then analyzed. The results show that both the brow beam height and drawpoint width had a noticeable influence on the RS magnitude, mainly on the tonnage of the flow and the distance reached by coarse particles dragged into the extraction drift. While the mass of fine material is crucial to the magnitude of RS events, results suggest that narrowing drawpoint width and/or increasing brow beam height can mitigate the impact of RS events.

Keywords: numerical modeling; discrete element method; granular material; mining risk

Citation: Castro, R.; Valdés, C.; Gómez, R.; Skrzypkowski, K.; Zagórski, K. Design Parameters Affecting Rill Swell Events for Block Caving Applications. *Appl. Sci.* **2024**, *14*, 8545. https://doi.org/10.3390/app14188545

Academic Editor: Tiago Miranda

Received: 23 June 2024
Revised: 2 September 2024
Accepted: 18 September 2024
Published: 23 September 2024

1. Introduction

Rill swell (RS) of fine material events are uncontrolled outflows of dry, fine-grained materials from drawpoints in underground mining, which can also transport large rocks interspersed with the fine material. The first events registered in Palabora Block Cave Lift 1 were described as fine rushes with material flowing in the air [1]; typical fine rushes were observed to flow across the width of the production drift up to the opposite sidewall. From May 2006 to 2020, more than 300 fine rushes occurred in Palabora, and those drawpoints classified as having a high risk of this type of event have subsequently been sealed off [1,2].

Other operations have also experienced fine rushes. For example, the mine site at Ridgeway Deeps has experienced these events since September 2014, with analysis showing that the fine material came from the SLC mine above [3]. Also, in Australia, Cadia East PC1 has experienced inrushes since February 2016, mainly at the cave-back boundary projection in the Production Level [4]. On the other hand, Mt. Wright has experienced inrushes since May 2014, which have been ascribed to poor performance of ring charging, the formation and release of boulders, and hang-up release procedures [5].

According to the literature, RS events are mainly related to two different mechanisms: (1) removal of hang-ups and (2) slope failure of the fine material at drawpoint [2,4–6]. Removal of hang-up activity generates free space through which large masses of fine material can fall and flow, and this has occurred in Ridgeway Deeps, Palabora, Mt. Wright, and Cadia East PC1. On the other hand, a slope failure mechanism can occur during load haul dump (LHD) loading, when fine material located over the drawpoint is destabilized and flows out. This kind of event has been observed at Mt. Wright and Cadia East PC1, and recently, minor runoff of fines has also been observed in the Chuquicamata underground mine. Both mechanisms require a previous accumulation of fine material in the drawbell, while the presence of coarse fragments can also contribute to the occurrence of RS in either mechanism.

The presence of fine material is critical in caving mines with inrush risk potential. Fine materials can appear due to the mining process, or they can originate from previous adjacent mine sectors [7]. Four sources of fine material have been identified in RS events: secondary fragmentation, fine material migration, fine material from open pits, and fine material from previous mine sectors. These sources can be independent or occur in combination to influence the quantity of fine material found in underground mines.

Secondary fragmentation is the last fragmentation stage that ore undergoes in the broken column before being extracted from the drawpoints. Here, the rock is mainly fragmented by compression and abrasion [8–10]. Additionally, some authors [10–12] include fragmentation by impact, when a rock block falls from the cave-back. Several models have been used to estimate these fragmentations in block caving mines [9,12–15]; however, none has been specifically calibrated to estimate fine fragments.

The main mechanism of fine material generation during secondary fragmentation is by abrasion generated by shear strain during gravity flow [13,16,17]. The problem is that shear strain and overload are difficult to estimate. Moreover, both variables are influenced by ore extraction. The shear strain can be determined based on the shear band during ore flow [12,13]. This approach has been used in a secondary fragmentation model [18] based on fragmentation studies involving shear [19,20]. This approach has improved the accuracy of fine material fragmentation models. However, fine material can also be observed under uniform draw due to large travel distances [21,22], which the previous models have failed to consider.

Fines migration occurs when fine materials flow more rapidly than coarse materials inside the broken column and eventually arrive at the drawpoint [7,23]. In block caving, this process has been studied mainly through physical modeling [1,24,25] and also through numerical modeling [26–28]. In cave mining, fine migration is mainly governed by the ratio between coarse and fine fragment size, the particle size distribution of ore, rock density, and draw strategies. Authors [12,13] suggest that fine migration also occurs around the ellipsoid of movement induced by shearing. Fine material migration can accumulate fine material in drawbells, increasing the risk of RS events.

Additionally, cave mining methods are sometimes developed after open-pit mining has ceased [29,30]. Due to the caving process, material from the pit slope can fail and become part of the caving-induced subsidence. Material incorporated from the pit is softer and more fractured than the in situ mineralized rock. In many cases, that softer, finer material is more susceptible to secondary fragmentation mechanisms. For example, Palabora Block Cave Lift 1 identified their RS events as being related to fine material from the pit slopes [1]. Abandoned cave mines are also sources of fine material for future deeper projects. For instance, Ridgeway Deeps' Block Cave suffered RS events related to fine material from the abandoned Ridgeway Gold Sublevel Cave from 2014 to 2016 [3].

The slope failure mechanics observed during the inrush of fine material may have certain similarities with rockslides that are well documented in the literature. At a large scale, rock avalanches can be found involving dry flows of fine granular material [31]. Rock avalanches are a type of landslide (large scale) in which a slope failure is produced [32]. This type of rock flow is affected by lithology [33,34], but its distance is commonly correlated with its debris mass [35]. Rockslides can occur in unconfined or confined conditions [32]. Additionally, particle sizes and shearing are key features in rockslides [31,36], along with a low friction coefficient [35]. Low mixing is commonly observed in landslides associated with laminar flow during slides. Commonly, in rock avalanches two motion mechanisms can be appreciated: sliding at the beginning, and then material flow [37]. Acoustic fluidization is one of the triggering mechanisms associated with the pseudo-viscous flow of dry rock debris moving long distances horizontally. In [38], a nonlinear model is proposed that considers the evolutionary characteristics of the slope failure. Large rock blocks can be also be associated with rockslides [33], similar to that observed in the inrush of fine reported in [3].

Studies focusing on understanding the key variables and mechanics in RS events are scarce, and although mine studies provide valuable information, the variables and mechanisms involved cannot be controlled for deeper analysis. This study focuses on the RS mechanism as it relates to hang-up removal, applying numerical modeling to analyze these events. The numerical model was calibrated based on available mine data, providing an opportunity to combine an in situ mine study with modeling to delve further into RS event occurrence and its mechanisms.

2. Methods

2.1. Granular Material

The definition of fine material in mining depends primarily on the operation or sector and the mine problem or phenomena being studied. For example, at Diablo Regimiento sector in El Teniente, fine materials are considered to be 7 cm in diameter or smaller [39], and mainly related to mud rush events. At Palabora Block Cave Lift 1, fine materials are considered to be 1 cm in diameter or smaller [2], and also related to mud rush problems. Some risk assessment studies have considered fine materials to be 25–30 cm in diameter or smaller [40]. Additionally, gravitational flow studies of dilution by fine migration have been used to define fine material size criteria [24,39,41,42]. Table 1 presents examples of fine material definitions in the cave mining industry and related studies.

Table 1. Fine material in cave mining.

Operation's Name/Study	Mining Method	Max. Size [cm]	Reference
Esmeralda sector (El Teniente mine)	Panel Caving	5	[39]
Diablo Regimiento sector (El Teniente mine)	Panel Caving	7	[39]
Mud-rush study	PC/BC (numerical modeling)	25	[40]
Palabora Lift 1	Panel Caving	1	[2]
Ridgeway Deeps	Block Caving	1 (d_{50})	[3]
Pipa Norte Extensión HW	Panel Caving	25	[43]
Mt Wright	Sublevel Shrinkage Stoping	1	[5]

As illustrated in Table 1, different fragment sizes are defined as fine material across cave mining environments. Given this variation, the size was chosen from within this range: For the numerical model, the fine material was set to 0.2 [m] in diameter and the coarse material was set to 0.75–1.5 [m] in diameter (mean size, d_{50} = 1.18 m). Both fragment size distributions can be observed in Figure 1.

The fine material (0.2 m) was selected as a mono-size mainly to achieve numerical stability and to reduce simulation times. Size distribution has been shown to influence the macro-mechanical properties of particulate material [44–47]; however, because this study focused on geometric parameters, only one material size was used, and this was calibrated with the case study. However, to evaluate the effect of the mechanical properties of the material, a friction sensitivity analysis was also performed to analyze its effect in this study.

2.2. Base Event

A large RS event at Ridgeway Deeps registered in September 2015 [3] was used for numerical model calibration. This event was identified as being caused by the outflow of dry fine material during removal of a hang-up (coarse arch). The event had a magnitude of 260 [t] of fine material flow through a drawpoint, and large rocks of 0.5–1.5 [m] diameter were dragged by the fines. The geometrical characteristics of this event are summarized in Table 2 and presented in Figure 2.

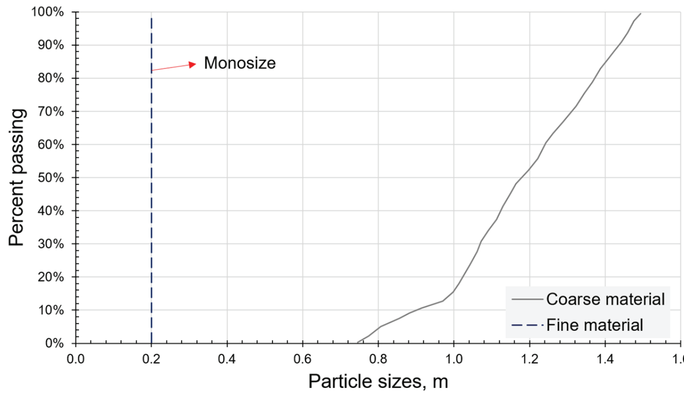

Figure 1. Fragment size distribution of the Numerical model material.

The flow was also described in terms of the distance reached and deposition angle in the production drift. Both of these were measured in the two senses of the production drift: towards the north, opposite to the direction of the extraction drift; and towards the south, in the same direction as the extraction drift (Figure 2). In Figure 2, the blue contour represents the fine material extension. The brow beam—in red—is located at the drawpoint where the RS event took place as the result of a hang-up removal. The hang-up was removed using a water cannon.

The run-out distance towards the south was not able to be determined because of the presence of the water cannon. Accordingly, the run-out distance towards the north was used in the calibration stage.

Table 2. Some base event characteristic used in calibration.

Parameter	Value	Unit
Tonnage	260	t
Real volume (non-apparent)	95	m^3
Run-out distance towards the north	-	m
Run-out distance towards the south	9.4	m
Large rocks in production drift?	Yes	-
Deposition angle towards the north, 1 [m] over the floor	19	$^\circ$
Deposition angle towards the south, 1 [m] over the floor	7	$^\circ$

2.3. Drawbell and Pillar Geometries

The production level of Ridgeway Deeps Block Cave is an offset herringbone layout, with 30 m between production drifts and 18 m between extraction drifts. Production and extraction drifts form 45-degree corners. The distance from one drawpoint to the next in the same drawbell is 11 m, and the drawbell height is 14 m from the drawpoint roof. Figure 3 presents detailed geometric characteristics of the drawbell and the pillar, respectively.

2.4. Numerical Model

The discrete element method (DEM) [48] is a numerical tool widely used for solving problems involving the flow of granular assemblies, represented as individual elements or particles. These particles interact with one another and other objects via contact force laws [48,49]. The basis of the DEM software is particle–pairs contact. When contact occurs, particles experience elastic repulsion and frictional forces, which are transformed into translational and rotational moments. Through the application of Newton's Second

Law, the particle's linear and angular accelerations are obtained. Then, through time integration of the acceleration, the particle's new velocity and new position are derived. These mathematical steps are known as Δt, with the following held to be true: The smaller the value of Δt, the greater the accuracy of the solution, and the longer the required computation time will be [49].

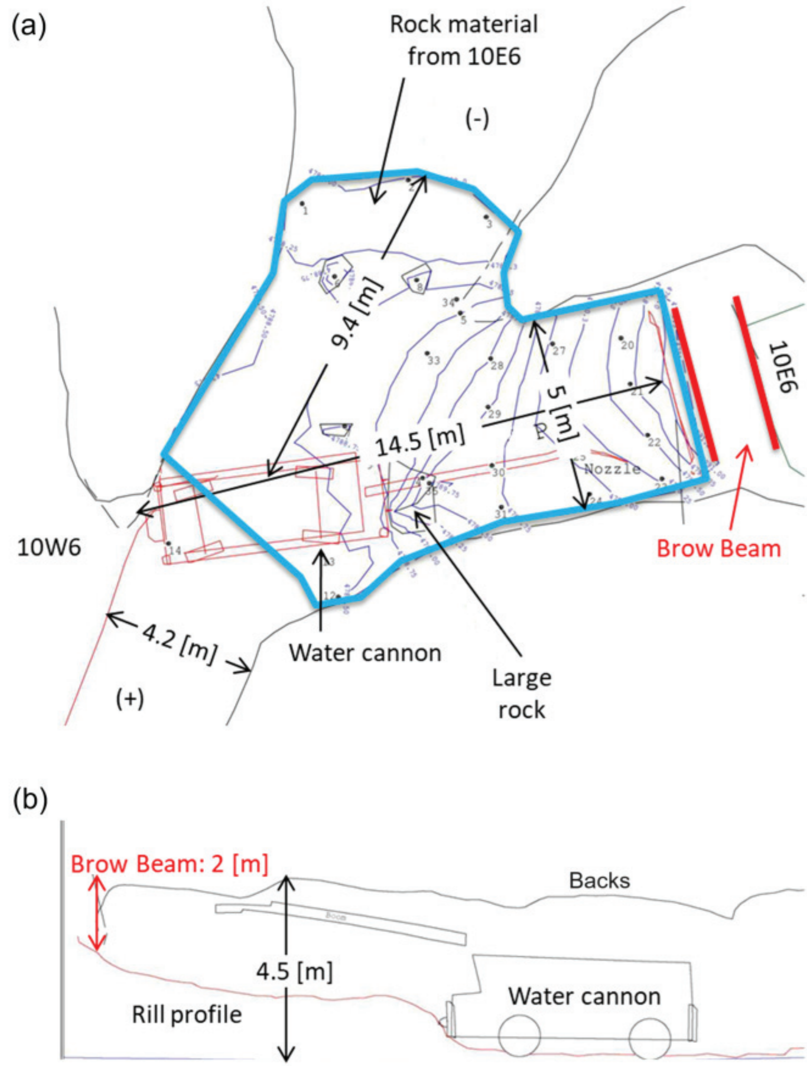

Figure 2. Geometric characteristics of the drawpoint and the event studied. (**a**) Plan view of the deposition profile (**b**) Lateral view of the deposition profile (after [3]).

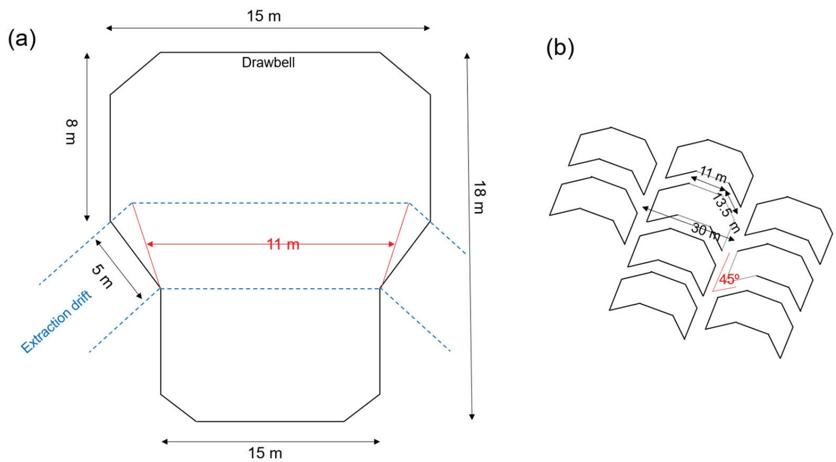

Figure 3. (**a**) Plan view of drawbell geometry, with red lines representing both drawpoints (**b**) Plan view of the pillar geometry and extraction level layout.

For this study, free-access ESyS-Particle software (version 2.3.5) was employed to implement DEM written in C++ with a Python API [50]. Using this program, it is possible to create bonded and non-bonded granular assemblies of spheres, assign contact coefficients such as friction and repulsion, model rotational and translational particles, and incorporate rigid structures into the simulations.

The setup of the numerical model (Figure 4) considers two drawpoints, one drawbell, two production drifts, two extraction drifts, two brow beams, coarse particles, fine particles, a hang-up at one of the two drawpoints composed of large particles (white), and a mass of fines (red) over the hang-up. The walls of the mine geometries are modeled with particles (blue) to assign mechanical properties to them.

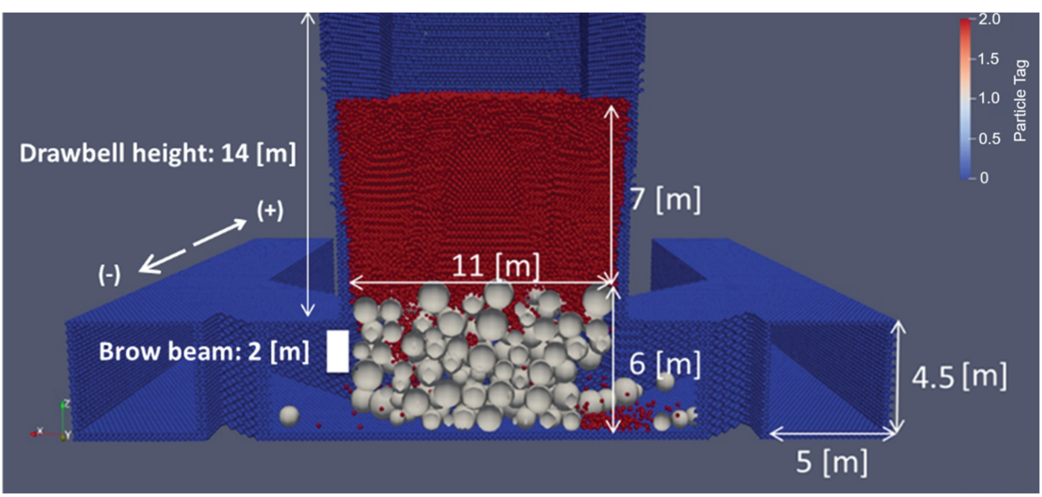

Figure 4. Initial setup of the numerical model developed in ESyS Particle. The red material is composed of fine particles. The white material is composed of coarse particles.

The hang-up was located at the drawpoint brow beam, and the experiments were focused on the behavior of the material flowing out from the drawpoint after part of the hang-up was removed. The coarse material was initially placed to create the hang-up, and then, the fine material was added. The hang-up volume removed was 4.5 m deep into the drawpoint (see yellow rectangle in Figure 5), a horizontal distance equivalent to 3 times the largest fragment size.

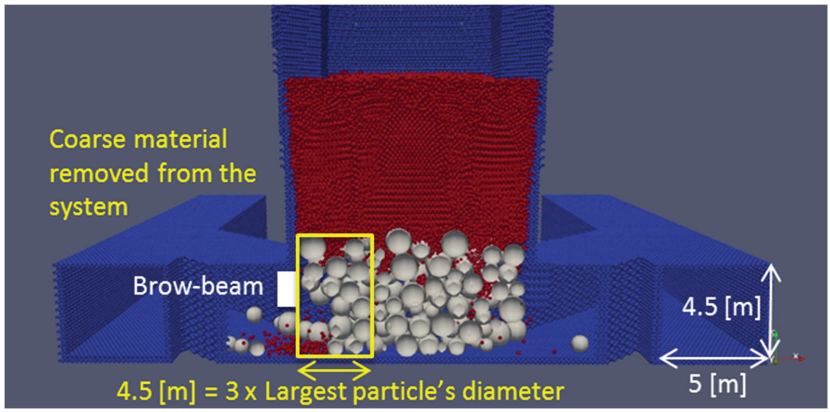

Figure 5. Volume of large particles removed to trigger the inrush event.

The RS magnitude was quantified by measuring 7 parameters described below (output variables):

- Tonnage of the event, including fine and coarse fragments (t)
- Run-out distance towards the north and the south, measured from the intersection of the extraction drift axis and production drift axis (m)
- Presence of large particles (>0.75 m diameter) in the production drift
- Height of the material in the production drift (m)
- Deposition angle towards the north and the south. This indicator was measured 1 m from the floor of the production drift (°).

The measurement procedures for the run-out distance, height of material, and deposition angle are illustrated graphically in Figure 6.

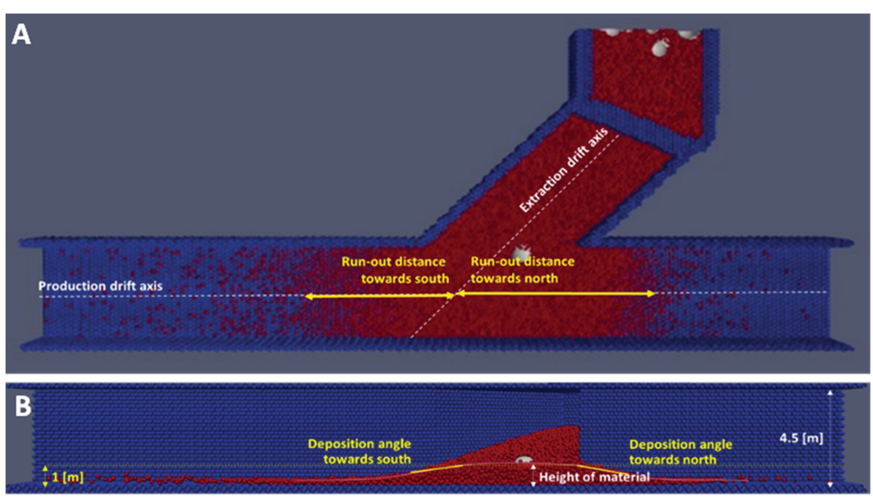

Figure 6. (**A**) Plan view of the measurement of run-out distance. (**B**) Profile view of the measurement of the height of flow and deposition angles.

The variables analyzed in this study were the following (control variables):

- The quantity of fine material over the hang-up. This variable was studied through its height, analyzing columns of 7 m, 15 m, and 30 m
- The effective height of the drawpoint. The effective drawpoint height is the nominal height of the drawpoint (4.5 m in this study) minus the brow-beam height. Brow beams are structures placed at the drawpoint brow to control RS or mud rush events
- The effective drawpoint width, which was measured wall-to-wall (3 and 5 m).

3. Numerical Calibration

The numerical model was calibrated according to the base event described in Section 2.2. Particle density was set to 2.7 t/m^3 and the Poisson ratio was set to 0.3. Drawpoint geometry and quantity/height of the fine material over the hang-up were set to the following values:

- Drawpoint width: 5 m;
- Nominal drawpoint height: 4.5 m;
- Brow beam: 2 m (effective drawpoint height: 2.5 m).

The numerical and material parameters adjusted in the calibration phase were the elastic repulsion module, damping, and the static and dynamic coefficients of friction. Additionally, the height of fine material over the hang-up was calibrated. Regarding this last parameter, although the amount of fine material that came out of the drawpoint is known, the amount of initial fine material that was over the hang-up is unknown (part of this fine material may have remained in the drawbell).

Table 3 presents the results for the best adjustment achieved. The results of the calibration phase achieved a 1% deviation in terms of the tonnage and a 1° deviation in terms of the deposition angle. As in the base event for calibration, fine material fell, flowed, and dragged large particles up to the extraction drift bullnose, as can be seen in Figure 7.

Table 3. Parameter results obtained during the calibration.

Parameters	Value	Unit
Elastic repulsion	4.5	MPa
Static friction	0.9	-
Dynamic friction	0.8	-
Damping	0.25	-
Height of fine material over hang-up	7	m
Time Step	0.0004	s

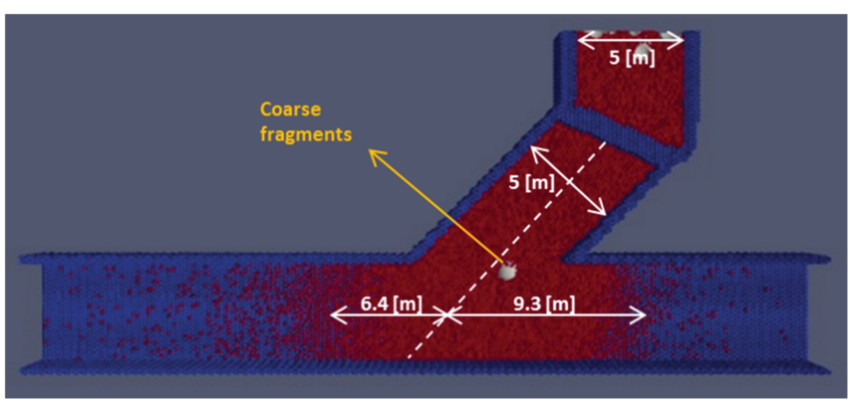

Figure 7. Plan view of the event modeled during calibration phase.

Additionally, Table 4 compares results obtained with the calibrated numerical model and the base event used in this study. Figure 7 and Table 4 demonstrate that coarse particles under the initial fine material were also dragged in the numerical simulation. The tonnage, run-out distance and deposition angle obtained in the numerical model are similar to the base event. The run-out distance to the south and the deposition angle were not reported in the base event because the water cannon interrupted the material flow.

Table 4. Results of main output variables calibrated with base event.

Parameters	Base Event	Numerical Model
Tonnage (t)	260	257
Run-out distance + (m)	-	6.4
Run-out distance − (m)	9.4	9.3
Large rocks in drift	yes	yes
Deposition angle + (°)	7	8
Deposition angle − (°)	-	7
Height of flow (m)	-	1.1

4. Results

This study focused on the relation between the drawpoint geometry and the quantity of fines over the hang-up with the magnitude of the RS event.

4.1. Drawpoint Geometry

Drawpoint height and drawpoint width were studied to analyze the magnitude of potential RS events. The quantity/height of fine material over the hang-up was adjusted at the calibration phase (7 m).

4.1.1. Drawpoint Height

Drawpoint height was analyzed in terms of the brow-beam height while the drawpoint width was fixed at 5 m and the amount of fine material over the hang-up was defined at a height of 7 m. Brow beams of 1 m, 2 m, and 3 m high were simulated. A brow beam of 2 m was the base case equivalent to the setup in the calibration phase. Table 5 presents the magnitude of the RS events simulated.

Table 5. RS magnitude for different brow beam (BB) heights.

Parameters	BB 1 m	BB * 2 m	BB 3 m
Tonnage	374	257	125
Run-out distance towards the north (+; m)	11	6.4	6.5
Run-out distance towards the south (−; m)	7.8	9.3	2.8
Large rocks in production drift?	Yes	Yes	No
Deposition angle in direction +, 1 (m) over the floor	14°	7°	-
Deposition angle in direction −, 1 (m) over the floor	17°	8°	-
Height of flow (m)	1.6	1.1	0.4

* Height of the base case.

Results showed a clear relation between the BB height and the RS magnitude. A brow beam of 1 m in height implied an RS event of 374 t, 46% larger than the event associated with the brow beam of 2 m in height. On the other hand, the 3 m high brow beam implied an RS event of 125 t, 51% smaller than the base case. In addition, in the event associated with the 1 m high brow beam, large particles were dragged to the production drift axis. On the contrary, the event associated with the brow beam of 3 m in height did not drag large particles through the extraction drift. Plan views of the material deposited are presented in Figure 8.

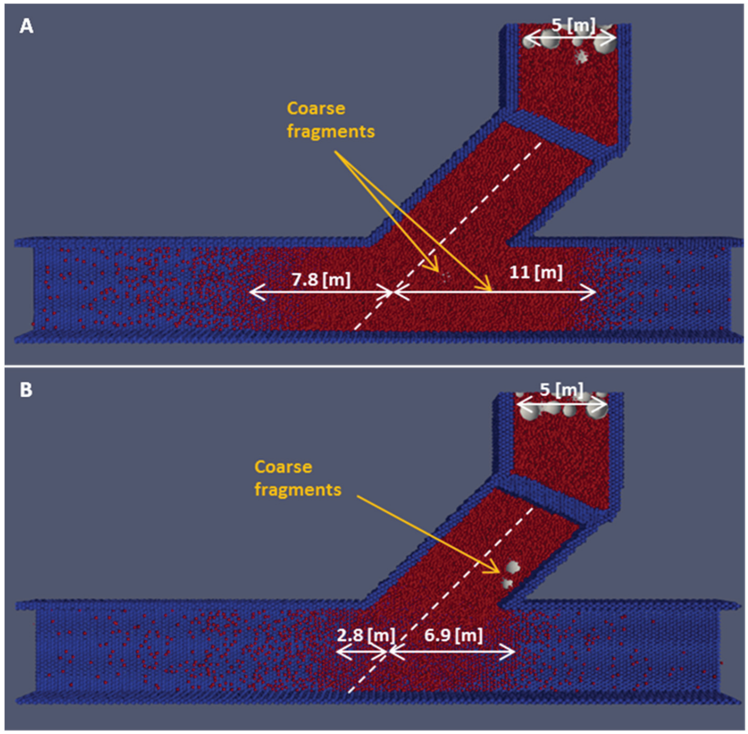

Figure 8. Plan views of the event modeled. (**A**) 1 m brow beam. (**B**) 3 m brow beam. Coarse fragments for the event associated with the brow beam of 1 m were of minor size.

4.1.2. Drawpoint Width

Two drawpoint widths were modeled. A small drawpoint width of 3 m was evaluated and compared with the large drawpoint width of 5 m used in Section 4.1.1. The effective drawpoint height was fixed at 2.5 m, the brow beam was fixed at 2 m, and the mass of fine material over the hang-ups at a height of 7 m.

Table 6 presents the magnitude of the RS events modeled. According to the results, the new event modeled (DP of 3 m) achieved a magnitude of 193 t, 25% smaller than the base event. Also, large rocks were dragged by the fines, but they did not arrive at the production drift, as can be observed in Figure 9.

Table 6. RS magnitude for different drawpoint widths.

Parameters	DP Width: 5 m *	DP Width: 3 m
Tonnage	257	193
Run-out distance towards the north (+; m)	6.4	3
Run-out distance towards the south (−; m)	9.3	6.9
Large rocks in production drift?	Yes	No
Deposition angle in direction +, 1 (m) over the floor	7°	-
Deposition angle in direction −, 1 (m) over the floor	8°	-
Height of flow (m)	1.1	0.8

* Height of the base case.

4.2. Available Fine-Grained Material

The number of fines over the hang-up was analyzed by height: columns of fines of 6 m, 15 m, and 30 m in height were studied and compared with the 7 m high columns used in previous sections. Brow beam heights of 1 m, 2 m, and 3 m and drawpoint widths of 5 m and 3 m were considered.

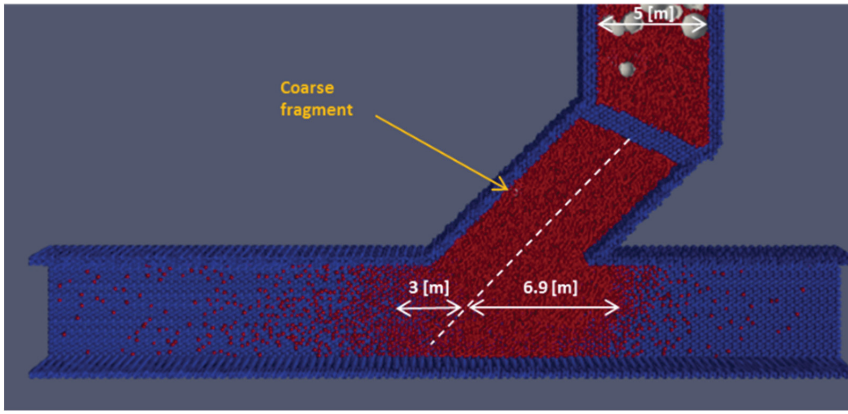

Figure 9. Plan view of the event modeled, with a drawpoint of 3 m in width. Coarse fragments that were dragged were covered by the fine material.

Table 7 presents the RS magnitude for events associated with columns of fines that were 6 m high, 15 m high, and 30 m high, respectively. According to the results, the RS magnitude expressed in tonnage was noticeably influenced by the drawpoint geometry, especially the brow beam height: For a brow beam of 1 m, the RS magnitude was 359–495 t depending on the available quantity of fines over the hang-up; for a brow beam of 2 m, the RS magnitude was 256–334 t; and for a brow beam of 3 m, the RS magnitude was 120–147 t. Thus, the smaller the brow beam, the larger the RS event.

Table 7. RS magnitude for different heights of fine material tested.

Height of Fine Material Over Drawpoint	Parameters	DP Width: 5 m			DP Width: 3 m
		BB 1 m	BB 2 m	BB 3 m	BB 2 m
6 m	Tonnage	359	256	120	190
	Run-out distance towards the north (+; m)	11	8.6	4.9	7.9
	Run-out distance towards the south (−; m)	5.7	4.6	2.1	2.2
	Large rocks in production drift?	Yes	Yes	No	Yes
	Deposition angle in direction +, 1 (m) over the floor	16	6	-	-
	Deposition angle in direction −, 1 (m) over the floor	15	6	-	-
	Height of flow (m)	1.4	1.1	0.4	0.9
15 m	Tonnage	446	287	137	212
	Run-out distance towards the north (+; m)	8.8	8.2	3.6	4
	Run-out distance towards the south (−; m)	13	9.8	6.5	7.3
	Large rocks in production drift?	Yes	Yes	No	Yes
	Deposition angle in direction +, 1 (m) over the floor	15°	7°	-	-
	Deposition angle in direction −, 1 (m) over the floor	17°	8°	-	-
	Height of flow (m)	2	1.1	0.4	0.5
30 m	Tonnage	495	334	147	234
	Run-out distance towards the north (+; m)	12.3	11.5	5	5.1
	Run-out distance towards the south (−; m)	13.3	10.6	6.5	9.4
	Large rocks in production drift?	Yes	Yes	No	Yes
	Deposition angle in direction +, 1 (m) over the floor	13°	7°	-	-
	Deposition angle in direction −, 1 (m) over the floor	16°	12°	-	-
	Height of flow (m)	2	1.4	0.5	1

The presence of large rocks in the production drift was observed for the brow beams of 2 m and 1 m, but not for the brow beam of 3 m, independently of the mass of fines over the hang-up. This phenomenon can be explained by the flowability of the fine material for different drawpoint opening widths.

5. Analysis

Figure 10 summarizes the magnitudes of all RS events modeled, including the drawpoint width of 3 m (dashed line). Here, the magnitudes increase according to the amount of fine material over the hang-up; hence, there was a maximum expected RS event for each drawpoint geometry. Considering drawpoints of 5 m in width, the maximum expected RS events would be 500 t, 350 t, and 150 t for brow beams of 1 m, 2 m, and 3 m high, respectively. Also, regarding drawpoints of 3 m in width and a brow beam of 2 m in height (effective drawpoint height of 2.5 m), the maximum expected RS event would be around 250 t.

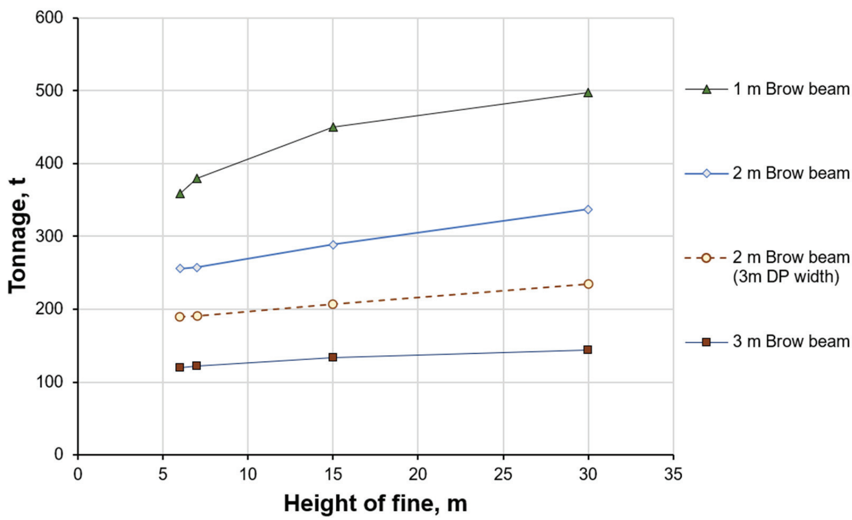

Figure 10. RS magnitude for different heights of fines over the hang-up and different drawpoint geometries.

On the other hand, the presence of large rocks in the production drift was observed to increase with a smaller brow beam and/or a larger amount of fine material over the hang-up. The observations in this study suggest an opportunity to define operational guidelines for mining sectors that have been classified as at high risk for RS events. The geometric characteristics of the drawpoints allow the maximum expected events to be estimated. Additionally—as a mitigation measure—results suggest the brow beam could be modified as caving progresses and finer fragmentation arrives at drawpoints.

The effect of rock density was quantified, and a sensitivity analysis of the density was performed. The density varied by +/−25% in simulating the case of a 2 m brow beam, 7 m of fine material height, and a drawpoint width of 5 m. The density was evaluated because it is known to influence fine migration [7,19]. Figure 11 shows the simulations for different rock densities. The red particles are the fine material, while the white ones are the coarse material present in the hang-up. For the lowest density (Figure 11a), coarse particles were not dragged to the production drift.

Table 8 shows the effect of particle density on RS events. It can be observed that at the lowest density the tonnage decreases by 28.5%, while at higher densities it increases by as much as 33%. It is possible that a lower density decreases the percolation and potential energy available to generate an RS event. Therefore, density is a variable that can have an important effect when this type of risk exists.

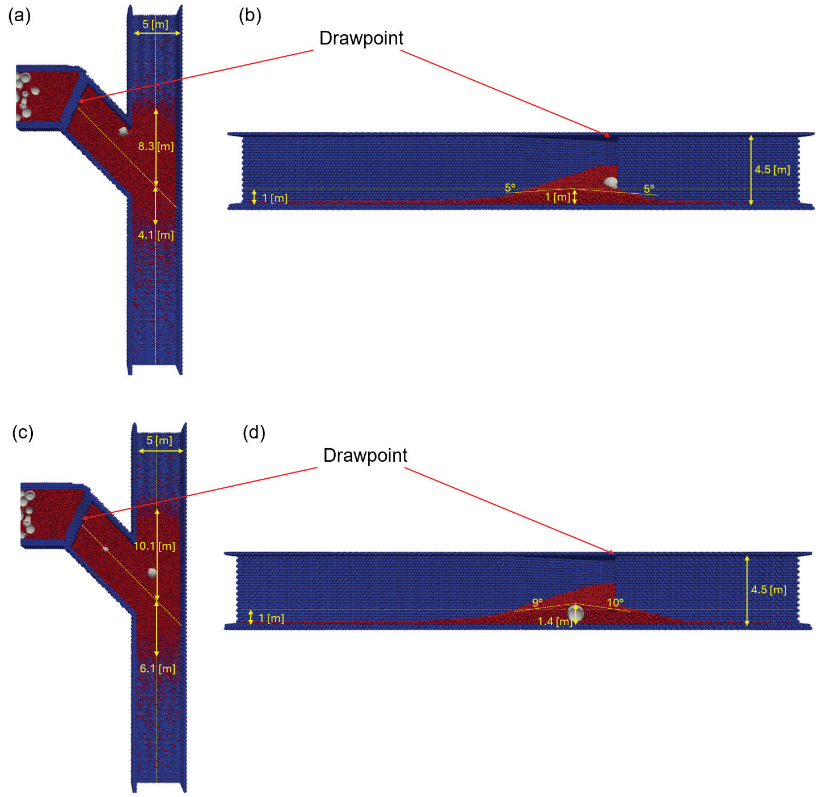

Figure 11. RS event simulation with different rock densities (**a**) plan view of RS event for rock density of 2.0 t/m^3, (**b**) profile view of RS event for rock density of 2.0 t/m^3, (**c**) plan view of RS event for rock density of 3.4 t/m^3, (**d**) profile view of RS event for rock density of 3.4 t/m^3.

Table 8. RS results simulating different rock densities.

Parameter	**Density (t/m^3)**		
	2.0	**2.7**	**3.4**
Tonnage	184	257	341
Run-out distance towards the north (+; m)	8.3	6.4	10.1
Run-out distance towards the south (−; m)	4.1	9.3	6.1
Large rocks in production drift?	No	Yes	Yes
Deposition angle in direction +, 1 (m) over the floor (°)	5	8	10
Deposition angle in direction −, 1 (m) over the floor (°)	5	7	10
Height of flow (m)	1	1.1	1.4

Being able to model rill swell of fine material events in mining contributes to a better understanding these phenomena. Although there is still much work to be done to achieve a thorough understanding in this area, the variables and results presented here enhance the comprehension of these critical events. However, one of the main variables associated with these phenomena is the uncertainty of the fine material accumulated at the drawpoints. It is advisable to use techniques to quantify this uncertainty [51,52] and thus minimize the risk through better estimates of the fine material generation and gravity flow.

6. Conclusions

This numerical study analyzed the magnitude of RS events associated with a hang-up release mechanism, modeling different drawpoint geometries and amounts of fine material over the hang-up. The numerical method was useful to replicate the RS events studied. Here, it was observed that the effective drawpoint height and the amount of fine material over the hang-up influenced the material flow. Based on the tonnage of fine material available over the hang-up, each drawpoint geometry was associated with a maximum expected RS event. The drawpoint geometry in terms of height and width were found to highly influence RS event magnitude, almost independently of the amount of fine material over the drawpoint. In our model, when the height of the brow beam increased by 50%, the amount of fine material in the RS event decreased by 51.4%. Given these results, the design of drawpoints should be evaluated and adjusted accordingly if there is a risk of RS events. Narrower drawpoints with higher brow beams could significantly decrease the magnitude of an RS event. If there is a potential risk of an RS event due to dry and fine material, the methodology used here can be used to anticipate the magnitude of an RS event.

Author Contributions: Conceptualization, R.C. and C.V.; Methodology, R.C. and C.V.; Software, C.V. and R.G.; Calibration, C.V.; Formal analysis, R.C., C.V. and R.G.; Investigation, R.C. and C.V.; Resources, R.C. and K.S.; Writing—original draft preparation, C.V. and R.G.; Writing—review and editing, K.S. and K.Z.; Visualization, C.V.; Supervision, R.C.; Funding acquisition, R.C. and K.S. All authors have read and agreed to the published version of the manuscript.

Funding: This research was funded by CONICYT/PIA Project AFB230001. This research was partially funded by the FONDECYT Regular 1230749. The APC was funded by AGH University of Krakow, scientific subsidy under number: 16.16.100.215.

Institutional Review Board Statement: Not applicable.

Informed Consent Statement: Not applicable.

Data Availability Statement: The raw data supporting the conclusions of this article will be made available by the authors on request.

Conflicts of Interest: The authors declare no conflicts of interest.

References

1. Pretorius, D.; Ngidi, S. Cave management ensuring optimal life of mine at Palabora. In Proceedings of the 5th Conference and Exhibition on Mass Mining, Lulea, Sweden, 9–11 June 2008; pp. 63–71.
2. Paetzold, H.; Lourens, P.; Brazier, R. Reopening and closure of a block cave. In Proceedings of the Eighth International Conference & Exhibition on Mass Mining, Massmin 2020, Santiago, Chile, 9–11 December 2020; pp. 103–114.
3. NSW Department of Industry, Skills and Regional Development. *Report into Death of Lee Peters at Ridgeway Mine*; NSW Department of Industry, Skills and Regional Development: Queanbeyan, NSW, Australia, 2017.
4. Lett, J.; Castro, R.; Pereira, M.; Osorio, A.; Alvarez, P. BCRisk applications for rill swell hazard analysis in PC1: Case study at Cadia East Operations. In Proceedings of the Caving 2022: Fifth International Conference on Block and Sublevel Caving, Adelaide, Australia, 30 August–1 September 2022; pp. 561–572. [CrossRef]
5. Long, S.; Carnovale, D.; Louwrens, L. Mt Wright–managing unique risks. In Proceedings of the 13th AUSIMM Underground Operators' Conference, Melbourne, Australia, 16–18 October 2017; pp. 295–304.
6. Gómez, R.; Loyola, M.; Palma, S.; Valdés, C. Experimental study of inrush of fines events in underground mining. *Int. J. Rock Mech. Min. Sci.* **2023**, *169*, 105436. [CrossRef]
7. Hashim, M.; Sharrock, G.; Saydam, S. A Review of Particle Percolation in Mining. In Proceedings of the SHIRMS: Southern Hemisphere International Rock Mechanics Symposium 2008, Perth, Australia, 16–19 September 2008; pp. 273–284. [CrossRef]
8. Laubscher, D.H. Cave mining-the state of the art. *J. South. Afr. Inst. Min. Metall.* **1994**, *94*, 279–293.
9. Eadie, B. A Framework for Modelling Fragmentation in Block Caving. Ph.D. Thesis, The University of Queensland, St Lucia, QLD, Australia, 2003.
10. Brown, E. Fragmentation Assessment. In *Block Caving Geomechanics*; Julius Kruttschnitt Mineral Research Centre: Queensland, Australia, 2007; pp. 184–228.
11. Laubscher, D.H. Secondary fragmentation. In *Block Cave Manual*; International Caving Study: Queensland, Australia, 2000.
12. Pierce, M.E. A Model for Gravity Flow of Fragmented Rock in Block Caving Mines. Ph.D. Thesis, University of Queensland, St Lucia, QLD, Australia, 2009.
13. Dorador, L. Experimental Investigation of the Effect of Broken Ore Properties on Secondary Fragmentation During Block Caving. Ph.D. Thesis, University of British Columbia, Vancouver, BC, Canada, 2016.
14. Gómez, R.; Castro, R.; Betancourt, F.; Moncada, M. Comparison of normalized and non-normalized block caving comminution models. *J. South Afr. Inst. Min. Metall.* **2021**, *121*, 581–588. [CrossRef]

15. Castro, R.; Gómez, R.; Castillo, J.J.; Jerez, O. Fragmentation model integrated in a gravity flow simulator for block caving planning. *Granul. Matter* **2024**, *26*, 20–22. [CrossRef]
16. Gómez, R.; Castro, R.L.; Casali, A.; Palma, S.; Hekmat, A. A Comminution Model for Secondary Fragmentation Assessment for Block Caving. *Rock Mech. Rock Eng.* **2017**, *50*, 3073–3084. [CrossRef]
17. Pierce, M.; Weatherley, D.; Kojovic, T. A hybrid methodology for secondary fragmentation prediction in cave mines. In Proceedings of the Second International Symposium on Block and Sublevel Caving, Perth, Australia, 20–22 April 2010; pp. 567–581. [CrossRef]
18. Pierce, M.; Fuenzalida, M. Application of a methodology for secondary fragmentation prediction in cave mines. In Proceedings of the 3rd International Symposium on Block and Sublevel Caving, Santiago, Chile, 5–6 June 2014; pp. 318–327.
19. Bridgwater, J.; Utsumi, R.; Zhang, Z.; Tuladhar, T. Particle attrition due to shearing-the effects of stress, strain and particle shape. *Chem. Eng. Sci.* **2003**, *58*, 4649–4665. [CrossRef]
20. Neil, A.U.; Bridgwater, J. Attrition of particulate solids under shear. *Powder Technol.* **1994**, *80*, 207–219. [CrossRef]
21. Gómez, R.; Castro, R. Experimental Quantification of Granular Material Fragmentation Due to Travel Distance. *Min. Metall. Explor.* **2022**, *39*, 615–623. [CrossRef]
22. Locat, P.; Couture, R.; Locat, J.; Leroueil, S. Assessment of the fragmentation energy in rock avalanches. In Proceedings of the 3rd Canadian Conference on Geotechnique and Geohazards, Edmonton, AB, Canada, 9–10 June 2003; pp. 261–268.
23. Laubscher, D. Dilution. In *Block Cave Manual, International Caving Study (1997–2000)*; International Caving Study: Brisbane, QLD, Australia, 2000.
24. Castro, R.; Arancibia, L.; Gómez, R. Quantifying fines migration in block caving through 3D experiments. *Int. J. Rock Mech. Min. Sci.* **2022**, *151*, 8–10. [CrossRef]
25. Hashim, M.; Sharrock, G. Dimensionless percolation rate of particles in block caving mines. In Proceedings of the 6th International Conference & Exhibition on Mass Mining, Massmin 2012, Sudbury, ON, Canada, 10–14 June 2012.
26. Leonardi, C.R.; Owen, D.R.J.; Feng, Y.; Ferguson, W.J. Computational modelling of fines migration in block caving operations. In Proceedings of the 5th Conference and Exhibition on Mass Mining, Lulea, Sweden, 9–11 June 2008; pp. 1063–1072.
27. Reyes, B. Caracterización de Elipsoides de Extracción con Material Cohesivo en Block/Panel Caving Utilizando Rocky Dem. Bachelor's Thesis, Universidad Técnica Federico Santa Maria, Santiago, Chile, 2021.
28. Castro, R.; Gómez, R.; Arancibia, L. Fine material migration modelled by cellular automata. *Granul. Matter* **2022**, *24*, 14. [CrossRef]
29. Flores, G. Rock Mass Response to the Transition from Open Pit to Underground Cave Mining. Ph.D. Thesis, University of Queensland, St Lucia, QLD, Australia, 2005.
30. Flores, G.; Catalan, A. A transition from a large open pit into a novel "macroblock variant" block caving geometry at Chuquicamata mine, Codelco Chile. *J. Rock Mech. Geotech. Eng.* **2019**, *11*, 549–561. [CrossRef]
31. Hungr, O.; Evans, S.G.; Bovis, M.J.; Hutchinson, J.N. Review of the classification of landslides of the flow type. *Environ. Eng. Geosci.* **2001**, *7*, 221–238. [CrossRef]
32. Strom, A. Rock Avalanches: Basic Characteristics and Classification Criteria. In *Understanding and Reducing Landslide Disaster Risk*; Springer: Cham, Switzerland, 2021; pp. 3–23. [CrossRef]
33. Strom, A.; Abdrakhmatov, K. *Rockslides and Rock Avalanches of Central Asia: Distribution, Morphology, and Internal Structure*; Elsevier: Amsterdam, The Netherlands, 2018.
34. Strom, A.; Li, L.; Lan, H. Rock avalanche mobility: Optimal characterization and the effects of confinement. *Landslides* **2019**, *16*, 1437–1452. [CrossRef]
35. Melosh, H.J. The mechanics of large rock avalanches. *Rev. Eng. Geol.* **1987**, *7*, 41–50.
36. Dubovskoi, A.N.; Pernik, L.M.; Strom, A.L. Experimental simulation of rockslide fragmentation. *J. Min. Sci.* **2008**, *44*, 123–130. [CrossRef]
37. Hungr, O.; Leroueil, S.; Picarelli, L. Varnes classification of landslide types, an update. *Landslides* **2012**, *1*, 47–58. [CrossRef]
38. Qin, S.Q.; Jiao, J.J.; Li, Z.G. Nonlinear evolutionary mechanisms of instability of plane-shear slope: Catastrophe, bifurcation, chaos and physical prediction. *Rock Mech. Rock Eng.* **2006**, *39*, 59–76. [CrossRef]
39. Sánchez, V.; Castro, R.L.; Palma, S. Gravity flow characterization of fine granular material for Block Caving. *Int. J. Rock Mech. Min. Sci.* **2019**, *114*, 24–32. [CrossRef]
40. Castro, R.; Perez, A.; Gómez, R. Evaluating Wet Muck Risk in Block Caving Mines: A New Model. *Int. J. Rock Mech. Min. Sci.* **2023**, *170*, 105485. [CrossRef]
41. Yu, K.; Zheng, C.; Ren, F. Numerical Experimental Study on Ore Dilution in Sublevel Caving Mining. *Min. Metall. Explor.* **2021**, *38*, 417–469. [CrossRef]
42. Lapčević, V.; Torbica, S. Numerical investigation of caved rock mass friction and fragmentation change influence on gravity flow formation in sublevel caving. *Minerals* **2017**, *7*, 56. [CrossRef]
43. Hidalgo, F.; Salina, I. Secondary rock ore reserve recovery using a primary rock layout: Extensión Hw Pipa Norte, a case study. In Proceedings of the Eighth International Conference & Exhibition on Mass Mining, Massmin 2020, Santiago, Chile, 9–11 December 2020; pp. 155–165.
44. Shahri, A.A.; Kheiri, A.; Hamze, A. Subsurface Topographic Modeling Using Geospatial and Data Driven Algorithm. *ISPRS Int. J. Geo-Inf.* **2021**, *10*, 341. [CrossRef]
45. Arrieta, M.; Zhang, Z.X. Particle size distribution (PSD) estimation using unmanned aerial vehicle (UAV) photogrammetry for rockfill shear strength characterization. *Acta Geotech.* **2024**, *19*, 6239–6258. [CrossRef]

46. Zhang, J.; Zhang, J. Particle size spatial distribution in landslide dams. *J. Mt. Sci.* **2024**, *21*, 1886–1903. [CrossRef]
47. Moncada, M.; Betancourt, F.; Rodríguez, C.G.; Toledo, P. Effect of Particle Shape on Parameter Calibration for a Discrete Element Model for Mining Applications. *Minerals* **2023**, *13*, 40. [CrossRef]
48. Cundall, P.A.; Strack, O.D.L. A discrete numerical model for granular assemblies. *Geotechnique* **1979**, *29*, 47–65. [CrossRef]
49. Hancock, W. Gravity Flow of Rock in Caving Mines: Numerical Modelling of Isolated, Interactive and Non-Ideal Draw. Ph.D. Thesis, University of Queensland, St Lucia, QLD, Australia, 2013.
50. Weatherley, D.; Boros, V.; Hancock, W.; Abe, S. Scaling benchmark of ESyS-Particle for elastic wave propagation simulations. In Proceedings of the 6th IEEE International Conference on e-Science, Brisbane, OLQ, Australia, 7–10 December 2010; pp. 277–283.
51. Emery, X.; Séguret, S.A. *Geostatistics for the Mining Industry: Applications to Porphyry Copper Deposits*, 1st ed.; CRC Press: London, UK, 2020. [CrossRef]
52. Shahri, A.A.; Chunling, S.; Larsson, S. A hybrid ensemble-based automated deep learning approach to generate 3D geo-models and uncertainty analysis. *Eng. Comput.* **2024**, *40*, 1501–1516. [CrossRef]

mining

MDPI

Article

Experimental Investigation into Deploying a Wi-Fi6 Mesh System for Underground Gold and Platinum Mine Stopes

Brenton Lloyd Chetty [1,2,*], Tom Mmbasu Walingo [1], Carel Phillip Kruger [2] and Sherrin John Isaac [2]

1 Department of Electrical, Electronic and Computer Engineering, University of KwaZulu-Natal, Durban 4041, South Africa; walingo@ukzn.ac.za
2 Next Generation Enterprises and Institutions, Council for Scientific and Industrial Research, Pretoria 0001, South Africa; ckruger1@csir.co.za (C.P.K.); sisaac@csir.co.za (S.J.I.)
* Correspondence: 214500040@stu.ukzn.ac.za

Abstract: Stopes suffer from unreliable wireless communication due to their harsh environment. There is a lack of confidence within industry regarding the effectiveness of existing solutions in providing reliable high-bandwidth performance in hard rock stopes. This work proposes that Wi-Fi6 is a good candidate for reliable high-bandwidth communications in underground hard rock stopes. Experiments in a tunnel and mine stope were conducted to evaluate the performance of Wi-Fi6 in terms of latency, jitter, and throughput. Different criteria, such as multi-hop systems, varying multipath, mesh routing protocols, and frequencies at different bandwidths, were used to evaluate performance. The results show that Wi-Fi6 performance is greater in stopes compared to tunnels. Signal quality evaluations were conducted using the Asus RT-AX53U running OpenWrt, and an additional experiment was conducted on the nrf7002dk running Zephyr OS to evaluate the power consumption of Wi-Fi6 against the industry standard for low-powered wireless communications, IEEE 802.15.4. Wi-Fi6 was found to be more power-efficient than IEEE 802.15.4 for Mbps communications. These experiments highlight the signal robustness of Wi-Fi6 in stope environments and also highlights its low-powered nature. This work also highlights the performance of the two most widely used open-source mesh routing protocols for Wi-Fi.

Keywords: B.A.T.M.A.N.; HWMP; jitter; latency; multipath; OpenThread; stope; throughput; Wi-Fi6

Citation: Chetty, B.L.; Walingo, T.M.; Kruger, C.P.; Isaac, S.J. Experimental Investigation into Deploying a Wi-Fi6 Mesh System for Underground Gold and Platinum Mine Stopes. *Mining* **2024**, *4*, 567–587. https://doi.org/10.3390/mining4030032

Academic Editors: Krzysztof Skrzypkowski, René Gómez, Fhatuwani Sengani, Derek B. Apel, Faham Tahmasebinia and Jianhang Chen

Received: 23 June 2024
Revised: 14 August 2024
Accepted: 15 August 2024
Published: 17 August 2024

1. Introduction

A high-bandwidth wireless solution would be of significant value in modern mining operations to enhance efficiency, safety, and productivity. They enable the real-time transmission of critical data, ensuring that information from various sensors and monitoring devices is swiftly communicated to control centres and decision-makers. This immediacy supports advanced automation technologies, allowing for the precise remote control of machinery and vehicles, and the seamless operation of automated processes. Furthermore, a high-bandwidth infrastructure ensures rapid and reliable safety communications, which is vital for protecting workers in the hazardous stope environment. It allows for instant alerts and emergency responses, enhancing the overall safety of mining operations. Additionally, a high-bandwidth infrastructure supports comprehensive data analysis, where the data can be analysed to optimize operations and inform strategic decisions. By leveraging a high-bandwidth wireless infrastructure, mining companies can significantly improve their operational effectiveness, reduce risks associated with equipment failures and environmental hazards, and achieve better overall performance, ultimately leading to increased productivity, profitability, and safety for stope activities. An example of an application could be the transmission of LiDAR data from robots to facilitate automation, mapping terrain, detecting potential obstacles, and determining safe pathways in real-time. These automated robots could be used to calculate the ideal locations to place dynamite in a stope, as well as facilitating the installation of the dynamite instead of using people, thus reducing risk to human lives. Another example could be the transmission of thermal and acoustic data to a processing node to identify loose rocks and trigger alarms if the area is unsafe. The transmission and analysis of geophone or accelerometer data could also be used to detect seismic activity and trigger appropriate alarms. Other applications include maintaining communication infrastructure; environmental monitoring using gas, temperature, and humidity sensors; and equipment monitoring to ensure high efficiency and safety. Due to the critical nature of these applications, the communication infrastructure would need to have excellent levels of jitter and latency; and if high-bandwidth applications such as LiDAR signal transmissions or geophone analysis are required then the infrastructure would need to support excellent levels of jitter and latency whilst transmitting at very high bandwidths.

The number of studies on wireless communication in stopes is extremely limited. While various technologies have been proposed for tunnels and soft rock mines such as coal mines [1,2], none have emerged as a mainstream solution for hard rock stopes such as the underground gold and platinum stope environment. Underground gold and platinum mine stopes are seen as much harsher environments due to their small size (approximately 1.5 m in height and 20 m in width), rough surfaces, as well as their irregular shape due to the requirement of blasting for hard rock mines, and frequent path blockages due to support pillars as well as large metallic mining equipment. Gold and platinum mines are also several kilometres underground; thus, it is vital to have an energy efficient system to prevent unnecessary battery replacements as it is not feasible to store large numbers of batteries underground due to health and safety reasons. To develop the best possible wireless solution for underground mine stopes, the technology would need to support high data rates for productivity-enhancement applications, low-power consumption to reduce battery replacements, and robustness to cope with the harsh stope environment.

Underground mines are dynamic, with each having peculiar conditions. They continue to involve extreme occupations in very hazardous environments, such as vehicle accidents, roof falls, fire, explosions, the release of toxic gases, and floods. Hard rock mines, particularly gold and platinum mine stopes, are very harsh environments. Mineral excavation in hard rock stopes is characterized by the usage of explosives. Due to the narrow and short nature of stopes and their rough, rocky surfaces, the wireless signals undergo excessive amounts of signal reflections and scatterings. For home usage, Wi-Fi signals can pass through layers of brick or blocks; however, in underground mines, wireless signals cannot pass through the thick layers of dense rock; thus, the signals are contained within a stope, which significantly increases the possibility of destructive interference alongside excessive multipath propagation. Wireless transmissions in confined areas tend to experience more multipath propagation as compared to spacious areas. In confined areas, the reflected signals have a much greater potential to interact with each other, and there is also the increased possibility of causing distortions, such as fading, ghosting, or signal dropout. For these reasons, stopes are seen as a difficult environment for wireless communications. Stopes are very small in size, and it is not feasible to install excess amounts of cabling in this environment as it would pose many health and safety risks. Cabling should be limited to high-powered equipment that are critical to the operation of the mine. A wireless solution is considered the most viable option for such an environment.

Coded Orthogonal Frequency Division Multiplexing (COFDM) has been identified as a promising technology for addressing the harsh conditions of underground hard rock stopes. This technology is well known for its role in the transformation of the terrestrial broadcasting domain [3,4]. However, the prohibitive cost associated with COFDM equipment limits its widespread adoption in the mining industry. In [5], Wi-Fi6 was shown to offer similar signal robustness as COFDM, However, the experiments were performed in a non-ideal office corridor. This work expands on [5] by performing the Wi-Fi6 experiments in a test stope. Additional experiments were also performed to give a more comprehensive analysis of Wi-Fi6 signal performance in a stope. The signal quality evaluations were performed on an Asus RT-AX53U using the open-source OpenWrt OS with open-source mesh routing protocols, namely B.A.T.M.A.N.-adv [6] and HWMP [7]. The industry standard for low-powered wireless communications was identified as IEEE 802.15.4 [8]. OpenThread was selected as the IEEE 802.15.4 variant. Wi-Fi6 was identified as the potential candidate for stope communications due to its potential for reliable high-bandwidth communications and power efficiency. This work compared the power consumption of Wi-Fi6 vs. OpenThread by using an identical setup. The nRF7002dk was used alongside Zephyr OS, since it supported both Wi-Fi6 and OpenThread. By using the same boards, same OS, same transmission frequencies, and same input voltage, we were able to achieve the accurate power consumption comparisons of the protocols.

2. Related Work

Due to the importance of communication in mining environments, wireless communication solutions have been developed and performance experiments have been conducted for different mining areas and categories in real mining environments [9]. Due to the costs of testing equipment, the unavailability of mining test sites, and the difficulty in experimental applications, practical mine test experimental results are wide and few, and this is especially true for underground gold and platinum mine stopes. In [10], an experimental study of the Line-of-Sight Millimetre-Wave Underground Mine Channel was conducted. In [11], experimental results for Zigbee in an underground mine are presented. The authors of [12] study Multiple-Input and Multiple-Output (MIMO) antenna configurations for underground mine communication and present measurements for a gold mine. Ref. [13] presents experimental results obtained from narrowband and wideband radio-channel measurements in an underground mine at 2.4 GHz. Ref. [14] explores and tests a smart phone network for communicating sensor data from the underground production environment to the surface, in a tunnel, stope, and shaft.

Power consumption is one of the major considerations for underground mine applications. The major drawbacks of high bandwidth wireless communications are that of high-power consumption as well as the inability to cope with excessive multipath propagation [15]. Low-power Wi-Fi6 systems have emerged as a potential candidate for the underground mine stope. Ref. [16] presented an empirical study of Wi-Fi performance where aerial-ground robots could be used to map, navigate, and search in an unknown underground environment in the experimental mine of the Colorado School of Mines. Laptops were used to represent the robots. The results show that the signal throughput drops significantly over large distances within line of sight and is non-existent around a corner. Ref. [17] performed measurements for mining Wi-Fi vehicle-to-vehicle (V2V) communication to be utilized in a tunnel to increase the safety and productivity of the transportation of mining goods. Furthermore, a signal performance analysis between COFDM [18] vs. Wi-Fi6 (IEEE 802.11ax) [19] demonstrated the potential performance of Wi-Fi6 for the underground mine stope [5]. In [5], the Asus RT-AX53U Wi-Fi6 device was compared with the SOL8SDR COFDM device. In this paper, Wi-Fi6 was shown to be more power efficient than the current industry standard of low power communications, IEEE 802.15.4 [8]. Even though Wi-Fi6 uses more peak power to transmit data, the total power consumed for sending data is much less due to the shorter transmission durations. The idle power consumption for both Wi-Fi6 and IEEE 802.15.4 (OpenThread [20]) were roughly the same.

It is also important to incorporate a mesh topology for stope communications due to its ability to enable multiple pathways between nodes and ease of network extensions and strategic node placement. Furthermore, a critical component of mesh topologies is its mesh routing protocol. These protocols are generally summarized into reactive and proactive protocols. For proactive routing protocols, every node keeps a current list of routes, and examples include the Optimized Link State Routing (OLSR) [21] and Destination-Sequenced Distance Vector (DSDV) [22]. For reactive routing protocols, the routes are only set up when necessary, and examples include Ad Hoc On-Demand Distance Vector (AODV) [23] and Dynamic Source Routing (DSR) [24]. In [25], the throughput of proactive routing was better than reactive routing with multipath fading. This research extends this by practically experimenting the performance of a decentralized proactive mesh routing protocol (B.A.T.M.A.N. advanced) vs. the hybrid approach of using both proactive and reactive routing (e.g., HWMP). For the highly regulated mining environment, where mining equipment is notably costly and typically vendor-controlled, there exists a compelling need for cost-effective alternatives to proprietary solutions. One such alternative is the adoption of a mesh system employing an open-source mesh routing protocol, such as the Hybrid Wireless Mesh Protocol (HWMP) or the Better Approach To Mobile Ad Hoc Networking—advanced (B.A.T.M.A.N.-adv) protocol. Renowned for their versatility and widespread adoption, these protocols offer the advantage of extended system lifespans, as a result of their continual development within the open-source community. This strategic shift not only mitigates cost concerns but also enhances adaptability and long-term viability within the mining infrastructure. To our knowledge, an experimental investigation of these two protocols has not been conducted in terms of multi-hop performance for the harsh underground gold and platinum stope environments. The performance of these protocols needs to be investigated for this type of stope environment; this is undertaken in this work.

3. Aim

The aim of this work is to demonstrate that Wi-Fi6 can offer reliable high-bandwidth performance in an underground hard rock stope using open-source mesh routing protocols, namely B.A.T.M.A.N.-adv and HWMP. This will be achieved by obtaining the fundamental characteristics of wireless performance, namely throughput, jitter, and latency results, in a stope and comparing them with the results from a more spacious tunnel which is considered a friendlier environment for wireless communications. The aim of this work is also to demonstrate that the Wi-Fi6 power efficiency rivals that of the industry standard for low-powered wireless communications, namely IEEE 802.15.4.

4. Scope of Work

This work develops experimental measurement results for the following:

- Performance of Wi-Fi6 in a test simulation mine developed with the intention of providing an easily accessible environment which closely resembled the conditions of a real mine with a stope. The experiments were conducted in a high multipath stope environment as well as a low multipath spacious tunnel environment within the mine to evaluate the impact of excessive multipath propagation on Wi-Fi6.
- The performance parameters of throughput, jitter, power consumption, and latency were considered. Different criteria such as the effects of channel bandwidths, transmission frequencies, mesh routing protocols, transport layer protocols, and multi-hop impact on the signal performance were investigated.
- The performance comparison of Wi-Fi6 and IEEE 802.15.4 (OpenThread) in terms of power consumption was performed. The experiment setup features the nRF7002dk alongside the Zephyr operating system transmitting at a frequency of 2.4 GHz. The results indicated that even though Wi-F6 has a greater instantaneous power consumption, its overall power consumption is much lower than that of OpenThread due to the shorter transmission times. The idle power consumption of both protocols was noted as being very similar.
- The performance comparison of HWMP and B.A.T.M.A.N.-adv routing protocols in terms of reactive and proactive routing for stope environments. The experimental test bed featured the open-source OpenWrt OS installed in the Wi-Fi6 nodes which were configured using the IEEE 802.11s mesh standard. The results indicate that even with the increased overhead of HWMP, it still outperforms B.A.T.M.A.N.-adv for stope environments.
- The throughput, latency, and jitter performance of the protocols was surprisingly found to be better in a stope than a spacious tunnel. This was attributed to the Wi-Fi6

technology taking advantage of the waveguide nature of a stope and its ability to efficiently handle the multipath signals.

5. Characteristics of the Applied Communication Technologies for the Underground Mine Stope

5.1. Wi-Fi6

Wi-Fi has evolved drastically over the years. Wi-Fi1 initially introduced Direct Sequence Spread Spectrum (DSSS) modulation [26], which spread a signal over a wider bandwidth as compared to its original size. This approach of spreading data reduced the effects of interference from other signals or noise, making the communication more robust. Wi-Fi2 uses Orthogonal Frequency Division Multiplexing (OFDM) [27], which enabled multi-user capabilities by allocating subcarriers to individual clients. For OFDM, the entire subcarrier could only be allocated to a single client. Wi-Fi3 uses the concept of channel bonding [28], which allows adjacent 20 MHz channels to be combined to create wider 40 MHz channels. This can effectively double the data throughput under optimal conditions. Wi-Fi4 applies Multiple-Input Multiple-Output (MIMO) technology [27], which allows for multiple streams of data to be transmitted simultaneously via multiple antennas. This improved spectral efficiency and greatly improved throughput. Wi-Fi5 introduced Multi-User MIMO (MU-MIMO) [29] for simultaneous data transmission to multiple clients. For MIMO, each antenna pair served a single client, whilst MU-MIMO serves multiple clients concurrently by spatially multiplexing the data streams. Whilst MIMO focused primarily on improving the performance of a single client, MU-MIMO enables simultaneous communication with multiple clients, thereby increasing overall network performance. Wi-Fi6 uses Orthogonal Frequency Division Multiple Access (OFDMA) [30] for improved efficiency in high-density environments. Wi-Fi6 also introduced BSS colouring [31], which is used to address co-channel interference. This helps devices make better decisions regarding channel access, hence reducing collisions and improving overall network efficiency in high-density environments. Due to the low-powered nature of Wi-Fi6, the devices can be installed in certain allocated points in stopes without being a burden to the miners. All these properties make Wi-Fi6 a good candidate for stopes.

Wi-Fi6 implements several technologies to address the concerns of multipath interference. Wi-Fi6 uses OFDMA, which allows for a single channel to be divided into smaller sub-channels known as Resource Units (RUs) [32]. These RUs can be transmitted to different users simultaneously, thus allowing for the increased utilization of the available spectrum, hence reducing the impact of multipath interference. Wi-Fi6 also introduced techniques such as BSS colouring with spatial frequency reuse [33] which enables multiple devices within close proximity to communicate simultaneously whilst limiting interference. This spatial reuse capability helps mitigate the effects of multipath interference by allowing the more efficient use of the available spectrum. Although MU-MIMO was introduced in Wi-Fi5; Wi-Fi6 expanded its capabilities by supporting MU-MIMO in both uplink and downlink transmissions. This functionality enables multiple devices to simultaneously receive and transmit data, even in environments with excessive multipath interference, by using multiple antennas to spatially separate the signals [34]. Wi-Fi6 also utilizes an improved beamforming technique, which enhances the reliability and efficiency of transmissions by directing signals towards the intended recipients [35]. For these reasons, Wi-Fi6 has become the perfect low-cost candidate for mine stope communications.

Previous research [5] has shown that COFDM offers slightly better signal robustness as compared to Wi-Fi6, which would have made COFDM the ideal choice for a stope. However, the cost of a COFDM device is much greater than that of a Wi-Fi6 device. Wi-Fi6 devices are substantially cheaper than COFDM devices whilst offering similar signal robustness. Wi-Fi6 devices also had substantially greater throughput than COFDM devices. The reason why Wi-Fi6 is so desirable for stopes is because the technology is mainstream, which prevents overly inflated prices. COFDM devices are expensive due to their niche market and limited consumer demand for the technology, i.e., a situation where a few vendors can dictate the price of the COFDM devices. Stopes are very harsh environments, where devices frequently become damaged. Due to the low cost of Wi-Fi6 devices, they are considered expendable whilst giving more emphasis to productivity. Whereas previous Wi-Fi generations focused mainly on speed improvements, Wi-Fi6 mainly focused on improved spectral efficiency, making it a good contender for a mine stope. Due to its characteristics, it is capable of dealing with harsh environments such as the underground gold and platinum mine stopes. Therefore, the practical performance of Wi-Fi6 needs to be investigated.

5.2. OpenThread

IEEE 802.15.4, alongside its variants, is well known for its place as the industry standard for low-powered wireless communications [8]. Its low power consumption makes it ideal for battery-operated devices and sensors, ensuring prolonged operation without frequent maintenance or battery replacements. OpenThread [36], an open-source implementation of the thread networking protocol, is an IEEE 802.15.4 variant that was engineered specifically for low-rate wireless personal area networks (LR-WPANs) [37]. OpenThread incorporates highly efficient modulation schemes optimized for long-range communication and minimal power consumption. Leveraging Offset Quadrature Phase Shift Keying (O-QPSK) [38], OpenThread achieves lower data rates tailored to the demands of Internet of Things (IoT) applications, distinguishing itself from the Quadrature Amplitude Modulation (QAM) utilized by Wi-Fi [39] within the same 2.4 GHz spectrum, albeit with reduced throughput. O-QPSK was primarily designed to reduce the peak-to-average power ratio (PAPR) in the transmitted signal [40]. By staggering the phase changes of the in-phase and quadrature components, O-QPSK ensures that the phase changes are more gradual compared to traditional QPSK. This results in a more constant envelope signal, which is easier for power amplifiers to handle efficiently without significant distortion. The authors of [41] demonstrate the low-powered nature of O-QPSK through the simulation of 180 nm, 90 nm, and 45 nm CMOS technologies and attempt to improve the power efficiency through reframing using a booth multiplier. This modulation scheme, combined with OpenThread's mesh networking capabilities, provides reliable and resilient communication by allowing devices to connect through multiple pathways, which is particularly advantageous in harsh and obstructed environments; however, its low throughput is a significant limitation. An experimental performance comparison of OpenThread and Wi-Fi6 is necessary to determine the feasibility of deployment of the two for the underground gold and platinum stope environments.

5.3. Mesh Routing Protocols

The Hybrid Wireless Mesh Protocol (HWMP) is the default mesh routing protocol for IEEE 802.11s. HWMP offers a combination of proactive routing (where nodes maintain routing tables with precalculated paths) and reactive routing (where routes are discovered on-demand) [7]. HWMP is an adaptation of the reactive Ad Hoc On-demand Distance Vector (AODV) routing protocol [42] called Radio-Metric AODV (RM-AODV) [43]. AODV operates in the IP layer and uses the hop count as its routing metric, whilst RM-AODV operates in the MAC layer and uses the radio-aware routing metric for its path selection.

The Better Approach To Mobile Ad Hoc Networking (B.A.T.M.A.N.) [6] protocol is a proactive mesh routing protocol. The main contribution of the B.A.T.M.A.N. mesh protocol was the decentralization of knowledge regarding the complete route of a message chain, from start to finish. A node in the network will not attempt to determine the complete path of the message it is passing, but rather it will only determine its best next hop towards the destination. The version known as B.A.T.M.A.N.-adv was used for this research. This version of B.A.T.M.A.N. operates in the MAC layer.

An experimental performance comparison of HWMP and B.A.T.M.A.N is necessary to determine the deployment of the two in different stope environments. Unfortunately, the short length of stopes limits the number of hops deployed to a minimum of three, considering the range of the deployed Wi-Fi6 systems.

6. Mine Layout

The layout of an underground platinum mine where room and pillar mining is being used, as shown in Figure 1. The tunnel is used to facilitate movement of machinery, personnel, and equipment, as well as ventilation and the removal of ore. A stope is the area where excavation and expansion occur. Stopes are within a room, a previously mined area, and the room is within a panel. Support structures are installed to stabilize the room whilst the stope is expanded. The entrance to the room is through a small tunnel called gully.

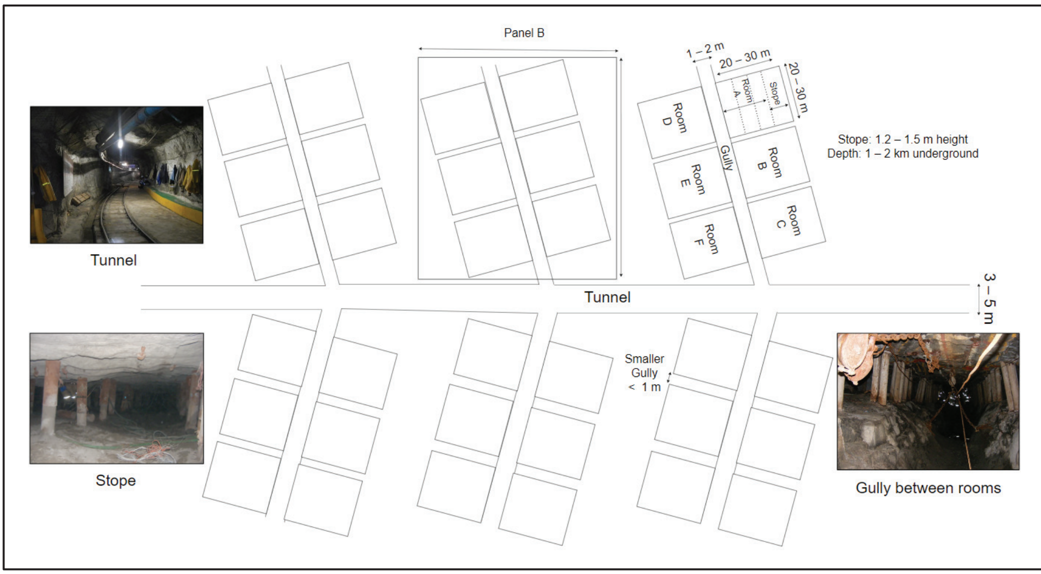

Figure 1. Mine layout.

7. Stope Characteristics

A stope in an underground hard rock mine is an area where blasting occurs; thus, it is the area of mine expansion and where the extraction of ore takes place. Figure 2 shows the stope, where support structures were installed to support the stope and prevent the collapsing of the stope. The stope is around 1.5 m in height and 20 m in width. The depth varies as the stope expands. The rooms, gulleys, etc., feature heavy machinery, ventilation pipes, and many other obstacles. All these obstacles present communication challenges.

The depth of a stope continually expands, necessitating the need for a dynamic mesh network. This area is very harsh for wireless communications as signals experience excessive contained reflections, resulting in great deal of signal attenuation due to the destructive interference that occurs as a result of the thick, layered walls and the large machinery deployed for mining. A wireless mesh system is suitable for ease of adaptability, route redundancy, and extensions required for such a system. The environment in a stope features high seismic activities, temperature, and humidity levels. This results in frequent breakdowns in communication system equipment, requiring a flexible ad hoc network communication system. A stope is also continuously expanded to areas rich in ore. As node distances increase, so does the path loss. A robust, low-powered, small-sized, self-healing wireless mesh system with ad hoc capabilities is required for a stope.

Figure 2. The stope.

8. Mine Wireless Communication Topology

Figure 3 shows the proposed mesh network topology for the mine stope. This architecture is universal by nature and should be adapted according to the specifications of the intended stope. The distance between nodes should be varied according to a stope's dimensions and characteristics. For short tunnels, the use of intermediate nodes is not encouraged, and they are only used as backup in the event of blocked nodes. A maximum of two to three hops is usually utilized. Research has shown that it is more efficient to transmit data via Wi-Fi6 over a long distance between two nodes directly rather than having additional repeater nodes installed with shorter wireless hops [5]. The nodes should be used for forwarding data packets to/from the client devices and the gateway node. The gateway node acts as a sink node which is used for processing the data. The gateway node is connected to the first node via a wired connection and is installed in an area a considerable distance away from the harsh stope environment. The wired cable should be installed in the gully. The whole system forms a mesh communication wireless network for a stope.

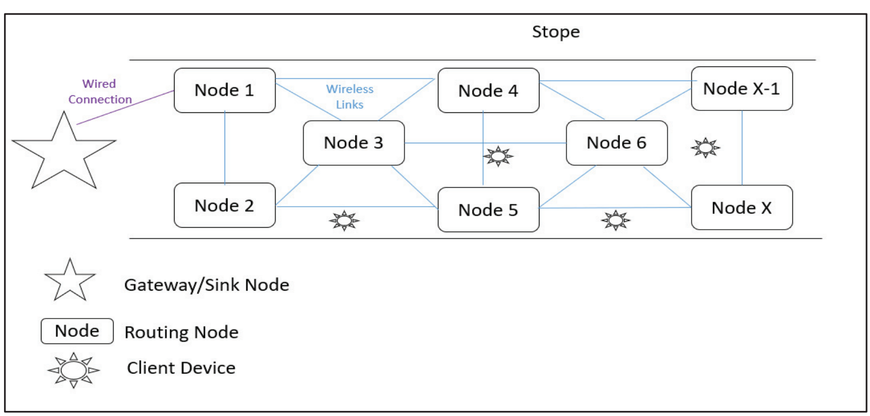

Figure 3. Wi-Fi6 intended deployment for a stope.

9. Materials and Methods

9.1. The Node Hardware

The nodes consisted of Wi-Fi6 routers for our signal quality experiments. The Asus RT-AX53U router was chosen for its ease of accessibility, low-cost, and support of the open-source OpenWrt [44] operating system. The Asus RT-AX53U is a 2 × 2 dual-band Wi-Fi6 router that provides 80 MHz channel bandwidth and 1024 QAM for fast wireless transmissions. The device was limited to an 80 MHz channel bandwidth due to an OpenWrt limitation. It supports OFDMA, BSS Colouring, and two spatial streams, which allows it to cope well with multi-hop performance in a stope environment. The throughput and jitter results were recorded using the iperf3 utility within OpenWrt, whilst the latency was obtained using the ping utility within OpenWrt. The utilized topology for signal quality evaluation is shown in Figure 4.

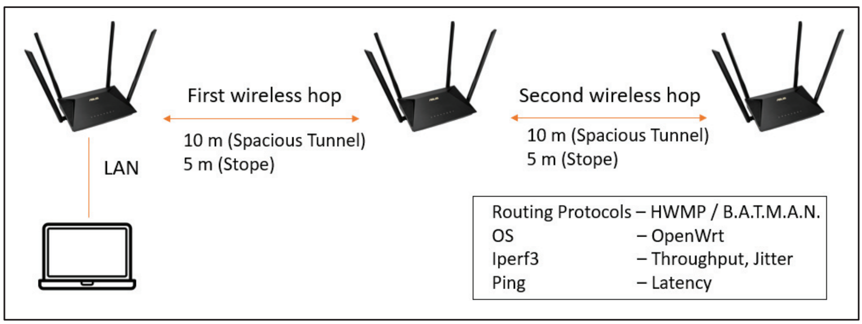

Figure 4. Asus RT-AX53U Wi-Fi6 router.

To achieve an accurate power consumption comparison, the nRF7002dk [45] device was used to evaluate both Wi-Fi6 and OpenThread protocols. The nRF7002dk is shown in Figure 5. The nRF7002dk was flashed with an open-source operating system known as Zephyr OS [46]. The boards were configured to transmit data via the 2.4 GHz channel for both protocols. By using the same OS, same transmission frequency, same input voltage, and same development kits, accurate power consumption comparison was achieved. The power evaluation setup is shown in Figure 5.

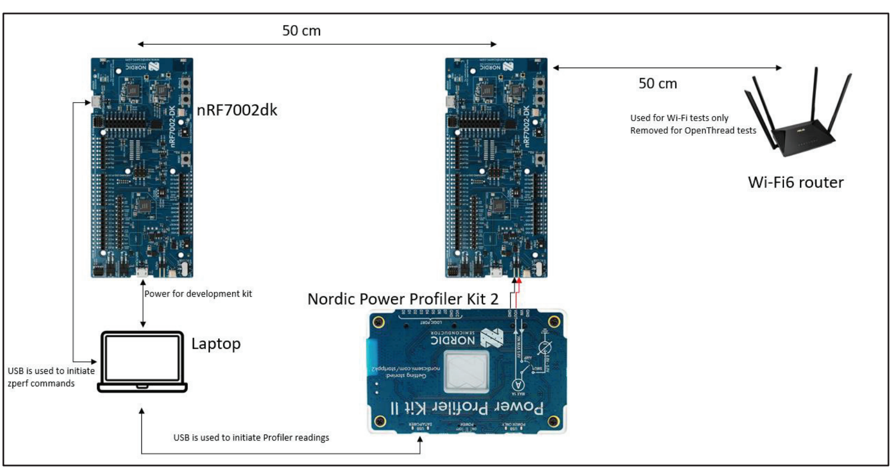

Figure 5. Power evaluation setup.

The Nordic Power Profiler Kit 2 (PPK2) was used to analyse the power consumption of the nRF7002dk. The PPK2 provides measurement with a resolution of 0.2 µA and allows for sampling at 100 KHz. Zephyr's zperf utility was used to transmit data at specific throughput values. The PPK2 was then used to record the power consumption for the different transmission rates. Nordic Power Profiler software [47] was used to analyse power consumption. The PPK2 powered the nRF7002dk with 3.3V for both of the Wi-Fi6 and OpenThread tests. The PPK2 only recorded the power consumption of the nRF7002dk that it was connected to during each test. At the time of performing the experiments, Zephyr OS did not support Wi-Fi directly, so an additional Wi-Fi6 router was used for the Wi-Fi6 test, but the results are still accurate since the receive power was obtained directly from the nRF7002dk and the transmit power was also obtained directly from the nRF7002dk during transmissions. The two nRF7002dk boards alternated between being transmitters and receivers. The PPK2 recorded the power consumption that the development kits used to send/receive 10 MB of data at different transmission rates. Each test case was performed several times, and the average results were recorded.

9.2. Test Environment

The performance comparison experiments to determine the effects of multipath fading were performed in a spacious tunnel (Figure 6), where there is less multipath, as well as a test stope (Figure 7), where there is severe multipath.

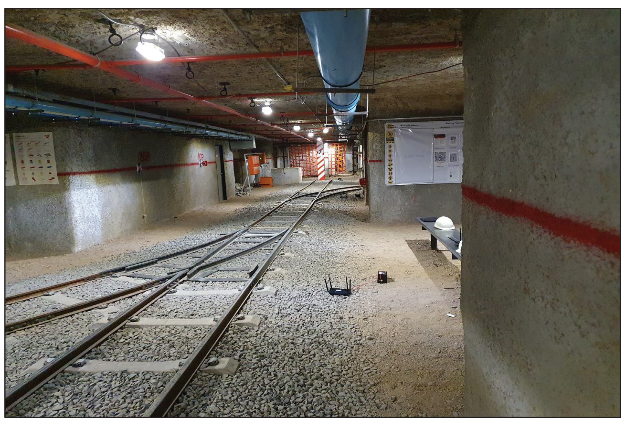

Figure 6. Test mine tunnel.

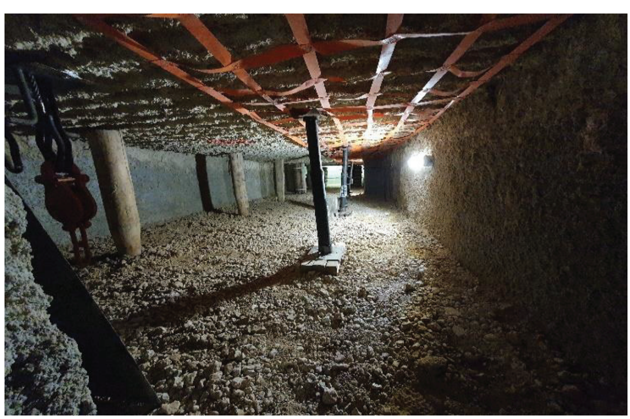

Figure 7. Stope.

The general experimentation parameters are shown in Table 1.

Table 1. General experimental parameters.

Hardware	Asus RT-AX53U, nRF7002dk, Nordic Power Profiler Kit 2
Software	OpenWrt, Zephyr OS, iperf3, zperf, ping, Nordic Power Profiler software
Frequency	2.4 GHz and 5 GHz
Node distance	5 m (stope) 10 m (spacious tunnel) 0.5 m (nRF power evaluations)
Routing protocols	HWMP (hybrid of reactive and proactive) B.A.T.M.A.N.-adv (proactive)
Packet size	Default iperf3 OpenWrt values (128 KB TCP, 1460 B UDP) 1 KB (nRF power evaluations)
Sample Rate	100 KHz (nRF power evaluations)

10. Results

10.1. Mesh Throughput Results

The average TCP and UDP throughput results for the tunnel as well as the stope are shown in Figure 8. Transmissions were automatically recorded at 1 s intervals, and a total of 120 samples were recorded for each test case. Each test was performed three times, after which the average throughput was calculated. The 2.4 GHz experiments in the tunnel proved ineffective in a multi-hop scenario due to the limitation of a 40 MHz channel bandwidth; hence, only the 5 GHz experiments were performed in the stope.

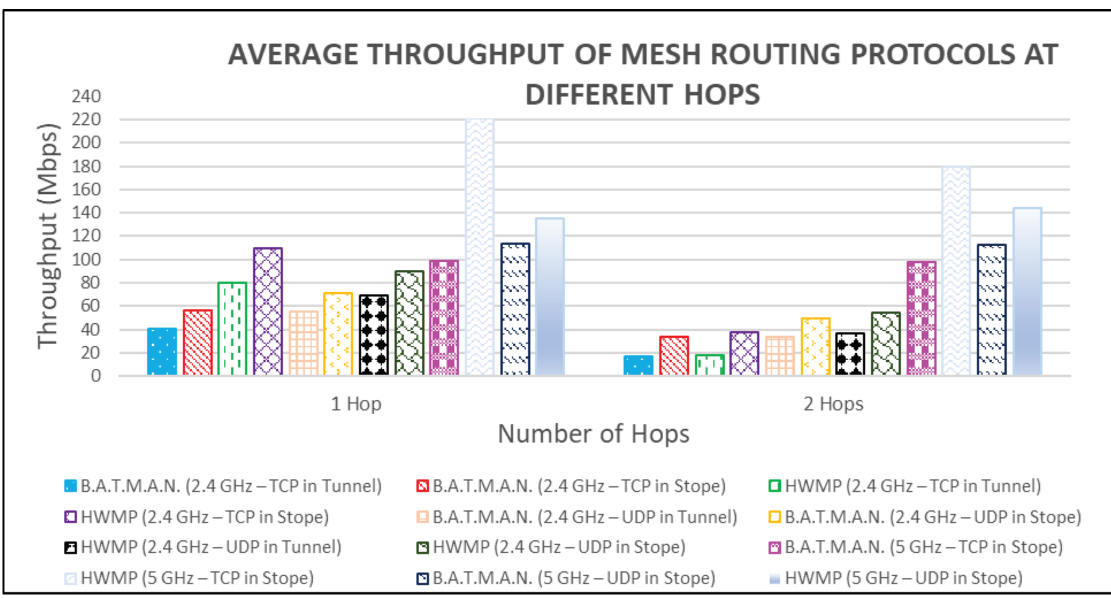

Figure 8. Average Wi-Fi6 throughputs for tunnel and stope.

Figure 9 shows the samples used to calculate the average results that were utilized in Figure 8. Each of the 120 samples from Figure 9 were averages calculated from three separate test cases.

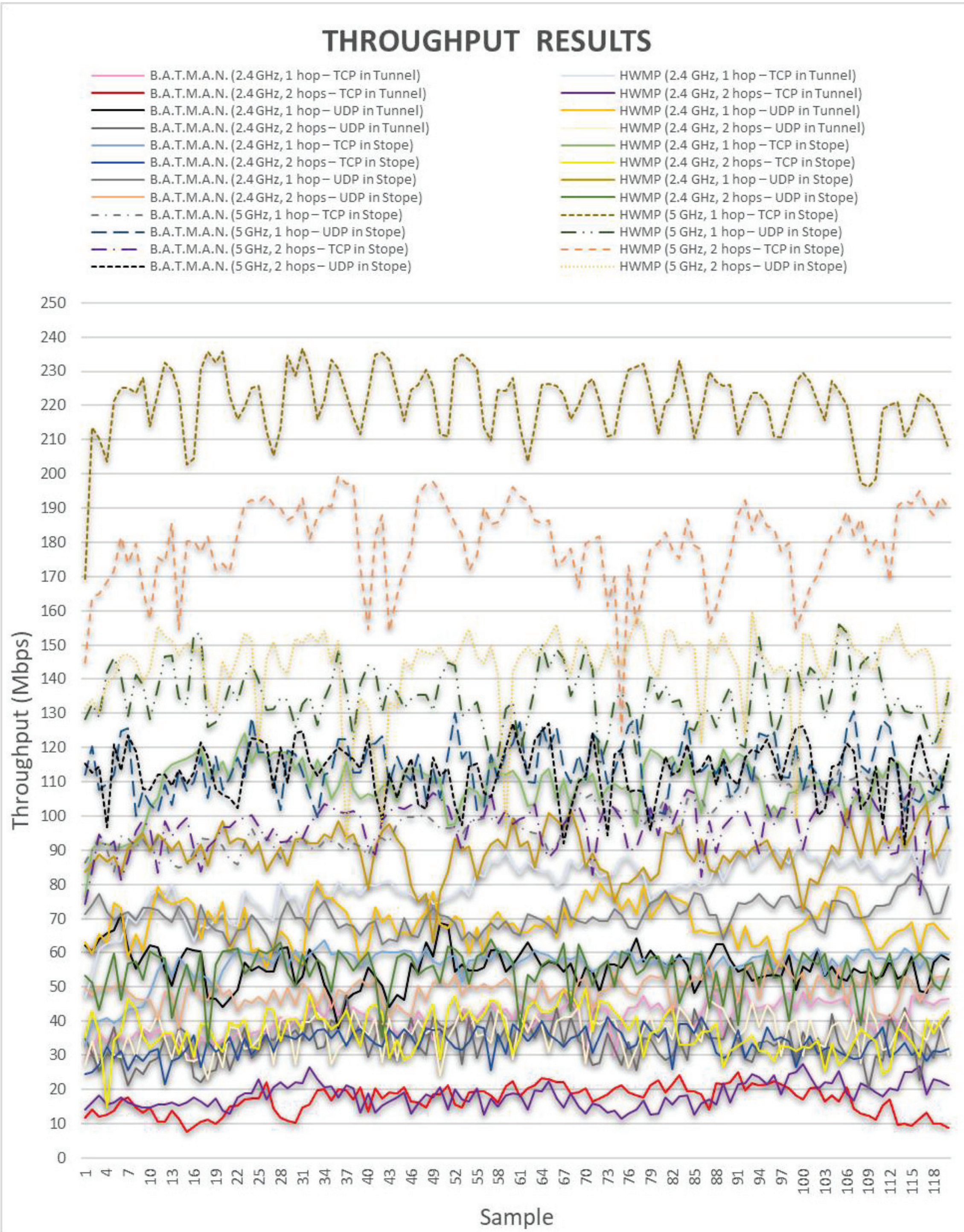

Figure 9. Wi-Fi6 sample throughput.

10.1.1. Frequency and Channel Bandwidth

At 2.4 GHz, the single hop throughput was significantly better than the double hop throughput. However, at 5 GHz, the single hop throughput was marginally better than the double hop throughput with the exception of HWMP UDP throughput in a stope, which was greater with a double hop. Static hops were assigned to ensure that a wireless hop did occur to ensure accurate results. To confirm the root cause behind the vast difference in multi-hop performance between the 2.4 GHz and 5 GHz experiments, an additional experiment was conducted. Multi-hop performance was recorded at different channel bandwidths, and the results are given in Table 2. The 5 GHz multi-hop experiments performed well due to it utilizing an 80 MHz channel bandwidth, whilst the 2.4 GHz experiments performed poorly due to its utilization of a 40 MHz channel bandwidth. For HWMP transmitting at 5 GHz, at a 20 MHz channel bandwidth, there was 50% loss of throughput across a wireless hop; at a 40 MHz channel bandwidth, there was 43% loss of throughput across a wireless hop; and at an 80 MHz channel bandwidth, there was 14% loss of throughput across a wireless hop. The higher channel bandwidth, alongside BSS Colouring, OFDMA, and beamforming, allowed for the efficient use of the spectrum, which enabled Wi-Fi6 to utilize the waveguide effect provided by the stope to enhance the signal quality rather than attenuating the signal.

Table 2. HWMP multi-hop performance using various channel bandwidths at 5 GHz.

CONFIGURATION	20 MHz	40 MHz	80 MHz
1 hop TCP	120 Mbps	210 Mbps	220 Mbps
2 hops TCP	60 Mbps	120 Mbps	190 Mbps
1 hop UDP	140 Mbps	140 Mbps	140 Mbps
2 hops UDP	80 Mbps	130 Mbps	130 Mbps

Table 2 shows the multi-hop performance which was recorded at different channel bandwidths.

10.1.2. Stope vs. Tunnel

The results also indicate that the throughput performance of both mesh routing protocols in the stope was better than in the tunnel. This is contrary to the previous belief that wireless communications suffer from degradation due to the nature of stopes. With Wi-Fi6's introduction of OFDMA, BSS Colouring, and MU-MIMO in both uplink and downlink, as well as improved beamforming technologies, it has become much smarter, with the ability to cope in high-density environments. This capability has resulted in Wi-Fi6 being able to make much more efficient use of the spectrum, which allows it to utilize the benefits of the waveguide affect provided by a stope. Wi-Fi6 recognizes and uses the waveguide properties of a stope to its advantage, improving signal quality and the resulting throughput results compared to the open tunnel.

10.1.3. UDP vs. TCP

The results also indicate that for both mesh routing protocols, a double hop resulted in better UDP performance as compared to TCP. This can be attributed to TCP's handshake acknowledgement packets being lost across wireless hops, which would result in retransmissions leading to a decrease in throughput. For single hop throughput performance, HWMP performed better with TCP, since there was a low risk of acknowledgement packets being lost due to no extra hops being required. B.A.T.M.A.N.-adv performed better with UDP for both single and double hops. This can be attributed to the B.A.T.M.A.N.-adv protocol's decentralized proactive nature.

10.1.4. HWMP vs. B.A.T.M.A.N.-Adv

The throughput performance of HWMP was better than B.A.T.M.A.N.-adv for all tests. This can be attributed to HWMP's utilization of a hybrid approach which uses both reactive and proactive mesh routing whilst B.A.T.M.A.N. only uses proactive mesh routing. The reactive component proved to be worth the expense of the additional overhead.

10.2. Mesh Jitter Results

The average jitter results for the tunnel as well the stope are shown in Figure 10. The jitter values were obtained from the iperf3 UDP throughput results, and the average values was calculated and plotted accordingly. The results show that the 5 GHz experiments performed the best for both B.A.T.M.A.N. and HWMP. The results were also better in the stope for both mesh routing protocols. The stope provided better results due to the waveguide effect that it offered. The jitter values increased across the double hop; however, this was expected due to the variation of latency caused by the additional signal processing across each wireless hop. Generally, the system exhibited good jitter performance results for all conducted experiments, enhancing the suitability of applying the system in mines.

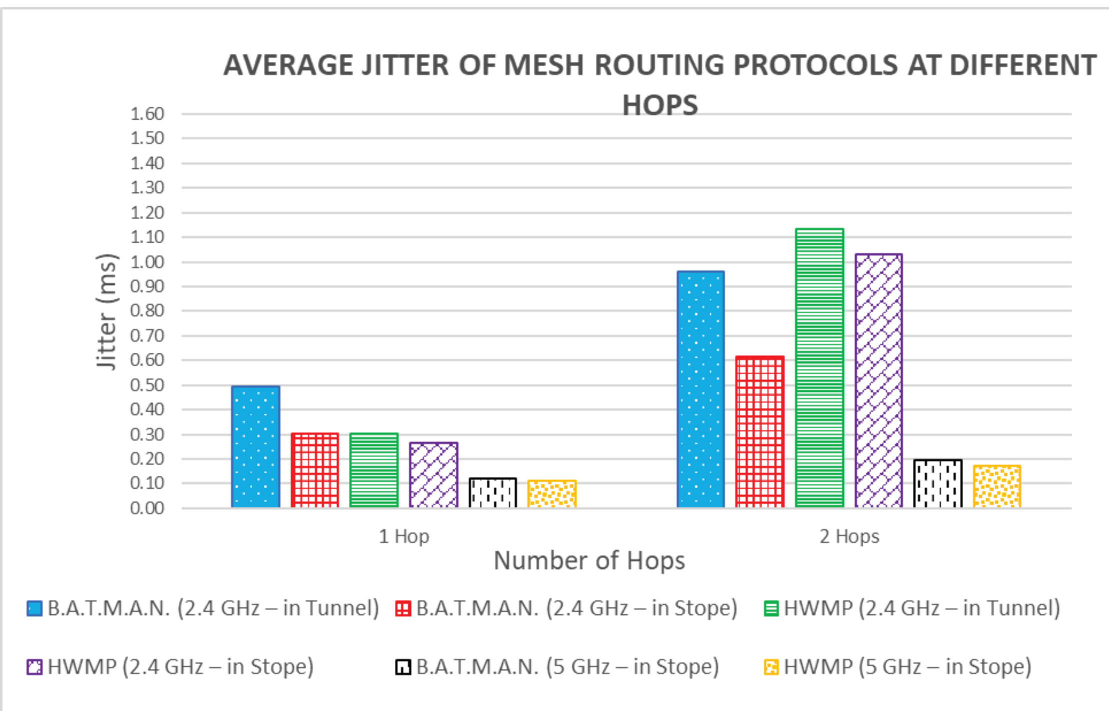

Figure 10. Average jitter.

Figure 11 shows the samples used to calculate the average results used in Figure 10. Each sample from Figure 11 were averages calculated from three separate test cases.

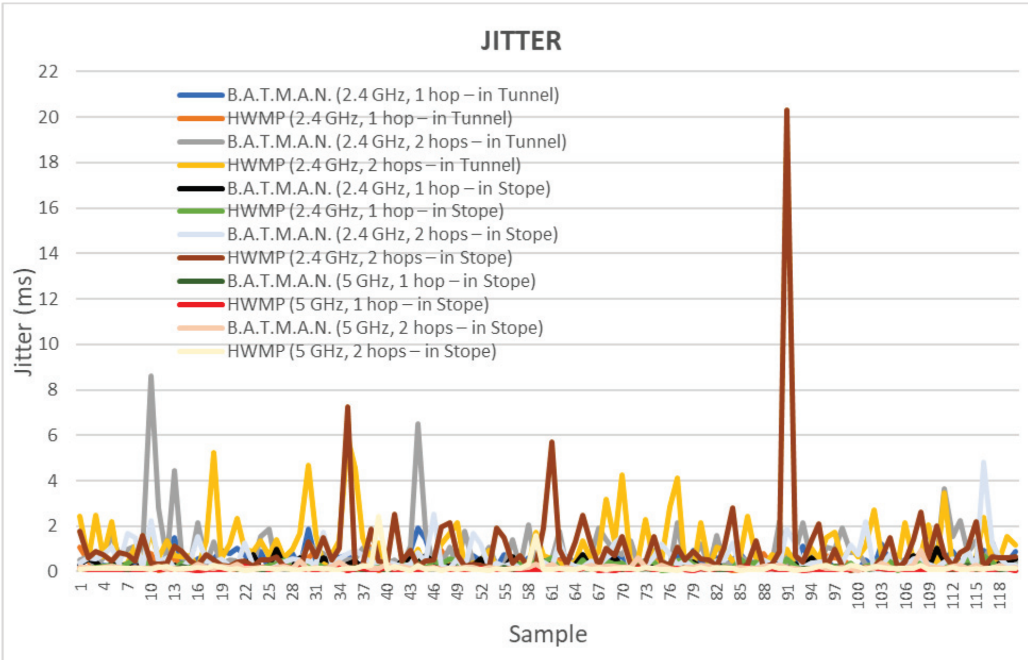

Figure 11. Wi-Fi6 jitter samples.

10.3. Mesh Latency Results

The average latency results for the tunnel as well as the stope are shown in Figure 12. The latency values were obtained using the OpenWrt ping utility. A total of 2000 samples were recorded for each latency test case. Each test case was also performed three times, after which the average latency was calculated. The results show that the double hop experiments had higher latency values as compared to a single hop; however, this was expected due to the additional signal processing that occurs across each wireless hop. The results also show that the best performance for both protocols were in the stope. This can be attributed to the waveguide effect provided by the stope. The 5 GHz experiments also gave the best results, and this is expected due to its higher transmission frequency. The difference in latency results for B.A.T.M.A.N.-adv and HWMP were found to be negligible (approximately 1 ms difference). Overall, the latency values were good for all conducted experiments, enhancing the applicability of technology in mining.

Figure 13 shows the samples used to calculate the average results used in Figure 12. Each sample from Figure 13 were averages calculated from three separate test cases.

10.4. Wi-Fi6 vs. OpenThread Power Results

The performance of Wi-Fi6 is evaluated against IEEE 802.15.4 (OpenThread), the industry standard for low-powered communications. The nRF7002dk was used since it supported both OpenThread and Wi-Fi6. An open-source operating system known as Zephyr OS was flashed onto the boards, and both protocols transmitted at 2.4 GHz. By using the same boards, same OS, and same input voltage, we were able to obtain an accurate power consumption comparison between the two protocols.

Figure 14 shows the total power for both protocols consumed to download 10 MB of data. Due to the modulation limitations inherent in OpenThread's O-QPSK scheme, its data rates remain notably low and lack competitiveness when compared to the QAM technique employed by Wi-Fi6. The OpenThread power evaluations were recorded from

20/40/80 Kbps data transmission rates, whilst the Wi-Fi6 power evaluations were recorded at 1/3 Mbps as well as 80 Kbps data transmission rates.

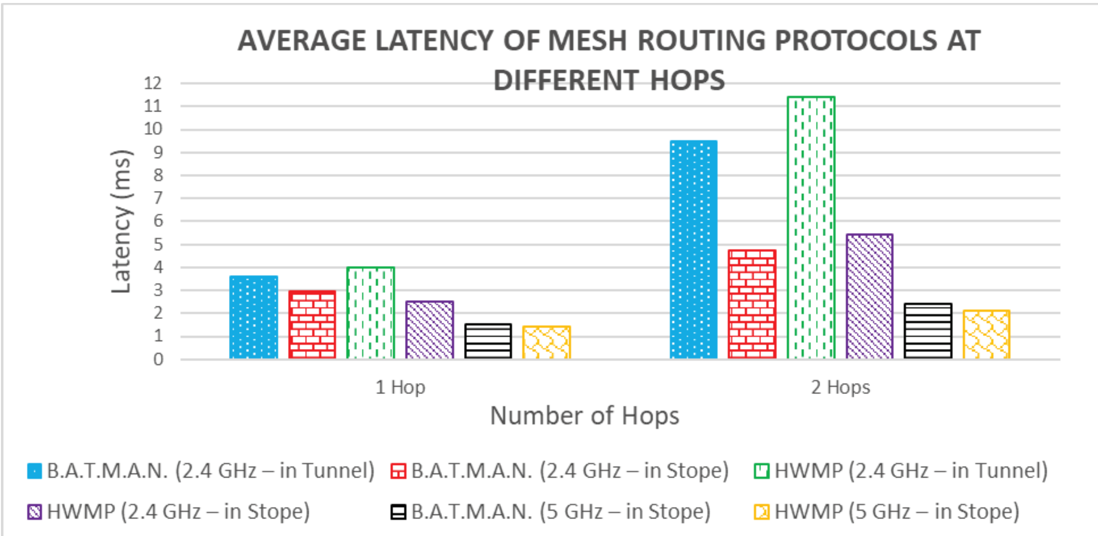

Figure 12. Average latency.

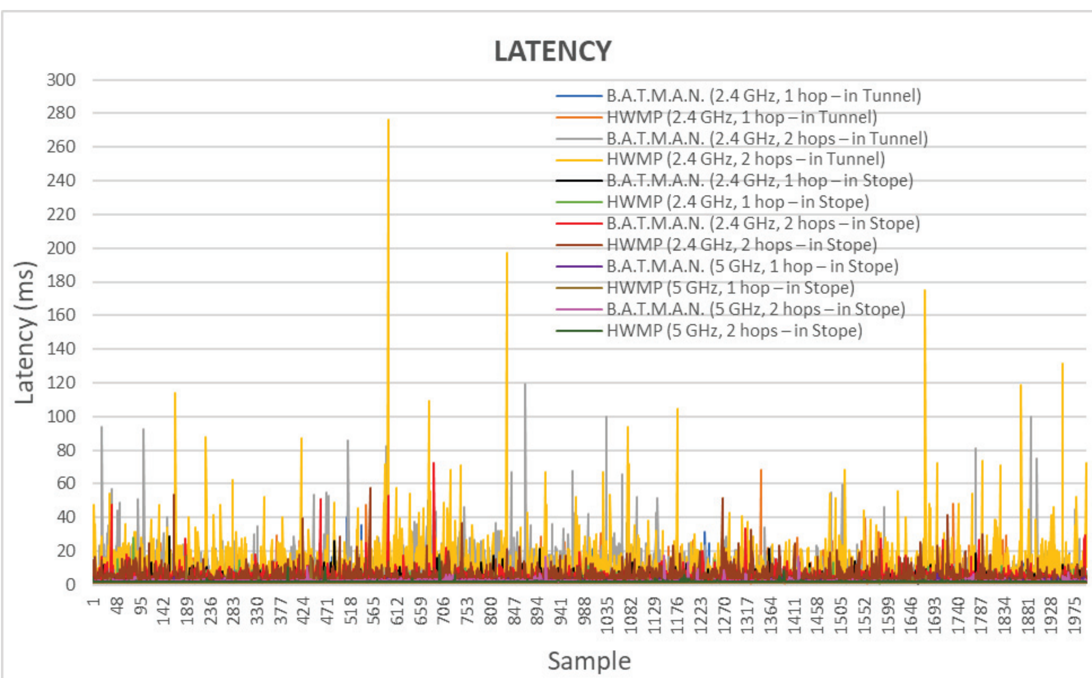

Figure 13. Wi-Fi6 latency samples.

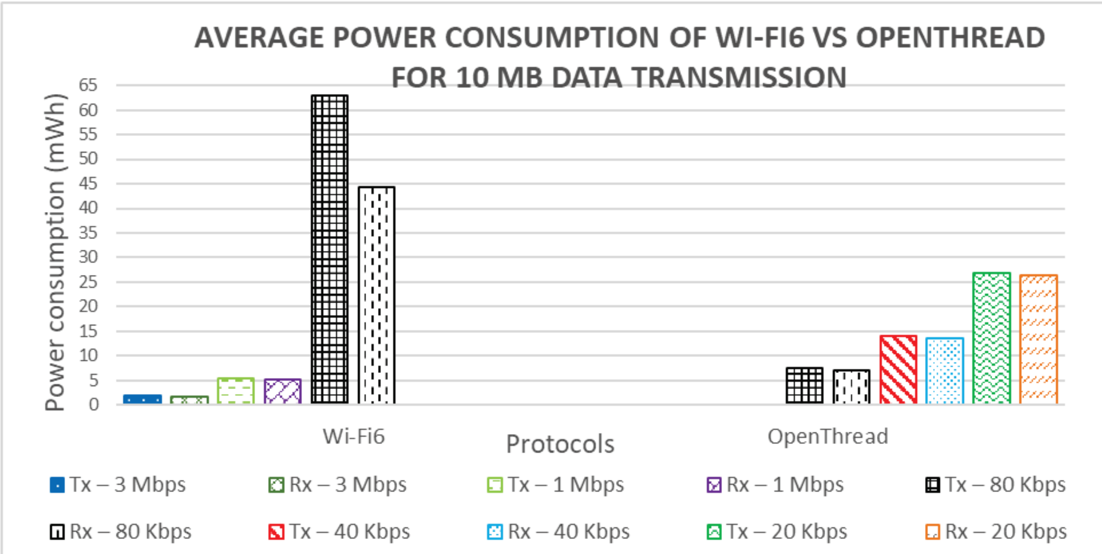

Figure 14. Power consumption for transmitting 10 MB of data.

The results show that both protocols performed best whilst transmitting at close to their peak transmission rates with no packets loss. When trying to send at rates faster than their peak transmission, they suffered from packet loss. The Wi-Fi6 device demonstrated a maximum transmission rate of 3.6 Mbps, whereas the OpenThread device peaked at 86 Kbps. From the results, it can be seen that Wi-Fi6 was the most power-efficient protocol with best transmission power consumption of 3.7 times less than that of OpenThread for the transmitter and 3.9 for the receiver. Despite Wi-Fi6 exhibiting higher instantaneous transmission power compared to OpenThread, its overall power consumption is significantly lower due to its shorter transmission times. For the idle power consumption evaluation, both OpenThread and Wi-Fi6 nodes operated as zperf servers; Wi-Fi6 exhibited an idle power consumption of 26.62 mW, whilst OpenThread recorded 22.61 mW, exhibiting a similar performance. Additionally, the results illustrate that at low transmission rates, specifically when both protocols transmit the same data amount at 80 Kbps, OpenThread consumed 8.3 times less power than Wi-Fi6. This can be attributed to the increased overhead requirements of Wi-Fi6. However, the viability of Wi-Fi6 is still better for mine applications.

11. Discussion

There is a significant research gap regarding high-bandwidth wireless communications for hard rock stope environments. Solutions have been proposed for tunnels and soft rock mines such as coal mines, but there is currently no mainstream high-bandwidth wireless solution for underground hard rock mine stopes, such as underground gold and platinum mines stopes, and little research has been conducted in these areas. This work provides real-world practical performance metrics of Wi-Fi6 in a tunnel and stope, and it was found that the Wi-Fi6 performance is greater in the stope as compared to the tunnel. This can be attributed to Wi-Fi6's newly introduced features which mainly focus on spectral efficiency which allowed it to utilize the waveguide nature of the stope to its advantage. This work also emphasizes the minimal feasible requirements for a mesh system in the stope, and it was found that the 5 GHz channel with 80 MHz channel bandwidth and two spatial streams provided good results even with a multi-hop scenario in the stope. This work also outlines the expected performances of using two of the most widely used open-source mesh routing protocols, namely B.A.T.M.A.N.-adv and HWMP alongside the IEEE 802.11s mesh standard.

This work emphasizes a wireless mesh solution for stopes. A wired connection should be used to interconnect the first node of the mesh to a gateway/sink node, which would be installed at a safe distance away from the stope. This work does not specify the routing method to the surface above the mine. In terms of high-bandwidth solutions, IEEE 802.15.4 and its variants cannot be used due to its modulation scheme throughput limitations. COFDM is a great solution for harsh environments, and [5] showcases its signal robustness. For critical mine safety applications, COFDM is still desirable; however, the technology is not available to the mainstream public as most vendors are of the broadcasting and military nature. Due to COFDM not being mainstream, there are wide fluctuations in price, and the technology is expensive. Wi-Fi6 is mainstream, and Wi-Fi has matured enough to be a good solution for stopes.

12. Conclusions

This research has provided experimental results for the viability of the application of Wi-Fi6 in underground gold and platinum mine stopes. This is due to its strong abilities, namely resilience to excessive multipath propagation alongside multiple wireless hops the ability to take advantage of the waveguide effect of stopes and its efficient spectrum usage due to BSS Colouring, OFDMA, uplink and downlink MU-MIMO, and enhanced beamforming techniques. Compared to other technologies like IEEE 802.15.4 (OpenThread), it was proven to be more energy-efficient and provides better throughput in a stope. For routing Wi-Fi6, the use of HWMP over B.A.T.M.A.N. is recommended due to HWMP's reactive nature, which establishes routes only when needed; this is crucial for stopes, as signals undergo excessive amounts of contained reflections which increases the risk of destructive interference. As for the Wi-Fi6 transport protocol, it is recommended that TCP as opposed to UDP is used due to stopes' waveguiding effect and Wi-Fi6's ability to make efficient use of its spectrum, which limit packet losses, ensuring that the robust performance of TCP is maintained in a multi-hop setup. This recommendation is based on a wide 80 MHz channel bandwidth. If a lower channel bandwidth must be used, then UDP should be the preferred choice due to the increased contention, resulting in dropped acknowledgement packets.

From the 5 GHz experimental results, it can be seen that the latency and jitter values were exceptional in the stope, even across multiple wireless hops. This informs us that real-time applications in a stope will work quite reliably. Furthermore, the exceptional jitter results were obtained at very high throughputs; thus, this indicates that the system will easily be able to handle real-time video processing. A low-spec Wi-Fi6 mesh system with two spatial streams utilizing an 80 MHz channel bandwidth should easily handle the processing of real-time LiDAR feedback, which is generally considered very bandwidth-intensive (e.g., 100 Mbps).

This work opens frontiers to the practical applications of high-bandwidth wireless communications in underground hard rock mine stopes. The world is rapidly advancing towards automation and integrated networks, yet stopes has been largely overlooked in this progress. It is crucial to demonstrate that incorporating automation and technology in stopes is not only financially feasible but also sustainable, aligning it with the advancements seen in other industries.

Wi-Fi7 has recently been released; however, there are currently very few development kits available, and none are currently supported by the open-source Wi-Fi operating system known as OpenWrt. This will be crucial for testing the open-source mesh standard, IEEE 802.11s, alongside mesh-routing protocols such as HWMP and B.A.T.M.A.N.-adv. When this technology is better established, it would be a good initiative to replicate these experiments with Wi-Fi7, as each iteration of Wi-Fi differs greatly.

Author Contributions: Conceptualization, B.L.C., C.P.K. and T.M.W.; methodology, B.L.C. and T.M.W.; software, B.L.C.; validation, B.L.C., T.M.W., C.P.K. and S.J.I.; formal analysis, B.L.C. and T.M.W.; investigation, B.L.C., T.M.W. and C.P.K.; resources, C.P.K. and S.J.I.; data curation, B.L.C.; writing—original draft preparation, B.L.C. and T.M.W.; writing—review and editing, B.L.C. and T.M.W.; visualization, B.L.C. and T.M.W.; supervision, T.M.W., C.P.K. and S.J.I.; project administration, S.J.I.; funding acquisition, T.M.W., C.P.K. and S.J.I. All authors have read and agreed to the published version of the manuscript.

Funding: This work was partially funded by the Council for Scientific and Industrial Research (CSIR) alongside the Mandela Mining Precinct and South African Mining Extraction Research, Development & Innovation (SAMERDI) strategy, under the Real-Time Information Management Systems (RTIMS) programme. The underlying research work was also partially funded by the Department of Science and Innovation under the Foundational Digital Capabilities Research Programme in its Distributed Networks and Processes Programme under project KR4EEMG.

Data Availability Statement: The data presented in this study are available on request from any of the authors. The data are not publicly available due to the research being funded by multiple parties mentioned above, each having different privacy policies.

Acknowledgments: The authors would like to thank and acknowledge the support provided by the Sibanye-Stillwater Mining Facility, as well as the South African Mining Extraction Research, Development & Innovation (SAMERDI) strategy alongside the Mandela Mining Precinct.

Conflicts of Interest: The authors declare no conflicts of interest.

References

1. Dohare, Y.S.; Maity, T.; Das, P.S.; Paul, P.S. Wireless Communication and Environment Monitoring in Underground Coal Mines—Review. *IETE Tech. Rev.* **2015**, *32*, 140–150. [CrossRef]
2. Misra, P.; Kanhere, S.; Ostry, D.; Jha, S. Safety assurance and rescue communication systems in high-stress environments: A mining case study. *IEEE Commun. Mag.* **2010**, *48*, 66–73. [CrossRef]
3. Wu, Y.; Pliszka, E.; Caron, B.; Bouchard, P.; Chouinard, G. Comparison of terrestrial DTV transmission systems: The ATSC 8-VSB, the DVB-T COFDM, and the ISDB-T BST-OFDM. *IEEE Trans. Broadcast.* **2000**, *46*, 101–113. [CrossRef]
4. Joshi, A.; Saini, D.S. Coded-OFDM in various multipath fading environments. In Proceedings of the 2010 the 2nd International Conference on Computer and Automation Engineering (ICCAE), Singapore, 26–28 February 2010; pp. 127–131.
5. Chetty, B.L.; Isaac, S.J.; Walingo, T. An Experimental Investigation into High Bandwidth Wireless Communication Standards for the Underground Mine Stope. In Proceedings of the 2023 IEEE AFRICON, Nairobi, Kenya, 20–22 September 2023; pp. 1–6.
6. Sanchez-Iborra, R.; Cano, M.-D.; Garcia-Haro, J. Performance Evaluation of BATMAN Routing Protocol for VoIP Services: A QoE Perspective. *IEEE Trans. Wirel. Commun.* **2014**, *13*, 4947–4958. [CrossRef]
7. Mozumder, A.H.; Acharjee, T.; Roy, S. Scalability performance analysis of BATMAN and HWMP protocols in wireless mesh networks using NS-3. In Proceedings of the 2014 International Conference on Green Computing Communication and Electrical Engineering (ICGCCEE), Coimbatore, India, 6–8 March 2014; pp. 1–5.
8. Singh, K.; Prabhakar, T.V.; Kuri, J. Improving Access to Network Resources in IoT Networks. In Proceedings of the 2020 International Conference on COMmunication Systems & NETworkS (COMSNETS), Bangalore, India, 7–11 January 2020; pp. 259–266.
9. Yarkan, S.; Guzelgoz, S.; Arslan, H.; Murphy, R.R. Underground Mine Communications: A Survey. *IEEE Commun. Surv. Tutor.* **2009**, *11*, 125–142. [CrossRef]
10. El Khaled, M.; Fortier, P.; Ammari, M.L. A Performance Study of Line-of-Sight Millimeter-Wave Underground Mine Channel. *IEEE Antennas Wirel. Propag. Lett.* **2014**, *13*, 1148–1151. [CrossRef]
11. Kawamura, Y.; Moridi, M.A.; Sharifzadeh, M.; Jang, H. Development of Underground Mine Communication and Monitoring Systems by Using ZigBee Technology. In Proceedings of the ISRM International Symposium—8th Asian Rock Mechanics Symposium, Sapporo, Japan, 14–16 October 2014; p. ISRM-166.
12. Ben Mabrouk, I.; Talbi, L.; Nedil, M. Performance Evaluation of a MIMO System in Underground Mine Gallery. *IEEE Antennas Wirel. Propag. Lett.* **2012**, *11*, 830–833. [CrossRef]
13. Nerguizian, C.; Despins, C.L.; Affes, S.; Djadel, M. Radio-Channel characterization of an underground mine at 2.4 GHz. *IEEE Trans. Wirel. Commun.* **2005**, *4*, 2441–2453. [CrossRef]
14. Ikeda, H.; Kolade, O.; Mahboob, M.A.; Cawood, F.T.; Kawamura, Y. Communication of Sensor Data in Underground Mining Environments: An Evaluation of Wireless Signal Quality over Distance. *Mining* **2021**, *1*, 211–223. [CrossRef]
15. Elazhari, M.E.; Talbi, L.; Nedil, M. Comparative study of Four Path Loss Models for UWB off-body Propagation Channel Inside a Mine. In Proceedings of the 2019 IEEE International Symposium on Antennas and Propagation and USNC-URSI Radio Science Meeting, Atlanta, GA, USA, 7–12 July 2019; pp. 2103–2104.

16. Zhu, L.; Wen, X.; Han, Q.; Fryer, A.; Suttora, N.; Petruska, A.J. Performance evaluation of wi-fi for underground robots. In *MobiQuitous '19: Proceedings of the 16th EAI International Conference on Mobile and Ubiquitous Systems: Computing, Networking and Services, Proceedings of the 16th EAI International Conference on Mobile and Ubiquitous Systems: Computing, Networking and Services, Houston, TX, USA, 12–14 November 2019*; Association for Computing Machinery: New York, NY, USA, 2020; pp. 498–503.
17. Viittala, H.; Soderi, S.; Saloranta, J.; Hamalainen, M.; Iinatti, J. An Experimental Evaluation of WiFi-Based Vehicle-to-Vehicle (V2V) Communication in a Tunnel. In Proceedings of the 2013 IEEE 77th Vehicular Technology Conference (VTC Spring), Dresden, Germany, 2–5 June 2013; pp. 1–5.
18. Sandoval, F.; Poitau, G.; Gagnon, F. Optimizing Forward Error Correction Codes for COFDM With Reduced PAPR. *IEEE Trans. Commun.* **2019**, *67*, 4605–4619. [CrossRef]
19. Magrin, D.; Avallone, S.; Roy, S.; Zorzi, M. Performance Evaluation of 802.11ax OFDMA through Theoretical Analysis and Simulations. *IEEE Trans. Wirel. Commun.* **2023**, *22*, 5070–5083. [CrossRef]
20. Biradar, A.G.; Johari, S.; Kulkarni, S.S.; Maheshwari, A.; Venkatesh, K. OpenThread Based Mesh Enabled IoT Smart Device Cluster for Health Monitoring of the Elderly in Old Age Homes. In Proceedings of the 2020 4th International Conference on Electronics, Materials Engineering & Nano-Technology (IEMENTech), Kolkata, India, 2–4 October 2020; pp. 1–6.
21. Gangopadhyay, S.; Jain, V.K. A Position-Based Modified OLSR Routing Protocol for Flying Ad Hoc Networks. *IEEE Trans. Veh. Technol.* **2023**, *72*, 12087–12098. [CrossRef]
22. Al-Zahrani, F.A. On Modeling Optimizations and Enhancing Routing Protocols for Wireless Multihop Networks. *IEEE Access* **2020**, *8*, 68953–68973. [CrossRef]
23. Santana, C.; Macedo, M.; Alves, E.; Guerreiro, M.T.; Valadares Siqueira, H.; Gokhale, A.; Bastos-Filho, C.J.A. Bio-Inspired Multi-Objective Algorithms Applied on the Optimization of the AODV's Routing Recovery Mechanism. *IEEE Access* **2023**, *11*, 116480–116496. [CrossRef]
24. Tan, X.; Zuo, Z.; Su, S.; Guo, X.; Sun, X.; Jiang, D. Performance Analysis of Routing Protocols for UAV Communication Networks. *IEEE Access* **2020**, *8*, 92212–92224. [CrossRef]
25. Istikmal; Subekti, A.; Perdana, D.; Ridha Muldina, N.; ArifIndra, I. Sussi Dynamic Source Routing and optimized Link State Routing Performance in Multipath Fading Environment with Dynamic Network Topology. In Proceedings of the 2019 4th International Conference on Information Technology, Information Systems and Electrical Engineering (ICITISEE), Yogyakarta, Indonesia, 20–21 November 2019; pp. 373–378.
26. Zhao, Y.-F.; Yin, S.-J.; Tao, W.; Li, X.-Y.; Meng, J. Gesture Recognition System Resilient to Interdevice Interference Based on Direct Sequence Spread Spectrum. *IEEE Sens. Lett.* **2023**, *7*, 1–4. [CrossRef]
27. He, Y.; Chen, Y.; Hu, Y.; Zeng, B. WiFi Vision: Sensing, Recognition, and Detection With Commodity MIMO-OFDM WiFi. *IEEE Internet Things J.* **2020**, *7*, 8296–8317. [CrossRef]
28. Barrachina-Muñoz, S.; Bellalta, B.; Knightly, E.W. Wi-Fi Channel Bonding: An All-Channel System and Experimental Study From Urban Hotspots to a Sold-Out Stadium. *IEEE/ACM Trans. Netw.* **2021**, *29*, 2101–2114. [CrossRef]
29. Piracha, A.Z.; Farid, H.; Shahzad, K.; Zeeshan, M. A Low Complexity Signal-to-Total Variance Precoding Scheme for Downlink Multi-Stream MU-MIMO Systems. In Proceedings of the 2022 3rd International Conference on Electrical Engineering and Informatics (ICon EEI), Virtual Conference, 19–20 October 2022; pp. 53–58.
30. Lee, K.-H. Using OFDMA for MU-MIMO User Selection in 802.11ax-Based Wi-Fi Networks. *IEEE Access* **2019**, *7*, 186041–186055. [CrossRef]
31. Behara, A.; Venkatesh, T.G. Performance Study of High-Efficiency IEEE 802.11ax WLAN Standard Using NS-3 Simulator. In Proceedings of the 2022 IEEE 27th International Workshop on Computer Aided Modeling and Design of Communication Links and Networks (CAMAD), Paris, France, 2–3 November 2022; pp. 226–231.
32. Chen, Q.; Ding, Z. Accommodating LAA within IEEE 802.11ax WiFi Networks for Enhanced Coexistence. *IEEE Trans. Wirel. Commun.* **2020**, *19*, 7621–7636. [CrossRef]
33. Šepić, N.; Kočan, E.; Pejanović-Djurišić, M. Evaluating spatial reuse in 802.11ax networks with interference threshold adjustment. In Proceedings of the 2020 24th International Conference on Information Technology (IT), Zabljak, Montenegro, 18–22 February 2020; pp. 1–4.
34. Yildirim, H.C.; Storrer, L.; Louveaux, J.; De Doncker, P.; Horlin, F. Impact of MU-MIMO on Passive Wi-Fi Sensing: Threat or Opportunity? In Proceedings of the 2022 2nd IEEE International Symposium on Joint Communications & Sensing (JC&S), Seefeld, Austria, 9–10 March 2022; pp. 1–6.
35. Tran, V.H.; Misra, A.; Xiong, J.; Balan, R.K. WiWear: Wearable Sensing via Directional WiFi Energy Harvesting. In Proceedings of the 2019 IEEE International Conference on Pervasive Computing and Communications (PerCom Workshops), Kyoto, Japan, 11–15 March 2019; pp. 1–10.
36. Kim, H.-S.; Kumar, S.; Culler, D.E. Thread/OpenThread: A Compromise in Low-Power Wireless Multihop Network Architecture for the Internet of Things. *IEEE Commun. Mag.* **2019**, *57*, 55–61. [CrossRef]
37. *IEEE Std 802.15.4-2020 (Revision of IEEE Std 802.15.4-2015)*; IEEE Standard for Low-Rate Wireless Networks. IEEE: Piscataway, NJ, USA, 2020.
38. Zhang, G.; Shi, C.; Han, C.; Li, X.; Wang, D.; Rabie, K.; Kharel, R. Implementation-Friendly and Energy-Efficient Symbol-by-Symbol Detection Scheme for IEEE 802.15.4 O-QPSK Receivers. *IEEE Access* **2020**, *8*, 158402–158415. [CrossRef]

39. Zhong, L.; Zou, Y.; Zhang, S.; Dai, X.; Zhang, J.; Cheng, M.; Deng, L.; Yang, Q.; Liu, D. An SNR-Improved Transmitter of Delta-sigma Modulation Supported Ultra-High-Order QAM Signal for Fronthaul/WiFi Applications. *J. Light. Technol.* **2022**, *40*, 2780–2790. [CrossRef]
40. Makarov, S.B.; Liu, M.; Ovsyannikova, A.S.; Zavjalov, S.V.; Lavrenyuk, I.L.; Xue, W.; Xu, Y. A Reduction of Peak-to-Average Power Ratio Based Faster-Than-Nyquist Quadrature Signals for Satellite Communication. *Symmetry* **2021**, *13*, 346. [CrossRef]
41. Usha, S.M.; Mahesh, H.B. Mahesh Low Power and Area Optimized Architecture for OQPSK Modulator. In Proceedings of the 2019 International Conference on Wireless Communications Signal Processing and Networking (WiSPNET), Chennai, India, 21–23 March 2019; pp. 123–126.
42. Atto, M.; Mstafa, R.J.; Alkhayyat, A. Improving AODV Routing Protocol for Image Transmission over Mobile Video Sensor Networks. *IEEE Access* **2020**, *8*, 169396–169407. [CrossRef]
43. Katila, C.J.; Di Gianni, A.; Buratti, C.; Verdone, R. Routing protocols for video surveillance drones in IEEE 802.11s Wireless Mesh Networks. In Proceedings of the 2017 European Conference on Networks and Communications (EuCNC), Oulu, Finland, 12–15 June 2017; pp. 1–5.
44. OpenWrt. Welcome to the OpenWrt Project. Available online: https://openwrt.org/ (accessed on 16 April 2024).
45. Nordic Semiconductor. nRF7002 DK. Available online: https://www.nordicsemi.com/Products/Development-hardware/nRF7002-DK (accessed on 16 April 2024).
46. Zephyr Project. About the Zephyr Project. Available online: https://www.zephyrproject.org/learn-about/ (accessed on 16 April 2024).
47. Nordic Semiconductor. nRF Connect for Desktop. Available online: https://www.nordicsemi.com/Products/Development-tools/nRF-Connect-for-Desktop (accessed on 16 April 2024).

sustainability

MDPI

Article

Improved Multi-Objective Beluga Whale Optimization Algorithm for Truck Scheduling in Open-Pit Mines

Pengchao Zhang [1], Xiang Liu [1,*], Zebang Yi [2] and Qiuzhi He [1,*]

1 School of Economics and Management, Guangxi University of Science and Technology, Liuzhou 545006, China; 19862523817@163.com
2 School of Earth Sciences, Guilin University of Technology, Guilin 541004, China; yizb@glut.edu.cn
* Correspondence: liux_600@163.com (X.L.); qzing600@163.com (Q.H.)

Abstract: Big data and artificial intelligence have promoted mining innovation and sustainable development, and the transportation used in open-pit mining has increasingly incorporated unmanned driving, real-time information sharing, and intelligent algorithm applications. However, the traditional manual scheduling used for mining transportation often prioritizes output over efficiency and quality, resulting in high operational expenses, traffic jams, and long lines. In this study, a novel scheduling model with multi-objective optimization was created to overcome these problems. Production, demand, ore grade, and vehicle count were the model's constraints. The optimization goals were to minimize the shipping cost, total waiting time, and ore grade deviation. An enhanced multi-objective beluga whale optimization (IMOBWO) algorithm was implemented in the model. The algorithm's superior performance was demonstrated in ten test functions, as well as the IEEE 30-bus system. It was enhanced by optimizing the population initialization, improving the adaptive factor, and adding dynamic domain perturbation. The case analysis showed that, in comparison to the other three conventional multi-objective algorithms, IMOBWO reduced the shipping cost from 7.65 to 0.84%, the total waiting time from 35.7 to 7.54%, and the ore grade deviation from 14.8 to 3.73%. The implementation of this algorithm for truck scheduling in open-pit mines increased operational efficiency, decreased operating costs, and advanced intelligent mine construction and transportation systems. These factors play a significant role in the safety, profitability, and sustainability of open-pit mines.

Keywords: improved multi-objective beluga whale algorithm; unmanned driving; open-pit mine; sustainable development

Citation: Zhang, P.; Liu, X.; Yi, Z.; He, Q. Improved Multi-Objective Beluga Whale Optimization Algorithm for Truck Scheduling in Open-Pit Mines. *Sustainability* **2024**, *16*, 6939. https://doi.org/10.3390/su16166939

Academic Editors: Krzysztof Skrzypkowski, René Gómez, Fhatuwani Sengani, Derek B. Apel, Faham Tahmasebinia and Jianhang Chen

Received: 26 June 2024
Revised: 4 August 2024
Accepted: 6 August 2024
Published: 13 August 2024

1. Introduction

Truck transportation is one of the main methods used in open-pit mining. In this field, conventional transportation techniques were inefficient, which worsened the effects on the environment and also consumed more energy and posed serious safety risks [1,2]. Truck schedule rigidity and reliance on manual operation frequently result in traffic jams and delays, raising operating expenses and lengthening waiting times [3–5]. Furthermore, it has been established that catastrophic geological occurrences such as landslides and ground collapses are dangerous for driver safety [6,7]. Mining transportation systems are going through a revolutionary age due to the rapid development of artificial intelligence and unmanned driving in recent years [8–10]. Newer intelligent mining transportation models maximize efficiency and safety while simultaneously consuming less energy [11–13]. Efficient data analytics can be used to enhance route planning and scheduling tactics, effectively mitigating truck congestion and minimizing transportation lag, thanks to the systems' constant monitoring of the logistical dynamics and mining terrain. In particular, the introduction of unmanned mining trucks not only has improved operational safety but also plays a vital role in material transportation, because transportation cost accounts for a sizeable share of mine operating expenses [14–16]. Nevertheless, there are certain drawbacks to the present scheduling procedures for the transferring of unmanned mining trucks, including some waiting time during operations and comparatively high shipping costs [17]. Therefore, it is crucial to design and optimize the unmanned mining truck dispatching model for use in open-pit mines in order to decrease operating costs, increase the effectiveness of ore transportation, decrease carbon emissions, and improve overall corporate performance [18–22].

To simulate real-world dispatch situations and develop scheduling models that align with real-world mining operations, researchers have undertaken in-depth investigations on truck dispatching models. In general, this paper focuses on methods for solving these models and optimizing goals [23–26]. Early research frequently described very simple models that primarily focused on single-objective constraints before progressively expanding to multi-objective, complex constraints. For instance, Temeng et al. developed and validated a nonpreemptive goal-programming approach for truck dispatching to ensure stable ore quality and maximize production [27]. Topal et al. concentrated on cutting overall truck maintenance costs and used case studies to demonstrate the efficacy of the mixed integer programming approach in doing so [28]. In order to solve energy difficulties while achieving production needs, Patterson et al. proposed a domain search-based algorithm to decrease the energy use of trucks and shovels required to reach production targets [29]. Yao et al. constructed a mine truck scheduling model under mixed transportation constraints based on allocation demand [30].

The dynamic and multidimensional nature of truck dispatching in open-pit mines still presents difficulties issues, despite the tremendous efforts of those researchers to introduce helpful algorithms for truck dispatching models, better adapting them to real mining transportation situations [13,18,22,31]. Environmental protection and worker safety are becoming increasingly important in the context of pursuing intelligent and unmanned mining operations. Increasing operational efficiency while minimizing environmental impact and optimizing operational safety has become a critical issue. As a result, appropriate models must be created and put into use that take safety regulations, production demands, environmental protection, technological advancements, and operation efficiency into account.

Integer programming and the linear programming method are frequently presented as solutions to these models [32–34]. Numerous studies have used artificial intelligence algorithms to handle truck scheduling issues as a result of the quick advancement of evolutionary computation techniques. In order to provide workable solutions for the allocation and real-time scheduling of mining trucks, for instance, Coelho et al. employed three multi-objective algorithms—2PPLSVNS, MOVNS, and NSGA-II—to solve dynamic truck allocation problems in open-pit mining operations [35]. Practical scheduling solutions were provided by Mendes et al. who proposed a multi-objective evolutionary algorithm for dynamic truck scheduling in open-pit mines [36]. Two multi-objective genetic algorithms were created by Alexandre et al. to handle scheduling schemes that maximize production and minimize expenses while allocating trucks and shovels in open-pit mining operations [37]. Furthermore, while managing multi-dimensional dispatch objectives, traditional algorithms frequently display subpar performance, lengthy calculation durations, and challenges in generating workable scheduling solutions that efficiently support intelligent dispatch systems. Therefore, there is an urgent need to introduce new solutions to address the challenges in solving mining truck scheduling models. Zhang et al. proposed a beluga optimization algorithm by observing a beluga group's swimming, feeding, and whale-falling activities [38]. Upon evaluation, the algorithm performed well, and case studies on distributed generation (DG) optimization [39], iron ore sintering batching [40], and anti-roll torsion bar optimization [41] were also carried out. Based on these factors, an improved multi-objective beluga whale optimization (IMOBWO) was introduced, wherein the population was initialized and its range expanded using logistic chaotic mapping. Adaptive factors were proposed to improve the algorithm's capacity for global searches and to quicken the algorithm's pace of convergence. The algorithm's solving power was improved by increasing the domain perturbation approach, broadening the pool of potential solutions. The algorithm's solution power was demonstrated using ten test functions and the IEEE 30-bus problem for thorough assessment before it was ultimately used with a real mining truck scheduling case.

In this study, a new open-pit mine truck scheduling model solved by the IMOBWO algorithm was proposed. The model took production demands, ore grade requirements, vehicle limitations, and route restrictions into account, aiming at achieving comprehensive optimization in terms of carbon emissions, shipping cost, total waiting time, and ore grade deviation. The IMOBWO algorithm performance was evaluated using test functions and the IEEE 30-bus problem, and a scheduling solution was provided following case analysis. This model enhanced operational safety and reduced transportation delays in the mining industry, which was of great significance for improving the overall operational efficiency of open-pit mines.

2. Problem Description and Model Establishment

2.1. Process Analysis of Truck Scheduling Problem

Trucking transportation scheduling is recognized as a multi-dimensional task encompassing path optimization, traffic flow coordination, and dynamic real-time decision making. These dimensions impose significant complexity on the scheduling domain, necessitating the pursuit of varied optimization goals amid numerous constraints. This paper has focused on the achievement of reduced shipping cost, the minimization of total waiting time, and the strict control of ore grade deviation. Furthermore, open-pit mine truck dispatching requires the consideration of complex constraints, such as truck transport capacity, ore supply at loading points, ore demand at crushing stations, and ore grade differences at different mining benches.

The research process followed in this article is shown in Figure 1, which outlines the study problem, data collection method, model building, problem solving, and solution results.

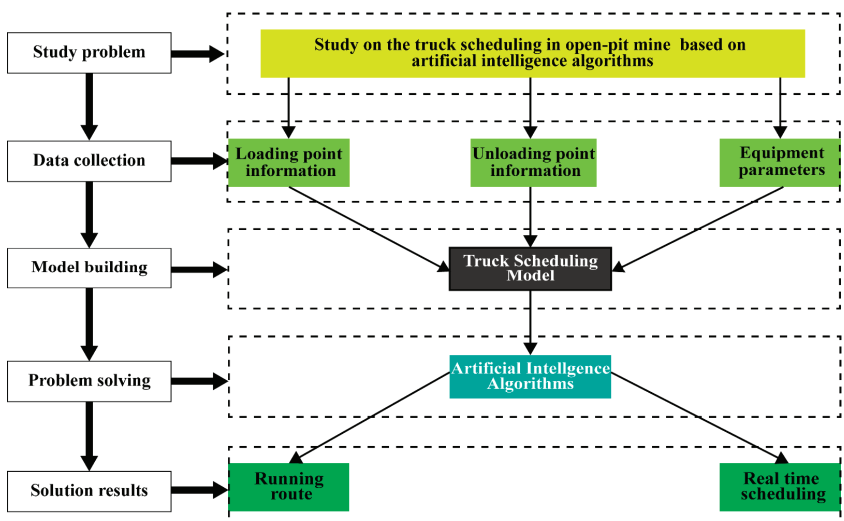

Figure 1. Research route for truck scheduling problem.

2.2. Description of Symbols

According to the actual state of the open-pit mine in Guigang, Guangxi, the parameters and the variables in the model are shown in Table 1.

Table 1. List of variable definitions.

Parameter Definition	Symbolic	Value	Unit
Working hours per shift	H	8	hour
Number of loading points	M	6	site
Number of crushing stations	N	4	site
Number of mine Trucks	K	13	vehicle
Truck load	G	50	ton
Fuel cost per liter	L	7.9	Yuan/L
Number of times truck k travels from loading point i to crushing station j	X_{kij}	Decision variable	times
Number of times truck k travels from crushing station j to loading point i	Y_{kij}	Decision variable	Times
Minimum ore grade	η	0.099	%
Fuel consumption of mine trucks with full load	Q_1	6.7	L/km
No-load fuel consumption of mine trucks	Q_2	3.9	L/km
Fuel Conversion Rate	λ	2.65	kg/L
Unit carbon trading cost	l	0.041	yuan/kg
Mine car full load speed	V_1	18	km/h
Mine car no full load speed	V_2	37	km/h
Unit truck loading time	t_l	5	min
Unit truck unloading time	t_s	3	min
Errors in ore grade allowed in the mine	w	0.05	%

2.3. Multi-Objective Truck Scheduling Model

In this study, to meet the demands of efficient and flexible mining transportation operations, a multi-objective scheduling model was established. The main optimization objectives were to optimize shipping cost, total waiting time, and ore grade deviation, while the main constraints were production constraints, transport capacity, and supply–demand balance.

2.3.1. Objective Function

Since diesel-powered trucks produce carbon emissions during operation, the cost of truck transportation carbon emissions (C) is due to the fuel conversion factor (λ) and the unit carbon transaction cost (l), as shown in Equation (1).

$$C = \sum_{k=1}^{K} \left(\sum_{i=1}^{M} \sum_{j=1}^{N} \lambda l (X_{kij} d_{ij} Q_1 + Y_{kij} d_{ij} Q_2)\right) \tag{1}$$

The truck shipping cost function is constructed by the truck driving cost and carbon emission treatment cost, as shown in Equation (2).

$$F(X_1) = MIN\left(\sum_{i=1}^{M} \sum_{j=1}^{N} \left(\sum_{k=1}^{K} X_{kij} d_{ij} Q_1 L + \sum_{n=1}^{k} Y_{kij} d_{ij} Q_2 L\right) + C\right) \tag{2}$$

X_1 is represented the truck transportation cost, and $F(X_1)$ is represented the truck cost function.

Since the number of ores transported per shift is constant, the ore transport task completed in limited working hours reduced operating costs and improved the equipment utilization rate, benefiting the company. However, irrational scheduling will lead to traffic jams in the process of loading or unloading the trucks, thus increasing non-working hours. As a result, the minimization of total waiting time for the trucks is considered as the optimization objective, and the total waiting time function is constructed, as shown in Equation (3).

$$F(X_2) = MIN\sum_{k=1}^{K}(H - \frac{\sum_{i=1}^{m}\sum_{j=1}^{n}[X_{ij}(d_{ij}+t_l V_2)]}{V_2} - \frac{\sum_{i=1}^{m}\sum_{j=1}^{n}[Y_{ij}(d_{ij}+t_s V_1)]}{V_1}) \tag{3}$$

X_2 represents the total waiting time of the trucks, and $F(X_2)$ represents the total waiting time function.

In order to improve the efficiency of ore allocation, neutralize the different tastes of ore, increase the output of qualified ores, reduce the amount of waste rock, meet the requirements of ore quality, improve the economic efficiency of the mine, and enhance the utilization rate of natural resources in the mine, the function with ore grade deviation as the optimization objective is established, as shown in Equation (4).

$$F(X_3) = \frac{\sum_{j=1}^{N}\sum_{i=1}^{M}\sum_{k=1}^{K}\left|GX_{kij}(R_i - r_j)\right|}{\sum_{j=1}^{N}\sum_{i=1}^{M}\sum_{k=1}^{K}GX_{kij}} \tag{4}$$

X_3 represents the ore grade deviation, and $F(X_3)$ represents the ore grade deviation function, R_i represents the i loading point ore grade, r_j represents the j crushing station specified grade.

2.3.2. Constraints

In order to satisfy the ore quantity demand constraints of each crushing station for each shift, the total ore car transportation quantity of each shift should be not less than the planned output of each crushing station F_j, the crushing stations demand constraint function is established, as shown in Equation (5).

$$\sum_{i=1}^{M}\sum_{k=1}^{K}(X_{kij}G) - F_j \geq 0 \tag{5}$$

In order to satisfy the ore volume supply constraints for each shift at each mining site, the total ore truck transportation volume for each shift should be no greater than the ore production W_i at each mining site. The mining site supply constraint function is established, as shown in Equation (6).

$$\sum_{i=1}^{M}\sum_{k=1}^{K}(X_{kij}G) - W_i \leq 0 \tag{6}$$

In order to meet the requirements of ore allocation, the overall grade of the transported ore and the error of the specified grade η the difference between the two should be no greater than the ore taste error w allowed in the mine, and the ore grade error constraint function is established, as shown in Equation (7).

$$\left|\frac{\sum_{k=1}^{K}\sum_{i=1}^{M}GX_{kij}R_{ki}}{\sum_{k=1}^{K}\sum_{i=1}^{M}GX_{kij}} - \min\eta\right| - w \leq 0 \tag{7}$$

The total number of transportation trucks in the mine is limited, and the number of trucks requires by the scheduling scheme should be less than the number of existing trucks K. The constraint on the number of transportation trucks is constructed, as shown in Equation (8).

$$\sum_{k=1}^{K} K_k \leq K \tag{8}$$

In order to satisfy the scheduling continuity, the kth truck should proceed to the i (j) crushing station (loading point) after completing the loading (unloading) of ore from the j (i) loading point (crushing station), the trucks are always active between the loading points and the crushing stations, the continuous trucking constraint is constructed as shown in Equation (9).

$$\sum_{j=1}^{M}\sum_{i=1}^{N} X_{kij} - \sum_{j=1}^{M}\sum_{i=1}^{N} Y_{kij} = 0 \tag{9}$$

3. Multi-Objective Beluga Whale Optimization

3.1. Beluga Whale Optimization

In 2022, Zhang et al. proposed a beluga whale optimization (BWO) algorithm upon observing the swimming, feeding, and whale-falling behaviors of beluga whales [42,43]. The algorithm has been tested and validated in engineering cases and has shown good results. Multiple objective beluga whale optimization (MOBWO) [44] is a fusion of the beluga whale optimization algorithm and the idea of multi-objective optimization. The beluga whale optimization algorithm contains the following four main steps.

3.1.1. Population Initialization

The algorithm is initialized by constructing a random population through an agent model, where each beluga whale in the population is an initial solution, X represents the agent position matrix, and the agent position matrix is built based on the population size n and solution dimension d, $x_{n,d}$ is candidate solution, as shown in Equation (10):

$$X = \begin{bmatrix} x_{1,1} & x_{1,2} & \cdots & x_{1,d} \\ x_{2,1} & x_{2,2} & \cdots & x_{2,d} \\ \vdots & \vdots & \vdots & \vdots \\ x_{n,1} & x_{n,2} & \cdots & x_{n,d} \end{bmatrix} \tag{10}$$

where n is the size of the population for which the algorithm is designed and d is the dimension of the problem to be solved. Fx is the fitness value matrix, and $f\ (x_{n,1}\ x_{n,2} \ldots x_{n,d})$ is the fitness value of each individual in the population, as shown in Equation (11).

$$Fx = \begin{bmatrix} f(x_{1,1} & x_{1,2} & \cdots & x_{1,d}) \\ f(x_{2,1} & x_{2,2} & \cdots & x_{2,d}) \\ \vdots & \vdots & \vdots & \vdots \\ f(x_{n,1} & x_{n,2} & \cdots & x_{n,d}) \end{bmatrix} \tag{11}$$

In the beluga whale optimization algorithm, the balancing factor B_f determines the degree of algorithm exploration and exploitation, as shown in Equation (12):

$$B_f = B_0(1 - t/2T) \tag{12}$$

where B_0 is a random number between (0,1), T is the maximum number of iterations, t is the current number of iterations, and B_f is the balancing factor that balanced the exploration and development phases. The exploration stage occurs when the balancing factor $B_f > 0.5$ and the development stage occurs when $B_f \leq 0.5$; when t gradually increases, B_f gradually decreases and the algorithm gradually transitions from the exploration stage to the development stage.

3.1.2. Exploration Phase

The exploration phase of the algorithm simulates the swimming behavior of a group of beluga whales, which is updated with the location of the beluga whales, as shown in Equation (13):

$$\begin{cases} X_{i,j}^{t+1} = X_{i,p_j}^{t} + (X_{r,p_1}^{t} - X_{i,p_j}^{t})(1+r_1)\sin(2\pi r_2) j = even \\ X_{i,j}^{t+1} = X_{i,p_j}^{t} + (X_{r,p_1}^{t} - X_{i,p_j}^{t})(1+r_1)\cos(2\pi r_2) j = odd \end{cases} \tag{13}$$

where $X_{i,j}^{t+1}$ denotes the position of the *i*th beluga after the *t*th iteration in the *j*th dimension, p_j denotes a random number from 1 to *d*, and r denotes a random number from 1 to *n*, X_{i,p_j}^{t} and X_{r,p_1}^{t} are the current positions of the *i*th and *r*th beluga, r_1 and r_2 are random operators for the enhanced exploration phase, taking values between (0,1), and sin ($2\pi r_2$) and cos ($2\pi r_2$) are used to average the random numbers between fins.

3.1.3. Development Phase

The development stage expands the candidate solutions by simulating the feeding behavior of beluga whales, where neighboring belugas cooperate and share information with each other. Levi's flight is introduced in the development phase of BWO to improve the convergence performance of the algorithm, as shown in Equation (14):

$$X_i^{t+1} = r_3 X_{best}^{t} - r_4 X_i^t + C_1 \times L_f \times (X_r^t - X_i^t) \tag{14}$$

where *t* is the current iteration number, X_i^{t+1} is the position of the next iteration of the *i*th beluga whale, X_{best}^{t} is the position of the optimal individual in the current population, X_r^t and X_i^t are the positions of a random beluga whale and the *i*th beluga whale, r_3 and r_4 are random numbers in the range of (0,1), $C_1 = 2r_4 \times (1 - t/T)$, which denotes the jumping intensity of the Lévy flight, and L_f is the Lévy flight function.

3.1.4. Whale-Fall Stage

The beluga whale group faces many external threats during migration and foraging, leading to the phenomenon of whale fall in some in the group. In order to ensure the stability of the population, the population has undergone position updates, as shown in Equations (15) and (16):

$$X_i^{t+1} = r_5 X_i^t - r_6 X_r^t + r_7 X_{step} \tag{15}$$

$$X_{step} = (u_b - l_b)\exp(-C_2 \times {}^{t}/_{T}) \tag{16}$$

where r_5 and r_6 are random numbers between (0,1), X_{step} is the beluga whale fall step, u_b is the upper limit of the variable, l_b is the lower limit of the variable, C_2 is the factor controlling the step size, $C_2 = 2W_f \times n$, W_f denotes the probability of beluga whales falling, $W_f = 0.1 - 0.05\ t/T$, and *n* is the population size.

3.2. Improved Beluga Whale Optimization Algorithm

It has been shown that variants of the BWO algorithm can effectively overcome the low accuracy and slow convergence of BWO, thus effectively solving multi-objection problems [39–41]. In this section, three improvements were made: (i) logistic chaotic [45] mapping was introduced to optimize the population distribution of BWO and enhance the algorithm's solution efficiency; (ii) the B_f factor was improved to balance the algorithm's global and local search capabilities; and (iii) domain perturbation was carried out during the development stage for the population update, aiming to expand the solution range and enhance the solution capability.

3.2.1. Optimized Population Initialization

The population initialization of BWO is introduced in Section 3.1.1, but BWO constructs the initial population randomly, resulting in an uneven distribution that affects the algorithm's solution efficiency. As a result, logistic chaotic mapping was introduced to carry out the population initialization of the algorithm, expanding the range of the initial population distribution and improving the algorithm's solving efficiency, as shown in Equation (17).

$$X_{k+1} = \lambda X_k \times (1 - X_k) \tag{17}$$

where $X_k \in$ (0,1), λ is a parameter that regulates the range of the mapping sequence, $\lambda \in [0, 4]$, and the mapping distribution becomes more uniform when λ increases; therefore, λ takes the value of 4.

3.2.2. Improved the B_f Factor

The B_f factor determines the extent of the role of algorithm exploration and exploitation and plays an important role in balancing the algorithm's global and local search abilities. According to Equation (12), B_f, depending on the number of current iterations, shows linear changes, and the linear balancing factor hinders the global search ability of the algorithm in the early stage and reduces the convergence speed of the algorithm in the later stage. As a result, B_f is improved, and a nonlinear balancing factor is proposed to enhance the performance of the algorithm, as shown in Equation (18).

$$B_f = B_0(1 - \frac{1}{2} \times ({}^{t}/{}_{T})^2) \tag{18}$$

3.2.3. Dynamic Domain Perturbation

As seen in Section 3.1.3, the BWO development phase expands the candidate solutions through beluga location sharing. As a result, a dynamic domain perturbation factor η was designed to further expand the solutions. The domain perturbation factor showed an increasing and then decreasing trend with the number of iterations, which accelerated the optimization speed of the algorithm in the early stage, enhanced the development ability in the middle stage, accelerated the convergence performance in the late stage, expanded the candidate solutions as a whole, and strengthened the algorithm's solving ability. The dynamic domain perturbation factor is shown in Equation (19):

$$\eta = \sin(\pi \times {}^{t}/{}_{T}) \tag{19}$$

With the inclusion of the dynamic domain perturbation factor, the beluga position update during the development stage is shown in Equation (20):

$$X_i^{t+1} = r_3 X_{best}^t - \eta X_i^t + C_1 \times L_f \times (X_r^t - X_i^t) \tag{20}$$

3.2.4. Flowchart for Improved Beluga Whale Optimization Algorithm

The beluga whale optimization algorithm was further improved and combined with the multi-objective idea of the non-dominated genetic algorithm, proposing an improved multi-objective beluga whale optimization algorithm. A flow chart of the algorithm is shown in Figure 2.

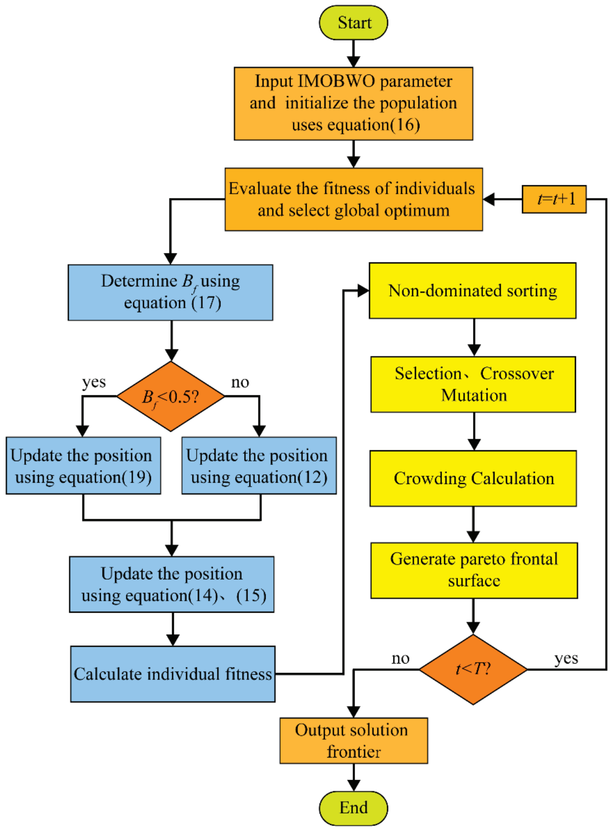

Figure 2. IMOBWO flow chart.

4. IMOBWO Performance Analysis

In this paper, the beluga whale optimization algorithm was enhanced from three aspects: initialization, adaptive factor, and development-stage domain perturbation. Upon integrating multi-objective optimization ideas, an improved multi-objective beluga whale algorithm was proposed. Ten multi-objective functions (ZDT1-ZDT4, Wfg5, Kursawe, Viennet2, Viennet3, DTLZ6, DTLZ7) [46–48] and IEEE-30bus [49,50] were selected. Their performance was analyzed to verify the solving capability of the IMOBWO.

4.1. Test Functions

The four main indexes for evaluating the performance of multi-objective algorithms, namely generation distance (GD), inverted generation distance (IGD), hypervolume (HV), and spacing (SP) were selected. The experimental software MATLAB 2022a was used, the number of iterations was 200, and the number of populations was 100. By analyzing multiple objective beluga whale optimization (MOBWO), multi-objective gray wolf optimization (MOGWO) [51], non-dominated sorting whale optimization (NSWOA) [52], and IMOBWO in 10 test functions were used, and the test results are shown in Table 2.

Table 2. Test results of the four algorithms on the 10 test functions.

Test Function	IMOBWO				MOBWO				MOGWO				NSWOA			
	GD	IGD	HV	SP	GD	IGD	HV	SP	GD	IGD	HV	SP	GD	IGD	HV	SP
ZDT1	6.473×10^{-5}	0.0015	0.7229	0.002	9.617×10^{-5}	0.0049	0.7192	0.0045	6.928×10^{-5}	0.0099	0.709	0.0132	5.257×10^{-4}	0.0057	0.7142	0.0058
ZDT2	2.661×10^{-5}	0.0022	0.4467	0.0057	4.809×10^{-5}	0.006	0.4436	0.0062	4.30×10^{-5}	0.0097	0.4353	0.0143	1.644×10^{-4}	0.0047	0.4436	0.0069
ZDT3	9.557×10^{-5}	0.0057	0.6045	0.0042	1.307×10^{-4}	0.1049	0.7784	0.005	1.726×10^{-4}	0.0117	0.5974	0.0225	3.921×10^{-4}	0.0069	0.5988	0.0064
ZDT4	4.958×10^{-5}	0.0022	0.7222	0.0034	5.562×10^{-5}	0.003	0.7214	0.0042	1.253×10^{-4}	0.0136	0.7089	0.0109	2.518×10^{-4}	0.0051	0.7182	0.0076
Wfg5	0.0045	0.0688	0.3092	0.0089	0.0052	0.0691	0.3086	0.0121	0.0068	0.0884	0.2994	0.0327	0.0064	0.0884	0.2994	0.0187
Kursawe	0.0015	0.0341	0.5062	0.0811	0.0021	0.0531	0.5048	0.103	0.0065	0.0817	0.4977	0.1199	0.0036	0.0555	0.5043	0.13334
Viennet2	2.052×10^{-4}	0.0256	3416	0.0069	4.657×10^{-4}	0.0694	0.3373	0.0171	2.611×10^{-4}	0.0227	0.3387	0.0172	0.0099	0.0191	0.3381	0.0439
Viennet3	2.212×10^{-4}	0.027	0.1835	0.0342	2.261×10^{-4}	0.0386	0.1834	0.0485	5.136×10^{-4}	0.0974	0.1827	0.0973	5.316×10^{-4}	0.0427	0.183	0.0619
DTLZ6	3.759×10^{-5}	0.0032	0.2013	0.0043	6.608×10^{-5}	0.0054	0.2008	0.0089	4.901×10^{-5}	0.0087	0.1946	0.0099	4.831×10^{-5}	0.0049	0.1999	0.0073
DTLZ7	0.0018	0.0854	0.2768	0.057	0.0019	0.2311	0.2599	0.0444	0.0071	0.0956	0.2596	0.0733	0.0055	0.0789	0.2673	0.0817

Among the 10 test functions, ZDT1-ZDT4 and Kursawe have two optimization objectives, and the other functions have three. The evaluation index values of the 10 test functions obtained using four algorithms were analyzed, and the following conclusions were drawn:

(i) The GD values obtained using IMOBWO were smaller than those obtained using the other algorithms for all 10 test functions, which was shown in Figure 3. The GD values obtained using IMOBWO for the functions ZDT2, ZDT3, Wfg5, and DTLZ6 were 2.661×10^{-5}, 9.557×10^{-5}, 0.0045, and 3.759×10^{-5}. Compared to the other three algorithms, IMOBWO showed significant performance advantages. According to Figure 3, the line of IMOBWO was always located at the lowest level, which showed that the average distance between the obtained solutions and the true Pareto solution set of the function was minimized, proving the superior convergence performance of IMOBWO.

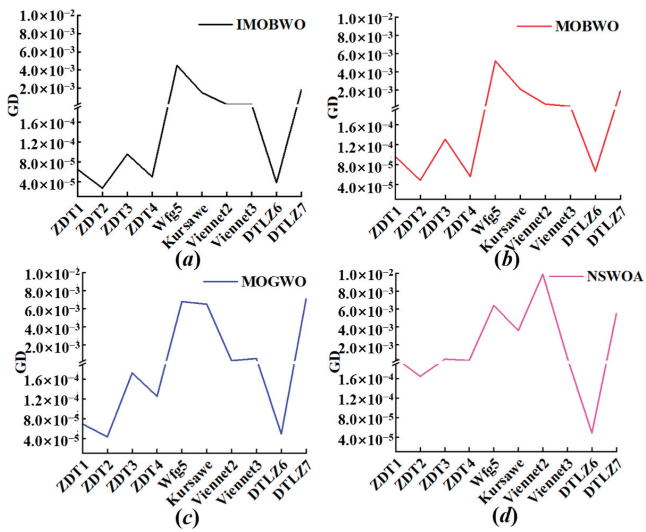

Figure 3. Line graph of GD values obtained using four algorithms.

(ii) The IGD values obtained using IMOBWO were smaller than those obtained using the other algorithms for eight of the test functions (excluding DTLZ7 and Viennet2), which was shown in Figure 4. The IGD values obtained using IMOBWO for the functions ZDT2, ZDT3, Kursawe, and Viennet3 were 0.0022, 0.0057, 0.0341, and 0.027. Compared to the other three algorithms, IMOBWO showed good performance, with the average distance from the set of Pareto solutions of the function to the solution obtained using the algorithm being the smallest, confirming that IMOBWO performed better than the other three algorithms in terms of diversity and convergence.

(iii) The HV values obtained using IMOBWO were greater than those obtained using the other algorithms for nine of the test functions (excluding ZDT3), which was shown in Figure 5. The HV values obtained using IMOBWO for the functions Wfg5, Viennet2, and DTLZ7 were 0.3092, 0.3416, and 0.2768. Compared to the other three algorithms, the HV values obtained using IMOBWO were always above the line graph, indicating that the distribution of the population in the target space was significantly better than that of the other algorithms.

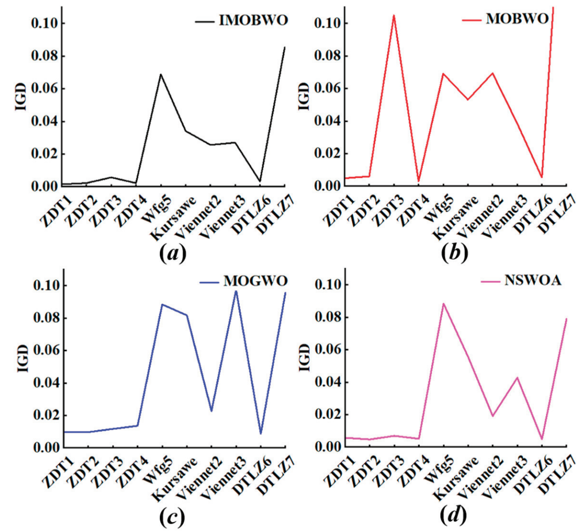

Figure 4. Line graph of IGD values obtained using four algorithms.

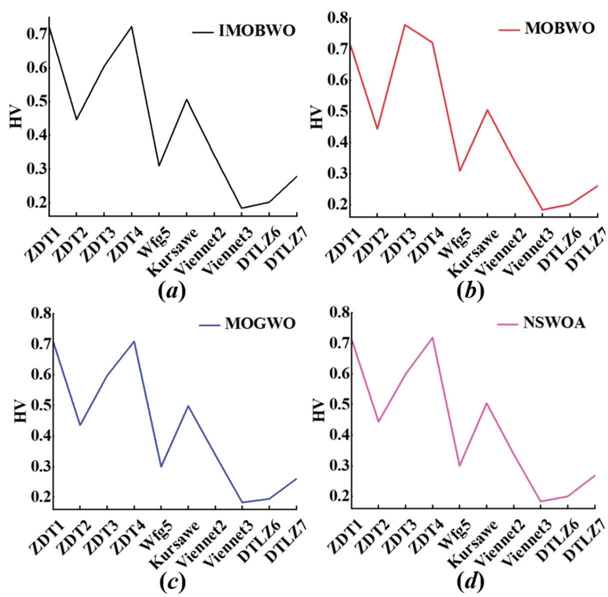

Figure 5. Line graph of HV values obtained using four algorithms.

(iv) The SP values obtained using IMOBWO were smaller than those obtained using the other algorithms for nine of the test functions (excluding DTLZ7), which was shown in Figure 6. The SP obtained values of IMOBWO on functions such as ZDT1, Wfg5, Kursawe, Vinnet2, and Vinnet3 were 0.0020, 0.0089, 0.0811, 0.0069, and 0.0342. Compared to the other three algorithms, the SP index values obtained using IMOBWO were significantly smaller, indicating that the distance between each solution of IMOBWO and the other solutions was the smallest and proved the homogeneity of the solution set. The performance of the 10 test functions proved that IMOBWO had better convergence performance in the multi-objective problem solving and the uniform distribution of the solution set possessed diversity.

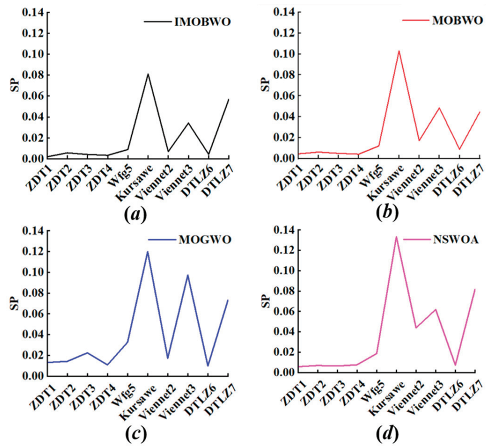

Figure 6. Line graph of SP values obtained by four algorithms.

4.2. IEEE 30-Bus

In order to test the ability of IMOBWO to solve engineering problems, the IEEE 30-bus problem was selected, and the Pareto frontier surfaces of the four algorithms were generated to analyze the distribution of the solution space and the dominant relationship between each multi-objective algorithm and verify the adaptability of IMOBWO for solving multi-objective engineering problems. The distribution of the frontier surfaces of the four algorithms were shown in Figure 7.

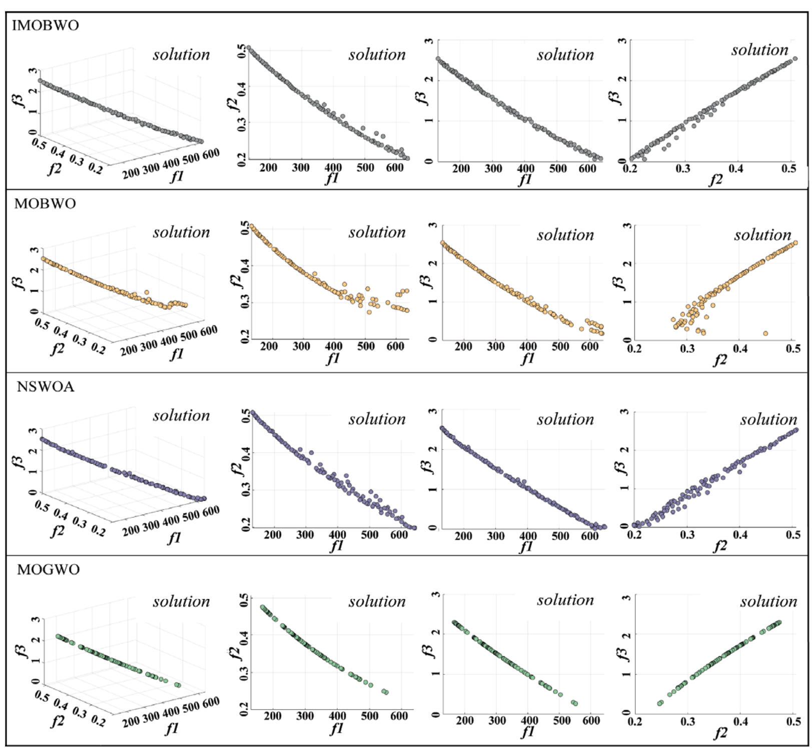

Figure 7. IEEE 30-bus test results.

The analysis in Figure 7 showed the excellent performance of IMOBWO for the IEEE 30-bus problem. When observing the Pareto frontier distributions of the four algorithms, the following could be seen: (i) a better solving ability of IMOBWO compared to MOBWO, with most of the solutions obtained using the former being dominated by the latter; (ii) strong solving ability of both IMOBWO and NSWOA for the test problem, with the latter having had more non-dominant distributions on the Pareto frontier than the former, and poor performance in terms of convergence performance; (iii) IMOBWO was better in both solution space distribution and convergence performance compared to MOGWO. The effective solving ability and superior convergence performance of IMOBWO for multi-objective problems were further verified.

5. Case Analysis

In this section, IMOBWO was applied to the truck scheduling problem of an open-pit mine in Guangxi, China. This section was divided into three parts; the first part provided a brief introduction of the basic situation of the mine, the second part showed the data needed for this study, and the third part introduced the research data and used IMOBWO to solve the scheduling model, as well as compared the solution results of the four algorithms and analyzed the application capabilities among the algorithms.

5.1. Introduction to an Open-Pit Mine

The mine is located in Guigang city in Guangxi, China, and is an open-pit mine production, with an overall flat mining environment. There are six loading points and four crushing stations in the mine, each of which is equipped with crushers and excavators, and all of which are capable of mining. The daily ore output from the six working faces satisfies the requirements of the mine's production. The current mining status of the mine is shown in Figure 8, letters A to E refer to the 6 loading point positions, while letters *a* to *d* refer to the 4 crushing station positions.

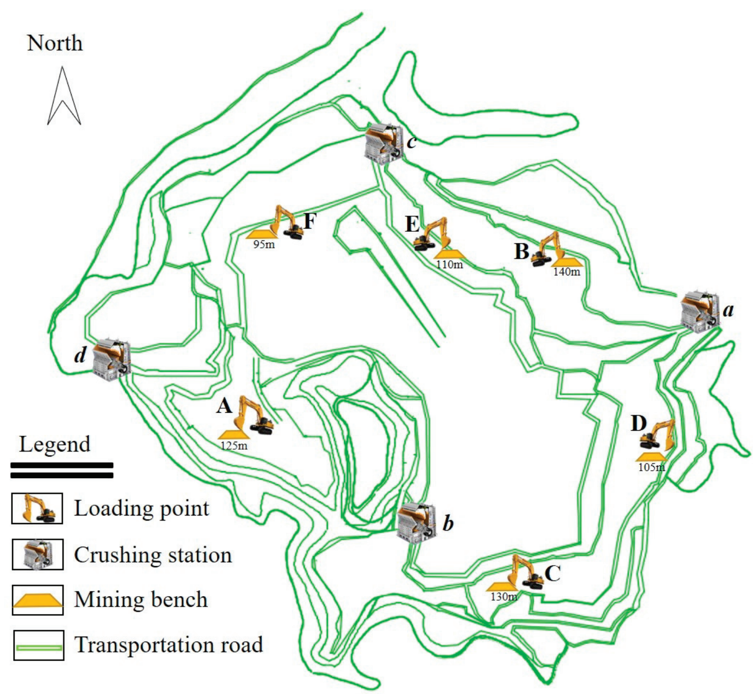

Figure 8. Schematic diagram of loading points and crushing stations.

The steps of ore production in this mine were as follows: after blasting, the ore was initially crushed into blocks using rock drills and crushing hammers, then loaded onto unmanned trucks using excavation shovels, and transported to the mine's crushing stations by road for granular crushing, in preparation for the subsequent extraction of minerals. However, the mine production was relatively sloppy; transportation truck scheduling relied on manual scheduling, and vehicle scheduling had the problems of high shipping cost and waiting time. Additionally, there was an obvious deficiency in the control of ore quality and the protection of transportation safety. As a result, a multi-objective scheduling model based on intelligent algorithms was applied to this open-pit mine to promote the intelligent transformation of truck scheduling, which was conducive to cost reduction, efficiency improvement, and synergistic development of open-pit mine production.

5.2. Presentation of Research Data

The research data were divided into two parts. First, the existing mechanical equipment in the mining area was considered, including data on the basic equipment such as the crushers, excavators, and transportation trucks used. Second, the parameter settings related to truck scheduling were included, such as the distance from each working face (loading point) to each crushing station, the ore grade provided by each working face and specified by each crushing plant, the amount of ore required to be supplied by the loading points and crushing plants in each shift, and other model-solving information.

5.2.1. Basic Data on Mining Equipment

The basic operation data of the crushers, dump trucks, excavators, etc., were obtained through field research on the current production status of the mine and combined with the preliminary information such as the mine development program, as shown in Table 3.

Table 3. Basic data of the equipment.

Equipment Name	Equipment Model	Equipment Parameters	
Crusher	PCF2022	Production capacity/t·h^{-1}	750~1000
		Feed size/mm	1200 × 1000 × 1500
		Discharge size/mm	≤40
Truck	YT3761	Load/t	50
		Full load speed/km·h^{-1}	18
		No-load speed/km·h^{-1}	37
Excavator	PC850-8E0	Working efficiency/t·h^{-1}	465
		Bucket volume/m^3	4.3
		Working weight/kg	78,300

5.2.2. Scheduling Model Parameterization

By collecting the location coordinates of each loading point and crushing station through a satellite cloud map of the mining area and combining them with the current production status of the mining area, the basic parameters such as the distance from each loading point to each crushing station, the supply of ore at the loading points, and the ore demand at the crushing stations was obtained, as shown in Tables 4–6.

Table 4. Distances between loading points and crushing stations.

Average Distance/km	Crushing Stations a	Crushing Stations b	Crushing Stations c	Crushing Stations d
Loading point A	3.251	2.694	2.838	1.543
Loading point B	1.902	2.264	3.031	3.194
Loading point C	2.861	1.348	2.984	2.142
Loading point D	1.596	3.689	1.865	3.065
Loading point E	1.64	2.87	2.716	2.887
Loading point F	3.227	1.658	1.334	1.793

Table 5. Ore supply at loading points.

	Loading Point A	Loading Point B	Loading Point C	Loading Point D	Loading Point E	Loading Point F
Supply/t	5100	6100	4200	5300	6500	7000
Grade/%	0.137	0.131	0.119	0.139	0.13	0.121

Table 6. Ore demand by crushing plant.

	Crushing Stations a	Crushing Stations b	Crushing Stations c	Crushing Stations d
Demand/t	3000	3000	3000	3000
Grade/%	0.125	0.125	0.125	0.125

5.3. Application Results

In this section, the results of four algorithms—IMOBWO, MOBWO, MOGWO, and NSWOA—for solving the truck scheduling problem for open-pit mines were shown. The experimental software was MATLAB 2022a was used, the number of iterations was 200, and the population size was 100. The results were shown in Figure 9.

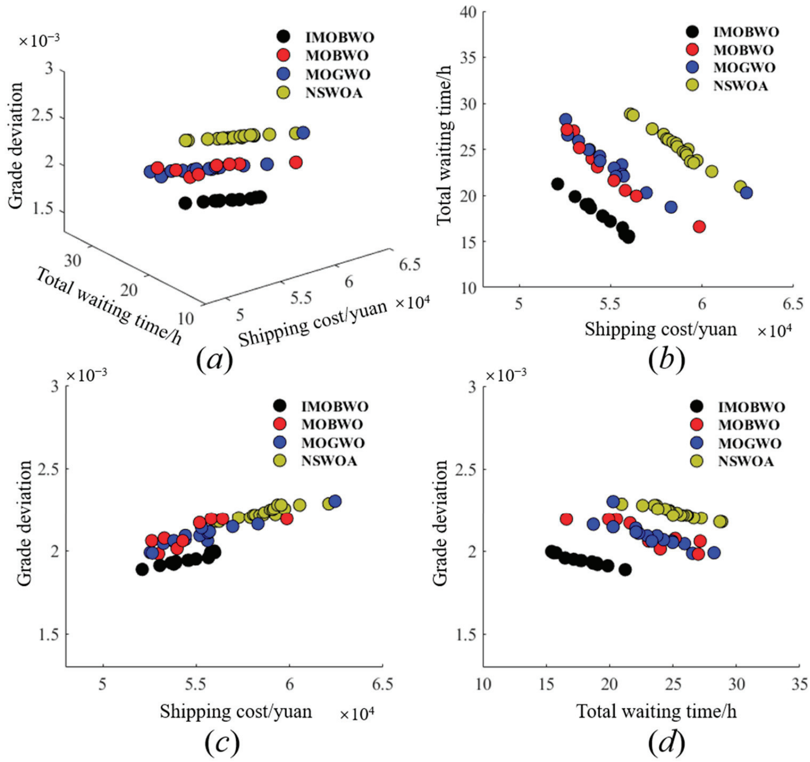

Figure 9. The solution results from four algorithms. (**a**) The objectives of shipping cost, total waiting time, and ore grade deviation. (**b**) The objectives of total waiting time and shipping cost. (**c**) The objectives of ore grade deviation and shipping cost. (**d**) The objectives of total waiting time and ore grade deviation.

In the analysis of the frontier surface distribution of the four algorithms, subplot (a) showed that feasible solutions to the scheduling problem were obtained in the three-dimensional objective space using all four algorithms, confirming the feasibility of the multi-objective algorithms for multi-objective problem solving. From an analysis of subplot (b), it was found that in terms of the total waiting time and the shipping cost, IMOBWO showed a dominant relationship over the other three algorithms. From an analysis of subplot (c), it was found that, in the two-dimensional objective space composed of ore grade deviation and shipping cost, all algorithms showed better solution results, while IMOBWO had better solution results. From an analysis of subfigure (d), it was found that IMOBWO had a significant dominance over MOBWO, MOGWO, and NSWOA in the two-dimensional objective space composed of total waiting time and ore grade deviation.

To demonstrate the solving ability of the improved algorithm, optimal solutions of the four algorithms on three objectives were listed in Table 7.

Table 7. The optimal values of four algorithms under three optimization objectives.

Optimization Objective	Solution Algorithm	Shipping Cost/Yuan	Total Waiting Time/h	Grade Deviation
Minimize Shipping cost	IMOBWO	52,108.4	21.2361	1.8878×10^{-3}
	MOBWO	52,617.1	27.1433	2.0602×10^{-3}
	MOGWO	52,544.4	28.2412	1.9897×10^{-3}
	NSWOA	56,094.9	28.8406	2.1777×10^{-3}
Minimize Total waiting time	IMOBWO	55,967.1	15.4318	1.9975×10^{-3}
	MOBWO	59,847.1	16.5958	2.1933×10^{-3}
	MOGWO	58,303.2	18.7224	2.1620×10^{-3}
	NSWOA	62,092.4	20.944	2.2873×10^{-3}
Minimize Grade deviation	IMOBWO	52,108.4	21.2361	1.8878×10^{-3}
	MOBWO	52,812.1	19.4529	1.9583×10^{-3}
	MOGWO	52,650.6	26.5475	1.9863×10^{-3}
	NSWOA	56,226.1	28.7033	2.1676×10^{-3}

The optimal values of the four algorithms were listed in detail in the bar chart in Figure 10.

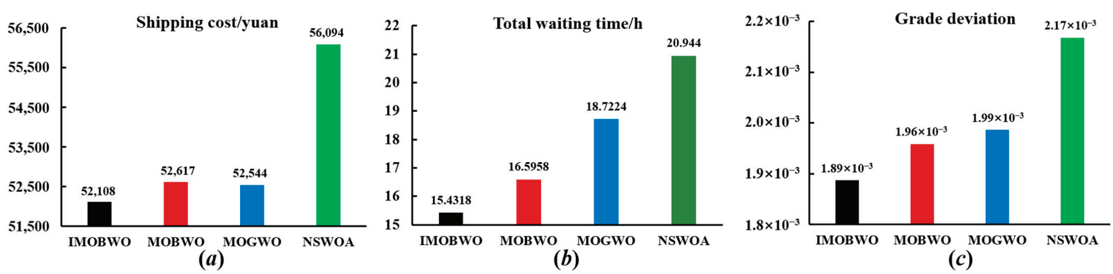

Figure 10. The optimal values of four algorithms under three optimization objectives.

From Figure 10, it could be seen that by applying IMOBWO for open-pit mine truck scheduling, the shipping cost decreased from 7.65 to 0.84%, the total waiting time decreased from 35.7 to 7.54%, and the ore grade deviation decreased from 14.8 to 3.73%. Figure 10 confirms the effectiveness of the IMOBWO algorithm in optimizing truck scheduling, which not only significantly reduced shipping cost but also optimized fuel consumption and carbon emission treatment cost that made up the shipping cost, thereby directly promoting mining environmental protection and sustainable development. In addition, through optimization, the idle time of trucks was significantly reduced, and the grade deviation of mined ore was better controlled. Compared to the other three algorithms, IMOBWO had the best solution for the open-pit mine truck scheduling problem.

To further demonstrate the solution results and to provide a basis for the development of a transportation truck scheduling scheme, the running routes of the trucks used for scheduling by IMOBWO under the objective of minimizing the shipping cost are shown in Table 8, and the Gantt chart of truck operation is shown in Figure 11.

Table 8. Optimized truck routes.

Vehicle Number	Optimized Trucks Route
1	AcEdDdAdCbCcCdEbAdFdDaEdEaCaBaCcAcBcCa
2	BdEdCaDaDdDbBcEbAcBbFaCbCdBbDdAaDbAdBd
3	CbBcBcAbCcCdCdEaFbDbEaCcEbCaFbBaBc
4	DdBaAbAdDdCdDdEaBaFdAbBcDbCaEbDaBdBcEdAa
5	EbAaFcAcBdDdEbEbBcDcCdAcCbCbFdEbBcBbCcCc
6	FaBdDbCbDbEbFaBaCaAdDaCbEaCcCbEbDa
7	AbBaAaAcCcBdAdEbCdBaEaDdBbAbBcAcAbCd
8	CdAbCdBcBcAdBaCbFcDbDaBaEaAcEbAc
9	DaCbDaBdEbAaAbCdEdBdFbEcDcDaCbAcCbDcDd
10	EaBbDcAaAbDbFcCbAaCcAaEaDcBdDcBaCcBc
11	FaCdBaBbFbFcBdFaEaCcFaCdDbFcFdFaBc
12	AdBcAdFaBcDcBaAdDcFdFcBdDcEdEdBbAaCaBbAd
13	BdEbDbBbFcAdEaAcAdAaFcBbFaBcCaFcBcDaBcCd

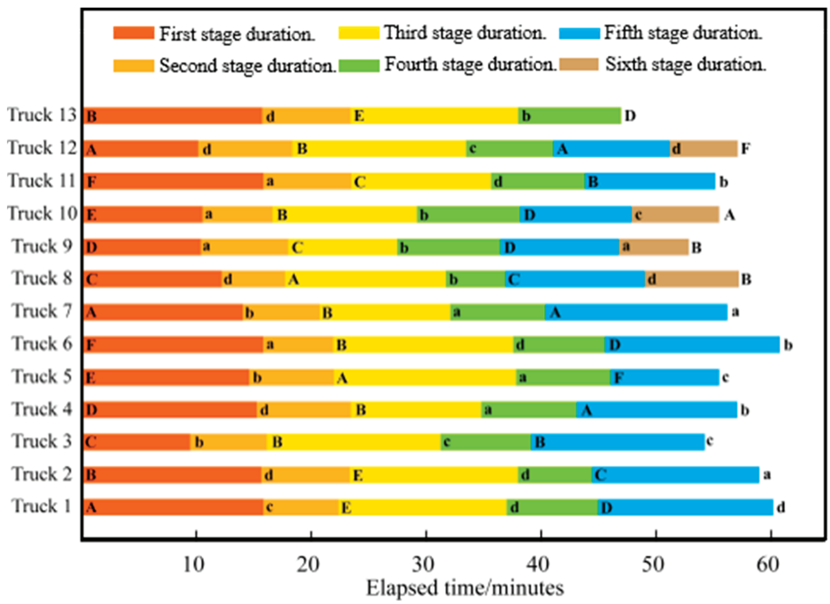

Figure 11. Gantt chart of truck operation.

In Table 8, the operating routes of unmanned trucks at the open-pit mine in Guigang are presented using the IMOBWO algorithm. In Figure 11, a progress schedule of the trucks within the first hour is shown. The above results demonstrated that the scheduling algorithm proposed in this paper could effectively solve the actual scheduling problem and provide certain decision support for production practice.

6. Conclusions and Future Directions

It has been acknowledged that planning transportation for mining trucks is essential to the output of open-pit mines. The utilization of intelligent technology in truck scheduling plays a crucial role in decreasing operational expenses, improving ore output, and reducing transportation delays. It also reduces environmental pollution and work-related safety risks. In order to overcome the challenges associated with the open-pit mine truck scheduling problem, this study proposed a novel multi-objective intelligence algorithm. The following conclusions were drawn:

(1) With the help of extensive empirical data from a mine in Guigang, Guangxi Province, China, a multi-objective truck scheduling model was built. This model was constructed to minimize ore grade deviation, total waiting time, and shipping cost. The fuel coefficient was used to convert truck fuel consumption into carbon emissions generated by vehicle operation, the truck shipping cost comprised two parts: the carbon emission treatment cost generated by fuel consumption and the truck driving cost, obviously, optimizing truck scheduling benefited the shipping cost, which could help diminish fuel consumption and carbon emission treatment cost. The model included constraints that take into account a number of factors, such as the availability of truck resources, the distance between each loading site and crushing station, the ore demand at crushing stations, and the supply of ore at loading locations.
(2) An improved multi-objective beluga whale optimization algorithm was proposed, and performance testing was conducted. Using logistic chaotic mapping, the initial population distribution was improved, and the distribution range of the solution was expanded. An adaptive factor was proposed that balanced the global and local search capabilities of the algorithm, overcoming the problem of slow convergence speed. The dynamic domain perturbation strategy was added to increase the number of potential solutions and improve the algorithm's ability to solve problems. The performance of IMOBWO was then investigated using IEEE 30-bus and 10 test functions, proving its superior problem-solving capability.
(3) When used for mine truck scheduling, IMOBWO demonstrated strong application skills. The shipping cost dropped from 7.65 to 0.84%, the total waiting time dropped from 35.7 to 7.54%, and the ore grade deviation dropped from 14.8 to 3.73% when compared to the other three algorithms.

This study's findings, taken together, show that IMOBWO performs exceptionally and has great value in mine scheduling applications. Future research directions might include improving the algorithm's solving capabilities. The applications of IMOBWO in other engineering scenarios will also be explored. The goal of this study was to promote the deep integration of intelligent scheduling algorithms and mine car scheduling, thereby promoting the sustainable development of the open-pit mining industry.

Author Contributions: Conceptualization, X.L. and Q.H.; methodology, X.L.; software, X.L.; validation, X.L. and Z.Y.; formal analysis, Z.Y.; investigation, X.L. and P.Z.; resources, X.L.; data curation, X.L.; writing—original draft preparation, P.Z.; writing—review and editing, X.L. and Q.H.; visualization, P.Z.; supervision, X.L.; project administration, X.L. and P.Z. All authors have read and agreed to the published version of the manuscript.

Funding: This research was funded by the National Natural Science Foundation of China (42003066), Guangxi Science and Technology Program (GuiKe AD21220109 and GuiKe AD21220147), Innovation Project of Guangxi Graduate education (YCSW2024518) and Guangxi Emergency Management Department Emergency Management Joint Innovation Technology Research Project (2024GXYJ011).

Institutional Review Board Statement: Not applicable.

Informed Consent Statement: Not applicable.

Data Availability Statement: The datasets generated and/or analyzed during the current research period can be obtained from the corresponding authors upon reasonable request.

Acknowledgments: We would like to thank Guigang Dingxiang mountain Mining Group for its help and support in this research.

Conflicts of Interest: The authors declare no conflicts of interest.

References

1. Purhamadani, E.; Bagherpour, R.; Tudeshki, H. Energy consumption in open-pit mining operations relying on reduced energy consumption for haulage using in-pit crusher systems. *J. Clean. Prod.* **2021**, *291*, 125228. [CrossRef]
2. Kuzmin, S.; Kadnikova, O.; Altynbayeva, G.; Turbit, A.; Khabdullina, Z. Development of a New Environmentally-Friendly Technology for Transportation of Mined Rock in the Opencast Mining. *Environ. Clim. Technol.* **2020**, *24*, 341–356. [CrossRef]

3. Fang, Y.; Peng, X. Micro-Factors-Aware Scheduling of Multiple Autonomous Trucks in Open-Pit Mining via Enhanced Meta-heuristics. *Electronics* **2023**, *12*, 3793. [CrossRef]
4. Moradi Afrapoli, A.; Askari-Nasab, H. Mining fleet management systems: A review of models and algorithms. *Int. J. Min. Reclam. Environ.* **2019**, *33*, 42–60. [CrossRef]
5. Bissiri, Y. Application of Agent-Based Modeling to Truck-Shovel Dispatching Systems in Open Pit Mines. Doctor of Philosophy—Ph.D. Thesis, University of British Columbia, Vancouver, BC, Canada, November 2022. [CrossRef]
6. Ismail, S.N.; Ramli, A.; Aziz, H.A. Research trends in mining accidents study: A systematic literature review. *Saf. Sci.* **2021**, *143*, 105438. [CrossRef]
7. Kasap, Y.; Subaşı, E. Risk assessment of occupational groups working in open pit mining: Analytic Hierarchy Process. *J. Sustain. Min.* **2017**, *16*, 38–46. [CrossRef]
8. Tang, J.; Zhao, B.; Yang, C.; Zhou, C.; Chen, S.; Ni, X.; Ai, Y. An Architecture and Key Technologies of Autonomous Truck Dispatching System in Open-pit Mines. In Proceedings of the 2022 International Conference on Cyber-Physical Social Intelligence (ICCSI), Nanjing, China, 18–22 November 2022. [CrossRef]
9. Chen, L.; Li, Y.; Silamu, W.; Li, Q.; Ge, S.; Wang, F.Y. Smart Mining With Autonomous Driving in Industry 5.0: Architectures, Platforms, Operating Systems, Foundation Models, and Applications. *IEEE Trans. Intell. Veh.* **2024**, *9*, 4383–4393. [CrossRef]
10. Noriega, R.; Pourrahimian, Y. A systematic review of artificial intelligence and data-driven approaches in strategic open-pit mine planning. *Resour. Policy* **2022**, *77*, 102727. [CrossRef]
11. Hartlieb-Wallthor, P.V.; Hecken, R.; Kowitz, S.F.; Suciu, M.; Ziegler, M. Sustainable Smart Mining: Safe, Economical, Environmental Friendly. In *Yearbook of Sustainable Smart Mining and Energy 2021: Technical, Economic and Legal Framework*; Springer International Publishing: Cham, Switzerland, 2022; pp. 37–79. [CrossRef]
12. Ertugrul, N.; Kani, A.P.; Davies, M.; Morán, L. Status of Mine Electrification and Future Potentials. In Proceedings of the 2020 International Conference on Smart Grids and Energy Systems (SGES), Guilin, China, 13–15 November 2020. [CrossRef]
13. Wang, Q.; Gu, Q.; Li, X.; Xiong, N. Comprehensive overview: Fleet management drives green and climate-smart open pit mine. *Renew. Sustain. Energy Rev.* **2024**, *189*, 113942. [CrossRef]
14. Mena, R.; Zio, E.; Kristjanpoller, F.; Arata, A. Availability-based simulation and optimization modeling framework for open-pit mine truck allocation under dynamic constraints. *Int. J. Min. Sci. Technol.* **2013**, *23*, 113–119. [CrossRef]
15. Zhang, L.; Shan, W.; Zhou, B.; Yu, B. A dynamic dispatching problem for autonomous mine trucks in open-pit mines considering endogenous congestion. *Transp. Res. Part C: Emerg. Technol.* **2023**, *150*, 104080. [CrossRef]
16. Ta, C.H.; Kresta, J.V.; Forbes, J.F.; Marquez, H.J. A stochastic optimization approach to mine truck allocation. *Int. J. Surf. Min. Reclam. Environ.* **2005**, *19*, 162–175. [CrossRef]
17. Huo, D.; Sari, Y.A.; Kealey, R.; Zhang, Q. Reinforcement Learning-Based Fleet Dispatching for Greenhouse Gas Emission Reduction in Open-Pit Mining Operations. *Resour. Conserv. Recycl.* **2023**, *188*, 106664. [CrossRef]
18. Munirathinam, M.; Yingling, J.C. A review of computer-based truck dispatching strategies for surface mining operations. *Int. J. Surf. Min. Reclam. Environ.* **1994**, *8*, 1–15. [CrossRef]
19. Alarie, S.; Gamache, M. Overview of solution strategies used in truck dispatching systems for open pit mines. *Int. J. Surf. Min. Reclam. Environ.* **2002**, *16*, 59–76. [CrossRef]
20. Shamsi, M.; Pourrahimian, Y.; Rahmanpour, M. Optimisation of open-pit mine production scheduling considering optimum transportation system between truck haulage and semi-mobile in-pit crushing and conveying. *Int. J. Min. Reclam. Environ.* **2022**, *36*, 142–158. [CrossRef]
21. Mirzaei-Nasirabad, H.; Mohtasham, M.; Askari-Nasab, H.; Alizadeh, B. An optimization model for the real-time truck dispatching problem in open-pit mining operations. *Optim. Eng.* **2023**, *24*, 2449–2473. [CrossRef]
22. Zhang, S.; Lu, C.; Jiang, S.; Shan, L.; Xiong, N.N. An Unmanned Intelligent Transportation Scheduling System for Open-Pit Mine Vehicles Based on 5G and Big Data. *IEEE Access* **2020**, *8*, 135524–135539. [CrossRef]
23. Nehring, M.; Topal, E.; Knights, P. Dynamic short term production scheduling and machine allocation in underground mining using mathematical programming. *Min. Technol.* **2010**, *119*, 212–220. [CrossRef]
24. Souza, M.J.; Coelho, I.M.; Ribas, S.; Santos, F.G.; Merschmann, L.H.C. A hybrid heuristic algorithm for the open-pit-mining operational planning problem. *Eur. J. Oper. Res.* **2010**, *207*, 1041–1051. [CrossRef]
25. Afrapoli, A.M.; Tabesh, M.; Askari-Nasab, H. A multiple objective transportation problem approach to dynamic truck dispatching in surface mines. *Eur. J. Oper. Res.* **2019**, *276*, 331–342. [CrossRef]
26. Choi, Y.; Nguyen, H.; Bui, X.N.; Nguyen-Thoi, T. Optimization of haulage-truck system performance for ore production in open-pit mines using big data and machine learning-based methods. *Resour. Policy* **2022**, *75*, 102522. [CrossRef]
27. Temeng, V.; Otuonye, F.; Frendewey, J. A nonpreemptive goal programming approach to truck dispatching in open pit mines. *Miner. Resour. Eng.* **1998**, *7*, 59–67. [CrossRef]
28. Topal, E.; Ramazan, S. A new MIP model for mine equipment scheduling by minimizing maintenance cost. *Eur. J. Oper. Res.* **2010**, *207*, 1065–1071. [CrossRef]
29. Patterson, S.R.; Kozan, E.; Hyland, P. Energy efficient scheduling of open-pit coal mine trucks. *Eur. J. Oper. Res.* **2017**, *262*, 759–770. [CrossRef]
30. Yao, J.; Wang, Z.; Chen, H.; Hou, W.; Zhang, X.; Li, X.; Yuan, W. Open-pit mine truck dispatching system based on dynamic ore blending decisions. *Sustainability* **2023**, *15*, 3399. [CrossRef]

31. Temeng, V.A.; Otuonye, F.O.; Frendewey, J.O. Real-time truck dispatching using a transportation algorithm. *Int. J. Surf. Min. Reclam. Environ.* **1997**, *11*, 203–207. [CrossRef]
32. Rehman, S.U.; Asad, M.W.A. A mixed-integer linear programming (MILP) model for short-range production scheduling of cement quarry operations. *Asia-Pac. J. Oper. Res.* **2010**, *27*, 315–333. [CrossRef]
33. Santelices, G.; Pascual, R.; Lüer-Villagra, A.; Cawley, A.M. Integrating mining loading and hauling equipment selection and replacement decisions using stochastic linear programming. *Int. J. Min. Reclam. Environ.* **2017**, *31*, 52–65. [CrossRef]
34. Li, Z. A methodology for the optimum control of shovel and truck operations in open-pit mining. *Min. Sci. Technol.* **1990**, *10*, 337–340. [CrossRef]
35. Coelho, V.N.; Souza, M.J.; Coelho, I.M.; Guimaraes, F.G.; Lust, T.; Cruz, R.C. Multi-objective approaches for the open-pit mining operational planning problem. *Electron. Notes Discret. Math.* **2012**, *39*, 233–240. [CrossRef]
36. Mendes, J.B.; D'Angelo, M.F.S.V.; Maia, N.A.; Veloso, R.R. A Hybrid Multiobjective Evolutionary Algorithm for Truck Dispatching in Open-Pit-Mining. *IEEE Lat. Am. Trans.* **2016**, *14*, 1329–1334. [CrossRef]
37. Alexandre, R.F.; Campelo, F.; Vasconcelos, J.A. Multi-objective evolutionary algorithms for the truck dispatch problem in open-pit mining operations. *Learn. Nonlinear Models* **2019**, *17*, 53–66. [CrossRef]
38. Zhong, C.; Li, G.; Meng, Z. Beluga whale optimization: A novel nature-inspired metaheuristic algorithm. *Knowl. Based Syst.* **2022**, *251*, 109215. [CrossRef]
39. Li, L.L.; Fan, X.D.; Wu, K.J.; Sethanan, K.; Tseng, M.L. Multi-objective distributed generation hierarchical optimal planning in distribution network: Improved beluga whale optimization algorithm. *Expert Syst. Appl.* **2024**, *237*, 121406. [CrossRef]
40. Li, Z.P.; Li, X.D.; Yan, X.T.; Wen, W.; Zeng, X.X.; Zhu, R.J.; Wang, Y.H.; Yi, L.Z. Optimal proportioning of iron ore in sintering process based on improved multi-objective beluga whale optimisation algorithm. *J. Iron Steel Res. Int.* **2024**, *31*, 1597–1609. [CrossRef]
41. Li, Y.; Chen, Z.; Hou, M.; Guo, T. Multi-objective optimization design of anti-roll torsion bar using improved beluga whale optimization algorithm. *Railw. Sci.* **2024**, *3*, 32–46. [CrossRef]
42. Hassan, M.H.; Kamel, S.; Jurado, F.; Ebeed, M.; Elnaggar, M.F. Economic load dispatch solution of large-scale power systems using an enhanced beluga whale optimizer. *Alex. Eng. J.* **2023**, *72*, 573–591. [CrossRef]
43. Li, Z.; Gao, J.; Guo, J.; Xie, Y.; Yang, X.; Li, M.J. Optimal loading distribution of chillers based on an improved beluga whale optimization for reducing energy consumption. *Energy Build.* **2024**, *307*, 113942. [CrossRef]
44. Xing, Q.; Huang, X.; Wang, J.; Wang, S. A novel multivariate combined power load forecasting system based on feature selection and multi-objective intelligent optimization. *Expert Syst. Appl.* **2024**, *244*, 122970. [CrossRef]
45. Kanso, A.; Smaoui, N. Logistic chaotic maps for binary numbers generations. *Chaos Solitons Fractals* **2009**, *40*, 2557–2568. [CrossRef]
46. Nebro, A.J.; Luna, F.; Alba, E.; Dorronsoro, B.; Durillo, J.J.; Beham, A. AbYSS: Adapting Scatter Search to Multiobjective Optimization. *IEEE Trans. Evol. Comput.* **2008**, *12*, 439–457. [CrossRef]
47. Cheng, R.; Li, M.; Tian, Y.; Xiang, X.; Zhang, X.; Yang, S.; Jin, Y.; Yao, X. *Benchmark Functions for the Cec'2018 Competition on Many-Objective Optimization*; University of Birmingham Edgbaston: Birmingham, UK, 2018.
48. Zitzler, E.; Deb, K.; Thiele, L. Comparison of Multiobjective Evolutionary Algorithms: Empirical Results. *Evol. Comput.* **2000**, *8*, 173–195. [CrossRef]
49. Flôr, V.B.B.; Do Coutto Filho, M.B.; de Souza, J.C.S.; Vergara, P.P. Critical Data Visualization to Enhance Protection Schemes for State Estimation. *IEEE Trans. Smart Grid* **2023**, *14*, 1249–1261. [CrossRef]
50. Hemeida, M.; Senjyu, T.; Alkhalaf, S.; Fawzy, A.; Ahmed, M.; Osheba, D. Reactive power management based hybrid GAEO. *Sustainability* **2022**, *14*, 6933. [CrossRef]
51. Mirjalili, S.; Saremi, S.; Mirjalili, S.M.; Coelho, L.D.S. Multi-objective grey wolf optimizer: A novel algorithm for multi-criterion optimization. *Expert Syst. Appl.* **2016**, *47*, 106–119. [CrossRef]
52. Islam, Q.N.U.; Ahmed, A.; Abdullah, S.M. Optimized controller design for islanded microgrid using non-dominated sorting whale optimization algorithm (NSWOA). *Ain Shams Eng. J.* **2021**, *12*, 3677–3689. [CrossRef]

applied sciences

MDPI

Article

Numerical Methods as an Aid in the Selection of Roof Bolting Systems for Access Excavations Located at Different Depths in the LGCB Mines

Daniel Pawelus * and Jan Butra

Faculty of Geoengineering, Mining and Geology, Wroclaw University of Science and Technology, 50-370 Wroclaw, Poland; jan.butra@pwr.edu.pl
* Correspondence: daniel.pawelus@pwr.edu.pl

Abstract: The values of primary stresses are not allowed for as a criterion in the selection of roof bolting systems in mining excavations located at various depths in Polish copper ore mines. Therefore, in order to ensure enduring and safe operation of excavations, in particular, those driven in unfavourable geological and mining conditions, this problem has required solutions based on numerical methods. This article presents an example of applying numerical simulations to the evaluation of the stability of headings in Polish copper ore mines. The analyses included mining excavations located at various depths in the rock mass. This issue is of great importance, as safety regulations are prioritised in mining excavations which remain in operation even for several decades. The stability of the headings was evaluated with the use of the RS2 specialist numerical simulation software. This computer program uses the finite element method (FEM) for calculations. The rock parameters used in the numerical models have been determined on the basis of the Hoek–Brown classification. For that purpose, the RocLab 1.0 software was used. The parameters of the stress field were identified from the profile of the GG-1 shaft with the assumed hydrostatic state of stress. The numerical modelling was performed in a triaxial stress state and in a plane strain state. The numerical analyses were based on the Mohr–Coulomb failure criterion. The rock medium was described with the elastic-plastic model with softening (roof and walls) and with the elastic-plastic model (floor). The results of the numerical analyses served to provide an example of the application of a roof bolting system to protect headings located at the depths of 1000 m b.g.l. and 1300 m b.g.l.

Keywords: stability of excavations; roof bolting systems; finite element method (FEM); numerical simulations; Polish copper ore mines

Citation: Pawelus, D.; Butra, J. Numerical Methods as an Aid in the Selection of Roof Bolting Systems for Access Excavations Located at Different Depths in the LGCB Mines. *Appl. Sci.* **2024**, *14*, 7052. https://doi.org/10.3390/app14167052

Academic Editor: Giuseppe Lacidogna

Received: 1 June 2024
Revised: 7 August 2024
Accepted: 8 August 2024
Published: 12 August 2024

1. Introduction

The copper ore deposit mined in Poland by KGHM Polska Miedz S.A. is located in Lower Silesia, between the towns of Lubin and Glogow. The Legnica-Glogow Copper Belt (LGCB) comprises three underground mining plants: Lubin, Polkowice-Sieroszowice and Rudna. The copper-bearing rocks are located at a depth from approx. 370 m b.g.l. (in the Lubin-Malomice mining area) to 1385 m b.g.l. (in the Deep Glogow mining area) [1].

Roof bolting is the most commonly used roof support system in the mines of the LGCB region. The selection of a roof bolt system is preceded by identifying the roof class of a mining excavation (from class 1—the worst—to class 5—the best) in accordance with the "Instructions on determining the geomechanical parameters of roof rocks with respect to roof classes in copper mines, as required in the selection of a roof bolting system design" [2]. Roof rocks are classified on the basis of such parameters as:

- Roof bedding (vertical split);
- Concentration of mineralised cracks;
- Fault concentration;
- Average fault throw;

- Tensile strength of the roof rock beam.

A particular design of the roof bolting system is selected in accordance with the "Regulations on the selection, construction and control of excavation support in the KGHM Polska Miedz S.A. mines" [3]. The roofs in the headings are protected with bolts at least 1.6 m long. The distance between the bolts (the bolting mesh) is adjusted depending on the class of the roof and on the width of the heading below the roof (Table 1).

Table 1. Selection of a roof bolting system for headings in the LGCB mines [3].

Roof Class	Maximum Excavation Width [m]	Bolting Mesh [m]
I	6.0	1.0 × 1.0
II	7.0	1.0 × 1.0
III	7.0	1.5 × 1.5
IV	7.0	2.0 × 2.0
V	8.0	2.0 × 2.0

Support is provided not only to the roof but also to the side walls of the heading in cases where the excavation height is greater than 4.5 m (regardless of the side wall inclination angle) or where the excavation height is not greater than 4.5 m and moving the side walls outwards by approximately 10° is not possible. The roof bolts have a length of at least 1.6 m and are spaced in the side walls at 1.5 × 1.5 m. The lower row of roof bolts is situated at a distance of approximately 1.8 m from the floor [3,4].

The regulations on the selection of roof support systems for the headings and production excavations in the LGCB mines do not allow for the values of primary stresses in the rock mass at the depth of the excavations. As a result, the roof support system may be inappropriately selected and lead to problems with the stability and functionality of the excavations. This fact may be of particular importance in the case of headings (both access and preparatory excavations) which have transport or ventilation functions. Their functionality must be ensured over a time spanning from several years to over a decade.

In recent years, owing to the increase in computing power, numerical methods have become a common tool in solving various problems related to rock mass mechanics. The advantage of such methods lies in their ability to analyse objects of practically any geometry, allowing for different models describing the behaviour of the material under load, spatial changes in rock mass properties, specific field of primary stresses, dynamic loads, etc. They also provide solutions to both two-dimensional and three-dimensional tasks [5–18]. Currently, the most popular numerical calculation methods employed in solving problems related to rock mass mechanics include the finite element method (e.g., PHASE2, RS2, RS3, NASTRAN, ANSYS, MIDAS GTS NX) and the finite difference method (e.g., FLAC software). Other methods include the boundary element method (e.g., EXAMINE) or the distinct element method (e.g., UDEC).

Numerical methods have significantly expanded research possibilities related to the analysis and evaluation of the stability of excavations in underground mines. They are frequently used, both in Poland and abroad, to solve problems related to driving excavations in underground mines in varying or difficult geological and mining conditions [19–30]. Numerical modelling allows predictions of the stress concentration zones and the potential locations in which the rock mass may become unstable in the vicinity of a mining excavation. The results of numerical simulations are used to plan and design inter alia access, preparatory, production, and other special-purpose excavations of various shapes and dimensions, as well as to aid the selection of adequate support systems [31–38].

2. Predictions of the Stability of Headings in the LGCB Mines

The decrease or the loss of stability in headings located at different depths (1000 m b.g.l. and 1300 m b.g.l.) in one of the LGCB mines were modelled with the use of numerical simulations. The numerical calculations were performed in the RS2 software, which is based on the finite element method (FEM), i.e., one of the most popular numerical methods.

Table 2 lists rock parameters used in the numerical simulations of the stability of headings in the conditions of one of the LGCB mines. The parameters were determined from geomechanical tests of rock samples. The rock samples for the laboratory tests were obtained from two boreholes: Jm-15/H-173 (rock layers in the roof and in the floor) and Jm-15-460 (rock layers in the walls). The rock parameters obtained from the Jm-15/H-173 and Jm-15-460 boreholes show the typical geological structure of the Fore Sudetic Monocline. In this structure, the access and preparatory excavations of the LGCB mines are driven. The immediate roof layers contain very strong carbonate formations (calcareous dolomite), as opposed to the rock layers which form the mined deposit and the floor layers.

Table 2. Mean strength and strain rock parameters for the Jm-15/H-173 borehole and the Jm-15-460 borehole.

Location	Rock Type	h [m]	ρ [MPa]	R_c [MPa]	R_r [MPa]	E_i [MPa]	ν [-]
Roof	Anhydrite I	0.70	2.94	132.49	6.43	42,420.00	0.24
	Anhydrite II	1.80	2.94	117.61	5.25	38,240.00	0.24
	Anhydrite III	3.00	2.94	97.88	5.58	40,600.00	0.24
	Anhydrite IV	9.30	2.94	86.93	5.94	38,300.00	0.24
	Dolomite I	1.20	2.81	175.86	7.20	68,400.00	0.26
	Dolomite II	1.70	2.79	156.21	8.03	47,290.00	0.25
	Dolomite III	0.60	2.63	194.22	10.05	89,800.00	0.27
	Dolomite IV	0.70	2.64	186.60	8.98	82,050.00	0.28
	Dolomite V	1.00	2.70	165.69	4.55	65,050.00	0.24
	Dolomite VI	0.70	2.73	126.89	9.59	23,400.00	0.22
	Dolomite VII	0.60	2.65	188.90	10.87	84,400.00	0.27
	Dolomite VIII	0.70	2.80	118.44	5.45	39,150.00	0.23
Walls	Dolomite IX	1.60	2.71	95.00	10.16	27,170.00	0.22
	Dolomitic shale	0.60	2.69	111.49	9.06	28,890.00	0.23
	Sandstone I	1.20	2.40	47.85	2.93	16,940.00	0.17
Floor	Sandstone II	9.50	2.33	36.19	2.78	13,600.00	0.14

The symbols used in the above table are as follows: h—thickness of rock layers, ρ—volume density, R_c—rock sample strength to uniaxial compression, R_r—tensile strength of the rock sample, E_i—longitudinal modulus of elasticity, v—Poisson's ratio.

Subsequently, the Hoek–Brown failure criterion, which is broadly used in geomechanical analyses of rock mass deformations and effort, was assumed for the rock mass. The generalised Hoek–Brown failure criterion for a fractured rock mass may be described with the following equation [39]:

$$\sigma_1 = \sigma_3 + \sigma_{ci} \cdot \left(m_b \cdot \frac{\sigma_3}{\sigma_{ci}} + s \right)^a \tag{1}$$

where:

σ_1—value of the maximum principal effective stress at failure,
σ_3—value of the minimum principal effective stress at failure,
m_b—the Hoek–Brown constant for the rock mass,
s and a—constants depending on the rock mass properties,
σ_{ci}—uniaxial compressive strength of the rock sample.

When rock mass tensile strength σ_{tm} is exceeded, the equation for a = 0.5 can be formulated as follows:

$$\sigma_{tm} = \frac{\sigma_{ci}}{2} \cdot \left(m_b - \sqrt{{m_b}^2 + 4s} \right) \tag{2}$$

After the failure criterion had been assumed, the RocLab 1.0 software and Hoek–Brown classification [39–42] were used to determine the rock mass parameters (strength and strain parameters) for each of the rock layers present in the Jm-15/H-173 and Jm-15-460 boreholes (Table 3).

Table 3. Rock mass parameters determined with the RocLab 1.0 software—the Jm-15/H-173 borehole and the Jm-15-460 borehole.

Location	Rock Type	c [MPa]	φ [°]	σ_t [MPa]	E_{rm} [MPa]
Roof	Anhydrite I	9.914	38.66	1.061	31,085.97
	Anhydrite II	8.801	38.66	0.942	28,022.81
	Anhydrite III	7.324	38.66	0.784	29,752.25
	Anhydrite IV	6.505	38.66	0.696	28,066.78
	Dolomite I	16.040	39.00	3.893	60,215.79
	Dolomite II	14.248	39.00	3.458	41,631.65
	Dolomite III	17.715	39.00	4.299	79,055.23
	Dolomite IV	17.020	39.00	4.131	72,232.54
	Dolomite V	15.113	39.00	3.668	57,266.63
	Dolomite VI	11.574	39.00	2.809	20,600.14
	Dolomite VII	17.229	39.00	4.182	74,301.36
	Dolomite VIII	10.803	39.00	2.622	34,465.62
Walls	Dolomite IX	7.579	37.69	1.442	22,180.23
	Dolomitic shale	6.447	30.41	1.327	18,250.37
	Sandstone I	3.589	40.54	0.180	10,701.33
Floor	Sandstone II	2.520	39.06	0.093	7072.00

The symbols used in the above table are as follows: c—cohesion, φ—internal friction angle, σ_t—uniaxial tensile strength of the rock mass, E_{rm}—rock mass modulus of elasticity.

The numerical model was constructed in the RS2 application, in a triaxial stress state and in a plane strain state. Numerical calculations were performed for an isotropic and for a uniform medium. The rock medium was described with the elastic-plastic model with softening (layers in the roof and walls) and with the elastic-plastic model (layers in the floor). Table 4 shows the strength and strain parameters of the rocks in the model. The numerical model was developed on the basis of the Mohr–Coulomb failure criterion, which states that rock may reach threshold effort under the following condition:

$$\sigma_1 = \sigma_3 \cdot \frac{1 + \sin\varphi}{1 - \sin\varphi} + \frac{2c \cdot \cos\varphi}{1 - \sin\varphi} \tag{3}$$

or

$$\sigma_3 = -\sigma_t \tag{4}$$

where:

σ_1—effective maximum stress at failure,
σ_3—effective minimum stress at failure,
φ—internal friction angle,
c—cohesion,
σ_t—uniaxial tensile strength of the rock mass.

Numerical analyses were performed for a group of four headings. The excavations have a trapezoidal shape. In the headings, the side walls were inclined at an angle of 10°. The adjacent excavations are separated by pillars 20 m in width. Table 5 lists the dimensions of headings in their assumed cross-sections. The headings were protected with full-length-grouted rockbolts in a 1.5 m × 1.5 m bolting grid (Figure 1). The parameters of the employed RM-18 1.8 m long bolts are shown in Table 6.

Table 4. Rock mass parameters adopted for the numerical modelling in the elastic-plastic medium with softening (the roof and the walls) and in the elastic-plastic medium (the floor), for the Coulomb–Mohr criterion.

Location	Rock Type	h [m]	E_s [MPa]	ν [-]	σ_t [MPa]	φ [°]	c [MPa]	δ [°]	φ_{res} [°]	c_{res} [MPa]
Roof	Anhydrite I-III	5.50	29,356.00	0.24	0.871	38.66	8.137	2.00	36.73	1.627
	Anhydrite IV	9.30	28,066.78	0.24	0.696	38.66	6.505	2.00	36.73	1.301
	Dolomite I-VIII	7.20	52,975.30	0.25	3.611	39.00	14.879	2.00	37.05	2.976
Walls	Dolomite—shale—sandstone formations	3.50	17,435.35	0.20	0.976	37.41	5.971	2.00	35.54	1.194
Floor	Sandstone	9.50	7072.00	0.14	0.093	39.06	2.520	2.00	39.06	2.520

The symbols used in the above table are as follows: h—thickness of rock layers, E_s—longitudinal modulus of elasticity, υ—Poisson's ratio, σ_t—tensile strength of the rock mass, φ—internal friction angle, c—cohesion coefficient, δ—dilatancy angle, ϕ_{res}—residual internal friction angle, c_{res}—residual cohesion coefficient.

Table 5. Dimensions of the analysed headings.

Excavation Height h_w [m]	Excavation Width Below the Roof d_r [m]	Excavation Width at the Floor d_f [m]	Mean Excavation Width d_a [m]	Excavation Surface Area S_r [m^2]
3.50	7.00	5.80	6.40	22.40

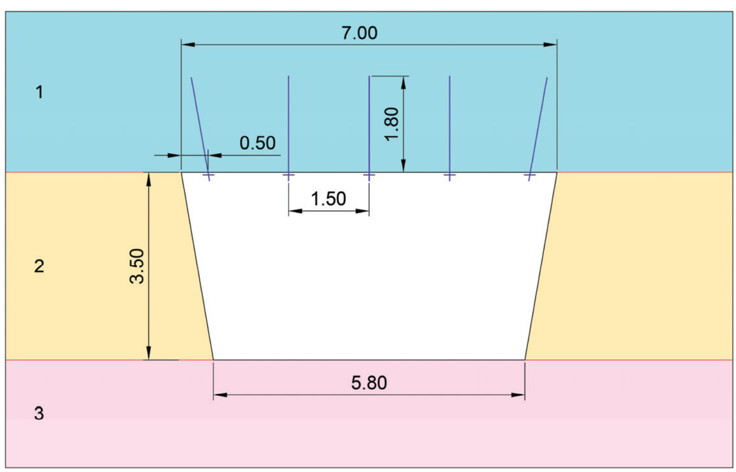

Figure 1. Heading protected with full-length-grouted rockbolts in the 1.5 m × 1.5 m bolting grid; legend: 1—dolomite I–VIII, 2—dolomite-shale-sandstone formations, 3—sandstone.

Table 6. Parameters of the RM-18 grouted rockbolts [43].

Parameter	Value
Bar diameter [mm]	18.2
Bar length [m]	1.8
Bar material	steel
Young's modulus [MPa]	210,000.0
Real load-capacity [kN]	170.0
Residual load-capacity [kN]	17.0
Pretension [kN]	30.0

The stress values were identified from the GG-1 shaft profile as per PN-G-05016:1997 [44]. The calculations included the porosity and water-logging of the rock layers. Table 7 shows the calculated primary stress values for two heading depths: 1000 m b.g.l. and 1300 m b.g.l. Owing to the deposit depth, the hydrostatic state of stress was assumed in the numerical models:

$$\sigma_z = \sigma_x = \sigma_y, \tag{5}$$

where:

σ_z—vertical stresses,
σ_x and σ_y—horizontal stresses.

Table 7. Primary stresses for two depths in the LGCB mines.

Depth H [m]	Vertical Stresses σ_z [MPa]	Horizontal Stresses σ_x [MPa]	Horizontal Stresses σ_y [MPa]
1000	22.11	22.11	22.11
1300	30.12	30.12	30.12

Two variants of loads acting on the group of headings were assumed for the numerical calculations. The flat, rectangular plate with openings shaped to correspond to the shapes of the analysed excavations located inside was assumed to be loaded on its edges:

- Load variant 1 (heading depth H = 1000 m b.g.l.):
  - side edges: p_x = 22.11 MPa;
  - upper edge and bottom edge: p_z = 22.11 MPa;
  - direction perpendicular to plate surface: p_y = 22.11 MPa.
- Load variant 2 (heading depth H = 1300 m b.g.l.):
  - side edges: p_x = 30.12 MPa;
  - upper edge and bottom edge: p_z = 30.12 MPa;
  - direction perpendicular to plate surface: p_y = 30.12 MPa.

The edges of the analysed plate were provided with supports which do not slide either in the vertical or in the horizontal direction. The numerical modelling employed finite elements having three nodes and a triangular shape. The plate edges were assumed to be at a 100 m distance from the extreme points on each side of the analysed excavations (the roof, the floor and the side walls). In all numerical models, the plate was 288.0 m $\times$ 203.5 m. Owing to the assumed dimensions of the plate, its edges (pillars) were not located excessively close to the excavations and thus had no influence on the results of calculations of the area of the excavations. In order to increase the accuracy of numerical calculations, smaller-size finite elements were used in the middle of the plate, in the area where the headings were driven (region of dense finite elements) (Figure 2). In each numerical model, the calculations were performed in two steps:

- Step 1: original state of the rock mass (no mining excavations present in the analysed plate);
- Step 2: state with the excavations present (four mining excavations present in the rock mass).

In the numerical simulations, it was assumed that the optimal measure of heading stability is the range of the yielded rock mass zone in the roof of the heading.

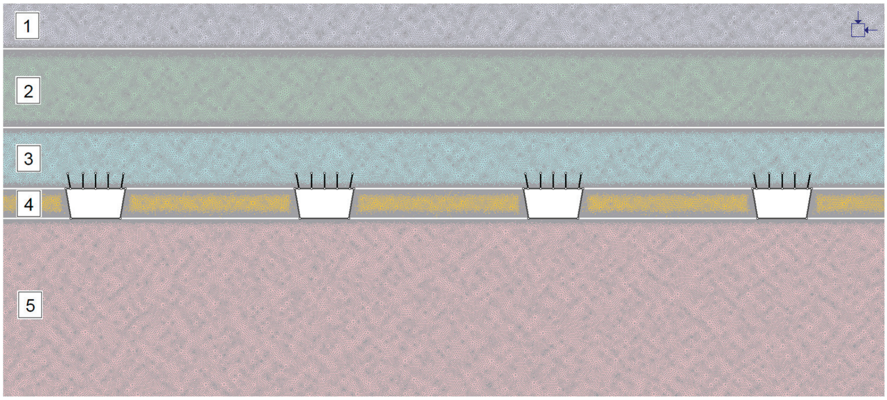

Figure 2. Numerical model of the group of headings generated in the RS2 software, the central part of the model and region of dense finite elements. Legend: 1—anhydrite II–IV, 2—anhydrite I, 3—calcareous dolomite I–VIII, 4—dolomite-shale-sandstone formations, 5—quartz sandstone.

3. Modelling Results

The numerical modelling of the stability of headings located at different depths in the rock mass (1000 m b.g.l. and 1300 m b.g.l.) in the geological and mining conditions assumed for the LGCB mines confirmed the results in a three-stage work: "Regulations on the selection of support systems for special-purpose room excavations in copper ore mines—Stage 1, Stage 2 and Stage 3" [45–47]. The numerical simulations also demonstrated that:

- The maximum range of the yielded rock mass (from 50% to 100%) in the roof (Table 8) of the headings located at the depth of 1000 m b.g.l. (load variant 1) was from 1.35 m to 1.54 m (Figures 3 and 4). For comparison, the maximum range of the yielded rock mass (from 50% to 100%) in the roof of the headings located at the depth of 1300 m b.g.l. (load variant 2) was from 1.97 m to 2.33 m (Figures 5 and 6). A change in the heading depth from 1000 m b.g.l. to 1300 m b.g.l. has thus caused the range of the yielded rock mass in the heading roof to increase from 0.43 m (heading 4) to 0.98 m (heading 2). The maximum range of the yielded rock mass in the roofs of all headings was greater than the 1.8 m range of the bolted zone. This fact indicates that in the LGCB mines, the heading depth in the rock mass may have a decisive impact on its stability. Problems with heading stability may occur when the yielded rock zone in the roof is larger than the bolted zone.
- The surface of the yielded rock area around a group of headings increases together with an increase in the excavation depth (increase in primary stress in the rock mass); this phenomenon negatively influences the stability of mining excavations and is strictly related to the stress and strain parameters of the rock layers surrounding the excavations.
- The maximum range of the yielded rock mass (from 50% to 100%) in the walls (Table 9) of the headings located at the depth of 1000 m b.g.l. was from 2.69 m to 3.02 m (Figures 3 and 4). For comparison, the maximum range of the yielded rock mass (from 50% to 100%) in the walls of the headings located at the depth of 1300 m b.g.l. was from 3.23 m to 3.47 m (Figures 5 and 6). A change in the heading depth from 1000 m b.g.l. to 1300 m b.g.l. has thus caused the range of the yielded rock mass in the walls to increase from 0.32 m (heading 4, left wall) to 0.62 m (heading 1, left wall).
- A more complex formation mechanism of yielded rock mass was observed in the floors of the excavations. A change in the heading depth from 1000 m b.g.l. to 1300 m b.g.l. has caused the vertical range of the yielded rock mass in the floors to increase only to a limited degree in comparison to the change in the horizontal range. The maximum vertical range of the yielded rock mass (from 50% to 100%) in the floors of the headings

(Table 10) was from 2.53 m to 2.58 m (for the depth of 1000 m b.g.l.) and from 2.92 m to 3.13 m (for the depth of 1300 m b.g.l.) A change in the heading depth caused the vertical range of the yielded rock mass to increase from 0.38 m (heading 1 and heading 4) to 0.60 m (heading 3).

- The horizontal ranges of the yielded rock mass in the floors changed more significantly due to the change in the heading depth (Table 11). The maximum horizontal range of the yielded rock mass (from 50% to 100%) in the floors of the headings located at the depth of 1000 m b.g.l. was 5.80 m and was equal to the width of the heading at the floor. In the headings located at the depth of 1300 m b.g.l., the horizontal range of the yielded rock mass in the floors increased significantly and was from 9.52 m to 10.25 m. A change in the heading depth has thus caused the horizontal range of the yielded rock mass to increase from 3.72 m (heading 1) to 4.45 m (heading 2).
- The results of the numerical analyses obtained for the plastic-elastic model with rock softening correspond best to the observed cases of stability loss in the mining excavations in the LGBC mines.

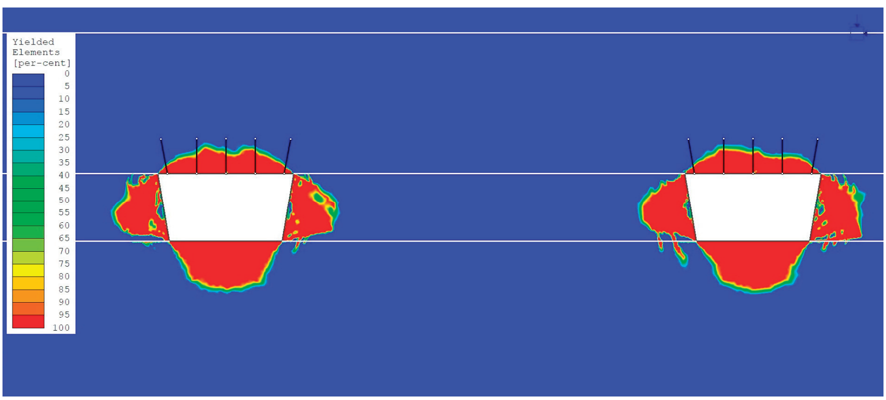

Figure 3. Yielded element area around headings 1 and 2, load variant 1.

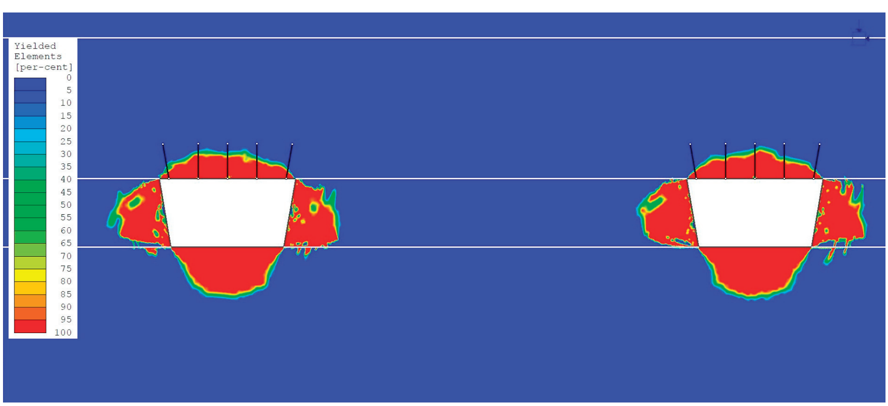

Figure 4. Yielded element area around headings 3 and 4, load variant 1.

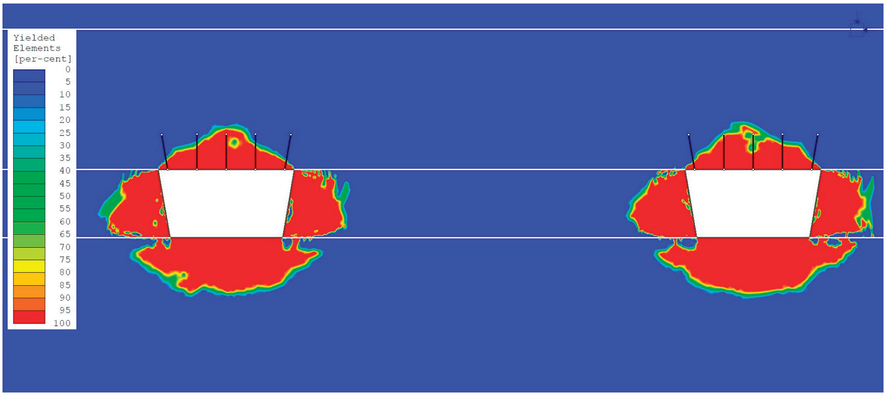

Figure 5. Yielded element area around headings 1 and 2, load variant 2.

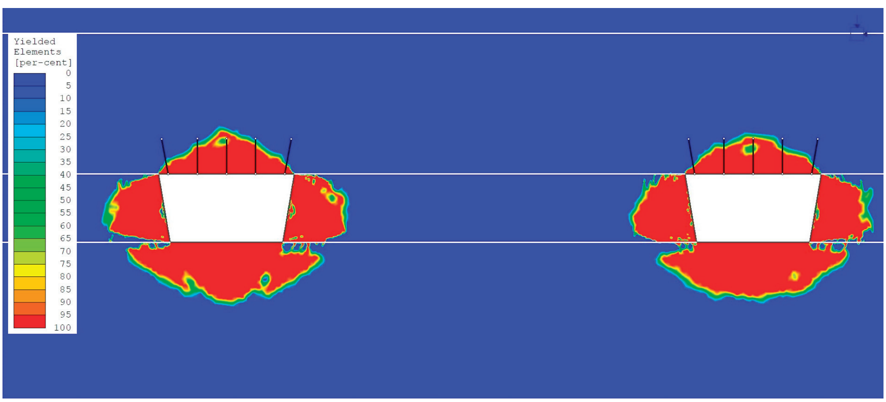

Figure 6. Yielded element area around headings 3 and 4, load variant 2.

Table 8. Yielded rock mass range in the roofs of the analysed excavations (yield between 50% and 100%).

Excavation	Yield Range in the Roof [m]		Increase in Yield Range in the Roof	
	Load Variant 1	Load Variant 2	[m]	[%]
1	1.42	2.15	0.73	51.41
2	1.35	2.33	0.98	72.59
3	1.36	2.27	0.91	66.91
4	1.54	1.97	0.43	27.92

Table 9. Yielded rock mass range in the walls of the analysed excavations (yield between 50% and 100%).

Excavation	Yield Range in the Wall [m]		Increase in Yield Range in the Wall	
	Load Variant 1	Load Variant 2	[m]	[%]
1 (left wall)	2.83	3.45	0.62	21.91
1 (right wall)	2.79	3.26	0.47	16.85
2 (left wall)	2.87	3.47	0.60	20.91
2 (right wall)	2.69	3.23	0.54	20.07
3 (left wall)	2.89	3.32	0.43	14.88

Table 9. *Cont.*

Excavation	Yield Range in the Wall [m]		Increase in Yield Range in the Wall	
	Load Variant 1	Load Variant 2	[m]	[%]
3 (right wall)	2.78	3.24	0.46	16.55
4 (left wall)	3.02	3.34	0.32	10.60
4 (right wall)	2.73	3.25	0.52	19.05

Table 10. Yielded rock mass range in the floors of the analysed excavations (yield between 50% and 100%).

Excavation	Yield Range in the Floor [m]		Increase in Yield Range in the Floor	
	Load Variant 1	Load Variant 2	[m]	[%]
1	2.54	2.92	0.38	14.96
2	2.58	2.97	0.39	15.12
3	2.53	3.13	0.60	23.72
4	2.58	2.96	0.38	14.73

Table 11. Horizontal range of yielded rock mass in the floors of the analysed excavations (yield between 50% and 100%).

Excavation	Horizontal Range of Yielded Rock Mass in the Floor [m]		Increase in Horizontal Yield Range in the Floor	
	Load Variant 1	Load Variant 2	[m]	[%]
1	5.80	9.52	3.72	64.14
2	5.80	10.25	4.45	76.72
3	5.80	9.98	4.18	72.07
4	5.80	9.71	3.91	67.41

4. Discussion

The numerical simulations allowed an optimal selection of the roof bolting design for headings driven at different depths in the rock mass in the conditions of the LGCB mines. For safety reasons, the simulations were based on an assumption that the bolted zone in the roof must be larger by at least 0.25 m than the maximum range of the yielded zone (yield from 50% to 100%). In the case of the headings driven at the depth of 1000 m b.g.l., the selection of 1.8 m long RM-18 grouted bolts in the 1.5 × 1.5 m grid (bolt distance) was proven correct. However, in the case of headings driven at 1300 m b.g.l., the range of the bolting zone should be increased. The selected bolts were 2.6 m long RM-18 grouted bolts in the 1.5 × 1.5 m grid (bolt distance).

The analysis of the results of numerical simulations also confirmed that a change in the heading depth from 1000 m b.g.l. to 1300 m b.g.l. caused the range of the yielded rock mass in the walls to increase. In actual mining conditions, the stability of the walls may be thus compromised. Observations in the LGCB mines indicate that in such cases, the walls may be effectively reinforced with the use of bolts not shorter than 1.6 m and installed in the 1.5 m × 1.5 m bolting grid (bolt spacing), with the bottom row of the bolts situated at a distance approximately 1.8 m from the floor. In justified cases, the walls may be reinforced with so-called deep bolts (longer than 2.6 m), e.g., cable bolts.

A change in the heading depth from 1000 m b.g.l. to 1300 m b.g.l. caused a limited increase in the vertical range and a significant increase in the horizontal range of the yielded rock mass in the floors. In situ observations in the LGCB mines indicate that in the case of deep headings (located more than 1000 m b.g.l.), the floor is uplifted more frequently than in the case of headings located at smaller depths. This phenomenon is also influenced by the low values of strength and deformation parameters of sandstones present in the floors of the headings.

In situ studies performed in the LGCB mines confirm that in the geological and mining conditions of the Polish copper ore mines, the stability of the heading is affected by its depth in the rock mass. In some cases, a loss of stability was observed for headings which were driven in similar geological and mining conditions but at different depths in the rock mass. The roof support system was, in these cases, selected in accordance with the binding regulations in the LGCB mines [3]. However, the regulations do not allow for the depth of the excavation in the rock mass and, thus, for the level of primary stresses in the mined rock mass.

Numerical modelling confirms that the stability of the heading is strictly related to its depth and, thus, to the level of primary stresses in the rock mass. Therefore, the regulations on the selection of roof bolting systems in the LGCB mines seem to require verification based on the results of numerical simulations, and a criterion should be added which would account for the depth of the heading in the selection process of such a roof bolting system.

The stability of the heading is also affected by its shape, height and width, as well as by the strength and strain parameters of the rocks around it. These parameters should be taken into consideration when selecting a roof support system for headings driven in the difficult geological and mining conditions of the LGCB mines.

Increased computing power and improved specialist software has allowed mining excavations and their roof support systems to be designed with the use of numerical methods. They enable broad and extensive analyses of heading stability in any geological and mining conditions. The results of such numerical analyses should be verified for correctness with the help of in situ observations of the stability of mining excavations in the LGCB mines.

Author Contributions: Conceptualization, D.P.; methodology, J.B. and D.P.; software, D.P.; validation, D.P.; formal analysis, J.B. and D.P.; investigation, D.P.; resources, D.P.; data curation, J.B. and D.P.; writing—original draft preparation, D.P.; writing—review and editing, J.B. and D.P.; visualization, D.P.; supervision, D.P.; project administration, D.P.; funding acquisition, J.B. and D.P. All authors have read and agreed to the published version of the manuscript.

Funding: The research work was co-founded with the research subsidy of the Polish Ministry of Science and Higher Education granted for 2024.

Institutional Review Board Statement: Not applicable.

Informed Consent Statement: Not applicable.

Data Availability Statement: The raw data supporting the conclusions of this article will be made available by the authors on request.

Conflicts of Interest: The authors declare no conflicts of interest.

References

1. KGHM Polska Miedz, S.A. Available online: https://kghm.com/pl/biznes/wydobycie-i-wzbogacanie (accessed on 20 April 2024).
2. Collaborative Publication. *Instructions on Determining the Geomechanical Parameters of Roof Rocks with Respect to Roof Classes in Copper Mines, as Required in the Selection of a Roof Bolting System Design*; KGHM Polska Miedz S.A.: Lubin, Poland, 2017. (In Polish)
3. Collaborative Publication. *Regulations on the Selection, Construction and Control of Excavation Support in the KGHM Polska Miedz S.A. Mines*; KGHM Polska Miedz S.A.: Lubin, Poland, 2017. (In Polish)
4. Pawelus, D. Stability assessment of headings situated in a field of high horizontal stress in Polish copper mines by means of numerical methods. *IOP Conf. Ser. Earth Environ. Sci.* **2019**, *221*, 012097. [CrossRef]
5. Pande, G.; Beer, G.; Williams, J. *Numerical Methods in Rock Mechanics*; Wiley: New York, NY, USA, 1990.
6. Zeller, S.S.; Pollard, D.D. Boundary conditions for rock fracture analysis using the boundary element method. *J. Geophys. Res. Solid Earth* **1992**, *97*, 1991–1997. [CrossRef]
7. Beer, G.; Pousen, A. Efficient numerical modelling of faulted rock using the boundary element method. *Int. J. Rock Mech. Min. Sci.* **1995**, *31*, 485–506. [CrossRef]
8. Cerrolaza, M.; Garcia, R. Boundary elements and damage mechanics to analyze excavations in rock mass. *Eng. Anal. Bound. Elem.* **1997**, *20*, 1–16. [CrossRef]

9. Pan, E.; Amadei, B.; Kim, Y.I. 2D BEM analysis of anisotropic half-plane problems—Application to rock mechanics. *Int. J. Rock Mech. Min. Sci.* **1998**, *35*, 69–74. [CrossRef]
10. Shou, K.J. A three-dimensional hybrid boundary element method for non-linear analysis of a weak plane near an underground excavation. *Tunn. Undergr. Space Technol.* **2000**, *15*, 215–226. [CrossRef]
11. Jing, L.; Hudson, J.A. Numerical methods in rock mechanics. *Int. J. Rock Mech. Min. Sci.* **2002**, *39*, 409–427. [CrossRef]
12. Jing, L. A review of technics, advances and outstanding issues in numerical modelling for rock mechanics and rock engineering. *Int. J. Rock Mech. Min. Sci.* **2003**, *40*, 283–353. [CrossRef]
13. Yasitli, N.E.; Unver, B. 3D numerical modelling of longwall mining with top-coal caving. *Int. J. Rock Mech. Min. Sci.* **2005**, *42*, 219–235. [CrossRef]
14. Henning, J.G.; Mitri, H.S. Numerical modelling of ore dilution in blasthole stoping. *Int. J. Rock Mech. Min. Sci.* **2007**, *44*, 692–703. [CrossRef]
15. Wang, J.; Apel, D.B.; Pu, Y.; Hall, R.; Wei, C.; Sepehri, M. Numerical modeling for rockbursts: A state-of-the-art review. *J. Rock Mech. Geotech. Eng.* **2021**, *13*, 457–478. [CrossRef]
16. Kruszewski, M.; Montegrossi, G.; Balcewicz, M.; Igbokwe, O.A.; Backers, T.; Saenger, E.H. 3D in situ stress state modelling and fault reactivation risk exemplified in the Ruhr region (Germany). *Geomech. Energy Environ.* **2022**, *32*, 100386. [CrossRef]
17. Wang, J.; Apel, D.B.; Dyczko, A.; Walentek, A.; Prusek, S.; Xu, H.; Wei, C. Analysis of the damage mechanism of strainbursts by a global-local modeling approach. *J. Rock Mech. Geotech. Eng.* **2022**, *14*, 1671–1696. [CrossRef]
18. Chen, D.; Zhu, J.; Ye, Q.; Ma, X.; Xie, S.; Guo, W.; Li, Z.; Wang, Z.; Feng, S.; Yan, X. Application of Gob-Side Entry Driving in Fully Mechanized Caving Mining: A Review of Theory and Technology. *Energies* **2023**, *16*, 2691. [CrossRef]
19. Shabanimashcool, M.; Li, C.C. Numerical modelling of longwall mining and stability analysis of the gates in a coal seam. *Int. J. Rock Mech. Min. Sci.* **2012**, *51*, 24–34. [CrossRef]
20. Zhu, D.; Tu, S. Mechanisms of support failure induced by repeated mining under gobs created by two-seam room mining and prevention measures. *Eng. Fail. Anal.* **2017**, *82*, 161–178. [CrossRef]
21. Feng, G.; Wang, P. Simulation of recovery of upper remnant coal pillar while mining the ultra-close lower panel using longwall top coal caving. *Int. J. Min. Sci. Technol.* **2020**, *30*, 55–61. [CrossRef]
22. Sepehri, M.; Apel, D.B.; Adeeb, S.; Leveille, P.; Hall, R.A. Evaluation of mining induced energy and rockburst prediction at a diamond mine in Canada using a full 3D elastoplastic finite element model. *Eng. Geol.* **2020**, *266*, 105457. [CrossRef]
23. Wang, J.; Qiu, P.; Ning, J.; Zhuang, L.; Yang, S. A numerical study of the mining-induced energy redistribution in a coal seam adjacent to an extracted coal panel during longwall face mining: A case study. *Energy Sci. Eng.* **2020**, *8*, 817–835. [CrossRef]
24. Wei, C.; Zhang, C.; Canbulat, I. Numerical analysis of fault-slip behaviour in longwall mining using linear slip weakening law. *Tunn. Undergr. Space Technol.* **2020**, *104*, 103541. [CrossRef]
25. Xiaojun, F.; Qiming, Z.; Muhammad, A. 3D modelling of the strength effect of backfill-rock on controlling rockburst risk: A case study. *Arab. J. Geosci.* **2020**, *13*, 128. [CrossRef]
26. Zhang, Z.; Deng, M.; Wang, X.; Yu, W.; Zhang, F.; Dao, V.D. Field and numerical investigations on the lower coal seam entry failure analysis under the remnant pillar. *Eng. Fail. Anal.* **2020**, *115*, 104638. [CrossRef]
27. Jendrys, M.; Hadam, A.; Cwiekala, M. Directional Hydraulic Fracturing (DHF) of the Roof, as an Element of Rock Burst Prevention in the Light of Underground Observations and Numerical Modelling. *Energies* **2021**, *14*, 562. [CrossRef]
28. Adach-Pawelus, K. Back-calculation method for estimation of geomechanical parameters in numerical modeling based on in-situ measurements and statistical methods. *Energies* **2022**, *15*, 4729. [CrossRef]
29. Wang, J.; Apel, D.B.; Xu, H.; Wei, C. Evaluation of the performance of yielding rockbolts during rockbursts using numerical modeling method. *Int. J. Coal Sci. Technol.* **2022**, *9*, 87. [CrossRef]
30. Guo, Y.; Luo, L.; Wang, C. Research on Fault Activation and Its Influencing Factors on the Barrier Effect of Rock Mass Movement Induced by Mining. *Appl. Sci.* **2023**, *13*, 651. [CrossRef]
31. Jaiswal, A.; Shrivastva, B.K. Numerical simulation of coal pillar strength. *Int. J. Rock Mech. Min. Sci.* **2009**, *46*, 779–788. [CrossRef]
32. Lucas, D.S.; Vakili, A.; Hutchison, B.J. Three-dimensional numerical modelling for successful design of steep slopes at the Kanmantoo copper mine. In *Slope Stability 2020: Proceedings of the 2020 International Symposium on Slope Stability in Open Pit Mining and Civil Engineering*; Dight, P.M., Ed.; Australian Centre for Geomechanics: Perth, Australia, 2020; pp. 1083–1096. [CrossRef]
33. Adach-Pawelus, K.; Pawelus, D. Influence of driving direction on the stability of a group of headings located in a field of high horizontal stresses in the Polish underground copper mines. *Energies* **2021**, *14*, 5955. [CrossRef]
34. Batugin, A.; Wang, Z.; Su, Z.; Sidikovna, S.S. Combined support mechanism of rock bolts and anchor cables for adjacent roadways in the external staggered split-level panel layout. *Int. J. Coal Sci. Technol.* **2021**, *8*, 659–673. [CrossRef]
35. Skrzypkowski, K. 3D Numerical modelling of the application of cemented paste backfill on displacements around strip excavations. *Energies* **2021**, *14*, 7750. [CrossRef]
36. Tahmasebinia, F.; Yang, A.; Feghali, P.; Skrzypkowski, K. A Numerical investigation to calculate ultimate limit state capacity of cable bolts subjected to impact loading. *Appl. Sci.* **2023**, *13*, 15. [CrossRef]
37. Tahmasebinia, F.; Yang, A.; Feghali, P.; Skrzypkowski, K. Structural evaluation of cable bolts under static loading. *Appl. Sci.* **2023**, *13*, 1326. [CrossRef]
38. Feng, C.; Liu, S.; Jia, H.; Fu, M.; He, D. Strengthening Device for Improving Shear Performance of Anchor Cable in Rock Support. *Materials* **2024**, *17*, 197. [CrossRef] [PubMed]

39. Hoek, E.; Carranza-Torres, C.T.; Corkum, B. Hoek-Brown failure criterion—2002 edition. In Proceedings of the North American Rock Mechanics Society Meeting, Toronto, ON, Canada, 7–10 July 2002.
40. Hoek, E. Strength of rock and rock masses. *ISRM News J.* **1994**, *2*, 4–16.
41. Hoek, E.; Brown, E.T. Practical estimates of rock mass strength. *Int. J. Rock Mech. Min. Sci.* **1997**, *34*, 1165–1186. [CrossRef]
42. Hoek, E.; Marinos, P. GSI: A geologically friendly tool for rock mass strength estimation. In Proceedings of the ISRM International Symposium, Melbourne, Australia, 19–24 November 2000.
43. Minova. Available online: https://www.minovaglobal.com/emea-cis/products/steel-gfrp/rock-bolts/resin-bolts-type-rm-18/ (accessed on 20 February 2024).
44. *Polish Standard PN-G-05016:1997*; Mining Shafts, Casing, Loads. Polish Committee for Standardization (PKN): Warsaw, Poland, 1997. (In Polish)
45. Pawelus, D.; Butra, J.; Madziarz, M.; Debkowski, R. *Regulations on the Selection of Support Systems for Special-Purpose Room Excavations in Copper Ore Mines—Stage 1*; KGHM Polska Miedz S.A.: Wroclaw, Poland, 2015. (In Polish)
46. Pawelus, D.; Butra, J.; Adach, K.; Madziarz, M.; Debkowski, R. *Regulations on the Selection of Support Systems for Special-Purpose Room Excavations in Copper Ore Mines—Stage 2*; KGHM Polska Miedz S.A.: Wroclaw, Poland, 2015. (In Polish)
47. Pawelus, D. *Regulations on the Selection of Support Systems for Special-Purpose Room Excavations in Copper Ore Mines—Stage 3*; KGHM Polska Miedz S.A.: Wroclaw, Poland, 2016. (In Polish)

minerals

MDPI

Article

Metallurgical Copper Recovery Prediction Using Conditional Quantile Regression Based on a Copula Model

Heber Hernández [1,*], Martín Alberto Díaz-Viera [2], Elisabete Alberdi [3], Aitor Oyarbide-Zubillaga [4] and Aitor Goti [4]

1 Facultad de Ingeniería y Arquitectura, Universidad Central de Chile, Santiago 8370178, Chile
2 Instituto Mexicano del Petróleo, Eje Central Lázaro Cárdenas No. 152, Ciudad de México 07730, Mexico; mdiazv@imp.mx
3 Department of Applied Mathematics, University of the Basque Country UPV/EHU, 48013 Bilbao, Spain; elisabete.alberdi@ehu.eus
4 Department of Mechanics, Design and Organization, University of Deusto, 48007 Bilbao, Spain; aitor.oyarbide@deusto.es (A.O.-Z.); aitor.goti@deusto.es (A.G.)
* Correspondence: heber.hernandez@ucentral.cl

Abstract: This article proposes a novel methodology for estimating metallurgical copper recovery, a critical feature in mining project evaluations. The complexity of modeling this nonadditive variable using geostatistical methods due to low sampling density, strong heterotopic relationships with other measurements, and nonlinearity is highlighted. As an alternative, a copula-based conditional quantile regression method is proposed, which does not rely on linearity or additivity assumptions and can fit any statistical distribution. The proposed methodology was evaluated using geochemical log data and metallurgical testing from a simulated block model of a porphyry copper deposit. A highly heterotopic sample was prepared for copper recovery, sampled at 10% with respect to other variables. A copula-based nonparametric dependence model was constructed from the sample data using a kernel smoothing method, followed by the application of a conditional quantile regression for the estimation of copper recovery with chalcocite content as secondary variable, which turned out to be the most related. The accuracy of the method was evaluated using the remaining 90% of the data not included in the model. The new methodology was compared to cokriging placed under the same conditions, using performance metrics RMSE, MAE, MAPE, and R^2. The results show that the proposed methodology reproduces the spatial variability of the secondary variable without the need for a variogram model and improves all evaluation metrics compared to the geostatistical method.

Keywords: metallurgical copper recovery; copula model; conditional quantile regression; kernel smoothing; collocated cokriging

Citation: Hernández, H.; Díaz-Viera, M.A.; Alberdi, E.; Oyarbide-Zubillaga, A.; Goti, A. Metallurgical Copper Recovery Prediction Using Conditional Quantile Regression Based on a Copula Model. *Minerals* **2024**, *14*, 691. https://doi.org/10.3390/min14070691

Academic Editors: Krzysztof Skrzypkowski, René Gómez, Fhatuwani Sengani, Derek B. Apel, Faham Tahmasebinia and Jianhang Chen

Received: 20 May 2024
Revised: 24 June 2024
Accepted: 25 June 2024
Published: 1 July 2024

1. Introduction

Metallurgical recovery, in the context of mineral mining, refers to the percentage of valuable metal extracted from the ore during the processing or beneficiation stage [1,2]. It is a crucial metric in the mining industry as it indicates the efficiency of the extraction process and ultimately affects the profitability of the mining operation.

From a mineral processing perspective, contemporary treatments for copper include the flotation of sulfide ores, leaching for oxide ores, and a hybrid approach that integrates flotation and magnetic separation for certain mixed ores [3]. Madenova and Madani (2021) [4] define metallurgical recovery as a vital geometallurgical variable for mine planning, representing a response to the processing plant design and the geological characteristics of the ore.

The process of extracting valuable metals from ore typically involves several stages, including crushing, grinding, concentration, and refining. Metallurgical recovery measures the effectiveness of these processes in separating and concentrating the valuable metal from the ore.

The calculation of metallurgical recovery involves comparing the amount of metal recovered from the ore to the total amount of metal present in the ore. This is often expressed as a percentage, where a higher percentage indicates a more efficient extraction process.

Factors influencing metallurgical recovery include the mineralogy and composition of the ore, the efficiency of the processing equipment and techniques used, and the expertise of the personnel involved in the operation. Improving metallurgical recovery is a key focus area for mining companies seeking to optimize their operations and maximize the value of their mineral resources.

To maximize profit, it is crucial to have a reliable estimation model for all variables involved, both primary (geological properties, mineral grades, densities, contaminants, etc.) and response variables (metallurgical recovery, bond work index, grindability index, processing capacity, milling performance, etc.) [5]. The combination of a geological model and metallurgical data is currently known as a geometallurgical model [6].

Metallurgical recovery is a critical feature in the evaluation and exploitation of mining projects, as it directly influences net economic benefit. This variable is expressed as a percentage and represents the yield of mineral processing, in the case of copper sulfides, by flotation along the mining value chain [7].

Incorporating metallurgical recovery into mine planning poses a challenge for resource modelers and mine planners. In most projects, the lack of proper collection and analysis of geometallurgical data leads to unreliable metallurgical response models [8]. Samples with this information are often scarce, costly, and highly heterotopic compared to primary variables [9,10]. However, these primary variables are known to be useful indicators for predicting metallurgical responses [11,12].

In the context of copper metallurgical recovery, a heterotopic sample refers to a sample taken from a location within a mineral deposit that is geologically distinct from the primary ore body being targeted for extraction.

For example, in a copper mining operation, the primary ore body may consist of a specific geological formation or vein where copper minerals are concentrated. A heterotopic sample, in this case, could be taken from a nearby area where copper mineralization occurs but in a different geological setting. This could include samples from adjacent rock formations, secondary veins, or areas with different mineralogical characteristics.

Analyzing heterotopic samples is important in copper metallurgical recovery because they can provide insights into the variability of copper mineralization within a mining area. Understanding the distribution and characteristics of copper mineralization in heterotopic samples can help optimize mining processes, improve recovery rates, and inform mine planning and development strategies.

Modeling metallurgical recovery is usually carried out using geostatistical techniques and, more recently, by machine learning methods. Machine learning methods seek to predict geometallurgical response variables using assay and mineralogy data [13–17]; however, they require a large number of variables and a considerable amount of data to consolidate a robust model [18]. On the other hand, geostatistics requires initially defining domains based on geometallurgical attributes [19] and then estimating indirectly, that is, by seeking mathematical arrangements forced to meet the required assumptions. Techniques like kriging are not usually recommended, as they can generate biased results due to the nonadditive nature of metallurgical recovery [20]. It has been observed that the weighted average of two sample values is not a good estimator of the corresponding value in the blend [21,22]. Additionally, cokriging and its variants have difficulties being applicable, mainly due to the subjectivity in modeling variograms with little information and nonlinear or complex dependency relationships with mineral grades and other geochemical variables [23].

Given the problems and limitations mentioned earlier, the application of copula-based methods emerges as a promising alternative in the mining industry [24]. As is usual in statistics and geostatistics, two approaches have been developed: one for estimation and the other for simulation. In particular, several geostatistical methods based on copulas have been published that have been successful in Earth sciences applications [25–29]. But above all, there are multiple developments in the sphere of finance using an estimation approach known as quantile regression based on copulas [30–32].

A copula is a multivariate cumulative distribution function for which the marginal probability distribution of each variable is uniform on the interval [0, 1]. They are functions that describe the underlying dependence between random variables. Sklar's theorem [33] states that any multivariate joint distribution can be expressed in terms of univariate marginal distribution functions and a copula that describes the dependency structure between the variables [34,35].

This research evaluates the performance of the conditional quantile regression method (CQRM) compared to the classical geostatistical collocated cokriging method (CCM) for modeling copper metallurgical recovery based on a predominantly measured geological attribute.

The structure of the paper is as follows. In the Section 2, the problem statement is established. The Section 3 presents the collocated cokriging and conditional quantile regression methods, and the general methodology of their application. The Section 4 gives a description of the dataset used in the comparative study. The Section 5 shows the results of the application of both methods to the case study. In the Section 6, the comparison of the performance of the two methods is discussed, and, finally, in the Section 7, the conclusions and future work are given.

2. Problem Statement

In a basic mining exploitation unit to calculate mining profit, Equation (1), metallurgical recovery, ore grade, and metal price are critical variables, all subject to significant uncertainty, as can be inferred from its own definition [36,37]:

$$Profit = R_{rc}^{Cu} \cdot P_{c}^{Cu} \cdot G^{Cu} \cdot T^{Cu} - C_{c}^{Cu} \tag{1}$$

where P_c^{Cu} is the price of the copper concentrate, G^{Cu} is the copper grade, T^{Cu} is the mineral tonnage, and C_c^{Cu} are the costs associated with the production, processing, and sale of the copper concentrate.

Due to the low sampling density, their strong heterotopic relationship with other mineral deposit measurements, and the nonlinearity in these relationships, geostatistical modeling appears to be a complex alternative.

Formally, metallurgical recovery can be defined for a copper mine by the following expression [8]:

$$R_{rc}^{Cu} = \frac{m_c^{Cu}}{m^{Cu}} = x_c^{Cu} f_c \frac{1}{x^{cu}} \tag{2}$$

where R_{rc}^{Cu} is the copper recovery, m_c^{Cu} is the mass of copper in the concentrate (i.e., the amount of recovered copper), and m^{Cu} is the initial mass of copper in the feed. x_c^{Cu} is the copper grade in the concentrate, x^{cu} is the feed grade, and f_c is the fraction of mass recovered.

Small variations in metallurgical recovery estimation will impact the profit valuation, which defines the material's destinations in strategic planning, whether as processed ore in the plant, waste rock extracted for deposition in dumps, or low-grade ore for stockpiling. Given the importance of this variable for downstream processes such as block model optimization, mine design, and mine life planning, it is essential to seek the best practices for its prediction.

3. Methodology

In this paper, a comparison of the conditional quantile regression method (CQRM) is made with respect to the traditional collocated cokriging method (CCM) in terms of accuracy and performance. To apply both methods, there are a series of steps that are common, as is shown in the general methodological workflow of Figure 1.

The first step, consisting of the exploratory analysis of the data, is standard for any statistical procedure and consists of a summary of its statistics and the probability distribution graphics with its boxplots and histograms. Also, an evaluation of the impact of the presence of outliers in the data sample on the statistics is also carried out.

In the variable selection step in both cases, the variable pair that has the greatest dependence is sought, but the difference is that for CCM it must be a linear dependence that should be estimated with the Pearson correlation coefficient, while for CQRM it is recommendable to use a more robust measure of dependence by using Spearman or Kendall rank correlation coefficients.

In the modeling part, different models are built. For CCM it is a spatial correlation model with the variogram of the primary variable, while for CQRM it is the dependence model that consists of the estimation and fitting of the marginal distributions of each variable as well as the copula.

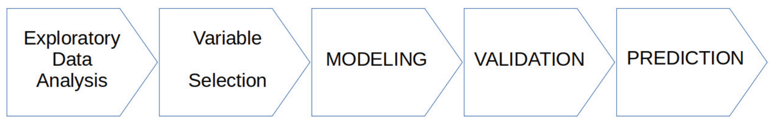

Figure 1. General methodological workflow.

The validation of the models is carried out for CCM with the usual cross-validation method, i.e., a leave one out method [38], while CQRM is validated performing an estimation with the same data used to build it. The quality of each method is evaluated in terms of performance metrics, such as root mean squared error (RMSE), mean absolute error (MAE), mean absolute percentage error (MAPE), and determination coefficient (R^2).

Finally, the prediction of copper metallurgical recovery conditioned by a secondary attribute is performed at each point where there are no sample values.

3.1. Collocated Cokriging Method

Collocated cokriging is a geostatistical method used for spatial interpolation or estimation of a target variable at unsampled locations based on available data from sampled locations [38]. This method is particularly useful when dealing with multiple correlated variables or when auxiliary information is available. In collocated cokriging, the relationship between the target variable and auxiliary variables is modeled using the concept of spatial dependence, which assumes that nearby locations tend to have similar values. The method estimates the target variable at an unsampled location by combining information from both the target variable and auxiliary variables at nearby sampled locations (see Appendix B).

The usual steps involved in the application of collocated cokriging method are the following:

- Data collection: Collect data on the target variable and auxiliary variables from sampled locations within the study area.
- Spatial correlation analysis: Assess the spatial correlation or dependence between the target variable and auxiliary variables using variograms or covariance functions.
- Modeling: Model the spatial dependence structure between the target variable and auxiliary variables using geostatistical techniques such as ordinary kriging.
- Validation: Validate the accuracy of the predictions using cross-validation or comparison with independent data, if available.
- Prediction: Estimate the value of the target variable at unsampled locations by combining information from nearby sampled locations and auxiliary variables, taking into account their spatial correlation.

Collocated cokriging offers advantages over traditional kriging methods by incorporating additional information from auxiliary variables, which can improve the accuracy of predictions, especially in areas with limited or sparse data coverage for the target variable.

3.2. Conditional Quantile Regression Method

Conditional quantile regression based on copulas is a statistical method used for modeling the relationship between variables, particularly when dealing with non-normal or skewed distributions, and when there are complex dependencies among variables. Copulas are mathematical functions that describe the dependence structure between random variables, independent of their marginal distributions. They capture the joint distribution of variables without making assumptions about their individual distributions. Copulas allow the modeling of both linear and nonlinear dependencies, making them useful for capturing complex relationships between variables.

Conditional quantile regression extends the concept of linear regression by estimating conditional quantiles of the response variable given the values of predictor variables. Unlike ordinary least squares regression, which models the conditional mean of the response variable, quantile regression models different quantiles (e.g., median, upper/lower quantiles), providing a more comprehensive understanding of the conditional distribution of the response variable. In quantile regression based on copulas, copulas are used to model the dependence structure between variables, while quantile regression is applied to estimate the conditional quantiles of the response variable given the values of predictor variables. This approach allows the capturing of the joint distribution and conditional distributions of variables simultaneously, taking into account complex dependencies among them.

Conditional quantile regression based on copulas offers several advantages:

- Flexibility: It can model nonlinear dependencies and account for heteroscedasticity.
- Robustness: It is robust to outliers and non-normality in the data.
- Interpretability: It provides insights into how different quantiles of the response variable are affected by changes in the predictor variables.
- Tail behavior: It can capture extreme events or tail behavior in the conditional distributions of variables.

This method is widely used in finance, economics, environmental science, and other fields where understanding the relationship between variables across different quantiles is essential. It can be used for risk management, forecasting, and decision making under uncertainty. Overall, quantile regression based on copulas is a powerful tool for modeling complex dependencies and understanding the conditional distribution of variables, especially in situations where traditional regression methods may not be adequate.

In this article, a nonparametric copula by the kernel smoothing method [39] is used, given its good adaptability to any type of distribution and computational efficiency. In particular, kernel smoothing, a type of weighted moving average method, is applied for probability density estimation, that is, to estimate the probability density function of a random variable based on kernels as weights, where the term kernel in this context means a window function.

A more detailed explanation of copula theory and the quantile regression method can be found in Appendix A. In particular, additional explanations about the kernel smoothing method can be found in Appendix A.2.

4. Dataset Description

With the purpose of carrying out the comparison between the collocated cokriging and conditional quantile regression methods with mining data, a dataset extracted from a synthetic porphyry copper deposit was selected, which was published in [19], and is openly available for academic use. From the three-dimensional block model, the level 2080 is chosen to configure a 2D space and we use it as experimental data for this application. This dataset consists of 3479 (71 × 49) cells of 20 × 20 meters, each spatially georeferenced by their X (easting) and Y (northing) coordinates. Each cell contains geochemical records of 1—clays, 2—chalcocite, 3—bornite, 4—chalcopyrite, 5—tennantite, 6—molybdenite, 7—pyrite, 8—copper (Cu), 9—molybdenum (Mo), and 10—arsenic (As), as well as the results of metallurgical tests for 11—copper recovery and 12—bond work index.

This exercise consists of extracting, in a random and spatially uniform manner, a sample equivalent to 10% of the total available information of the metallurgical recovery, constructing a strongly heterotopic case with respect to the other variables. Figure 2 shows the copper recovery maps for the complete dataset on the left side and the corresponding map for the 10% sampling on the right side, respectively.

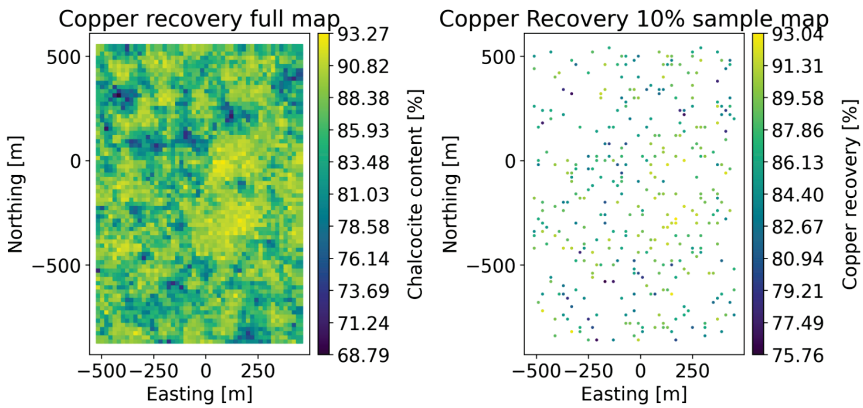

Figure 2. Copper recovery for the 100% (**in the left**) and 10% (**in the right**) sample maps, respectively.

The comparison of the CCM and CQRM methods is carried out by applying them to the rest of the data corresponding to 90% of the dataset, allowing a direct comparison between the real information and the results obtained by the two methods under the same heterotopic sampling conditions and validation metrics.

A comparative statistical summary between the full (100%) dataset and the 10% sample for copper recovery is shown in Table 1 and Figures 3 and 4, respectively. It can be seen that the 10% subset of data is statistically equivalent to the total dataset in terms of the statistical values and probability distribution. Hereinafter, the subset corresponding to 10% of the dataset will be referred to as “10% sample”.

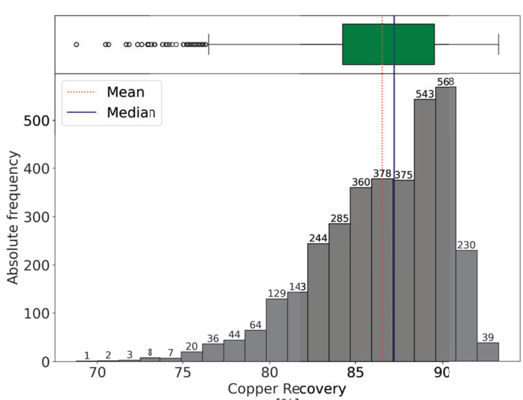

Figure 3. Copper recovery histogram and boxplot for the full (100%) dataset.

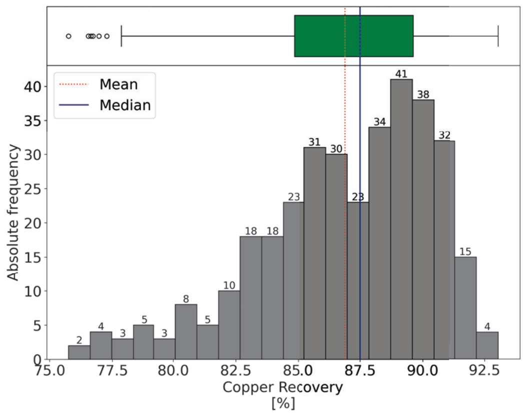

Figure 4. Copper recovery histogram and boxplot for 10% sample dataset.

Table 1. Copper recovery statistics summary for the total and 10% sample, respectively.

Statistics	Total Sample	10% Sample
Size	3479	347
Minimum	68.7907	75.7572
1st quartile	84.2624	84.8486
Median	87.2162	87.503
Mean	86.5376	86.8988
3rd quartile	89.5262	89.6185
Maximum	93.2732	93.0413
Range	24.4825	17.2841
Interquartile range	5.2638	4.7699
Variance	13.8434	12.3059
Standard deviation	3.7207	3.508
Skewness	−0.8964	−0.8003
Kurtosis	0.6558	0.2731

5. Case Study Application

5.1. Exploratory Data Analysis

A statistical summary of the geochemical attributes for the 10% sample is shown in Table 2.

Table 2. Statistics summary for a 10% sample for all geochemical attributes, where the numbering corresponds to: 1—clays, 2—chalcocite, 3—bornite, 4—chalcopyrite, 5—tennantite, 6—molybdenite, 7—pyrite, 8—copper (Cu), 9—molybdenum (Mo), and 10—arsenic (As), 11—copper recovery and 12—bond work index.

Statistics	1	2	3	4	5	6	7	8	9	10	11	12
Size	347	347	347	347	347	347	347	347	347	347	347	347
Minimum	0.7294	0.0045	0.0047	0.205	0.0046	0.0047	0.0053	0.0766	0.0028	0.0009	75.7572	11.39
1st quartile	2.1378	0.009	0.0674	0.5892	0.005	0.0089	0.6665	0.3199	0.0054	0.001	84.8486	12.5312
Median	3.2251	0.0457	0.1308	0.789	0.0067	0.0127	1.6151	0.4129	0.0076	0.0014	87.503	12.8145
Mean	4.08	0.0804	0.1733	0.9003	0.0128	0.0185	1.8393	0.4569	0.0111	0.0026	86.8988	12.9392
3rd quartile	5.0217	0.1261	0.2246	1.0561	0.0123	0.0218	2.7769	0.5312	0.0131	0.0025	89.6185	13.1052
Maximum	20.7767	0.7682	0.9131	3.6683	0.133	0.125	7.1561	1.6023	0.075	0.027	93.0413	22.2781
Range	20.0473	0.7637	0.9084	3.4633	0.1285	0.1203	7.1509	1.5257	0.0722	0.0261	17.2841	10.8881
Interquartile range	2.884	0.1172	0.1571	0.4669	0.0072	0.0129	2.1103	0.2113	0.0077	0.0015	4.7699	0.5739
Variance	8.0645	0.0101	0.0255	0.2463	0.0003	0.0002	1.911	0.0461	0.0001	0	12.3059	0.9168
Standard deviation	2.8398	0.1003	0.1597	0.4963	0.0174	0.0153	1.3824	0.2146	0.0092	0.0035	3.508	0.9575
Skewness	1.7563	2.9569	1.7926	2.3118	4.4297	2.4914	0.664	1.7473	2.4914	4.4297	−0.8003	5.058
Kurtosis	4.3005	14.3695	3.6934	7.8782	23.0514	9.0065	−0.1015	4.9835	9.0065	23.0514	0.2731	36.8668

5.2. Variable Selection

A bivariate analysis is carried out to select the geochemical attribute that has a greater dependence relationship with respect to copper recovery. For this purpose, heat maps of the Pearson, Kendall, and Spearman correlation coefficients are obtained (see the latter in Figure 5).

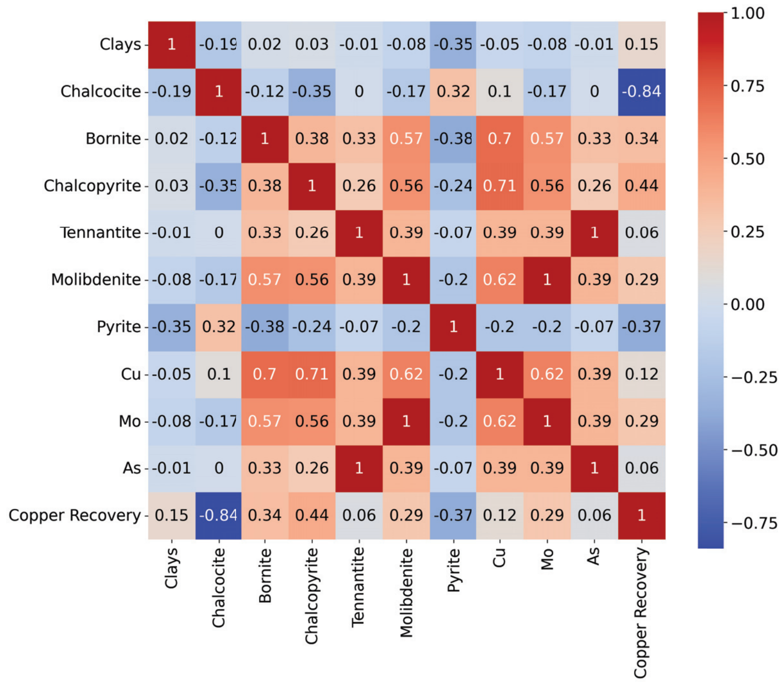

Figure 5. Spearman correlation heat map of all geochemical attributes for a 10% sample.

The geochemical attribute that shows the strongest correlation with copper recovery is chalcocite, with correlation coefficients of −0.75, −0.84, and −0.63 according to Pearson, Spearman, and Kendall, respectively (see Table 3). However, it is important to note that the dependency relationship between the variables, as shown in Figure 6, presents a clearly nonlinear behavior. The variable chalcocite, which is mostly sampled, is selected to perform the comparison between the collocated cokriging and conditional quantile regression methods.

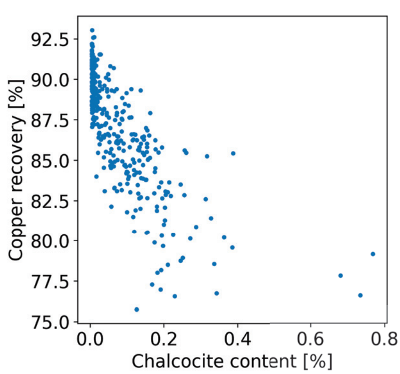

Figure 6. Copper recovery vs. chalcocite scatterplot for 10% sample dataset.

Table 3. Copper recovery and chalcocite correlation coefficients.

Primary Variable	Secondary Variable	Pearson	Kendall	Spearman
Copper recovery	chalcocite	−0.75	−0.63	−0.84

5.3. Modeling

As was mentioned in Section 3, the modeling step is different for each method. CCM corresponds to a *spatial correlation modeling* step, while CQRM to a *dependence modeling* step, as shown below.

5.3.1. Spatial Correlation Modeling

The spatial correlation model for CCM consists of estimating the sample variogram and optimally adjusting a variogram model to the primary variable, which in this case is copper recovery.

The chalcocite spatial distribution for the complete dataset on the left side and the corresponding map for the 10% sampling on the right side are shown in Figure 7, while Figure 8 shows the copper recovery empirical variogram calculated by Matheron estimator and a spherical fitted model with an effective range of 141.12 m, a sill of 12.20, and no nugget effect. This spatial correlation model is used in conjunction with Pearson's correlation coefficient in the collocated cokriging application to chalcocite complete dataset (left side of Figure 7).

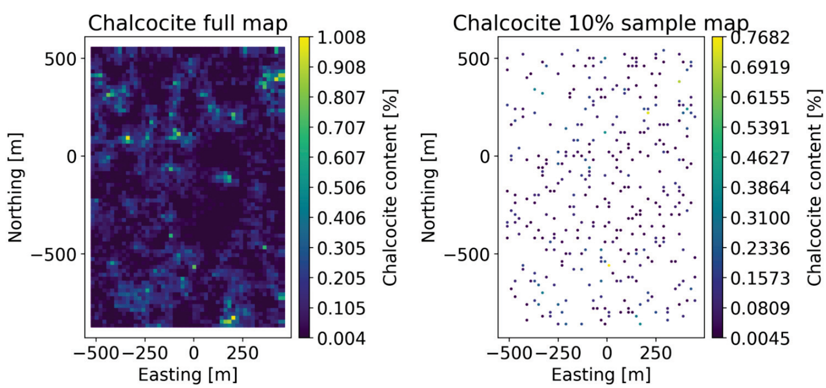

Figure 7. Chalcocite for the 100% (**in the left**) and 10% (**in the right**) sample maps, respectively.

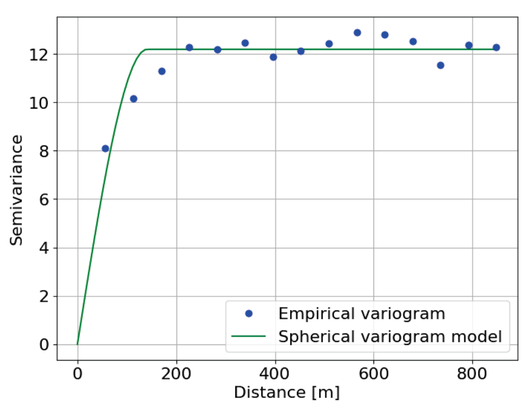

Figure 8. Copper recovery variogram model. The blue dots are the empirical variogram and the continuous green line is the fitted variogram model.

5.3.2. Dependence Modeling

The distribution of chalcocite shows a strong positive skewness (see Figure 9), which probably will not fit a parametric distribution, while copper recovery presents a slight negative skewness (see Figure 10).

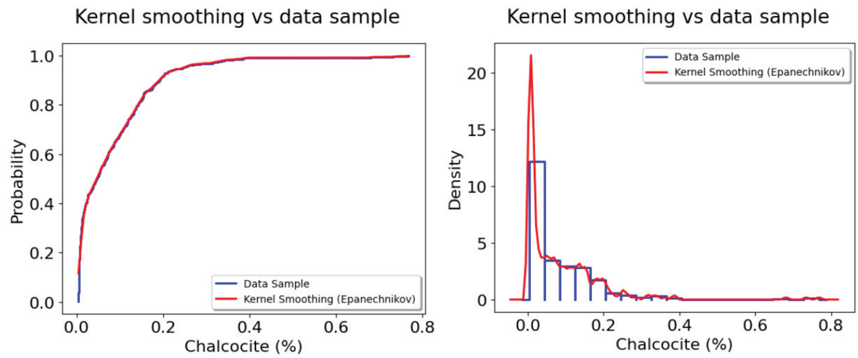

Figure 9. Model fitting of the chalcocite marginal using the kernel smoothing method with the Student function. The cumulative distribution function is on the left side and the probability density function is on the right side.

For both chalcocite and copper recovery, marginal distributions are fitted using the nonparametric method of kernel smoothing, which estimates a probability density function (PDF) from data without assuming a specific form. In particular, an Epanechnikov kernel [40] is the best fitting function for both marginals using the Bayesian information criterion (see Figures 9 and 10). Subsequently, a copula model is fitted using the same kernel smoothing method and criterion, but the best kernel is a Student function [41], which shows a better fit than other evaluated kernels, including the Epanechnikov one (see Figure 11).

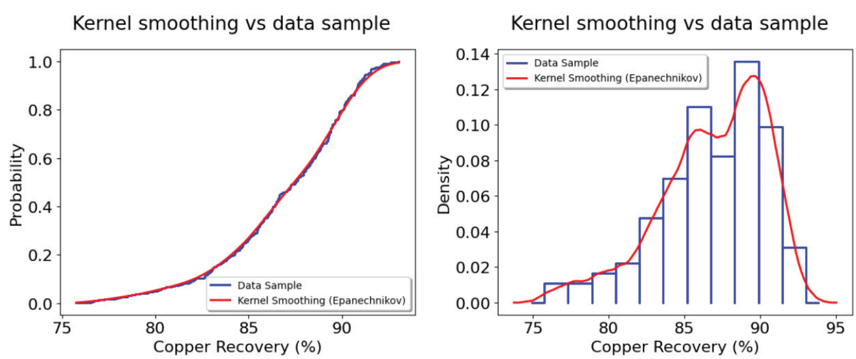

Figure 10. Model fitting of the copper recovery marginal using the kernel smoothing method with the Student function. The cumulative distribution function is on the left side and the probability density function is on the right side.

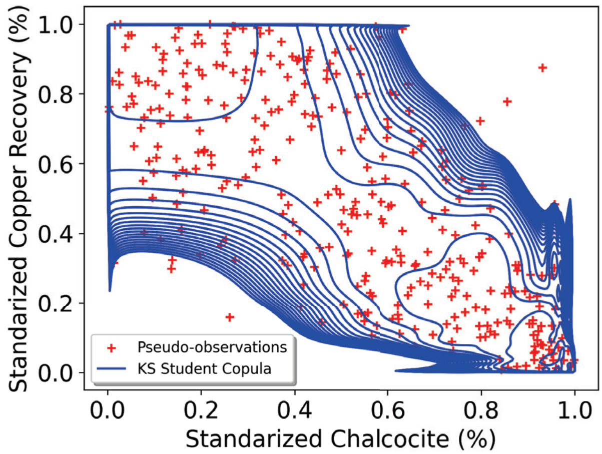

Figure 11. Copula model fitting using kernel smoothing method with a kernel Student function.

5.4. Validation

The validation stage consists of two parts. The first part involves verifying that the dependency model accurately reproduces both the univariate statistics of the marginal variables (chalcocite and copper recovery) and the bivariate statistics of the data sample. This is achieved through a joint nonconditional simulation using the dependency model (Appendix A.3). The second part assesses the predictive power of the quantile regression method by comparing its results with the 10% data sample (Appendix A.4). Specifically, copper recovery values are estimated by applying the quantile regression method conditioned on the chalcocite data from the 10% sample and are then compared with the actual copper recovery values from that sample.

The nonconditional simulation is generated using the bivariate probability distribution function of chalcocite and copper recovery from the previous section. To ensure comparability, the unconditional simulation produces a sample of the same size as the 10% data sample. The resulting simulation is statistically equivalent to the 10% data sample (see Tables 4 and 5). Additionally, the dependency model accurately reproduces the dependence pattern between the chalcocite data and copper recovery (see Figure 12), thereby validating both the models of the marginal distributions and the copula model.

Table 4. Statistics summary for copper recovery and chalcocite nonconditional joint simulation.

Statistics	Chalcocite	Copper Recovery
Size	347	347
Minimum	−0.0051	75.8326
1st quartile	0.0109	84.4898
Median	0.0540	87.522
Mean	0.0872	86.8948
3rd quartile	0.1440	89.7867
Maximum	0.7676	93.2552
Range	0.7727	17.4227
Interquartile range	0.1331	5.2969
Variance	0.0108	13.7954
Standard deviation	0.1040	3.7142
Skewness	2.5942	−0.6636
Kurtosis	14.6298	2.8307

Table 5. Copper recovery and chalcocite nonconditional simulation correlation coefficients.

Primary Variable	Secondary Variable	Pearson	Kendall	Spearman
Copper recovery	Chalcocite	−0.69	−0.52	−0.73

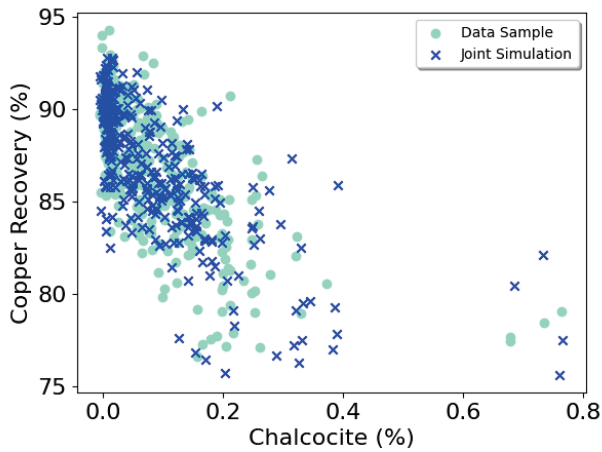

Figure 12. Joint copper recovery and chalcocite nonconditional simulation. The aquamarine circles are the data sample values and blue crosses are the copper–chalcocite joint bivariate unconditional simulation values.

Conditional quantile regression is applied to predict copper recovery conditional on chalcocite data values. These results are compared to actual copper recovery values, which are not used in the modeling. The estimated values of the median and the first (Q1) and third (Q3) quartiles (50% quantile, 25% quantile and 75% quantile, respectively) by CQRM follow the global trend of the real data (Figure 13) and their spatial distribution.

When comparing the omnidirectional variogram obtained from the copper recovery of the complete dataset with the copper recovery variogram estimated through the CQRM, it is observed that both are quite close (see Figure 14). This finding demonstrates the excellent ability to reproduce spatial variability using CQRM at unsampled locations.

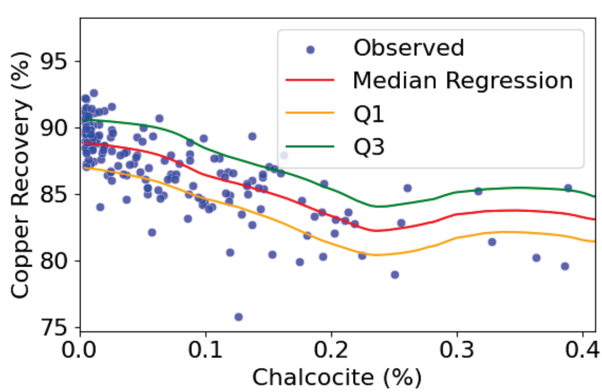

Figure 13. Scatterplot of copper recovery vs. chalcocite. The blue dots are the observed data values, the red line is the median estimated values, and the orange and green lines are the first (Q1) and third (Q3) quartiles, respectively, by CQRM application.

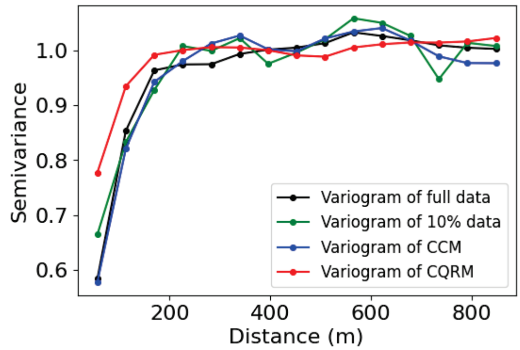

Figure 14. Copper recovery empirical variograms from full data, 10% sample, CCM and CQRM.

5.5. Prediction

The collocated cokriging method (CCM) was applied with the Markov 1 model, described in detail in [42], where chalcocite was employed as an exhaustive secondary variable. The co-estimation plan considered a search neighborhood equivalent to the effective range of the spherical variogram, at 145 radial meters, using a limit of 20 observations as the maximum for each co-estimation. Similarly, the conditional quantile regression method (CQRM) was applied to each chalcocite cell using the dependence model obtained in Section 5.3.2 for the estimation of the median and interquartile range of copper recovery.

The results of the application of both methods are shown numerically in terms of performance metrics in Table 6 and graphically in Figures 15 and 16.

Table 6. Performance metrics of collocated cokriging vs. quantile regression method for copper recovery estimation conditioned by chalcocite for 10% sample data, where RMSE is the root mean squared error, MAE is the mean absolute error, MAPE is the mean absolute percentage error, and R^2 is the determination coefficient.

Performance Metrics	CCM	CQRM
RMSE	3.85	2.86
MAE	3.03	1.71
MAPE	3.58	2.04
R^2	0.09	0.67

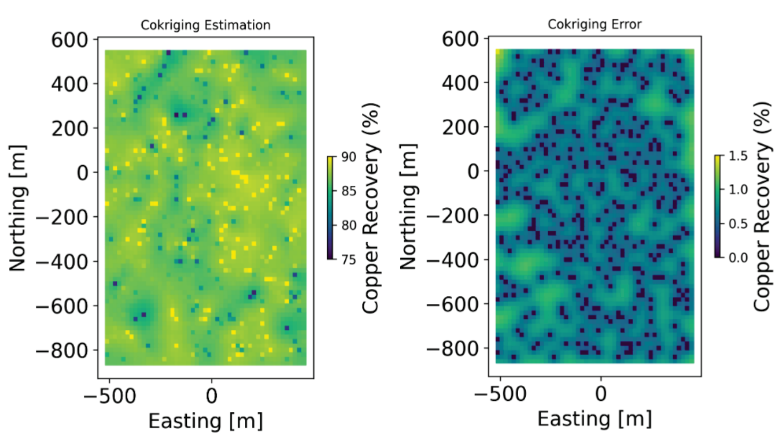

Figure 15. Mean estimation (**on the left side**) and standard deviation (**on the right side**) for copper recovery conditioned by chalcocite using CCM.

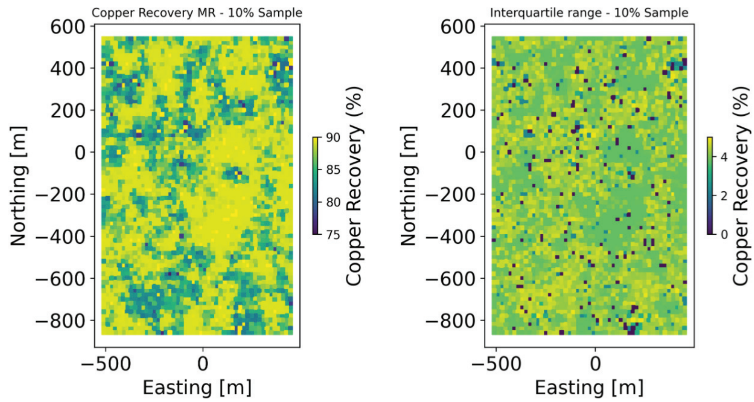

Figure 16. Median estimation (**on the left side**) and interquartile range (**on the right side**) for copper recovery conditioned by chalcocite using CQRM.

The performance metrics (RME, MAE, and MAPE) in Table 6 are significantly lower for CQRM relative to CCM, meaning that CQRM is a much more accurate method, and R^2 corroborates that CQRM has a better goodness of fit. Or, in other words, it explains a greater percentage of the variance in the data than the CCM. This is complemented graphically, since it can be seen that the spatial distribution pattern of the copper recovery estimate using CCM (Figure 15) is very different from that of Figure 2 of the dataset complete, while the CQRM estimation (Figure 16) has a much closer spatial distribution.

Performance Evaluation

By reducing heterotopy through an increase in the sampling of the primary variable, a substantial decrease in error is observed. This improvement is logical and is due to the fact that a greater amount of data for the primary variable allows for a better understanding of its behavior and its relationship with other variables.

A comparison of CQRM performance under different scenarios is shown in Figure 17. In particular, five scenarios were evaluated with a considerably high heterotopia, with different percentages (1%, 5%, 10%, 15%, and 20%) of the primary copper recovery variable, but preserving the set of complete data for the secondary variable chalcocite. It can be seen that with more information, the CQRM can more accurately estimate the primary copper recovery variable, resulting in a significant reduction in uncertainty and, therefore, the associated error. This is clearly demonstrated in Table 7, where the performance metrics consistently improve as the percentage of data for the primary variable increases.

Table 7. Performance metrics of quantile regression method for copper recovery estimation conditioned by chalcocite under different scenarios: 1%, 5%, 10%, 15%, and 20% sample data, where RMSE is the root mean squared error, MAE is the mean absolute error, MAPE is the mean absolute percentage error, and R^2 is the determination coefficient.

Performance Metrics	1%	5%	10%	15%	20%
RMSE	3.78	2.97	2.86	2.35	2.24
MAE	2.64	1.92	1.71	1.52	1.41
MAPE	3.16	2.29	2.04	1.81	1.68
R^2	0.39	0.63	0.67	0.79	0.81

The results are notable considering the simplicity of this approach, as it depends only on a single secondary variable, and the computational efficiency it presents.

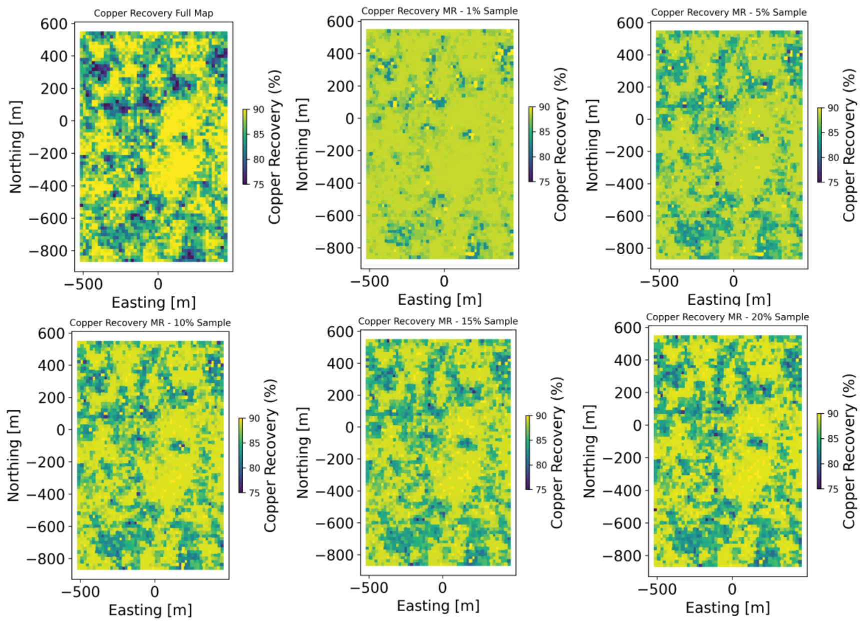

Figure 17. Median quantile regression estimation for copper recovery conditioned by chalcocite under different scenarios. The figures are arranged from left to right and from top to bottom: full (100%) map, 1%, 5%, 10%, 15%, and 20% sample data.

6. Discussion

The results of the CCM, under the same heterotopic sampling conditions of 10%, did not surpass those of the CQRM, even when the latter was used under less favorable sampling conditions (Table 7). In particular, it can be observed that the performance metrics for the 1% sample data are even better for CQRM than those for the 10% sample data for CCM. This is because methods like the CCM depend on strictly linear relationships between variables and are not competitive in this case, where there is no linearity and the dependencies are complex.

Although the CQRM does not explicitly incorporate a spatial correlation model for copper metallurgical recovery, it reproduces its variability quite well. When observing Figure 14, there is a high similarity between the data sample and prediction variograms. This occurs because the primary variable (copper recovery) inherits the spatial correlation through the secondary variable using the joint dependence model. By not requiring a spatial correlation model, a certain degree of subjectivity is eliminated from the process, adding practicality and efficiency. It is shown that a copula-based dependence model can reproduce spatial variability, provided that the joint dependence model is established following the proposed methodological guidelines. This includes appropriately selecting the predictor variable based on maximum dependence, correctly modeling marginal distributions, and choosing an appropriate bivariate model, as well as validating the model through simulation to reproduce the dependence of the sampling data.

7. Conclusions

Copper metallurgical recovery is a key variable in defining the cutoff grade for mining operations, directly influencing the amount of copper that can be profitably extracted and processed. Consequently, it is critical in the economic evaluation of a project. In this context, an accurate estimation of metallurgical recovery is vital for strategic planning and decision making.

The approach proposed in this article consists of the application of a novel conditional quantile regression method for metallurgical copper recovery conditioned on a secondary variable that is widely sampled and exhibits the maximum possible dependence. The particularity of this approach lies in the optimal estimation of the codependency model of the variables using a kernel smoothing method for the marginals as well as for the copula.

The presented application is based on a synthetic but realistic case of a porphyry copper deposit, where the median regression for copper recovery is estimated at all known chalcocite locations, used as an explanatory variable. The comparison of the results obtained by CQRM versus CCM shows that, both in terms of precision and efficiency, as well as reproduction of spatial variability, the method proposed in this article is superior when the dependencies are nonlinear.

Although this is a specific application to a case study, the methodology can be extended to other scenarios, such as an exploration drilling campaign, where the largest scale of information comes from drilling interval logs, with metallurgical recovery measured in fewer quantities and not necessarily in the same locations.

CQRM is an innovative, practical, efficient, and versatile approach. It avoids strong assumptions about the data and theoretical constraints in its implementation, demonstrating a clear capacity to adapt to different levels of information and scales, making it applicable to a wide variety of scenarios.

As future work, the implementation of conditional quantile regression method based on copula model with multivariate dependencies is proposed. This model extension is expected to further improve the accuracy of predictions while maintaining practicality, versatility, and computational efficiency.

As can be deducted from the Funding section of this manuscript, this research has raised the interest of other sectors, such as the steel industry, who wishes to maximize the efficiency of all its processes in terms of both industrial and social impact.

Author Contributions: Conceptualization, H.H. and M.A.D.-V.; methodology, M.A.D.-V.; software, M.A.D.-V.; validation, H.H.; formal analysis, M.A.D.-V.; writing—original draft preparation, H.H. and M.A.D.-V.; writing—review and editing, E.A., A.G., and A.O.-Z.; supervision, E.A.; funding acquisition, A.G. and A.O.-Z. All authors have read and agreed to the published version of the manuscript.

Funding: Work funded by project SILENCE—European Commission—Research Program of the Research Funds for Coal and Steel—Prj. No.: 101112516.

Data Availability Statement: Data used in this article are taken from the publication [19] and are publicly available.

Conflicts of Interest: The authors declare no conflicts of interest.

Abbreviations

The following abbreviations are used in this manuscript:

CCM	Collocated cokriging method
CQRM	Conditional quantile regression method based on copulas
MAE	Mean absolute error
MAPE	Mean absolute percentage error
PDF	Probability density function
R^2	Determination coefficient
RMSE	Root mean squared error

Appendix A. Conditional Quantile Regression Method Based on Copulas

Sklar in 1959 [33] established a theorem indicating a functional relationship between the joint probability distribution function of a random vector and its univariate marginal distribution functions. For instance, in the case of two variables, if (X, Y) is a random vector with a joint probability distribution $H_{XY}(x, y) = P(X \leq x, Y \leq y)$, then the marginal distribution functions of X and Y are $F_X(x) = P(X \leq x) = H_{XY}(x, \infty)$ and $G_Y(y) = P(Y \leq y) = H_{XY}(\infty, y)$, respectively. However, when marginalizing H_{XY}, some information is lost, as the marginal distributions F_X and G_Y generally do not suffice to fully determine H_{XY}. This is because the marginal distributions only describe the individual probability behavior of the random variables they represent. Sklar's theorem demonstrates that there exists a function C_{XY}: $[0,1]^2 \longmapsto [0,1]$ such that

$$H_{XY}(x,y) = C_{XY}(F_X(x), G_Y(y)) \tag{A1}$$

where C_{XY} is the *copula* function associated with the bivariate random vector (X, Y) and describes its dependence relationship, H is the bivariate probability distribution function, and F and G are the univariate (marginal) probability distributions.

Copula functions are a valuable tool for constructing joint probability models with greater flexibility. They allow us to independently select univariate models for the random variables of interest and choose a copula function that best represents their dependence, either parametrically or nonparametrically. For example, in a multivariate normal model, all marginal distributions must be normal, with no tail dependence and finite second moments for well-defined correlations. The multivariate normal model is a specific instance where the underlying copula is Gaussian and all univariate marginals follow a normal distribution.

When F_X and G_Y are continuous, elementary probability theory tells us that $U = F_X(X)$ and $V = G_Y(Y)$ are continuous uniform random variables on $(0,1)$. The underlying copula C for the random vector (U, V) is the same copula corresponding to (X, Y). According to Sklar's theorem, the joint probability distribution function for (U, V) is given by $H_{UV}(u, v) = C(F_U(u), G_V(v)) = C(u, v)$. Therefore, if F_X and G_Y are known but H_{XY} is unknown, and we have an observed random sample $\{(x_1, y_1), \ldots, (x_n, y_n)\}$ of (X, Y), the set $\{(u_k, v_k) = (F_X(x_k), G_Y(y_k)) : k = 1, \ldots, n\}$ will be an observed random sample of (U, V) with the same underlying copula C as (X, Y). Since $C = F_{UV}$, we can use the values (u_k, v_k) (known as copula observations) to estimate C as a joint empirical distribution:

$$\hat{C}(u,v) = \frac{1}{n} \sum_{k=1}^{n} \mathbb{I}_{\{u_k \leq u, v_k \leq v\}} \tag{A2}$$

Strictly, the estimate $\hat{C}$ is not a copula since it is discontinuous and copulas are always continuous. If F_X, G_Y, and H_{XY} are all unknown, which is the most common case, F_X and G_Y are estimated by their empirical univariate distribution functions:

$$\hat{F}_X(x) = \frac{1}{n} \sum_{k=1}^{n} \mathbb{I}\{x_k \leq x\}, \quad \hat{G}_Y(y) = \frac{1}{n} \sum_{k=1}^{n} \mathbb{I}\{y_k \leq y\} \tag{A3}$$

where $\mathbb{I}$ represents an indicator function equal to 1 when its argument is true and 0 otherwise.

We will refer to the set of pairs $\left\{(\hat{u}_k, \hat{v}_k) = (\hat{F}_X(x_k), \hat{G}_Y(y_k)) : k = 1, \ldots, n\right\}$ as pseudo observations of the copula. It can be verified directly that $\hat{F}_X(x_k) = \frac{1}{n} rank(x_k)$ and $\hat{G}_Y(y_k) = \frac{1}{n} rank(y_k)$. In this case, the concept of empirical copula, see [34], is defined as the following function C_n: $I_n^2 \longmapsto [0,1]$, where $I_n = \left\{\frac{i}{n} : i = 0, \ldots, n\right\}$, given by

$$C_n\left(\frac{i}{n}, \frac{j}{n}\right) = \frac{1}{n} \sum_{k=1}^{n} \mathbb{I}_{\{rank(x_k) \leq i, rank(y_k) \leq j)\}} \tag{A4}$$

Again, C_n is not a copula but is an estimate of the underlying copula in the mesh I_n^2 that can be extended to a copula in $[0,1]^2$of, for example, Bernstein polynomials, as proposed and studied in [43], leading to what is known as a nonparametric estimate of the Bernstein copula $\tilde{C}$: $[0,1]^2 \longmapsto [0,1]$ given by

$$\tilde{C}(u,v) = \sum_{i=0}^{n}\sum_{j=0}^{n} C_n\left(\frac{i}{n},\frac{j}{n}\right)\binom{n}{i}u^i(1-u)^{n-i}\binom{n}{j}v^j(1-v)^{n-j} \tag{A5}$$

Appendix A.1. Three Approaches to Building a Copula-Based Dependency Model

There are three approaches to building a copula-based dependency model: parametric, nonparametric, and semiparametric.

The parametric approach consists of being able to fit a known copula model to the empirical copula, such as the Frank, Gumbel, or Clayton copulas, which belong to the family of Archimedean copulas [34,35], as well as being able to fit the empirical marginal probability distributions to known distribution functions such as normal or Gaussian, lognormal, gamma, Weibull, etc. In this way, a joint probability distribution model is obtained.

The nonparametric approach consists of numerically approximating the empirical copula and its marginals, usually by means of some polynomial expression. In this approach, Bernstein polynomials [28,43] and splines [44], as well as the kernel smoothing method, have been used [35], where kernel smoothing is a type of weighted moving average.

While a semiparametric approach is a combination of the two previous approaches, this allows two options, that is, a model could be fitted to the empirical copula and approximate the marginals with a polynomial, or the empirical copula could be approximated by a polynomial expression and adjust the marginals with a known distribution model [45].

Appendix A.2. Kernel Density Estimation with Kernel Smoothing Method

Consider $(x_1, x_2, \ldots, x_n)$ as independent and identically distributed samples drawn from a univariate distribution characterized by an unknown density function f at any arbitrary point x. Our focus lies in approximating the shape of this function f. Its kernel density estimator is expressed as follows:

$$\widehat{f}_h(x) = \frac{1}{n}\sum_{i=1}^{n} K_h(x-x_i) = \frac{1}{nh}\sum_{i=1}^{n} K\Big(\frac{x-x_i}{h}\Big), \tag{A6}$$

In this context, K denotes the kernel, a function that yields only non-negative values, while $h > 0$ represents a smoothing parameter referred to as the bandwidth. A kernel labeled with the subscript h is termed the scaled kernel, defined by $K_h(x) = \frac{1}{h}K(\frac{x}{h})$. In essence, one aims to select h to be as small as the data permits intuitively; nevertheless, there invariably exists a trade-off between the estimator's bias and its variance.

Appendix A.3. Copula Simulation Algorithm

As summarized in [45], in order to simulate the repetitions of the random vector (X, Y) with the dependence structure inferred from the observed data $(x_1, y_1), \ldots, (x_n, y_n)$, we have the following algorithm:

(i) Generate two independent and continuous random variables u and t uniformly distributed in $(0, 1)$.
(ii) Set $v = c_u^{-1}(t)$, where $c_u(v) = \frac{\partial \tilde{C}(u,v)}{\partial u}$.
(iii) The desired pair is $(x, y) = (\tilde{Q}_n(u), \tilde{R}_n(v))$, where $\tilde{Q}_n$ and $\tilde{R}_n$ are the empirical quantile functions for X and Y, respectively.

Appendix A.4. Conditional Quantile Regression Algorithm

For a value x in the range of the random variable X and a given $0 < \alpha < 1$, let $y = \varphi_\alpha(x)$ be the solution of the equation $P(Y \leq y|X = x) = \alpha$. Then the graph of

$y = \varphi_\alpha(x)$ is the *quantile regression* curve α of Y conditional on $X = x$. In [34] it is proven that

$$P(Y \le y|X = x) = c_u(v)|_{u=F_X(x),v=G_Y(y)} \tag{A7}$$

This result leads to the following algorithm to obtain *quantile regression* curve α of Y conditional on $X = x$:

(i) Set $c_u(v) = \alpha$.
(ii) Solve the regression curve for v:

$$v = g_\alpha(u). \tag{A8}$$

(iii) Replace u by $\tilde{Q}_n^{-1}(x)$ and v by $\tilde{R}_n^{-1}(y)$.
(iv) Solve the regression curve for y:

$$y = \varphi_\alpha(x). \tag{A9}$$

Appendix B. Collocated Cokriging Method with Markov Model

The kriging method is well known as the best unbiased linear spatial estimator of a single random function and the cokriging method is its generalization for two or more random functions. This requires calculating the primary variogram (e.g., copper recovery), the secondary variogram (e.g., geochemical attribute), and the cross-variogram [38,46]. In particular, the cross-variogram takes into account the spatial dependence between the two random functions and is defined as follows:

$$\gamma_{12}(h) = \frac{1}{2N(h)} \sum_{\alpha=1}^{N} (Z_1() - Z_1(x_\alpha + h))(Z_2(x_\alpha) - Z_2(x_\alpha + h)) \tag{A10}$$

where γ_{12} is the semivariance between the random functions Z_1 (copper recovery) and Z_2 (geochemical attribute), h is the lag distance, x_α is a spatial location, and N is the number of lag distances.

The rigorous application of the ordinary cokriging method is frequently very difficult and complicated since it also requires that the set of variograms comply with the linear coregionalization model. This model is very restrictive since it requires that all variograms fit the same model with a common range.

A more efficient and practical alternative is the collocated cokriging method that was introduced by Almeida and Journel (1994) [47]. It is a variant of cokriging method for spatial interpolation that leverages both primary and secondary data. But it simplifies the computation by using only the secondary variable's value that is collocated (at the same location) as the primary variable. This method is particularly useful when secondary data are more densely sampled than primary data.

However, this approach requires a conditional independence between the primary variable and the secondary variable, given their collocated values. This is known as a Markov assumption of conditional independence, which simplifies the modeling process. There are two types of Markov models: Markov models 1 and 2, respectively. Here, Markov model 1 (MM1) is used as it is the simplest and most straightforward option.

In Markov model 1, the following conditional independence assumption is made:

$$E(Z_2(u)|Z_1(u) = z_1, Z_1(u') = z_1(u')) = E(Z_2(u)|Z_1(u) = z_1) \tag{A11}$$

This implies, under the assumptions of MM1, a simplification in the statistical relationship between the primary and secondary variables. Thus, the cross-correlogram model can be written as

$$\rho_{12}(h) = \rho_{12}(0)\rho_1(h) \tag{A12}$$

where the correlogram ρ is expressed by

$$\rho(h) = 1 - \gamma(h) \tag{A13}$$

Assuming that $\gamma(h)$ is the variogram for data with a standard normal distribution, the correlogram is simply the variogram inverted and shifted upward by one. While the variogram measures spatial covariance, the correlogram measures spatial correlation. Therefore, $\rho_{12}(0)$, the correlogram at a lag distance of zero, is equivalent to the correlation coefficient between variables 1 and 2.

In summary, to apply the collocated cokriging method with Markov model 1 (MM1), all that is needed is the primary variable variogram and the linear correlation coefficient between the primary and secondary variables. The variogram for secondary variable is not necessary.

Note that you MUST to perform a normal score transformation for the primary and secondary data prior to invoking MM1.

References

1. Kasa, F.K.; Dağ, A. Appraising economic uncertainty in open-pit mining based on fixed and variable metallurgical recovery. *Arch. Min. Sci.* **2022**, *67*, 699–713.
2. Gholami, A.; Asgari, K.; Khoshdast, H.; Hassanzadeh, A. A hybrid geometallurgical study using coupled Historical Data (HD) and Deep Learning (DL) techniques on a copper ore mine. *Physicochem. Probl. Miner. Process.* **2022**, *58*, 147841. [CrossRef]
3. Oumesaoud, H.; Faouzi, R.; Aboulhassan, M.A.; Naji, K.; Benzakour, I.; Faqir, H.; Oukhrib, R.; Elboughdiri, N. Iron Oxide–copper Mineral Associations in Supergene Zones: Insights into Flotation Challenges and Optimization Using Response Surface Methodology. *ACS Omega* **2024**, *9*, 24438–24452. [CrossRef]
4. Madenova, Y.; Madani, N. Application of Gaussian Mixture Model and Geostatistical Co-simulation for Resource Modeling of Geometallurgical Variables. *Nat. Resour. Res.* **2021**, *30*, 1199–1228. [CrossRef]
5. Ramos Armijos, N.J.; Calderón Celis, J.M. Revisión del modelo geometalúrgico para la estimación de recursos minerales en depósitos pórfido cupríferos. *Rev. Del Inst. De Investig. De La Fac. De Minas Metal. Y Cienc. Geográficas* **2022**, *25*, 445–459. [CrossRef]
6. Mu, Y.; Salas, J.C. Data-Driven Synthesis of a Geometallurgical Model for a copper Deposit. *Processes* **2023**, *11*, 1775. [CrossRef]
7. Hunt, J.A.; Berry, R.F. Economic Geology Models #3. Geological Contributions to Geometallurgy: A Review. *Geosci. Can.* **2017**, *44*, 103–118. [CrossRef]
8. Hoffimann, J.; Augusto, J.; Resende, L.; Mathias, M.; Mazzinghy, D.; Bianchetti, M.; Mendes, M.; Souza, T.; Andrade, V.; Domingues, T.; et al. Modeling Geospatial Uncertainty of Geometallurgical Variables with Bayesian Models and Hilbert-Kriging. *Math. Geosci.* **2022**, *54*, 1227–1253. [CrossRef]
9. Hunt, J.; Kojovic, T.; Berry, R. Estimating comminution indices from ore mineralogy, chemistry and drill core logging. In Proceedings of the Second AusIMM International Geometallurgy Conference (GeoMet), Carlton, VIC, Australia, 30 September–2 October 2013; Dominy, S., Ed.; The Australasian Institute of Mining and Metallurgy (AusIMM): Carlton, Australia, 2013; pp. 173–176.
10. Garrido, M.; Ortiz, J.; Sepúlveda, E.; Farfán, L.; Townley, B. An overview of good practices in the use of geometallurgy to support mining reserves in copper sulfides deposits. In Proceedings of the Conference: Procemin Geomet 2019, Santiago, Chile, 20–22 November 2019. [CrossRef]
11. Dowd, P.A.; Xu, C.; Coward, S. Strategic mine planning and design: Some challenges and strategies for addressing them. *Min. Technol.* **2016**, *125*, 22–34. [CrossRef]
12. Little, L.; Mclennan, Q.; Prinsloo, A.; Muchima, K.; Kaputula, B.; Siame, C. Relationship between ore mineralogy and copper recovery across different processing circuits at Kansanshi mine. *J. S. Afr. Inst. Min. Metall.* **2018**, *118*, 1155–1162. [CrossRef]
13. Adeli, A.; Dowd, P.; Emery, X.; Xu, C. Using cokriging to predict metal recovery accounting for non-additivity and preferential sampling designs. *Miner. Eng.* **2021**, *170*, 106923. [CrossRef]
14. Dachri, K.; Bouabidi, M.; Naji, K.; Nouar, K.; Benzakour, I.; Oummouch, A.; Hibti, M.; El Amari, K. Predictive insights for copper recovery: A synergistic approach integrating variability data and machine learning in the geometallurgical study of the Tizert deposit, Morocco. *J. Afr. Earth Sci.* **2024**, *212*, 105208. [CrossRef]
15. Lishchuk, V.; Lund, C.; Ghorbani, Y. Evaluation and comparison of different machine-learning methods to integrate sparse process data into a spatial model in geometallurgy. *Miner. Eng.* **2019**, *134*, 156–165. [CrossRef]
16. Chehreh Chelgani, S.; Nasiri, H.; Alidokht, M. Interpretable modeling of metallurgical responses for an industrial coal column flotation circuit by XGBoost and SHAP-A "conscious-lab" development. *Int. J. Min. Sci. Technol.* **2021**, *31*, 1135–1144. [CrossRef]
17. Cook, R.; Monyake, K.C.; Hayat, M.B.; Kumar, A.; Alagha, L. Prediction of flotation efficiency of metal sulfides using an original hybrid machine learning model. *Eng. Rep.* **2020**, *2*, e12167. [CrossRef]

18. Flores, V.; Leiva, C. A Comparative Study on Supervised Machine Learning Algorithms for copper Recovery Quality Prediction in a Leaching Process. *Sensors* **2021**, *21*, 2119. [CrossRef] [PubMed]
19. Garrido, M.; Sepúlveda, E.; Ortiz, J.; Townley, B. Simulation of synthetic exploration and geometallurgical database of porphyry copper deposits for educational purposes. *Nat. Resour. Res.* **2020**, *29*, 3527–3545. [CrossRef]
20. Campos, P.H.A.; Costa, J.F.C.L.; Koppe, V.C.; Bassani, M.A.A. Geometallurgy-oriented mine scheduling considering volume support and non-additivity. *Min. Technol.* **2022**, *131*, 1–11. [CrossRef]
21. Tavares, L.M.; Kallemback, R.D. Grindability of binary ore blends in ball mills. *Miner. Eng.* **2013**, *41*, 115–120. [CrossRef]
22. Carrasco, P.; Chilès, J.P.; Séguret, S.A. Additivity, metallurgical recovery, and grade. In Proceedings of the 8th International Geostatistics Congress, Santiago, Chile, 1–5 December 2008; pp. on CD. hal-00776943
23. Rossi, M.E.; Deutsch, C.V. *Mineral Resource Estimation*; Springer: Dordrecht, The Netherlands, 2014. [CrossRef]
24. Sohrabian, B.; Soltani-Mohammadi, S.; Pourmirzaee, R.; Carranza, E.J.M. Geostatistical Evaluation of a Porphyry Copper Deposit Using Copulas. *Minerals* **2023**, *13*, 732. [CrossRef]
25. Bárdossy, A.; Li, J. Geostatistical interpolation using copulas. *Water Resour. Res.* **2008**, *44*. [CrossRef]
26. Hernández-Maldonado, V.; Díaz-Viera, M.A.; Erdely, A. A joint stochastic simulation method using the Bernstein copula as a flexible tool for modeling nonlinear dependence structures between petrophysical properties. *J. Pet. Sci. Eng.* **2012**, *90–91*, 112–123. [CrossRef]
27. Kazianka, H.; Pilz, J. Spatial Interpolation Using Copula-Based Geostatistical Models. In *geoENV VII—Geostatistics for Environmental Applications*; Atkinson, P.M., Lloyd, C.D., Eds.; Springer: Dordrecht, The Netherlands, 2010; pp. 307–319. [CrossRef]
28. Díaz-Viera, M.A.; Erdely, A.; Kerdan, T.; del Valle-García, R.; Mendoza-Torres, F. Bernstein Copula-Based Spatial Stochastic Simulation of Petrophysical Properties Using Seismic Attributes as Secondary Variable. In *Geostatistics Valencia 2016. Quantitative Geology and Geostatistics, vol 19*; Gómez-Hernández, J., Rodrigo-Ilarri, J., Rodrigo-Clavero, M., Cassiraga, E., Vargas-Guzmán, J., Eds.; Springer International Publishing: Berlin/Heidelberg, Germany, 2017; pp. 487–504.
29. Le, V.H. Copula-Based Modeling for Petrophysical Property Prediction Using Seismic Attributes as Secondary Variables. Ph.D. Thesis, Instituto de Geofísica, UNAM, Mexico City, Mexico, 2021.
30. Kolev, N.; Paiva, D. Copula-based regression models: A survey. *J. Stat. Plan. Inference* **2009**, *139*, 3847–3856. [CrossRef]
31. Kim, J.M.; Cho, C.; Jun, C.; Kim, W.Y. The Changing Dynamics of Board Independence: A Copula Based Quantile Regression Approach. *J. Risk Financ. Manag.* **2020**, *13*, 254. [CrossRef]
32. Tepegjozova, M.; Czado, C. Bivariate vine copula based regression, bivariate level and quantile curves. *arXiv* **2022**, arXiv:2205.02557.
33. Sklar, A. Fonctions de répartition á n dimensions et leurs marges. *Publ. Inst. Stat. Univ. Paris* **1959**, *8*, 229–231.
34. Nelsen, R.B. *An Introduction to Copulas*; Springer: New York, NY, USA, 2006. [CrossRef]
35. Joe, H. *Dependence Modeling with Copulas*; Chapman and Hall/CRC: Amsterdam, The Netherlands, 2014.
36. Tholana, T.; Musingwini, C. A Probabilistic Block Economic Value Calculation Method for Use in Stope Designs under Uncertainty. *Minerals* **2022**, *12*, 437. [CrossRef]
37. Jamshidi, M.; Osanloo, M. Determination of block economic value in multi-element deposits. In Proceedings of the 6th International Conference on Computer Applications in the Minerals Industries, CAMI2016-06, Istanbul, Turkey, 5–7 October 2016.
38. Wackernagel, H. Collocated Cokriging. In *Multivariate Geostatistics: An Introduction with Applications*; Springer: Berlin/Heidelberg, Germany, 2003; pp. 165–169. [CrossRef]
39. Wand, M.; Jones, M. *Kernel Smoothing*; Chapman and Hall/CRC: New York, NY, USA, 1994.
40. Scott, D.W. *Multivariate Density Estimation: Theory, Practice, and Visualization*; Wiley Series in Probability and Statistics; John Wiley & Sons, Inc.: Hoboken, NJ, USA, 1992. [CrossRef]
41. Li, R.; Nadarajah, S. A review of Student's t distribution and its generalizations. *Empir. Econ.* **2020**, *58*, 1461–1490. [CrossRef]
42. Shmaryan, L.; Journel, A. Two Markov Models and Their Application. *Math. Geol.* **1999**, *31*, 965–988. [CrossRef]
43. Sancetta, A.; Satchell, S. The bernstein copula and its applications to modeling and approximations of multivariate distributions. *Econom. Theory* **2004**, *20*, 535–562. [CrossRef]
44. Shen, X.; Zhu, Y.; Song, L. Linear B-spline copulas with applications to nonparametric estimation of copulas. *Comput. Stat. Data Anal.* **2008**, *52*, 3806–3819. [CrossRef]
45. Erdely, A.; Diaz-Viera, M. Nonparametric and Semiparametric Bivariate Modeling of Petrophysical Porosity-Permeability Dependence from Well Log Data. In *Copula Theory and Its Applications: Proceedings of the Workshop, Warsaw, Poland, 25–26 September 2009*; Jaworski, P., Durante, F., Härdle, W.K., Rychlik, T., Eds.; Springer: Berlin/Heidelberg, Germany, 2010; pp. 267–278.
46. Babak, O.; Deutsch, C.V. Improved spatial modeling by merging multiple secondary data for intrinsic collocated cokriging. *J. Pet. Sci. Eng.* **2009**, *69*, 93–99. [CrossRef]
47. Almeida, A.S.; Journel, A.G. Joint simulation of multiple variables with a markov-type coregionalization model. *Math. Geol.* **1994**, *26*, 565–588. [CrossRef]

applied sciences

Article

Determination of the Ground Reaction Curve for an Elasto-Plasto-Fractured Rock Mass

Paweł Kamiński [1], Aleksandra Otto [2], Piotr Dawidziuk [2], Leszek Malinowski [3], Kinga Stecuła [4,*] and Artur Dyczko [3]

1 KOMAG Institute of Mining Technology, Pszczynska 37, 44-101 Gliwice, Poland; pkaminski@komag.eu
2 Przedsiębiorstwo Budowy Szybów SA, Hutnicza 5-9, 42-600 Tarnowskie Góry, Poland; aotto@jswpbsz.pl (A.O.); pdawidziuk@jswpbsz.pl (P.D.)
3 Mineral and Energy Economy Research Institute, Polish Academy of Sciences, Wybickiego 7a, 31-261 Krakow, Poland; malinowski@meeri.com (L.M.); arturdyczko@min-pan.krakow.pl (A.D.)
4 Faculty of Organization and Management, Silesian University of Technology, 44-100 Gliwice, Poland
* Correspondence: kinga.stecula@polsl.pl

Abstract: Polish National Standards for underground excavation support design outline the deformational pressure model for assessing loads acting on the support systems of deep underground excavations. They distinguish two different rock mass models, highlighting the pivotal role of the critical longitudinal strain of the rock mass in appropriate model selection. A comparison between the design method given by Polish Standards and the widely recognized convergence–confinement method, consisting of a ground reaction curve (GRC), longitudinal displacement profile (LDP), and support characteristics curve (SCC), reveals the advantages of the latter in capturing the three-dimensional nature of underground excavations. The following study presents a method for establishing a GRC curve for the elasto-plasto-fractured rock mass model, featured in Polish Standards, demonstrating its applicability through analyses of a typical circular roadway under varying rock mass conditions. Practical implications are discussed, including the design of yielding steel arches as the primary support system and the calculation of safety factors for both the support system and the surrounding rock mass, considered as a natural support component. Overall, the study contributes to a deeper understanding of the actions of rock masses in the vicinity of excavations located at great depths. Furthermore, it provides practical insights for engineering applications.

Keywords: rock mechanics; convergence–confinement method; ground reaction curve; elasto-plasto-fractured model; excavation support

Citation: Kamiński, P.; Otto, A.; Dawidziuk, P.; Malinowski, L.; Stecuła, K.; Dyczko, A. Determination of the Ground Reaction Curve for an Elasto-Plasto-Fractured Rock Mass. *Appl. Sci.* **2024**, *14*, 5409. https://doi.org/10.3390/app14135409

Academic Editors: Jianhang Chen, Krzysztof Skrzypkowski, René Gómez, Fhatuwani Sengani, Derek B. Apel and Faham Tahmasebinia

Received: 21 May 2024
Revised: 19 June 2024
Accepted: 20 June 2024
Published: 21 June 2024

1. Introduction

The development of the pressure of a rock mass that acts on an excavation support depends on various factors, including the physical and mechanical properties of the rock mass, the mining technology used, and the characteristics of the support [1]. As the excavation face advances, the rock mass gradually moves toward the excavation axis. The increment of the displacement of the rock mass is influenced by both the distance to the excavation face and the time. However, in practical applications, the influence of time is often overlooked [2]. An analysis of the impact of the time factor on the growth of the displacement of rock masses requires the utilization of various rheological models—as discussed, for example, in [3–7].

The development of a deformational pressure acting on an excavation support is the result of the suppression of the increase in the displacement of the rock mass increment caused by the installation of the support [1]. The magnitude of the deformational pressure acting on a support system decreases as the ground displacement increases. Consequently, its value is a function of the distance between the excavation face and the support location during installation [2,8,9].

Up to a certain level of ground displacement, the rock mass in the vicinity of an excavation acts as an elastic medium. Once the displacement of the ground exceeds a certain threshold, inelastic zones begin to form around the excavation, which could lead to a reduction in the rock mass within these zones [4,10]. Therefore, four different types of inelastic zones can be identified:

- The compressive strength of the rock mass within the inelastic zone is equal to the compressive strength in the elastic zone, satisfying the condition:

$$R_{cg} = R_{cg}^{'} \tag{1}$$

  This scenario characterizes the elasto-perfectly plastic medium.

- The compressive strength of the rock mass within the inelastic zone is lower than the compressive strength in the elastic zone, meeting the following condition:

$$R_{cg} > R_{cg}^{'} \tag{2}$$

  This represents the softening elasto-plastic medium.

- The rock mass within the inelastic zone exhibits no compressive strength:

$$R_{cg}^{'} = 0 \tag{3}$$

  This represents the elasto-fractured medium.

- Two coaxial inelastic zones form around the excavation. In the immediate vicinity of the excavation, there exists a fractured rock mass zone without compressive strength. At a certain distance from the excavation boundary, a zone of plastic rock mass develops, retaining some residual compressive strength. This scenario denotes an elasto-plasto-fractured medium [11].

The development of inelastic zones around the excavation corresponds to the occurrence of a static rock mass pressure, which arises from the gravitational load of plasticized and fractured roof rocks. As the value of the ground displacement increases, the extent of the inelastic zones, and thus the level of static pressure, also increases. The elasto-plastic rock mass exhibits a boundary displacement value at which the static pressure reaches its maximum, while the deformational pressure diminishes. Therefore, the elasto-plastic model produces a paradox, since it suggests that the value of the support pressure always decreases along with an increase in ground displacement, whereas according to practical engineering, the support pressure is expected to increase significantly after reaching a certain value of ground displacement as a result of the loss of confinement and the detrimental loosening of the rock mass.

Meanwhile, in elasto-fractured and elasto-plasto-fractured media, as displacements increase, the static pressure theoretically tends toward infinity, while the deformational pressure approaches zero. Therefore, the final value of the support pressure increases after reaching a certain value of ground displacement, which seems to be consistent with engineering practice [12,13].

2. Deformational Pressure Model According to Polish Standards

In the late 1970s, the Industrial Standards BN-78/0434-07 [14] and BN-79/0434-04 [15] were introduced into Polish engineering practice. Their aim was to regulate and organize the various methods for calculating loads acting on the support systems of underground roadways and chambers. Previously used rheological models were replaced with the so-called deformational pressure model, which was later implemented in the National Standards PN-G-05600 [16] and PN-G-05020 [17], which remain in use up to today. The equations used to calculate the radii of the inelastic zones and the values of deformational and static pressure acting on excavation supports were based on the solution of a disk of uniform thickness initially subjected to a hydrostatic far-field (primary) stress. Calculations were performed under the following assumptions [18]:

- the plain strain condition,
- the hydrostatic far-field (primary) stress condition,
- the circular shape of the excavation section,
- the homogeneity, isotropy and weightlessness of the rock mass,
- that rock mass destruction occurs in cases of exceeding its compressive strength (based on the Mohr–Coulomb yield criterion).

The Polish Standards PN-G-05600 and PN-G-05020 distinguish between the following rock mass models [16,17], depending on the characteristics of the rock mass within the inelastic zone:

- the elasto-plastic model with softening (referred to simply as elasto-plastic model),
- the elasto-plasto-fractured model.

A schematic representation of the rock mass models as provided by the Polish Standards is depicted in Figure 1.

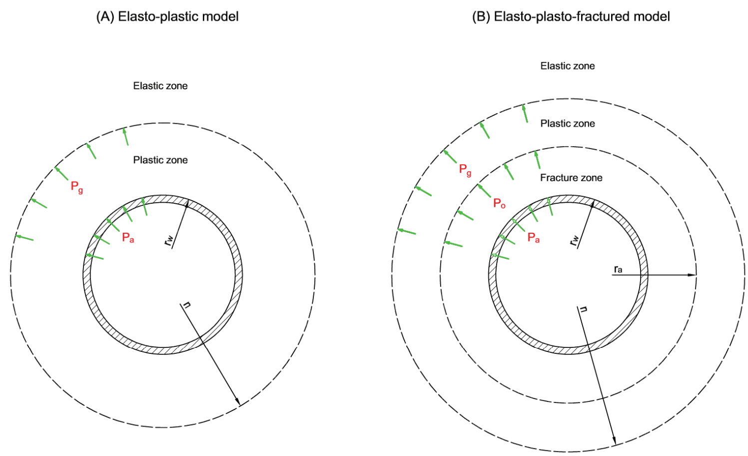

Figure 1. Deformational pressure model according to Polish Standards.

The choice of the appropriate rock mass model is dependent on the value of the critical longitudinal strain of the rock mass. This strain value marks the point at which the rock mass transitions from a plastic to a fractured medium in terms of its strength properties [18]. The critical longitudinal strain of the rock mass can be calculated using the equation provided by the PN-G-05020 standard [17]:

$$\varepsilon_{ng} = 1.5 \cdot \varepsilon_{ns}, \tag{4}$$

where:

ε_{ns}—the value of critical longitudinal strain of the intact rock, evaluated by loading the rock sample to a value of around 95% of its compressive strength.

The PN-G-05020 Standard recommends employing the elasto-plasto-fractured model when the following condition is satisfied [17]:

$$u_w > r_w \cdot \varepsilon_{ng}, \tag{5}$$

where:

u_w—value of ground displacement, m,
r_w—excavation radius, m.

Similarly, the PN-G-05600 Standard advises using the elasto-plasto-fractured model under the condition outlined as follows [16]:

$$0 < p_o \leq p_g \tag{6}$$

where:

p_g—radial stress on the boundary of plastic and elastic zone, MPa,

p_o—radial stress on the boundary of fractured and plastic zone, MPa.

In accordance with the PN-G-05600 Standard, the dimensioning of the so-called shell lining (comprising a thin layer of shotcrete with supplementary steel arches and rockbolts) is based solely on the value of the static roof pressure. Deformational pressure can be disregarded since the entire displacement of the rock mass must be transferred by the supporting structure. Therefore, the following condition must be satisfied [16]:

$$u^{ob} \geq k \cdot u_w \tag{7}$$

where:

u^{ob}—radial deformability of the support, m.

To incorporate a portion of the displacement of the rock mass that occurs before support installation, a coefficient k is introduced into Formula (7). This introduction can be viewed as an attempt to crudely include the three-dimensional effect of road excavation in an otherwise two-dimensional analysis. The PN-G-05600 standard assumes a fixed value of the k factor, set at 0.9. However, the authors of this article regard such an assumption as oversimplified, as it may lead to either overestimation or underestimation of the required deformability of the roadway support. The actual value of the k coefficient depends on numerous factors, including the rock mass and support properties, as well as the distance between the location of the support installation and the excavation face [8,9,12,19]. This topic has been extensively discussed in [20].

The dimensioning of the so-called vaulted lining (constructed of brick or a thick layer of unreinforced or reinforced concrete) according to the PN-G-05020 Standard should be carried out while considering the following load combinations [17]:

- simultaneous loading of the lining's self-weight and the static pressure of the rock mass,
- simultaneous loading of the lining's self-weight and the deformational pressure of the rock mass,
- simultaneous load of the lining's self-weight and the injection pressure.

Since the PN-G-05020 standard does not provide suitable formulas, the influence of deformational pressure on the vaulted lining is sometimes overlooked by engineers [21]. This practice may be justified due to the utilization of a yieldable primary lining, which is capable of accommodating the entirety of the initial displacement of the rock mass (associated with the advancement of the excavation face). According to the recommendation outlined in the Polish Standard, secondary support can only be constructed once an equilibrium state is reached between the primary layer and the rock mass [17]. Therefore, if a primary lining with appropriate deformability is installed beforehand, the deformational pressure acting on the secondary lining should be eliminated or significantly reduced.

In summary, according to Polish National Standards, the primary lining of an underground roadway or chamber must always be designed as a yieldable structure in order to eliminate the occurrence of deformational pressure. This assumption accounts for a significant weakness of the discussed solution. Determining the value of the deformational pressure acting on the support of limited deformability (for which condition (7) is not met) is not possible using the equations provided by Polish Standards only. Additionally, it must be noted that in engineering practice, the geotechnical properties of rock masses are never constant, as they may be reduced due to mining activities, rock delamination, water inflow, and contact with the mine's atmosphere [10]. Therefore, in many cases, the use of shell support with limited deformability, which allows for the rapid suppression of rock mass displacement, may be highly desirable. This solution is widely employed in the worldwide tunneling industry, constituting one of the basic principles of the new Austrian tunneling method [22].

3. Theoretical Background for the Convergence Confinement Method

The convergence confinement method (CCM) serves as a straightforward analytical tool capable of estimating the deformational load acting on an excavation support. Initially, the CCM method was based on the stress state solution of anelastic disc of a uniform thickness proposed by Kirsch [23]. Over subsequent years, the method underwent further refinement and enhancement, including considerations such as the development of the plastic zone around the excavation [24–28]. Regardless of the specific yield criterion used, these adaptations were based on the fundamental assumption of rock mass continuity [8]. Pacher [29] conducted research on potential disruptions in this continuity, leading to the formulation of the hypothesis that appropriate radial deformability and the timing of support installation are critical factors in ensuring both safety and cost-effectiveness in excavation design.

CCM is a graphical method consisting of three basic components [22,30]:

- Ground reaction curve (GRC)—illustrates the correlation between fictitious support pressure and the radial displacement of the excavation boundary. In essence, fictitious pressure refers to the internal support pressure required to prevent further ground displacement.
- Support characteristics curve (SCC)—depicts the relationship between increases in the radial displacement of the support and the external radial stress applied to the support (deformational pressure).
- Longitudinal displacement profile (LDP)—depicts the correlation between the radial displacement of the excavation boundary and the longitudinal distance from the excavation face.

In comparison to the design method advocated by Polish Standards, the convergence–confinement method is capable of:

- More accurately considering the three-dimensional character of an underground roadway or chamber excavation.
- Considering rigid support systems, which enable the quick suppression of rock mass displacement.
- Considering the correlation between support system stiffness and the value of the excavation boundary displacement.
- Considering the deformational load acting on the designed support system.

4. Algorithm for the Establishment of a Ground Reaction Curve for an Elasto-Plasto-Fractured Rock Mass

An important issue connected with the use of the CCM method is the difficulty in evaluating the real actions of rock masses within inelastic zones [31]. The simplest procedure for determining a GRC curve is based on the model of an elasto-perfectly-plastic medium [2]. Hoek and Brown claim that such a model can only be used for rock masses of low quality (GSI < 30) [32]. Therefore, for a rock mass of medium (30 < GSI < 70) or high (GSI > 70) quality, a number of alternative equations have been introduced over the years, considering such issues as post-failure acting, including rock mass softening, stiffness degradation, and dilatancy [31,33].

The development of a three-phase rock mass model, based on the model of elasto-plasto-fractured medium, was considered an important achievement of Polish mining engineering [18]. This three-phase model was introduced into Polish Standards [14–17] and successfully applied in the design of underground roadways and chambers located at significant depths in the vicinity of low and medium-quality rock masses. The properties of an elasto-plasto-fractured medium may by depicted by polyline (Figure 2) [18]:

- Within the elastic, the zone action of the rock mass is depicted by a straight line inclined by the angle $arctg(E_g)$, where E_g is a rock mass deformation modulus.
- Within the plastic zone a following condition, depicting rock mass action, is met:

$$\frac{R_{cg}}{E_g} < \varepsilon_t < \varepsilon_{ng}, \tag{8}$$

where:

R_{cg}—rock mass compressive strength in the elastic zone, MPa,
E_g—rock mass Young modulus, MPa,
ε_t—longitudinal strain of the rock mass.

- Within the fracture zone a following condition, depicting rock mass action, is met:

$$\varepsilon_t > \varepsilon_{ng}. \tag{9}$$

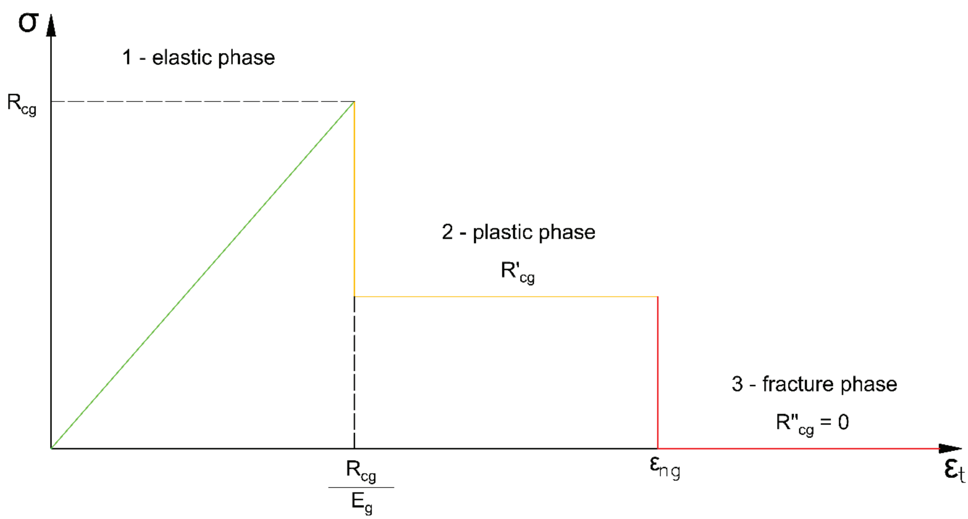

Figure 2. Stress–strain characteristics for a rock mass described by the elasto-plasto-fractured model.

This paper aims to present a guideline for the determination of a ground reaction curve for an elasto-plasto-fractured rock mass model, employed by Polish Standards, which, however, neither incorporate the convergence confinement method of support design nor the concept of the ground reaction curve.

The presented solution of a ground reaction curve for a rock mass described by an elasto-plasto-fractured model is based on the Mohr–Coulomb yield criterion. The compressive strength of the rock mass is determined by the following equation:

$$R_{cg} = \frac{2 \cdot c \cdot cos\phi}{1 - sin\phi} \tag{10}$$

where:

c—cohesive strength of the rock mass, MPa,
ϕ—angle of internal friction of the rock mass, °.

According to the PN-G-05020 Standard, the residual compressive strength of the rock mass is given by the following equation [17]:

$$R'_{cg} = (0.4 \div 0.6) \cdot R_{cg} \tag{11}$$

Alternatively, if the mechanical properties of a rock mass are determined based on the Geological Strength Index (GSI), a residual GSI factor may be applied to estimate the residual compressive strength of the rock mass [34]. Such an approach has been introduced in various tunneling projects worldwide [35–38].

In order to simplify the calculation further, factor β, given by the following equation, shall be introduced:

$$\beta = \frac{2 \cdot sin\phi}{1 - sin\phi} \tag{12}$$

The critical radial stress (or radial stress on the boundary between the elastic and plastic zones) is determined by the following equation:

$$p_g = \frac{2 \cdot p_z - R_{cg}}{2 + \beta} \tag{13}$$

where:

p_z—in situ hydrostatic stress, MPa.

The radial stress on the boundary between the fractured and plastic zones is determined by the following formula:

$$p_o = \frac{p_g \cdot \beta + R'_{cg}}{\beta} \cdot \left[\frac{(1+\nu) \cdot (p_z - p_g)}{E_g \cdot \varepsilon_{ng}} \right]^{\frac{\beta}{2}} - \frac{R'_{cg}}{\beta} \tag{14}$$

where:

ν—rock mass Poisson's ratio.

The value of the ground displacement is a function of the radial stress that needs to be applied to the excavation boundary to prevent further movement (fictitious pressure p_a):

- if $p_a > p_g$, the rock mass acts as an elastic medium;
- if $p_g > p_a > p_o$, the rock mass acts as a plastic medium;
- if $p_a < p_o$, the rock mass acts as a fractured medium.

The value of the ground displacement for an elastic medium is given by the following equation:

$$u(p_a) = \frac{r_w \cdot (1+\nu)}{E_g} \cdot (p_z - p_a) \tag{15}$$

where:

r_w—excavation radius, m.

For a plastic medium, the plastic zone radius r_l (which is a function of the fictitious pressure p_a) must be calculated beforehand:

$$r_l(p_a) = r_w \cdot \left(\frac{p_g \cdot \beta + R'_{cg}}{p_a \cdot \beta + R'_{cg}} \right)^{\frac{1}{\beta}} \tag{16}$$

The fracture zone radius r_a is a function of the fictitious pressure p_a and may be calculated using the following equation:

$$r_a(p_a) = r_w \cdot \left(\frac{p_o}{p_a} \right)^{\frac{1}{\beta}} \tag{17}$$

As shown in Formula (17), with reductions in the fictitious pressure, the radius of the fracture zone tends to infinity. At the equilibrium state, the value of the deformational pressure is equal to the value of the static pressure of the fractured rock mass within the fracture zone. The radius of the fracture zone in the equilibrium state $r_{a_{eq}}$ may be determined based on the equation given by the PN-G-05600 Standard [16]:

$$\left(\frac{r_a}{r_w}\right)^{\beta+1} - \left(\frac{r_a}{r_w}\right)^{\beta} = \frac{p_o}{\gamma_s \cdot r_w} \tag{18}$$

where:

γ_s—average bulk density of the roof rocks, MN/m^3.

The static pressure of the rock mass within the fracture zone for the radius determined from Formula (18) is equal to the value of the deformational pressure at the equilibrium state:

$$p_{a_{min}} = q_{za} = (r_a - r_w)\cdot\gamma_s \tag{19}$$

The radius of the plastic zone developed outside the range of the fracture zone is a function of the fracture zone radius:

$$r_l(r_a) = r_a \cdot \left(\frac{p_g \cdot \beta + R'_{cg}}{p_o \cdot \beta + R'_{cg}}\right)^{\frac{1}{\beta}} \tag{20}$$

The static pressure of the plastic and fractured rock masses within the inelastic zones (both plastic and fracture zone) is a function of the plastic zone radius:

$$q_{zl}(r_l) = (r_l - r_w)\cdot\gamma_s \tag{21}$$

Ultimately, the value of the ground displacement for both plastic and fractured media is a function of the plastic zone radius:

$$u(r_l) = \frac{r_w \cdot (1+\nu)}{E_g} \cdot \left[2\cdot(1-\nu)\cdot(p_z - p_g)\cdot\left(\frac{r_l}{r_w}\right)^2 - (1 - 2\cdot\nu)\cdot(p_z - p_a)\right] \tag{22}$$

Formulas (10) to (22) constitute all the essential relationships for the establishment of a GRC curve for an elasto-plasto-fractured medium. The featured algorithm may be introduced to the calculation sheet for rock masses fulfilling the conditions given by Formulas (5) or (6).

5. Application of the Developed Approach

In order to verify the algorithm featured in Section 4, a series of analyses were performed involving a typical circular roadway of radius r_w = 3 m excavated at a depth of 1000 m, where the in situ hydrostatic stress equaled p_z = 25 MPa. Three cases considering rock mass classes with different mechanical properties were investigated for comparative purposes:

- class I—competent rock mass,
- class II—fair rock mass,
- class III—weak rock mass.

Input parameters for different rock mass classes were selected based on Polish Industrial Standard BN-78/0434-07 [14], which provides guidelines for the crude approximation of basic rock mass parameters such as an internal friction angle, cohesive strength, Young modulus, Poisson's ratio and critical longitudinal strain. These approximations are derived from the uniaxial compressive strength (UCS) of an intact rock and the Rock Quality Designation (RQD) of the rock mass. Input parameters selected for different rock mass class parameters are presented in Table 1.

Table 1. Input parameters for exemplary calculation of GRC curves for different rock mass classes.

Parameter	Symbol	Unit	Rock Mass Class		
			I	II	III
Cohesive strength of the rock mass	c	MPa	6.39	5.18	2.65
Internal friction angle of the rock mass	ϕ	^{0}	38.67	33.73	29.30
Rock mass Young modulus	E	MPa	7667	5409	3338
Rock mass Poisson's ratio	ν	-	0.20	0.20	0.20
Critical longitudinal strain of the rock mass	ε_{ng}	-	0.0046	0.0051	0.0054

The GRC curves for different rock mass classes were calculated based on the elasto-plastic-fractured model of the rock mass and the procedure featured in Section 4. The calculation results of basic GRC curves parameters are presented in Table 2.

Table 2. Calculation results of basic GRC parameters for elasto-plasto-fractured model for different rock mass classes.

Parameter	Symbol	Unit	Rock Mass Class		
			I	II	III
Compressive strength of the rock mass within the elastic zone	R_{cg}	MPa	26.60	19.37	9.05
Compressive strength of the rock mass within the plastic zone	R'_{cg}	MPa	13.30	9.69	4.53
Computational factor	β	-	3.33	2.50	1.92
Radial stress on the boundary between plastic and elastic zone	p_g	MPa	4.39	6.81	10.45
Radial stress on the boundary between fracture and plastic zone	p_o	MPa	0.65	4.10	10.03
Deformational pressure at the equilibrium state	$p_{a_{eq}}$	MPa	0.071	0.284	0.354
Fracture zone radius at the equilibrium state	$r_{a_{eq}}$	m	5.83	10.39	17.17
Plastic zone radius at the equilibrium state	$r_{l_{eq}}$	m	6.96	11.68	17.47
Rock mass displacement at the equilibrium state	$u\left(p_{a_{eq}}\right)$	m	0.076	0.217	0.833

The results of the GRC calculations based on the proposed elasto-plasto-fractured model were compared with the typical elasto-plastic solution for the displacement of a circular roadway. GRC curves obtained for both the elasto-plasto-fractured and elasto-plastic model for different rock mass classes are depicted on Figures 3–5.

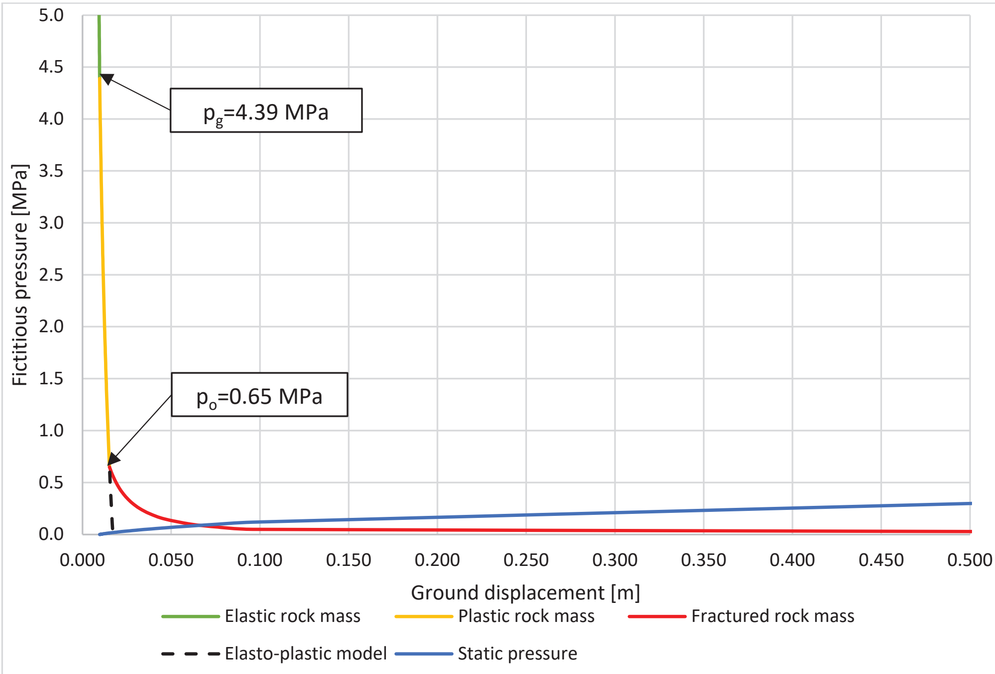

Figure 3. GRC curves for the competent rock mass (class I).

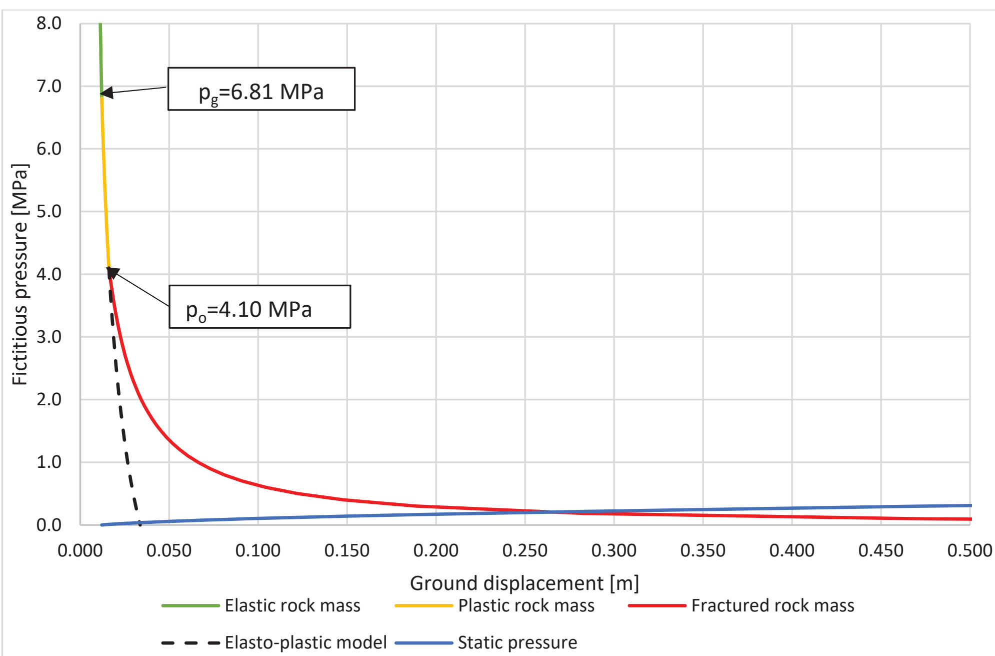

Figure 4. GRC curves for the fair rock mass (class II).

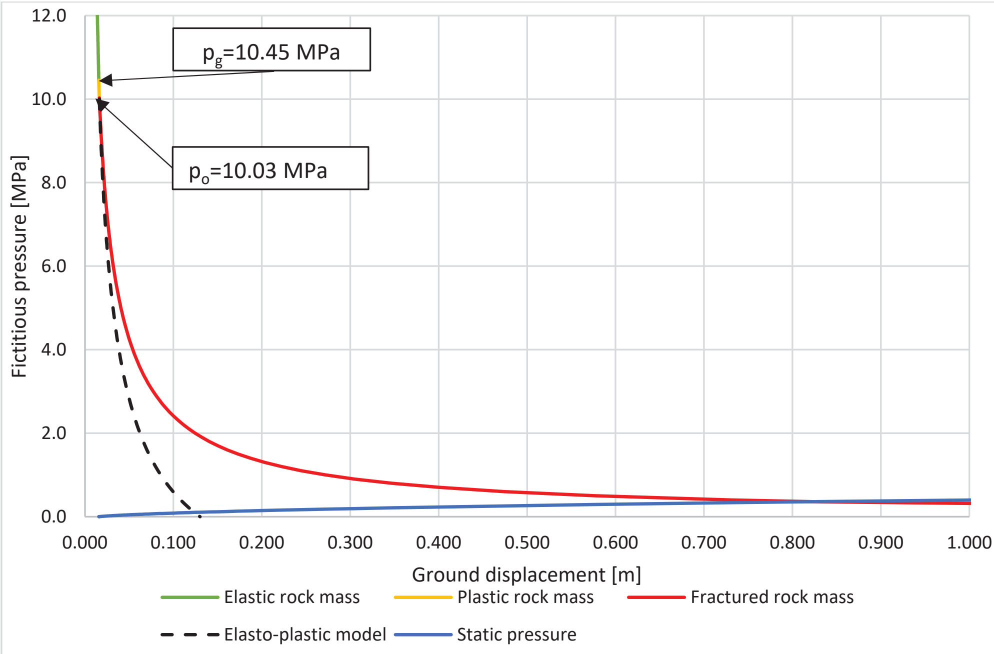

Figure 5. GRC curves for the weak rock mass (class III).

The analysis of Figures 3–5 highlights the importance of the proper selection of the rock mass model used in geotechnical calculations. The initial portions of the GRC curves for both the elasto-plasto-fractured model and the elasto-plastic model were identical. According to the elasto-plasto-fractured model, once the fictitious pressure reached the theoretical value of the radial stress at the boundary between the fracture and plastic zone p_o (which is dependent on the value of the critical longitudinal strain of the rock mass ε_{ng}), a fracture zone began to develop in the vicinity of the roadway. Since the rock mass within the fracture zone lacked cohesion (and thus compressive strength), a portion of the GRC curve associated with the fractured rock mass exhibited a rapid displacement increase.

Along with the decrease in rock mass strength, a simultaneous increase was observed in both the displacement of the rock mass and the values of deformational pressure occurring at the equilibrium state between the static and deformational pressures. In practice, the roadway support has to be installed before reaching an equilibrium point—especially in the case of fair and weak rock mass. Otherwise, excess displacement may lead to the dissipation of rock mass confinement, thereby allowing detrimental loosening and ultimately ground failure.

Figure 6 illustrates the comparison of GRC (ground reaction curve) plots derived from the elasto-plasto-fractured model for different rock mass classes.

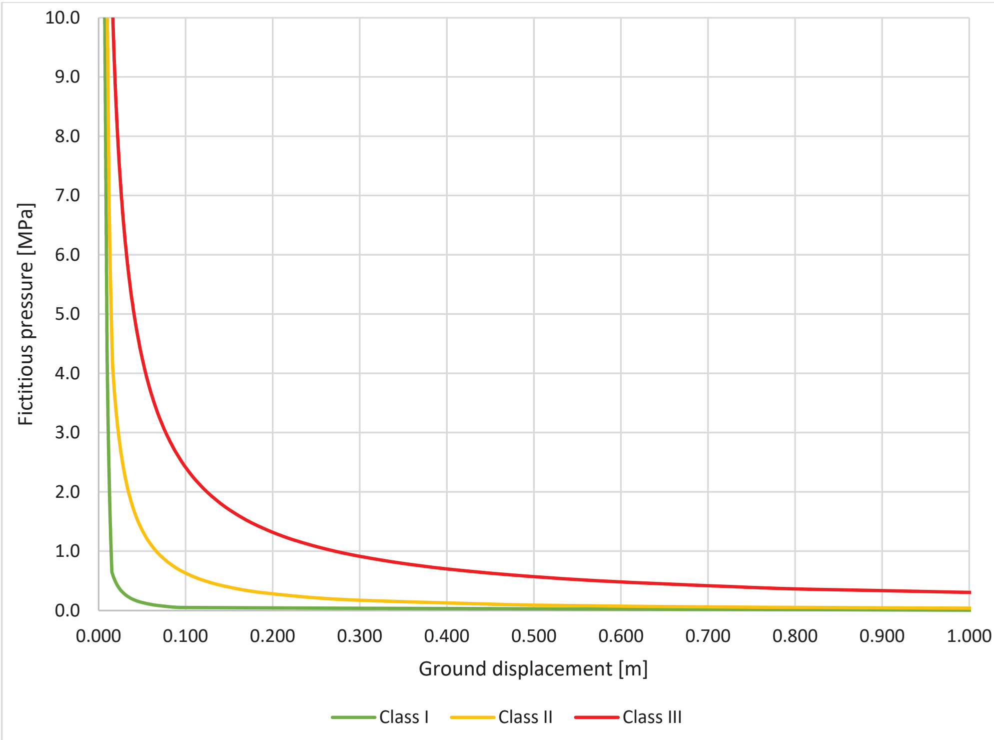

Figure 6. Comparison of GRC curves for different rock mass classes.

It is evident that with decreases in the mechanical parameters of the rock mass, there was an increase in rock mass displacement observed at consistent values of fictitious pressure. Regardless of the rock mass class under consideration, along with the reduction in fictitious pressure, the radius of the fracture and the plastic zones—and thereby the value of the displacement—tended to infinity, thereby indicating the need for support installation. This feature of the GRC curve based on the elasto-plasto-fractured model distinguishes it from a typical elasto-plastic GRC curve. In the latter, there is always a theoretical equilibrium point where the fictitious pressure equals zero, while the radius of the plastic zone and the value of ground displacement reach their maximum value (in most cases, in practical applications, before such an equilibrium point is reached, excessive displacements may lead to detrimental loosening and ground failure).

In the subsequent stage of the analysis, in order to determine the optimal moment for the installation of the support, longitudinal deformation profiles (LDP) were established for different rock mass classes. The determination of the LDP curve followed the algorithm outlined in [8].

Considering that for the rock mass model based on an elasto-plasto-fractured medium, the plastic zone radius and the value of the ground displacement consistently tended towards infinity, a maximum value of these parameters could not be unambiguously determined. Therefore, a plastic zone radius and the value of the ground displacement at the equilibrium point between the static and deformational pressures were adopted for the calculations. Although this assumption was simplified, further exploration into the solution of LDP for elasto-plasto-fractured media seems to be necessary. An exemplary LDP curve based on the solution given by [8] is illustrated in Figure 7.

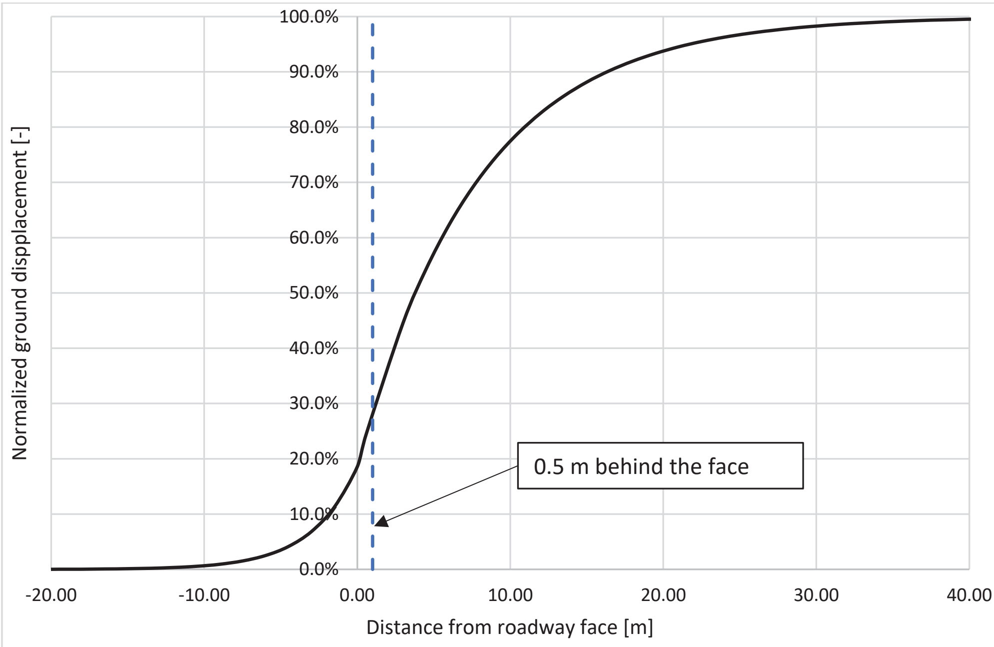

Figure 7. Exemplary LDP curve for a fair rock mass (class II).

The extent of the plastic and fracture zones, as well as the magnitude of rock mass displacement, can be mitigated by the application of an appropriate support system. In Polish underground coal mines, the most prevalent support system for long-lasting roadways and chambers consists of yielding steel arches, sometimes combined with a thin layer of shotcrete.

Since a large amount of support deformation is to be expected, it was assumed that the roadway support system should consist of yielding steel sets fitted with sliding joints. These sets are installed immediately behind the roadway face, ensuring safety for personnel working at the face.

Support characteristics curves (SCC) for yielding steel sets, determined using the algorithm outlined in [39], consist of four parts:

(1) First part involves elastic deformation, where steel arches act as rigid elements.
(2) Second part involves yielding, where overlapped segments of the steel sets start to slide and the arch section diminishes.
(3) Third part once again involves elastic deformation, wherein the maximum yielding capacity of the steel arch is reached, and therefore, it acts again as a rigid element.
(4) Fourth part involves plastic deformation, wherein the bearing capacity of the rigid steel support is reached, and therefore, a certain amount of plastic deformation occurs.

The input parameters and calculation results for SCC curves are shown in Table 3. The resulting SCC curves, in conjunction with GRC curves, obtained for different mass classes are depicted in Figures 7–9.

Table 3. Input parameters and calculation results of the basic parameters of SCC curves for different rock mass classes.

Parameter	Symbol	Unit	Rock Mass Class		
			I	II	III
Cross sectional area of the section	A_s	m^2		0.00452	
Young's modulus of the steel	E_s	MPa		210,000	
Yield strength of the steel	σ_{ys}	MPa		440	
Yielding force of the sliding joint	N_{lim}	MN		0.35	
Maximum sliding length	s_{lim}	m		0.30	
Number of sliding joints in the steel set	n	-		3	
Initial overlapped length	s_0	m		0.6	
Steel set spacing	d	m	1.0	0.6	0.4
Support capacity at 1st part of elastic deformation	p_1	MPa	0.117	0.199	0.307
Maximum support capacity at yielding part	p_2	MPa	0.176	0.299	0.461
Support capacity at 2nd part of elastic deformation	p_3	MPa	0.701	1.192	1.842

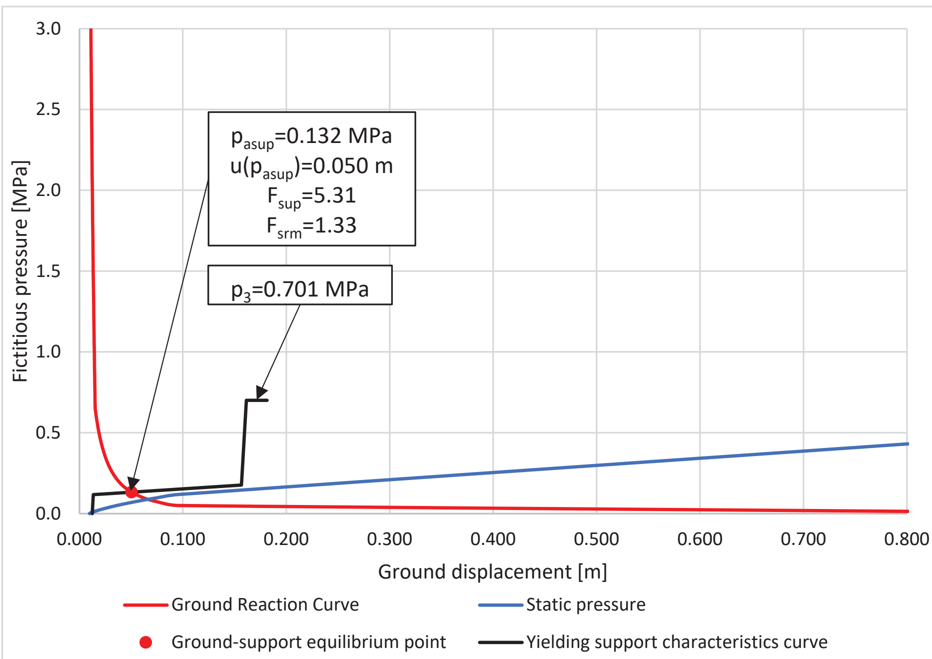

Figure 8. SCC curve coupled with GRC curve for a competent rock mass (class I).

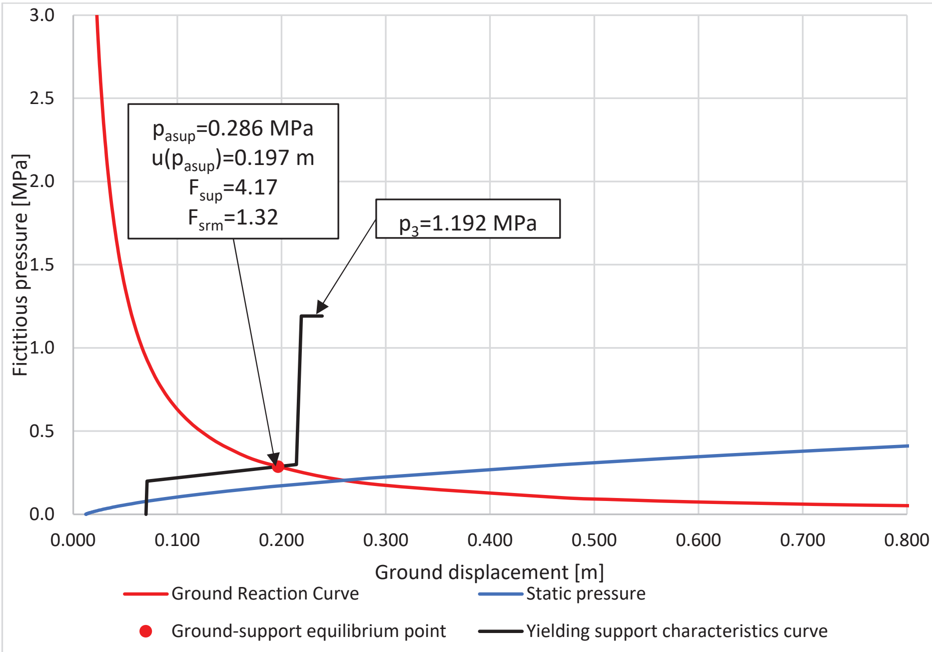

Figure 9. SCC curve coupled with GRC curve for a fair rock mass (class II).

The graphical interpretation of the SCC and GRC curves along with the ground-support equilibrium point included in Figures 8–10 allows for the estimation of the deformational pressure applied to the roadway support (p_{asup}). The factors of safety for both the designed support system (F_{sup}) and the surrounding rock mass, considered as the natural support component (F_{srm}), can be derived from the following equations:

$$F_{sup} = \frac{p_3}{p_{a_{sup}}} \tag{23}$$

$$F_{srm} = \frac{p_{a_{sup}}}{p_{a_{eq}}} \tag{24}$$

In cases of competent and fair rock masses (classes I and II), the ground-support equilibrium point was located on the yielding part of the SCC curve. This is in contrast to weak rock masses, where the ground-support equilibrium point was situated on the 2nd elastic deformation part of the SCC curve. This indicates that the maximum yielding capacity of the support was reached, due to the large value of the ground displacement. Consequently, the steel sets are no longer able to slide, thus acting like a rigid element. As a result, the factor of the safety of the roadway support ($F_{sup} = 2.00$) for a weak rock mass was significantly lower than in case of a fair ($F_{sup} = 4.17$) or competent rock mass ($F_{sup} = 5.31$). Meanwhile the factor of the safety of the surrounding rock mass component was greater in the case of the weak rock mass ($F_{srn} = 2.54$) than in cases of a fair ($F_{srm} = 1.32$) or competent rock mass ($F_{srm} = 1.33$).

In all analyzed cases, the support capacity at the yielding part of the SCC curve exceeded the static load exerted on the steel arches at a certain value of ground displacement. This observation, connected with the calculated values of the factors of safety, suggests that the designed support system effectively ensures roadway stability—thereby mitigating ground failure resulting from the loss of confinement and the eventual collapse of the fractured rock mass.

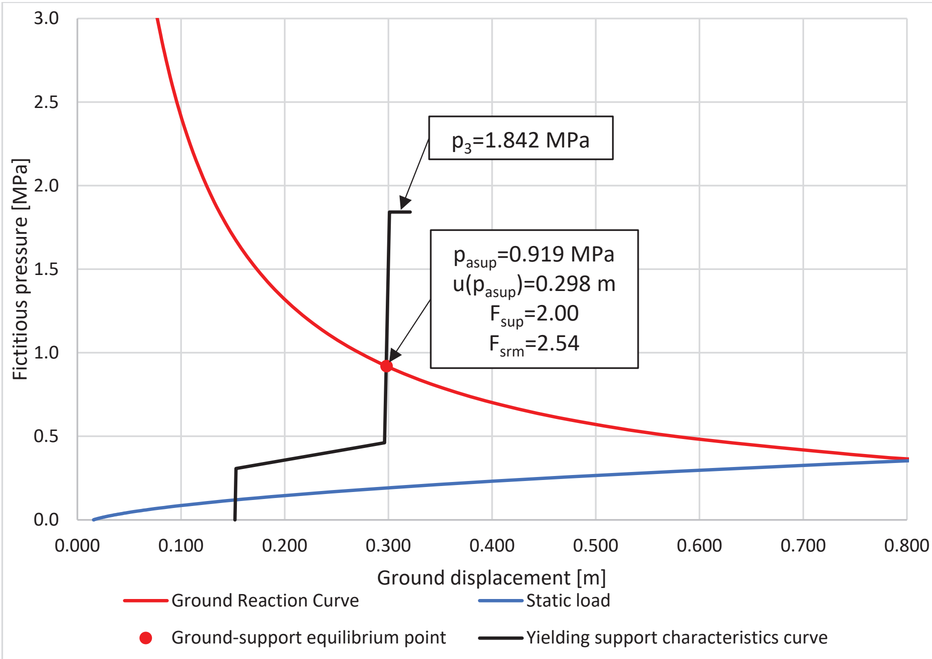

Figure 10. SCC curve coupled with GRC curve for the weak rock mass (class III).

After reaching the equilibrium point between the rock mass and yielding steel support, a more rigid and durable support may be employed, such as a thin layer of shotcrete or a thick layer of in situ-made concrete. Embedding steel sets in shotcrete or concrete may yield some additional advantages:

- creation of a favorable, triaxial state of stress on the roadway boundary,
- protection of steel arches from corrosion,
- shielding the rock mass from the influence of water inflow and the mine's atmosphere.

6. Engineering Application—Ventilating a Roadway in the "Knurów" Coal Mine

The "Knurów" coal mine is located in the western part of the Upper Silesian Coal Basin in Poland. An elasto-plasto-fractured model of the rock mass was employed for the initial support design of a ventilating roadway situated near the "Aniołki" ventilation shaft. This roadway is to be excavated at a depth of 474 m using the conventional "drill and blast" method. The roadway has a horseshoe shape with a maximum height of approximately 6.05 m and a width of approximately 6.09 m, corresponding to a circular geometry with a radius of 3.13 m (Figure 11).

According to the geological survey, the roadway will be excavated in a thick layer of claystone characterized by an uniaxial compressive strength (UCS) of at least 21.98 MPa. Other geotechnical parameters of the rock mass, such as its cohesive strength, internal friction angle, and Young's modulus, were determined using the guidelines provided by the Polish Industrial standard BN-78/0434-07 [14]. The input parameters and basic calculation results of the Ground Reaction Curve (GRC), utilized in the initial design of the roadway support structure, are listed in Table 4.

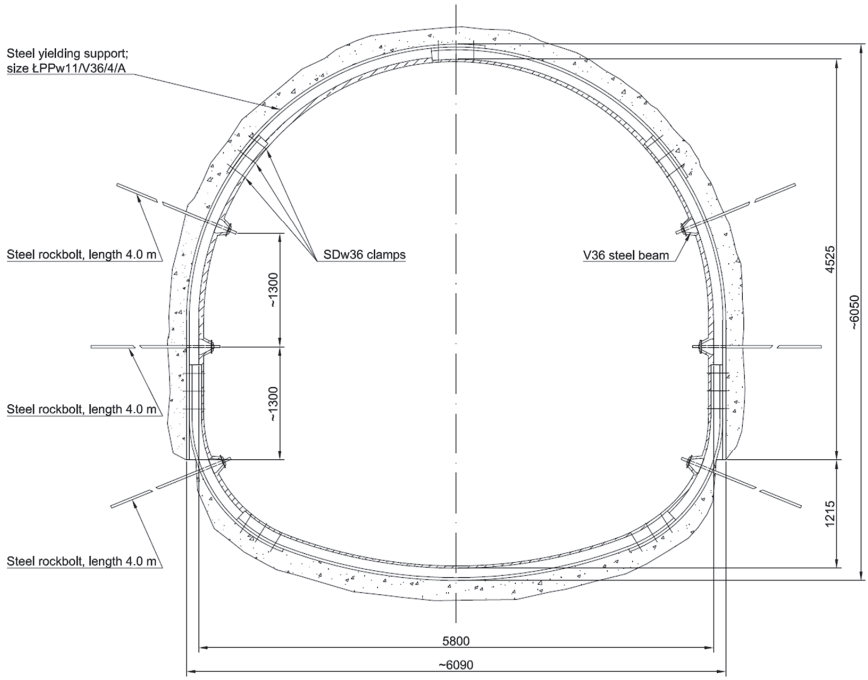

Figure 11. Cross-section of the ventilating roadway in the "Knurów" coal mine.

Table 4. Input parameters for the calculation of the GRC curve for the ventilating roadway in the "Knurów" coal mine.

Parameter	Symbol	Unit	Value
Input Parameters			
Excavation radius	r_w	m	3.13
In situ hydrostatic stress	p_z	MPa	11.39
Cohesive strength of the rock mass	c	MPa	2.65
Internal friction angle of the rock mass	ϕ	°	29.30
Rock mass Young's modulus	E	MPa	3347.83
Rock mass Poisson's ratio	ν	-	0.24
Critical longitudinal strain of the rock mass	ε_{ng}	-	0.0054
Results			
Compressive strength of the rock mass within the elastic zone	R_{cg}	MPa	9.05
Compressive strength of the rock mass within the plastic zone	R'_{cg}	MPa	3.62
Computational factor	β	-	1.92
Radial stress on the boundary between plastic and elastic zone	p_g	MPa	3.504
Radial stress on the boundary between fracture and plastic zone	p_o	MPa	1.103
Deformational pressure at the equilibrium state	$p_{a_{eq}}$	MPa	0.143
Fracture zone radius at the equilibrium state	$r_{a_{eq}}$	m	9.09
Plastic zone radius at the equilibrium state	$r_{l_{eq}}$	m	12.35
Rock mass displacement at the equilibrium state	$u\left(p_{a_{eq}}\right)$	m	0.210

The support structure of the roadway under consideration consists of yielding steel arches made from V36 profiles, spaced 0.50 m apart. After reaching an equilibrium point between the rock mass and steel yielding support, additional steel arches shall be embedded in fiber-reinforced shotcrete (Figure 12). The input parameters and basic calculation results of SCC curve for the designed support structure are listed in Table 5.

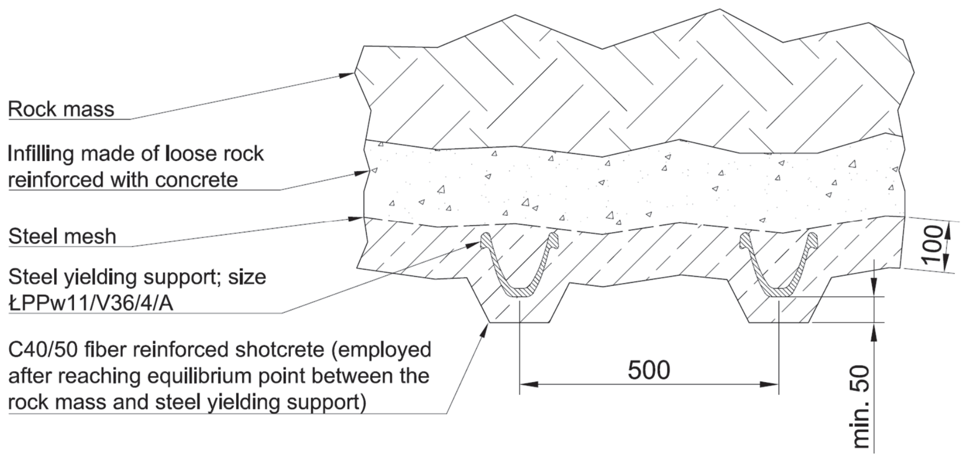

Figure 12. Support scheme of the ventilating roadway in the "Knurów" coal mine.

Table 5. Input parameters and calculation results of the basic parameters of the SCC curve for the ventilating roadway in the "Knurów" coal mine.

Parameter	**Symbol**	**Unit**	**Value**
Input Parameters			
Cross sectional area of the section	A_s	m^2	0.00452
Young's modulus of the steel	E_s	MPa	210,000
Yield strength of the steel	σ_{ys}	MPa	440
Yielding force of the sliding joint	N_{lim}	MN	0.35
Maximum sliding length	s_{lim}	m	0.15
Number of sliding joints in the steel set	n	-	7
Initial overlapped length	s_0	m	0.60
Steel set spacing	d	m	0.50
Results			
Support capacity at 1st part of elastic deformation	p_1	MPa	0.227
Maximum support capacity at yielding part	p_2	MPa	0.299
Support capacity at 2nd part of elastic deformation	p_3	MPa	1.364

The SCC curve coupled with the GRC curve calculated for the geological conditions of the ventilation roadway in the "Knurów" coal mine is depicted in Figure 13.

As a result of the application of the convergence–confinement method and the employment of the elasto-plasto-fractured rock mass model, the initial choice of the support scheme—consisting of yielding steel arches made from V36 profiles with a spacing of 0.50 m—was confirmed to be correct. The factors of safety for the roadway support ($F_{sup} = 5.39$) and the rock mass ($F_{srm} = 1.78$) indicate that the designed support structure can be successfully employed in a ventilation roadway under the given geological conditions.

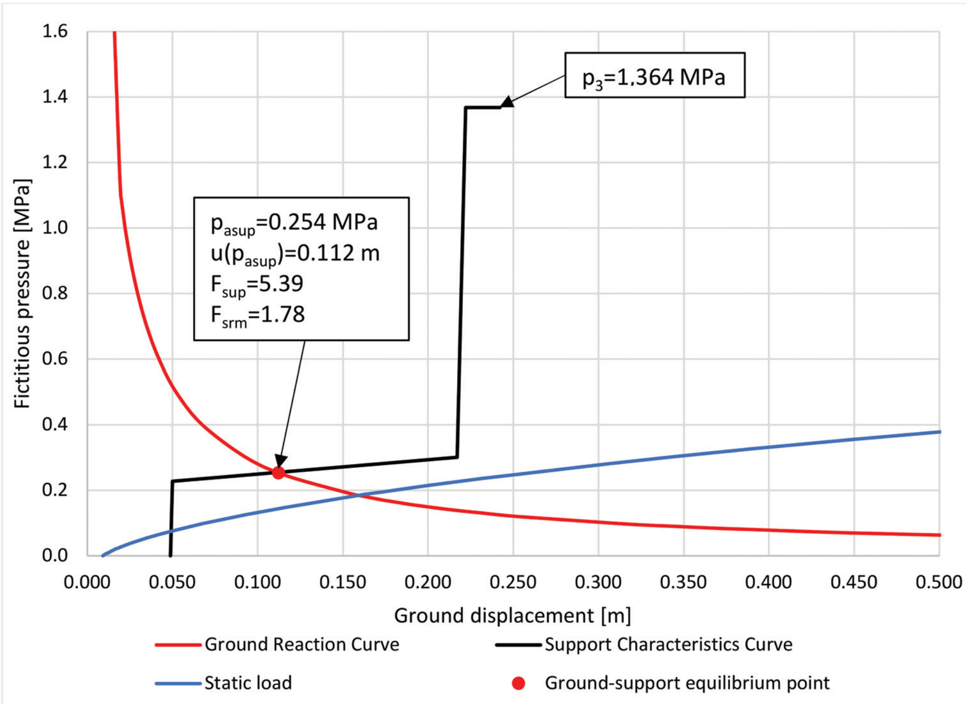

Figure 13. SCC curve coupled with the GRC curve for the ventilation roadway in the "Knurów" coal mine.

7. Conclusions

Based on the conducted study, the following conclusions can be inferred:

(1) Polish National and Industrial Standards introduced the deformational pressure model for calculating loads acting on the support systems of underground excavations located at significant depths. These Standards distinguish between the softening elasto-plastic and elasto-plasto-fractured models. The choice of the appropriate rock mass model is contingent upon the value of the critical longitudinal strain of the rock mass, which marks the point at which the rock mass transitions from a plastic to a fractured medium. Since Equation (4), provided by the National Standards to calculate the value of the critical longitudinal strain of the rock mass, is not supported by any empirical studies, further investigation on this topic may be necessary.

(2) The three-phase rock mass model outlined in the Polish National and Industrial Standards is based on the assumption that under certain conditions, a rock mass may act as an elasto-plasto-fractured medium. In this scenario, two coaxial inelastic zones form around the excavation: a fracture zone, where the rock mass lacks cohesion and therefore is devoid of its compressive strength, and a plastic zone, where the rock mass can retain its residual compressive strength. For an elasto-plasto-fractured model of the rock mass, the support pressure value increases after reaching a certain ground displacement threshold, which appears to align with engineering practice.

(3) The convergence–confinement method (CCM) is a widely recognized, straightforward analytical tool for predicting the ground action and support design of underground roadways, chambers, and tunnels. Compared to the method outlined in Polish National Standards, it can more accurately capture the three-dimensional nature of underground excavations. Furthermore, it facilitates the design of a rigid support system, unlike the

method prescribed by Polish Standards, which requires the support system to be able to transfer the entirety of the predicted rock mass displacement.

(4) In Section 4 of this paper, a method for the establishment of the ground reaction curve for an elasto-plasto-fractured rock mass model was presented; this detailed equations for determining the value of ground displacement and the radii of the plastic and fracture zones, which are dependent on the value of fictitious pressure. These formulations provide a basis for establishing the ground reaction curve and can be applied in practical engineering calculations.

(5) In Section 5 of this paper, a series of analyses were conducted on a typical circular roadway to verify the algorithm proposed in Section 4. Three rock mass classes with different mechanical properties were considered. Ground reaction curves for each rock mass class were calculated based on the elasto-plasto-fractured model. These curves were compared with the GRC curves obtained for the typical elasto-plastic model. The elasto-plasto-fractured model showed distinct action compared to the elasto-plastic model—most importantly in terms of displacement increments.

(6) In the second part of the analyses conducted for the various rock mass classes, exemplar calculations of a support system were performed. Yielding steel arches were considered as the primary support system due to the expected large deformations. Support characteristics curves were determined for different rock mass classes, taking into account the action of the yielding steel sets. Based on ground-support equilibrium points, the factors of safety for the designed support system and the surrounding rock mass were calculated, indicating the correct choice of support parameters. Additionally, a real engineering case of a ventilation roadway in the "Knurów" coal mine was introduced. The engineering calculations, based on the convergence–confinement method and elasto-plasto-fractured model of the rock mass, indicated that the designed support structure can be successfully employed in the roadway under the given geological conditions.

Author Contributions: Conceptualization, P.D. and P.K., Methodology, P.D., A.O. and A.D., formal analysis, A.O. and L.M., Project Administration, A.D. and K.S., Supervision, P.K., Validation, L.M. and P.K., Writing—original draft, A.O., P.D. and P.K., Writing—review and editing, L.M., A.D. and K.S. All authors have read and agreed to the published version of the manuscript.

Funding: This research was funded by KOMAG Institute of Mining Technology and Mineral and Energy Economy Research Institute, Polish Academy of Sciences.

Institutional Review Board Statement: Not applicable.

Informed Consent Statement: Not applicable.

Data Availability Statement: The data presented in this study are available on request from the corresponding author. The data are not publicly available due to privacy.

Conflicts of Interest: Authors Aleksandra Otto and Piotr Dawidziuk was employed by the company Przedsiębiorstwo Budowy Szybów SA. The remaining authors declare that the research was conducted in the absence of any commercial or financial relationships that could be construed as a potential conflict of interest.

References

1. Gałczyński, S. Geotechnika górnicza. In *Ćwiczenia Projektowe z Mechaniki Górotworu*; Wydawnictwa Politechniki Wrocławskiej: Wrocław, Poland, 1970.
2. Hoek, E. *Practical Rock Engineering [e-Book]*; Rocscience Inc.: Vancouver, BC, Canada, 2007. Available online: https://www.rocscience.com/learning/hoeks-corner (accessed on 26 February 2024).
3. Barla, G.; Bonini, M.; Debernardi, D. Time Dependent Deformations in Squeezing Tunnels. *Int. J. Geoeng. Case Hist.* **2010**, *2*, 40–65. [CrossRef]
4. Chudek, M.; Głuch, P.; Szczepaniak, Z. *Projektowanie i Wykonywanie Wyrobisk Komorowych*, 2nd ed.; Wydawnictwo Politechniki Śląskiej: Gliwice, Poland, 1991.
5. Paraskevopoulou, C. Time-dependent behaviour of rock materials. In *Engineering Geology*; Lwisa, E., Arman, H., Eds.; IntechOpen: Rijeka, Croatia, 2021. [CrossRef]

6. Paraskevopoulou, C.; Diederichs, M.S. Long-term behaviour in tunnelling: Limitations in using creep parameters. In Proceedings of the 66th Canadian Geotechnical Conference, GeoMontreal on Geoscience for Sustainability, Montreal, QC, Canada, 29 September–3 October 2013.
7. Schubert, W.; Button, E.A.; Sellner, P.J.; Solak, T. Analysis of time dependent displacements of tunnels. *Felsbau* **2003**, *21*, 96–103.
8. Vlachopoulos, N.; Diederichs, M.S. Improved Longitudinal Displacement Profiles for Convergence Confinement Analysis of Deep Tunnels. *Rock. Mech. Rock. Eng.* **2009**, *42*, 131–146. [CrossRef]
9. Vlachopoulos, N.; Su, Y. Longitudinal Displacement Profiles for Convergence-Confinement Analysis of Excavations: Applicability to Tunnelling, Limitations and Current Advancements. In Proceedings of the 72st Annual Conference of the Canadian Geotechnical Society, St John's, NL, Canada, 29 September–2 October 2019.
10. Chudek, M.; Mateja, J.; Rułka, K. Podstawy teoretyczne oraz nowe zasady doboru, ustalenia obciążeń i wymiarowania obudów długotrwałych wyrobisk korytarzowych i komorowych. *Zesz. Nauk. Politech. Śląskiej* **1985**, *761*, 1–178.
11. Duży, S. Studium niezawodności konstrukcji obudowy i stateczności wyrobisk korytarzowych w kopalniach węgla kamiennego z uwzględnieniem niepewności informacji. *Zesz. Nauk. Politech. Śląskiej* **2007**, *1750*, 1–221.
12. Oke, J.; Vlachopoulos, N.; Diederichs, M.S. Improvement to the Convergence-Confinement Method: Inclusion of Support Installation Proximity and Stiffness. *Rock. Mech. Rock. Eng.* **2018**, *51*, 1495–1519. [CrossRef]
13. Su, Y.; Su, Y.; Zhao, M.; Vlachopoulos, N. Tunnel Stability Analysis in Weak Rocks Using the Convergence Confinement Method. *Rock. Mech. Rock. Eng.* **2021**, *54*, 559–592. [CrossRef]
14. *BN-78/0434-07*; Wyrobiska Korytarzowe i Komorowe w Kopalniach. Obudowa Powłokowa. Wytyczne Projektowania i Obliczeń Statycznych. Główne Biuro Studiów i Projektów Górniczych: Katowice, Poland, 1978.
15. *BN-79/0434-04*; Wyrobiska Korytarzowe i Komorowe w Kopalniach. Obudowa Sklepiona. Wytyczne Projektowania i Obliczeń Statycznych. Główne Biuro Studiów i Projektów Górniczych: Katowice, Poland, 1979.
16. *PN-G-05600:1998*; Podziemne Wyrobiska Korytarzowe i Komorowe. Obudowa Powłokowa. Zasady Projektowania i Obliczeń Statycznych. Polski Komitet Normalizacyjny: Warszawa, Poland, 1998.
17. *PN-G-05020:1997*; Podziemne Wyrobiska Korytarzowe i Komorowe. Obudowa Sklepiona. Zasady Projektowania i Obliczeń Statycznych. Polski Komitet Normalizacyjny: Warszawa, Poland, 1997.
18. Wichur, A. Zagadnienia projektowania obudowy długotrwałych wyrobisk podziemnych. *Górnictwo i Geoinżynieria* **2009**, *33*, 407–436.
19. Wichur, A.; Bajorek, M.; Frydrych, K. Metoda sprawdzania podatności obudowy powłokowej. *Górnictwo i Geoinżynieria* **2007**, *31*, 459–468.
20. Dawidziuk, P.; Otto, A.; Kamiński, P.; Małkowski, P. Zastosowanie metody sterowania konwergencją do projektowania obudowy wyrobisk kapitalnych w kopalniach podziemnych na przykładzie kopalń JSW S.A. *Przegląd Górniczy* **2022**, *77*, 29–43.
21. Wichur, A.; Domańska, D.; Frydrych, K.; Bugiel, A.; Oślizło, K.; Franiel, J. Budowa wlotu w szybie VI JSW S.A. KWK "Budryk"" poz. 1290. In Proceedings of the XXV Mineral Resources & Energy Congress (SEP), Kraków, Poland, 26–28 February 2016.
22. Tajduś, A.; Cała, M.; Tajduś, K. Geomechanika w budownictwie podziemnym. In *Projektowanie i Budowa Tuneli*; Wydawnictwo AGH: Kraków, Poland, 2012.
23. Kirsch, G. Die Theorie der Elastizität und die Bedürfnisse der Festigkeitslehre. *Zeitshrift Des Vereines Dtsch. Ingenieure* **1898**, *42*, 797–807.
24. Carranza-Torres, C.; Fairhurst, C. Application of the Convergence-Confinement Method of Tunnel Design to Rock Masses that Satisfy The Hoek-Brown Failure Criterion. *Tunn. Undergr. Space Technol.* **2000**, *15*, 187–213. [CrossRef]
25. Duncan Fama, M.E. Numerical modelling of yield zones in weak rock. In *Comprehensive Rock Engineering: Principles, Practice and Projects. Analysis and Design Methods*; Fairhurst, C., Ed.; Pergamon Press: Oxford, UK, 1995; pp. 49–75.
26. Fenner, R. Untersuchungen zur Erkenntnis des Gehirndruckes. *Glückauf. Berg-Und Hüttenmännische Z.* **1938**, *74*, 681–695.
27. Panet, M.; Guenot, A. Analysis of convergence behind the face of a tunnel. In Proceedings of the International Symposium Tunnelling, Brighton, VIC, Australia, 7–11 June 1982.
28. Brown, E.; Bray, J.; Landayi, B.; Hoek, E. Ground response curves for rock tunnels. *J. Geotech. Eng.* **1983**, *109*, 15–39. [CrossRef]
29. Pacher, F. Deformationsmessungen im Versuchsstollen als Mittel zur Erforschung des Gebirgsverhaltens und zur Bemessung des Ausbaus. *Felsmech. u Ing. Geol.* **1964**, *1*, 149–161.
30. Chang, L.; Alejano, L.R.; Cui, L.; Sheng, Q.; Xie, M. Limitation of convergence-confinement method on three-dimensional tunnelling effect. *Sci. Rep.* **2023**, *13*, 1988. [CrossRef]
31. Alejano, L.R. Why the convergence confinement method is not much used in practice. In *Rock Mechanics in Civil and Environmental Engineering*; Zhao, J., Labiouse, V., Dudt, J.P., Mathier, J.F., Eds.; CRC Press: London, UK, 2010; pp. 347–350. [CrossRef]
32. Hoek, E.; Brown, E.T. Practical estimates of rock mass strength. *Int. J. Rock Mech. Min. Sci.* **1997**, *34*, 1165–1186. [CrossRef]
33. Molladavoodi, H. Ground Response Curve (GRC) and Excavation Damage Zone Based on an Isotropic Damage Model. In *Constitutive Modeling of Geomaterials*; Yang, Q., Zhang, J.M., Zheng, H., Yao, Y., Eds.; Springer: Berlin, Germany, 2013; pp. 741–750. [CrossRef]
34. Cai, M.; Kaiser, P.K.; Tasaka, Y.; Minami, M. Determination of residual strength parameters of jointed rock masses using the GSI system. *Int. J. Rock Mech. Min. Sci.* **2007**, *44*, 247–265. [CrossRef]
35. Gkikas, V.I.; Nomikos, P.P. Primary Support Design for Sequentially Excavated Tunnel Junctions in Strain-Softening Hoek–Brown Rock Mass. *Geotech. Geol. Eng.* **2021**, *39*, 1997–2018. [CrossRef]

36. Karki, S.; Karki, B.; Chhushyabaga, B.; Khadka, S.S. Design and Analysis of Squeezing Ground Hydropower Tunnel in the Himalaya through a Case Study. *Lowl. Technol. Int.* **2020**, *21*, 268–278.
37. Marini, D.; Zurlo, R.; Rivoltini, M.; Pizzarotti, E.M. Brenner Base Tunnel, Italian Side: Mining methods stretches—Design procedures. In *Tunnels and Underground Cities. Engineering and Innovation Meet Archaeology, Architecture and Art. Volume 7: Long And Deep Tunnels*; Peila, D., Viggiani, G., Celestino, T., Eds.; CRC Press: London, UK, 2020. [CrossRef]
38. Sebbeh-Newton, S.; Shehu, S.A.; Ayawah, P.; Kaba, A.A.; Zabidi, H. Analytical and numerical assessment of a preliminary support design—A case study. *Cogent Eng.* **2021**, *8*, 1869367. [CrossRef]
39. Rodríguez, R.; Díaz-Aguado, M.B. Deduction and use of an analytical expression for the characteristic curve of a support based on yielding steel ribs. *Tunn. Undergr. Space Technol.* **2013**, *33*, 159–170. [CrossRef]

applied sciences

MDPI

Article

Floor Heave Control in Gob-Side Entry Retaining by Pillarless Coal Mining with Anti-Shear Pile Technology

Ivan Sakhno [1,*], Svitlana Sakhno [1], Krzysztof Skrzypkowski [2,*], Oleksandr Isaienkov [1], Krzysztof Zagórski [2] and Anna Zagórska [3]

[1] Faculty of Mining, Donetsk National Technical University, Sofia Kovalevska Street 29, 43012 Lutsk, Ukraine; svitlana.sakhno@donntu.edu.ua (S.S.); oleksandr.isaienkov@donntu.edu.ua (O.I.)
[2] Faculty of Civil Engineering and Resource Management, AGH University of Krakow, Mickiewicza 30 Av., 30-059 Krakow, Poland; zagkrzys@agh.edu.pl
[3] Research Centre in Kraków, Institute of Geological Sciences, Polish Academy of Science, Senacka 1, 31-002 Kraków, Poland; a.zagorska@ingpan.krakow.pl
* Correspondence: ivan.sakhno@donntu.edu.ua (I.S.); skrzypko@agh.edu.pl (K.S.)

Abstract: The severe floor heave in gob-side entry retaining is the major restriction factor of the wide application of pillarless mining thin coal seams. Reinforcement and stress-relief floor heave control methods are the most promising. However, in practice, floor restoration is widely used. Therefore, floor heave control technology in gob-side entry retaining needs to be improved. This study proposes anti-shear pile technology to control floor heave in gob-side entry retaining. The research was mainly carried out by numerical simulation. It was found that the transformation of high vertical stresses in the entry floor underneath the filling wall and coal seam body into horizontal stresses starts the floor heave process. The vertical dilatancy of rocks under the roadway span and their subsequent unloading lead to the delamination of the floor strata and uplift of the entry contour. In this paper, the best pile installation scheme was found. It is a 2pile 5+2 scheme with the installation of two piles, each 2 m long. After that, it was shown that filling piles are more than 3.3 times cheaper than comparable analogs, and pile installation is less labor-intensive. The implementation of the proposed floor heave control method leads to a reduction in heaving by 2.47 times.

Keywords: gob-side entry retaining; pillarless mining; floor heave control; mine roadway stability; thin coal seam mining; steel pile; filling pile; anti-shear pile technology

Citation: Sakhno, I.; Sakhno, S.; Skrzypkowski, K.; Isaienkov, O.; Zagórski, K.; Zagórska, A. Floor Heave Control in Gob-Side Entry Retaining by Pillarless Coal Mining with Anti-Shear Pile Technology. *Appl. Sci.* **2024**, *14*, 4992. https://doi.org/10.3390/app14124992

Academic Editors: Andrea Carpinteri and Paulo Santos

Received: 5 April 2024
Revised: 24 May 2024
Accepted: 5 June 2024
Published: 7 June 2024

1. Introduction

Nowadays, coal provides about a quarter of the world's energy generation. The transition to renewable energy sources is inevitable. However, in reality, the pace of this transition turned out to be slower than expected. The European energy crisis that was caused by the war in Ukraine has shown that in the near future, abandoning coal as an important source of energy is not possible. At the same time, certain types of coal are important raw materials for the metallurgical and chemical industries. Therefore, coal mining will be quite relevant in the near future.

To reduce the negative impact of mining on the environment, governments of various coal-mining countries are introducing increasingly stringent restrictions and environmental regulations. Also, every year, safety requirements in mining become more and more stringent. This leads to an increase in the cost of coal, which stimulates the search and implementation of new technological solutions.

A major part of the world's underground coal is mined from longwall. The US, China, Australia, Poland, and Ukraine use the longwall method. The modern trend in longwall mining is the pillarless mining technology. Its advantages are the following:

- Reduced expenses to mine roadway excavation and, therefore, reduced coal cost;
- An increase in the pace of longwall panel preparation;

- Improvement of the coal recovery ratio;
- Application of effective Y-shaped ventilation systems in the panel, which allows longwall production to be increased by the ventilation factor.

The pillarless method has been known for over 70 years. Experience in its application has been gained in traditional coal-mining countries. Scholars from Germany and Great Britain have made a great scientific contribution to the development of this method [1,2]. Most progress was achieved through the implementation of goaf filling technology and the installation of filling walls. In the 1950s–1960s in Germany, quick-setting materials based on phosphogypsum were developed, from which filling walls were constructed. However, pillarless systems were initially applied with an advancing-type layout of longwall in which gateroads were formed as the coal face advanced (Figure 1a). The majority of such methods were used in thin coal seam mining. However, the absence of a pre-prepared panel and the complexity due to simultaneous roadway excavation and longwall mining in the same panel result in a reduction in the pace of coal mining. Therefore, small coal pillar methods have become more widely used (Figure 1b). In the 1970–1980s, traditional wide pillars were reduced from 20 m to 2–3 m and were applied in many coal basins of Europe and China [3,4]. In the 1970s, Ukrainian mines completely abandoned wide pillars. The elaboration of technologies for the creation of new quick-setting materials has ensured a gradual increase in non-pillar method application (Figure 1c) [5]. Many scholars have researched the efficiency of the filling wall body of gob-side entry retaining in fully mechanized longwalls [6–8].

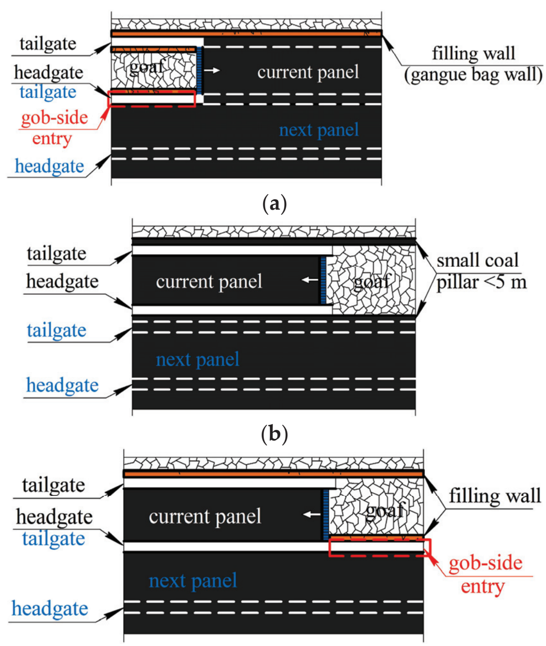

Figure 1. Evolution of thin coal seam longwall mining methods: (**a**)—pillarless method with advancing mining type; (**b**)—small coal pillar method; (**c**)—modern pillarless method.

Additional possibilities for using pillarless methods have appeared in recent years thanks to Chinese scientists. Song and He [9] proposed new pillarless coal-mining technologies. Among them, the N110 construction method is currently the most used pillarless coal-mining technology, which has many advantages [2,10,11]. The essence of this technique is to cut off the connection between the partial roof of the gob and the roof of the roadway by directional roof cutting so that the roof in a certain range above the roadway forms a short-arm beam structure [12].

The widespread application of pillarless coal mining is restricted mainly by the difficulty of ensuring the stability of gob-side entry [13,14]. The problem of gob-side entry retaining stability is aggravated by the constant increase in the mining depth and the natural deterioration of geological conditions. The deformation and failure of the roof and wall sides of the entry in most cases are effectively controlled by a multi-level support system (steel arch, rock bolt, cable bolt), while the entry floor often remains free. Therefore, severe floor heave is an unsolved problem in gob-side entry retaining. Floor heave control will significantly increase the application of progressive pillarless mining technologies.

Many scholars have studied the floor heave mechanism in gob-side entry retaining [15–17]. It can be concluded that failure or plastic flow of the immediate floor, caused by stresses exceeding the strength limit of the rock, is a prerequisite for floor heave [18]. Li et al. [19] pointed out that the key factors of floor heave are changes in the stress–strain state of surrounding rocks after roof failure. This causes an increase in vertical stress in the roadway side walls, which affects the floor strata state. Li et al. 2023 [16] found that the floor is squeezed by the two sides to form an asymmetric sliding force towards the free face of the floor.

Most scientists agree that high horizontal stresses in the immediate floor are one of the main factors that cause severe floor heave. The magnitude of heaving depends on the vertical–horizontal stress ratio [20,21]. Mo et al. [22] proposed the Horizontal Stress Rating (HSR), which represents the magnitude of horizontal stress by statistical analysis on an Australian database. Zhang and Shimada [23] found that variations in the horizontal–vertical stress ratio in the floor strata are the main cause of large floor heave. Gong et al. [15] found that horizontal stress in the immediate floor is the root factor that causes floor heave. Chen et al. [24] proved that squeezing and fluid floor heave play an important role in the stable stage of gob-side entry retaining. Gao et al. [25] defined the main role of shear failure in roadway failure.

Traditional ideas about floor heave identify three main floor heave mechanisms: bearing capacity failure, swelling, and buckling [26]. Each of these mechanisms is associated with a key factor that causes it. Bearing capacity failure cases are associated with the shear failures of the floor strata underneath the coal pillars when the vertical stress exceeds the bearing capacity of the floor. Swelling occurs in wet rocks containing clay minerals. Buckling occurs under the influence of high horizontal stresses on the floor strata [27].

However, in situ, the mechanisms of heaving are not so clear. In gob-side entry retaining, different factors often have simultaneous influence. In each local case, this leads to different magnitudes of floor heave. In addition, the headgate has different media from the two wall sides (solid coal on one side and filling wall on another); it also has different vertical pressure, which leads to asymmetry in the entry deformation.

In this paper, it was accepted that the main cause of floor heave is a change in the stress field in surrounding rocks; moisture is still considered an additional negative factor.

Reinforcement and stress-relief methods have the greatest potential for the control of floor heave in gob-side entry retaining. However, despite the significant scientific substantiation of these methods, in practice, they are not widely used. Floor restoration has been widely implemented. Therefore, scientists from different countries have searched for new effective reinforcement schemes.

Traditional floor reinforcement schemes with rock bolts are modified by combining them with flexible anchor supports [28], shotcrete and steel frames [29], concrete inverted arches [30], pressure-relief holes [31], etc.

Zhu et al. [32] proposed the control method of "bottom lifting + bottom angle bolt + floor bolt" based on the results of a numerical simulation. Wang et al. [33] proposed an asymmetric floor heave control scheme of "floor leveling + anchor cable support + concrete hardening" on the basis of the control principle of "roof + two sides + floor". Wei et al. [34] used 3DEC discrete-element software to simulate and analyze the characteristics and evolution of asymmetric roadway floor heave under dynamic-load disturbance, and proposed the asymmetric control scheme of “slurry anchor reinforcement + top cutting and pressure relief”. Zhang et al. [35] used UDEC software to study the floor failure mechanism under the influence of superimposed dynamic and static loads. Full-section anchor cables and inverted arches were proposed to maintain the stability of the surrounding rock. Qin et al. [36] proposed the zonal reinforcement scheme of “fix cable to shed, floor pressure relief, deep-shallow composite grouting” and implemented it in practice, with good results.

It was also proposed to control heaving by installing bolts in the roadway corners. Kang et al. [37] proposed the combined support method of grouting on the floor plate and installing anchor rock bolts in floor corners. Yang et al. [38] studied the mechanical properties of different types of floor corner bolts. However, in high-horizontal-stress conditions, the rock bolts are easy to bend and yield, which reduces the supporting effect.

To control floor heave in gob-side entry retaining, Xu et al. [13] proposed a new steel pile method that was similar to the anti-sliding pile method applied in slope engineering. In this method, steel piles are installed in roadway floor corners before the dynamic pressure zone has an influence.

Kang et al. [39] have shown that the floor angle pile with floor grouting can effectively control the deformation of the roadway floor and two sides. Compared with the rock bolt, the floor corner pile can effectively cut off the sliding line of the floor due to its high bending shear capacity [39]. Guo et al. [40], based on the results of a numerical simulation, field tests, and microseismic monitoring, proposed a floor pressure relief borehole with a large diameter and a concrete-filled steel tube pile support to control floor rock burst. Summing up, it can be seen that floor reinforcement methods in gob-side entry retaining still need to be improved.

This paper is focused on the evolution of floor heave in gob-side entry retaining. Floor heave control with an anti-shear pile method was studied. The numerical simulation with ANSYS code was used for the stress–strain analysis of the surrounding rock. Previous articles researching the effectiveness of pile methods as a method for floor heave control in underground roadways have mainly focused on floor corner piles. The main novelty of this paper is the study of a highly effective floor heave control scheme in which piles were installed not only in the floor corners but in five different positions along the entry span. At the same time, the length and type of the piles varied. Based on the analysis of floor heave causes, promising schemes of pile installation in the immediate floor were proposed and a study of their effectiveness was carried out. As a result, the most effective floor control scheme was determined.

2. Engineering Background

2.1. Geological and Engineering Conditions

The Pivdennodonbasskaya mine is a typical underground coal mine with a depth of 800 m, in the Donbas region of Ukraine. The coal seam has a thickness of 1.3 m and an average inclination of 6°. The immediate roof strata and floor strata of the coal seam are both soft mudstone with thicknesses of 8.2 m and 6.0 m, respectively, as shown in Figure 2a.

Typically, longwall panels have a U-shaped layout where fresh air flows through the headgate to the longwall face, taking away methane, coal dust, and heat, and then flows through the tailgate. At the same time, the small coal pillar method is used with a pillar width of 1.5–3 m. With this system, the daily extraction of coal from the longwall is limited by the gas factor.

Eleven- and twelve-longwall panels have more advanced Y-type longwall mining systems (Figure 2b) based on a retained gob-side entry. Y-type systems contribute to reducing gas accumulation and loss of coal resources in pillars. In Y-shaped systems, fresh air can flow in through two gateroads before the coal face and then flow out through gob-side entry retaining. After the longwall panel mining finishes, gob-side entry retaining can be reused for the next longwall panel.

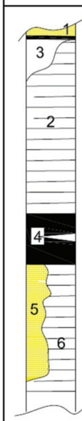

Column	Lithology	Thickness (m)	Average thinkness (m)	Geologic description, uniaxial strength of intact rock σ_c, (MPa)
	1. sandstone	6.7–8.1	7.4	gray, horizontal bedding, σ_c=57 MPa
	2. sandy mudstone	6.2–10.4	8.2	gray, horizontal bedding, σ_c=45 MPa
	3. sandy mudstone	22–24	20	dark gray, σ_c=36 MPa
	4. coal	1.15–1.45	1.3	semibright coal, fractured, σ_c=12 MPa
	5. mudstone	4–8	6.0	gray, horizontal laminated σ_c=30 MPa
	6. sandstone	16.0–24.0	18	gray, horizontal bedding, σ_c=60 MPa

(**a**)

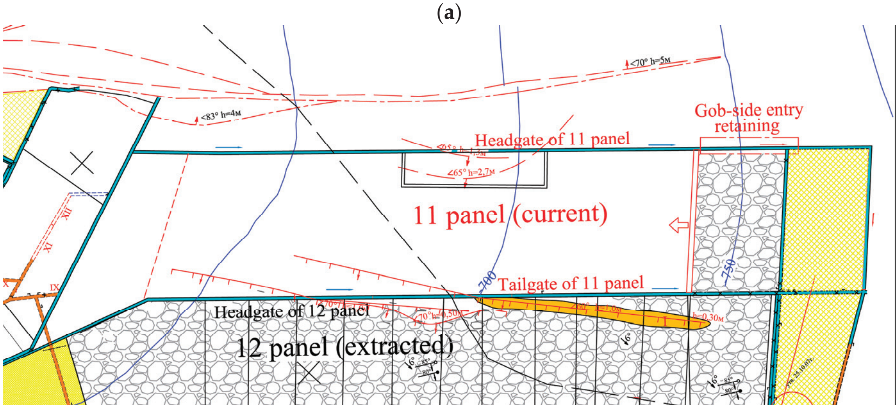

(**b**)

Figure 2. The geological and engineering conditions of a mine: (**a**) strata histogram; (**b**) layout of longwall panels.

2.2. Supporting Parameters and Deformation of Gob-Side Entry Retaining

A U-shaped steel arch support (U33) with steel mesh was used in the entry. The width and height of the entry were 5.2 m and 3.65 m, respectively. The cross-sectional area of the entry during the excavation stage was 15.1 m^2. The distance between the steel arch frames was 0.67 m. After coal mining in the longwall face, an artificial filling wall was built to maintain the gob-side entry. Figure 3a shows the original design of the support scheme. However, at a longwall retreat with a distance of 200 m, the width and height of the headgate of the 12-panel longwall were 2.6 m and 1.29 m, respectively. The total vertical convergence was about 64% of the initial roadway height. The average floor uplift was 1.04 m, and the average roof lowering was 1.32 m. The headgate deformed asymmetrically. The steel arches were critically bent and irreversibly deformed. The yielding nodes failed, and the steel mesh was disrupted. The entry required repair. The failure of the headgate support system and the floor heave consequences are shown in Figure 3b. To increase the load-bearing capacity of the steel arch frames, wooden pillars were installed. Floor restoration was carried out with a Hasemag EL160 loader machine to ensure the required cross-sectional area in the gob-side entry retaining. This practice is typical for coal mines in Ukraine [41]. Scholars from other countries report similar cases of critical floor heave [16,18,27,42,43].

Floor heave monitoring was performed in the headgate of the 12 panels. Measurements were carried out at three monitoring stations. The distance between stations was 9.6 m. Each station consisted of 4 marker points installed in the roof, floor, and both wall sides of the gateroad. The measurements were carried out over 4 months. The graphs of floor heave evolution in the center of the headgate span in front of the longwall face and behind it are presented in Figure 3c. The floor uplift in front of the longwall influence zone was 95 mm (9% of the total floor heave) and occurred during the roadway excavation stage. The monitoring results show that the main part of the floor uplift occurred at a distance of +40 m in front of the longwall face and −50 m behind it. In total, 35% of the floor uplift occurred at a distance of "+40" m in front of the longwall face to the intersection of the headgate with the face. Another 28% of floor uplift appears in the section of the headgate "0"–"−50" m behind the longwall face. The floor uplift has a damping tendency and stabilizes at a distance of 260–300 m behind the longwall face. At the stage of maintaining the headgate behind the longwall face, 56% of the total floor uplift occurs.

An analysis of the floor heave dynamic monitoring showed that this phenomenon evolved with different intensities at different stages of the gateroad's life. This is generally consistent with previous studies [15,17,27,41]. The gateroad that was an object of study had no water inflows. Therefore, the swelling mechanism of heaving is not typical for it. The greatest increase in gateroad floor heave was associated with the longwall face influence. The abutment pressure changed the equilibrium state of rock masses, increased vertical stress concentration and led to post-elastic deformation of rocks. In this case, the immediate floor lost its continuity and became discontinued. This was visually confirmed after rock excavation during floor restoration, similar to previous studies [41]. Post-elastic deformation (pseudoplastic flow) and dilatancy are the main causes of floor heave. Floor heave in the gob-side entry is complicated by the asymmetrical stress–strain state. In this case, the heaving mechanism is close to bearing capacity in failure cases. However, due to the stress asymmetry, failures of the floor strata underneath the coal body and the filling wall body are different.

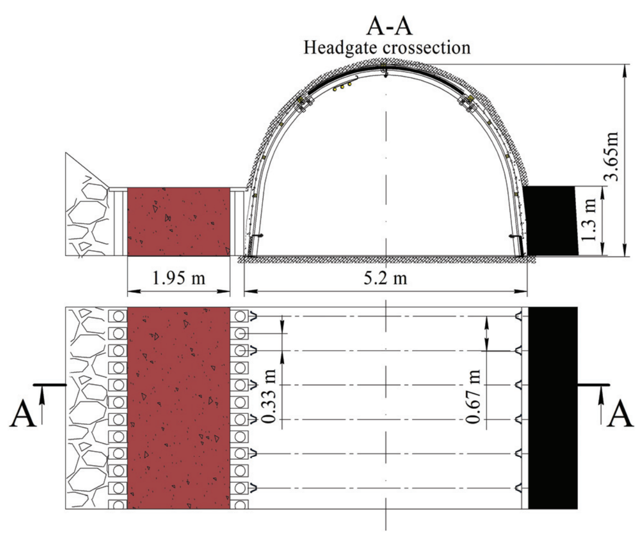

(a)

Figure 3. *Cont.*

(**b**)

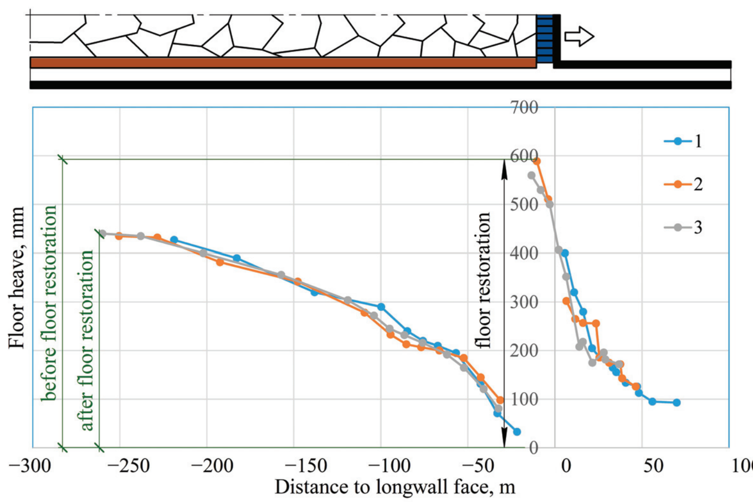

(**c**)

Figure 3. The parameters of the original support system (**a**), view on gob-side entry at a retreat of the longwall at a distance of 200 m (**b**), monitoring curve of floor heave in headgate in longwall face influence zone (**c**). 1, 2, 3—monitoring stations.

To control the lowering of the roof, the distance between the steel arch frames was reduced to 0.5 m in the gateroad of 11 panels. However, the floor of entry remained unsupported. So, the main problem for entry stability was the large floor heave. Floor restoration with dinting loaders is an ineffective passive method, which requires additional labor and material resources, organization of transport of the excavated rock, and time. Therefore, optimization of the support scheme to control floor heave is an important problem.

3. Study of the Floor Heave in Gob-Side Entry Retaining

3.1. Numerical Model

The geotechnical conditions of the 11-longwall panel of the Pivdennodonbasskaya coal mine were the basis of the numerical model that was realized by ANSYS 17.2 software. The simulation zone is indicated in Figure 4a, and the numerical model is shown in Figure 4b.

The model was three-dimensional (3D). The size is 250 m along the x direction, 60 m along the y direction, and 25 m along the z direction. Half of the panel width was simulated due to symmetry. The height and width of the gob-side entry were 3.65 m and 5.2 m, respectively. The height and width of the filling wall were 1.3 m and 1.95 m, respectively. The bottom boundary of the model was fixed vertically; displacements of lateral boundaries were constrained in the normal direction. Vertical pressure, which was equivalent to the strata weight at a depth of 900 m (22.5 MPa), was applied to the top boundary.

To simulate the behavior of rock mass, filling wall material, and gangue in the goaf, the Drucker–Prager model was applied. The capability of the Drucker–Prager model to adequately simulate the behavior of pressure-dependent materials (like rocks) has been shown in previous studies [44–46]. The bilinear isotropic hardening model was used to simulate the behavior of the steel arch frame, rock bolt, and steel pile.

The surrounding rocks of gob-side entry retaining were failured and discontinuous. Therefore, the mechanical parameters of intact rock (Figure 2a) should have been corrected. The Hoek–Brown Failure Criterion [47] was used to calculate the properties of rock mass in gob-side entry retaining. The Geological Strength Index (GSI), the "mi" constant, and the disturbance factor (D) were determined.

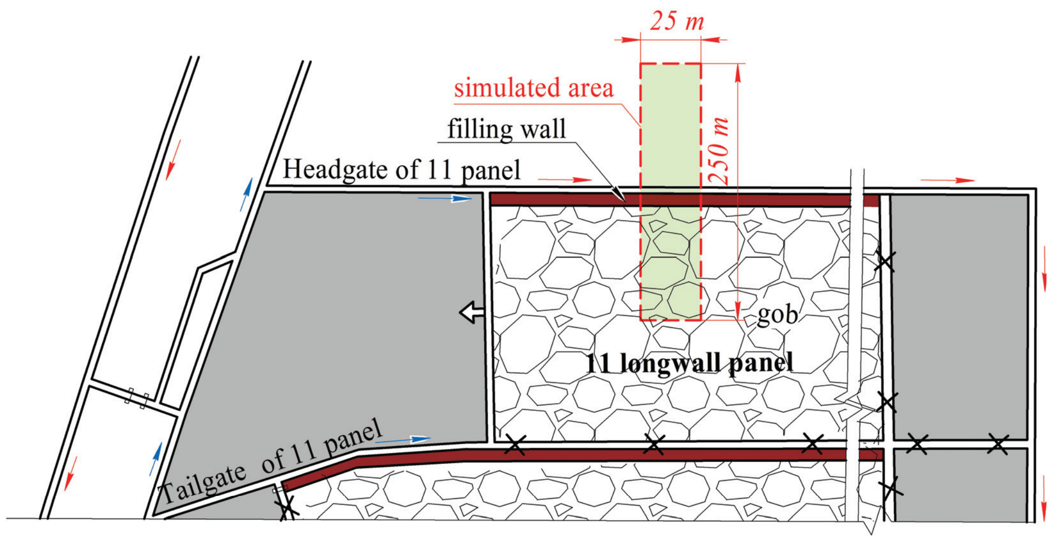

(**a**)

Figure 4. *Cont.*

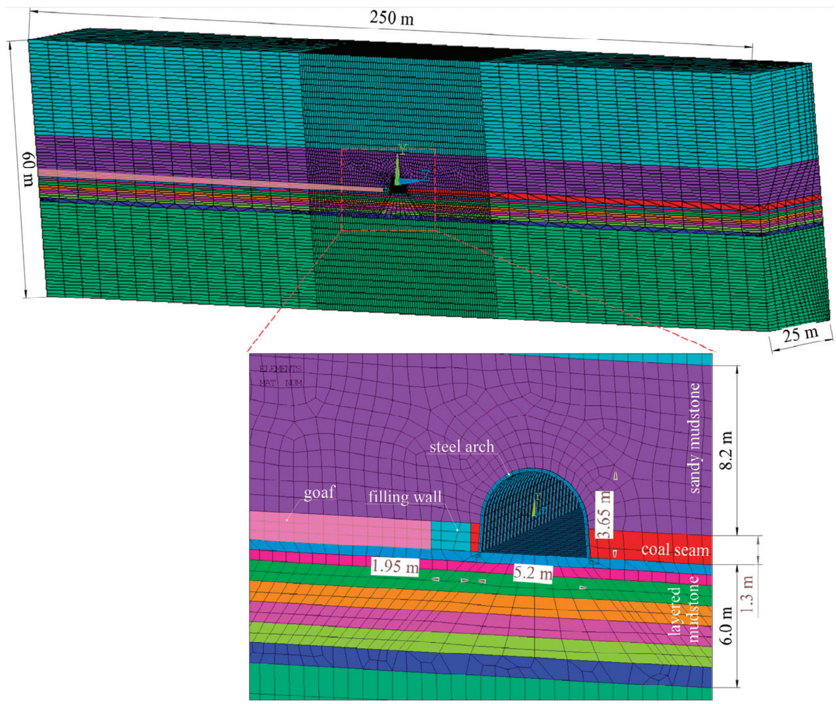

(**b**)

Figure 4. Plan of the simulated area (**a**); numerical model and support elements (**b**).

The GSI was calculated as RMR89-5 [48]. RMR89 was determined on the basis of geological documentation, results of the uniaxial strength tests, tests of the drill cores, and the observation of exposure of rock mass during gateroad repairs according to the Bieniawski method [49].

The "mi" constant was 8 for mudstones, 17 for coal, and 12 for sandstone. The D parameter corresponded to Hoek's classification categories: "squeezing problems result in significant floor heave, disturbance can be severe unless a temporary invert is placed" for mudstone and sandstone; "mechanical excavation in poor quality rock masses resulting in minimal disturbance to the surrounding rock mass" for coal seams [47].

The deformation modulus (E_{rm}), friction angle (φ), and cohesive strength (c) were calculated according to Hoek and Diederichs' empirical method [48]. The calculation procedure was described in previous studies [18,50]. The calculated rock mass properties are presented in Table 1. The filling wall body in the case of a longwall retreat with a distance of 100 m was fissured and discontinuous. Therefore, the same method was applied for the filling wall material. The properties of the filling wall are shown in Table 1. To simulate the behavior of the broken gangue in the goaf, Poisson's ratio = 0.45, and E_{rm} = 30 MPa were applied [51]. The properties of the steel arch frame are shown in Table 2.

3.2. Simulation Results

The stress–strain distributions in the surrounding rocks are shown in Figures 5 and 6. The initial position of the rock layers during the excavation of the gateroad is shown in Figure 5a,b by the dashed line. In these figures, the movement of rock strata can be tracked comparative to the initial state. Specific displacements of rock strata are marked with arrows in Figure 5a. The subsidence of the roof above the longwall goaf, caused by coal mining, leads to loading of the filling wall body. As a result, the filling wall is pressed into the immediate floor, which causes an increase in the concentration of vertical stresses in it (Figure 5a). The magnitude of vertical pressure on the filling wall body depends on the length of the roof console above the goaf and the rigidity of the filling wall material [5]. This issue is not discussed in this paper.

Table 1. Rock mass and filling wall material parameters for numerical simulation.

GSI	D	Compressive Strength (MPa)	Tensile Strength (MPa)	Deformation Modulus (GPa)	Poisson's Ratio	Cohesion Value (MPa)	Angle of Internal Friction (deg)	Dilatancy Angle (deg)
Main roof (sandy mudstone)								
52	0.5	1.75	0.09	1.19	0.3	2.83	24	24
Immediate roof (sandy mudstone)								
52	0.5	1.48	0.08	0.97	0.3	2.45	27	27
Coal seam c_{11}								
35	0	0.32	0.006	0.22	0.3	1.13	20	20
Immediate floor (mudstone)								
47	0.5	0.87	0.04	0.50	0.3	1.61	22	22
Main floor (sandstone)								
55	0.5	2.90	0.11	1.80	0.3	3.90	34	34
Filling wall material								
66	0.5	3.62	0.16	1.48	0.3	3.33	29	-

Table 2. Steel arch frame parameters for numerical simulation.

Primary Support	Type of Elements	Material Behavior Option	Elastic Modulus (GPa)	Poisson's Ratio	Yield Strength (MPa)	Tangent Modulus (GPa)
U-shaped steel support	Beam	Bilinear isotropic hardening	200	0.27	295	52.2

From the side of the coal seam body, vertical stresses also increase in the roof and floor. Increased vertical stresses in the floor strata underneath the gateroad walls cause lateral expansion of rocks in the horizontal direction. Thus, the horizontal stresses in the immediate floor underneath the filling wall and coal seam body increase. Moreover, the magnitude of these stresses underneath the filling wall is higher than underneath the coal seam body, as can be seen from Figure 5b. High horizontal stresses under the steel arch legs provoke transverse expansion of the rocks (in the vertical direction) and their displacement towards the gateroad cavity. This causes stress relief in the rock mass as it approaches the entry contour and changes stress sign in the near-contour area (Figure 5a,b). The zone of vertical rock expansion and elevation in the immediate floor covers 5 m in depth according to the numerical modeling results, which are shown in Figure 5b. As a result of the filling wall body indentation in the immediate floor underneath the wall, a zone of rock subsidence is formed, up to 3.5 m deep, as shown in Figure 5b. The floor heave was 948 mm. This is 9.7% lower than the results of in situ monitoring. Overall, it can be concluded that the numerical model is adequate.

The mechanism described above is confirmed by analyzing the strain distribution (Figure 5c,d).

The results of rock specimen tests show [52–55] that for mudstone, siltstone, argillite, and sandstone with a uniaxial strength of 25–40 MPa, the failure criterion for strain is about 0.02-0.03. Therefore, in the numerical simulation, the post-peak limit was accepted in the range of "−0.02"–"+0.02". In this paper, the authors do not study the failure of rocks in detail. The authors understand that in a triaxial stress field, failure will depend on the ratio of stress components and can vary. In the context of this study, it is important to recognize the post-elastic stage. Therefore, the post-peak strain is analyzed. In the Drucker–Prager model, pseudoplastic deformation is accepted for analyzing the behavior of rock mass beyond the elastic stage, including discontinuous rock.

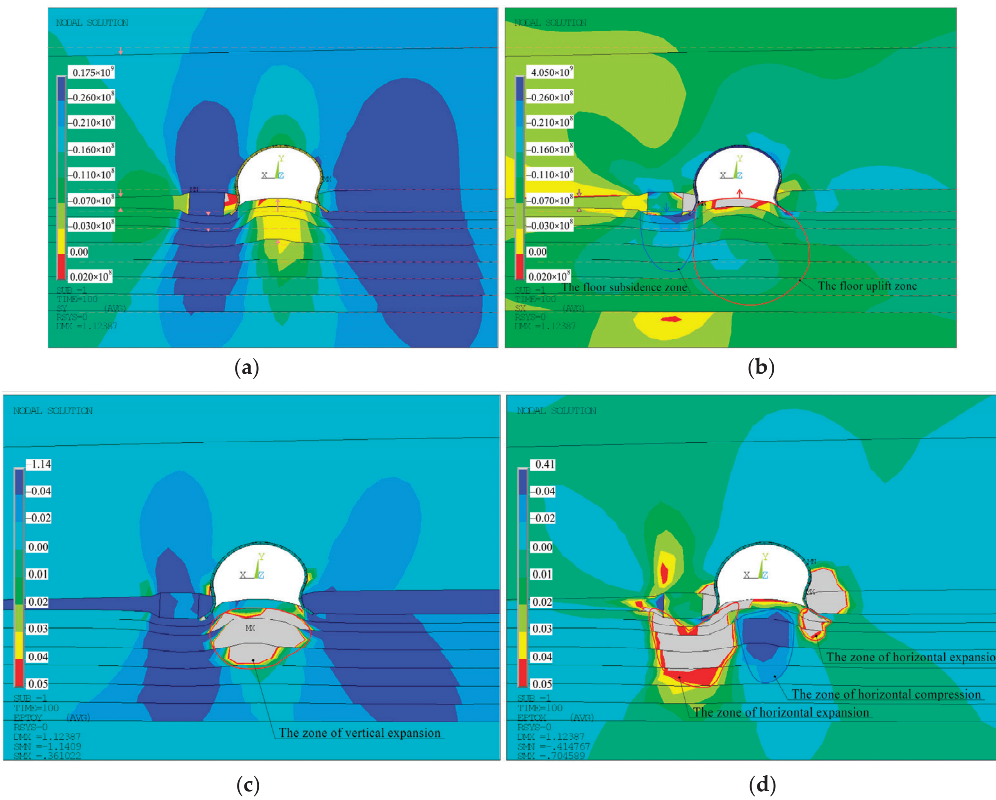

Figure 5. Stress–strain distributions around the gob-side entry retaining: (**a**) vertical stress; (**b**) horizontal stress; (**c**) vertical strain; (**d**) horizontal strain.

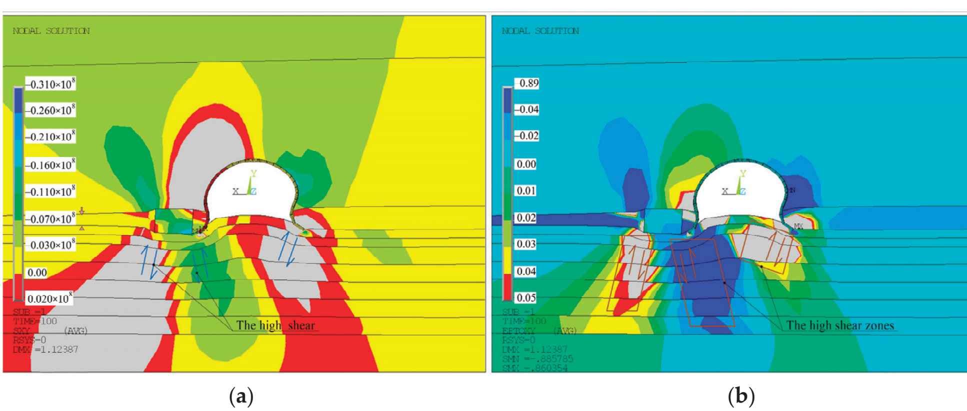

Figure 6. Shear stress (**a**) and shear strain (**b**) distributions around the gob-side entry retaining.

The contour of the vertical expansion zone with post-peak strain is shown in Figure 5c. The positive strain scale in the figures is limited to “+0.05”. All strains that are greater than +0.05 are indicated in gray. Vertical strains in this zone exceed the post-peak strain for mudstone by more than two times. In this zone, post-elastic deformation and delamination of rocks occur.

Zones of horizontal post-peak expansion of rocks are formed under the filling wall body and coal seam body. In these zones, dilatancy expansion of rock is observed under the influence of high vertical stresses (Figure 5d). The expansion of rocks in these zones leads to compression of the rocks between them, underneath the entry span. The post-peak horizontal compression zone is shown in Figure 5d. Dilatancy in this zone is caused by the horizontal stresses.

Zones of post-peak horizontal strains also form in the side walls of the entry. This causes deformation of the legs of the steel arch frame. The stress asymmetry not only leads to floor heave asymmetry but also irregular curvature of the support frame, which confirms the results of in situ observations in the gob-side entry retaining.

Analysis of Figure 5 shows that counter-movements of rocks occur on the entry floor. Such movements cause shear deformations. Therefore, to analyze them, the distributions of shear stresses and strains in the surrounding rocks are shown in Figure 6. The main interest in this study is the central high-shear zone that occurs between the zone of uplift and the zone of subsidence of the immediate floor. This zone originates in the corner of the filling wall body and extends into the depth of the entry floor at an angle (Figure 6a). The post-peak shear strain zones are shown in Figure 6b. On the opposite side of the filling wall body and underneath the arch frame leg on the coal seam side, zones of increased shear stress and strain are also formed, as shown in Figure 6. Thus, shear has an important role in the deformation and failure of immediate floors.

The simulation results lead to comprehension of the floor heave mechanism in gob-side entry retaining. The main processes on the entry floor and their cause-and-effect relationships have been identified. The floor heave most likely corresponds to a buckling mechanism. Such findings are consistent with those reported by Mo et al. [22,27] regarding cases of floor heave in Australian mines. Since the main cause of heaving is horizontal stress, it can be concluded that a high degree of deformation is caused by rock mass buckling due to the failure of the floor materials in accordance with Mo et al.'s hypothesis [22].

3.3. Simulation Discussions

Several conclusions can be drawn according to the above analyses:

(1) The main reason for dramatic floor heave in gob-side entry retaining is the vertical loading of the filling wall by the weight of the roof that has lost its support after coal extraction in the longwall face. The high pressure of the roof leads to the indentation of the filling wall body into the immediate floor and the formation of a zone of increased vertical stresses underneath it. These stresses are higher than those on the side of the coal seam body, which is the main reason for the asymmetry of the gateroad deformation. Further redistribution of stresses in the immediate floor leads to an increase in horizontal stresses, which have a key role in floor heave.

(2) High vertical stresses underneath the filling wall and coal seam body lead to dilatancy expansion of rocks in the horizontal direction. High horizontal stresses in the immediate floor under the side wall provoke the formation of a post-peak horizontal compression zone under the entry span. In this zone, the dilatancy and lateral expansion of rocks in the vertical direction cause delamination of the immediate floor and uplift of discontinuous rocks.

(3) A zone of high shear occurs between the zone of rock uplift under the entry span and the zone of rock subsidence underneath the filling wall body. A zone of high shear stress and strain is also formed under the steel arch leg on the solid coal side. The rock failure in these zones complicates the floor heave mechanism described above. In shear strain zones, vertical stresses are transformed into horizontal ones.

(4) Numerical simulation results are valid only for geostress, geological and mechanical parameters of rock mass, filling wall setting, and support elements that were applied. However, the mechanism of floor heave is typical for similar engineering conditions.

4. Floor Heave Control with Anti-Shear Pile Technology

4.1. Design and Parameters of Floor Heave Control Schemes

The analysis of stresses and strains given in the previous section showed that the key factor of floor heave in gob-side entry retaining is the transmission of stresses from under the filling wall body to the zone under the entry span, which causes delamination, vertical expansion, and uplift of the discontinuous rocks in the immediate floor. A reinforcement method with anti-shear pile installation was proposed for the floor heave control.

The study of the effectiveness of the anti-shear pile was carried out in three stages. In the first stage, three floor heave control schemes with one anti-shear pile were studied. Each scheme was simulated twice: with a pile length of 2 m and 4 m. The distance between piles was equal to the distance between steel arch frames. Figure 7a–f show the support schemes that were studied. The parameters of the schemes are presented in Table 3.

Table 3. The parameters of floor heave control schemes for numerical simulation.

Scheme	Number of Piles	Pile Position	Pile Length (m)	Summary Length of Piles (m)	Pile Type	Class Of Concrete in the Pile	Deformation Modulus (GPa)	Poisson's Ratio
				1st simulation stage				
1pile 5 (4)	1	#5	4	4	Steel pile	B-60	72	0.25
1pile 4 (4)	1	#4	4	4	Steel pile	B-60	72	0.25
1pile 3 (4)	1	#3	4	4	Steel pile	B-60	72	0.25
1pile 5 (2)	1	#5	2	2	Steel pile	B-60	72	0.25
1pile 4 (2)	1	#4	2	2	Steel pile	B-60	72	0.25
1pile 3 (2)	1	#3	2	2	Steel pile	B-60	72	0.25
				2nd simulation stage				
2pile 5+1	2	#5, #1	2	4	Steel pile	B-60	72	0.25
2pile 5+2	2	#5, #2	2	4	Steel pile	B-60	72	0.25
2pile 5+3	2	#5, #1	2	4	Steel pile	B-60	72	0.25
				3rd simulation stage				
2pile 5+2	2	#5, #2	2	4	Steel pile	B-60	72	0.25
2pile 5+2(tube)	2	#5, #2	2	4	Steel tube	-	200	0.3
2pile 5+2(B-20)	2	#5, #2	2	4	Filling pile	B-20	27.5	0.19
2pile 5+2(B-40)	2	#5, #2	2	4	Filling pile	B-40	36.0	0.19
2pile 5+2(B-60)	2	#5, #2	2	4	Filling pile	B-60	39.5	0.19

In the second stage, three floor heave control schemes with two anti-shear piles were modeled. The length of each pile was 2.0 m. Thus, the summary pile length in the first simulation stage and in the second simulation stage was equal. Schemes of the second simulation stage are shown in Figure 7g–i.

In the third simulation stage, the investigation of the optimal type of pile was carried out. In this case, a comparison of three pile types was conducted:

- "Steel pile"—steel tube with a diameter of 200 mm and a wall thickness of 4 mm, filled with concrete (for this type of pile, two previous simulation stages were performed);
- "Steel tube"– steel tube with a diameter of 200 mm and a wall thickness of 4 mm;
- "Filling pile"—a pile of reinforced concrete (simulation was carried out for concrete classes B-20, B-40, and B-60).

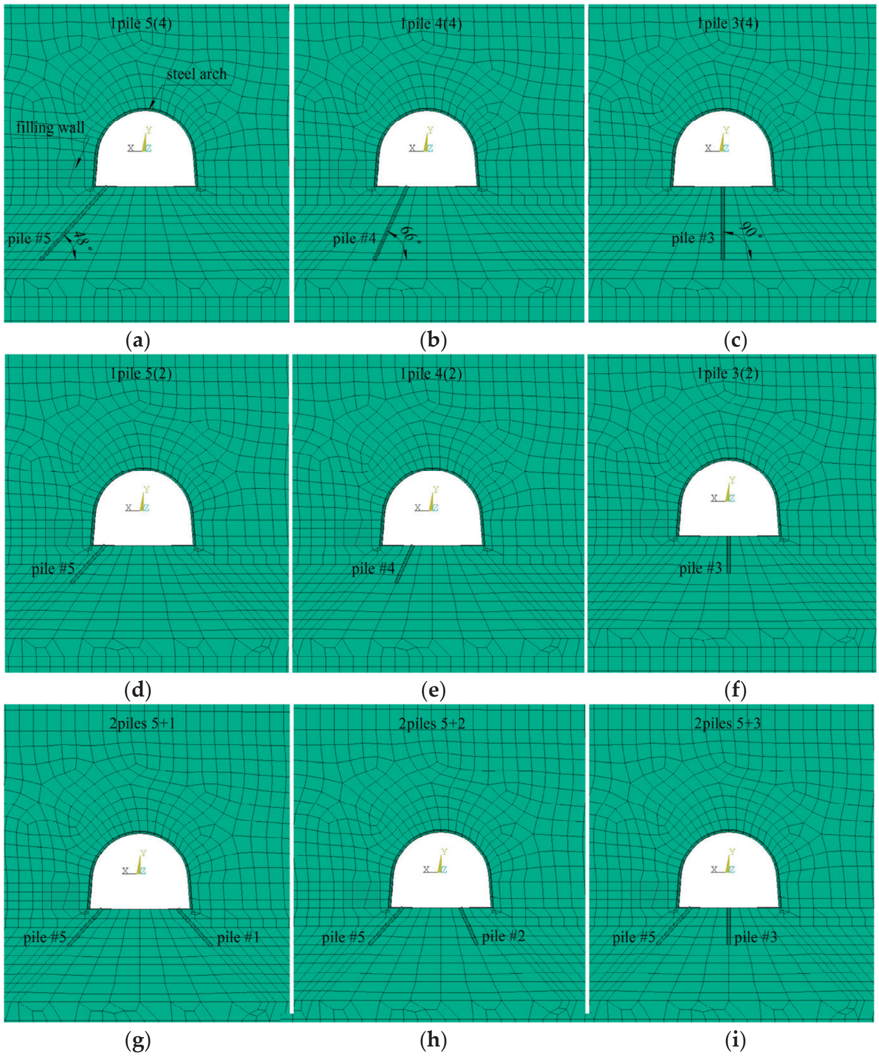

Figure 7. Finite-element models for simulated floor heave control schemes: (**a**) scheme 1pile 5 (4); (**b**) scheme 1pile 4 (4); (**c**) scheme 1pile 3 (4); (**d**) scheme 1pile 5 (2); (**e**) scheme 1pile 4 (2); (**f**) scheme 1pile 3 (2); (**g**) scheme 2pile 5+1; (**h**) scheme 2pile 5+2; (**i**) scheme 2pile 5+3.

The plan of the numerical experiment is presented in Table 3.

The pile positions were numbered in the direction from the solid coal body to the filling wall body. The central pile (position #3) has a vertical orientation along the axis of the roadway cross-section. The piles that were installed in floor corners (position #1, position #5) were inclined 48 degrees to the horizon. The piles in the position between the central pile and floor corner pile (position #2, position #4) were inclined 66 degrees to the horizon. The pile inclination was chosen by taking into account the simulation results presented in the previous section.

The original U-shaped steel arch was not changed. Table 3 shows the mechanical parameters of floor support components in the numerical model. The piles were modeled as beam elements. In this case, the deformation modulus was calculated as a weighted average between steel and concrete for each pile type structure separately according to the theory of elasticity.

4.2. Effectiveness of Anti-Shear Pile Method

First simulation stage.

In the first simulation stage, the search for the best floor control scheme was carried out while installing one pile.

The distributions of vertical strain and shear strain around the entry before and after pile installation are shown in Figures 8 and 9. It can be seen that the installation of the pile in any of the positions significantly reduces the size of the post-peak strain zone on the immediate floor. Pile installation does not significantly affect the distribution of compressive stresses; however, the zone of tensile stresses underneath the entry span is reduced. The smallest dimensions of this zone are for the 1pile 4 scheme (4) (Figure 8c). The pile installed in the entry corner (scheme 1pile 5 (4)) bends at a depth of 1–2 m in the zone of high horizontal stresses. This pile orientation effectively restricts floor delamination on the side of the filling wall, but practically does not restrain expansion on the side of the coal seam body (Figure 8b). Pile installation in the center of the entry span (scheme 1pile 3 (4)) restricts floor delamination on the side of the coal seam body, but on the side of the filling wall, vertical delamination remains significant (Figure 8d).

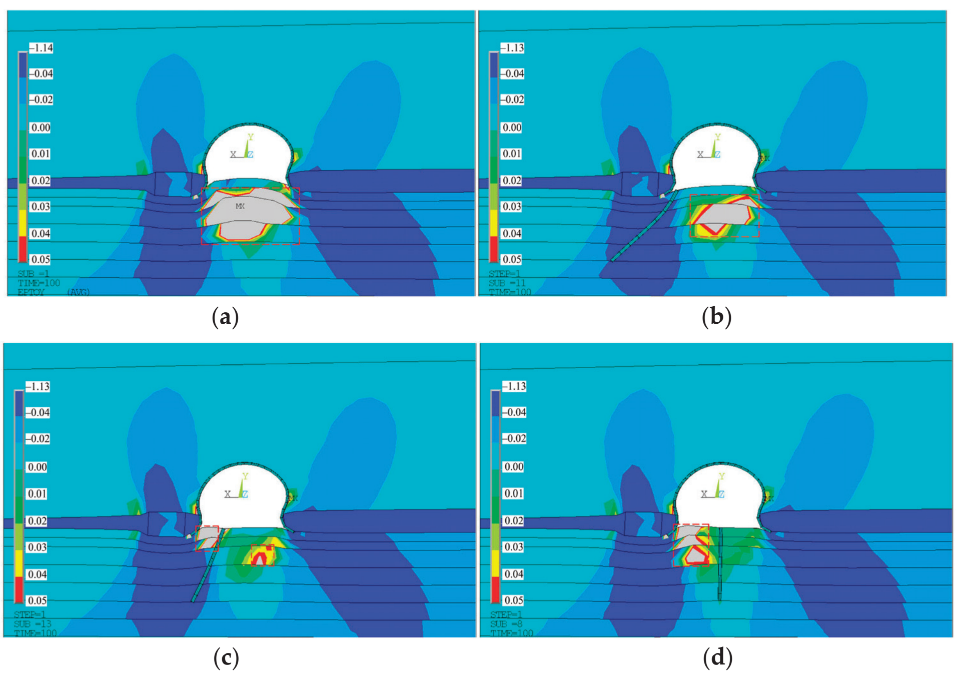

Figure 8. The vertical strain distributions in surrounding rock in gob-side entry retaining: (**a**) before pile installation; after pile installation with schemes (**b**) 1pile 5 (4); (**c**) 1pile 4 (4); (**d**) 1pile 3 (4).

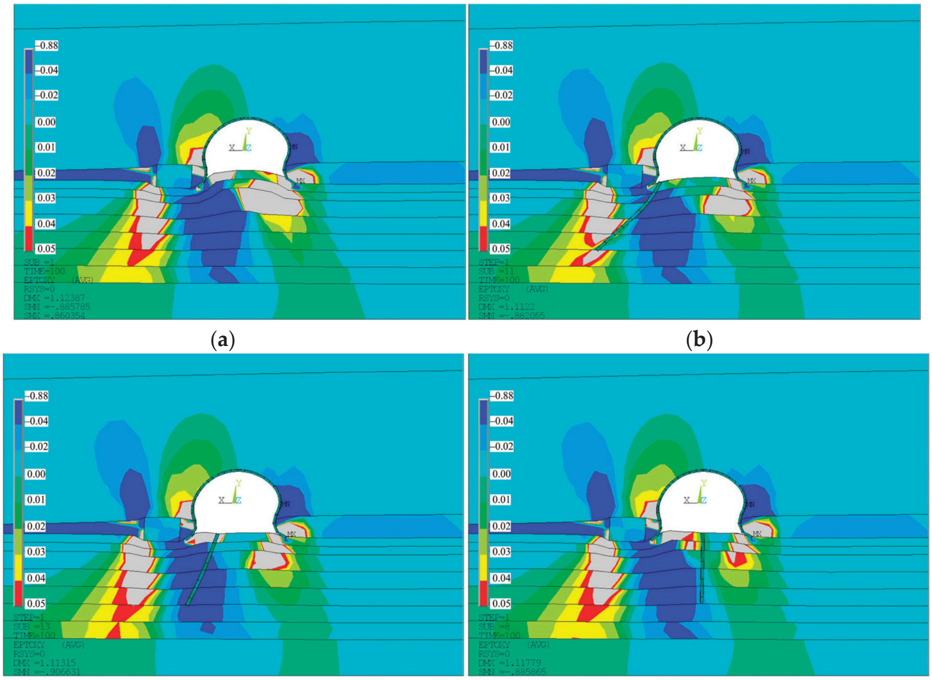

(**a**) (**b**)
(**c**) (**d**)

Figure 9. The shear strain distributions in surrounding rock in gob-side entry retaining: (**a**) before pile installation; after pile installation with schemes (**b**) 1pile 5 (4); (**c**) 1pile 4 (4); (**d**) 1pile 3 (4).

Pile installation has a similar effect on shear strain in the geometric sense. The smallest dimensions of the post-peak shear strain zone are for the 1pile 4 (4) scheme (Figure 9c). The pile in the center of the entry span (scheme 1pile 3 (4)) does not reduce the floor heave by the anti-shear (anti-slide) effect (Figures 8d and 9d). It is more likely that such pile installation halves the entry span, which ensures a reduction in floor delamination.

The discussed stress–strain distributions are in accordance with the results of the floor heave analysis. The floor heave before and after pile installation at the first simulation stage is shown in Figure 10a. The smallest contour uplifts among schemes with piles 4 m long are noted for the 1pile 4 (4) scheme. In this case, the smallest dimensions of the horizontal compression zone on the entry floor are observed (Figure 10b). However, the smallest dimensions of the horizontal post-peak expansion zone are observed in scheme 1pile 5 (4) (Figure 10b). This scheme is worthy of interest since the post-peak horizontal strain is the key factor of the floor heave in the gob-side entry, which was discussed in the previous section.

The vertical strain distributions around the gob-side entry retaining after installation of 2 m long piles are shown in Figure 11. Reducing the length of the piles to 2 m for schemes 1pile 4(2) and 1pile 3(2) led to a significant decrease in the efficiency of counteraction to immediate floor delamination. The 1pile 3(2) scheme affects only the local maximum of floor heave in the center of the entry (Figure 10a) and the vertical floor delamination in the central part of the entry span (Figure 11c). The size of the post-peak strain zone in the immediate floor does not decrease significantly compared to the case before pile installation (Figure 8a). Pile installation with the 1pile 4(2) scheme reduces the size of the vertical post-peak strain zone on the filling wall body side (Figure 11b), which leads to a decrease in floor heave on the filling wall side (Figure 10a). However, the length of the pile is insufficient to counteract the delamination of the floor from the side of the coal seam body

(Figure 11b) and reduce the size of the horizontal expansion zones under the filling wall (Figure 10b). At the same time, the scheme 1pile 5(2) is as effective as the scheme 1pile 5(4). Reducing the pile length at this position does not have a significant effect on the floor heave (Figure 10a) and the configuration of the post-peak strain zones (Figure 10b, Figure 11a). The maximum floor heaves in the 1pile 4(4) and 1pile 5(2) schemes differ by only 60 mm, i.e., by 14%; at the same time, the pile length differs by 2.0 m, i.e., 50%. Therefore, it can be concluded that the 1pile 5(2) scheme is more effective. The obtained results were the basis for the elaboration of schemes that were studied at the second simulation stage.

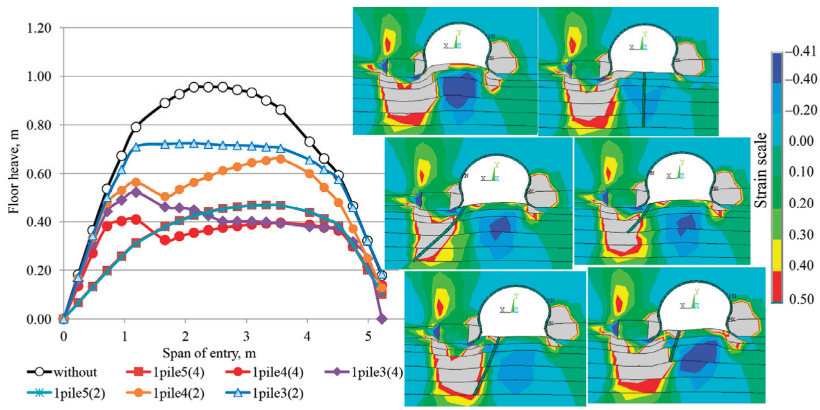

(**a**) (**b**)

Figure 10. The entry floor heave (**a**) and horizontal strain distributions in surrounding rock (**b**) before and after pile installation at the 1st simulation stage.

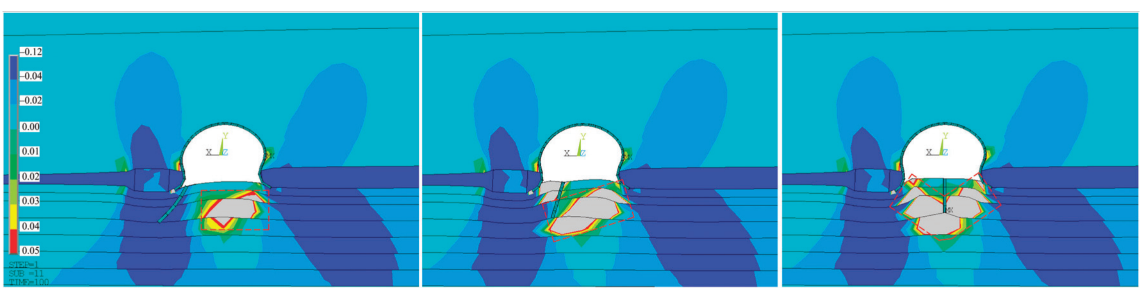

(**a**) (**b**) (**c**)

Figure 11. The vertical strain distributions around the gob-side entry retaining after pile installation with schemes (**a**) 1pile 5 (2); (**b**) 1pile 4 (2); (**c**) 1pile 3 (2).

Second simulation stage.

The elaboration of schemes for the second simulation stage was based on the concept that the summary length of the piles should not be more than 4.0 m (more than at the first simulation stage), since the borehole drilling and pile consumption depend on it. At this stage, it was assumed that two piles would be installed on the immediate floor. The position of one of these piles was determined in the results of the analysis of the investigation at the first simulation stage. This was position #5. Pile installation in this position leads to the highest efficiency among the compared ones. Thus, the most effective position for the second pile was searched for in the second simulation stage. The distributions of vertical strain and shear strain around the entry before and after pile installation are shown in Figures 12 and 13.

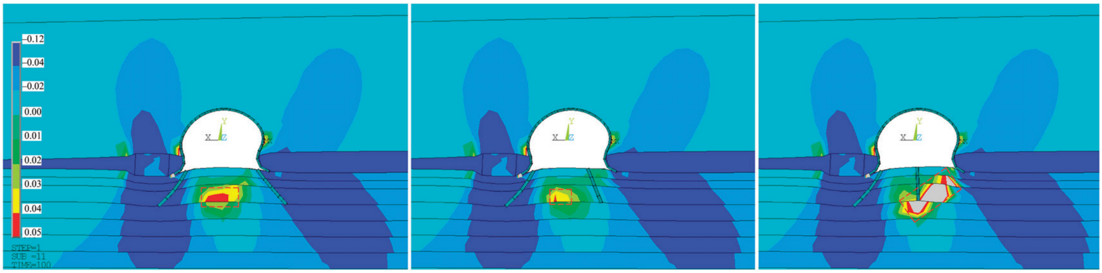

(**a**) (**b**) (**c**)

Figure 12. The vertical strain distributions around the gob-side entry retaining after pile installation with schemes (**a**) 2pile 5+1; (**b**) 2pile 5+2; (**c**) 2pile 5+3.

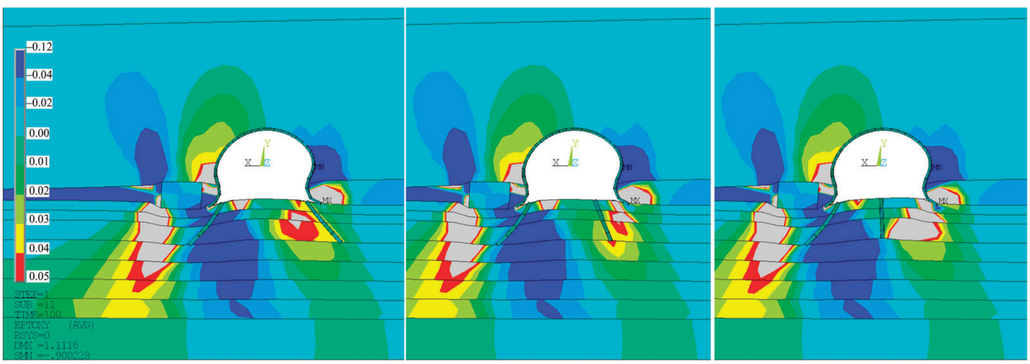

(**a**) (**b**) (**c**)

Figure 13. The shear strain distributions around the gob-side entry retaining after pile installation with schemes (**a**) 2pile 5+1; (**b**) 2pile 5+2; (**c**) 2pile 5+3.

It can be seen that installing a second pile in any of the compared positions reduces the size of the post-peak strain zone on the immediate floor. The best effect is obtained in the case of the 2pile 5+2 scheme. The size of the vertical delamination zone (Figure 12b) and the post-peak shear strain zone (Figure 13b) is the smallest in this case. It is clear that this is reflected in the size of the floor heave, which is minimal for this scheme. The scheme 2pile 5+1 is less effective, as can be seen from the larger size of the post-peak shear strain (Figure 13a) and post-peak vertical strain (Figure 12a) on the entry floor. However, the 2pile 5+1 scheme is better than the scheme 2pile 5+3. The post-peak strain zones in the 2pile 5+3 scheme (Figures 12c and 13c) are the largest among the compared schemes. It can be concluded that the anti-shear effect of pile installation is more efficient than the span-lowering effect for floor heave control in gob-side entry retaining.

The entry floor heave before and after pile installation at the second simulation stage is shown in Figure 14a. The scheme 2pile 5+2 is the most effective one. With this scheme, the maximum floor heave is 361 mm (Figure 14a), and the size of the horizontal post-peak strains is the smallest (Figure 14b). Thus, the most efficient scheme has been determined.

Third simulation stage.

For the practical implementation of the proposed method, it must satisfy two conditions: be technologically simple and inexpensive. There is no doubt that the piles should be installed in the gateroad outside the longwall influence zone. This will allow us to start floor heave control in a timely manner. Hole drilling for piles is a necessary process for floor support technology, and there is only one possible way to implement it. Therefore, the attention at the third simulation stage was focused on finding the optimal type of pile. In order to find more economical and simple solutions, a technical and economic comparison of different types of piles was carried out. A metal tube with a concrete filling was the initial pile type, for which all previous simulation stages were carried out. This type of pile was called the "steel pile" (Figure 15a). As an alternative, pile variants were proposed, such as tubes without filling (scheme 2pile 5+2(tube)), called "steel tubes" (Figure 15b). Concrete filling piles with different concrete classes (2pile 5+2(B-20...B-60)) were also studied. In these piles, five main steel bars for longitudinal reinforcement and spiral lateral reinforcement stirrups were used (Figure 15c).

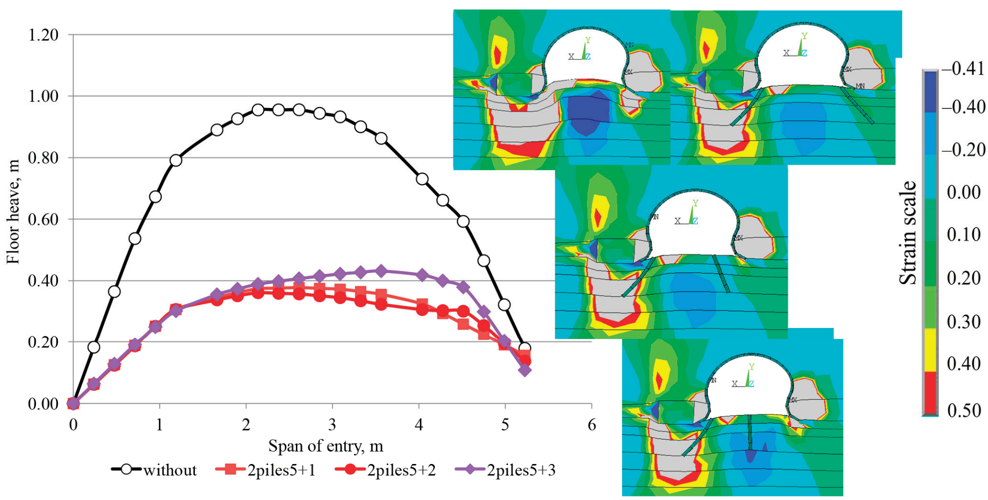

Figure 14. The entry floor heave and horizontal strain distributions in surrounding rock before and after pile installation at the 2nd simulation stage.

The entry floor heave after pile installation with different schemes is shown in Figure 16. The form of the floor contour is the same for all pile variants. Steel piles have the best counteraction to heaving (the maximum floor heave is 361 mm). The worst variant is the "steel tube" (the maximum floor heave is 399 mm). The effectiveness of the "filling pile" depends on the class of concrete. Thus, the floor heave for the B-20 class is 397 mm, and for the B-60 class, it is 386 mm. An increase in the class of concrete leads to a decrease in the size of the vertical post-peak strain zone in the entry floor (Figure 17b,c) and a decrease in floor uplift. The localization and size of the post-peak strain zone for the steel tube pile and filling pile with B-20 concrete do not differ (Figure 17a,b). However, the cost of piles varies significantly. A comparison of costs for one set of piles (2 × 2 m) for different types is shown in Table 4. The prices are correct for Ukraine as of March 2024.

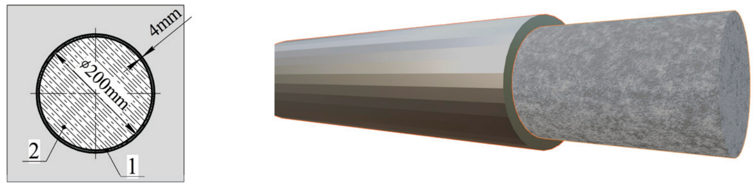

(**a**)

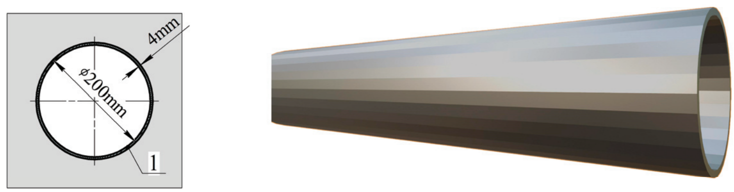

(**b**)

(**c**)

Figure 15. Pile design in numerical simulation: (**a**) steel pile; (**b**) steel tube; (**c**) filling pile. 1—steel tube (diameter 200 mm); 2—concrete; 3—main steel bars (5 × 14 mm); 4—lateral reinforcement stirrups (spiral length 14 m, diameter 6 mm).

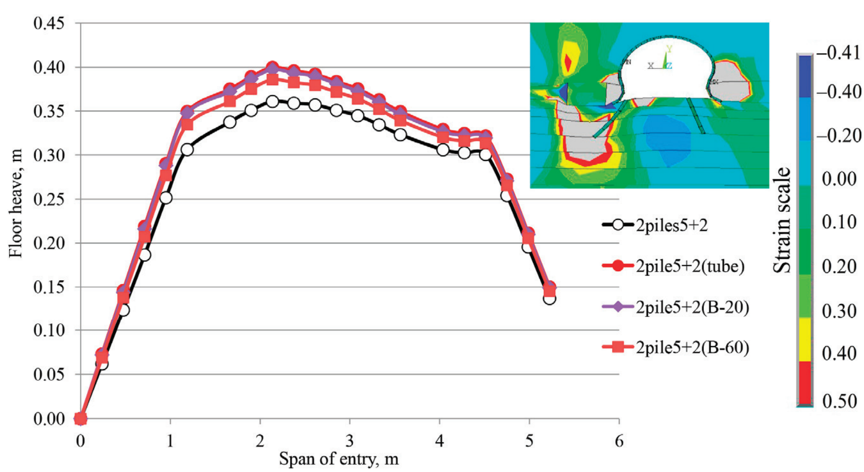

Figure 16. The entry floor heave after pile installation at the 3rd simulation stage with different schemes.

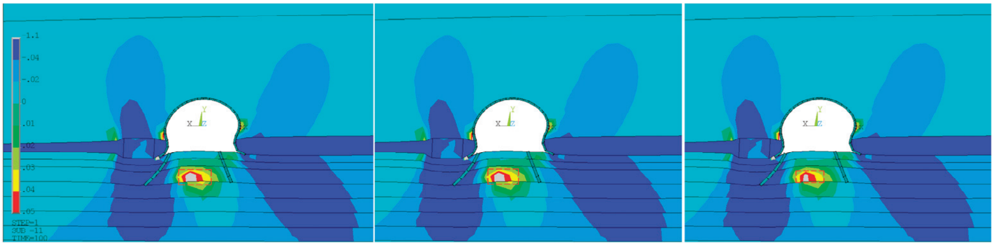

(**a**) (**b**) (**c**)

Figure 17. The vertical strain distributions around the gob-side entry retaining after pile installation with schemes (**a**) 2pile 5+2(tube); (**b**) 2pile 5+2(B-20); (**c**) 2pile 5+2(B-60).

Table 4. Comparison of the costs of materials for different types of piles with scheme 2pile 5+2.

Scheme	Pile Type	Class of Concrete in the Pile	Cost of Concrete, EUR	Cost of Tube, EUR	Cost of Longitudinal and Lateral Reinforcement, EUR	Total Cost, EUR	Maximal Floor Heave, mm
2pile 5+2	Steel pile	B-60	9.35	116.81		126.16	361
2pile 5+2(tube)	Steel tube	-	-	116.81		116.81	399
2pile 5+2(B-20)	Filling pile	B-20	8.48	-	25.92	34.40	397
2pile 5+2(B-40)	Filling pile	B-40	8.78	-	25.92	34.70	389
2pile 5+2(B-60)	Filling pile	B-60	9.35	-	25.92	35.27	386

Filling piles have a minimal cost, which gives them an advantage. So, with the 2pile 5+2(B-60) scheme, the cost of the pile is 3.57 times less than with the 2pile 5+2 scheme. Installation of the filling pile is easier, since the weight of reinforcement elements is less, which also reduces transportation costs. In addition, the installation of reinforcement of filling piles, unlike the installation of tubes, can be carried out without significant labor costs. Thus, filling piles are more beneficial for floor heave control. The design of the proposed pile is shown in Figure 15c. Optimization of pile reinforcement design requires additional research and is not studied in this article.

4.3. Filling Pile Floor Support Scheme

The analysis of monitoring of gob-side entry retaining shows that the main gateroad stability problem is dramatic floor heave. Therefore, the modification of the current support system of the entry is necessary.

Based on numerical simulation results, it was found that the most effective floor support scheme is the 2pile 5+2 (B-60) scheme. Additional installation of piles in the original support system was proposed. The rationale for the effectiveness of this scheme is presented in the previous section of this paper. Figure 18 shows the proposed design of the support scheme. Drilling of boreholes for piles into the entry floor can be carried out with a machine for drilling degassing wells. SBG-1M is an example of such a machine.

According to the authors, the proposed anti-shear pile technology does not require significant investment. Investments are required to purchase an SBG-1M-type drilling machine. The approximate cost of such equipment in Ukraine, taking into account transportation costs, is EUR 15,000. Taking into account the service life, residual value, average monthly depreciation, and downtime, the depreciation expense will be EUR 205/month. The machine repairs and maintenance expenses, taking into account planned repairs, are 0.012 man-hours. Taking into account wages in Ukraine, monthly maintenance expenses will be EUR 119/month. Electric energy consumption and the salary of a worker operating the drilling machine depend on local wages and the quantities of drilling work. Three workers per shift are involved in the implementation of the proposed technology.

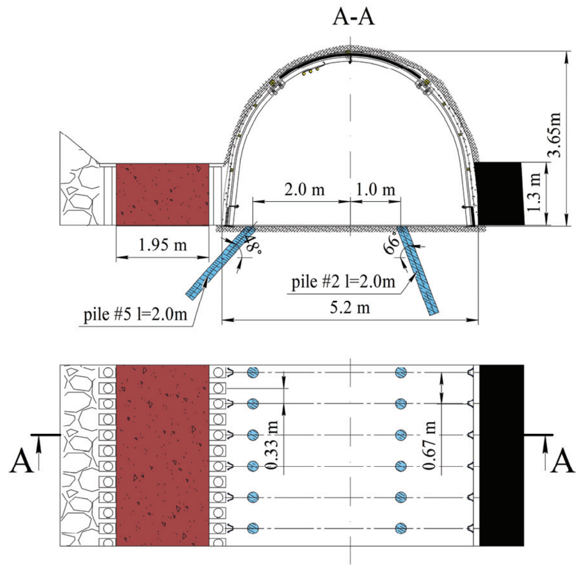

Figure 18. Design of support scheme.

Pile installation must be carried out after the roadway excavation stage, and before the longwall mining stage. Therefore, the production schedule of the working face does not affect the schedule of pile installation. The estimated pace of installation of piles in a gateroad in a three-shift operating mode is 819 m/month.

5. Conclusions

This study was focused on floor heave evolution and its restriction in gob-side entry retaining. Floor heave control with anti-shear pile technology was studied. Numerical simulation by ANSYS 17.2 software was used for the stress–strain analysis of the surrounding rock. As a result, a floor heave mechanism was proposed. Based on the analysis of the floor heave causes, perspective schemes for immediate floor reinforcement were proposed and a study of their effectiveness was conducted. Based on the results of this investigation, the following conclusions can be drawn:

(1) The transformation of high vertical stresses, which arise in the entry floor underneath the filling wall and coal seam body, into horizontal stresses starts the floor heave process. Increased vertical stresses under the filling wall and coal seam body cause the dilatancy expansion of rocks in the horizontal direction. As a result, a zone of horizontal compression underneath the entry span occurs. Rocks within this zone, in the process of dilatancy expansion to relieve stress, displace towards the entry cavity. This leads to the delamination of rocks in the vertical direction and uplift of the entry contour. Between the zone of rock uplift under the entry span and the zones of rock subsidence underneath the filling wall body and coal seam body, high-shear zones arise, in which vertical stresses are transformed into horizontal ones. The rock failure in these zones complicates the floor heave mechanism described above.

(2) The ways to control floor heave are (1) restricting stress transformation in the entry floor; (2) increasing the bearing capacity of the immediate floor to counteract rock dilatation and delamination. A floor heave control method with anti-shear pile installation was proposed. The numerical simulation results confirmed the efficiency of pile installation. This makes it possible to significantly reduce the floor heave and the size of the zone of horizontal post-peak strain. As a result of numerical simulation, the most effective scheme (2pile 5+2) was found. A technical and economic comparison of different types of piles was carried out to find the most economical and simple solutions for the practical

implementation of this scheme. Analysis of the numerical simulation results and the cost comparison of different types of piles shows that filling piles are the most effective ones. The cost of filling piles is more than 3.5 times less than the steel pile cost. In addition, the installation of filling piles does not require significant labor costs; the weight of the reinforcement used in this scheme is less than the weight of tubes in analog piles, which also reduces transportation costs. The implementation of the proposed floor heave control method with anti-shear piles leads to a significant reduction in heaving in gob-side entry retaining. The results of this study can be used to design a support system in gob-side entry retaining.

(3) Anti-shear pile technology is at the stage of elaboration and justification of parameters. In situ tests are planned for the future. Therefore, the above-described effect is based only on the results of numerical simulation so far. Further research will aim to study the effectiveness of the proposed floor heave control method in situ in coal mines. The best design for filling piles will also be found.

Author Contributions: Conceptualization, I.S. and S.S.; methodology, I.S. and O.I.; software, I.S. and K.S.; validation, I.S., K.S., K.Z. and A.Z.; formal analysis, S.S.; investigation, I.S.; resources, K.Z. and A.Z.; writing—original draft preparation, I.S.; writing—review and editing, K.S. and S.S.; visualization, O.I.; supervision, I.S.; project administration, I.S.; funding acquisition, K.S., K.Z. and A.Z. All authors have read and agreed to the published version of the manuscript.

Funding: This research received no external funding.

Data Availability Statement: The original contributions presented in this study are included in the article; further inquiries can be directed to the corresponding author.

Acknowledgments: The authors are grateful to the administration of Donetsk National Technical University and AGH University of Science and Technology for supporting this research.

Conflicts of Interest: The authors declare no conflicts of interest.

References

1. Yang, X.; Huang, R.; Yang, G.; Wang, Y.; Cao, J.; Liu, J.; He, M. Validation study of no-pillar mining method without advance tunneling: A case study of a mine in China. *Energy Sci. Eng.* **2021**, *9*, 1761–1772. [CrossRef]
2. He, M.; Wang, Q.; Wu, Q. Innovation and future of mining rock mechanics. *J. Rock Mech. Geotech. Eng.* **2021**, *13*, 1–21. [CrossRef]
3. Chen, A. Width Design of Small Coal Pillar of Gob-Side Entry Driving in Soft Rock Working Face and Its Application of Zaoquan Coal Mine. *Adv. Civ. Eng.* **2021**, *2021*, 9999957. [CrossRef]
4. Wang, D.; Li, S.; Wang, Q.; Li, W.; Wang, F.; Wang, H.; Peng, P.; Ruan, G. Experimental study of reasonable coal pillar width in fully mechanized top coal caving face of deep thick coal seam. *Chin. J. Rock Mech. Eng.* **2014**, *33*, 539–548.
5. Sakhno, I.; Sakhno, S.; Kamenets, V. Stress environment around head entries with pillarless gobside entry retaining through numerical simulation incorporating the two type of filling wall. *IOP Conf. Ser. Earth Env. Sci.* **2022**, *1049*, 012011. [CrossRef]
6. Xie, S.R.; Wang, E.; Chen, D.D.; Li, H.; Jiang, Z.S.; Yang, H.Z. Stability analysis and control technology of gob-side entry retaining with double roadways by flling with high-water material in gently inclined coal seam. *Int. J. Coal Sci. Technol.* **2022**, *9*, 52. [CrossRef]
7. Ning, J.; Wang, J.; Bu, T.; Hu, S.; Liu, X. An innovative support structure for gob-side entry retention in steep coal seam mining. *Minerals* **2017**, *7*, 75. [CrossRef]
8. Kong, D.; Pu, S.; Cheng, Z.; Wu, G.; Liu, Y. Coordinated Deformation Mechanism of the Top Coal and Filling Body of Gob-Side Entry Retaining in a Fully Mechanized Caving Face. *Int. J. Geomech.* **2021**, *21*, 04021030. [CrossRef]
9. He, M.; Song, S.; Wang, Q.; Yang, H.; Qi, H.; Guo, Z. Theory of longwall mining by using roof cuting shortwall team and 110 method—The third mining science and technology reform. *Coal Sci. Technol. Mag.* **2017**, *1*, 13. [CrossRef]
10. Wang, M.; Xu, Y.L.; Xu, Q.Y.; Shan, C.F.; Li, Z.H.; Nan, H.; Li, Y.F.; Liu, H.L.; Chu, T.X. Stability control of overburden and coal pillars in the gob-side entry under dynamic pressure. *Int. J. Rock Mech. Min. Sci.* **2023**, *170*, 105490. [CrossRef]
11. Zhang, Z.; Shimada, H.; Sasaoka, T.; Hamanaka, A. Stability Control of Retained Goaf-Side Gateroad under Different Roof Conditions in Deep Underground Y Type Longwall Mining. *Sustainability* **2017**, *9*, 1671. [CrossRef]
12. Hu, J.; He, M.; Wang, J.; Ma, Z.; Wang, Y.; Zhang, X. Key Parameters of Roof Cutting of Gob-Side Entry Retaining in a Deep Inclined Thick Coal Seam with Hard Roof. *Energies* **2019**, *12*, 934. [CrossRef]
13. Xu, Y.; Chen, J.; Bai, J. Control of floor heaves with steel pile ingob-side entry retaining. *Int. J. Min. Sci. Technol.* **2016**, *26*, 527–534. [CrossRef]
14. Hao, J.; Zhang, P.; Song, Y.; Liu, H.; Shi, Y.; Liu, J.; Lu, G. Research on Pillarless Mining by Gob-Side Caving under Soft Rock Roof Conditions: A Case Study. *Appl. Sci.* **2023**, *13*, 2816. [CrossRef]

15. Gong, P.; Ma, Z.; Ni, X.; Zhang, R.R. Floor heave mechanism of gob-side entry retaining with fully-mechanized backfilling mining. *Energies* **2017**, *10*, 2085. [CrossRef]
16. Li, Z.; Zhang, Y.; Ma, Q.; Zheng, Y.; Song, G.; Yan, W.; Zhang, Y.; Hu, L. The floor heave mechanism and control technology of gob-side entry retaining of soft rock floor. *Sustainability* **2023**, *15*, 6074. [CrossRef]
17. Yu, G.; Wang, J.; Hu, J.; Zhu, D.; Sun, H.; Ma, X.; Ming, W.; Li, W. Innovative control technique for the floor heave in goaf-side entry retaining based on pressure relief by roof cutting. *Math. Probl. Eng.* **2021**, *2021*, 7163598. [CrossRef]
18. Małkowski, P.; Ostrowski, Ł.; Stasica, J. Modeling of floor heave in underground roadways in dry and waterlogged conditions. *Energies* **2022**, *15*, 4340. [CrossRef]
19. Li, C.; Zuo, J.; Chunchan, W.; Xu, X. Fracture Development at Laminated Floor Layers Under Longwall Face in Deep Coal Mining. *Nat. Resour. Res.* **2020**, *29*, 3857–3871. [CrossRef]
20. Guo, G.; Kang, H.; Qian, D.; Gao, F.; Wang, Y. Mechanism for Controlling Floor Heave of Mining Roadways Using Reinforcing Roof and Sidewalls in Underground Coal Mine. *Sustainability* **2018**, *10*, 1413. [CrossRef]
21. Kang, Y.; Liu, Q.; Gong, G.; Wang, H. Application of a combined support system to the weak floor reinforcement in deep underground coal mine. *Int. J. Rock Mech. Min. Sci.* **2014**, *71*, 143–150. [CrossRef]
22. Mo, S.; Ramandi, H.L.; Oh, J.; Masoumi, H.; Canbulat, I.; Hebblewhite, B.; Saydam, S. A new coal mine floor rating system and its application to assess the potential of floor heave. *Int. J. Rock Mech. Min.* **2020**, *128*, 104241. [CrossRef]
23. Zhang, Z.Y.; Shimada, H. Numerical study on the effectiveness of grouting reinforcement on the large heaving floor of the deep retained goaf-side gateroad: A case study in China. *Energies* **2018**, *11*, 1001. [CrossRef]
24. Chen, Y.; Bai, J.B.; Yan, S.; Xu, Y.; Wang, X.Y.; Ma, S. Control mechanism and technique of floor heave with reinforcing solid coal side and floor corner in gob-side coal entry retaining. *Int. J. Min. Sci. Technol.* **2012**, *22*, 841–845. [CrossRef]
25. Gao, F.; Stead, D.; Kang, H.; Wu, Y. Discrete element modelling of deformation and damage of a roadway driven along an unstable goaf—A case study. *Int. J. Coal Geol.* **2014**, *127*, 100–110. [CrossRef]
26. Faria Santos, C.; Bieniawski, Z.T. Floor design in underground coal mines. *Rock Mech. Rock Eng.* **1989**, *22*, 249–271. [CrossRef]
27. Mo, S.; Sheffield, P.; Corbett, P.; Ramandi, H.L.; Oh, J.; Canbulat, I.; Saydam, S. A numerical investigation into floor buckling mechanisms in underground coal mine roadways. *Tunn. Undergr. Space Technol.* **2020**, *103*, 103497. [CrossRef]
28. Zhai, W.; He, F.; Xu, X.; Lv, K.; Li, L.; Song, J. Floor heave mechanism in water-rich soft rock roadways and a DS-IBA control approach. *Geomat. Nat. Hazards Risk* **2022**, *13*, 2107–2123. [CrossRef]
29. Wang, C.; Chen, X.Y.; Zhang, J.D.; Wu, Y.P. Stability Mechanism and Repair Method of U-Shaped Steel Reverse Arch Support in Soft Floor Roadway. *Adv. Civ. Eng.* **2020**, *2020*, 8814365. [CrossRef]
30. Zheng, W.; Zhao, Y.; Bu, Q. The coupled control of floor heave based on a composite structure consisting of bolts and concrete antiarches. *Math. Probl. Eng.* **2018**, *2018*, 3545423. [CrossRef]
31. Zhai, X.X.; Qin, L.T.; Chen, C.Y. Combined Supporting Technology of Anchoring and Grouting and Floor Relief in Deep Chamber of Belt Conveyor. *Chin. J. Undergr. Space Eng.* **2017**, *5*, 67. [CrossRef]
32. Zhu, L.; Liu, C.; Gu, W.; Yuan, C.; Wu, Y.; Liu, Z.; Song, T.; Sheng, F. Research on Floor Heave Mechanisms and Control Technology for Deep Dynamic Pressure Roadways. *Processes* **2023**, *11*, 467. [CrossRef]
33. Wang, D.; Zheng, Y.; He, F.; Song, J.; Zhang, J.; Wu, Y.; Jia, P.; Wang, X.; Liu, B.; Wang, F.; et al. Mechanism and Control of Asymmetric Floor Heave in the Gob-Side Coal Roadway under Mining Pressure in Extra-Thick Coal Seams. *Energies* **2023**, *16*, 4948. [CrossRef]
34. Wei, W.; Zhang, G.; Li, C.; Zhang, W.; Shen, Y. Mechanism and Control of Asymmetric Floor Heave in Deep Roadway Disturbed by Roof Fracture. *Sustainability* **2023**, *15*, 6357. [CrossRef]
35. Zhang, D.; Bai, J.; Yan, S.; Wang, R.; Meng, N.; Wang, G. Investigation on the Failure Mechanism of Weak Floors in Deep and High-Stress Roadway and the Corresponding Control Technology. *Minerals* **2021**, *11*, 1408. [CrossRef]
36. Qin, D.; Wang, X.; Zhang, D.; Chen, X. Study on Surrounding Rock-Bearing Structure and Associated Control Mechanism of Deep Soft Rock Roadway Under Dynamic Pressure. *Sustainability* **2019**, *11*, 1892. [CrossRef]
37. Kang, H.; Wang, J.; Lin, J. Case studies of rock bolting in coal mine roadways. *Chin. J. Rock Mech. Eng.* **2010**, *29*, 649–664.
38. Yang, J.; Shi, H.; Gan, Q.I. Research on mechanism for floor heave control in the roadway by base-angel-bolt and its type selection test. *J. Min. Saf. Eng.* **2016**, *33*, 643–648.
39. Kang, X.; Guo, D.; Lu, Z. Mechanism of roadway floorheave controlled by floor corner pile in deep roadway underhigh horizontal stress. *Adv. Civ. Eng.* **2021**, *2021*, 6669233. [CrossRef]
40. Guo, D.; Kang, X.; Lu, Z.; Chen, Q. Mechanism and Control of Roadway Floor Rock Burst Induced by High Horizontal Stress. *Shock Vib.* **2021**, *2021*, 6745930. [CrossRef]
41. Sakhno, I.; Isayenkov, O.; Rodzin, S. Local reinforcing of footing supported in the destroyed rock massif. *Min. Miner. Depos.* **2017**, *11*, 9–16. [CrossRef]
42. Małkowski, P.; Ostrowski, Ł.; Bednarek, Ł. The effect of selected factors on floor upheaval in roadways-in situ testing. *Energies* **2020**, *13*, 5686. [CrossRef]
43. Liu, H.; Zhang, B.; Li, X.; Liu, C.; Wang, C.; Wang, F.; Chen, D. Research on roof damage mechanism and control technology of gob-side entry retaining under close distance gob. *Eng. Fail. Anal.* **2022**, *138*, 106331. [CrossRef]

44. Liu, Q.; Fu, Q.; Yang, K.; Wei, Q.; Liu, H.; Wu, H. Geomechanical Modeling and Inversion Analysis of the *in-situ* Stress Field in Deep Marine Shale Formations: A Case Study of the Longmaxi Formation, Dingshan Area. *China Front. Earth Sci.* **2022**, *9*, 808535. [CrossRef]
45. Sakhno, I.G.; Molodetskyi, A.V.; Sakhno, S.V. Identification of material parameters for numerical simulation of the behavior of rocks under true triaxial conditions. *Naukovyi Visnyk NHU* **2018**, *5*, 48–53. [CrossRef]
46. Zhu, B.; Weifeng, K.; Jiami, X.; Yanjun, S. Numerical simulation research of construction method for shallow buried large section tunnel. *Open Civ. Eng. J.* **2016**, *10*, 578–597. [CrossRef]
47. Hoek, E.; Carranza-Torres, C.; Corkum, B. Hoek-Brown failure criterion—2002 edition. In Proceedings of the 5th North American Rock Mechanics Symposium and the 17th Tunnelling Association of Canada Conference, NARMS-TAC, Toronto, ON, Canada, 7–10 July 2002; pp. 267–271.
48. Hoek, E.; Diederichs, M. Empirical estimates of rock mass modulus. *Int. J. Rock Mech. Min. Sci.* **2006**, *43*, 203–215. [CrossRef]
49. Bieniawski, Z.T. *Engineering Rock Mass Classifications*; Wiley: New York, NY, USA, 1989.
50. Sakhno, I.; Sakhno, S. Numerical studies of floor heave control in deep mining roadways with soft rocks by the rock bolts reinforcement technology. *Adv. Civ. Eng.* **2023**, *2023*, 2756105. [CrossRef]
51. Li, J.; Huang, Y.; Zhai, W.; Li, Y.; Ouyang, S.; Gao, H.; Li, W.; Ma, K.; Wu, L. Experimental study on acoustic emission of confined compression of crushed gangue under different loading rates: Disposal of gangue solid waste. *Sustainability* **2020**, *12*, 3911. [CrossRef]
52. Zhou, H.; Zhang, C.; Li, Z.; Hu, D.; Hou, J. Analysis of mechanical behavior of soft rocks and stability control in deep tunnels. *J. Rock Mech. Geotech. Eng.* **2014**, *6*, 219–226. [CrossRef]
53. Josh, M.; Esteban, L.; Delle Piane, C.; Sarout, J.; Dewhurst, D.N.; Clennell, M.B. Laboratory characterisation of shale properties. *J. Pet. Eng.* **2019**, *88–89*, 107–124. [CrossRef]
54. Almisned, O.A.; Alqahtani, N. Rock analysis to characterize Saudi soft sandstone rock. *J. Petrol. Explor. Prod. Technol.* **2021**, *11*, 2381–2387. [CrossRef]
55. Liu, Q.; Liang, B.; Sun, W.; Zhao, H. Experimental study on the difference of shale mechanical properties. *Adv. Civ. Eng.* **2021**, *2021*, 6677992. [CrossRef]

applied sciences

MDPI

Article

Reinforcement Learning Based Speed Control with Creep Rate Constraints for Autonomous Driving of Mining Electric Locomotives

Ying Li [1], Zhencai Zhu [1,*] and Xiaoqiang Li [2]

[1] School of Mechanical and Electrical Engineering, China University of Mining and Technology, Xuzhou 221116, China; lycumt@cumt.edu.cn
[2] School of Electrical Engineering, China University of Mining and Technology, Xuzhou 221116, China; xiaoqiangli@cumt.edu.cn
* Correspondence: zhuzhencaijs@163.com

Abstract: The working environment of mining electric locomotives is wet and muddy coal mine roadway. Due to low friction between the wheel and rail and insufficient utilization of creep rate, there may be idling or slipping between the wheels and rails of mining electric locomotives. Therefore, it is necessary to control the creep rate within a reasonable range. In this paper, the autonomous control algorithm for mining electric locomotives based on improved ε-greedy is theoretically proven to be convergent and effective firstly. Secondly, after analyzing the contact state between the wheel and rail under wet and slippery road conditions, it is concluded that the value of creep rate is an important factor affecting the autonomous driving of mining electric locomotives. Therefore, the autonomous control method for mining electric locomotives based on creep control is proposed in this paper. Finally, the effectiveness of the proposed method is verified through simulation. The problem of wheel slipping and idling caused by insufficient friction of mining electric locomotives in coal mining environments is effectively suppressed. Autonomous operation of vehicles with optimal driving efficiency can be achieved through quantitative control and utilization of the creep rate between wheels and rails.

Keywords: autonomous driving; creep rate; mining electric locomotive; reinforcement learning; speed control

Citation: Li, Y. ; Zhu, Z.; Li, X. Reinforcement Learning Based Speed Control with Creep Rate Constraints for Autonomous Driving of Mining Electric Lovomotives. *Appl. Sci.* **2024**, *14*, 4499. https://doi.org/10.3390/app14114499

Academic Editor: Krzysztof Skrzypkowski, René Gómez, Fhatuwani Sengani, Derek B. Apel, Faham Tahmasebinia and Jianhang Chen

Received: 18 April 2024
Revised: 22 May 2024
Accepted: 23 May 2024
Published: 24 May 2024

1. Introduction

Mining electric locomotives have the transportation function of materials, equipment, and people in roadway. Safe driving of mining electric locomotives is crucial. However, the method of underground mining is often used in the Chinese coal mining industry [1]. In deep underground confined spaces, there are unfavorable conditions for driving in coal mine roadway, such as slippery, muddy, dusty, foggy, and complex human behavior, which lead to frequent accidents. Reducing personnel participation and ensuring the safe operation of production and transportation equipment are necessary to ensure the safety production of coal mines. At present, the intelligent development of coal mine equipment has become an inevitable trend [2]. Unmanned transportation of coal mine equipment can fundamentally solve the problem of personnel participation and reduce casualties in the event of inevitable accidents. We have conducted relevant research on autonomous mining electric locomotives [3]. The mining electric locomotive has achieved functions based on Reinforcement Learning (RL) and improved ε-greedy such as autonomous and efficient operation on speed limited sections, maintaining a safe distance from vehicle in front, and avoiding obstacles.

However, problems such as slipping of autonomous vehicles and wheel idling caused by slippery roadway in deep mines have not been addressed in a targeted manner. Manually driven mining electric locomotives rely on the driver's experience to sprinkle sand to increase wheel rail friction. But this method is a remedial measure taken when slipping/idling occurs during driving. And there is no quantitative evaluation standard for actions judged by human subjectivity. Moreover, actions based on human subjective judgment cannot be used as a quantifiable evaluation criterion applicable to machine autonomous decision-making. In the autonomous driving control process of mining electric locomotives, it is necessary to make decisions that can actively control the interaction between wheels and rails to prevent slipping, idling, and other phenomena caused by external environment.

For rail vehicles, the destruction of the adhesion between the wheel and rail is the basic reason of wheel slip/idling [4]. One of the reasons for the traction and braking forces of wheelsets is the presence of contact and friction between the wheel and rail [5]. This kind of wheel rail interaction force is not pure friction, but a phenomenon called creep caused by deformation after wheel rail contact [6]. Reasonably utilizing the creep rate can improve the efficiency and safety of vehicle operation [7]. Nowadays, to prevent train wheel slipping or idling, scholars have conducted research on algorithms related to adhesion control. According to different control methods, adhesion control algorithms are generally divided into re-adhesion control and optimized adhesion control [8]. Re-adhesion control is a method that can quickly adjust the motor torque to achieve balance with the current adhesion conditions, and avoid wheel idling when determining whether the locomotive's wheels are idling/slipping. The research on this method is relatively mature [9–11], but it belongs to passive adhesion control method, with a low adhesion utilization rate and long algorithm response time. The purpose of optimizing adhesion control is to achieve the peak point of the optimal adhesion utilization, which is of great significance for the operation control of trains under wet, muddy and emergency braking conditions. Mehmet Ali Çimen et al. [12] analyzed the input and output phase shift dynamic characteristics of the traction system. They also proposed an adaptive control method that effectively controls the adhesion utilization rate of the traction system. Song Wang et al. [13] proposed an adhesion control method based on optimal torque search for high-speed trains, which can achieve stable operation of trains in the optimal adhesion state under changes of track surface and high-speed driving conditions, effectively reducing the idle rate of the wheel and improving train adhesion utilization. Shuai Zhang et al. [14] proposed a sliding mode control method, which used recursive least squares method based on enhanced forgetting factor to solve the problem of wheel anti lock on heavy-duty trains. This algorithm can obtain the optimal creep rate and construct a PI closed-loop observer to estimate the unmeasured adhesion torque, enabling the locomotive to adjust to the optimal creep rate when the contact of wheel and rail changes. The optimized adhesion control algorithm can suppress the sliding and idling of the wheel. However, the maximum adhesion point in the contact area of wheel and rail is at the junction of creep and sliding, making it difficult to ensure that the contact state of wheel and rail is always creep during the actual control process. Therefore, this method still belongs to passive adhesion control. In addition, there are certain differences in the utilization of adhesion capacity among the axles of the train. The existing methods have insufficient control accuracy, as most of the adhesive characteristic curves relied on are empirical formulas obtained through experiments.

Therefore, this paper proposes a creep control method for mining electric locomotives based on RL. This method converts the impact of complex driving environments on mining electric locomotives into reward feedback values obtained by the electric locomotives from the environment. The impact of creep conditions that are difficult to quantify and evaluate on vehicles has been particularly considered in this method. The optimal range of creep rate is tried to achieve after training the mining electric locomotive to adjust the driving torque of the wheelset in this method. To achieve maximum driving efficiency under safe operating conditions is the goal of this method.

The overall structure of this paper is shown in Figure 1. Firstly, the autonomous control method of mining electric locomotives based on improved ε-greedy is analyzed from the theoretical perspective. By changing environmental variables and replicating algorithms, the important factor affecting the operation of mining electric locomotive on wet and slippery tracks is identified. Secondly, a mining electric locomotives autonomous control algorithm based on creep control is proposed, which can effectively improve the safety and reliability of autonomous driving of mining electric locomotives. Finally, based on the three-dimensional dynamic model of mining electric locomotives modeled using Simpack, the feasibility of the proposed algorithm is verified using a multi software (PyCharm2021, MATLAB R2014b and Simpack 2018) co-simulation platform.

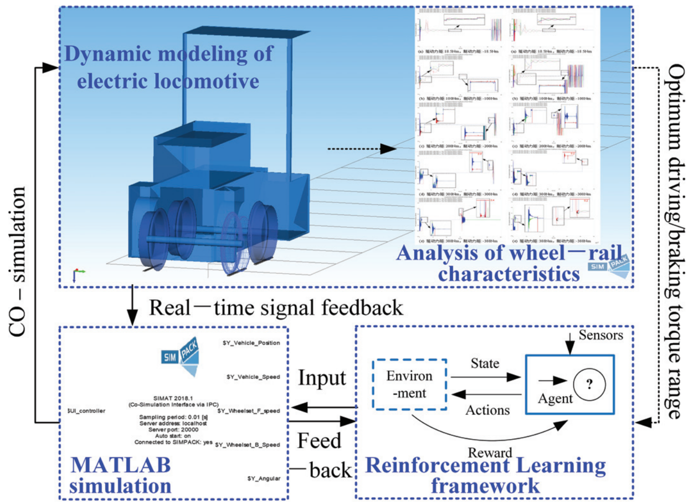

Figure 1. The framework of creep control method for autonomous driving of the mining electric locomotive.

Compared to [3], this paper identifies the creep rate, a key factor affecting the autonomous operation of mining electric locomotives, through theoretical verification of the algorithm and practical analysis of operating conditions. This paper also proposes a creep control method suitable for mining electric locomotives, which improves the accuracy of autonomous operation control for mining electric locomotives.

2. Analysis of Autonomous Control Algorithm for Mining Electric Locomotives

In this section, an important factor is found through theoretical analysis and simulation, which was not particularly considered in the previous algorithm design but affected the autonomous driving of mining electric locomotives. First, in reproducing the autonomous control algorithm of mining electric locomotives based on RL, we find that changing the friction between the wheels and rails can lead to poor control performance. Second, this algorithm has been theoretically proven to be reasonable and convergent. Mining electric locomotives can stably achieve autonomous driving under the control of this algorithm. Third, the relationship between creep rate and adhesion coefficient of rail vehicles is analyzed. It is necessary to take the creep rate between the wheel and rail into the autonomous control algorithm. Finally, we conclude that the improved control objective is to achieve the optimal control range of creep rate.

2.1. Problem Formulation

As shown in Figure 2, RL was adopted to solve the autonomous control problem of mining electric locomotives, and the ε-greedy strategy was improved to balance the relationship of exploration and exploitation better in reference [3]. This control method is reproduced in this paper on the condition that the friction of wheel and rail is adjusted from 0.4 to 0.3. Under this working condition, the autonomous control state curve of the mining electric locomotive shown in Figure 3 is obtained. It can be seen that mining electric locomotive operates safely and efficiently on speed limited sections, and can maintain a safe distance from obstacles when using the autonomous control method based on the improved ε-greedy strategy. However, it is found that the mining electric locomotive is unable to control the acceleration duration correctly when accelerating and reaching the maximum speed limit, and the running speed of the electric locomotive would slightly exceed the maximum speed limit. Moreover, the mining electric locomotive cannot control the deceleration duration to reach the maximum speed on the next speed limit section when decelerating.

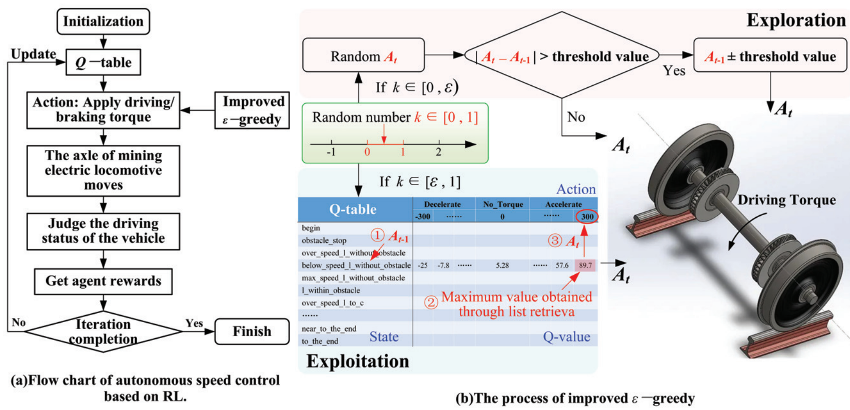

Figure 2. Improved ε-greedy strategy [3].

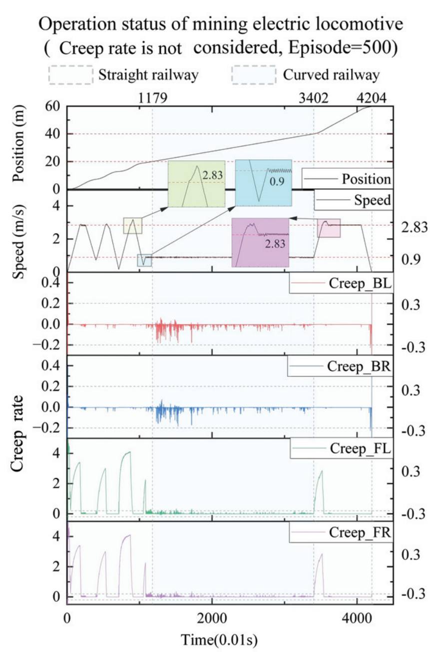

Figure 3. The autonomous control state curve of the mining electric locomotive without creep control.

2.2. Theoretical Analysis

In order to find out the reasons for the problem above, we first verify whether the algorithm structure is designed reasonably from the perspective of algorithm theory. If the structural design is reasonable, the results of the algorithm will tend to converge with the training process of the agent. In this section, the convergence of the algorithm is demonstrated from two aspects: RL and improved ε-greedy strategy.

2.2.1. Reinforcement Learning

RL is a method for studying how an agent maximizes its reward in a complex and uncertain environment [15,16]. Figure 4 shows the process of RL. The agent interacts with the environment, obtains the current state S_t and reward R_t at moment t, and takes action A_t based on certain strategies. After the agent takes action A_t, the environment obtains the latest state S_{t+1} and reward R_{t+1} at moment t + 1, and passes them to the agent. This interaction process can be represented by the Markov Decision Process (MDP).

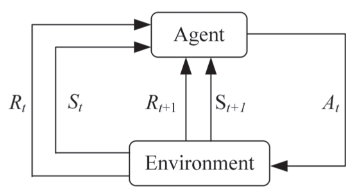

Figure 4. Reinforcement Learning.

The MDP adds a decision layer to the commonly used Markov Process/Markov Reward Process, which is the action a shown in the Figure 5. This means that when the agent is in the state S_t at time t, it must first decide on a specific action a to take in order to reach the middle layer, which is the black node in the diagram. After reaching the black node, the state of the agent at the moment t+1 also depends on the probability distribution.

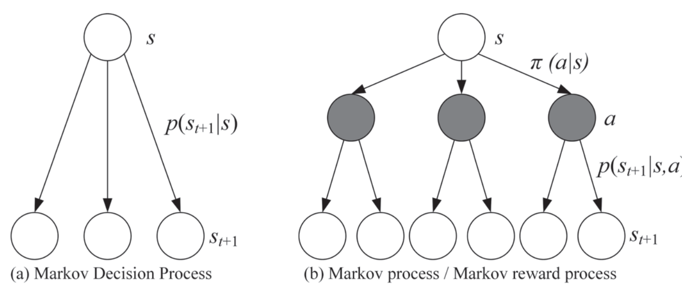

Figure 5. The Markov Decision Process and Markov Process/Markov Reward Process.

RL, as a trial and error learning method, continuously repeats the above interaction process between agents and the environment to find a mapping that can maximize the cumulative sum G_t of benefits R_t over time.

$$G_t = \sum_{i=0}^{T-i-1} \gamma^i R_{t+i+1}. \tag{1}$$

where, T is the total time, γ is the discount factor.

However, the sum of cumulative returns, also known as value return G_t, is not easily obtained. To solve this problem, researchers propose two value functions for estimating the sum of cumulative returns: the state value function $V_\pi(s)$ and the action value function $Q_\pi(s,a)$. The state value function $V_\pi(s)$ is the expected value of the sum of the reward functions under π strategy and s state. The action value function $Q_\pi(s,a)$ represents the expected value of the sum of the benefit functions of action a under the π strategy and s state.

$$V_\pi(s) = \mathbb{E}_\pi[G_t|S_t = s] = \sum_{a\in\mathcal{A}} \pi(a|s) \cdot Q_\pi(s,a). \tag{2}$$

$$Q_\pi(s,a) = \mathbb{E}_\pi[G_t|S_t = s, A_t = a] = \sum_{r,s_{t+1}} p(s_{t+1}, r|s,a) \cdot [R + \gamma V_\pi(s_{t+1})]. \tag{3}$$

where, $\mathcal{A}$ is the set of action a.

According to the value function, the Bellman equation is derived as follows:

$$V(s) = R(s) + \gamma \sum_{s_{t+1} \in \mathcal{S}} p(s_{t+1}|s) \cdot V(s_{t+1}). \tag{4}$$

where, $\mathcal{S}$ is the set of state s.

The Bellman equation for the Q-function is as follows:

$$Q(s,a) = R(s,a) + \gamma \max_{a_{t+1}} Q(s_{t+1}, a_{t+1}). \tag{5}$$

We adopt Theorem - Cauchy's convergence Test to verify the convergence of RL we design to apply in the field of autonomous control of mining electric locomotives. The specific steps to prove the convergence of RL are detailed in Appendix A.

The RL algorithm focuses on the feedback information obtained by the agent from the environment for decision-making, without relying on the agent and the environment model. This method does not require modeling of the intelligent agent, directly avoiding control bias caused by inaccurate modeling. In addition, this algorithm idea enables the algorithm proposed in this paper to be applicable to different types of mining electric locomotives driving on different road sections. So this method is universally applicable in complex mine conditions. The method proposed in this paper is applied in the actual field based on the results of laboratory simulation training, which greatly reduces the debugging time of the algorithm in the actual application process.

2.2.2. Improved ε-Greedy

In reference [3], in order to balance the relationship between exploration and exploitation, the traditional ε-greedy algorithm was improved by changing the value of ε in Formula (6) to the value of ε in Formula (7).

$$\varepsilon_1 = (\varepsilon_{\text{initial}} - \varepsilon_{\text{final}}) \cdot (1 - episode/max\_episodes) \tag{6}$$

$$\varepsilon_2 = \begin{cases} (\varepsilon_{\text{initial}} - \varepsilon_{\text{final}}) \cdot (0.5 + \sqrt{0.25 - (episode/max\_episodes)^2}), & (episode/max\_episodes) \in [0, 0.5] \\ (\varepsilon_{\text{initial}} - \varepsilon_{\text{final}}) \cdot (0.5 - \sqrt{0.25 - (1 - episode/max\_episodes)^2}), & (episode/max\_episodes) \in (0.5, 1] \end{cases} \tag{7}$$

For the improved ε-greedy, the selection of actions follows the following rules:

$$a_t = \begin{cases} \operatorname{argmax}_a Q(s_{t+1}, a), for \quad probability \quad 1 - \varepsilon_t \\ random \quad from \quad \mathcal{A}, for \quad probability \quad \varepsilon_t \end{cases} \tag{8}$$

We can obtain the probability distribution of whether an action is the optimal action:

$$\pi(a|s) = \begin{cases} 1 - \varepsilon + \frac{\varepsilon}{|\mathcal{A}(s)|}, if \ a = \operatorname{argmax}_a Q(s,a) \\ \frac{\varepsilon}{|\mathcal{A}(s)|}, if \ a \neq \operatorname{argmax}_a Q(s,a) \end{cases} \tag{9}$$

The specific steps to prove the convergence of improved ε-greedy strategy are detailed in Appendix B.

In summary, RL and improved ε-greedy strategy applied to autonomous control of mining electric locomotives is convergent. The autonomous control method for mining electric locomotives based on the improved ε-greedy strategy is feasible.

2.3. Adhesion and Creep

After the analysis, we will focus on the constraints considered in the algorithm design process. When designing the algorithm, conditions are taken into consideration, such as speed limits, road obstacles, and safe following of mining electric locomotives. However, the road surface of the coal mine roadway is very slippery and muddy. The contact condition between the wheels and rails is also one of the factors that needs to be carefully considered.

Two conditions must be met simultaneously to enable rail vehicles to run along the track [17]. One is that the rotating torque is applied to the moving wheel, and the other is that the contact between the moving wheel and the steel rail has a frictional effect. As shown in Figure 6, the moving wheel is in contact with the track due to the vertical force P applied by the vehicle body, and generates a motion trend under the torque M transmitted by the transmission device [18]. Assuming that there is static friction between the wheel and rail, the force F' generated by the moving wheel on the track is equal in magnitude to the force F generated by the track on the moving wheel, but in opposite directions. For the mining electric locomotive, rim traction force F is the driving traction force. But the wheels of rail vehicles mostly have conical tread, which can cause elastic-plastic deformation when the wheels come into contact with the rail. The mining electric locomotive is subjected to shock and vibration during operation. When the wheel set rolls on the rail, it is accompanied by longitudinal and transverse sliding. There is no pure static friction state between the wheel and rail, but rather 'slight movement in stillness' and 'slight sliding in rolling'. This phenomenon is creep, also known as adhesion between wheel and rail. The maximum longitudinal horizontal force in the adhesive state is the adhesive force, and the ratio of adhesive force F_μ to vertical load P is the adhesive coefficient μ. According to Hertz elasticity contact theory [19], the contact area between the wheel and rail is approximately elliptical. The area where the wheel and rail are relatively stationary and do not slide under the action of positive pressure is called the adhesion zone. The area where slight sliding occurs is called the creep zone. As the driving torque M increases, the creep zone becomes larger and the adhesion zone decreases to 0, and the wheels are in a sliding state. Therefore, when the vehicle is in traction or braking conditions, if the traction or braking force is greater than the adhesion between the wheels and rails, the wheels will idling or slip. This phenomenon can cause damage to the wheel rail tread and even affect the safety of rail vehicles.

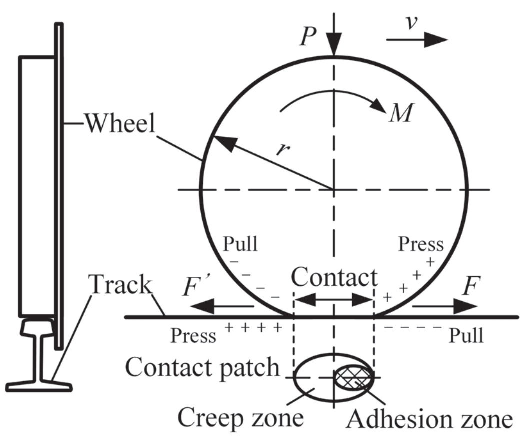

Figure 6. Schematic diagram of adhesion between wheels and rails.

According to the International Union of Railways (UIC) definition of creep rate, the creep rate is represented as follows:

$$\begin{cases} CR_{longitudinal} = \frac{(VW_{longitudinal} - VT_{longitudinal})_{At\ the\ contact\ patch}}{Nominal forwardvelocity} \\ CR_{lateral} = \frac{(Wheel\ lateral\ velocity - Track\ lateral\ velocity)_{At\ the\ contact\ patch}}{Nominal forwardvelocity} \\ CR_{spin} = \frac{(Wheel\ angular\ velocity - Track\ Wheelangularvelocity\ velocity)_{At\ the\ contact\ patch}}{Nominal forwardvelocity} \end{cases} \quad (10)$$

Based on the operating results when the friction between the wheel and rail is 0.3 (Figure 2), it can be observed that there is a sudden change in the interaction of wheel and rail during vehicle acceleration, and the creep rate value is abnormal.

2.4. Control Objectives

As the main auxiliary transportation tool in the coal mine roadway, the mining electric locomotive is greatly affected by the humid, muddy and other harsh environment during driving. When there are pedestrians or obstacles, the tram can't bypass to avoid them, but only take emergency braking. Wet and slippery road surface may lead to insufficient wheel/rail adhesion of mining electric locomotive. When the vehicle is in traction condition and the traction force is greater than the wheel/rail adhesion, the wheel will idling. When the vehicle is in braking condition and the braking force is greater than the adhesion, the wheels will slip. The occurrence of these situation will cause the wheel tread and rail surface to be scratched, which will seriously affect the safety and stability of the vehicle. Therefore, the most critical control factor for the safe running of mining electric locomotive on the track is the value of the driving/braking torque applied on the axle. In this way, we can directly control the driving acceleration and speed of the vehicle by controlling the torque to avoid driving accidents such as vehicle braking failure and vehicle rollover.

As shown by the adhesion characteristic curves under dry and wet rail surface conditions in Figure 7, when the creep rate is within the range of −10% to 10%, the absolute value of the adhesion coefficient between the wheel and rail rapidly increases under braking/traction conditions [20]. When the creep rate is within the range of −30% to −10% and 10% to 30%, the absolute value of the adhesion coefficient between the wheel and rail reaches its optimal value under braking/traction conditions. When the creep rate is around ±20%, the wheel rail adhesion coefficient will reach its peak, and at this time, the vehicle can obtain maximum ground braking/traction force, which can minimize the braking distance. Therefore, controlling the creep rate within the range of ±10% to ±30% is an ideal control goal.

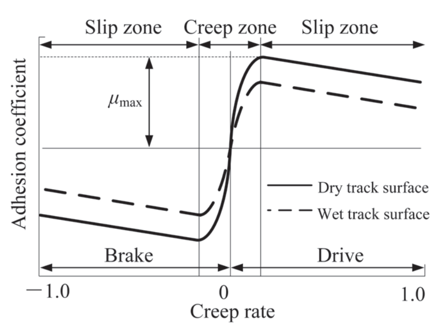

Figure 7. The adhesion characteristic curves under dry and wet rail surface conditions.

3. Creep Controller Model

In this section, an RL speed control method for mining electric locomotives based on the optimal creep rate is proposed. For mining electric locomotives, there are many turns and narrow sections in coal mine roadway, and there are many emergencies during the operation of the locomotives. This method can fully utilize the advantage of RL that does not rely on models. The impact of complex mine environments on vehicle driving processes, especially the impact of slippery wheel/rail conditions that are difficult to quantify and evaluate on vehicle safety and autonomous operation, is converted into reward feedback obtained by vehicles from the environment. This method simplifies the modeling process of vehicle driving conditions and improves the efficiency of intelligent algorithm calculation. There are three major elements in RL, including state, reward, and strategy for selecting actions. When using RL method for creep control of the mining electric locomotive, the mining electric locomotive is considered as an intelligent agent, and the algorithm components are designed as follows.

3.1. State and Action

According to the starting or stopping of the mining electric locomotive, whether the driving section is a curve or a straight road, whether there are obstacles, whether the operating speed reaches the speed limit of the corresponding section, and whether the electric locomotive reaches the destination, the state of the RL creep control algorithm for the mine electric locomotive is set to 16 as shown in the Table 1. In addition, the torque applied on the axle has three forms: positive, negative, and zero, corresponding to the three actions of vehicle acceleration, deceleration, and uniform speed.

Table 1. State Design of the Mining Electric Locomotive Autonomous Control Based on RL

State	Meaning
begin	Electric locomotive start
to_the_end	Electric locomotive reaches the destination
obstacle_stop	Stop when encountering obstacles
c_within_obstacle	Close to the vehicle in front on curves
max_spd_c_no_obstacle	The maximum set speed is reached on curves
over_spd_c_no_obstacle	Overspeed on curves
below_spd_c_no_obstacle	The maximum set speed is not reached on curves
l_within_obstacle	Keep close to the obstacle in front when driving straight
near_to_the_end_brake	The speed is greater than 0 when approaching the terminal
near_to_the_end_drive	The speed is less than 0 when approaching the terminal
max_spd_l_to_c	The maximum speed allowed in the curve is reached when preparing to turn
over_spd_l_to_c	Overspeed when preparing to turn
below_spd_l_to_c	The maximum speed allowed in the curve is not reached when the vehicle is preparing to turn
max_spd_l_no_obstacle	The maximum set speed is reached on the straight track
over_spd_l_no_obstacle	Overspeed on the straight
below_spd_l_no_obstacle	The maximum set speed is not reached on the straight track

During the execution of the algorithm, the real-time position and speed of the mining electric locomotive are recorded every 0.01s to determine the changes of electric locomotive state during the sampling interval. At the same time, the algorithm will also timely provide the actions that should be applied within the sampling time of 0.01s, ensuring the timeliness of control.

It is worth pointing out that 'Technical Conditions for Explosion-proof Special Battery Electric Locomotives in Coal Mines' (JB/T 4091-2014, published by Ministry of Industry and Information Technology of the People's Republic of China in Jul. 2014) stipulates that mining electric locomotives should pass through the curve radius at a 50% of hourly speed.

For the CTY1.5/6 electric locomotive used in this case, the maximum speed of the vehicle is 2.83 m/s (10.2 km/h), and the hourly speed of the vehicle is 1.80 m/s (6.5 km/h). Therefore, when the mining electric locomotive passes a curve with a radius of curvature greater than 4m, the minimum speed of the vehicle is 0.90 m/s.

3.2. Features of Reward Function

The appropriate definition of the reward function can directly determine whether the learning process of RL algorithms can efficiently and quickly achieve the desired training objectives. The main task of RL is to maximize rewards by selecting the best action at each sampling time. The ultimate goal of control algorithm for the electric locomotive is to achieve the optimal creep rate utilization in uncertain and harsh roadway environments, reduce the occurrence of slip and idling phenomena, and achieve the best operating efficiency under the premise of safe operation. Therefore, the reward function is directly related to the control effect of the mining electric locomotive's driving speed and creep rate under different states.

Whether the mining electric locomotive has encountered obstacles or reached the maximum speed of the corresponding road section is classified during the state setting. When setting the reward function, whether the vehicle is accelerating, decelerating, or running at the uniform speed in the current state should be considered. The vehicle changing at a faster speed to achieve the desired control purpose will present a better training effect. The following speed reward conditions is defined based on repeated experiments. The main way to measure the size of the reward value is to calculate the speed change that occurs during the unit sampling interval for the vehicle to achieve control objectives.

$$reward_{\mathrm{speed}} = c_{\mathrm{speed}} \times (v_{\mathrm{record}} - v_{\mathrm{current}}) \tag{11}$$

where, c_{creep} represents the speed reward coefficient, which can be obtained through multiple experiments.

According to the control goal proposed in Section 2.4 of the paper to control the creep rate within the range of ±10% to ±30%, the creep control reward conditions are set. We have comprehensively considered the creep rate of four wheels, and the evaluation criteria for the creep rate reward are set as follows.

When the absolute values of the creep rate of the left front wheel $|\xi_{\mathrm{FL}}|$, right front wheel $|\xi_{\mathrm{FR}}|$, left rear wheel $|\xi_{\mathrm{BL}}|$, and right rear wheel $|\xi_{\mathrm{BR}}|$ are all approximately equal to the optimal creep rate of 0.2 when taking two decimal places, the reward value can be set to:

$$reward_{\mathrm{creep}} = c_{\mathrm{creep\_max}} \tag{12}$$

In other cases, the reward value is set to:

$$reward_{\mathrm{creep}} = \frac{c_{\mathrm{creep\_max}}}{\sqrt{(|\xi_{\mathrm{FL}}| - 0.2)^2 + (|\xi_{\mathrm{FR}}| - 0.2)^2 + (|\xi_{\mathrm{BL}}| - 0.2)^2 + (|\xi_{\mathrm{BR}}| - 0.2)^2}} \tag{13}$$

where, $c_{\mathrm{creep\_max}}$ and c_{creep} represent the reward coefficient for optimal creep rate and the reward coefficient for creep rate respectively, which can be obtained through multiple experiments.

We add the evaluation results of speed and creep with ratio of 1:1 to obtain the final reward function formula:

$$reward = reward_{\mathrm{speed}} + reward_{\mathrm{creep}} \tag{14}$$

3.3. Structure of the Creep Control Method

After setting up the intelligent agent, state, action, and reward function, a complete creep control framework for mining electric locomotives should be designed. As shown in the Figure 8, the mining electric locomotive serves as an intelligent agent to determine the current state S_t based on the conditions of the environment at the current moment t. Then the intelligent agent uses an improved ε-greedy method to select the actions to be executed, obtain the current action A_t, and apply it to the axle. Finally, the intelligent agent obtains the corresponding reward value R_{t+1} based on the current environment and state. This reward is used to update Q-table.

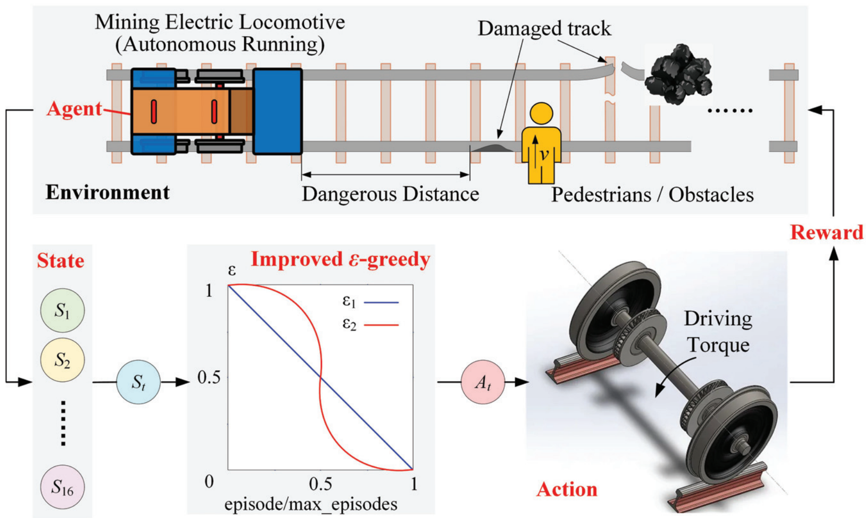

Figure 8. Details of the CTY1.5/6 creep control method.

4. Simulation Verification and Results

In this section, we verify the proposed RL based creep control method for autonomous operation of mining electric locomotives through simulation experiments. A dynamic model of the CTY1.5/6 mining electric locomotive is built through Simpack. And the algorithm framework based on the Python language environment is designed. MATLAB is used as the intermediate carrier for connecting the algorithm and model, mainly responsible for the collection of dynamic model data and the output of algorithm operation results. Therefore, in this paper, the validation of the algorithm will be carried out through a co-simulation platform built by Simpack, MATLAB, and Python. The simulation platform is used to verify the effectiveness of the creep control method for autonomous operation of mining electric locomotives. The creep control method is compared with traditional ε-greedy algorithms to highlight the advantages of the improved ε-greedy algorithm in terms of learning efficiency.

4.1. Simulation Platform and Setup

The Windows 11 Professional 64 bit system is used as a simulation platform operating system, equipped with an Intel (R) Core (TM) i9-9900K CPU @ 3.60 GHz CPU and NVIDIA GeForce RTX 2070 SUPER GPU. The composition software of the co-simulation platform is PyCharm Community Edition, MATLAB R2014b and Simpack 2018.1. The language environment of Python 2.7 and its equipped third-party libraries such as Matlabengine for Python R2014b and Openpyxl 2.6.4 provide the foundation for the operation of simulation platform algorithms.

We use the RL algorithm based on the improved ε-greedy mentioned above to train the creep control of the CTY1.5/6 mining electric locomotive. The number of iterations is 500, with a maximum runtime of 45 s and a sampling interval of 0.01 s. The learning rate of this algorithm is set to 0.2, and the Q-learning discount rate is 0.8. The initial and final values of ε are set to 0.01 and 1, respectively. The driving section of the mining electric locomotive is composed of a combination of 20 m straight road-20 m curved road-20 m straight road. In general, the friction between the rail and the wheel is 0.2–0.4. Therefore, the friction coefficient on the track surface is set to 0.3.

4.2. Simulation Results

The reward values for creep control of the mining electric locomotive obtained through simulation using traditional ε-greedy and improved ε-greedy algorithms are shown in the Figure 9. It can be seen that under the condition of training 500 times, the agent obtains larger reward values in the first half of the training using traditional ε-greedy. The increasingly stable creep control reward value is obtained in the later stages of training during the use of improved ε-greedy algorithm for autonomous driving simulation in mining electric locomotives. This indicates that the improved ε-greedy algorithm we have designed can fully utilize the experience gained from exploration in the first half of the training, while the exploration of traditional ε-greedy in the first half of the training is clearly limited. And towards the end of the training stage, the reward value tends to stabilize to ensure the reliability of the training results, allowing the agent to repeatedly train and verify the optimal value.

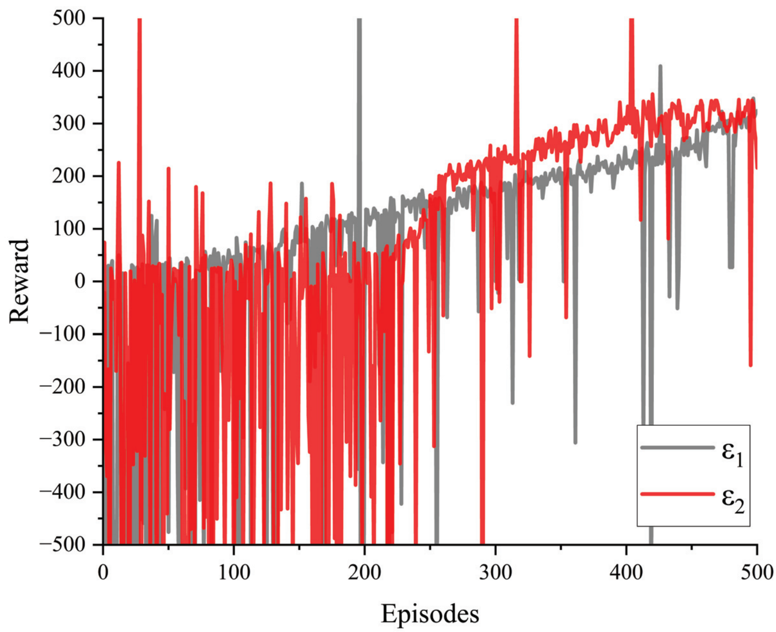

Figure 9. Results of reward with different values of ε.

We take the results every 125 iterations and plot the real-time position, speed, and creep rate of each wheel of the mining electric locomotive. From the 125th iteration to the 500th iteration (Figures 10 and 11), the mining electric locomotive can achieve their destination. However, the speed change is different. It can be easily observed that the mining electric locomotive cannot fully achieve the maximum speed limit for straight or curved roads during the initial training stage, and the vehicle cannot stop at its destination. As the training progresses, the mining electric locomotive acceleration increases.It can operate efficiently on speed limited sections, with accurate braking at the destination. On the first straight section of the road, the mining electric locomotive can maintain a safe distance when encountering obstacles.

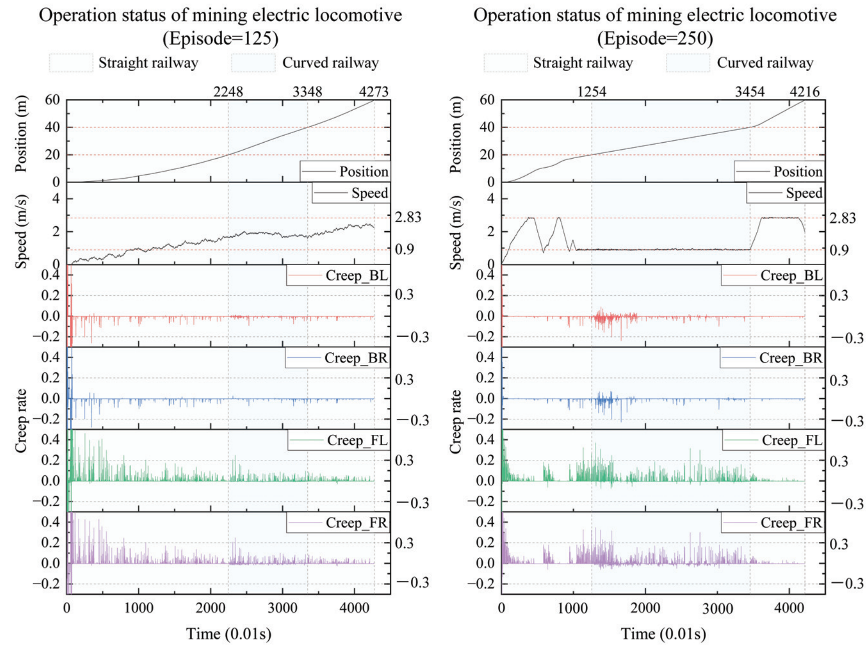

Figure 10. The operating status of mining electric locomotives with episode = 125 and episode = 250.

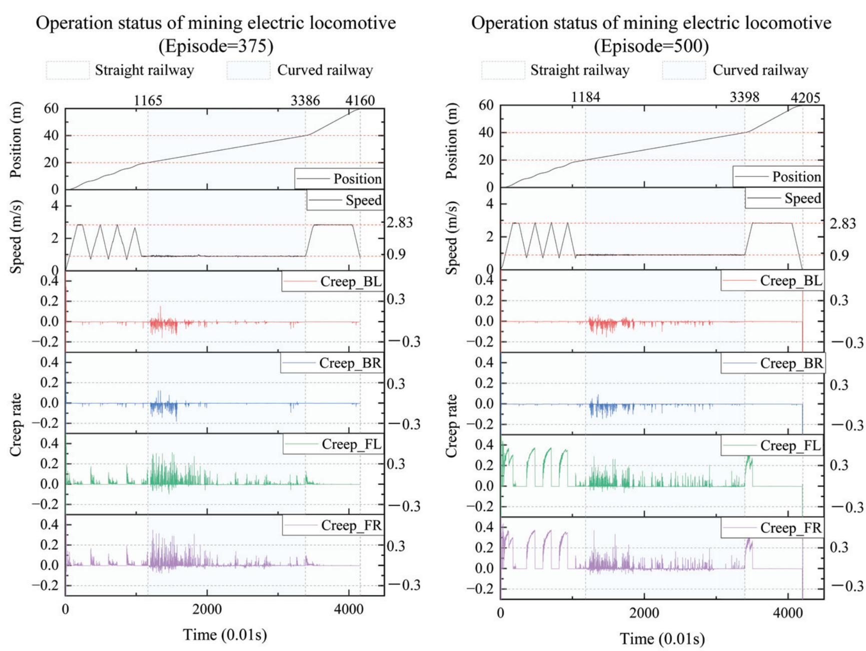

Figure 11. The operating status of mining electric locomotives with episode = 375 and episode = 500.

In terms of controlling the creep rate, it can be seen that the creep rate fluctuates greatly during vehicle acceleration, which can easily lead to wheel spin. Meanwhile, when the vehicle is driving in a bend, there is also a fluctuation in creep rate, indicating the possibility of some wheels slipping at certain times during the turning process. After training the agent, it can be seen that as the number of iterations increases, the idle time during the vehicle acceleration process significantly decreases, almost eliminating the phenomenon of the vehicle slipping on curves. When the intelligent agent is trained 500 times, the creep rate of the vehicle during acceleration can be controlled within the range of 0.1 to 0.4. This indicates that the creep rate between the wheels and rails is well controlled during vehicle operation and is well utilized to drive wheel acceleration. This proves that the design of our learning algorithm is reasonable and effective, which can better utilize the creep rate and achieve the goal of safe and efficient creep control.

We also conduct simulation experiments on the driving results of an 8-ton electric locomotive in an 86 m tunnel with a friction coefficient of 0.2. The results are detailed in Appendix C. From the results in Appendix C, it can be concluded that this method can be applied to different mining electric locomotives traveling on different track conditions. This method has good universal applicability in the control of creep rate and obstacle avoidance of mining electric locomotives.

5. Conclusions

In order to reduce the occurrence of idling or slipping caused by wet track surface and improve vehicle safety when mining electric locomotive is driving, an improved ε-greedy of creep control strategy for mining electric locomotives based on RL algorithm is designed in this paper. By reproducing and proving the autonomous control method of mining electric locomotives based on improved ε-greedy, the analysis of the operating conditions of mining electric locomotives shows that creep rate is an important influencing factor on the operation of electric locomotives in wet and slippery tunnels. An RL based creep control method is proposed, which considers the efficiency of vehicle driving speed and the effectiveness of creep control in the algorithm design process. Finally, simulation verification is conducted based on a co-simulation platform that can simulate the dynamic process of mining electric locomotives underground. The results show that this method can achieve safe operation of mining electric locomotives in complex and ever-changing mine environments, including being able to drive with maximum efficiency on speed limited sections, follow at a safe distance, and reduce the occurrence of dangerous phenomena such as slipping and idling during vehicle driving.

In addition, coal mine tunnels have harsh environmental conditions such as small cross-sections, high pressure, and easy deformation. The coal mine tracks are slippery and muddy, with many turns, and the behavior of nearby personnel is complex. The road environment for coal mine electric locomotives is difficult to predict. Therefore, we use real-time perception of vehicle driving conditions instead of predictive analysis, which is limited by sensor accuracy. In the future, we plan to adopt a data-driven fusion analysis method based on multi-source sensor information to improve the real-time perception accuracy of mining electric locomotives.

We will also apply the control strategy proposed in this article to coal mines in the future, and further optimize and improve the algorithm based on on-site test results. We will import the training results of the algorithm, namely the generated Q-table, into the industrial control computer of the electric locomotive to guide the vehicle to operate autonomously underground in the coal mine. At the same time, the actual operation data of the electric locomotive will also be continuously updated to optimize the Q-table.

Author Contributions: Conceptualization, Y.L.; methodology, Y.L.; software, Y.L.; validation, Y.L.; formal analysis, Y.L.; investigation, Y.L.; resources, Y.L., Z.Z. and X.L.; data curation, Y.L.; writing—original draft preparation, Y.L.; writing—review and editing, Y.L. and X.L.; visualization, Y.L. and X.L.; supervision, Z.Z.; project administration, Z.Z.; funding acquisition, Z.Z. All authors have read and agreed to the published version of the manuscript.

Funding: This research was funded by NATIONAL KEY R&D PROGRAM of funder grant number 2020YFB1314100, CHINA.

Institutional Review Board Statement: Not applicable.

Informed Consent Statement: Not applicable.

Data Availability Statement: Data are contained within the article.

Conflicts of Interest: The authors declare no conflicts of interest.

Abbreviations

The following abbreviations are used in this manuscript:

RL	Reinforcement Learning
MDP	Markov Decision Process
UIC	International Union of Railways

Appendix A

Assumption A1. *Define H as the contraction operator, the following formula is easily obtained:*

$$HQ(s,a) = R(s,a) + \gamma \mathbb{E}_{s_{t+1} \sim p(\cdot|s,a)}[\max_{a_{t+1}} Q(s_{t+1}, a_{t+1})]. \tag{A1}$$

Assuming that the optimal value function Q^* is a fixed point of H, it means:

$$Q^* = HQ^*. \tag{A2}$$

That is, Q^* remains at its original value after any multiplication with the H operator.

$$(Hq)(s,a) = \sum_{s_{t+1} \in \mathcal{S}} p_a(s, s_{t+1})[r(s,a,s_{t+1}) + \gamma \max_{a_{t+1} \in \mathcal{A}} q(s_{t+1}, a_{t+1})]. \tag{A3}$$

Lemma A1. ***Theorem-Cauchy's convergence Test:*** *The necessary and sufficient condition for the convergence of a sequence is that for any positive number ε, there must be a positive integer N that satisfies the following equation under the condition of $n > m \geqslant N$:*

$$|x_n - x_m| < \varepsilon. \tag{A4}$$

We refer to $\{x_n\}$ that satisfies this condition as a Cauchy sequence. So the theorem can be expressed as: the necessary and sufficient condition for the convergence of sequence $\{x_n\}$ is that the sequence is a Cauchy sequence.

Theorem A1. *In the Q-learning algorithm, $Q(s,a)$ can converge to Q^* when the agent accesses any action in any state multiple times.*

Proof. The convergence of the Q function is proved:

$$\begin{aligned} ||Hq_1 - Hq_2||_\infty &= \max_{s,a} \gamma | \sum_{s_{t+1} \in \mathcal{S}} p_a(s, s_{t+1})[\max_{a_{t+1} \in \mathcal{A}} q_1(s_{t+1}, a_{t+1}) - \max_{a_{t+1} \in \mathcal{A}} q_2(s_{t+1}, a_{t+1})]| \\ &\leq \max_{s,a} \gamma \sum_{s_{t+1} \in \mathcal{S}} p_a(s, s_{t+1}) | \max_{a_{t+1} \in \mathcal{A}} q_1(s_{t+1}, a_{t+1}) - \max_{a_{t+1} \in \mathcal{A}} q_2(s_{t+1}, a_{t+1})| \\ &\leq \max_{s,a} \gamma \sum_{s_{t+1} \in \mathcal{S}} p_a(s, s_{t+1}) \max_{a_{t+1} \in \mathcal{A}} |q_1(s_{t+1}, a_{t+1}) - q_2(s_{t+1}, a_{t+1})| \\ &= \gamma ||q_1 - q_2||_\infty. \end{aligned} \tag{A5}$$

According to the Theorem-Cauchy's convergence Test, any q_1 function can ultimately converge to Q^* when q_2 is the optimal function of Q^*. □

Appendix B

In order to evaluate the balance effect of exploration and exploitation, regret l_t is defined to represent the average possible loss at each step:

$$l_t = \mathbb{E}[V^* - Q(a_t)] \tag{A6}$$

where, $V^* = Q^*(a^*) = \max_{a \in \mathcal{A}} Q^*(a)$ represents the expected return value corresponding to the optimal action.

Total regret L_t is defined to represent the total loss:

$$L_t = \mathbb{E}[\sum_{\tau=1}^{t} V^* - Q(a_\tau)] = \sum_{a \in \mathcal{A}} \mathbb{E}[N_t(a)](V^* - Q(a)) = \sum_{a \in \mathcal{A}} \mathbb{E}[N_t(a)]\Delta_a \tag{A7}$$

where, $\Delta_a = (V^* - Q(a))$ represents the gap between the value of the action and the optimal action, and $N_t(a)$ represents the number of times that the action a has been selected. The goal of maximizing cumulative returns is actually equivalent to minimizing total regret, and an excellent algorithm is hoped to reduce the number of choices for actions with large gaps. For such an evaluation system, the most crucial issue is that the gap in practical problems is difficult to obtain, as V^* is unknown and $Q^*(a)$ also needs to be estimated. However, this evaluation system can still have guiding significance for the evaluation of strategies. It is usually assumed that Δ_a is a known constant value when discussing.

If the total regret L_t increases linearly with the increase of iteration, it indicates that the probability of selecting each action in the algorithm does not change at each time interval. That is, the regret l_t at each step does not change, and the information obtained from exploration is not better utilized. A strategy that can better balance exploration and exploitation should have a sublinear total regret. As the iteration progresses, the regret l_t for each time interval gradually decreases, and the selection of algorithms will gradually abandon those that are likely to achieve lower returns.

Lai and Robbins has proven that for all total regrets that may become an optimal strategy, an asymptotic lower bound in the form of logarithmic growth is required [16,21,22]:

$$\lim_{t \to \infty} L_t \leq 8 \ln t \sum_{a|\Delta_a} \frac{\Delta_a}{KL(R^a || R^{a^*})} \tag{A8}$$

The strategy of ε-greedy strategy can ensure that all actions are sampled infinitely as the number of iterations increases. Thereby the convergence of $Q(a)$ is ensured. This means that the probability of selecting the optimal action can converge to greater than 1 - ε, which is close to certainty. However, the probability of selecting the optimal action is only approaching a value, and its effectiveness cannot be guaranteed in practice. Obviously, the probability of each choice of action by ε-greedy is more than $\frac{\varepsilon}{\mathcal{A}}$. So the regret l_t is more than $\frac{\varepsilon}{\mathcal{A}} \sum_{a \in \mathcal{A}} \Delta_a$, which is a linear total regret. However, although ε-greedy is not the optimal method in theory, Kuleshov and Precup [23] have demonstrated through extensive experimental data that ε-greedy can often achieve better results than some complex methods in practice.

Set $episode = t$, $max\_episodes = T$. We will write the value of ε in the improved ε-greedy as follows:

$$\varepsilon_t = \begin{cases} (0.5 + \sqrt{0.25 - (t/T)^2}),\ (t/T) \in [0, 0.5] \\ (0.5 - \sqrt{0.25 - (1 - t/T)^2}),\ (t/T) \in (0.5, 1] \end{cases} \tag{A9}$$

To demonstrate the convergence of the improved ε-greedy strategy, we calculate the regret of the strategy:

$$l_t = \pi(a|s) \sum_{a \in \mathcal{A}} \Delta_a = \begin{cases} (1 - \varepsilon + \frac{\varepsilon}{|\mathcal{A}(s)|}) \sum_{a \in \mathcal{A}} \Delta_a,\ if\ a = \underset{a}{\operatorname{argmax}} Q(s,a) \\ \frac{\varepsilon}{|\mathcal{A}(s)|} \sum_{a \in \mathcal{A}} \Delta_a,\ if\ a \neq \underset{a}{\operatorname{argmax}} Q(s,a) \end{cases} \tag{A10}$$

$$L_t \approx \int\limits_t l_t \mathrm{d}t = \int\limits_t \frac{\varepsilon}{|\mathcal{A}|} \sum_{a \in \mathcal{A}} \Delta_a \mathrm{d}t$$
$$= \begin{cases} \int\limits_t \frac{\sum\limits_{a\in\mathcal{A}} \Delta_a}{|\mathcal{A}|}(0.5 + \sqrt{0.25 - (t/T)^2})\mathrm{d}t, \ (t/T) \in [0, 0.5] \\ \int\limits_t \frac{\sum\limits_{a\in\mathcal{A}} \Delta_a}{|\mathcal{A}|}(0.5 - \sqrt{0.25 - (1-t/T)^2})\mathrm{d}t, \ (t/T) \in (0.5, 1] \end{cases} \tag{A11}$$
$$\rightarrow \begin{cases} \frac{\sum\limits_{a\in\mathcal{A}} \Delta_a}{|\mathcal{A}|}(\frac{t}{2} + \frac{1}{8}T\arcsin(\frac{2t}{T}) + \frac{t}{4}\sqrt{1-4(\frac{t}{T})^2}), \ (t/T) \in [0, 0.5] \\ \frac{\sum\limits_{a\in\mathcal{A}} \Delta_a}{|\mathcal{A}|}(\frac{t}{2} + \frac{1}{8}T\arcsin(2(1-\frac{t}{T})) + \frac{T}{4}(1-\frac{t}{T})\sqrt{1-4(1-\frac{t}{T})^2}), \ (t/T) \in (0.5, 1] \end{cases}$$

Plot the trends of L_t and its derivative $L_\mathrm{t}{}'$ as the number of iterations increases. In Figure A1, it can be seen that $L_\mathrm{t}{}'$ is 0 in the later stage of iteration, and the value of L_t no longer increases, indicating that the improved ε-greedy tends to converge.

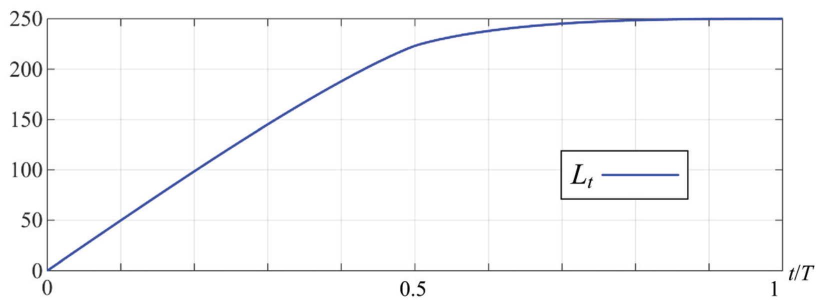

(a) L_t

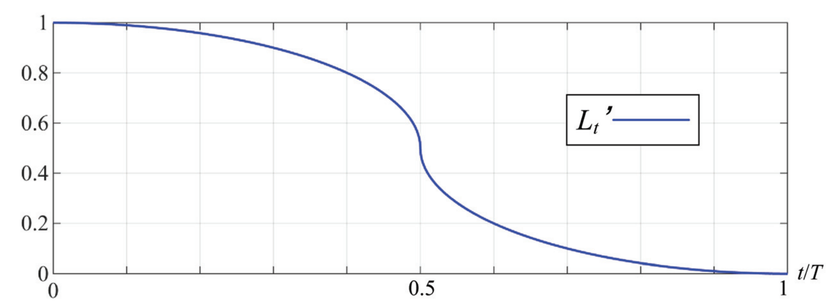

(b) L_t'

Figure A1. The trend of total regret L_t and its derivative $L_\mathrm{t}{}'$.

Appendix C

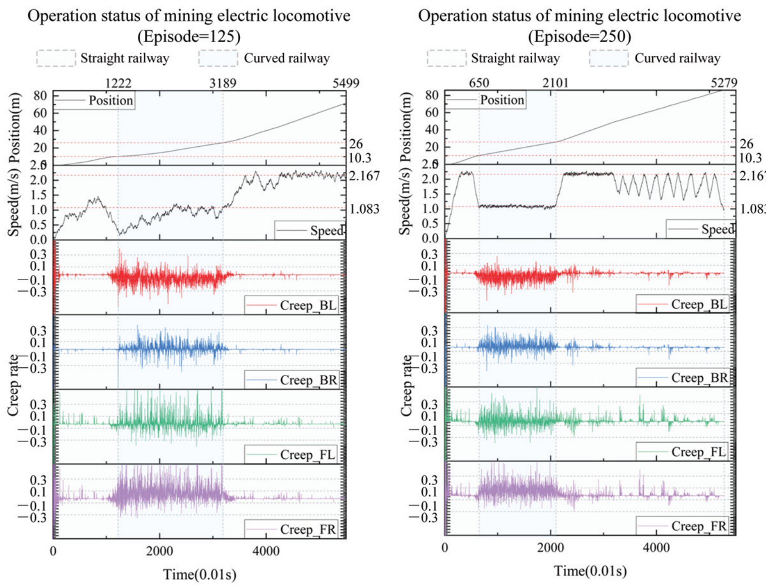

Figure A2. The operating status of 8t mining electric locomotives with episode = 125 and episode = 250.

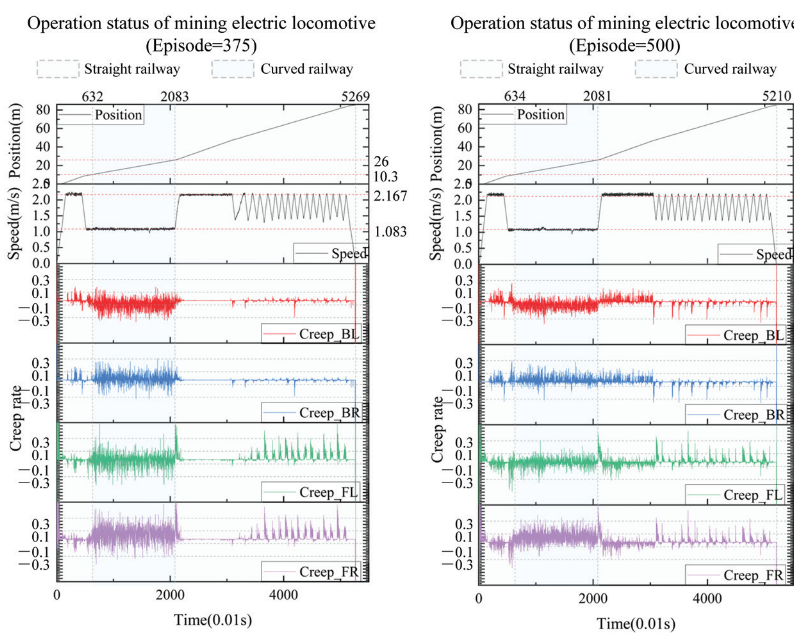

Figure A3. The operating status of 8t mining electric locomotives with episode = 375 and episode = 500.

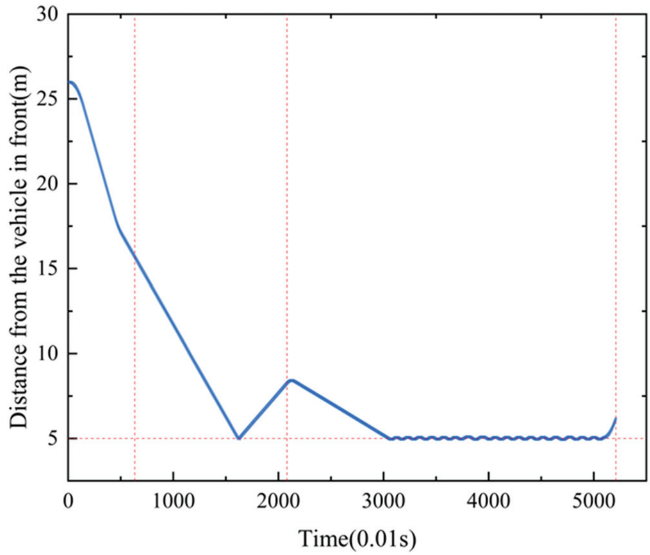

Figure A4. The distance from the vehicel in front of 8t mining electric locomotives.

In order to verify the universal applicability of the creep control based unmanned speed control method for mining electric locomotives proposed in this paper on different vehicles and road sections, we conduct simulation experiments on the autonomous operation of an 8-ton mining electric locomotive in this section. The hourly speed of the electric locomotive is 7.8 km/h (2.167 m/s). From the Figures A2 and A3, it can be seen that the intelligent agent can control the creep rate within ±10%∼±30% during acceleration/deceleration sections. This indicates that our speed control method for autonomous operation of electric locomotives is effective in controlling creep rate.

In addition, to verify the effectiveness of this method in ensuring driving safety, we set the safety distance to 5 m when encountering obstacles or maintaining a safe distance from the preceding vehicle. From the Figure A4, it can be seen that the autonomous driving of the electric locomotive using this method is safe and effective, ensuring that the vehicle always maintains a distance of 5 m from obstacles or the preceding vehicle.

Therefore, this method can be applied to different vehicles traveling on different track conditions. This method has good universal applicability in the control of creep rate and obstacle avoidance of mining electric locomotives.

References

1. Wang, G.F.; Liu, F.; Meng, X.J.; Fan, J.; Wu, Q.; Ren, H.; Pang, Y.; Xu, Y.; Zhao, G.; Zhang, D.; et al. Research and practice on intelligent coal mine construction (primary stage). *Coal Sci. Technol.* **2019**, *47*, 1–36.
2. Ge, S.R. Present situation and development direction of coal mine robots. *China Coal* **2019**, *45*, 18–27.
3. Li, Y.; Zhu, Z.C.; Li, X.Q.; Yang, C.Y.; Lu, H. When mining electric locomotives meet reinforcement learning. *arXiv* **2023**, arXiv:2311.08153. https://doi.org/10.48550/arXiv.2311.08153.
4. Fang, C.C.; Jaafar, S.A.; Zhou, W.; Yan, H.K.; Chen, J.; Meng, X.H. Wheel-rail contact and friction models: A review of recent advances. *Proc. Inst. Mech. Eng. Part J. Rail Rapid Transit* **2023**, *237*, 1245–1259. [CrossRef]
5. Vollebregt, E.; Six, K.; Polach, O. Challenges and progress in the understanding and modelling of the wheel-rail creep forces. *Veh. Syst. Dyn.* **2021**, *59*, 1026–1068. [CrossRef]
6. Zhao, Y.H.; He, X.; Zhou, D.H.; Pecht, M.G. Detection and Isolation of Wheelset Intermittent Over-Creeps for Electric Multiple Units Based on a Weighted Moving Average Technique. *IEEE Trans. Intell. Transp. Syst.* **2022**, *23*, 3392–3405. [CrossRef]
7. Lu, C.X.; Chen, D.L.; Shi, J.; Li, Z.Q. Research on wheel-rail dynamic interaction of high-speed railway under low adhesion condition. *Eng. Fail. Anal.* **2024**, *157*. [CrossRef]
8. Gao, X.; Lu, Y. Study of locomotive adhesion control. *Railw. Locomot. Car* **2017**, *3*, 35–39.

9. Yamazaki, O.; Ohashi, S.; Fukasawa, S.; Kondo, K. The proposal of re-adhesion control method with the advantage of individual control system. In Proceedings of the International Conference on Electrical Systems for Aircraft, Railway, Ship Propulsion and Road Vehicles (ESARS), Aachen, Germany, 3–5 March 2015.
10. Yamashita, M.; Soeda, T. Anti-slip re-adhesion control method for increasing the tractive force of locomotives through the early detection of wheel slip convergence. In Proceedings of the 17th European Conference on Power Electronics and Applications (EPE ECCE-Europe), Geneva, Switzerland, 8–10 September 2015.
11. Wen, X.K.; Huang, J.C.; Zhang, S. Anti-slip re-adhesion control strategy of electric locomotive based on distributed MPC. In Proceedings of the 2019 IEEE 21st International Conference on High Performance Computing and Communications, Zhangjiajie, China, 10–12 August 2019.
12. Çimen, M.A.; Ararat, Ö.; Söylemez, M.T. A new adaptive slip-slide control system for railway vehicles. *Mech. Syst. Signal Process.* **2018**, *111*, 265–284. [CrossRef]
13. Wang, S.; Wang, X.G.; Huang, J.C.; Sun, P.F.; Wang, Q.Y. Adhesion Control of High Speed Train Based on Vehicle-control System. In Proceedings of the 2021 IEEE 16th Conference on Industrial Electronics and Applications (ICIEA), Chengdu, China, 1–4 August 2021.
14. Zhang, S.; Huang, Z.W.; Yang, Y.Z.; Gao, K.; Zhu, C. A Safe and Reliable Anti-Lock Wheel Control with Enhanced Forgotten Factor for Brake Operation of Heavy Train. In Proceedings of 2017 IEEE International Symposium on Parallel and Distributed Processing with Applications, Guangzhou, China, 12–15 December 2017.
15. Martin-Guerrero, J.D.; Lamata, L. Reinforcement Learning and Physics. *Appl. Sci.* **2021**, *11*, 8589. [CrossRef]
16. Kulkarni, S.R.; Lugosi, G. Finite-time lower bounds for the two-armed bandit problem. *IEEE Trans. Autom. Control.* **2000**, *45*, 711–714. [CrossRef]
17. Malvezzi, M.; Pugi, L.; Papini S.; Rindi A.; Toni P. Identification of a wheel-rail adhesion coefficient from experimental data during braking tests. *Proc. Inst. Mech. Eng. Part J. Rail Rapid Transit* **2013**, *227*, 128–139. [CrossRef]
18. Polach, O. Creep forces in simulations of traction vehicles running on adhesion limit. *Wear* **2005**, *258*, 992–1000. [CrossRef]
19. Fu, G.H. An extension of Hertz's theory in contact mechanics. *J. Appl. Mech. Trans. ASME* **2007**, *74*, 373–374. [CrossRef]
20. Polach, O. A fast wheel-rail forces calculation computer code. *Veh. Syst. Dyn.* **1999**, *33*, 728–739. [CrossRef]
21. Tze, L.L.; Herbert, R. Asymptotically efficient adaptive allocation rules. *Adv. Appl. Math.* **1985**, *6*, 4–22.
22. Auer, P.; Cesa-Bianchi, N.; Fischer, P. Finite-time analysis of the multiarmed bandit problem. *Mach. Learn.* **2002**, *47*, 235–256. [CrossRef]
23. Volodymyr, K.; Doina, P. Algorithms for multi-armed bandit problems. *arXiv* **2014**, arXiv:1042.6028.

minerals

MDPI

Article

Numerical Simulation of Air–Water–Flake Graphite Triple-Phase Flow Field in a Homemade Double-Nozzle Jet Micro-Bubble Generator

Xing Dong [1,*], Chenhao Guo [2], Deqiang Peng [3] and Yun Jiang [2]

1 School of Mechanical Engineering, Heilongjiang University of Science and Technology, Harbin 150022, China
2 School of Safety Engineering, Heilongjiang University of Science and Technology, Harbin 150022, China; 18145974766@163.com (C.G.),
3 School of Mining Engineering, Heilongjiang University of Science and Technology, Harbin 150022, China
* Correspondence: dongxingwrh@163.com; Tel.: +86-13069897538

Abstract: The essential part of the flake graphite flotation apparatus is a micro-bubble generator. Developing a micro-bubble generator with a reasonable structure and superior self-absorption performance is crucial to improving flake graphite sorting. In this study, to realize the integrated treatment of the grinding and mineralization of flake graphite, the development and manufacturing of a double-nozzle jet micro-bubble generator were based on the concepts of shear-type cavitation water jets and jet pumps, among other theories. A numerical simulation of the air–water–flake graphite triple-phase flow field of the generator was conducted using the CFD method. The goal was to investigate the grinding and mineralization process of flake graphite by analyzing the distribution of the air phase's volume percentage and the speed distribution of the air–water–flake graphite triple-phase flow field. The findings indicate that the air-phase volume percentage produced by the generator ranges from 98.3% to 99.9%, and the air-phase volume percentage is evenly distributed within the steady flow tube, achieving the mineralization function. Additionally, the flake graphite particles are dissociated from the flake graphite under the combined effect of friction shear and cavitation of the internal nozzles, thereby achieving the grinding function.

Keywords: double-nozzle jet micro-bubble generator; flake graphite; air–water–flake graphite triple-phase flow; grinding; mineralization; numerical simulation

Citation: Dong, X.; Guo, C.; Peng, D.; Jiang, Y. Numerical Simulation of Air–Water–Flake Graphite Triple-Phase Flow Field in a Homemade Double-Nozzle Jet Micro-Bubble Generator. *Minerals* **2024**, *14*, 533. https://doi.org/10.3390/min14060533

Academic Editor: Krzysztof Skrzypkowski

Received: 1 April 2024
Revised: 11 May 2024
Accepted: 17 May 2024
Published: 22 May 2024

1. Introduction

Graphite is an allotrope of carbon and a crucial non-metallic mineral resource [1]. Flake graphite is an essential branch of natural graphite, formed by combining many single layers of graphite with a distinctly oriented crystal structure. Flake graphite's floatability, lubricity, and plasticity are superior to those of other types of graphite. However, the grade of the flake graphite ore is quite low, posing challenges to its direct utilization. To satisfy industrial manufacturing demands, flake graphite needs to be purified by multistage grinding and multistage flotation beneficiation processes [2–4], such as seven grinding, eight flotation, nine grinding, and ten flotation processes. These beneficiation processes can improve the grade of flake graphite; however, the process is long and complex, and it is straightforward to damage the graphite structure on large scales. Therefore, optimizing the beneficiation process while ensuring the grade recovery and extraction of the flake graphite concentrate has emerged as a pressing issue that necessitates resolution within the existing flake graphite beneficiation procedure [5,6].

Flotation via froth serves as the primary sorting approach in the flake graphite beneficiation process [7,8], which involves the creation of micro-bubbles by micro-bubble generators that are beneficial to flake graphite mineralization. Therefore, micro-bubble generators are known as the core technology of froth flotation [9,10]. Micro-bubble generators are categorized into internal and external based on the bubble generation method. Internal micro-bubble generators are subdivided into riser micro-bubble generators, filter disk micro-bubble generators, gravel bed micro-bubble generators, etc. [11]. Internal micro-bubble generators are prone to scaling and clogging of the flow channel [12], which often leads to the failure of the flotation column within a flotation system. External micro-bubble generators are subdivided into jet micro-bubble generators, cyclone micro-bubble generators, air–water micro-bubble generators, etc. [11]. They effectively resolve the issue of frequent clogging [13], which has withstood the test of industrial practice and lays the foundation for the industrial application of high-efficiency jet flotation columns. Among them, the jet micro-bubble generator harnesses the vacuum produced by the high-velocity jet to draw in the air as well as crush it into minuscule bubbles, which has the advantages of a smaller bubble diameter, high volume fraction of gas phase, simple structure, and low energy consumption [14,15]. Therefore, the current study on jet micro-bubble generators has become one of the essential study contents of micro-bubble generators.

The jet micro-bubble generator's structural arrangement impacts the dimension of the created bubbles and the air phase's volume percentage and directly affects the flotation effect of minerals; as a result, scholars in the field have conducted several related study efforts. Wu et al. [16] added a variable pitch spiral guide vane inside the conventional jet bubble generator to generate a vortex jet, which enhanced the shear-crushing effect of the bubbles. Sadatomi et al. [17] designed a new type of jet micro-bubble generator. The study conducted micro-bubble measurement tests in order to examine the influence of tubular size ratio, air-intake port diameter, and axial position on the number and size of micro-bubbles generated. Gordiychuk et al. [18] evaluated the impact of the air-intake port diameter on the venturi jet micro-bubble producer and the gas–liquid rate of flow upon the distribution of particle sizes of the micro-bubbles generated. Deng et al. [19] utilized the AFM to investigate the cavitation-generated micro-nanobubbles by a particular structured venturi jet micro-bubble generator and observed a positive correlation with water flow velocity and cavitation cloud density. Fujiwara et al. [20] employed a fast-speed digital camera to investigate the dynamic development of micro-bubbles at the venturi jet micro-bubble producer's throat and concluded that microbubble diameter is inversely proportional to flow velocity at the throat. Tsave et al. [21] combined the traditional jet bubble generator and the micro-bubbles generated by water electrolysis to produce a new micro-bubble generator device, which can generate 76 μm micro-bubbles and enhance the flotation efficiency of materials with fine grains to a great extent. Fu et al. [22] employed a fast-speed digital camera in combination with dissolved oxygen analysis to study the self-absorption and foaming performance of a self-designed venturi jet micro-bubble generator. The findings indicated that the generator's self-absorption ability and foaming performance had a positive correlation with the flow velocity, and the maximum dissolved oxygen could be up to 14.4 mg/L. Li et al. [23] optimized the design based on the structure of a conventional venturi micro-bubble generator to increase the number of micro-bubbles and micro-bubble dispersion effectively. They determined that the breaking of bubbles primarily takes place within the diffusion section of the venturi bubble producer through numerical analog and visualization tests.

CFD has become a crucial approach for optimizing structural design due to the advent of computational fluid dynamics and advancements in computer technology. It is applied in the analysis of the fluid pattern exhibited by the micro-bubble generator. Xu et al. [24] employed a CFD-PBM model to analyze and solve the kinematic law of the flow field within the jet bubble generator and found that the air bubbles produced inside the bubble generator's dimensions are 0.99–140 μm. The air is sheared and broken into micro-bubbles after being injected into the generator from the suction tube under negative pressure, and the micro-bubbles gradually move from the center of the tube to the peripheral wall. Li et al. [25] employed CFD in conjunction with the PIV technique to investigate the foaming performance of single- and dual-port jet micro-bubble generators. The findings demonstrated that the gas-phase velocity vector distribution of the dual-port jet micro-bubble generator is more symmetric, which improves the dispersion of micro-bubbles. Basso et al. [26] conducted a CFD simulation to analyze the air–water double-phase stream field of a novel venturi jet micro-bubble producer with a helix angle and found that compared with the conventional venturi micro-bubble producer the average size of the bubbles produced by the novel venturi jet micro-bubble producer is smaller, which can solve the problem of the unstable foaming performance of a venturi bubble generator at a low flow rate. Wang et al. [27] simulated the kinetic energy of turbulence in various configurations of cyclonic bubble generators using the CFD method, and the findings from the simulation indicate that the turbulent kinetic energy of the staggered array design was found to be optimal, which was more conducive to the collision and adhesion between bubbles and mineral grains. Alam et al. [28] employed a CFD-PBM model to examine the distribution of bubble dimensions in a cyclonic nanobubble producer and found that the standardized k-Ω model is suitable for bubble dispersion analysis at high flow velocities, and the micro-bubble dispersion increases proportionally with the turbulence dissipation rate. Al-Azzawi et al. [29] applied CFD to computationally analyze the flow field for a cyclonic nanobubble generator with three types of air-intake structures: single inlet, double inlet, and tangential inlet. The simulation results revealed that a clear vortex appeared in the low-pressure region of the micro-bubble generator with the tangential inlet, and the self-absorption performance was optimal.

Through the optimization of the structure of the jet micro-bubble generator and the study of its internal flow characteristics, it was found that the jet micro-bubble generator can achieve a higher air intake through self-absorption at a lower working pressure. At the same time, the micro-bubbles generated possess a substantial specified area of surface and exhibit exceptional mass transmission efficiency, making it suitable for the flotation of diverse minerals. Palazuelos et al. [30] applied a jet bubble generator to the flotation of metallic silver, and under the optimal process conditions, the optimal recovery rate of silver reached 93%. Taghavi et al. [31] investigated the application of a jet micro-bubble producer in the flotation process of phosphorite, and the findings demonstrated that the jet micro-bubble producer's generation of micro-bubbles could significantly improve the recovery of phosphorite flotation and concentrate grade. Parga et al. [32] applied their bubble generator to the flotation machine for the sorting of pyrite, and the test showed that this sorting method decreased the cost of flotation compared with the traditional flotation machine by two-thirds, concentrate quality exhibited a 7% rise, and recuperation improved by 5%. Ni et al. [33], to improve the crude coal recovery and grade, connected a self-absorbing jet micro-bubble producer to the entry tube of a conventional flotation column to realize the coal pre-mineralization process. A comparison with the conventional coal slurry flotation column found that the refined coal recovery rate improved by 9.29%. Ma et al. [34] utilized a nanojet micro-bubble generator for a graphite flotation test. The results show that the nanobubbles effectively reduce the electrostatic rejection among graphite particles and promote the process of agglomerating fine-grained graphite, resulting in a notable enhancement in both graphite recovery and concentrate grade.

In summary, at present, scholars in this field have carried out some structural optimization of jet micro-bubble generators, numerical simulation analysis of the gas–liquid dual-phase flow, research on the flotation tests of different minerals, etc. It has not been found that the structure of the micro-bubble producer can simultaneously achieve the dissociation of flake graphite by jet flow and the mineralization of flake graphite by the jet flow of negative-pressure-induced air. In this paper, a double-nozzle jet micro-bubble generator was designed and fabricated using the principles of grinding dynamics, shear cavitation water jet theory, jet pump principle, and bubble generator principle. A numerical simulation of the air–water–flake graphite triple-phase flow field of the homemade double-nozzle jet micro-bubble generator using the CFD method and ANSYS FLUENT software was carried out. This simulation allowed for the determination of the air phase's volume percentage within the generator, as well as the velocity distribution of the air–water–flake graphite triple-phase flow. A comparative analysis was carried out with the existing jet micro-bubble generator to validate the homemade double-nozzle jet micro-bubble generator's design rationality. In order to integrate the current conventional flake graphite grinding and mineralization of two step-by-step independent operations of the process to solve the problem of flake graphite grinding, the flotation process is long and complex to provide a specific reference.

2. Materials and Methods

2.1. Simulation Parameters

The flake graphite samples were sourced from the Liumao graphite pit in Jixi, Heilongjiang Province, China. The main product of this graphite mine is large flake graphite. The product selection from the first stage of the beneficiation plant was taken as the parameter value of solid-phase flake graphite for the numerical simulation. In the numerical simulation, liquid-phase water is set as the main phase density value at 1000 kg/m^3, and the viscosity value is 1×10^{-3} Pa·s; solid-phase flake graphite is set as the secondary phase density value at 2100 kg/m^3, and the viscosity value is 1×10^{-5} Pa·s, with a volume concentration of 30% and an equivalent diameter of 0.1 mm. Gas-phase air is set as the secondary phase density value at 1.225 kg/m^3, and the viscosity value is 1.8×10^{-5} Pa·s, by varying the double-nozzle jet micro-bubble generator's inlet pressure to examine the flow field.

2.2. Double-Nozzle Jet Micro-Bubble Generator

2.2.1. Overall Structure

Figure 1 illustrates the schematic configuration of the homemade double-nozzle jet micro-bubble generator. As depicted in Figure 1, the homemade double-nozzle jet micro-bubble generator consists of two parts: an internal tandem friction shear cavitation nozzle and an external negative-pressure-induced air nozzle. The internal tandem friction shear cavitation nozzle consists of four levels of nozzles: the first level for the cone-convergence-type nozzle, the second and third levels for the rectangular convergence of the flat friction nozzle, and the fourth level for the friction shear cavitation nozzle. The external negative-pressure ejection air nozzle consists of two air-intake pipes, a suction mixing chamber, throat, diffusion tube, and flow regulator tube. The physical diagram of the double-nozzle jet micro-bubble generator is shown in Figure 2.

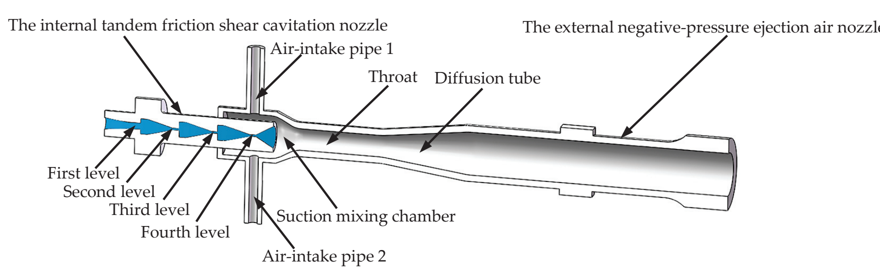

Figure 1. Structure of the double-nozzle jet micro-bubble genrator.

Figure 2. Image of the double-nozzle jet micro-bubble generator.

The homemade double-nozzle jet micro-bubble generator has two functions. Firstly, the internal tandem friction shear cavitation nozzles make full use of the characteristics of the laminated structure of the flake graphite, the application of friction on the nozzle's interior wall, and the dissociation of flake graphite through the cavitation of water jets to achieve the function of grinding. Secondly, the external negative-pressure-induced air nozzle can continuously and stably generate and release micro-bubbles of a suitable size and uniform distribution, which can fully collide and adhere with the dissociated flake graphite particles in the internal nozzle to form mineralized bubbles and realize the mineralization function.

The geometrical model of the inner fluid channel of the homemade double-nozzle jet micro-bubble generator is given in Figure 3. In Figure 3, for the internal tandem friction shear cavitation nozzles, the inlet diameter of the first-stage conical convergent nozzle is 5.3 mm, the flat section of the second third-stage rectangular convergent flat friction nozzles has a straight notch shape, and the diffusion section of the fourth-stage friction shear cavitation nozzle's outlet diameter is 10 mm. The interior nozzles' total length is 78 mm. For the external negative-pressure-induced air nozzle, the inlet diameter of both induced air tubes is 4 mm, and the suction mixing chamber's diameter value is 20 mm. The double-nozzle jet micro-bubble's total length value is 288 mm.

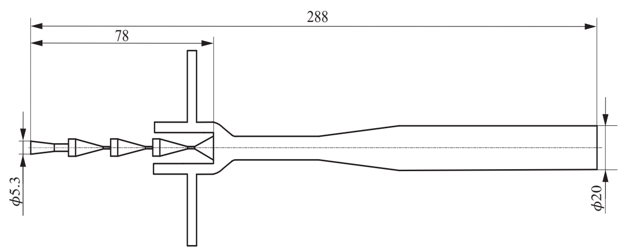

Figure 3. Geometric model of the inner channel of the double-nozzle jet micro-bubble generator.

2.2.2. Internal Tandem Friction Shear Cavitation Nozzle Design

The internal tandem friction shear cavitation nozzle is made up of four sections. The first section of the cone convergent nozzle is designed according to the design guidelines of the cone convergent water nozzle and the actual demand to realize the acceleration of the flake graphite slurry. When the inlet pressure and flow rate of the first-stage cone-convergent nozzle are specific, the nozzle outlet diameter d is as follows [35]:

$$d = \sqrt{\frac{4Q}{\pi\mu\sqrt{\frac{2p}{\rho}}}} \tag{1}$$

where Q represents the nozzle flow rate (m^3/s); μ represents the flow coefficient, 0.80; p represents the inlet pressure (Pa); and ρ represents the density of flake graphite (kg/m^3).

For the second- and third-level rectangular convergent flat friction nozzles, according to the characteristics of the laminated structure of flake graphite and the principle of grinding dynamics on the rectangular convergence of flat friction nozzle flat section of the straight groove design, enhance the friction shear effect of flake graphite particles and the nozzle channel wall, the dissociation of flake graphite. For the fourth level of the friction shear cavitation nozzle, due to the nozzle channel structure before the diffusion section with the second- and third-level nozzle structure being the same, the design method is the same as the second- and third-level nozzle, and for the fourth-level nozzle diffusion section, based on the theory of shear-type cavitation water jet design, the use of cavitation water jet bubbles produced by the collapse of the jet impact dissociates the flake graphite further. Simultaneously, the first-, second-, third-, and fourth-level nozzles are connected in a series to enhance the effect of the dissociation of the flake graphite, realizing the grinding function of the double-nozzle jet micro-bubble generator.

2.2.3. External Negative-Pressure-Induced Air Nozzle Design

The external negative-pressure-induced air nozzle is designed based on the jet pump and bubble generator principles. According to the exit diameter of the diffusion section of the fourth-stage nozzle of the internal tandem friction shear cavitation nozzle and taking into account that the solid-phase flake graphite particles should be in suspension during the conveying process, it is required that the mixed triple-phase flow velocity is not less than the critical velocity in the tube. Therefore, the diameter of the suction mixing chamber can be determined.

The external negative-pressure-induced air nozzle adopts a long throat design to enhance the likelihood of the colliding and adhesion of flake graphite particles and micro-bubbles and strengthen the mineralization effect. The throat's diameter d_h according to the empirical formula for jet pumps is as follows [36,37]:

$$d_h = d\sqrt{\varepsilon m} \tag{2}$$

$$m = 0.981\left(p_c - p_{atm}\right) + 1 \tag{3}$$

where ε is the throat shrinkage coefficient (0.6~0.72); m is the optimal area ratio of the throat and inner nozzle outlet section; p_c is the external negative-pressure-induced air nozzle outlet pressure (Pa); and p_{atm} is the atmospheric pressure (Pa).

The optimal throat length L is as follows [38]:

$$L = (7.77 + 2.42m)d_h \tag{4}$$

The external negative-pressure-induced air nozzle is designed with a diffusion tube cone angle of 14°, and given the diffusion tube outlet diameter, the diffusion tube length L_d is determined by the results of the laboratory tests in this project and by referring to the literature [37]:

$$L_d = k(d_d - d_h) \tag{5}$$

where k is the diffusion angle coefficient, take 7~10; d_d is the outlet inner diameter of the diffusion angle (mm); and d_h is the diameter of the throat (mm), according to Equations (2) to (5). The throat diameter, throat length, and diffusion tube length can be calculated, respectively.

2.3. Calculation Method and Boundary Condition Setting

To determine the calculation method and boundary condition setting, a separation solver is applied to the air–water–flake graphite triple-phase flow field characteristics of the double-nozzle jet micro-bubble generator and the Eulerian multiphase flow model is selected. Moreover, the default first-order accuracy windward differential format is used, and the standardized k-ε model is selected for the turbulence model [39]. The convergence criterion for the numerical simulation is the residual $R \leq 10^{-6}$, the relaxation factors are all adopted as default values, and the pressure–velocity coupling approach employs the phase-coupled SIMPLE algorithm [40].

The inlet of the internal cavitation nozzle of the double-nozzle jet micro-bubble generator is set as the liquid-solid two-phase pressure inlet, and the two air inlets and nozzle outlets of the external air nozzle of the double-nozzle jet micro-bubble generator are set as the air-phase pressure inlet and the air–water–flake graphite triple-phase pressure outlet, respectively. The double-nozzle jet micro-bubble generator's interior wall is slid without velocity, and a standard wall function is selected near the inner wall surface of the nozzle.

3. Mathematical Mode

3.1. Control Equations for the Three-Phase Flow of Air–Water–Flake Graphite

The double-nozzle jet micro-bubble generator's internal field of flow is a hybrid triple-phase highly turbulent jet, with interpenetrations and interactions between air-phase, water-phase, and flake-graphite-phase media. The hybrid triple-phase media are all approximate to a continuous medium. Furthermore, the solid-phase flake graphite slurry in the mixed three-phase has a volume percentage of 30%, which is more than 10%. These conditions are suitable for the Eulerian multiphase flow model [41]. Therefore, the Eulerian model is chosen in this study to investigate the triple-phase flow characteristics of the air, water, and flake graphite phases.

(1) The equations for the conservation of mass for air, water, and flake graphite are as follows [42]:

$$\frac{\partial}{\partial t}(\alpha_a \rho_a) + \nabla \cdot (\alpha_a \rho_a v_a) = 0 \quad (6)$$

$$\frac{\partial}{\partial t}(\alpha_w \rho_w) + \nabla \cdot (\alpha_w \rho_w v_w) = 0 \quad (7)$$

$$\frac{\partial}{\partial t}(\alpha_s \rho_s) + \nabla \cdot (\alpha_s \rho_s v_s) = 0 \quad (8)$$

where t represents the time (s); α_a represents the volume ratio occupied by the air phase (%); ρ_a represents the air density (kg/m^3); v_a represents the air velocity (m/s); α_w represents the volume ratio occupied by the water (%); ρ_w represents the water density (kg/m^3); v_w represents the water velocity (m/s); α_s represents the volume ratio occupied by the flake graphite (%); ρ_s represents the flake graphite density (kg/m^3); and vs. represents the flake graphite velocity (m/s).

(2) The equations for the conservation of momentum for air, water, and flake graphite are as follows [42]:

$$\frac{\partial}{\partial t}(\alpha_a \rho_a v_a) + \nabla \cdot (\alpha_a \rho_a v_a v_a) = -\alpha_a \nabla p - \nabla(\alpha_a \tau_a) + \alpha_a \rho_a g + M_{i,a} \quad (9)$$

$$\frac{\partial}{\partial t}(\alpha_w \rho_w v_w) + \nabla \cdot (\alpha_w \rho_w v_w v_w) = -\alpha_w \nabla p - \nabla(\alpha_w \tau_w) + \alpha_w \rho_w g + M_{i,w} \quad (10)$$

$$\frac{\partial}{\partial t}(\alpha_s \rho_s v_s) + \nabla \cdot (\alpha_s \rho_s v_s v_s) = -\alpha_s \nabla p - \nabla(\alpha_s \tau_s) + \alpha_s \rho_s g + M_{i,s} \quad (11)$$

where p represents the working pressure (Pa); τ_a represents the air shear stress (Pa); g represents the acceleration of gravity (m/s^2); $M_{i,a}$ represents the air-phase interphase force (N); τ_w represents the water-phase shear stress (Pa); $M_{i,w}$ represents the water-phase interphase force (N); τ_s represents the flake-graphite-phase shear stress (Pa); and $M_{i,s}$ represents the flake-graphite-phase interphase force (N).

The shear stresses τ_a, τ_w, and τ_s in Equations (9) to (11) for air, water, and flake graphite are as follows [43]:

$$\tau_a = \alpha_a \mu_a \left(\nabla v_a + \nabla {v_a}^T\right) + \alpha_a \left(\lambda_a - \frac{2}{3} v_a\right) \nabla v_a I \quad (12)$$

$$\tau_w = \alpha_w \mu_w \left(\nabla v_w + \nabla {v_w}^T\right) + \alpha_w \left(\lambda_w - \frac{2}{3} v_w\right) \nabla v_w I \quad (13)$$

$$\tau_s = \alpha_s \mu_s \left(\nabla v_s + \nabla {v_s}^T\right) + \alpha_s \left(\lambda_s - \frac{2}{3} v_s\right) \nabla v_s I \quad (14)$$

where μ_a represents the air shear viscosity (Pa·s); λ_a represents the air bulk viscosity (Pa·s); μ_w represents the water shear viscosity (Pa·s); λ_w represents the water bulk viscosity (Pa·s); μ_s represents the flake graphite shear viscosity (Pa·s); λ_s represents the flake graphite bulk viscosity (Pa·s); and I represents the unit tensor.

(3) Interphase forces of air, water, and flake graphite

In the air–water–flake graphite Eulerian triple-phase flow model, as a result of the phases' different velocities, a velocity difference occurs between the phases so that interaction forces are generated between the phases, and momentum exchange is induced between the phases. To study the interphase forces between the three phases, it is now expected to take the interaction between two phases into account first and then analyze the impact of the presence of the third phase on the interplay between the other two phases to establish the interphase force equation for the coupling of the air–liquid–solid three phases. Therefore, this study is divided into air phase–water phase, water phase–flake graphite phase, and air phase–flake graphite phase to establish the interphase force equations.

Interphase forces in the air phase–water phase

① The gas–liquid added mass force is caused by the acceleration difference between the water and air phases in the internal flow field of the double-nozzle jet micro-bubble generator. When the bubble accelerates, part of the fluid in the trailing vortex accelerates to increase its resistance, equivalent to increasing the bubble mass. The gas–liquid additional mass force $F_{vm,a\text{-}w}$ is as follows [43]:

$$F_{vm,a\text{-}w} = \alpha_a \rho_w C_M \frac{\partial}{\partial t}(v_w - v_a) \tag{15}$$

where C_M represents the additional mass force coefficient, which is taken to be 0.5 by default.

There are traction forces between air and water, and the Schiller–Naumann traction model can better describe air–liquid traction, which is $F_{drag,a\text{-}w}$ as follows [43–45]:

$$F_{drag,a\text{-}w} = C_D(v_w - v_a) \tag{16}$$

$$C_D = \begin{cases} 24(1 + 0.15Re^{0.687})/Re & Re < 1000 \\ 0.44 & Re \geq 1000 \end{cases} \tag{17}$$

where C_D represents the gas–liquid traction coefficient, and Re represents the Reynolds number.

Interphase forces in the water phase–flake graphite phase

② In the internal flow field of the double-nozzle jet micro-bubble generator, the trailing force between liquid and solid is minimal, and due to the small diameter of the flake graphite mineral particles, which has a robust flow-following property, the interphase force of the water phase–flake graphite phase in this environment can be neglected as a trailing force; only the shear lift of the water phase–flake graphite phase will be examined, and the liquid–solid shear lift $F_{lift,w\text{-}s}$ is as follows [43]:

$$F_{lift,w-s} = \alpha_w \rho_s C_L (v_s - v_w)(\nabla \times v_s) \tag{18}$$

Interphase forces in the air phase–flake graphite phase

③ The force between the air phase–flake graphite phase in the inner flow field of the double-nozzle jet micro-bubble generator is mainly a trailing force generated due to the velocity gradient between the air bubbles and the flake graphite particles. This air–solid trailing force $F_{drag,a\text{-}s}$ is as follows [43,46]:

$$F_{drag,a\text{-}s} = \frac{3}{4} C_D \frac{\alpha_s \alpha_a \rho_a |v_a - v_s|}{d_s} {\alpha_a}^{-2.65} \tag{19}$$

$$C_D = \begin{cases} \frac{24}{\alpha_s Re_s}\left[1 + 0.15(\alpha_s Re_s)^{0.687}\right] & Re_s < 1000 \\ 0.44 & Re_s \geq 1000 \end{cases} \tag{20}$$

$$Re_s = \frac{\rho_a d_s |v_s - v_a|}{\mu_a} \tag{21}$$

where C_D represents the gas–solid tracer coefficient, Re_s represents the gas–solid relative Reynolds number, and d_s represents the flake graphite particles' diameter (mm).

3.2. Turbulence Model

The double-nozzle jet micro-bubble generator's inner flow field in this study belongs to the complex gas–liquid–solid three-phase turbulent suspension flow, which contains multifactorial physical processes such as turbulent jets, particle collisions, jet swirling suction, turbulent mixing, etc. At the same time, a high Reynolds number exists in the multiphase flow, so the standardized k-ε model for computing is selected as the turbulence model. This turbulence model contains two basic equations, the transport equations for turbulent kinetic energy k and dissipation rate ε [47]:

$$\frac{\partial}{\partial t}(\rho k) + \frac{\partial}{\partial x_i}(\rho k u_i) = \frac{\partial}{\partial x_j}\left[\left(\mu + \frac{\mu_t}{\sigma_k}\right)\frac{\partial k}{\partial x_j}\right] + G_k + G_b - \rho\varepsilon - Y_M \tag{22}$$

where μ represents the kinetic viscosity coefficient (Pa·s); μ_t represents the turbulent viscosity (Pa·s); σ_k represents the turbulent Platt's number of turbulent kinetic energy; G_k represents the turbulent kinetic energy produced by the average velocity gradient; G_b represents the turbulent kinetic energy generated by the buoyancy force; and Y_M represents the contribution of pulsating expansion to the total dissipation rate in compressible turbulence.

$$\frac{\partial}{\partial t}(\rho\varepsilon) + \frac{\partial}{\partial x_i}(\rho\varepsilon u_i) = \frac{\partial}{\partial x_i}\left[\left(\mu + \frac{\mu_t}{\sigma_\varepsilon}\right)\frac{\partial\varepsilon}{\partial x_j}\right] + C_{1\varepsilon}\frac{\varepsilon}{k}(G_k + C_{3\varepsilon}G_b) - C_{2\varepsilon}\rho\frac{\varepsilon^2}{k_\varepsilon} \tag{23}$$

where σ_ε represents the turbulent Prandtl number of the dissipation rate; and $C_{1\varepsilon}$, $C_{2\varepsilon}$, and $C_{3\varepsilon}$ are the experimentally measured constant coefficients. For numerical simulations, $C_{1\varepsilon}$ = 1.44, $C_{2\varepsilon}$ = 1.92, σ_k = 1.0, and σ_ε = 1.3.

4. Simulation Results and Discussion

4.1. Finite Element Model

This study applies Solidworks to establish a geometric model of the flow field inside the double-nozzle jet micro-bubble generator. ICEM is used to perform tetrahedral unstructured meshing on the model. For the internal tandem friction shear cavitation nozzle rectangular convergence flat section and the external negative-pressure-induced air nozzle throat and other turbulence intensity regions for local encryption, this is to enhance the precision of calculations. Figure 4 depicts the finite element model of the double-nozzle jet micro-bubble generator.

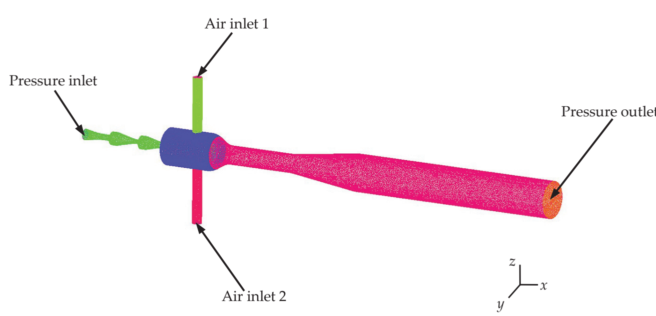

Figure 4. The finite element model.

4.2. Mesh-Independence Test

A high-quality mesh is critical to the impact of computational results. In practical fluid dynamics computational applications, it is necessary to find the threshold value to reach mesh irrelevance [48]. Mesh-independence verification is a common method to solve this problem, and the most reasonable meshing scheme is selected based on the computational accuracy of numerical simulations with different numbers of meshes [49]. This study examines the mesh independence of the maximal axis velocity of the air–water–flake graphite triple-phase flow field under the inlet pressure of 45 MPa for five different grid number conditions, and the results of the simulation calculations after reaching the steady state can be seen in Table 1.

Table 1. Mesh-independence test results.

Maximum Axial Velocity ($m{\cdot}s^{-1}$)	Number of Meshes				
	1,568,291	**2,068,291**	**2,568,291**	**3,068,291**	**3,568,291**
Air-phase flow field	174.135	180.011	187.355	187.358	187.359
Water-phase flow field	169.418	175.213	183.615	183.619	183.620
Flake-graphite-phase flow field	166.254	172.201	180.606	180.607	180.609

The maximal axis velocity variation curves of the air–water–flake graphite triple-phase flow field for five different mesh numbers are given in Figure 5. According to Figure 5 and Table 1 when the number of meshes is less than 2,568,291, the numerical simulation values of the maximal axis velocity of the water–air–flake graphite triple-phase flow field have a significant difference; when the number of meshes is greater than or equal to 2,568,291, the numerical simulation values of the maximal axis velocity of the air–water–flake graphite triple-phase flow field have a minimal difference. Therefore, considering the computational efficiency and precision of the simulation, it is determined that the number of meshes is 2,568,291 to meet the requirement of mesh number irrelevance, and the corresponding number of nodes is 356,453.

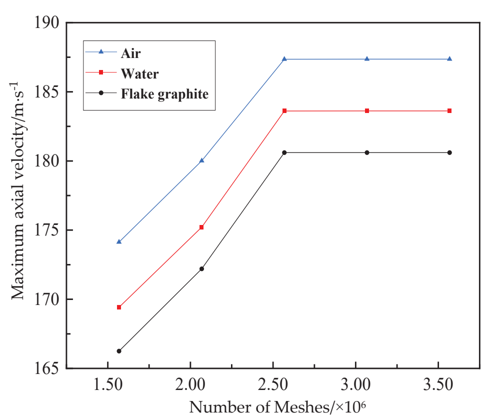

Figure 5. Speed curves of the three-phase flow field with different meshes.

4.3. Effect of Inlet Pressure on the Air Flow Field

With different inlet pressures of the double-nozzle jet micro-bubble generator, the flake graphite slurry is ejected from the internal nozzles at different speeds, with varying air intake and air-phase volume fractions. Figure 6 depicts a cloud chart of the air volume fraction distribution when the inlet pressure of the micro-bubble generator is 5, 15, 25, 35, and 45 MPa, respectively. According to the data demonstrated in Figure 6, the air volume fraction in the flow field of the double-nozzle jet micro-bubble generator is more significant than 98% under different inlet pressures, and it is approximately uniformly distributed in the steady flow tube. Specifically, when the flake graphite slurry is ejected from the internal series friction shear cavitation nozzle at high speed, the cavitation nozzle's exit point experiences negative pressure due to the high-speed flow of the slurry. The ejection generates a negative pressure, causing the outside air to be drawn into the mixing chamber via the entrance of the double-input pipe of the external air nozzle.

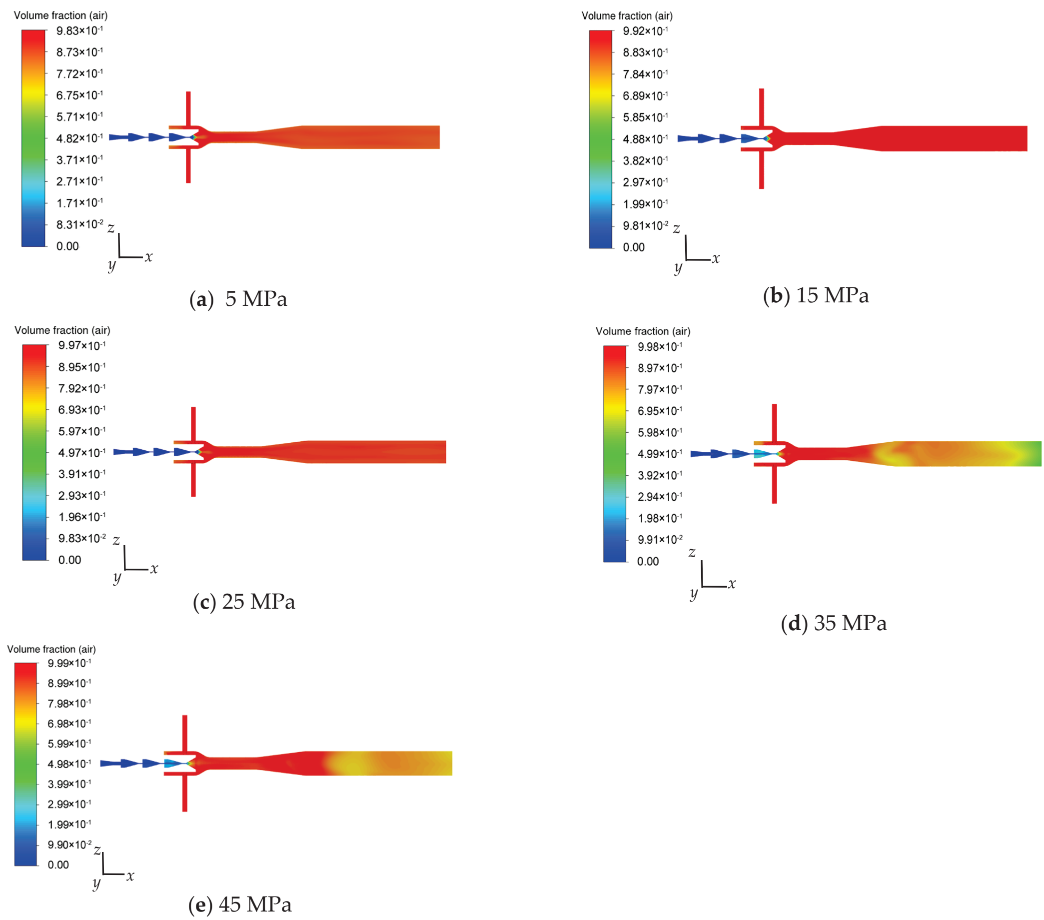

Figure 6. Cloud chart of the air volume fraction distribution.

The air entering the mixing chamber is fully collided and sheared by the graphite slurry sprayed out from the cavitation nozzle at high speed, and split into countless tiny bubbles to form an air–water–flake graphite triple-phase flow into the throat and then into the diffusion tube and the steady flow tube; in the throat, diffusion tube, and the continuous flow tube, due to the fluid role of the high turbulence intensity of the air–water–flake graphite triple-phase media to enhance further mixing to promote a more even distribution of bubbles, the bubbles in the steady flow tube show an approximate uniform distribution. The results obtained by Li et al. [25] align with the present study, as they found that the dual-intake tube configuration yields a more homogeneous dispersion of bubbles compared to the jet micro-bubble generator with a single-intake tube configuration.

At the same time, as seen in Figure 6, the negative-pressure ejection effect of the flake graphite slurry from the cavitation nozzle at high speed is directly proportional to the inlet pressure. As the inlet pressure increases, a greater influx of air results in a more substantial air-phase volume percentage. When the inlet pressure is 5, 15, 25, 35, and 45 MPa, the resulting air-phase volume fraction is 98.3%, 99.2%, 99.7%, 99.8%, and 99.9%, respectively, which indicates that the homemade double-nozzle jet micro-bubble generator has good self-absorption performance. Sufficient air intake by the high-speed flow of flake graphite slurry fully collision shears into tiny bubbles, which is conducive to the mineralization of flake graphite, to achieve the mineralization function of the double-nozzle jet micro-bubble generator.

Figure 6 also shows a significant air-phase volume percentage close to the wall of the diffusion portion of the internal tandem friction shear cavitation nozzle. This is because the flake graphite slurry is ejected from the friction portion of the fourth-stage nozzle of the internal tandem friction shear cavitation nozzle into the diffusion portion. In the diffusion portion, the slurry's axial velocity in the radial direction exhibits a substantial velocity gradient. This gradient is further amplified in the shear layer, producing a notable structural vortex ring. The pressure in the center of the vortex ring is lower than the saturated vapor pressure of the water, forming numerous bubbles due to cavitation. This finding aligns with the result drawn by Yasunari et al. [50], which suggests that the primary site for vacuole formation inside the depressurized nozzle is the low-pressure area of the flow channel, as seen by a high-speed camera.

Figure 7 gives the vector diagram of air flow field velocity distribution in the mixing chamber of the external negative-pressure-induced air nozzle at the inlet pressure of 25 MPa of the double-nozzle jet micro-bubble generator. As seen in Figure 7, there is obvious air reflux near the wall of the diffusion section of the internal tandem friction shear cavitation nozzle; the refluxed air is superimposed with the air bubbles generated during the cavitation of the diffusion section and under the hostage effect of the slurry to form an air–water–flake graphite triple-phase flow to the downstream throat, diffusion tube up to the stabilizer tube, and the bubbles exhibit a uniform spread in the flow stabilizer tube. Therefore, the vacuoles generated by cavitation are an essential part of the gas volume percentage in the homemade double-nozzle jet micro-bubble generator. This is in agreement with Deng [19], who found that the cavitation effect of the micro-bubble generator assumes a crucial function in micro-bubble production and the mineralization process during mineral flotation when simulated.

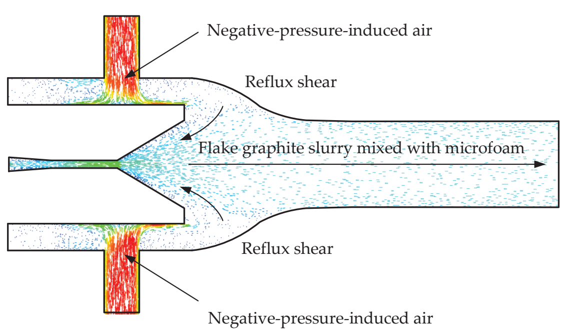

Figure 7. Vector diagram of air flow velocity in the mixing chamber.

4.4. Effect of Inlet Pressure on the Flow Field of Water and the Flow Field of Flake Graphite

As shown in Figure 8, the axis velocity of the water of the double-nozzle jet micro-bubble generator shows a symmetrical distribution up and down at inlet pressures of 5, 15, 25, 35, and 45 MPa, respectively, and the maximum axis velocity of the water is proportional to the inlet pressure. Specifically, the liquid-phase water in the slurry enters the slurry through the inlet of the tandem friction shear cavitation nozzles inside the double-nozzle jet micro-bubble generator. After entering the water first through the internal nozzle of the first stage of the nozzle, the first stage of the nozzle convergence section of the axis velocity of the water increases rapidly. In the cylindrical section, the axis velocity basically remains unchanged; this is due to the cylindrical section of the entrance position. In the inertial effect of the water, the water can only exhibit a gradual, smooth, and continuous bending of the water flow so that the fluid cross-section of the contraction is of a certain degree. Then, into the second level of the rectangular convergence flat friction nozzle, because the second level of the nozzle entrance in the flow channel cross-section expands and then gradually contracts, the axis velocity of the water in the second level of the nozzle first decreases and then gradually increases in the friction section of the axial velocity, which remains unchanged. After entering the third level of the rectangular convergence flat friction nozzle, because the third level of the nozzle structure is the same as the second-level nozzle, the axis velocity of the water in the third level of the rule of change and the second level of the rule of change of is the same. Finally, the water enters the fourth level of friction shear cavitation nozzle because the fourth level of nozzle channel structure in the before diffusion section with the second level and the third level of nozzle structure, so in this part of the channel in the axis velocity change rule of the water with the second level, the third level of the axis velocity change rule of the nozzle is the same; in the nozzle diffusion section of the axis velocity of the water is rapidly decreasing.

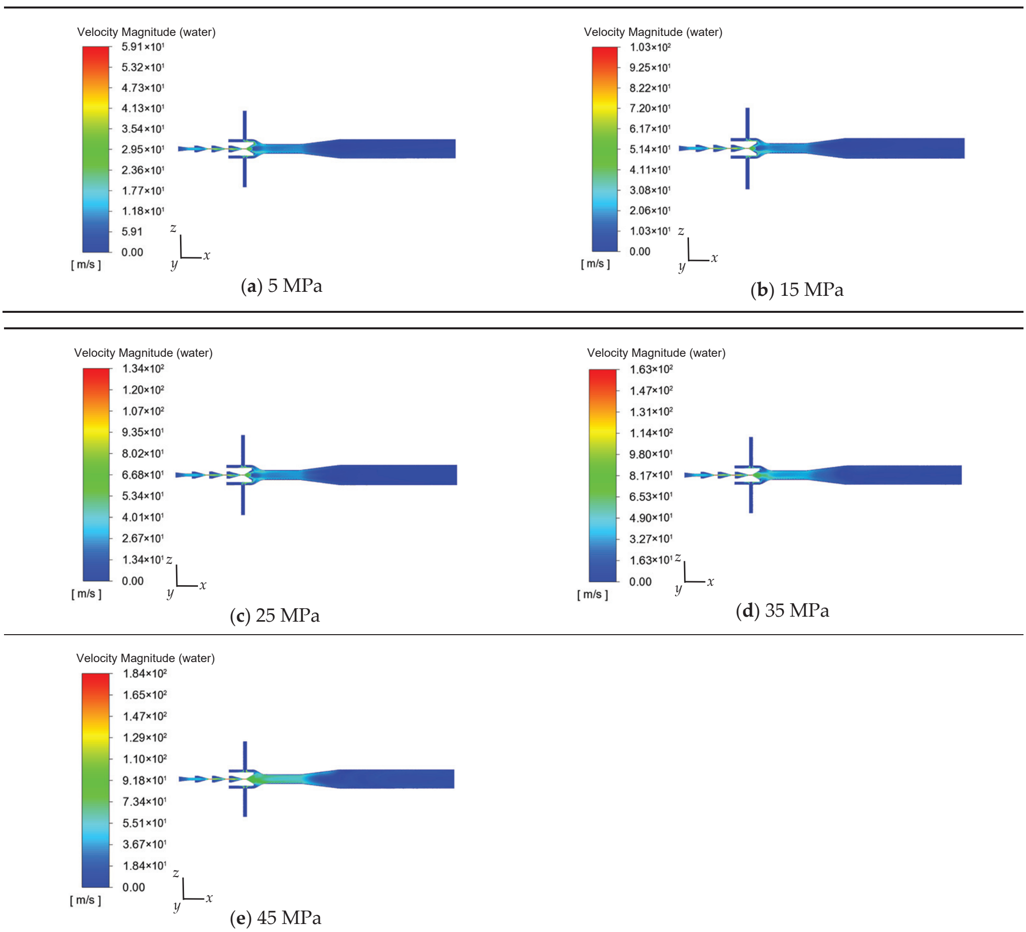

Figure 8. Water axial velocity distribution cloud diagram.

The water from the fourth-stage nozzle in the mixing chamber of the external air nozzle is strongly mixed with the air introduced under negative pressure, and then flows into the throat through the mixing chamber contraction section to realize the second acceleration, and then flows through the downstream diffusion section and the steady flow tube out of the double-nozzle jet micro-bubble generator. The axial velocity is basically kept unchanged in the throat and decreases because of the gradual expansion of the cross-section in the diffusion tube, which basically keeps the axial velocity constant in the steady flow tube. The maximum axial velocities of the water are 59.1, 103.0, 134.0, 163.0, and 184.0 m/s when the inlet pressures are 5, 15, 25, 35, and 45 MPa, respectively.

As shown in Figure 9, the change rule and distribution of axis velocity of the flake graphite of the double-nozzle jet micro-bubble generator is the same as that of the water when the inlet pressures are 5, 15, 25, 35, and 45 MPa, respectively. The maximum axis velocity of the flake graphite is proportional to the inlet pressure. The maximum axis velocities of the flake graphite are 58.5, 101.0, 132.0, 161.0, and 181.0 m/s when the inlet pressures are 5, 15, 25, 35, and 45 MPa, respectively.

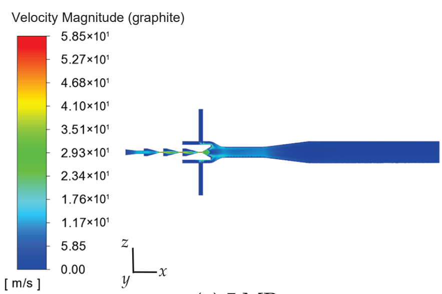

(a) 5 MPa

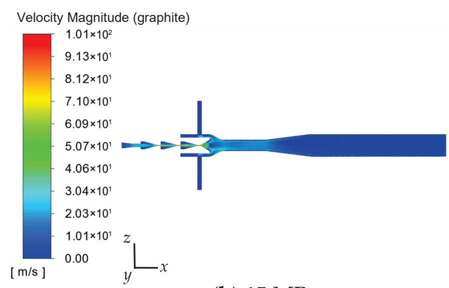

(b) 15 MPa

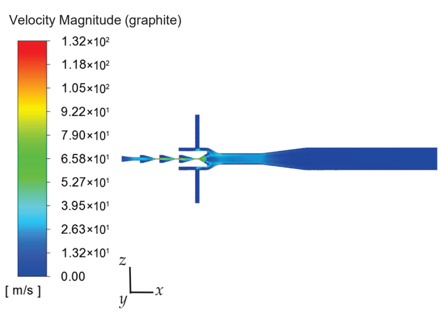

(c) 25 MPa

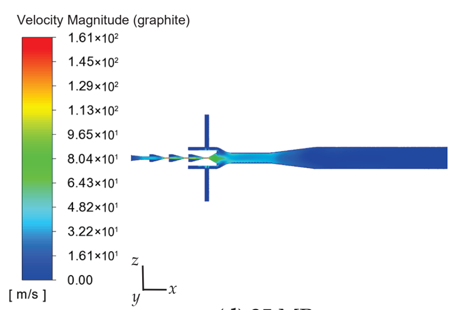

(d) 35 MPa

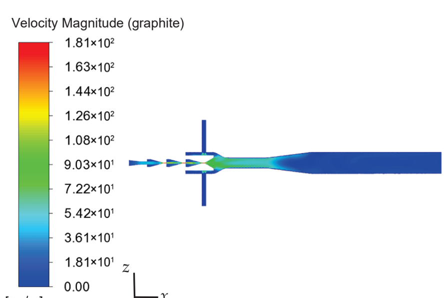

(e) 45 MPa

Figure 9. Flake graphite axial velocity distribution cloud diagram.

It should be emphasized that first, under the same inlet pressure conditions, the maximum axis velocity of the flake graphite is slightly smaller than the maximum axis velocity of the water. This is due to the density of flake graphite being 2.1 times the density of water, and the inertia of flake graphite is greater than the inertia of water in the water–flake graphite liquid–solid two-phase flow and air–water–flake graphite gas–liquid–solid three-phase flow process. Secondly, the slurry composed of water and flake graphite is sprayed from the internal nozzle at high speed into the suction mixing chamber of the external nozzle, which is strongly combined with the air inhaled from the double-inlet pipe to form the air–water–flake graphite triple-phase flow field, and then flows into the throat through the suction mixing chamber contraction tube to realize the secondary acceleration and the stabilized flow adjustment of the three-phase fluid flow in the throat. Third, the air–water–flake graphite triple-phase fluid enters the downstream diffusion tube after stabilizing the flow through the throat. The axis velocity of the air–water–flake graphite triple-phase fluid in the diffusion tube has a large radial velocity gradient. A sizeable structural vortex ring is formed by the velocity gradient in the shear layer. The vortex ring generates a region of reduced pressure at its central region, resulting in the roll suction effect on the surrounding fluid. The air has a significantly lower density compared to the water and the flake graphite, so the air bubbles are first rolled into the vortex ring, realizing intense collisions between bubbles, crushing and prolonging the residence time of bubbles. This coincides with the findings of Huang et al. [51] that the reflux coiling suction impact observed in the diffusion zone of the micro-bubble generator can effectively enhance the interaction between bubbles while prolonging the bubble residence time and significantly increasing the collision probability. Fourthly, the flake graphite particles in the friction region of level two to level four of the internal nozzle and the convergence region of level one to level four of the nozzles all generate strong friction and shear effects between the flake graphite particles and the interior portion of the nozzle to dissociate the flake graphite, and at the same time, the cavitation effect generated in the diffusion section of the fourth-stage nozzles of the internal nozzles also dissociates the flake graphite. This comprehensive dissociation of flake graphite realizes the micro-bubble generator's grinding function.

After studying the law of the inlet pressure on the triple-phase velocity flow field, the influence of the inlet pressure on the turbulence intensity of the law was further studied. Figure 10 provides an example of the turbulence kinetic energy distribution of the double-nozzle jet micro-bubble generator inlet pressure of 15 MPa in a cloud diagram. As can be seen from Figure 10, the turbulent kinetic energy reaches its maximum at the joint of the double air-intake pipe and the mixing chamber, and the maximum value is generated due to the low-speed airflow being sucked, collided, and sheared by the high-speed jet slurry. The high turbulence intensity is conducive to promoting the air–water–flake graphite mixing, thus improving the shear effect on the airflow introduced by the negative pressure, which is conducive to the realization of the generation and uniform distribution of micro-bubbles.

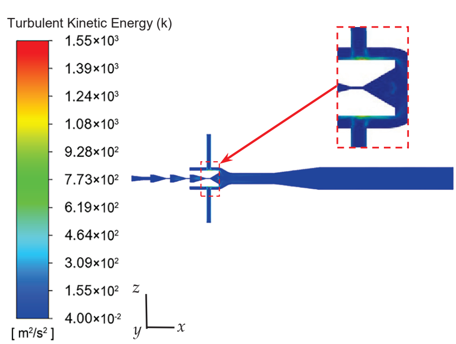

Figure 10. Cloud of the turbulence intensity distribution at 15 MPa.

4.5. Experimental Validation

4.5.1. Bubble Cluster Visualization Test

The bubble visualization test system for the homemade double-nozzle jet micro-bubble generator is shown in Figure 11. As seen in Figure 11, the system mainly consists of a water tank, a high-pressure pump, a high-pressure control valve, a high-pressure tube, a double-nozzle jet micro-bubble generator, a float flow meter, a flotation column unit, a high-frequency LED light source, a light plate, a high-speed camera, and a computer PC port. During the test, the inlet pressure of the double-nozzle jet micro-bubble generator was 15 MPa, and the air inlet of the float flow meter was 20 LPM. The high-speed camera captured a photo of the bubble group morphology generated by the air–water two-phase fluid injected into the capture area of the flotation column unit through the double-nozzle jet micro-bubble generator.

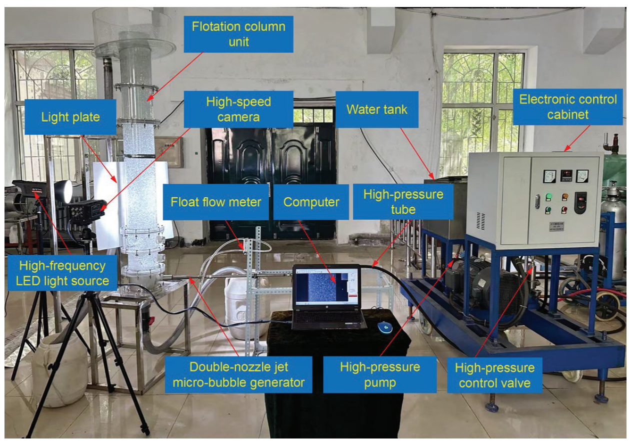

Figure 11. Bubble visualization test system for the double-nozzle jet micro-bubble generator.

The working principle of the double-nozzle jet micro-bubble generator is that the high-pressure water generated by the high-pressure pump enters the double-nozzle jet micro-bubble generator through the high-pressure tube into the internal tandem friction shear cavitation nozzle and is then sprayed out at the fourth cavitation nozzle at a very high speed. The negative-pressure ejection of high-speed jets causes the outside air to enter into the double air-intake pipe through the float flow meter, and at the inlet of the double air-intake pipe, a relatively uniform flow rate is sucked into the mixing chamber of the external negative-pressure ejection air nozzle of the double-nozzle jet micro-bubble generator. Near the outlet of the fourth-stage cavitation nozzle, there is a significant velocity difference between the high-speed jet and the airflow introduced by the negative pressure. The low-speed airflow is carried by the high-speed jet and crushed into countless tiny bubbles. The contraction section of the throat promotes the gas–liquid two-phase flow to contact and mix further fully, and then it is injected into the flotation column device through the outlet of the double-nozzle jet micro-bubble generator. The bubble group morphology photos of the double-nozzle jet micro-bubble generator taken by the high-speed camera are shown in Figure 12. It can be seen from Figure 12 that under the combined action of the internal tandem friction shear cavitation nozzle diffusion section and the external negative-pressure ejection air nozzle steady flow tube, the jet produced a dense and uniform bubble group. The area percentage, aspect ratio, and bubble spacing of the bubble group were good, indicating that the self-suction performance of the homemade double-nozzle jet micro-bubble generator was good. The sufficient air intake was fully collided and sheared into tiny bubbles by the high-speed jet, which could produce a bubble group with uniform dispersion, which verified the accuracy of the numerical simulation results.

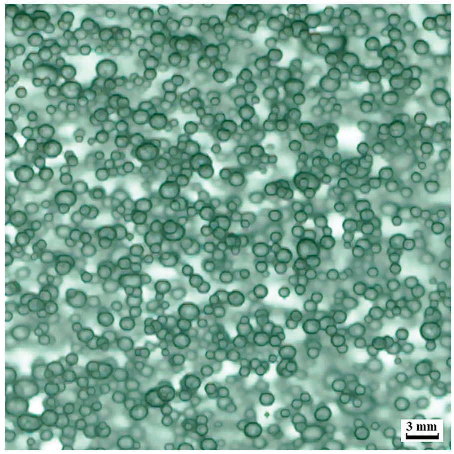

Figure 12. Photograph of bubble cluster morphology.

Since the bubble size determines the surface area of the bubble in contact with the flake graphite particles, it plays a crucial role in the flotation flake graphite environment. Therefore, to evaluate the bubble size generated by the double-nozzle jet micro-bubble generator, Image-Pro Plus software was used to obtain the average bubble size, and the bubble size distribution graph was plotted, to visually characterize the diameter of micro-bubbles generated by the double-nozzle jet micro-bubble generator. The histogram of bubble diameter distribution is shown in Figure 13, from which it can be seen that the bubble size distribution is unimodal, and the average size of bubbles less than or equal to 1 mm accounted for 71.26% of the total number of bubbles, indicating that the bubble size distribution is centralized, presenting a uniform bubble group dispersion distribution state and a good specific surface area, which is conducive to the realization of the sorting of the flake graphite.

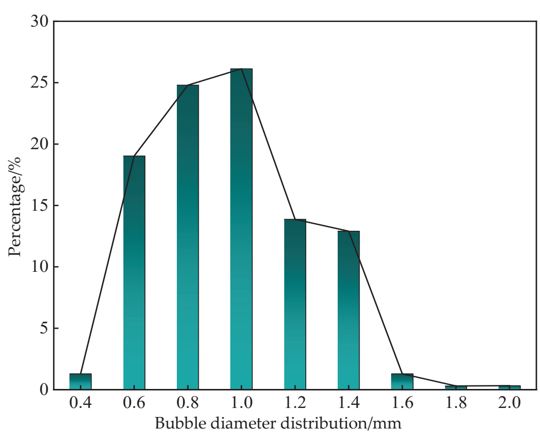

Figure 13. Histogram of bubble diameter distribution.

4.5.2. Integration Test of Flake Graphite Grinding and Floating

The integrated test system of the double-nozzle jet micro-bubble generator on flake graphite grinding and floating is shown in Figure 14. As can be seen in Figure 14, the system mainly consists of a water tank, high-pressure pump, electronic control cabinet, high-pressure pipe, high-pressure control valve, flake graphite slurry tank, double-nozzle jet micro-bubble generator, a float flow meter, flotation column unit, concentrate collection bucket, and tailings collection bucket and other components. The test process is as follows: a high-pressure pump to pressurize the water to the working pressure of 15 MPa, pressurized high-pressure water into the flake graphite slurry tank to complete the mixing with the flake graphite after the flow to the double-nozzle jet micro-bubble generator, the internal tandem friction shear cavitation nozzle for multistage dissociation of the flake graphite to achieve the function of grinding, while at the same time, a graphite slurry high-speed flow of the negative pressure generated by the air sucked into the external negative-pressure ejection air nozzle inside the mixing chamber, air from the high-speed flow of the graphite slurry impact and shear action to form tiny bubbles, and gas–liquid two-phase accumulation to form a high gas capacity, conducive to the formation of mineralization bubbling and mineralization function. The flake graphite slurry after grinding and mineralization is discharged to the flotation column device through the double-nozzle jet micro-bubble generator, the graphite concentrate and tailings are separated in the flotation column device, the graphite concentrate is collected in the concentrate tank at the upper end of the flotation column device, and the tailings are discharged from the tailings tank at the lower end of the flotation column device, which realizes the integration of grinding and flotation in the processing of flake graphite.

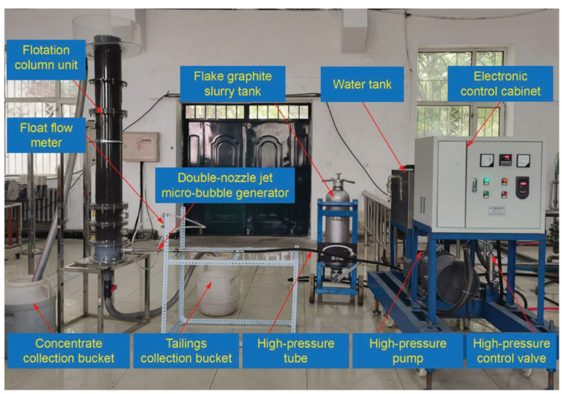

Figure 14. Integration test of flake graphite grinding and floating.

In this study, the fixed carbon content of flake graphite was used as an evaluation index. By measuring the fixed carbon content of flake graphite samples before and after the test, the grinding and mineralization effect of flake graphite by the double-nozzle jet micro-bubble generator was obtained. Since the test sample is the first stage of the beneficiation product of Jixi Liumao graphite ore, the fixed carbon content of the flake graphite sample after the test was compared with the fixed carbon content of the secondary and tertiary stage of the beneficiation products in the actual industrial beneficiation process of Jixi Liumao graphite, and the optimization effect of the double-nozzle jet micro-bubble generator on shortening the flake graphite beneficiation process was evaluated.

In order to ensure the accuracy of the measurement results of the fixed carbon content of flake graphite, the flake graphite samples before the grinding and flotation integration test and the flake graphite concentrate samples after the grinding and flotation integration test were divided into two groups, with 1 g for each group. The fixed carbon content of each group of samples was determined by using the subtraction method, and the average value was calculated. The fixed carbon content of the flake graphite samples before the test and the flake graphite concentrate samples after the test were 49.11% and 80.70%, respectively. Moreover, the fixed carbon content of the concentrate samples after the test increased by 31.59%, indicating that the double-nozzle jet micro-bubble generator can effectively dissociate the vein stone impurities on the surface of flake graphite, and at the same time, the generator can realize the mineralization function of flake graphite, which greatly improves its grade. In addition, the fixed carbon content of the flake graphite concentrate samples after the grinding and flotation integration test was higher than the fixed carbon content of the secondary and tertiary stages of the beneficiation products of Jixi Liumao graphite ore. This result indicates that conducting the single grinding and flotation integration test on flake graphite by using the double-nozzle jet micro-bubble generator can replace the three beneficiation steps of primary grinding, secondary flotation, and secondary grinding in the actual beneficiation process; moreover, the generator can achieve the aim of shortening the actual conventional flake graphite beneficiation process.

5. Conclusions

In this study, a homemade double-nozzle jet micro-bubble generator was proposed to integrate the existing independent operations of conventional flake graphite grinding and mineralization into one process. The CFD method was used to solve the micro-bubble generator air–water–flake graphite triple-phase flow, and the results were compared with those from an existing jet micro-bubble generator to validate the reasonableness of the design of the homemade double-nozzle jet micro-bubble generator.

A positive correlation exists between the air-phase volume percentage and the inlet pressure produced by the double-nozzle jet micro-bubble generator. The air-phase volume percentage is approximately uniformly distributed in the stabilizer tube. The air-phase volume percentages produced by the micro-bubble generator are 98.3, 99.2, 99.7, 99.8, and 99.9% when the inlet pressures are 5, 15, 25, 35, and 45 MPa, respectively. This indicates a homemade double-nozzle jet micro-bubble generator has an excellent self-absorption performance to achieve the mineralization function.

The axis velocities of the water and the flake graphite inside the homemade double-nozzle jet micro-bubble generator were distributed symmetrically upward and downward, and both positively correlated with the inlet pressure for the same inlet pressure. The maximum axial velocity of the flake graphite was slightly smaller than that of the water. The flake graphite is dissociated under the combined effect of friction shear and cavitation in the internal nozzle to realize the grinding function.

Author Contributions: Conceptualization, X.D.; methodology, X.D. and C.G.; software, C.G.; validation, X.D. and C.G.; formal analysis, C.G.; investigation, X.D., C.G., D.P. and Y.J.; resources, X.D. and D.P.; data curation, C.G.; writing—original draft preparation, C.G.; writing—review and editing, X.D. and D.P.; visualization, C.G. and Y.J.; supervision, X.D.; project administration, X.D.; funding acquisition, X.D. All authors have read and agreed to the published version of the manuscript.

Funding: This research was supported by the National Natural Science Foundation of China (No. 52075151) and the Natural Science Foundation of Heilongjiang Province (No. LH2020E123).

Data Availability Statement: The data presented in this study are available on request from the corresponding author. As the data in this paper belongs to the National Natural Science Foundation of China, it involves related privacy and is not owned by individuals.

Conflicts of Interest: The authors declare no conflicts of interest.

References

1. Bernard, A.; Khalil, N.; Ahmed, I.; McCalden, D.; Haelssig, J.; Macchi, A.; Duchesne, M. Gas fluidization of natural graphite flakes. *Powder Technol.* **2024**, *431*, 119097. [CrossRef]
2. Sun, K.K.; Qiu, Y.S.; Zhang, L.Y. Preserving Flake Size in an African Flake Graphite Ore Beneficiation Using a Modified Grinding and Pre-Screening Process. *Minerals* **2017**, *7*, 115. [CrossRef]
3. Al-Ani, T.; Leinonen, S.; Ahtola, T.; Salvador, D. High-Grade Flake Graphite Deposits in Metamorphic Schist Belt, Central Finland-Mineralogy and Beneficiation of Graphite for Lithium-Ion Battery Applications. *Minerals* **2020**, *10*, 680. [CrossRef]
4. Vasumathi, N.; Sarjekar, A.; Chandrayan, H.; Chennakesavulu, K.; Reddy, G.R.; Kumar, T.V.V.; El-Gendy, N.S.; Gopalkrishna, S.J. A Mini Review on Flotation Techniques and Reagents Used in Graphite Beneficiation. *Int. J. Chem. Eng.* **2023**, *2023*, 1007689. [CrossRef]
5. Srikant, S.S.; Rao, R.B. Preparation of High Purity Graphite using Comminution, Pressure Leaching and Flotation. *J. Min. Environ.* **2023**, *14*, 2461. [CrossRef]

6. Peng, Z.M.; Li, D.S.; Fang, W.J.; Zhang, J.; Zhang, R.Y.; Qiu, Y.S.; Sun, K.K. Improved Flotation of Fine Flake Graphite Using a Modified Thickening Process. *Separations* **2023**, *10*, 275. [CrossRef]
7. Ghosh, A.K. Literature quest and survey on graphite beneficiation through flotation. *Renew. Sustain. Energy Rev.* **2024**, *189*, 113980. [CrossRef]
8. Gao, J.X.; Bu, X.N.; Dong, L.S.; Qiu, Y.S.; Xie, G.Y.; Chelgani, S.C. Natural Graphite Froth Flotation—An Overview. *Miner. Process. Extr. Metall. Rev.* **2024**, 1–18. [CrossRef]
9. Yoon, R.H. Microbubble flotation. *Miner. Eng.* **1993**, *6*, 619–630. [CrossRef]
10. Lee, J.E.; Choi, W.S.; Lee, J.K. A study of the bubble properties in the column flotation system. *Korean J. Chem. Eng.* **2003**, *20*, 942–949. [CrossRef]
11. Gui, X.H.; Liu, J.T.; Cao, Y.J.; Ding, Q.P. Research and Progress on the Structural Properties of Bubble Generators. *Coal Prep. Technol.* **2009**, *2*, 66–70+81. [CrossRef]
12. Matiolo, E.; Couto, H.J.B.; Lima, N.; Silva, K.; de Freitas, A.S. Improving recovery of iron using column flotation of iron ore slimes. *Miner. Eng.* **2020**, *158*, 106608. [CrossRef]
13. Tortorelli, J.P.; Craven, J.W.; Toguri, J.M.; Dobby, G.S.; Agar, G.E. The effect of external gas/slurry contact on the flotation of fine particles. *Miner. Eng.* **1997**, *10*, 1127–1138. [CrossRef]
14. Shuai, Y.; Wang, X.Y.; Huang, Z.L.; Yang, Y.; Sun, J.Y.; Wang, J.D.; Yang, Y.R. Structural Design and Performance of a Jet-Impinging TypeMicrobubble Generator. *Ind. Eng. Chem. Res.* **2022**, *61*, 4445–4459. [CrossRef]
15. Chen, W.Y.; Wang, J.B.; Jiang, N.; Zhao, B.; Wang, Z.D. Numerical simulation of gas-liquid two-phase jet flow in air-bubble generator. *J. Cent. South Univ. Technol.* **2008**, *15*, 140–144. [CrossRef]
16. Wu, M.; Yuan, S.Y.; Song, H.Y.; Li, X.B. Micro-nano bubbles production using a swirling-type venturi bubble generator. *Chem. Eng. Process.-Process Intensif.* **2022**, *170*, 108697. [CrossRef]
17. Sadatomi, M.; Kawahara, A.; Kano, K.; Ohtomo, A. Performance of a new micro-bubble generator with a spherical body in a flowing water tube. *Exp. Therm. Fluid Sci.* **2005**, *29*, 615–623. [CrossRef]
18. Gordiychuk, A.; Svanera, M.; Benini, S.; Poesio, P. Size distribution and Sauter mean diameter of micro bubbles for a Venturi type bubble generator. *Exp. Therm. Fluid Sci.* **2016**, *70*, 51–60. [CrossRef]
19. Deng, X.W.; Lv, B.; Cheng, G.; Lu, Y. Mechanism of micro/nano-bubble formation and cavitation effect on bubbles size distribution in flotation. *Physicochem. Probl. Miner. Process.* **2020**, *56*, 504–512. [CrossRef]
20. Fujiwara, A.; Okamoto, K.; Hashiguchi, K.; Peixinho, J.; Takagi, S.; Matsumoto, Y.; ASME. Bubble breakup phenomena in a venturi tube. In Proceedings of the 5th Joint ASME/JSME Fluids Engineering Summer Conference, San Diego, CA, USA, 30 July–2 August 2007.
21. Tsave, P.K.; Kostoglou, M.; Karapantsios, T.D.; Lazaridis, N.K. A Hybrid Device for Enhancing Flotation of Fine Particles by Combining Micro-Bubbles with Conventional Bubbles. *Minerals* **2021**, *11*, 561. [CrossRef]
22. Fu, X.Z.; Niu, Z.; Lin, M.; Gao, Y.; Sun, W.; Yue, T. Strengthened Oxygen Oxidation of Ferrous Ions by A Homemade Venturi Jet Microbubble Generator towards Iron Removal in Hydrometallurgy. *Minerals* **2021**, *11*, 1342. [CrossRef]
23. Li, Q.; Guo, X.; Zhang, J.; Lei, M.; Liu, J.L.; Ming, D.Z.; Fang, L. Mechanism of Microbubbles and Cavitation Effect on Bubble Breakage in a Venturi Bubble Generator. *J. Appl. Fluid Mech.* **2023**, *16*, 778–793. [CrossRef]
24. Xu, W.G.; Li, W.J.; Wang, J.W.; Song, Y.S.; Wu, B.A.; Wen, J.K.; Li, K.G.; Li, B. Numerical Simulation of Gas-Liquid Two-Phase Flow CFD-PBM Model in a Micro-Nanobubble Generator. *Minerals* **2022**, *12*, 1270. [CrossRef]
25. Li, X.H.; Su, W.B.; Liu, Y.; Yan, X.K.; Wang, L.J.; Zhang, H.J. Comparison of bubble velocity, size, and holdup distribution between single- and double-air inlet in jet microbubble generator. *Asia-Pac. J. Chem. Eng.* **2021**, *16*, e2611. [CrossRef]
26. Basso, A.; Hamad, F.; Ganesan, P. Effects of the geometrical configuration of air-water mixer on the size and distribution of microbubbles in aeration systems. *Asia-Pac. J. Chem. Eng.* **2018**, *13*, e2259. [CrossRef]
27. Wang, L.J.; Wang, Y.H.; Yan, X.K.; Wang, A.; Cao, Y.J. A numerical study on efficient recovery of fine-grained minerals with vortex generators in pipe flow unit of a cyclonic-static micro bubble flotation column. *Chem. Eng. Sci.* **2017**, *158*, 304–313. [CrossRef]
28. Alam, H.S.; Sutikno, P.; Soelaiman, T.A.F.; Sugiarto, A.T. CFD-PBM Coupled modeling of bubble size distribution in a swirling-flow nanobubble generator. *Eng. Appl. Comput. Fluid Mech.* **2022**, *16*, 677–693. [CrossRef]
29. Al-Azzawi, A.; Al-Shimmery, A.; Alshara, A.; Mohammed, M.R. Computational Fluid Dynamics Simulation Assessment of Inlet Configuration Influence on Enhancing Swirl Flow Microbubble Generator Performance. *J. Eng.* **2023**, *2023*, 1457986. [CrossRef]
30. Palazuelos, L.P.A.; Guerrero, M.U.F.; Labra, M.P.; Domínguez, I.A.R.; García, R.E.; Cardona, F.P.; Hernández, F.R.B.; Tapia, J.C.J.; Pérez, M.R. Silver(I) Recovery by Ion Flotation Process from Aqueous Solutions in Cells with Spargers. *Minerals* **2023**, *13*, 572. [CrossRef]
31. Taghavi, F.; Noaparast, M.; Pourkarimi, Z.; Nakhaei, F. Comparison of mechanical and column flotation performances on recovery of phosphate slimes in presence of nano-microbubbles. *J. Cent. South Univ.* **2022**, *29*, 102–115. [CrossRef]
32. Parga, J.R.; Valenzuela, J.L.; Aguayo, S. Bacis flotation cell for gold- and silver-beard pyrite recovery. *Miner. Metall. Process.* **2009**, *26*, 25–29. [CrossRef]
33. Ni, C.; Jin, M.G.; Chen, Y.R.; Xie, G.Y.; Peng, Y.L.; Xia, W.C. Improving the Recovery of Coarse-Coal Particles by Adding Premineralization Prior to Column Flotation. *Int. J. Coal Prep. Util.* **2017**, *37*, 87–99. [CrossRef]
34. Ma, F.Y.; Tao, D.P. A Study of Mechanisms of Nanobubble-Enhanced Flotation of Graphite. *Nanomaterials* **2022**, *12*, 3361. [CrossRef] [PubMed]

35. Wang, P.F.; Han, H.; Liu, R.H.; Gao, R.Z.; Wu, G.G. Effect of outlet diameter on atomization characteristics and dust reduction performance of X-swirl pressure nozzle. *Process Saf. Environ. Prot.* **2020**, *137*, 340–351. [CrossRef]
36. Zhang, H.Y.; Zou, D.H.; Yang, X.L.; Mou, J.G.; Zhou, Q.W.; Xu, M.S. Liquid-Gas Jet Pump: A Review. *Energies* **2022**, *15*, 6978. [CrossRef]
37. Lu, H.Q. *Theory and Application of Jet Pump Technology*; Water Resources and Electric Power Press: Beijing, China, 1989; p. 316.
38. Liu, J.Z. Research on performance of liquid-air jet pump. *J. Wuhan Inst. Water Conserv. Electr. Power.* **1982**, *3*, 105–114.
39. Wu, Y.X.; Chen, H.; Song, X.F. An investigation on the effect of open hole number and scheme on single-phase flow of a swirl flow bubble generator. *Korean J. Chem. Eng.* **2023**, *40*, 754–769. [CrossRef]
40. Cheng, J.C.; Li, Q.; Yang, C.; Zhang, Y.Q.; Mao, Z.S. CFD-PBE simulation of a bubble column in OpenFOAM. *Chin. J. Chem. Eng.* **2018**, *26*, 1773–1784. [CrossRef]
41. Mutharasu, L.C.; Kalaga, D.V.; Sathe, M.; Turney, D.E.; Griffin, D.; Li, X.L.; Kawaji, M.; Nandakumar, K.; Joshi, J.B. Experimental study and CFD simulation of the multiphase flow conditions encountered in a Novel Down-flow bubble column. *Chem. Eng. J.* **2018**, *350*, 507–522. [CrossRef]
42. Muthiah, P.; Ponnusamy, K.; Radhakrishnan, T.K. CFD Modeling of Flow Pattern and Phase Holdup of Three Phase Fluidized Bed Contactor. *Chem. Prod. Process Model.* **2009**, *4*, 1366. [CrossRef]
43. Fluent, A. *Ansys Fluent Theory Guide*; Ansys Inc.: Canonsburg, PA, USA, 2020; pp. 724–746.
44. Mwandawande, I.; Akdogan, G.; Bradshaw, S.M.; Karimi, M.; Snyders, N. Prediction of gas holdup in a column flotation cell using computational fluid dynamics (CFD). *J. S. Afr. Inst. Min. Metall.* **2019**, *119*, 81–95. [CrossRef]
45. Zhang, X.; Yu, T.; Cong, T.L.; Peng, M.J. Effects of interaction models on upward subcooled boiling flow in annulus. *Prog. Nucl. Energy* **2018**, *105*, 61–75. [CrossRef]
46. Du, W.; Bao, X.J.; Xu, J.; Wei, W.S. Computational fluid dynamics (CFD) modeling of spouted bed: Assessment of drag coefficient correlations. *Chem. Eng. Sci.* **2006**, *61*, 1401–1420. [CrossRef]
47. Zhu, Z.Y.; Qin, B.; Li, S.H.; Liu, Y.G.; Li, X.; Cui, P.Z.; Wang, Y.L.; Gao, J. Multi-dimensional analysis of turbulence models for immiscible liquid-liquid mixing in stirred tank based on numerical simulation. *Sep. Sci. Technol.* **2021**, *56*, 411–424. [CrossRef]
48. Lee, M.; Park, G.; Park, C.; Kim, C. Improvement of Grid Independence Test for Computational Fluid Dynamics Model of Building Based on Grid Resolution. *Adv. Civ. Eng.* **2020**, *2020*, 8827936. [CrossRef]
49. Zulkifli, Z.; Halim, N.H.A.; Solihin, Z.H.; Saedon, J.; Ahmad, A.A.; Abdullah, A.H.; Raof, N.A.; Hadi, M.A. The analysis of grid independence study in continuous disperse of MQL delivery system. *J. Mech. Eng. Sci.* **2023**, *17*, 9586–9596. [CrossRef]
50. Maeda, Y.; Hosokawa, S.; Baba, Y.; Tomiyama, A.; Ito, Y. Generation mechanism of micro-bubbles in a pressurized dissolution method. *Exp. Therm. Fluid Sci.* **2015**, *60*, 201–207. [CrossRef]
51. Huang, J.; Sun, L.C.; Du, M.; Liang, Z.; Mo, Z.Y. An investigation on the performance of a micro-scale Venturi bubble generator. *Chem. Eng. J.* **2020**, *386*, 120980. [CrossRef]

mining

MDPI

Article

The Development of a New Smart Evacuation Modeling Technique for Underground Mines Using Mathematical Programming

Richard Meij [1], Masoud Soleymani Shishvan [1,*] and Javad Sattarvand [2]

[1] Faculty of Civil Engineering and Geosciences, Delft University of Technology, 628 Delft, The Netherlands
[2] Department of Mining and Metallurgical Engineering, University of Nevada, Reno, NV 89557, USA; jsattarvand@unr.edu
* Correspondence: m.soleymanishishvan@tudelft.nl

Abstract: Navigating miners during an evacuation using smart evacuation technology can significantly decrease the evacuation time of an underground mine in case of emergency hazards. This paper presents a mathematical programming model to calculate the most efficient escape path for miners as a critical component of smart evacuation technology. In this model, the total evacuation distance of the crew is minimized and scenarios with blocked pathways and stamina categories for the miners are simulated. The findings revealed that all the tested scenarios were technically feasible. Using the feature that filters out blocked pathways has no downsides as safer routes are calculated and there is no penalty in the computation time. This paper also discusses the social and technical issues that must be resolved before the algorithm can be implemented as an actual escape solution.

Keywords: smart evacuation; mathematical programming; hazards; underground mines

Citation: Meij, R.; Shishvan, M.S.; Sattarvand, J. The Development of a New Smart Evacuation Modeling Technique for Underground Mines Using Mathematical Programming. *Mining* **2024**, *4*, 106–119. https://doi.org/10.3390/mining4010008

Academic Editors: Krzysztof Skrzypkowski, René Gómez, Fhatuwani Sengani, Derek B. Apel, Faham Tahmasebinia and Jianhang Chen

Received: 27 November 2023
Revised: 16 February 2024
Accepted: 19 February 2024
Published: 23 February 2024

1. Introduction

Current strategies for mine evacuation are blind and outdated technologies that only require people to run to predefined locations such as escape ways or refugee chambers during emergencies [1]. An evacuation is usually initiated by an explosion [2,3] and the release of a stench gas [4]. Upon smelling the stinky gas, miners leave their workplaces and start moving to predefined locations. This is quite a blind methodology because (i) it takes a relatively long time for the air current to reach the people underground [5]; (ii) not all people may be familiar with the layout of the mine, which may lead to confusion when trying to find the route to a safe haven; (iii) some of the predefined escape paths may cross danger zones (such as fires), and miners may approach the danger instead of running away from it; and (iv) people may get confused while navigating when the visibility decreases, which could lead to them making decisions while panicking.

Currently, several methods are used to guide miners to a safe haven during an emergency. These conventional technologies can be divided into passive and active guidance systems [1]. One passive method is to hang signs with directions to the nearest exit at intersections in the mine [4]. These, however, may be hard to read when dirty or when the visibility in the mine is limited (for instance, because of smoke). Another passive method is the use of lifelines [6]. These lines lead the miner from the workstations to the safe havens and use cones to indicate the direction of egress. Active guidance methods give the miners visual and audible cues about the route to safety. For visible cues, LEDs, lasers, or strobe lights may be used. These visual aids have a green color when one is heading towards a safe haven and a red color when one is moving away from it. Audible cues are given to augment the visual cues and use the pitch of sound to guide miners in the right direction.

In a virtual reality environment, it has been proven that smart evacuation is faster than conventional methods of evacuation [7]. According to Gaab (2019), smart evacuation systems are real-time evacuation guidance systems that are adaptable to changing conditions such as location and spreading of fire and resulting safest and fastest exit routes. To employ smart evacuation, an algorithm is needed to determine the safest and fastest exit routes.

In order to utilize smart evacuation, the real-time localization of individuals underground is needed. There are different methods for localization:

- Radio Frequency Identification (RFID): RFID systems make a connection between what are called tags and readers [8–10]. Tags can be worn by miners or attached to vehicles and contain information about the wearer. Tags communicate with readers using electromagnetic waves. The location of the wearer of the tag can be calculated using the difference in time of arrival, the received signal strength indicator (RSSI), or the time-of-flight method.
- Wi-Fi: Uses the RSSI principle [11]. In this case, access points of the wireless local area network measure the signal strength of smart devices (e.g., smartwatches and smartphones) [9].
- Bluetooth: Uses the RSSI principle in a similar way to Wi-Fi, but can use multiple channels (which is an advantage when there is a lot of background noise) [9]. Bluetooth offers good signal detection, is relatively cheap, and enables the easy introduction of new applications [12]. Also, Bluetooth devices can communicate with each other.
- Wireless Sensor Networks (WSNs): Uses fingerprinting, which is a localization method based on the RSSI principle [13–15]. In this case, a map of sensor patterns (that is, signal strengths of tags at known locations in the mine) is made before the operation is started. These maps compare the actual signals in the mine, giving an idea of where miners or vehicles may be located.
- Image-Assisted Person Location: Identifies miners by the lamp on their helmet (each of which has a unique shape) [16].

There are a number of the shortest path algorithms that could be used for smart evacuation. Three notable examples will be given here:

- Dijkstra's Algorithm: Dijkstra's algorithm is a well-established and popular shortest path algorithm [17–20]. The algorithm assumes a network of nodes, which are connected to one another by arcs. It consists of two methods: one for tree networks (where only one path between two nodes is possible) and one for more complicated networks (such as in underground mines) [21]. The algorithm will always return the shortest path possible but is computationally inefficient (with a running time of $O(n^3)$) [22]. Many shortest path algorithms are derived from Dijkstra's algorithm, each with its own advantages and disadvantages.
- Floyd–Warshall Algorithm: Another method that can be used to compute the shortest path is the Floyd–Warshall algorithm [23]. According to Hougardy (2010), it is widely used and relatively simple. Just like Dijkstra's algorithm, Floyd–Warshall's method works on a network of nodes that are connected by arcs (again, it will be assumed that one is not dealing with tree networks). The worst-case runtime of the algorithm is $O(n^3)$. If used correctly, the method will always return the shortest route between all nodes in a network. However, it does not work in networks where some of the edges have negative values. This, however, is not the case in underground mines.
- Ant Colony Optimization (ACO): ACO can also be used to find a route of egress in case of an underground mine emergency [24]. ACO is inspired by foraging ants [25]. Ants are blind and, therefore, initially, seek food at random. However, they do leave a trail of pheromones while they are on their way. Once they have found food they follow the pheromone trail back to their anthill, leaving new pheromones, making the trail stronger. The crux of the matter is that ants are more likely to follow the stronger pheromone trails. As, over time, the shorter routes to food will have more deposited pheromones on them, more ants will use the more efficient routes. The main advantage of this method is that it is relatively fast; the main disadvantage is that the final solution may be suboptimal [26].

It is clear, then, that each shortest path algorithm has its own advantages and disadvantages. In this paper, a new method based on mathematical programming will be introduced. More specifically, the method will be used to calculate the escape strategy for an underground mine. The development of this method will be presented as a part of a larger project to develop practical smart evacuation technology, supported by the US National Institute of Occupational Health and Safety (NIOSH) at the University of Nevada, Reno. A case study was executed for a drift and fill gold mine located in north-central Nevada, USA. For the case study, a CAD model of the mine containing information on the network of the underground tunnels was used. The locations of the miners, fires, and their destinations in case of an emergency (refugee chambers and shafts) were randomized. This paper investigates if mathematical programming can be used to determine the most efficient escape solution in case of an evacuation.

2. Method

This section outlines a step-by-step procedure for the proposed technique in this study. Figure 1 illustrates this process, which includes gathering necessary data, acquiring the digital mine model, investigating triggered hazards, identifying personnel and hazard location data, constructing the mathematical model, developing and evaluating diverse scenarios, utilizing optimization techniques to solve the built model for each scenario, disseminating results to individuals, guiding individuals to their destinations, and, ultimately, receiving updated hazard locations and furnishing new results if necessary.

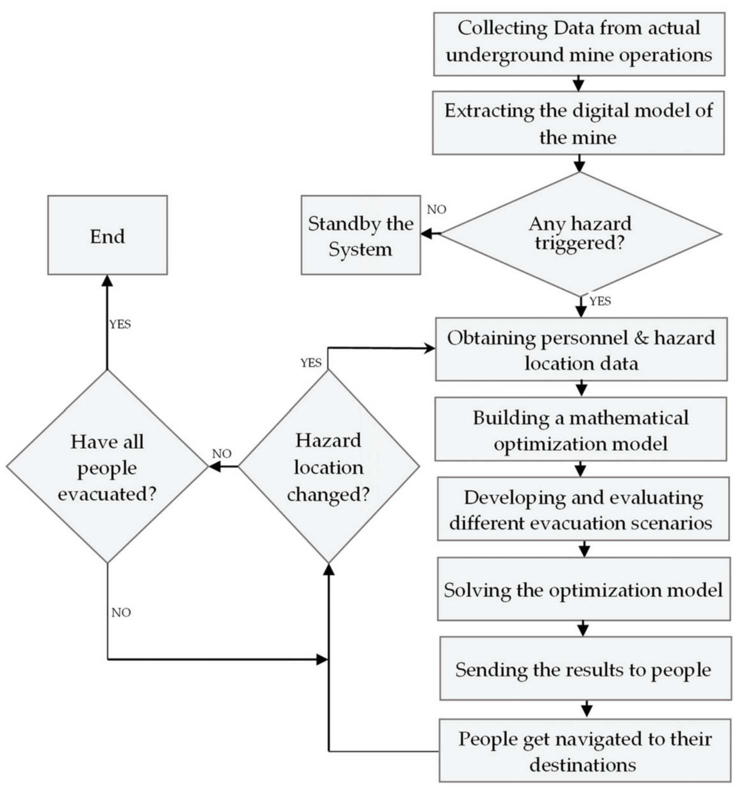

Figure 1. A step-by-step flowchart for the proposed procedure in this study.

2.1. Digital Model of the Mine

The digital modeling process started by constructing a network model that reflected the physical model of the access roads within the mine. The data concerning the dimensions of the mine used for the case study was delivered in an AutoCAD file (in a '.dxf' format). Then, the AutoCAD file was loaded onto the Python environment. Subsequently, the data were converted to an Excel file ('.xlsx' format), serving as the source of data for the main programming file. Converting the data to the Excel format made it easier to comprehend and manipulate the data.

A visual inspection of the file revealed that it contained three categories of data: 'AIR-DATA', '2DARROW', and 'AIRLINES'. The first category contained points in space, while the latter two were line strings, with a beginning and an end node. It was found that 'AIR-DATA' and '2DARROW' were used merely for ventilation purposes, while the 'AIRLINES' dataset contained the drifts making up the mine used for the case study. Therefore, all further use and manipulation of data were performed solely with the 'AIRLINES' category. A plot of the 'AIRLINES' data is given in Figure 2.

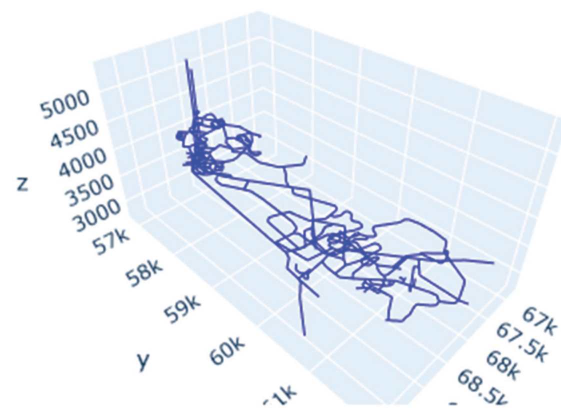

Figure 2. 'AIRLINES' data, with the unit being 'Meter' (k stands for 1000).

The next step was to build a model in which optimization models could be run. It must be noted that although line strings had been drawn, they had not been quantified yet. The only information that was known at this point was the start and end coordinates of each arc. The first step that needed to be taken, then, was to identify each individual node in the network. This was done using a function in Python specifically designed for this purpose. This function first runs through all coordinates of the starting nodes of the line strings. If a combination of coordinates does not occur, it is added to a list. After implementing this process, a sweep is made through the tail nodes to see if any original nodes can be found there. These are also added to the list. In total, 453 nodes were found using this function.

Afterwards, it was essential to find which nodes were combined to form arcs. This procedure was conducted by using another Python function. Firstly, the nodes that were found before were stored in a Pandas data frame. Secondly, the coordinates of each begin and end node of the arcs in the 'AIRLINES' data were compared to their position in the data frame. In this way, a list could be made with the relative positions of the node pairs. For instance, node zero was connected to node six. This appeared as [0, 6] in the list of arcs. In total, there were 522 arcs. Also, the pairs were reversed, as it was assumed that miners could travel in both directions on each arc. In this case, both directions of a pathway could be used during the evacuation optimization process.

Finally, the distance between the connected nodes, the slope of the particular path, and a correction to the distance for this slope needed to be calculated. The calculations for the distances between the nodes were performed using the Euclidian method. The slope angle of each path was calculated using the tangent. Adjiski et al. (2015) [27] devised a formula that makes a correction to the Euclidian distance to give paths that go more steeply upwards more weight. The correction factor was calculated using the following equation:

$$k_{gi} = \frac{m \times g \times v_0 \times sin\theta_i}{P_0} + cos\theta_i \tag{1}$$

where

- k_{gi} is the correction factor
- m is the mass of the miner (taken to be eighty kilograms on average)
- g is the gravitational constant (9.81 m/s^2)
- v_0 is the average walking speed (taken to be 1.35 m per second [28])
- θ_i is the slope angle of the path in degrees
- P_0 is the human's walking power (taken to be 200 Watts)

The correction factor was only used for slopes that rose upwards. Slopes going downwards were kept at their original length. The correction for the slope was linked to a maximum angle (taken to be 80 degrees). This was done to prevent the weights for the shafts, which went steeply upwards, becoming erratic. The Euclidian distances corrected by Adjiski's formula were used as the definitive distances between the nodes to be used in the optimization model.

2.2. Mathematical Model

The task of finding the optimal evacuation routes for each specific miner during an emergency in an underground mine can be modeled as a 'Minimum-Cost Network Flow Problem' (MCNFP). This mathematical programming model can be solved with different approaches, such as linear programming and integer programming [29].

The divisibility assumption is an important characteristic of mathematical programming. This assumption states that each variable x_i is allowed to take fractional values. This, of course, is not the case in mine evacuation scenarios (one cannot split miners into fractions). Therefore, a special type of mathematical programming, called integer programming, will be used for all optimization problems in this paper.

The mathematical programming representation of an MCNFP is stated as follows:

$$min \sum_{all\ arcs} c_{ij} * x_{ij} \tag{2}$$

subject to

$$\sum_j x_{ij} - \sum_k x_{ki} = b_i \tag{3}$$

where

- x_{ij} is the number of units of flow sent from node i to node j through arc (i, j)
- c_{ij} is the cost of transporting one unit of flow from node i to node j via arc (i, j)
- b_i is the net supply (outflow minus inflow) at node i

In the objective function (Expression (2)), the total distance that miners needed to travel altogether was minimized as the length of the arc between two nodes, c_{ij}, was multiplied by the number of miners, x_{ij}, that took this route when they were heading for the exit. It should be noted that c_{ij}, as mentioned, was not only based on the distance between nodes [27]. Influences like the slope angle of the path, the temperature, and the quality of the air could be incorporated into this parameter. This allowed for the calculation of not only the shortest route but also one that prioritized safety and efficiency. In this paper, only slope angle, closed pathways, and the stamina of the miners are considered.

Constraint (3) describes the difference between the flows that led towards a node (x_{ij}) and the flows that led away from it (x_{ki}). By setting parameter b_i to a certain value, places where miners are located at the time of an emergency and the nodes where they can find a safe haven could be simulated. For instance, if a worker was present at node 1, b_1 could be set to one. In this way, the workers were introduced into the network of nodes and arcs. If a refugee chamber at node i could house 10 people, b_i needed to be set to greater or equal to -10. Also, if a miner reached a safe haven, this individual 'disappeared' from the system. A relatively large coefficient was assigned to the mine shaft due to its high capacity. Keeping b_i zero at nodes that served no particular purpose made sure that all miners arriving at this node would have to leave as well. This way, miners had to keep passing 'empty' nodes until they found a safe haven.

2.3. Implementing the Built Model

Two pieces of code were written to perform the optimizations: one where all miners were assumed to have the same stamina and one where the miners were divided into stamina categories. In this sub-chapter, a brief overview will be presented, outlining the design process of both codes.

2.3.1. Common Stamina

Although different methods of localizing miners underground were briefly given previously, the exact locations of workers or workstations were not available for this study. Moreover, the locations of safe havens and possible safety hazards were also not known. Therefore, a lot of randomizations were used in the optimization processes. The locations of safe havens were chosen by the author at random nodes in the network and kept equal for all optimizations. The positioning of miners was a bit more complicated as the workers needed to be located at the nodes of the network and always exactly halfway down an arc. This problem was solved by letting the computer pick two things at random: the arc where a miner was located and a number between 0 and 1, which indicated how far a miner was along the specific arc. At this location, a temporary node was created together with two temporary arcs, which connected the temporary node with the two adjacent ordinary nodes. To simulate a safety hazard (for instance, a fire), a random arc was selected and subsequently removed (in both directions) from the network. This arc could not be used in escape routes.

Now that the miners and safety hazards had been introduced to the underground tunnel network, the objective function and constraints (as given in Expression (2) and Constraint (3)) could be set. The linear functions were loaded onto GUROBI, which is a Python application that can be used to solve linear optimization problems. Subsequently, a first optimization attempt could be undertaken. This could lead to two situations: an escape solution being determined or the model being found to be infeasible, which would mean that one or more miners could not reach a safe haven without crossing a safety hazard. If the model came back as infeasible, two things needed to happen: the trapped miners needed to be localized and their colleagues needed to be directed to a safe haven. This could be done by linear relaxation, where GUROBI filters out the constraints that cannot be met and optimizes the model without these. As the violated constraints were linked to the temporary nodes where miners were trapped, it was quite easy to locate these workers.

At this point, the routes for the miners that had a means of escape were calculated and the trapped miners were localized. The route for each individual miner could be plotted, an example of which is given in Figure 3. The red dot indicates the initial location of the miner, while the red lines indicate the route that the miner needed to take to reach safety. In the case of a trapped miner, only a red dot is shown.

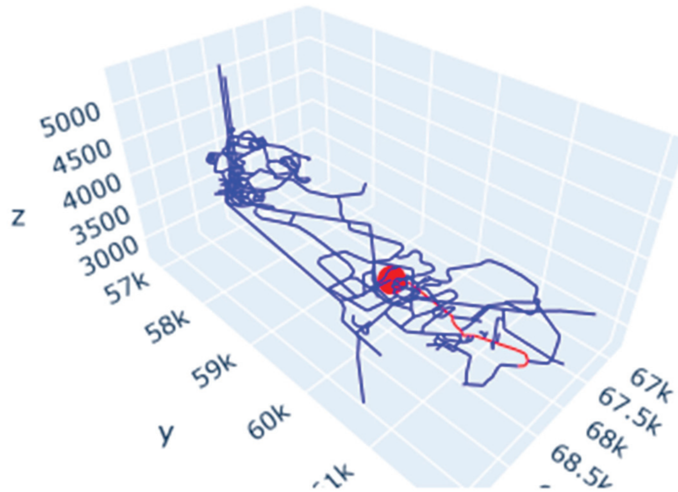

Figure 3. Example of route plot, with the unit being 'Meter' (k stands for 1000).

2.3.2. Stamina Categories

In the second piece of code, stamina categories were introduced. Miners could have stamina with a factor of 0.8, 0.9, 1.0, 1.1, or 1.2. A stamina of 0.8 (or 80 percent) meant that the stamina of the miner was low, while a stamina of 1.2 (or 120 percent) meant that the miner was in very good shape. The stamina values were used to correct the distances that the miners needed to travel, which will be explained later in this sub-chapter.

The localization of miners and safety hazards was performed in the same manner as when no stamina categories were used. However, to each individual miner, an extra piece of data was added: an integer between zero and four (which was also chosen by the computer at random). A zero indicated that a miner was in the lowest stamina category, while a four indicated that he or she was in the highest category. Afterwards, five spin-offs needed to be created for each drift in the mine (one for each stamina category). For instance, if a drift was 100 m long, the spin-off drift for miners in the lowest stamina category would be 125 m (which is $\frac{100}{0.8}$) . For miners in the highest stamina category, this would be 83.3 m (which is $\frac{100}{1.2}$). In this way, the routes for miners with low stamina were made artificially longer, while, for miners with high stamina, they were made shorter. The purpose of this was to assign relatively lower weight to miners with higher stamina levels in the objective function (as given in Constraint (2)). This approach ensured that such miners were directed towards a distant safe haven if the closest option was almost their capacity. For instance, if two miners (one in a high and one in a low stamina category) were at location A, while the safe haven at location B could only harbor one more individual, the miner in the lower stamina category would be favored for this spot. Indeed, it was less expensive to send a miner in the higher category to a safe haven farther away.

At this point, the objective function and the constraints could be fed to the GUROBI application. This, however, was a bit more complicated than previously. This was because miners needed to take only the spin-off path that belonged to their stamina category. This meant a large increase in the constraints of the optimization problem (which were multiplied by a factor of five). This situation led to longer computation times (which will be further elaborated on in the Results section). The final result, however, was the same as in the version of the code without stamina categories: trapped miners were located, and all others received directions for a safe haven.

2.4. Scenarios and Situations

A total of four scenarios were tested:

- Scenario 1: No correction to the pathlengths for the stamina of the miners and no blocked pathways.
- Scenario 2: No correction to the pathlengths for the stamina of the miners and 10 blocked pathways.
- Scenario 3: Pathlengths corrected for the stamina of the miners and no blocked pathways.
- Scenario 4: Pathlengths corrected for the stamina of the miners and 10 blocked pathways.

Each of the scenarios was run for five different situations. In each situation, the miners and fires were located differently. The situations remained consistent across all scenarios, and optimizations were run with 1, 5, 10, 50, 100, 200, 500, and 1000 underground workers. The locations of the safe havens were kept the same in all optimizations.

3. Results

In this section, three different types of results relevant to utilizing a smart evacuation algorithm will be analyzed. Firstly, the division of miners among the safe havens in the different scenarios for a specific situation will be looked at. This is done for two reasons: firstly, to see how various scenarios influence the escape solution and, secondly, to see what the impact of an increasing number of miners is on this solution. After completing this step, the paths of an individual miner (called Miner X) in the different scenarios are analyzed to characterize how blocked paths and the use of stamina categories influence the route to safety for a specific miner. Finally, the computation times of the different situations will be compared to see how added features influence the efficiency of the algorithms.

3.1. Distribution of Miners among Safe Havens

Five safe havens were used in each of the optimizations: two shafts (located at nodes 200 and 250) and three refugee chambers (located at nodes 120, 150, and 300). The refugee chambers were assumed to have a capacity of 30 miners, while the shafts had infinite capacity. Tables 1–4 provide the distribution of miners among the safe havens for different scenarios in Situation 3.

Table 1. Defined destinations for Scenario 1 in Situation 3.

Refuge/# of Miners	1	5	10	50	100	200	500	1000
Chamber 120	0	2	3	10	22	30	30	30
Chamber 150	0	0	0	4	11	30	30	30
Chamber 300	0	0	0	2	5	16	30	30
Shaft 200	0	0	4	22	42	85	223	482
Shaft 250	1	3	3	12	20	39	187	428
Total	1	5	10	50	100	200	500	1000

Table 2. Defined destinations for Scenario 2 in Situation 3.

Refuge/# of Miners	1	5	10	50	100	200	500	1000
Chamber 120	0	2	3	9	18	30	30	30
Chamber 150	0	0	0	4	11	21	30	30
Chamber 300	0	0	0	3	8	24	30	30
Shaft 200	0	0	4	22	44	87	242	503
Shaft 250	1	3	3	11	18	35	163	402
Total	1	5	10	49	99	197	495	995

Table 3. Defined destinations for Scenario 3 in Situation 3.

Refuge/# of Miners	1	5	10	50	100	200	500	1000
Chamber 120	0	2	3	10	22	30	30	30
Chamber 150	0	0	0	4	11	30	30	30
Chamber 300	0	0	0	2	5	16	30	30
Shaft 200	0	0	4	22	42	85	224	475
Shaft 250	1	3	3	12	20	39	186	435
Total	1	5	10	50	100	200	500	1000

Table 4. Defined destinations for Scenario 4 in Situation 3.

Refuge/# of Miners	1	5	10	50	100	200	500	1000
Chamber 120	0	2	3	9	18	30	30	30
Chamber 150	0	0	0	4	11	21	30	30
Chamber 300	0	0	0	3	8	24	30	30
Shaft 200	0	0	4	22	44	87	243	502
Shaft 250	1	3	3	11	18	35	162	403
Total	1	5	10	49	99	197	495	995

The first point that one should notice is that for up to 200 underground workers, the capacities of the refugee chambers were sufficient. This meant that each miner could be sent to the safe haven closest to them. From 500 miners and up, the refugee chambers reached capacity, which led to more miners being sent to a shaft. In Scenarios 2 and 4, not all miners could make it to a safe haven. This was, as mentioned, due to the blocked paths in these scenarios, which led to miners getting trapped.

In order to compare the scenarios, Tables 5–8 present the absolute differences in the number of miners located in a specific safe haven across all scenarios.

Table 5. The difference in the number of miners located in a safe haven between Scenarios 1 and 2 in Situation 3.

Refuge/# of Miners	1	5	10	50	100	200	500	1000
Chamber 120	0	0	0	1	4	0	0	0
Chamber 150	0	0	0	0	0	9	0	0
Chamber 300	0	0	0	1	3	8	0	0
Shaft 200	0	0	0	0	2	2	19	21
Shaft 250	0	0	0	1	2	4	24	26

Table 6. The difference in the number of miners located in a safe haven between Scenarios 3 and 4 in Situation 3.

Refuge/# of Miners	1	5	10	50	100	200	500	1000
Chamber 120	0	0	0	1	4	0	0	0
Chamber 150	0	0	0	0	0	9	0	0
Chamber 300	0	0	0	1	3	8	0	0
Shaft 200	0	0	0	0	2	2	19	27
Shaft 250	0	0	0	1	2	4	24	32

Tables 5 and 6 compare the scenarios with and without blocked paths. According to these tables, the blocked paths caused a significant shift in how miners were divided among the safe havens. This circumstance occurred due to two reasons. The first, and most important, was that miners may have needed to take detours due to blocked pathways. On their new route, the safe haven that was previously closest may then have been relatively farther away. Moreover, the route to a safe haven may have been blocked entirely for a specific miner. This could lead to miners heading to a different destination than the one they would have gone to when all paths were available. The second, and less important, reason for the differences was the trapped miners. These miners did not make it to a safe haven at all, which can be found back in the numbers.

Table 7. The difference in the number of miners located in a safe haven between Scenarios 1 and 3 in Situation 3.

Refuge/# of Miners	1	5	10	50	100	200	500	1000
Chamber 120	0	0	0	0	0	0	0	0
Chamber 150	0	0	0	0	0	0	0	0
Chamber 300	0	0	0	0	0	0	0	0
Shaft 200	0	0	0	0	0	0	1	7
Shaft 250	0	0	0	0	0	0	1	7

Table 8. The difference in the number of miners located in a safe haven between Scenarios 2 and 4 in Situation 3.

Refuge/# of Miners	1	5	10	50	100	200	500	1000
Chamber 120	0	0	0	0	0	0	0	0
Chamber 150	0	0	0	0	0	0	0	0
Chamber 300	0	0	0	0	0	0	0	0
Shaft 200	0	0	0	0	0	0	1	1
Shaft 250	0	0	0	0	0	0	1	1

Tables 7 and 8 give the differences with and without the use of stamina categories in the algorithms. In these cases, no differences could be seen for the optimizations with up to 200 miners. Minimal differences could be seen for the shafts for optimizations with 500 miners or more. This was attributed to the fact that the refugee chambers could accommodate enough miners, up to a capacity of 200. This meant that miners were sent to the safe haven closest to them, regardless of their stamina category. In the optimizations where the refugee chambers were full, miners that had lower stamina were favored for a spot in the refugee chambers (if this was relatively closer by). This meant that a miner with better stamina would be sent to a shaft in his/her place. However, it is essential to note that this shaft may not have been the same one the weaker miner would have gone to. This led to some differences in the division of miners around the shafts.

3.2. Miner X

The purpose of this section is to investigate how blocked pathways and stamina categories influenced the path of an individual miner. Miner X was part of the optimizations executed in the second situation. This individual was in the highest stamina category, and his/her path was determined in the case where 500 miners were present. The different paths are presented in Table 9.

Table 9. Destinations of Miner X.

Scenario	Distance in Meters	Final Destination Node
1	2502.7	150 (Refugee Chamber)
2	2502.7	150 (Refugee Chamber)
3	4285.1	250 (Shaft)
4	6821.1	250 (Shaft)

According to Table 9, there was no difference between Scenarios 1 and 2. This means that, despite the fires, Miner X encountered no blocked paths on his/her route to safety in Scenario 2. When evaluating Scenario 3, it becomes evident that the distance Miner X needed travel increased significantly compared to Scenarios 1 and 2. This was because a weaker miner was favored for a spot in refugee chamber 150, and Miner X had to head to a shaft in his/her place. Finally, in Scenario 4, the path for Miner X was longer than in Scenario 3. This was because one or more pathways on his/her original route were blocked because of fire, which meant that he/she needed to take a detour to get to the shaft at node 250.

It can be concluded from Table 9 that both blocked pathways and stamina categories added significantly to the path of an individual miner. In the case of blocked pathways, this was not necessarily undesirable. Although the route for the individual miner may have been longer, it did avoid hazardous situations such as fires. Therefore, pathlength was exchanged for safety. That said, the added pathlength due to the stamina categories does raise social and ethical questions. Can you expect a miner to travel farther in favor of a weaker colleague?

It should be noted that the pathlengths for Miner X seem unrealistically long. The reason for these unrealistic pathlengths is the randomization that was used in the optimizations for the locations of miners and safe havens. In this randomization, safety standards were disregarded. Naturally, when implementing this system in an actual underground mine, the locations of workstations and safe havens are known, and all pathlengths in case of an evacuation would be within the limits stated in safety regulations.

3.3. Computation Times

The average times to run the algorithms for different scenarios are indicated in Figure 4.

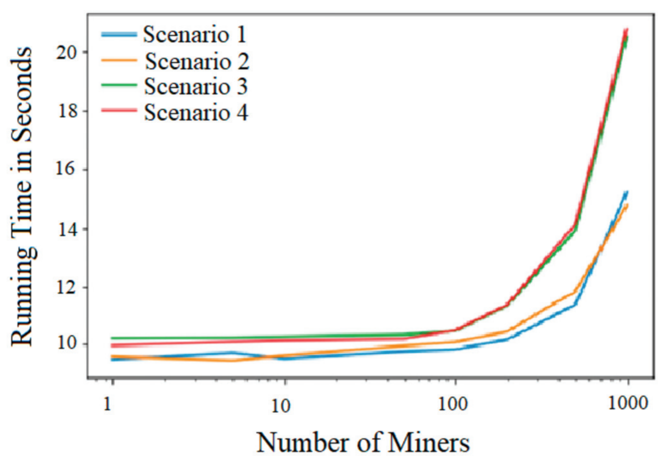

Figure 4. Average computation times for different scenarios.

As shown in Figure 4, blocked pathways had a negligible effect on the computation time of the algorithms. This is remarkable as these scenarios required more execution of code. This means that there is virtually no downside to including the feature that filters out blocked pathways. Trapped miners are localized, and their colleagues are sent on routes that avoid hazardous situations, without overly complicating the algorithm. It is therefore highly recommended to use this feature in escape solutions.

Using stamina categories, on the other hand, did add to the computation time (up to 5 s in optimizations with 1000 miners underground). Although this time difference would most likely not result in a matter of life and death, it does, again, raise some questions about desirability. Firstly, if the refugee capacity is sufficient, the final solution that the algorithm generates will be the same. In this case, it is undesirable to have the added computation time. Secondly, if the capacity of the refugee chambers is insufficient, added computation time is just one of the objections one can have against the use of stamina categories.

A final note is that the optimizations were run on an ordinary, everyday-use laptop. If this system were to be implemented in an actual mining operation, most likely, a specialized computer would be used. This could lead to a significant decrease in the time it takes for the algorithms to run.

4. Discussion

This paper raises some ethical and social questions about the obtained solutions. Firstly, there is the issue of using stamina categories. It has been proven that using this type of category is technically feasible, but one could question whether it is desirable to employ sexual and/or fitness discrimination in decision-making. Furthermore, they can have an adverse effect on the path of an individual miner (who has good stamina). Is it ethical or socially acceptable to expect a miner to accept a longer path of escape in favor of a weaker colleague? However, it is worth noting that these categories may be useful in cases where the operation employs vehicles, such as underground trucks. These categories, then, might not be used for dividing miners but can be used for a different purpose.

Using the algorithm without stamina categories also raises ethical issues. For instance, if five miners are positioned at the same workstation, the closest refugee chamber can only harbor four more workers. In this case, a decision would have to be made about which miner misses out on a spot in this safe haven. This can present a tough ethical dilemma. Who is entrusted with making the decision about which miner cannot access the closest safe haven—the algorithm, the miners themselves, or the emergency controller? There is, probably, not a single definitive answer to this question. Nevertheless, this issue must be addressed and resolved before implementing a smart evacuation system.

Another issue is how to classify which paths are suitable to use for escape and which are not. Naturally, in the case of a fire or toxic gases, the exclusion of a path is obvious. However, what if a path is partly blocked by machinery or other obstacles? What if a drift is partly filled with water? This issue can partly be resolved by giving these paths extra weight in the objective function, but it requires that the conditions for every underground location are extensively monitored. A system would need to be devised that assigns certain penalties to certain situations. It can be argued, then, that the current system of assigning weights to the pathways is not yet complete.

5. Conclusions

In this paper, a mathematical programming component for a new smart evacuation algorithm for underground mines was proposed. The algorithm set the evacuation model as a 'Minimum-Cost Network Flow Problem' that can be solved using any mathematical programming solver. This was conducted by setting the evacuation as an objective function that was subject to several constraints. The objective function minimized the total distance traveled by all underground miners. The constraints were used to indicate the locations of workers and safe havens. The algorithms for this paper were written in the Python programming language and solved by use of the GUROBI library.

A total of four scenarios were tested: with and without blocked pathways and with and without dividing the miners up into stamina categories. Each of the scenarios was run for five different situations, with optimizations for 1, 5, 10, 50, 100, 200, 500, and 1000 miners. The locations of miners and blocked pathways were chosen randomly by the computer in different situations. The safe havens were chosen randomly by the author and kept the same for all optimizations.

It was found that in optimizations with up to 200 miners, the capacity of the refugee chambers was sufficient. For optimizations with 500 miners or more, the refugee chambers reached the designated capacity, which led to more miners heading to the shafts. The introduction of blocked pathways had a significant influence on how the miners were divided up among the safe havens. There were two reasons for this. Firstly, blocked paths may cause a safe haven that was once closest to become relatively farther away or entirely unreachable. This can lead to miners being sent to a different safe haven. The second reason is that blocked pathways may cause miners to get trapped. Therefore, they will not reach a safe haven, which can be found back in the numbers. Stamina categories only had some effect on the division of miners around the shafts in optimizations with 500 miners and more. This is because when a stronger miner was sent to a shaft in favor of a weaker miner, this did not need to be the same shaft as that the latter would have originally gone to.

To give an idea of how the different scenarios influence the path of an individual worker, Miner X was introduced (who came from an optimization with 500 miners and was in the highest stamina category). It was found that both blocked pathways and stamina categories may add significantly to the path of an individual miner. This is not that big of an issue in the case of blocked paths as pathlength is exchanged for a safer route. However, in the case of stamina categories, there are some social and ethical objections that can be raised.

Introducing a feature that filters out blocked pathways and localizes trapped miners does not give a penalty to the computation time of the algorithms. This means that there is virtually no downside to using this feature. Stamina categories add to the computation time. If there is sufficient refugee capacity, this is undesirable, as there will be no impact on the final solution. If the capacity is insufficient, the time penalty will most likely not result in a matter of life and death. However, social and ethical objections play a role here as well.

Author Contributions: All authors contributed to the study conception and design. R.M. participated in all phases of the study, including modeling, analysis, and interpreting the results. M.S.S. participated in data collection and analysis of the results. J.S. developed the research methodology and validated the models and outcomes. All authors have read and agreed to the published version of the manuscript.

Funding: The authors declare that no funds, grants, or other support were received during the preparation of this manuscript.

Data Availability Statement: The data presented in this study are available on request from the corresponding author (accurately indicate status).

Acknowledgments: This research is based on the MSc thesis of the first author and is part of a capacity-building project supported by the US National Occupational Safety and Health (NIOSH) at the University of Nevada, Reno. The authors acknowledge NIOSH for making this research happen. We would also like to thank Marco Keersemaker for his feedback on the thesis.

Conflicts of Interest: The authors have no relevant financial or non-financial interests to disclose.

References

1. Brenkley, D.; Bennett, S.; Jones, B. Enhancing mine emergency response. In Proceedings of the 28th International Conference on Safety in Mines Research Institutes, Sinaia, Romania, 7–11 June 1999.
2. Hao, J.; Du, Z.; Zhang, T.; Li, H. Influence of $NH_4H_2PO_4$ powder on the laminar burning velocity of premixed CH_4/Air flames. *Int. J. Hydrogen Energy* **2022**, *47*, 38477–38493. [CrossRef]
3. Jiang, H.; Bi, M.; Li, B.; Ma, D.; Gao, W. Flame inhibition of aluminum dust explosion by $NaHCO_3$ and $NH_4H_2PO_4$. *Combust. Flame* **2019**, *200*, 97–114. [CrossRef]
4. Conti, R.S.; Chasko, L.L.; Wiehagen, W.J.; Lazzara, C.P. *Fire Response Preparedness for Underground Mines*; US Department of Health and Human Services: Washington, DC, USA, 2005.
5. Conti, R.S.; Yewen, R.G. *Evaluation of a Signaling and Warning System for Underground Mines*; US Department of Health and Human Services: Washington, DC, USA, 1997.
6. Conti, R.S. Emerging technologies: Aiding responders in mine emergencies and during the escape from smoke-filled passageways. In Proceedings of the Northwest Mining Association's 107th Annual Meeting, Spokane, WA, USA, 3–7 December 2001.
7. Gaab, S.J. Evaluation of Smart Underground Mine Evacuation Efficiency through Virtual Reality. Ph.D. Thesis, University of Nevada, Reno, NV, USA, 2019.
8. Radinovic, G.; Kim, K. Feasibilty study of RFID/Wi-Fi/BlueTooth wireless tracking system for underground mine mapping–Oklahoma. In Proceedings of the 2008 Incorporating Geospatial Technologies into SMCRA Business Processes, Atlanta, GA, USA, 25–27 March 2008.
9. Rusu, S.R.; Hayes, M.J.D.; Marshall, J.A. Localization in large-scale underground environments with RFID. In Proceedings of the 2011 24th Canadian Conference on Electrical and Computer Engineering (CCECE), Niagara Falls, Canada, 8–11 May 2011.

10. Yan, N.; Chen, H.; Lin, K.; Ni, Z.; Li, Z.; Xue, H. BFSearch: Bloom filter based tag searching for large-scale RFID systems. *Ad Hoc Netw.* **2023**, *139*, 103022. [CrossRef]
11. Mohapatra, A.G.; Keswani, B.; Nanda, S.; Ray, A.; Khanna, A.; Gupta, D.; Keswani, P. Precision local positioning mechanism in underground mining using IoT-enabled WiFi platform. *Int. J. Comput. Appl.* **2020**, *42*, 266–277. [CrossRef]
12. Baek, J.; Choi, Y.; Lee, C.; Suh, J.; Lee, S. BBUNS: Bluetooth beacon-based underground navigation system to support mine haulage operations. *Minerals* **2017**, *7*, 228. [CrossRef]
13. Chehri, A.; Fortier, P.; Tardif, P.M. UWB-based sensor networks for localization in mining environments. *Ad Hoc Netw.* **2009**, *7*, 987–1000. [CrossRef]
14. Yiu, S.; Dashti, M.; Claussen, H.; Perez-Cruz, F. Wireless RSSI fingerprinting localization. *Signal Process.* **2017**, *131*, 235–244. [CrossRef]
15. Aroba, O.J.; Nalindren, N.; Timothy, A.; Avintha, G.; Khadija, K. A review: The bibliometric analysis of emerging node localization in wireless sensor network. *Int. J. Comput. Inf. Syst. Ind. Manag. Appl.* **2023**, *15*, 141–153.
16. Niu, Q.; Yang, X.; Yin, Y. IPL: Image-Assisted Person Localization for Underground Coal Mines. *Sensors* **2018**, *18*, 3679. [CrossRef] [PubMed]
17. Dramski, M. A comparison between Dijkstra algorithm and simplified ant colony optimization in navigation. *Zesz. Nauk. Akad. Morska Szczecinie* **2012**, *29*, 25–29.
18. Fan, D.; Shi, P. Improvement of Dijkstra's algorithm and its application in route planning. In Proceedings of the 2010 Seventh International Conference on Fuzzy Systems and Knowledge Discovery, Yantai, China, 10–12 August 2010.
19. Hong, Y.; Li, D.; Wu, Q.; Xu, H. Dynamic route network planning problem for emergency evacuation in restricted-space scenarios. *J. Adv. Transp.* **2018**, *2018*, 4295419. [CrossRef]
20. Hughes, T.M. Graph processing by which to evacuate a mine. In Proceedings of the 1990 Symposium on Applied Computing, Fayetteville, AR, USA, 5–6 April 1990.
21. Dijkstra, E.W. A note on two problems in connexion with graphs. *Numer. Math.* **1959**, *1*, 269–271. [CrossRef]
22. Bari, A. 4.2 All Pairs Shortest Path (Floyd-Warshall)—Dynamic Programming. Youtube. 2018. Available online: https://www.youtube.com/watch?v=oNI0rf2P9gE (accessed on 20 February 2022).
23. Hougardy, S. The Floyd–Warshall algorithm on graphs with negative cycles. *Inf. Process. Lett.* **2010**, *110*, 279–281. [CrossRef]
24. Guangwei, Y.; Dandan, F. Escape-route planning of underground coal mine based on Improved Ant Algorithm. *Swarm Intell. Eng.* **2013**, *2013*, 687969.
25. Mirjalili, A. Inspiration of Ant Colony Optimization. 2018. Available online: https://www.youtube.com/watch?v=1qpvpOHGRqA (accessed on 10 September 2023).
26. Abdmouleh, Z.; Gastli, A.; Ben-Brahim, L.; Haouari, M.; Al-Emadi, N.A. Review of optimization techniques applied for the integration of distributed generation from renewable energy sources. *Renew. Energy* **2017**, *113*, 266–280. [CrossRef]
27. Adjiski, V.; Mirakovski, D.; Despodov, Z.; Mijalkovski, S. Simulation and optimization of evacuation routes in case of fire in underground mines. *J. Sustain. Min.* **2015**, *14*, 133–143. [CrossRef]
28. Cronkleton, E. What Is the Average Walking Speed of an Adult? Available online: https://www.healthline.com/health/exercise-fitness/average-walking-speed (accessed on 14 January 2023).
29. Winston, W.L.; Goldberg, J.B. *Operations Research: Applications and Algorithms*; Thomson Brooks/Cole Belmont: Belmont, CA, USA, 2004; Volume 3.

mining

Article

Mechanical and Microstructural Response of Iron Ore Tailings under Low and High Pressures Considering a Wide Range of Molding Characteristics

Giovani Jordi Bruschi [1,*], Carolina Pereira Dos Santos [1], Hugo Carlos Scheuermann Filho [1], Camila da Silva Martinatto [1], Luana Rutz Schulz [1], João Paulo de Sousa Silva [2] and Nilo Cesar Consoli [1]

1 Graduate Program in Civil Engineering, Universidade Federal do Rio Grande do Sul, Porto Alegre 90035-190, RS, Brazil; camilamartinatto@hotmail.com (C.d.S.M.); consoli@ufrgs.br (N.C.C.)
2 Exploration and Mineral Projects—Mineral Development Centre, VALE S.A., BR-381, Santa Luzia 33040-900, MG, Brazil; joao.paulo.silva@vale.com
* Correspondence: gio.bruschi@gmail.com

Abstract: The dry stacking of filtered tailings is an option to deal with safety-related issues involving traditional slurry disposition in impoundments. Filtered tailings can be compacted to pre-define design specifications, which minimizes structural instability problems, such as those related to liquefaction. Yet, comprehending the tailing's response under various stress states is essential to designing any dry stacking facility properly. Thus, the present research evaluated the mechanical response of cemented and uncemented compacted filtered iron ore tailings, considering different molding characteristics related to compaction degree and molding moisture content. Therefore, a series of one-dimensional compression tests and consolidated isotropically drained triaxial tests (CID), using 300 kPa and 3000 kPa effective confining pressures, were carried out for different specimens compacted at various molding characteristics. In addition, changes in gradation owing to both compression and shearing were evaluated using sedimentation with scanning electron microscope tests. The overall results have indicated that the 3% Portland cement addition enhanced the strength and stiffness of the compacted iron ore tailings, considering the lower confining pressure. Nevertheless, the same was not evidenced for the higher confining stress. Moreover, the dry-side molded specimens were initially stiffer, and significant particle breakage did not occur owing to one-dimensional compression but only due to shearing (triaxial condition).

Keywords: iron ore tailings; dry staking; filtered tailings; tailings dam; Portland cement

Citation: Bruschi, G.J.; Santos, C.P.D.; Filho, H.C.S.; da Silva Martinatto, C.; Schulz, L.R.; Silva, J.P.d.S.; Consoli, N.C. Mechanical and Microstructural Response of Iron Ore Tailings under Low and High Pressures Considering a Wide Range of Molding Characteristics. *Mining* **2023**, *3*, 712–730. https://doi.org/10.3390/mining3040039

Academic Editors: Mostafa Benzaazoua, Krzysztof Skrzypkowski, René Gómez, Fhatuwani Sengani, Derek B. Apel, Faham Tahmasebinia and Jianhang Chen

Received: 24 August 2023
Revised: 14 November 2023
Accepted: 16 November 2023
Published: 18 November 2023

1. Introduction

The dry stacking of filtered tailings has become feasible due to the recent evolution of dewatering technologies, which enables the obtainment of an unsaturated material, known as 'cake,' that can be compacted to form stackings of hundreds of meters [1,2]. Hence, this technique can potentially overcome most safety-related drawbacks associated with traditional slurry disposal in pounds. That is, the stored tailings are no longer found saturated and in a loose condition susceptible to liquefaction. They are arranged according to design specifications, such as dry density and compaction water content [3,4]. In addition, dry stacking requires less physical space for tailings storage. It involves recovering substantial amounts of water that can be later reused in the extraction and beneficiation processes [5].

The dry stacking of mining tailings has become an attractive alternative, especially considering that more rigid regulations/laws have been recently introduced prohibiting the construction of new tailings dams using the upstream method while demanding the de-characterization and decommissioning of existing ones in countries such as Brazil [6]. This was motivated by the recent catastrophic incidents that occurred in the Fundão dam

(2015) and Mina do Córrego do Feijão (2019) dam, both of which stored iron ore tailings and were constructed using the upstream method [7–9]. In this sense, Brazil has been one of the top three global iron ore suppliers, with the Quadrilátero Ferrífero (Iron Quadrangle) region (located in the province of Minas Gerais) accounting for around 65% of the Brazilian iron ore production [10,11]. This scenario highlights the need to reallocate the vast amount of iron ore tailings already stored in upstream dams and provide a proper destination for the upcoming tailings.

The appropriate conception of a tailings storage facility (*TSF*) relies upon comprehending the tailings' mechanics under operational boundary conditions, which involves, among other aspects, knowing the material's response under various stress states [12,13]. In this regard, dry stacking tailings have the advantage over hydraulic disposal in dams concerning spatial predictability of the tailing's properties. The first involves the compaction of a well-characterized material. In contrast, the latter comprehends the hydraulic deposition, sedimentation, and subsequent consolidation over a vast impoundment, enhancing the problem's inherent complexity [14,15]. Still, a resilient design of a dry stacking facility demands an understanding of the filtered tailings response over a wide range of stresses and the effect of the compaction characteristics on the mechanical response. Eventually, it is also possible to incorporate a cementitious material into the tailings to enhance the material's strength and stiffness [16–20].

The behavior of artificially cemented geomaterials is well-known and extensively documented: developing a cementitious matrix in a granular media leads to significant strength and stiffness gains until cementing bond degradation, accompanied by a more dilatative response and post-peak brittleness [21,22]. Naturally, once the bonds are degraded, the cement is ineffective in providing actual enhancements in the material's mechanical response; that is, the cement may be useless for higher confinement levels [23]. In general, artificially cemented tailings behave like cemented soils and can be analyzed using the same approaches [18]. Nonetheless, despite a variety of studies concerning the response of cemented tailings for mine backfill [19,24–29], few have been carried out on the behavior of artificially cemented filtered tailings for dry staking purposes, particularly for high-stress levels and different compaction conditions.

Accordingly, the present study evaluated the mechanical response of cemented (C = 3%) and uncemented (C = 0%) compacted filtered iron ore tailings under low (p'_0 = 300 kPa) and high (p'_0 = 3000 kPa) confining pressures. Both cemented and uncemented test specimens were molded considering various compaction characteristics that involved compaction degrees (97% and 100%) for modified and standard Proctor compaction efforts and moisture contents (dry, optimum, and wet sides of the compaction curve). A series of 1-D consolidation tests were carried out for all the test specimens and consolidated isotropically drained triaxial tests (*CID*) under two different confinement levels (p'_0 = 300 kPa and p'_0 = 3000 kPa). Particle breakage analysis was carried out for both stress paths with sedimentation and scanning electron microscope tests.

2. Experimental Program

Three phases compose the experimental program. The first comprehended the physical characterization of the iron ore tailings (*IOTs*), in which the molding points were determined based on the compaction characteristics obtained using the standard and modified Proctor compaction efforts—the second consisted of the conduction of the 1-D compression tests and the triaxial tests, both executed on the cemented and uncemented tailings compacted under different conditions. In the third phase, the possibility of particle breakage during the compression and shearing of the specimens was evaluated using the analysis of grain size distribution with the aid of scanning electron microscope (*SEM*) tests.

3. Materials

The iron ore tailings utilized herein come from a filtration plant in the Province of Minas Gerais (southeast Brazil). Table 1 summarizes the main physical characteristics of these tailings.

Table 1. Physical properties of the iron ore tailings.

Physical Properties	Iron Ore Tailings	Test Method
Liquid limit (%)	-	
Plastic limit (%)	-	ASTM D4318
Plastic index (%)	non-plastic	
Specific gravity	2.72	ASTM D854
Coarse Sand (2.00 mm < diameter < 4.75 mm) (%)	0.0	
Medium Sand (0.425 mm < diameter < 2.00 mm) (%)	0.0	
Fine Sand (0.075 mm < diameter < 0.425 mm) (%)	8.0	ASTM D7928
Silt (0.002 < diameter < 0.075 mm) (%)	88.7	
Clay (diameter < 0.002 mm) (%)	3.3	
Maximum dry unit weight at standard effort (kN/m^3)	17.4 (w = 15.2%)	ASTM D1557
Maximum dry unit weight at modified effort (kN/m^3)	18.5 (w = 11.6%)	ASTM D698

The gradation was evaluated through sedimentation and sieve analysis following ASTM D7928 [30]. The Atterberg limits and the specific gravity were analyzed following ASTM D4318 [31] and ASTM D854 [32], respectively. According to the Unified Soil Classification System [33], the studied IOTs can be classified as silty sand once non-plastic and around 83% of their particles are in the silt-size range. Figure 1 depicts the compaction characteristics obtained using the standard ASTM D698 [34] and the modified ASTM D1557 [35] Proctor compaction efforts.

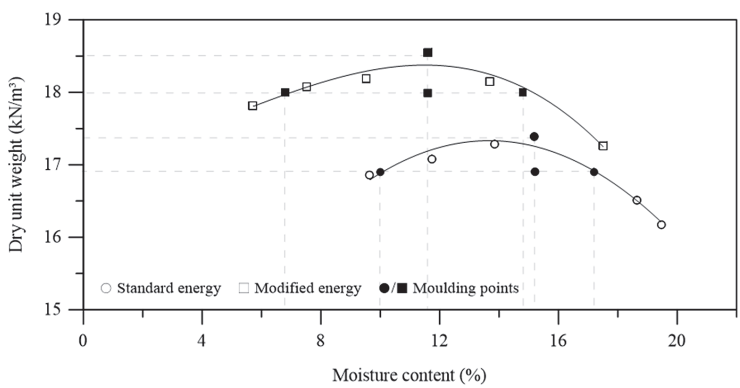

Figure 1. Compaction characteristics of the iron ore tailings and molding points.

Chemically, the X-ray fluorescence (XRF) test has revealed that the *IOTs* are mainly constituted of silicon (Si = 57%), iron (Fe = 36%), and aluminum (Al = 5%), as well as other minor constituents. Mineralogically, X-ray diffraction analysis (XRD), combined with a semi-quantification using the reference intensity ratio (RIR) method, have attested the presence of quartz (85%), kaolinite (13%), and hematite (3%). Figure 2 exhibits the scanning electron microscope (SEM) micrographs of the iron ore tailings at 100× (Figure 2a), 500× (Figure 2b), and 5000× (Figure 2c) magnification rates. The IOTs are composed primarily of flattened-angular quartz grains and a lesser amount of smaller hematite particles (Figure 2c).

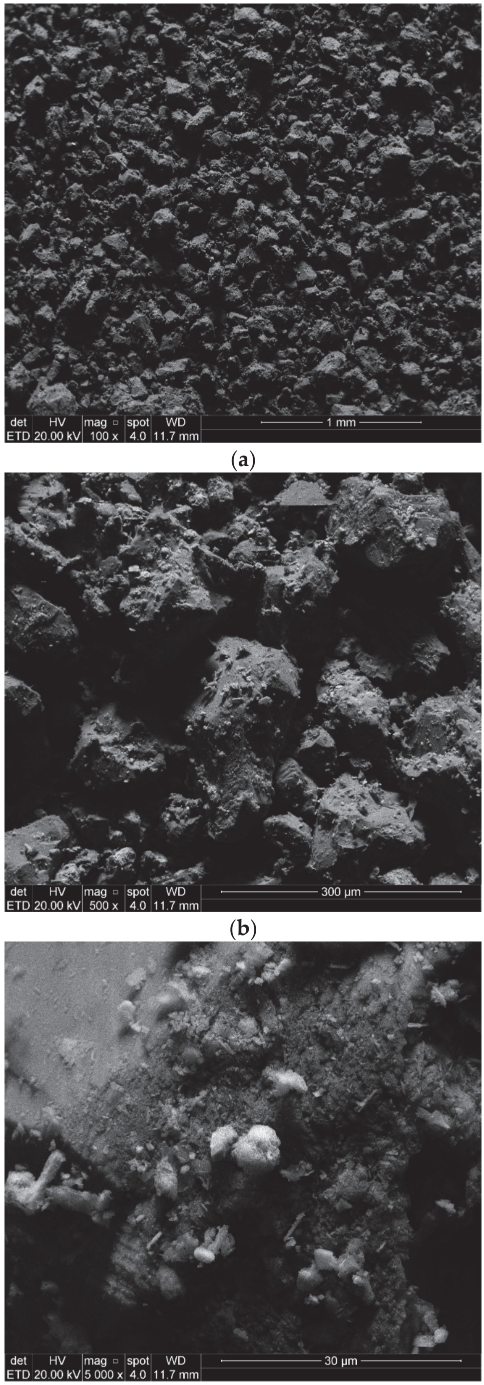

(**c**)

Figure 2. SEM micrographs of the iron ore tailings magnified by (**a**) 100× and (**b**) 500×; (**c**) 5000×.

The XRF tests were conducted on a WDS spectrometer model *RIX* 2000 from Rigaku®. A D-500 Siemens® X-ray diffractometer (Akishima-shi, Tokyo, Japan), equipped with a fixed Cu anode tube, was used in the XRD tests, whereas a scanning electron microscope with an electron beam of 20 kV using gold-coated samples (Q150 and JMS-6610 models) was used for the SEM tests. Commercially available high early strength Portland cement (type III) was used as the cementing agent. The cement's specific grain unit weight was 3.15 g/cm^3. Distilled water was used for molding and saturating the test specimens and throughout the physical characterization tests.

4. Methods

4.1. Molding Characteristics

Characteristics of the filtered cake, such as gradation and moisture content, may vary across a particular range owing to inherent variations related to the filtration plant and the tailings' nature [36–38]. As a result, the filtered tailings moisture content (w) is a crucial variable in affecting the compaction process and, thus, the in situ mechanical response of the compacted material, as it is intimately linked to both the attainable compaction degrees and the compacted materials fabrics [39–41]. Therefore, understanding the iron ore tailings response under certain compaction conditions is essential to guarantee a rational design of filtered STF.

Considering the cemented and uncemented specimens, the molding points were based on the compaction tests and are depicted in Figure 1. For both compaction efforts, the highest dry density values and the corresponding optimum moisture contents were chosen. In addition, within each curve, three points with a degree of compaction of around 97% were chosen: one located on the dry side of the curve, one located on the wet side of the curve, and the other presenting the same dry unit weight of those two but molded using the corresponding optimum moisture content. Therefore, those three additional points obtained for each compaction curve have the same molding void ratio but different molding moisture contents. This enables the assessment of the influence of molding characteristics on the response of the cemented and uncemented iron ore tailings.

4.2. Specimen Molding and Curing

Cylindrical specimens were statically molded for the one-dimensional compression tests (5 cm in diameter and 2 cm in height) and the triaxial tests (5 cm in diameter and 10 cm in height). For the first, the material was directly compacted in one layer inside the oedometric ring. For the latter, the compaction was carried out in three layers in a cylindrical split mold, with the top of the first and second layers slightly scarified to guarantee the adherence of the subsequent layer. Still, before compaction, the correct amount of distilled water, iron ore tailings, and cement (when needed) were manually mixed until a homogeneous material of a homogeneous aspect was obtained. For the cemented samples (containing 3% of cement based upon the mass of dry tailings), the oedemetric ring or the retrieved specimen from the split mold was sealed inside a plastic bag and forwarded to be cured in a room with a controlled environment (23 ± 2 °C and 95% of relative moisture). All cemented specimens were cured for seven days. Otherwise, the specimens were ready to be tested. As an acceptance criterion, each sample was considered suitable for testing if the following requirements were met: dry unit weight (γ_d) within ±1% of the target value and moisture content (w) within ±0.5% of the assigned value.

4.3. One-Dimensional Compression Tests

The one-dimensional compression tests agreed with the procedures stated by ASTM D2435 [42] using a setup composed of a consolidometer, a load device, and a linear variable differential transformer (LDVT) used to measure the vertical displacement. Porous discs and filter papers were utilized at the bottom and top of the testing ring to permit the drainage of the compacted specimen during the loading stages. After applying a setting stress of 5 kPa, the loading schedule was: 50 kPa, 100 kPa, 200 kPa, 400 kPa, 800 kPa, 1600 kPa, 3200 kPa, and 6400 kPa.

4.4. Triaxial Tests

Consolidated isotropically drained (CID) triaxial tests were carried out according to the recommendations preconized by ASTM D7181 [43] in a triaxial test apparatus capable of attaining high confining pressures and in which all the data were digitally monitored and recorded. The test samples were entirely saturated by a process involving CO_2 percolation, distilled water percolation, and the increment of backpressure (maintaining p' = 20 kPa) at a rate of 1.5 kPa/min. Irrespective of the test specimen configuration, a backpressure of 400 kPa was sufficient to guarantee the obtainment of B values greater than 0.95. The consolidation stage consisted of incrementing the chamber confining pressure at a 2 kPa/min rate up to the desired initial mean effective stress (p'_0) value. At this rate, no excess pore pressure was developed. The shearing followed a conventional loading path, maintaining the confining pressure constant, conducted at a strain rate of 1.0 mm/hour. Hall effect sensors [44], attached directly to the test specimen (two in the axial direction and one in the radial direction), enabled the local strain assessment along all the test phases. Also, the volumetric strains during the consolidation and shearing phases were measured by the flow volume of water leaving/entering the specimen. Both confining pressure and backpressure were digitally monitored by pressure transducers and were applied using general-purpose water pressure sources. The axial load was also digitally scanned using a 100 kN load cell.

4.5. Particle Breakage Analysis

The possibility of particle breakage owing to the one-dimensional consolidation and the shearing phase on the triaxial test was evaluated for some representative specimens. Quantitatively, the after-test gradation was compared to the natural (untested) iron ore tailings grain size distribution using the particle breakage factor (B_f). The breakage factor is defined as the difference between the amount of the finer particles after testing compared to the original content of finer particles [45]. Qualitatively, SEM micrographs were carried out on some specimens to study the particle breakage, as shown in Section 5.3.

5. Results and Discussions

The notation used to characterize a test specimen takes the form of A_B_C. **A** is the corresponding compaction energy (S = standard; M = modified), **B** refers to the molding moisture content relative to the compaction curve depicted in Figure 1 (W = wet side; O = optimum; R = optimum but with reduced density; D = dry side), and **C** concerns the amount of cement required (3C = 3%; 0C = 0%).

5.1. One-Dimensional Compression Tests

Figure 3a depicts the one-dimensional compression tests for the uncemented iron ore tailings specimens, and Figure 3b exhibits the same results, considering the samples containing 3% cement. Initially, the cemented samples were substantially less compressible until cementing bond breakage, which occurred at vertical pressures below 800 kPa.

Table 2 summarizes the values of the compression indexes (C_c). These C_c values indicate that, at higher pressures, the molding void ratio appears to influence the slope of the one-dimensional normal compression line (1D-NCL).

In other words, the C_c values of the denser samples are very similar, as are the C_c values of the looser specimens. Nevertheless, the compression curves converge towards a unique 1D-NCL, indicating that the initial fabric effects created by the cement addition and compaction characteristics would be erased at higher stresses [46]. This is reinforced when calculating the m parameter [47], obtained by plotting a specific volume at the most elevated pressure versus a specific volume at 20 kPa. Considering the test specimens' data, no linear trend was obtained, and the resultant m was close to zero, indicating no transitional behavior of the studied iron ore tailings [48]. In this regard, at the highest vertical pressure, the difference between the highest and lowest e values was only 0.024.

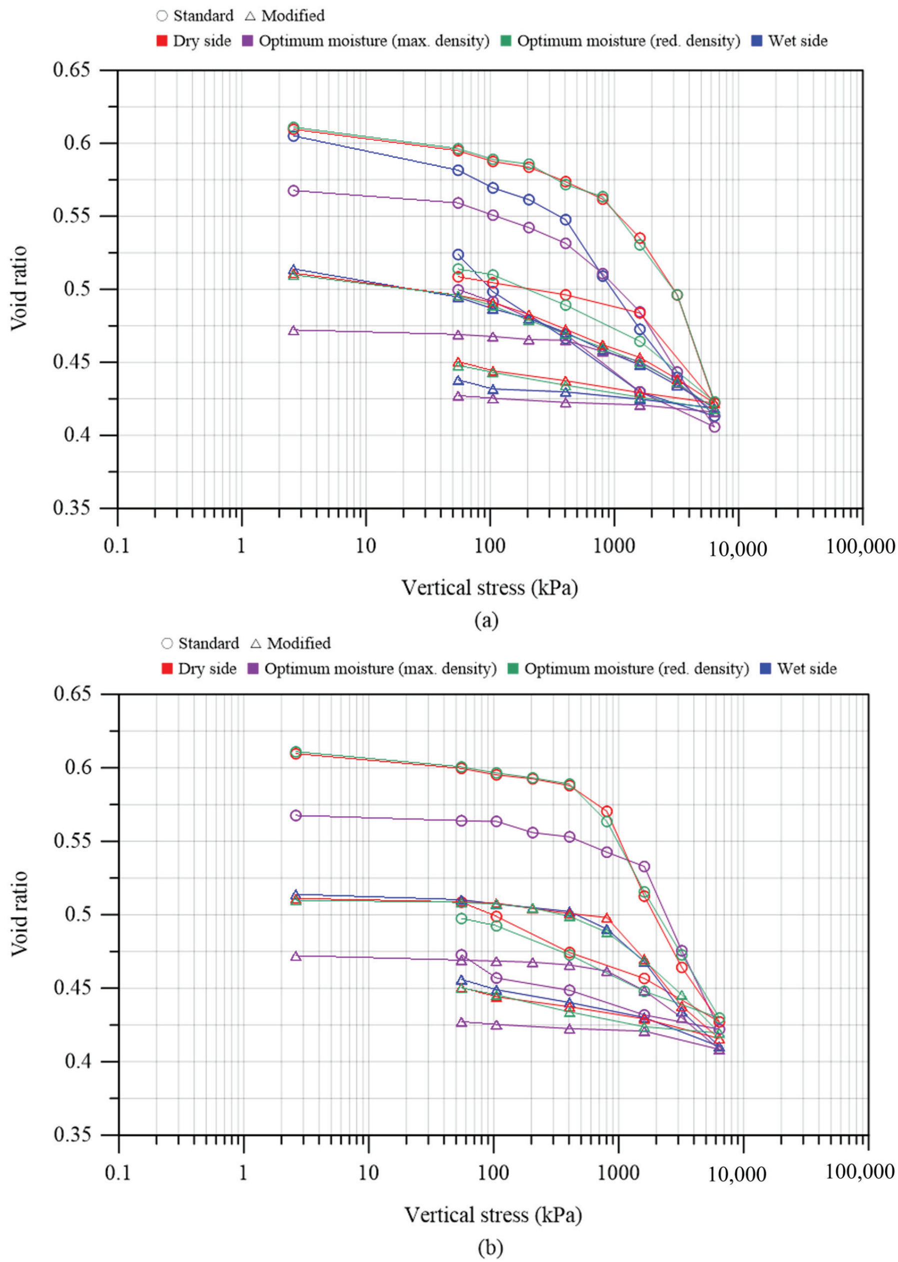

Figure 3. One-dimensional compression tests (**a**) uncemented and (**b**) cemented specimens.

Table 2. One-dimensional compression characteristics.

Specimen	e_0	e_{6400}	C_c
S_W_3C	0.605	0.412	0.14
S_O_3C	0.568	0.422	0.14
S_R_3C	0.608	0.428	0.14
S_D_3C	0.610	0.427	0.14
M_W_3C	0.512	0.410	0.10
M_O_3C	0.471	0.408	0.07
M_R_3C	0.511	0.412	0.11
M_D_3C	0.509	0.414	0.10
S_W_0C	0.603	0.412	0.11
S_O_0C	0.566	0.403	0.14
S_R_0C	0.608	0.421	0.12
S_D_0C	0.609	0.421	0.12
M_W_0C	0.512	0.426	0.04
M_O_0C	0.473	0.419	0.04
M_R_0C	0.514	0.421	0.04
M_D_0C	0.514	0.422	0.04

5.2. Triaxial Tests

5.2.1. Stress–Strain Data

The stress–strain ($\varepsilon_a \times q$) response and the volume change behavior ($\varepsilon_a \times \varepsilon_v$) are plotted in Figure 4a (p'_0 = 300 kPa, uncemented), Figure 4b (p'_0 = 300 kPa, cemented), Figure 4c (p'_0 = 3000 kPa, uncemented), and Figure 4d (p'_0 = 3000 kPa, cemented). Table 3 summarizes the main data relative to the triaxial testing program.

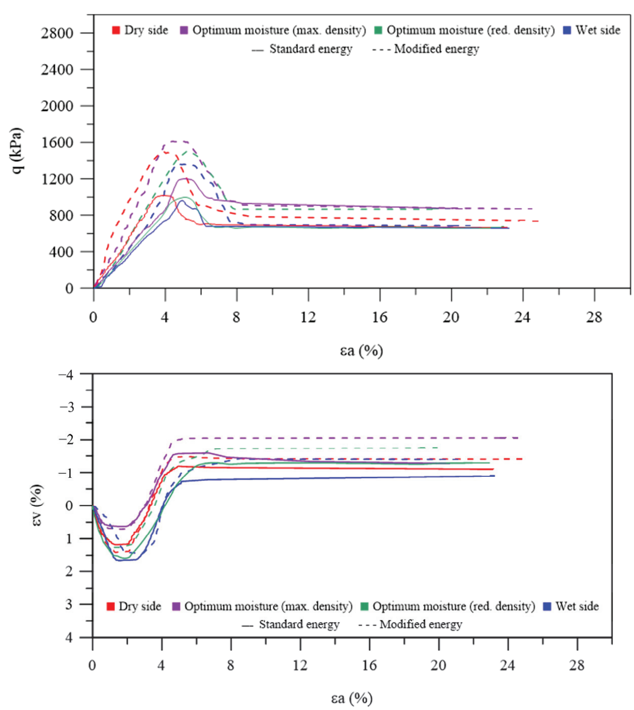

(**a**)

Figure 4. *Cont.*

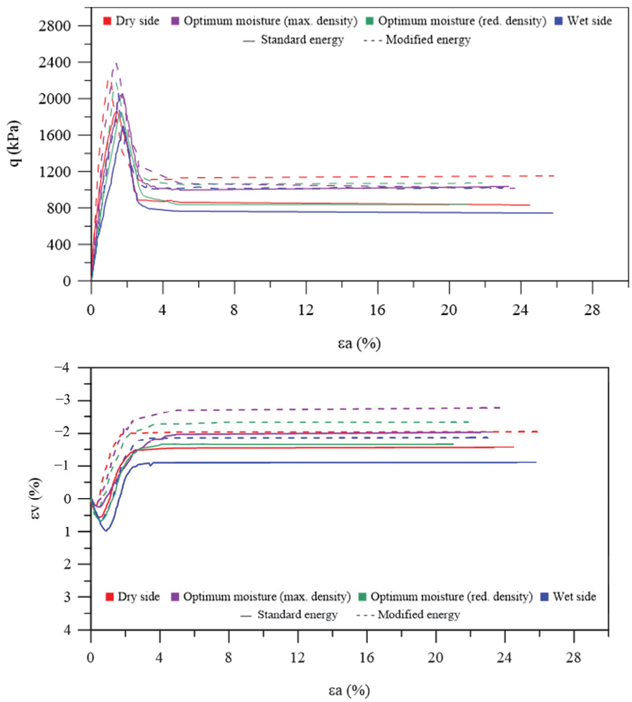

(**b**)

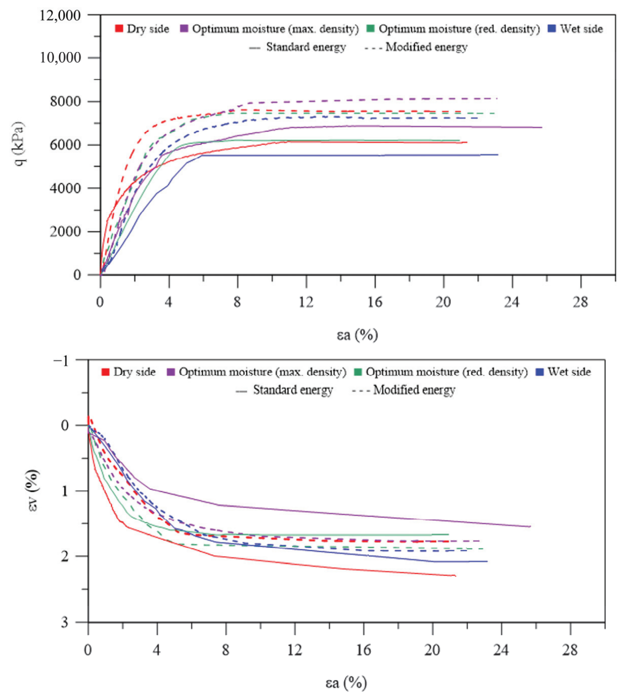

(**c**)

Figure 4. *Cont.*

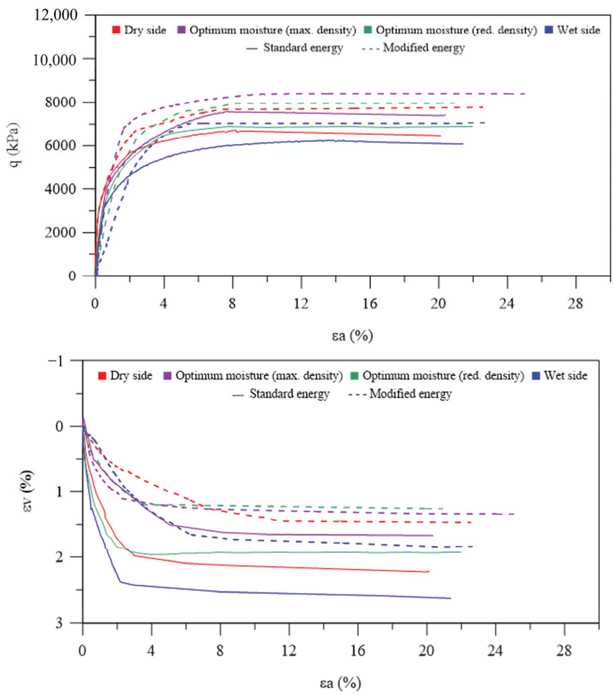

(**d**)

Figure 4. Triaxial stress–strain data and volume change response: (**a**) p'_0 = 300 kPa, uncemented; (**b**) p'_0 = 300 kPa, cemented; (**c**) p'_0 = 3000 kPa, uncemented; (**d**) p'_0 = 3000 kPa, cemented.

Considering the lowest confinement level, all specimens have shown an initial brittle response, presenting well-defined peak stress, followed by post-peak strain softening. This was accompanied by an initial contraction, followed by a dilatative trend. For the uncemented samples, the peak stress coincides with the highest dilation rate, which is the typical response of purely frictional granular materials. This was not the case for the cement-containing specimens [21,22]. For both cemented and uncemented samples, the top deviatoric stress (q_{max}) was proportional to the molding void ratio when considering the optimum molding conditions at standard and modified compaction efforts (i.e., γ_{dmax} and w_{opt}). Moreover, slightly higher strengths were obtained for the specimens molded at the optimum moisture content but with reduced dry unit weight, followed by the dry side samples and, ultimately, the wet side ones. The addition of cement has also led to a substantial increment in the strength and pre-peak stiffness of the samples, has augmented the dilation rate, and has enhanced the brittleness. This suggests that the cement bonds have remained intact during the consolidation phase up to the attainment of p'_0 = 300 kPa [23]. In other words, the cement bonds were responsible for the reported strength and stiffness gains as they only degraded during the shearing [22,49].

Concerning the highest confinement, both uncemented and cemented specimens have not presented a well-defined peak strength and have shown a fully contractive response, characterizing a ductile behavior. For most of the tests conducted at p'_0 = 3000 kPa, the deviatoric stress (q) and the volumetric strain (ε_v) seem to stabilize for axial strain (ε_a) values greater than 15%. Moreover, the cement addition appeared to have negligible influence on the iron ore tailings' responses to this high confinement level, indicating that the bonds were probably broken during the consolidation phase [49–51]. This is corroborated by the quantitively and qualitatively similar responses of the cemented and uncemented samples under the highest confining stress that attained deviatoric stresses of the same order of magnitude and comparable compression during shear. The top strength value followed the previously discussed trend for the p'_0 = 300 kPa tests.

Table 3. Triaxial test specimens' characteristics.

Specimen	p'_0 (kPa)	e_0	e_c	$G\varepsilon_s = _{0.5\%}$ (MPa)
S_W_3C	300 kPa	0.59	0.57	56.1
S_O_3C		0.54	0.53	63.8
S_R_3C		0.58	0.57	68.8
S_D_3C		0.58	0.57	76.6
M_W_3C		0.49	0.49	63.1
M_O_3C		0.44	0.43	75.2
M_R_3C		0.44	0.43	83.5
M_D_3C		0.49	0.47	88.8
S_W_0C		0.58	0.57	7.5
S_O_0C		0.54	0.53	9.4
S_R_0C		0.58	0.57	11.1
S_D_0C		0.58	0.56	15.2
M_W_0C		0.48	0.48	21.4
M_O_0C		0.44	0.43	9.8
M_R_0C		0.44	0.43	11.2
M_D_0C		0.48	0.47	38.5
S_W_3C	3000 kPa	0.59	0.41	188.5
S_O_3C		0.54	0.43	261.5
S_R_3C		0.58	0.43	282.4
S_D_3C		0.58	0.43	303.9
M_W_3C		0.49	0.42	170.5
M_O_3C		0.44	0.41	264.7
M_R_3C		0.48	0.42	221.5
M_D_3C		0.49	0.41	351.3
S_W_0C		0.58	0.43	33.5
S_O_0C		0.54	0.43	66.6
S_R_0C		0.58	0.43	69.8
S_D_0C		0.58	0.42	146.6
M_W_0C		0.48	0.43	46.8
M_O_0C		0.44	0.40	71.6
M_R_0C		0.48	0.42	74.8
M_D_0C		0.48	0.41	109.7

5.2.2. Effect of Molding Characteristics

For the uncemented samples, within each confinement level and separately considering each compaction energy, the highest strength was attained at the optimum molding conditions (i.e., lowest void ratio and optimum moisture content). This reinforces the role of the degree of interlocking in the strength of purely frictional materials, which contributes to minimizing the compressive trend and assists in enhancing the strength associated with dilation, particularly for lower confinement pressures [52–54]. For the 97% compaction degree, the specimens assembled using the optimum moisture content and the dry side samples attained comparable top strength values. They were slightly less compressible and more dilatant than the wet-side ones, thus more resistant. The fabrics that have arisen when compacting the samples using lower moisture contents have favored this trend because the particles are less lubricated than in the wet-side arrangement and, as a reason, less likely to compress during shear. Considering the cemented samples, the same trend regarding the strength response was obtained, but with the addition of a cohesion-related strength parcel for the p'_0 = 300 kPa tests [18,21,55]. This has substantially increased the top strength in comparison to the uncemented samples.

In contrast, the initial stiffness does not follow the above trend for the strength data. For both the cemented and uncemented specimens, and within the same compaction energy, the dry-side samples were initially stiffer, followed by the ones molded at the optimum conditions, the ones compacted at the optimum moisture content but with reduced dry density, and, ultimately, the ones compacted on the wet side. This indicates that the fabric created by the compaction on the dry side of the compaction curves has favored the stiffness. The lack of lubrication between the particles on the dry side has somewhat restrained the relative movement between the constituent grains, enhancing the stiffness in this condition. Consoli et al. [50] reported a similar trend for conventional geotechnical materials. Likewise, the cement addition enhanced the initial stiffness of the iron ore tailings, particularly in p'_0 = 300 kPa tests, in which the cemented samples were initially much stiffer than the uncemented ones. This difference is not as pronounced for the highest level of confinement since most of the cement bonds were broken during consolidation. The shear modulus values corroborate these for a distortional strain of ε_s = 0.5%, summarized in the last column of Table 3.

5.3. Particle Breakage Analysis

Figure 5 depicts the grain size distribution of the specimens submitted to the one-dimensional compression tests, and Figure 6 exhibits the same regarding the triaxial tests conducted at p'_0 = 3000 kPa. Both figures contain the gradation of the natural (untested) iron ore tailings. Table 4 summarizes the particle breakage factor (B_f) calculated based on those curves.

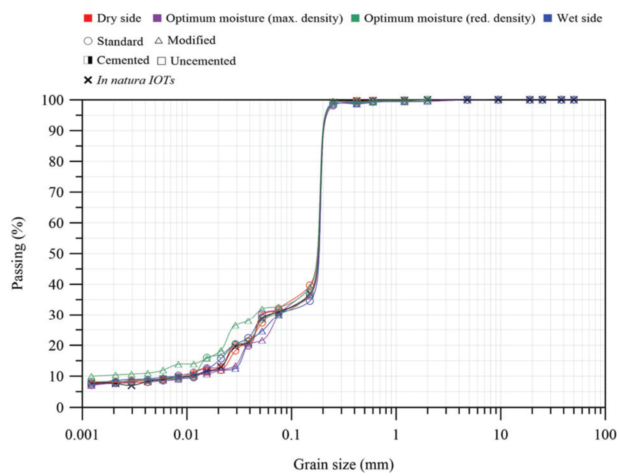

(**a**)

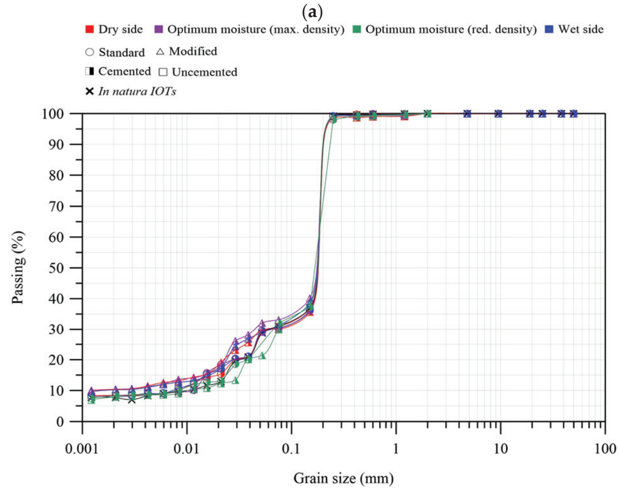

(**b**)

Figure 5. Grain size distribution test conducted after the one-dimensional compression test: (**a**) uncemented and (**b**) cemented.

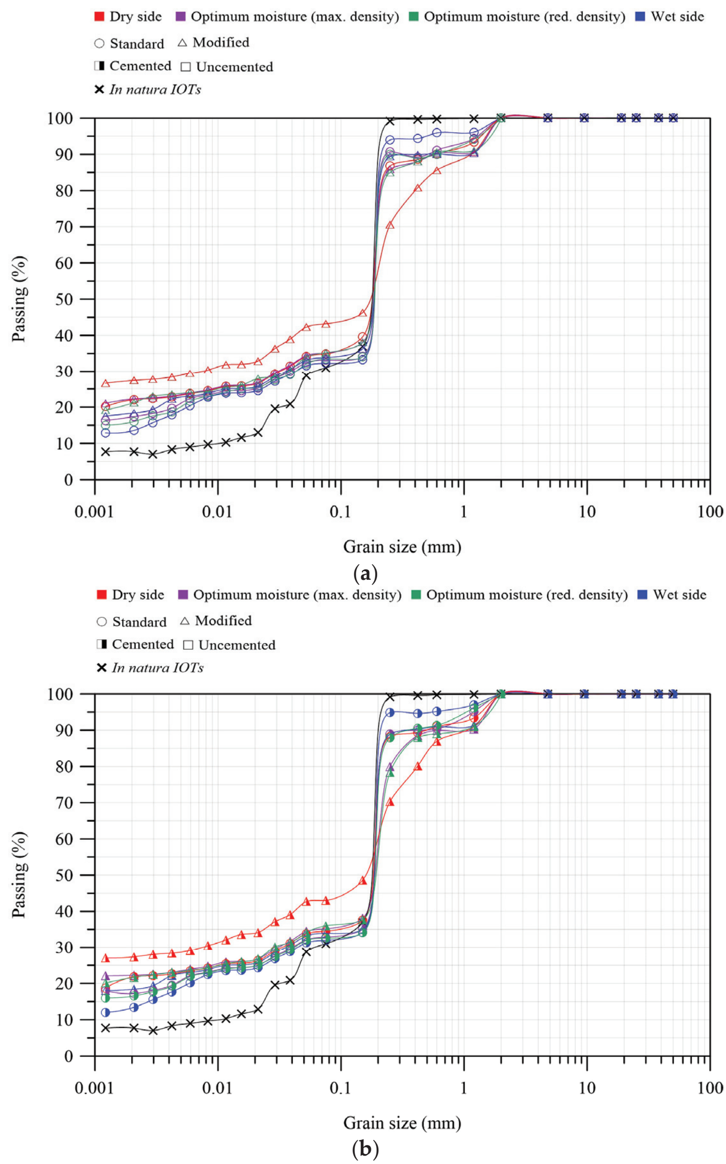

Figure 6. Grain size distribution test conducted after the triaxial test: (**a**) uncemented and (**b**) cemented.

The amount of grain crushing due to one-dimensional compression is negligible, as evidenced by the near-zero values of the B_f, regardless of the specimen's characteristics. This is corroborated by the SEM micrographs of specimens M_D_3C and M_D_0C, shown in Figure 7a and 7b, respectively. Features of the tested material, such as particle size, shape, and surface roughness, have remained unaltered when vertically compressed up to 6400 kPa. Higher pressures would probably cause grain breakage for this loading condition [56,57].

Table 4. Particle breakage factor.

Specimen	Particle Breakage Factor (B_f)	
	Test Type	
	1-D Comp.	Triaxial
S_W_3C	0.02	0.04
S_O_3C	0.02	0.10
S_R_3C	0.01	0.08
S_D_3C	0.02	0.11
M_W_3C	0.01	0.10
M_O_3C	0.01	0.14
M_R_3C	0.02	0.11
M_D_3C	0.01	0.19
S_W_0C	0.00	0.05
S_O_0C	0.00	0.09
S_R_0C	0.00	0.07
S_D_0C	0.00	0.12
M_W_0C	0.00	0.10
M_O_0C	0.00	0.13
M_R_0C	0.00	0.11
M_D_0C	0.00	0.19

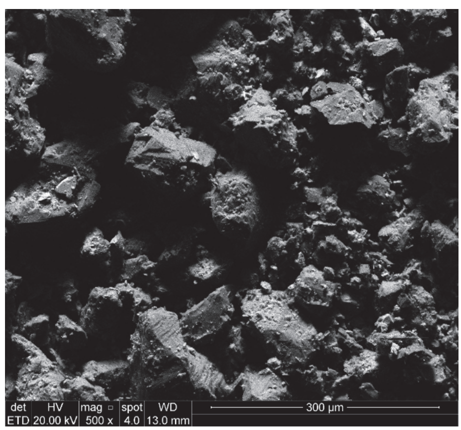

(**a**)

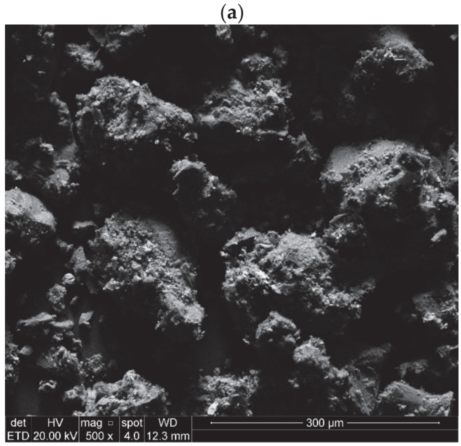

(**b**)

Figure 7. SEM micrographs after one-dimensional compression tests at 500× magnification rate: (**a**) M_D_0C and (**b**) M_D_3C.

In contrast, shearing at p'_0 = 3000 kPa caused grain breakage, which varied according to the molding specimen's characteristics, suggesting that B_f values ranged from 4% to 19%. The amount of particle crushing was higher when the specimens were molded at a modified energy (97% or 100% of compaction degree), which is probably related to the denser packing that favored inter-particle contact [58]. Considering the moisture content, the specimens compacted on the wet side presented slightly lower B_f values, which is probably related to the higher degree of lubrication between the particles in this condition. Moreover, the cement-containing specimens showed marginally higher B_f values than the uncemented samples compacted at the same density and using the same moisture content. However, this difference was practically negligible. The after-shearing SEM micrographs of samples M_D_3C and M_D_0C are presented in Figure 8a and 8b, respectively.

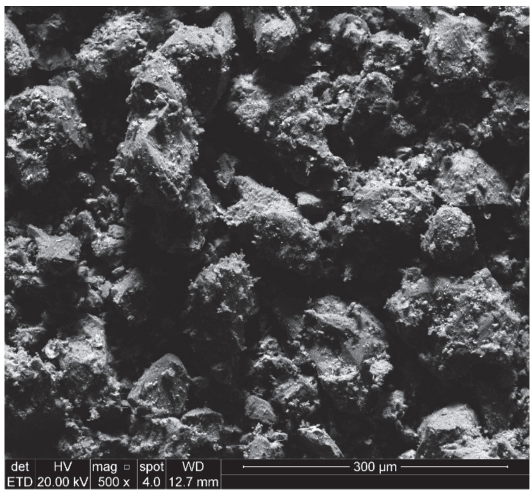

(**a**)

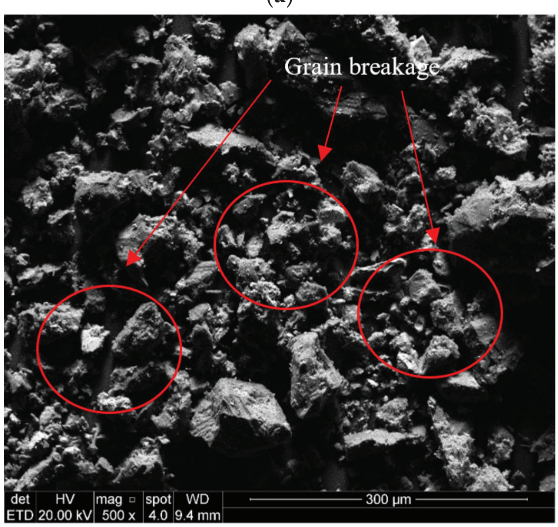

(**b**)

Figure 8. SEM micrographs after triaxial testing at 500× magnification rate: (**a**) M_D_0C and (**b**) M_D_3C. Red circles and arrows represent the grain breakage of the samples.

It is noticeable that the particles became smaller and slightly more angular owing to the breakage that occurred during shearing. Again, no differences between the cemented and uncemented samples can be noticed, indicating that the cement bonds were thoroughly broken during the 3000 kPa consolidation stage.

6. Concluding Remarks

From the data presented herein and considering the boundaries of the present research, the following conclusions can be drawn:

- Despite the non-convergent behavior of all samples up to the attained vertical stress (σ'_v = 6400 kPa), as indicated by the different compression index values between the denser and looser samples, the studied iron ore tailings appear to be non-transitional since a near-zero m parameter value was obtained. This indicates that fabric-related differences resulting from various molding conditions (such as compaction degree, initial moisture content, and cement addition) diminish at higher stress levels during one-dimensional compression.
- The molding characteristics appeared to have significantly influenced the stress–strain response of the triaxial tests considering the lowest confining pressure (p'_0 = 300 kPa). At the highest confinement level (p'_0 = 3000 kPa), most of the cement bonds were broken during the consolidation phase, exerting a marginal effect on the shearing phase.
- For lower confinement levels, the cement addition appears to be an interesting option to enhance the strength and stiffness of the compacted iron ore tailings. Compacting the samples at the optimum conditions maximizes the top strength. In contrast, the initial stiffness is enhanced when the compaction is performed on the dry side of the compaction curve.
- The one-dimensional compression tests did not reveal substantial particle breakage, regardless of the initial molding characteristics. On the other side, shearing at p'_0 = 3000 kPa generated a considerable grain breakage, particularly in the densest samples. In this regard, the cement addition appeared to have exerted a marginal influence concerning preventing particle breakage due to shearing at p'_0 = 3000 kPa.
- Despite the differences arising from using distinct compaction characteristics, the overall volume change response was not profoundly altered by adding cement and altering the molding moisture content. In other words, all the specimens sheared at p'_0 = 300 kPa initially contracted and then dilated, whereas all the specimens sheared at p'_0 = 3000 kPa contracted.
- The durability of artificially cemented filtered iron ore tailings is relevant for adequately designing and maintaining dry stacking facilities. Particularly those submitted to harsh environmental conditions. Therefore, it is an exciting topic for future research.

Author Contributions: Conceptualization, G.J.B., H.C.S.F. and N.C.C.; methodology, G.J.B., C.P.D.S., H.C.S.F., C.d.S.M., L.R.S., J.P.d.S.S. and N.C.C.; validation, G.J.B. and H.C.S.F.; formal analysis, G.J.B., C.P.D.S., H.C.S.F., C.d.S.M. and L.R.S.; investigation, G.J.B., C.P.D.S., H.C.S.F., C.d.S.M. and L.R.S.; resources, J.P.d.S.S. and N.C.C.; data curation, G.J.B. and H.C.S.F.; writing—original draft preparation, G.J.B. and H.C.S.F.; writing—review and editing, G.J.B., C.P.D.S., H.C.S.F., C.d.S.M., L.R.S., J.P.d.S.S. and N.C.C.; visualization, J.P.d.S.S. and N.C.C.; supervision, N.C.C.; project administration, N.C.C. All authors have read and agreed to the published version of the manuscript.

Funding: This research received no external funding.

Data Availability Statement: Some or all data, models, or codes that support the findings of this study are available from the corresponding author upon reasonable request.

Acknowledgments: The authors wish to express their appreciation for VALE S.A. and the Brazilian Research Council (CNPq) for supporting the research group.

Conflicts of Interest: João Paulo de Souza Silva employed by the company VALE S.A. The remaining authors declare that the research was conducted in the absence of any commercial or financial relationships that could be construed as a potential conflict of interest.

Notations

γ_d	dry unit weight
γ_s	unit weight of solids of the iron ore tailings
w	moisture content
G	initial shear modulus
γ	bulk density
1-D	one-dimensional
CID	consolidated isotropically drained
SEM	scanning electron microscope
XRD	X-ray diffraction
XRF	X-ray fluorescence
IOT	iron ore tailings
NCL	normal compression line
M	modified compaction energy
S	standard compaction energy
W	wet side
D	dry side
O	optimum molding conditions
e_0	molding void ratio
e_c	after consolidation, the void ratio
B_f	breakage factor
C	amount of cement expressed in percentage
C_c	compression index
p'	mean effective stress
p'_0	initial mean effective stress
q	deviatoric stress
q_{max}	peak deviatoric stress
ε_a	axial strain
ε_v	volumetric strain
ε_s	distortional strain
σ'_v	vertical stress
σ_1, σ_3	principal stresses

References

1. Cacciuttolo Vargas, C.; Pérez Campomanes, G. Practical Experience of Filtered Tailings Technology in Chile and Peru: An Environmentally Friendly Solution. *Minerals* **2022**, *12*, 889. [CrossRef]
2. Gomes, R.B.; De Tomi, G.; Assis, P.S. Iron Ore Tailings Dry Stacking in Pau Branco Mine, Brazil. *J. Mater. Res. Technol.* **2016**, *5*, 339–344. [CrossRef]
3. Bedin, J.; Schnaid, F.; Da Fonseca, A.V.; Costa Filho, L.D.M. Gold Tailings Liquefaction under Critical State Soil Mechanics. *Géotechnique* **2012**, *62*, 263–267. [CrossRef]
4. Carrera, A.; Coop, M.; Lancellotta, R. Influence of Grading on the Mechanical Behaviour of Stava Tailings. *Géotechnique* **2011**, *61*, 935–946. [CrossRef]
5. Oldecop, L.; Rodari, G. Unsaturated Mine Tailings Disposal. *Soils Rocks* **2021**, *44*, 1–12. [CrossRef]
6. Schaper, D.; Lessa, R.; Freitas, A.; Weeks, B. De-Characterization and Closure of TSF: Concepts of the Brazilian Legislation and International Criteria. *Plan. Clos.* **2020**, *3*.
7. Armstrong, M.; Petter, R.; Petter, C. Why Have so Many Tailings Dams Failed in Recent Years? *Resour. Policy* **2019**, *63*, 101412. [CrossRef]
8. Islam, K.; Murakami, S. Global-Scale Impact Analysis of Mine Tailings Dam Failures: 1915–2020. *Glob. Environ. Chang.* **2021**, *70*, 102361. [CrossRef]
9. Lyu, Z.; Chai, J.; Xu, Z.; Qin, Y.; Cao, J. A Comprehensive Review on Reasons for Tailings Dam Failures Based on Case History. *Adv. Civ. Eng.* **2019**, *2019*, 4159306. [CrossRef]
10. Dauce, P.D.; De Castro, G.B.; Lima, M.M.F.; Lima, R.M.F. Characterisation and Magnetic Concentration of an Iron Ore Tailings. *J. Mater. Res. Technol.* **2019**, *8*, 1052–1059. [CrossRef]
11. Vilaça, A.S.I.; Simão, L.; Montedo, O.R.K.; Novaes de Oliveira, A.P.; Raupp-Pereira, F. Waste Valorization of Iron Ore Tailings in Brazil: Assessment Metrics from a Circular Economy Perspective. *Resour. Policy* **2022**, *75*, 102477. [CrossRef]
12. Kossoff, D.; Dubbin, W.E.; Alfredsson, M.; Edwards, S.J.; Macklin, M.G.; Hudson-Edwards, K.A. Mine Tailings Dams: Characteristics, Failure, Environmental Impacts, and Remediation. *Appl. Geochem.* **2014**, *51*, 229–245. [CrossRef]
13. Santamarina, J.C.; Torres-Cruz, L.A.; Bachus, R.C. Why Coal Ash and Tailings Dam Disasters Occur. *Science* **2019**, *364*, 526–528. [CrossRef] [PubMed]
14. Ahmed, S.I.; Siddiqua, S.; Renner, S. Development of a Model to Predict Consolidation of Tailings. *Environ. Geotech.* **2018**, *5*, 271–284. [CrossRef]
15. Ledesma, O.; Sfriso, A.; Manzanal, D. Procedure for Assessing the Liquefaction Vulnerability of Tailings Dams. *Comput. Geotech.* **2022**, *144*, 104632. [CrossRef]

16. Bruschi, G.J.; Dos Santos, C.P.; Tonini de Araújo, M.; Ferrazzo, S.T.; Marques, S.F.V.; Consoli, N.C. Green Stabilization of Bauxite Tailings: Mechanical Study on Alkali-Activated Materials. *J. Mater. Civ. Eng.* **2021**, *33*, 06021007. [CrossRef]
17. Consoli, N.C.; Da Silva, A.P.; Nierwinski, H.P.; Sosnoski, J. Durability, Strength, and Stiffness of Compacted Gold Tailings—Cement Mixes. *Can. Geotech. J.* **2018**, *55*, 486–494. [CrossRef]
18. Consoli, N.C.; Vogt, J.C.; Silva, J.P.S.; Chaves, H.M.; Scheuermann Filho, H.C.; Moreira, E.B.; Lotero, A. Behaviour of Compacted Filtered Iron Ore Tailings–Portland Cement Blends: New Brazilian Trend for Tailings Disposal by Stacking. *Appl. Sci.* **2022**, *12*, 836. [CrossRef]
19. Festugato, L.; Fourie, A.; Consoli, N.C. Cyclic Shear Response of Fibre-Reinforced Cemented Paste Backfill. *Géotech. Lett.* **2013**, *3*, 5–12. [CrossRef]
20. Pereira dos Santos, C.; Bruschi, G.J.; Mattos, J.R.G.; Consoli, N.C. Stabilization of Gold Mining Tailings with Alkali-Activated Carbide Lime and Sugarcane Bagasse Ash. *Transp. Geotech.* **2022**, *32*, 100704. [CrossRef]
21. Schnaid, F.; Prietto, P.D.M.; Consoli, N.C. Characterization of Cemented Sand in Triaxial Compression. *J. Geotech. Geoenviron. Eng.* **2001**, *127*, 857–868. [CrossRef]
22. Lade, P.V.; Trads, N. The Role of Cementation in the Behaviour of Cemented Soils. *Geotech. Res.* **2014**, *1*, 111–132. [CrossRef]
23. Rotta, G.V.; Consoli, N.C.; Prietto, P.D.M.; Coop, M.R.; Graham, J. Isotropic Yielding in an Artificially Cemented Soil Cured under Stress. *Géotechnique* **2003**, *53*, 493–501. [CrossRef]
24. Behera, S.; Mishra, D.; Singh, P.; Mishra, K.; Mandal, S.K.; Ghosh, C.; Kumar, R.; Mandal, P.K. Utilization of mill tailings, fly ash and slag as mine paste backfill material: Review and future perspective. *Constr. Build. Mater.* **2021**, *309*, 120–125. [CrossRef]
25. Ercikdi, B.; Cihangir, F.; Kesimal, A.; Deveci, H. Practical Importance of Tailings for Cemented Paste Backfill. In *Paste Tailings Management*; Yilmaz, E., Fall, M., Eds.; Springer International Publishing: Cham, Switzerland, 2017; pp. 7–32, ISBN 978-3-319-39680-4.
26. Jiang, H.; Fall, M. Yield stress and strength of saline cemented tailings in sub-zero environments: Portland cement paste backfill. *Int. J. Miner. Process.* **2017**, *160*, 68–75. [CrossRef]
27. Kasap, T.; Yilmaz, E.; Guner, N.U.; Sari, M. Recycling Dam Tailings as Cemented Mine Backfill: Mechanical and Geotechnical Properties. *Adv. Mater. Sci. Eng.* **2022**, *2022*, 6993068. [CrossRef]
28. Mitchell, R.J.; Olsen, R.S.; Smith, J.D.; Li, L.; Aubertin, M.; Thompson, B.; Bawden, W.; Grabinsky, M. Model studies on cemented tailings used in mine backfill. *Can. Geotech. J.* **1982**, *19*, 14–28. [CrossRef]
29. Qi, C.; Fourie, A. Cemented paste backfill for mineral tailings management: Review and future perspectives. *Miner. Eng.* **2019**, *144*, 106025. [CrossRef]
30. *ASTM D7928*; Test Method for Particle-Size Distribution (Gradation) of Fine-Grained Soils Using the Sedimentation (Hydrometer) Analysis. ASTM International: West Conshohocken, PA, USA, 2021.
31. *ASTM D4318*; Test Methods for Liquid Limit, Plastic Limit, and Plasticity Index of Soils. ASTM International: West Conshohocken, PA, USA, 2017.
32. *ASTM D854*; Test Methods for Specific Gravity of Soil Solids by Water Pycnometer. ASTM International: West Conshohocken, PA, USA, 2014.
33. *ASTM D2487*; Practice for Classification of Soils for Engineering Purposes (Unified Soil Classification System). ASTM International: West Conshohocken, PA, USA, 2017.
34. *ASTM D698*; Test Methods for Laboratory Compaction Characteristics of Soil Using Standard Effort (12,400 Ft-Lbf/Ft3 (600 KN-m/M3)). ASTM International: West Conshohocken, PA, USA, 2021.
35. *ASTM D1557*; Test Methods for Laboratory Compaction Characteristics of Soil Using Modified Effort (56,000 Ft-Lbf/Ft3 (2700 KN-m/M3)). ASTM International: West Conshohocken, PA, USA, 2021.
36. Carmignano, O.; Vieira, S.; Teixeira, A.P.; Lameiras, F.; Brandão, P.R.; Lago, R. Iron Ore Tailings: Characterization and Applications. *J. Braz. Chem. Soc.* **2021**, *32*, 1895–1911. [CrossRef]
37. Chang, N.; Heymann, G.; Clayton, C. The Effect of Fabric on the Behaviour of Gold Tailings. *Géotechnique* **2011**, *61*, 187–197. [CrossRef]
38. Nie, W.; Li, C.; Hu, J.; Saffari, P.; Wang, W.; Luo, M. Spatial Variation of Physical and Mechanical Properties of Tailings under Different Rainfall Intensities and the Interaction Pattern. *Geomech. Geophys. Geo-Energy Geo-Resour.* **2023**, *9*, 86. [CrossRef]
39. Li, Y.; Otsubo, M.; Kuwano, R. Evaluation of Soil Fabric Using Elastic Waves during Load-Unload. *J. Rock Mech. Geotech. Eng.* **2023**, *15*, 2687–2700. [CrossRef]
40. Shaker, A.A.; Elkady, T.Y. Hydraulic Performance of Sand–Clay Mixtures: Soil Fabric Perspective. *Géotech. Lett.* **2015**, *5*, 198–204. [CrossRef]
41. Yimsiri, S.; Soga, K. Effects of Soil Fabric on Behaviors of Granular Soils: Microscopic Modeling. *Comput. Geotech.* **2011**, *38*, 861–874. [CrossRef]
42. *ASTM D2435*; Test Methods for One-Dimensional Consolidation Properties of Soils Using Incremental Loading. ASTM International: West Conshohocken, PA, USA, 2011.
43. *ASTM D7181*; Test Method for Consolidated Drained Triaxial Compression Test for Soils. ASTM International: West Conshohocken, PA, USA, 2020.
44. Clayton, C.R.I.; Khatrush, S.A. A New Device for Measuring Local Axial Strains on Triaxial Specimens. *Géotechnique* **1986**, *36*, 593–597. [CrossRef]

45. Nakata, A.F.L.; Hyde, M.; Hyodo, H.; Murata. A Probabilistic Approach to Sand Particle Crushing in the Triaxial Test. *Géotechnique* **1999**, *49*, 567–583. [CrossRef]
46. Li, W.; Coop, M.R. Mechanical Behaviour of Panzhihua Iron Tailings. *Can. Geotech. J.* **2019**, *56*, 420–435. [CrossRef]
47. Ponzoni, E.; Nocilla, A.; Coop, M.R.; Colleselli, F. Identification and Quantification of Transitional Modes of Behaviour in Sediments of Venice Lagoon. *Géotechnique* **2014**, *64*, 694–708. [CrossRef]
48. Todisco, M.C.; Coop, M.R. Quantifying "Transitional" Soil Behaviour. *Soils Found.* **2019**, *59*, 2070–2082. [CrossRef]
49. Malandraki, V.; Toll, D. Drained Probing Triaxial Tests on a Weakly Bonded Artificial Soil. *Géotechnique* **2000**, *50*, 141–151. [CrossRef]
50. Alvarado, G.; Coop, M.R.; Willson, S. On the Role of Bond Breakage Due to Unloading in the Behaviour of Weak Sandstones. *Géotechnique* **2012**, *62*, 303–316. [CrossRef]
51. Alvarado, G.; Lui, N.; Coop, M.R. Effect of Fabric on the Behaviour of Reservoir Sandstones. *Can. Geotech. J.* **2012**, *49*, 1036–1051. [CrossRef]
52. Reza Fotovvat, A.; Sadrekarimi, A. Instability of a Gold Mine Tailings Subjected to Different Stress Paths. *J. Geotech. Geoenviron. Eng.* **2022**, *148*, 04022020. [CrossRef]
53. Salvatore, E.; Modoni, G.; Andò, E.; Albano, M.; Viggiani, G. Determination of the Critical State of Granular Materials with Triaxial Tests. *Soils Found.* **2017**, *57*, 733–744. [CrossRef]
54. Wagner, A.C.; De Sousa Silva, J.P.; De Azambuja Carvalho, J.V.; Cezar Rissoli, A.L.; Cacciari, P.P.; Chaves, H.M.; Scheuermann Filho, H.C.; Consoli, N.C. Mechanical Behavior of Iron Ore Tailings under Standard Compression and Extension Triaxial Stress Paths. *J. Rock Mech. Geotech. Eng.* **2023**, *15*, 1883–1894. [CrossRef]
55. Lade, P.V.; Overton, D.D. Cementation Effects in Frictional Materials. *J. Geotech. Eng.* **1989**, *115*, 1373–1387. [CrossRef]
56. Kikumoto, M.; Wood, D.M.; Russell, A. Particle Crushing and Deformation Behaviour. *Soils Found.* **2010**, *50*, 547–563. [CrossRef]
57. Zhang, T.; Yang, W.; Zhang, C.; Hu, C. Particle Breakage Effect on Compression Behavior of Realistic Granular Assembly. *Int. J. Geomech.* **2021**, *21*, 04021105. [CrossRef]
58. Wei, H.; Li, X.; Zhang, S.; Zhao, T.; Yin, M.; Meng, Q. Influence of Particle Breakage on Drained Shear Strength of Calcareous Sands. *Int. J. Geomech.* **2021**, *21*, 04021118. [CrossRef]

applied sciences

Article

Solid Backfilling Efficiency Optimization in Coal Mining: Spatiotemporal Linkage Analysis and Case Study

Tingcheng Zong [1,2], Gaolei Zhu [3], Qiang Zhang [1,2,*], Kang Yang [1,2], Yunbo Wang [1,2], Yu Han [1,2], Haonan Lv [1,2] and Jinming Cao [1,2]

[1] School of Mines, China University of Mining and Technology, Xuzhou 221116, China; ts21020078a31@cumt.edu.cn (T.Z.); tb22020033a41ld@cumt.edu.cn (K.Y.); wangyunbo@cumt.edu.cn (Y.W.); ts22020117p21@cumt.edu.cn (Y.H.); ts22020048a31@cumt.edu.cn (H.L.); ts22020097p21@cumt.edu.cn (J.C.)

[2] State Key Laboratory of Coal Resources and Safe Mining, China University of Mining and Technology, Xuzhou 221116, China

[3] Anhui RONDS Technology Co., Ltd., Hefei 230088, China; ts20020081a31tm@cumt.edu.cn

* Correspondence: zhangq@cumt.edu.cn; Tel.: +86-137-7598-1147

Abstract: In coal mining, solid backfilling technology is widely used. However, its efficiency is seriously hindered by the following two factors. Firstly, the process flow of the solid backfilling operation is more complicated in the back, and the spatiotemporal linkage (SPL) between actions of the cylinders powering each support and between hydraulic supports in the whole face lacks continuity. Secondly, the coal mining process in the front has a higher level of intelligence and technical maturity than the backfilling operation in the back, the latter permanently staying behind the former. To this end, the present study investigates the SPL of the mining and backfilling operations for single supports in the working and whole faces. The SPL of cylinder actions is analyzed for intelligent backfilling using hydraulic supports. We also investigate the SPL of the positions of each piece of key equipment involved in different steps of intelligent backfilling in the whole face. Formulas are derived for calculating the time required to complete the cyclic hydraulic support movement–discharge–filling operation for single supports and the whole face. The key factors influencing the time required to complete a hydraulic support movement–discharge–filling cycle are analyzed. On this basis, a backfilling efficiency optimization scheme is proposed. It envisages reducing the number of tampings and time gaps in actions of single supports and cylinders, increasing the number of hydraulic supports in parallel operation, and intelligent upgrading of the backfilling operation. These findings help synchronize coal mining and backfilling operations.

Keywords: intelligent backfilling; mining and backfilling operation; spatiotemporal linkage; parallel mining and filling

Citation: Zong, T.; Zhu, G.; Zhang, Q.; Yang, K.; Wang, Y.; Han, Y.; Lv, H.; Cao, J. Solid Backfilling Efficiency Optimization in Coal Mining: Spatiotemporal Linkage Analysis and Case Study. *Appl. Sci.* **2023**, *13*, 12298. https://doi.org/10.3390/app132212298

Academic Editor: Nikolaos Koukouzas

Received: 27 September 2023
Revised: 8 November 2023
Accepted: 9 November 2023
Published: 14 November 2023

1. Introduction

Due to the tendency to minimize heaps on the surface, solutions are being sought to manage waste rocks in mining technologies [1–3] both in preparatory excavations and exploitation systems; studies on the automation of mining and backfilling operations mainly focus on paste transport and backfilling and cemented backfilling [4]. Solid backfilling still needs to be fully automated. The research progress in automated backfilling is reviewed below. For automated paste backfilling, Chang et al. [5] introduced the technology principles and technological process of paste backfilling mining in coal mines and discussed the components and features of backfill materials, the constitution of the backfilling system, and the backfilling process. Qing et al. [6] optimized the transport process in high-efficiency automated paste filling with double pumps working in parallel by reasonably laying backfill pipelines. For automated cemented backfilling, Dong et al. [7] utilized a signal transmission network, intelligent instrumentation, and a control software algorithm to realize fault self-diagnosis and processing for long-distance, large diameter backfill pipelines and a fast and precise preparation and control technique for non-cemented slurry. Shi et al. [8] employed automatic control technology and intelligent recognition and processing technology for the automated control of cemented backfilling, improving the tailings backfill quality. Zhang et al. [9] systematically elaborated on an overall framework for underground intelligent sorting and an in situ backfill for deep coal mines for solid backfilling and mining–selection–filling processes. They built an overall research framework and equipment system for underground intelligent sorting and in situ backfill for deep coal mines. A novel solid backfilling mining technology that integrated mining, sorting, and backfilling and achieved the original underground gangue's sorting and an in situ backfill was proposed in works [10,11] Yao et al. [12] installed support pressure, angle, stroke, and blanking height sensors to transmit data to the central controller. A control program was used for conditional judgment of the gangue filling rate and compaction degree, thereby realizing the process flow of gangue backfilling control automation. Gao et al. [13] studied machine-following automation for fully mechanized mining hydraulic supports that consisted of three stages: automation of center following, automation of head following, and automation of tail following. Then, based on the action flow for hydraulic supports and the motion trajectory of the shearer, the automated process flow of the machine head and tail following was subdivided into six stages. Liu et al. [14] proposed a collaborative control technology for the shearer and hydraulic supports in a fully mechanized working face based on memory cutting performed by the shearer and automated following control technology for hydraulic supports. Shi et al. [15] analyzed the process of following automation for hydraulic supports in the middle of the working face and presented a mathematical model for following automated control in the middle of the fully mechanized working face.

Despite significant progress achieved in the above studies, the mechanism of spatiotemporal linkages (SPL) of mining and backfilling operations in the solid backfilling working face in fully mechanized mining remains unclear. A method to quantify the time required to complete parallel mining and backfilling operations and reduce the time gap between the two operations to improve the backfilling efficiency is very topical.

To this end, the current study analyzes the SPL of different cylinders involved in sequential actions for intelligent backfilling using single supports in parallel mining and backfilling operations in fully mechanized mining. We also investigate the SPL of the positions of each piece of key equipment involved in different steps of intelligent backfilling in the whole face. Formulas for calculating the time of a complete hydraulic support movement–discharge–filling cycle for single supports and the whole face are derived. The influencing factors of the time required to complete a hydraulic support movement–discharge–filling cycle are identified. On this basis, we propose an optimization scheme to improve the backfilling efficiency, which consists in reducing the number of tampings, reducing the time gaps in the actions of single supports and cylinders, increasing the number of hydraulic supports in parallel operation, and intelligent upgrading.

2. Evolution of Intelligent Mining and Backfilling Operations in Fully Mechanized Mining and the Connotation of the Mechanism of SPL

2.1. Evolution of Intelligent Mining and Backfilling Operations in Fully Mechanized Mining

Early mining and backfilling operations have been carried out by manually operating a hydraulic valve control lever. Along with the applications of electrohydraulic control technology, there has been an evolution toward automatic filling based on electrohydraulic control [16,17]. In recent years, intelligent backfilling has emerged due to advances in intelligent perception and control technology [18–20].

In teams of mining workers involved in mechanized backfilling, each worker usually operates a filling hydraulic support and observes the field environment with the naked eye [21]. The workers manually operate the valve lever based on their experiences in controlling hydraulic valve reversion, stretching out, and drawing back the cylinders. Common deficiencies of mechanized backfilling technology include the disordered actions of cylinders powering single supports and frame supports, prolonged time gap between cylinder actions (sum of human response time and actuating time), heavy reliance of the backfilling effect upon subjective experiences, and high labor intensity.

Compared with mechanized solid backfilling, automated solid backfilling involves an electrohydraulic control system, greatly simplifying manual operations. Processes that were once accomplished by workers manually operating different valve levers are now carried out by pushing buttons, which means a higher level of automation. However, there is still a need for manual observation, decision-making, and manipulation, apart from the long-standing problems of disordered actions of cylinders powering single hydraulic supports and frame supports and prolonged time gaps in cylinder actions.

In intelligent solid backfilling mining [22–24], to intelligently control the backfilling process, travel sensors are often installed on the hydraulic cylinders of backfilling hydraulic supports to monitor their real-time stroke values. Tilt sensors are installed on the base and front and rear beams to monitor the tilt angles. Pressure sensors are installed inside the hydraulic cylinder cavities or at the outlet of the oil supply pipelines to monitor the loads on the hydraulic cylinders. In addition, to monitor other abnormal conditions in the backfilling space, computer vision technology can also be used to assist [25]. Furthermore, for intelligent control of the coal mining process, the relatively mature LASC (Longwall Automation Steering Committee) [26,27] automated coal mining technology is usually adopted, and image recognition and other technologies are utilized to assist in improving the intelligibility of the coal mining process. Various sensors are installed to acquire the status and position information of hydraulic supports, and the host computer optimizes the execution sequences for cylinders. The electrohydraulic control system powered by the host computer executes the cylinder actions. There is no need to stop the shearer or for human involvement during the operations. Intelligent backfilling optimizes the sequences of cylinder actions and reduces the time gaps between cylinder actions.

2.2. Connotation of the SPL of Sequential Processes of Intelligent Mining and Backfilling Operations

The basic principle of SPL of sequential processes of intelligent mining and backfilling operations is that the mining and backfilling operations are carried out simultaneously between different frames, whereas either mining or backfilling is carried out within the same frame at a time [28]. The SPL is defined to determine the spatial sequence of processes executed by mining and backfilling equipment at different frame positions in the working face at different nodes of the process flow for a complete cycle that consists of end coal cutting, central coal cutting, opposite coal cutting, and backfilling operations within a mining and backfilling footage. The time frame for executing different steps of the mining and backfilling processes should be determined for a specific frame position, including coal cutting, push-pull, support moving, dumping, tamping, operation of the perforated bottom discharge scraper conveyor, and operation of the self-moving redoming conveyor. The time sequence of steps of a specific process executed by an actuator should be established. Based on the above, one can define the mechanism of SPL for the automated organization of the mining and backfilling operations. Then, by incorporating the automated coal mining process, one can design the automated process flow of the whole mining and backfilling operations. Finally, intelligent upgrading of solid backfilling mining is carried out to improve the backfilling efficiency, which can resolve the difficulty in parallel operations in conventional mechanized solid backfilling mining technology.

3. Spatiotemporal Linkage between Different Steps of Intelligent Backfilling Operation Using Single Hydraulic Supports

3.1. Division of Sequential Actions of Filling Using Single Hydraulic Supports

In the solid backfilling working face, the roof is supported by the solid backfilling mining hydraulic support (SBMHS). The front space is used for coal mining, and the rear space is used for backfilling. The gangue materials used for filling are transported by the belt conveyor for transporting gangue from the tail gate to the backfilling scraped conveyor, and then dumped to the gob area and then compacted densely by the tamping mechanism of the SBMHS [29], as shown in Figure 1.

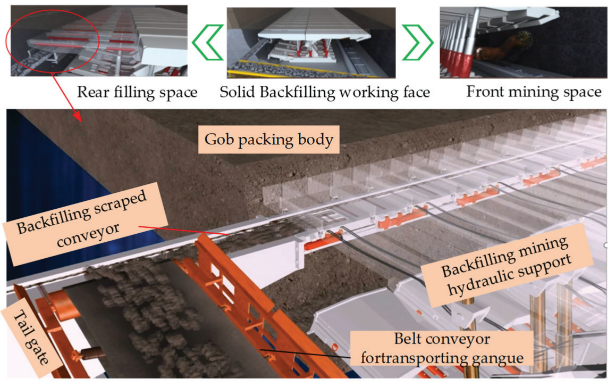

Figure 1. Schematic diagram of solid backfilling material transportation in working face.

The mining and filling actions executed by the SBMHS are realized by stretching out and drawing back each hydraulic cylinder. A typical cylinder configuration of the hydraulic support is shown in Figure 2, where the front and rear columns, cylinders, and various types of jacks are all hydraulic jacks.

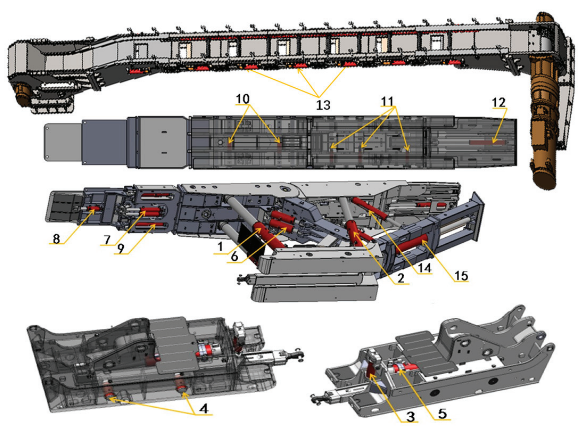

Figure 2. Schematic diagram of the cylinder configuration of the backfilling mining hydraulic support.

The names of the hydraulic cylinders No.1–15 in Figure 2 are 1. front column; 2. rear column; 3. bottom-lifting jack; 4. bottom-adjustment jack; 5. push jack; 6. equilibrium jack; 7. first-level protection jack; 8. secondary protection jack; 9. hydraulic support telescopic beam jack; 10. front roof beam-side push jack; 11. rear roof beam-side push jack; 12. expansion jack of the backfilling scraped conveyor; 13. discharge jack of the backfilling scraped conveyor; 14. swing beam jack; 15. compaction jack.

To analyze the SPL of the backfilling operation, the backfilling operation is first subdivided into the following four processes: (i) hydraulic support motion process, (ii) hydraulic support adjusting process, (iii) dumping process, and (iv) tamping process. The cylinders involved in each process and their functions are listed in Table 1.

Table 1. Functionality list of cylinders of the four-column, four-bar linkage backfilling mining hydraulic support.

Serial No.	Process	Specification	Number	Functions
1	Hydraulic support motion process	Front column	2	Lift the support canopy
2		Rear column	2	Lift the support canopy
3		Bottom-lifting jack	1	Lift the bottom up during support movement to facilitate the movement
4		Bottom-adjustment jack	2	Maintain a proper distance between the supports, and adjust the bottom as appropriate during support movement
5		Push jack	1	Pull the support
6	Hydraulic support adjusting process	Equilibrium jack	2	Adjust the support pose so that the canopy is better connected to the roof
7		Hydraulic support first-level protection jack	2	Drive the first-level face guard to protect the coal walls and prevent rib spalling. Retrieve the jack before the shearer passes through and stretch out again to protect the coal walls after the shearer passes through
8		Hydraulic support secondary protection jack	1	Drive the secondary face guard to protect the coal walls and prevent rib spalling. Retrieve the jack before the shearer passes through and stretch out again to protect the coal walls after the shearer passes through
9		Hydraulic support telescopic beam jack	2	After the coal cutting and before support pulling, drive the telescopic beam to stretch out and temporarily support the roof; retrieve the telescopic beam during support pulling
10		Front roof beam-side push jack	2	Front roof beam stretches out and retrieves the mobile side guard
11		Rear roof beam-side push jack	3	Rear roof beam stretches out and retrieves the mobile side guard
12	Dumping process	Expansion jack of Backfilling scraped conveyor	1	Pull the filling conveyor, fulfilling similar functions as the push jack
13		Expansion jack of Backfilling scraped conveyor	1	The backfilling scraped conveyor dumps the backfill material
14	Tamping process	Swing beam jack	2	Adjust the angle of the tamping mechanism
15		Compaction jack	1	Make the backfill material compact

The hydraulic support motion process refers to a series of actions moving the hydraulic support forward. After the shearer has finished coal cutting, the support is moved forward to cover the exposed roof seam to ensure mining space safety. The front and rear columns are intended to lift the support canopy up and down. The columns lift the support canopy to cover the coal seam roof to ensure mining space safety. The bottom-lifting jack reaches out to lift the bottom during support movement, thereby reducing the contact area between the support bottom and the coal seam floor. This further reduces the frictional resistance to support movement and facilitates movement. The bottom-lifting jack is intended to maintain a proper distance between the supports. During support movement, the bottom spacing should be adjusted as appropriate. The push jack is used for pulling the support so that the support slides forward. The support movement process consists of the following steps: push jack (push-pull) → lift the front and rear columns by hydraulic operation → bottom-lifting jack → the bottom-lifting jack makes adjustments → push jack (pull the support) → the bottom-lifting jack makes adjustments → bottom-lifting jack→front and back columns rise. A flowchart of the cylinder actions for the hydraulic support motion process is depicted in Figure 3.

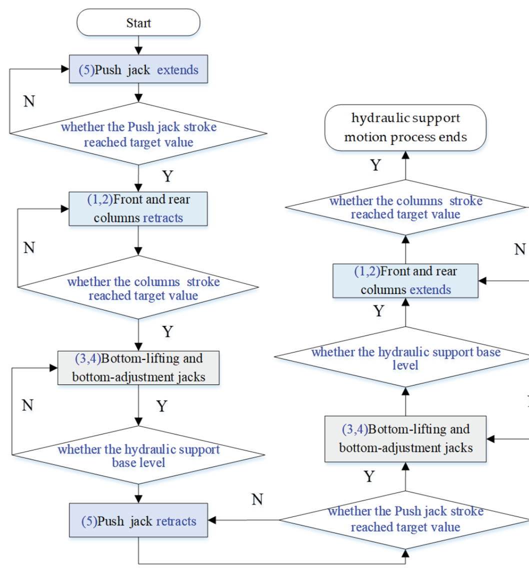

Figure 3. Flowchart of cylinder actions for the hydraulic support motion process.

It needs to be noted that the numbers in Figures 3 and 4 correspond to the serial numbers (Serial No.) in Table 1, representing the columns or jacks participating in the current process action. In addition, the text in blue font within the rectangular boxes is used to emphasize the movement direction of the columns or jacks, while the text in blue font within the diamond-shaped boxes represents the judgment logic of whether the process can enter the next step.

Adjustment refers to adjusting support positions, once before and once after the hydraulic support motion process. The equilibrium jack adjusts support positions so that the canopy is better connected to the roof. The first-level and secondary face guards are intended to protect the coal walls and prevent rib spalling. They are retrieved before the shearer passes through and stretched out again to protect the coal walls after the shearer passes through. The hydraulic support telescopic beam jack drives the telescopic beam to stretch out and temporarily support the roof after coal cutting and before support pulling; it retrieves the telescopic beam during support pulling. The front and rear roof beam-side push jacks are used to stretch out and retrieve the mobile side guards. The hydraulic support adjusting process involves the sequential actions of the following jacks: equilibrium jack → first level protection jack → secondary projection jack → front and rear roof beam-side push jacks → telescopic beam jack.

Dumping refers to the orderly discharge of solid backfill material from the backfilling scraped conveyor. The expansion jack of the backfilling scraped conveyor is used to pull the filling conveyor in the back before the support moves to enter the support-moving state. After the support is made straight in the working face, the expansion jack pushes the filling support to the back to enter the dumping state. The discharge jack of the backfilling scraped conveyor is used to open the discharge port and dump the backfill material. The dumping process consists of the following steps: the rear roof beam-side push jack pushes backward, the discharge jack of the backfilling scraped conveyor starts working, the discharge jack of the backfilling scraped conveyor stops working, and the rear roof beam-side push jack pulls forward.

The tamping process refers to the push and compaction of the solid backfill material so that the backfill material is tightly connected to the roof and becomes compacted [25,26]. The swing beam jack is used to adjust the angle of the tamping mechanism. The compaction jack is used to compact the backfill material. Cyclic compaction is carried out to have the solid backfill material in full and tight connection to the roof and become compacted, thereby achieving a satisfactory backfilling effect. The tamping process involves the sequential actions of the following jacks: compaction jack → swing beam jack → compaction jack → swing beam jack. A flowchart of the cylinder actions for the tamping process is shown in Figure 4.

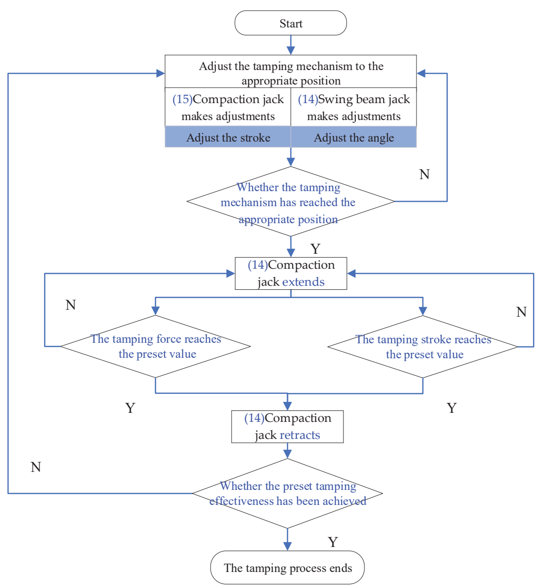

Figure 4. Flowchart of cylinder actions for the tamping process.

3.2. Theoretical Analysis of the Actuation Time of Sequential Actions of the Backfilling Operation Using Single Hydraulic Supports

The complete support movement–discharge–filling cycle for a single hydraulic support consists of the following: adjusting process, motion process, adjusting process, dumping process, and tamping process. The time needed to complete the cyclic operation is derived as follows:

$$\begin{cases} T_s = 2T_a + T_m + T_u + T_c \\ T_a = T_{af} + n_a \frac{T_r}{\lambda} \\ T_m = T_{mf} + n_m \frac{T_r}{\lambda} \\ T_u = T_{uf} + n_u \frac{T_r}{\lambda} \\ T_c = n \cdot \left(T_{cf} + n_c \frac{T_r}{\lambda}\right) \end{cases} \quad (1)$$

where T_s is the time required for a single support to complete the entire cycle; T_a is the time required to complete the adjusting process; T_m is the time required to complete the motion process; T_u is the time required to complete the dumping process; T_c is the time required to complete the tamping process; T_{af} is the total actuating time of cylinders to complete the adjusting process; T_{mf} is the total actuating time of cylinders to complete the motion process; T_{uf} is the total actuating time of cylinders to complete the dumping process; T_{cf} is the actuating time of cylinders to complete tamping once; T_r is the time gap in the actions of the cylinders to complete mechanized processes, that is, the human response time; n is the number of tampings completed by the tamping mechanism in one cycle; n_a, n_m, n_u, and n_c are numbers of connections between cylinder actions to complete the adjusting, moving, dumping, and tamping processes, respectively; and λ is the intelligence index; the higher the index is, the higher the intelligence level.

For the entire working face, the complete work cycle time of the working face is affected by many factors such as the working face length, coal seam mining height, shearer cutting depth, and the number of supports for parallel operations. For a single hydraulic support, different mining parameters of the working face will lead to changes in the time for the hydraulic support to execute the step actions. The larger the shearer cutting depth, the longer the moving support step takes. The greater the mining thickness, the longer the unloading and tamping steps take. For the entire working face, the longer the working face length, the more hydraulic supports there are, and the longer the complete work cycle time. In addition, given the complexity of underground mining conditions, the actuating time of cylinders in any single hydraulic support varies in the same working face. The speed of cylinder action is related to the oil pump pressure and the number of cylinders operating simultaneously in unit time. Therefore, when using the above formulas for calculation, the mining parameters of the working face and the structural parameters of the hydraulic supports need to be considered.

During the field measurement at the Xingdong Mine, the actuating time of a four-column, four-bar linkage backfilling mining hydraulic support was averaged. The results were used for a quantitative analysis of the actuating time of the cylinders and the time gaps between cylinder actions. The action sequence of the cylinders is optimized. The time sequence of the actions of all cylinders in a complete process cycle for a single support is designed, as shown in Figure 5.

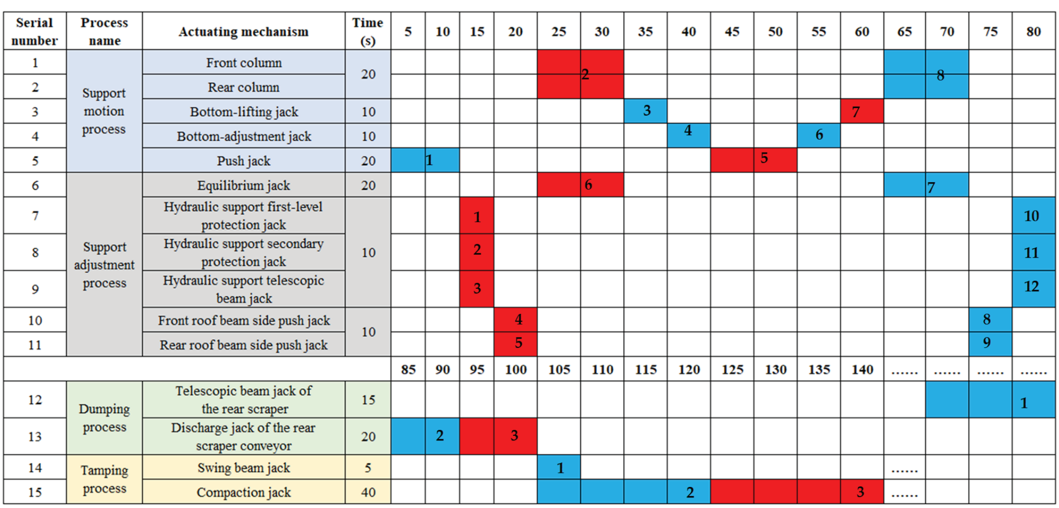

Figure 5. Time sequence of all actions of the cylinders involved in a complete hydraulic support movement–discharge–filling cycle for a single support.

In Figure 5, the different colors of rectangles in the same row represent that the movement directions of the corresponding columns or jacks are different.

It can be seen from Figure 5 that the total actuation time T_{mf} of the cylinders involved in the support motion process is 60 s; the number n_a of connections between cylinder actions is 8. The total actuation time T_{af} of the cylinders involved in the support adjustment process is 40 s; the number n_m of connections between cylinder actions is 12. The total actuating time T_{uf} of the cylinders in the dumping process is 35 s, and the number n_u of connections between cylinder actions is 3. For the dumping process, the tamping mechanism should execute the tamping actions n times to achieve a satisfactory effect. The actuation time T_{cf} of the cylinder for each tamping is 45 s. For this process, the number n_c of connections between cylinder actions is 3, the total time of the tamping process is 45 times n s, and the number of connections between cylinder actions is 3 times n.

From the system of Equation (1), the time required to complete a mining and backfilling cycle for a single solid filling support in mechanized operation is derived as follows:

$$T_S = 175 + 31T_r + (45 + 3T_r) \cdot n \tag{2}$$

The time required to complete a mining and backfilling cycle for a single solid filling support in automated operation is given by Formula (3):

$$T_S = 175 + 31\frac{T_r}{\lambda} + (45 + 3\frac{T_r}{\lambda}) \cdot n \tag{3}$$

In theory, the intelligent solid backfilling process does not require human participation. That is, at λ = +∞, the time gap between cylinder actions approaches 0 s. Hence, the time required to complete a mining and backfilling cycle for intelligent operation is given by Formula (4):

$$T_S = 175 + 45n \tag{4}$$

It can be deduced from Formulas (2)–(4) that the time required to complete an intelligent operation cycle for single support is only directly proportional to the number of tampings. However, for mechanized and automated operations, the time to complete an operation cycle for single support is directly proportional to the time gaps between cylinder actions and the number of tampings. We then optimize the time sequence of cylinder actions so that the cylinders can operate in parallel, reducing the number of tampings and improving the intelligence level of the supports. This way, one can reduce the time required to complete a mining and backfilling cycle.

4. SPL between Different Steps of Intelligent Mining and Backfilling Operations for the Whole Face

4.1. Division of Sequential Actions of the Intelligent Backfilling Operation for the Whole Face

The overall cycling operation time of the backfilling working face includes the cycling time of coal mining and backfilling operations. The coal mining by the coal shearer can be considered as a continuous operation. The time it takes is relatively short compared with the hydraulic support motion process, hydraulic support adjusting process, dumping process, and tamping process. Therefore, the cutting depth and mining height of the coal shearer have little impact on the sequential operation time of the solid backfilling working face. However, the length of the working face is the main factor affecting the cycling operation time. It determines the advance length that can be achieved daily. According to the working face length and the cycling operation time of the backfilling process, three shifts of production (18 h) are usually arranged per day with one shift for maintenance (6 h) or two shifts for production (16 h), with one shift for maintenance (8 h). Therefore, the maximum shutdown time, i.e., maintenance time, of the backfilling working face per day is 6–8 h. The daily advance length that can be achieved is mainly determined by the cycling time of the backfilling process.

For the whole backfilling working face, the optimal operation implies achieving parallel, autonomous execution of the mining and filling processes through the shearer, scraper conveyor, hydraulic supports, and perforated bottom discharge scraper conveyor. For this purpose, one should ensure that the equipment and mechanisms executing different mining and filling processes do not interfere with each other and fulfill specified functions in a spatially and temporally organized manner. The spatial sequence refers to an appropriate spatial alternation of processes executed by different equipment at different frame positions in the working face. Temporal sequence refers to the chronological order of specific processes involving different mechanisms within a specific frame, which are organized temporally to complete the mining and backfilling operations. Based on the above principles, this study designed the cyclic parallel mining and backfilling operations in the fully mechanized mining face, as shown in Figure 6.

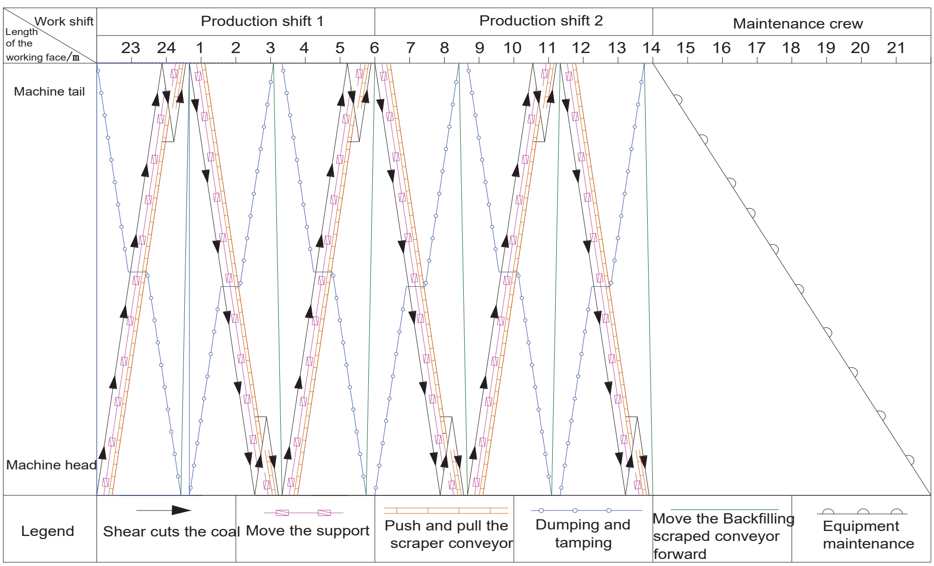

Figure 6. Illustration of the cyclic parallel mining and backfilling operations in the intelligent backfilling face.

It is easy to see that the operation cycle is divided into distinct stages. Representative time points demarcating different stages are chosen as the benchmarks for analysis: 23:52 (end-oblique cutting knife stage), 00:14 (cutting triangular coal stage), 00:32 (end-brake bottom coal-cleaning stage), and 01:13 (central coal-cutting stage). Over the longitudinal section of the working face, we can divide the mining and intelligent solid backfilling operation cycle into four distinct stages. Thus, we obtain the relationship between the spatial positions of the equipment executing the corresponding processes at different stages, as shown in Figure 7.

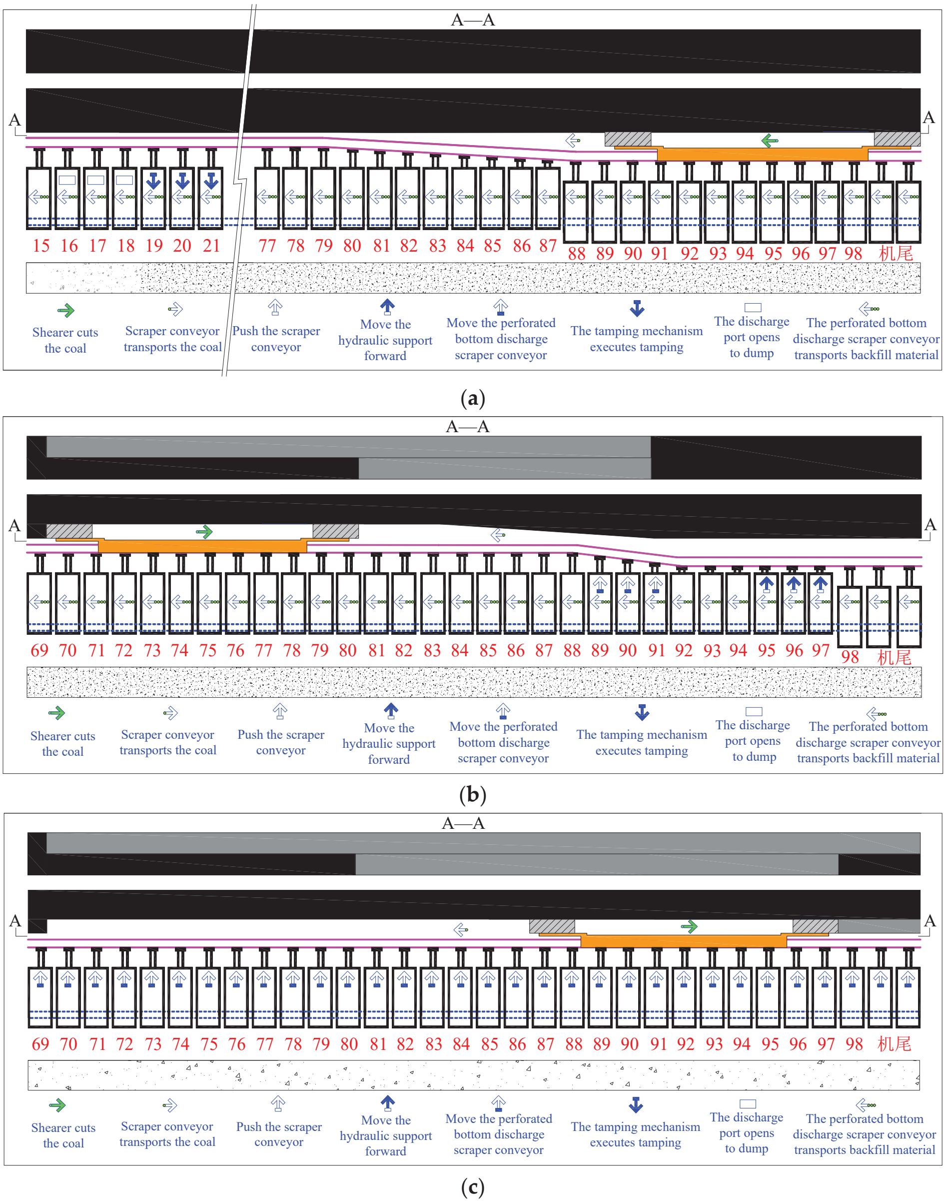

Figure 7. *Cont.*

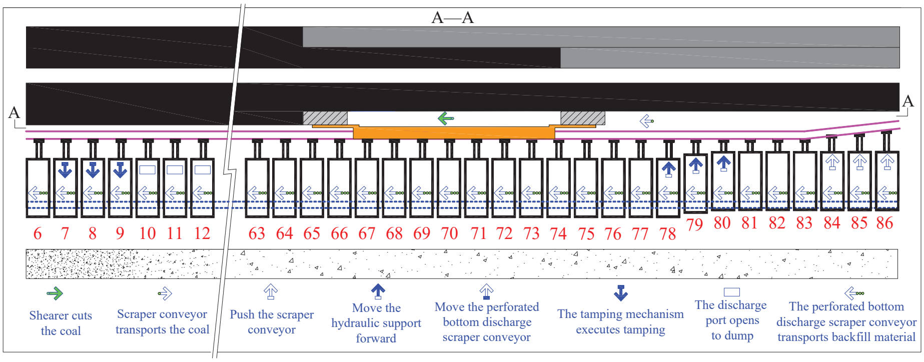

(**d**)

Figure 7. Relationship between spatial positions of the mining and backfilling equipment executing corresponding processes at different stages in the working face, (**a**) end-oblique cutting knife stage, (**b**) cutting triangular coal stage, (**c**) cutting residual triangular coal at the bottom, (**d**) central coal-cutting.

(1) End-oblique cutting knife stage: When the shearer moves to the end of the working face, the hydraulic support behind it follows the shearer and moves to the position of the rear drum. The scraper conveyor follows accordingly, and a curved segment for oblique knife-cutting is formed at the end. The shearer moves reversely, obliquely cutting the coal bodies ahead via the curved segment. As the end-oblique cutting knife stage is completed, the backfilling operation is orderly. The perforated bottom discharge scraper conveyor dumps the backfill material in groups, followed by tamping by the tamping mechanism.
(2) Cutting triangular coal stage: Following the end-oblique cutting knife stage, the supports, located from the end of the working face to the position of oblique knife cutting, push the scraper conveyor forward to form a straight line. The shearer moves in the reverse direction, cutting the triangular coal left by oblique knife cutting. The backfilling operation is conducted in an orderly manner. The perforated bottom discharge scraper conveyor dumps the backfill material in groups, followed by tamping by the tamping mechanism.
(3) End-brake bottom coal cleaning: After the shearer returns to cut triangular coals, the front drum drops down, cutting the triangular residual coal equal in length and height to the shearer's body. The backfilling operation is conducted in an orderly manner. The perforated bottom discharge scraper conveyor dumps the backfill material in groups, followed by tamping by the tamping mechanism.
(4) Central coal-cutting stage: The front drum of the shearer is lifted to cut the coal bodies in the reverse direction. The hydraulic supports behind the shearer follow, and the scraper conveyor is pushed accordingly. The backfilling operation is conducted in an orderly manner. The perforated bottom discharge scraper conveyor dumps the backfill material in groups, followed by tamping by the tamping mechanism.

4.2. Theoretical Analysis of the Time of Cyclic Backfilling Operation for the Whole Face

The total time of cyclic operation in the whole face is the sum of the time required to complete the cycle for all supports. Since several supports can operate in parallel, the total time for the cyclic operation in the working face can be estimated as follows:

$$\begin{cases} T_w = \frac{L}{NA}(T_s + T_R) \\ T_R = 3T_r \end{cases} \quad (5)$$

where T_w is the total time of cyclic operation in the whole face; L is the length of the working face; N is the number of supports in parallel operation; A is the distance between support centers; and T_R is the time gap between supports.

The time required for a complete operation cycle for mechanized solid backfilling can be assessed from Formulas (2) and (5), yielding Equation (6), while that for automated solid backfilling is obtained from Equations (3) and (5), yielding Equation (7):

$$T_w = \frac{L}{NA}[175 + 34T_r + (45 + 3T_r) \cdot n] \tag{6}$$

$$T_w = \frac{L}{NA}\left[175 + 34\frac{T_r}{\lambda} + (45 + 3\frac{T_r}{\lambda}) \cdot n\right] \tag{7}$$

For intelligent solid backfilling, the time gap T_r in cylinder actions approaches zero, and the time gap T_R for supports also approaches 0 s. Combining Formulas (4) and (5), we estimate the time required for a complete operation cycle for intelligent solid backfilling, as given by Formula (8):

$$T_w = \frac{L}{NA}(175 + 45n) \tag{8}$$

If the length of the working face and the distance between support centers are fixed, the time required for a complete cycle of automated solid backfilling is directly proportional to the time gap in cylinder actions and the number of tampings. It is inversely proportional to the number of parallel operations and intelligence level supports. For intelligent solid backfilling, the time required to complete an operation cycle is irrelevant to the time gap in cylinder actions but directly proportional to the number of tampings and inversely proportional to the number of supports in parallel operation.

5. Analysis of Key Factors Influencing the Cyclic Operation Time

For the time for cyclic operation for intelligent solid backfilling, the influencing factors include geological conditions, working face layout, filling equipment and processes used, backfill material, and intelligence level.

When the integrity of the roof strata in the working face is poor or causes the rear beam of the SBMHS to rotate and sink, and the caving of roof rocks into the goaf reduces the space available for backfilling operations, it will lead to increased interference between the tamping mechanism and the backfilling scraper conveyor, resulting in an increased number of connections for the tamping cylinder. In addition, an uneven roof will increase the time for the hydraulic support adjusting process [30].

With the constant geological conditions, working face layout, and filling equipment, we can shorten the time of the operation cycle by upgrading the intelligence level and optimizing the processes. We change the parameters of the filling technology to analyze the influence of upgrading the intelligence level and optimizing the processes on the backfilling efficiency. The filling process parameters include the following: time gap in cylinder actions, number of tampings, number of supports in parallel operation, and intelligence index.

Univariate analysis was performed, and the values of the parameters were preset as follows: length of the working face of 58 m, distance between support centers of 1.5 m, number of supports of 39, and time gap in cylinder actions of 5.0 s; the number of tampings required to achieve a satisfactory filling effect was 10; the number of supports in parallel operation was 3; and the intelligence indices of the mechanized, automated, and intelligent operations were 1, 2, and ∞, respectively.

5.1. Time Gaps in Cylinder Actions

The actuation time of the cylinder is related to the pump pressure. The greater the pressure, the faster the cylinder expansion and the shorter the actuation time of the cylinder. Under a given pressure, the time required for a complete operation cycle can be reduced by minimizing the time gap in cylinder actions. The relationship between the two is plotted in Figure 8.

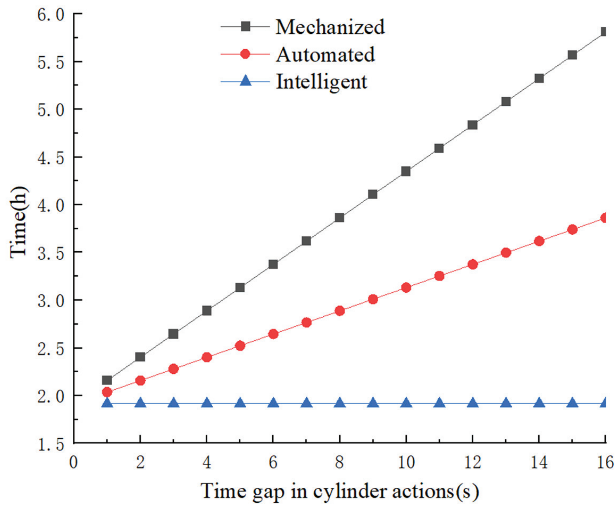

Figure 8. Relationship between the time of cyclic operation and time gap in cylinder actions.

It can be seen in Figure 8 that for mechanized and automated solid backfilling operations, the time of cyclic operation is directly proportional to the time gap in cylinder actions. However, for intelligent operation, the time gap in cylinder actions approaches zero. When the time gap in cylinder actions is 5 s, the times of cyclic operation for mechanized, automated, and intelligent solid backfilling technologies are 3.13, 2.52, and 1.92 h, respectively. Compared with mechanized backfilling, the backfilling efficiency of automated and intelligent operations is improved by 19% and 39%, respectively.

5.2. Number of Tampings

The number of tampings has a significant impact on the backfilling efficiency. However, if the number of tampings is low and the total time required for completing one intelligent operation cycle is short, one has to improve the cohesiveness of the backfill material to meet the requirements for the compaction ratio. The relationship between the time of cyclic operation and the number of tampings is plotted in Figure 9.

As shown in Figure 8, the time of cyclic operation was directly proportional to the number of tampings for all three backfilling operations. When the number of tampings is 5, the times of cyclic operation for mechanized, automated, and intelligent solid backfilling technologies are 2.15 h, 1.67 h, and 1.20 h, respectively. Compared with mechanized filling, the backfilling efficiency of automated and intelligent operations is improved by 22% and 44%, respectively.

5.3. Number of Supports in Parallel Operation

The higher the number of supports in parallel operation per unit time and the higher the number of cylinders in simultaneous operation, the shorter the time of cyclic operation. Intelligent solid backfilling technology can optimize the action sequences of cylinders and single supports and increase the number of supports in parallel operation. The relationship between the time of the cyclic backfilling operation and the number of supports in parallel operation is plotted in Figure 10.

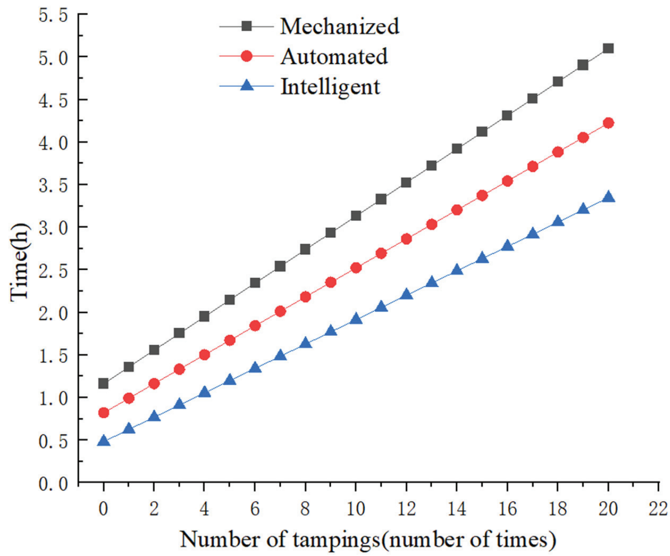

Figure 9. Relationship between the time of cyclic operation and the number of tamping.

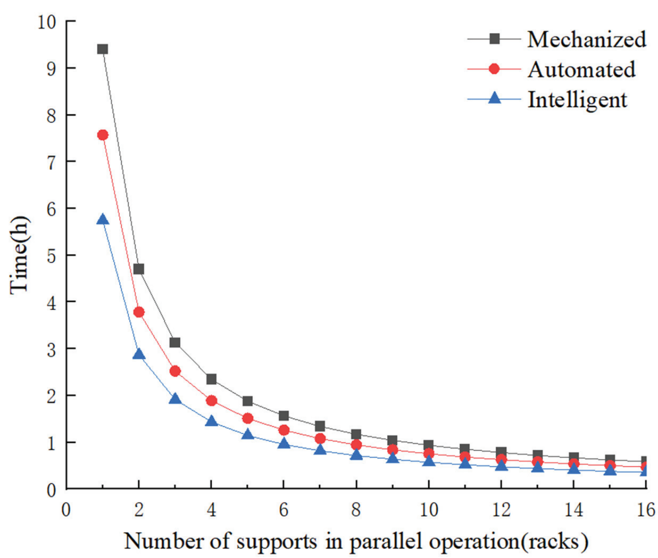

Figure 10. Relationship between the time of the cyclic backfilling operation and the number of supports in parallel operation.

It can be seen in Figure 9 that the time of cyclic operation in the three backfilling techniques is hyperbolically related to the number of supports in parallel operation. When the number of supports in parallel operation is 4, the times of cyclic operation in the three backfilling techniques are 2.35, 1.89, and 1.43 h, respectively. Compared with mechanized filling, the backfilling efficiency of automated and intelligent operations is improved by 20% and 39%, respectively.

5.4. Degree of Intelligence

The higher the intelligence level, the less human participation in observation, decision-making, and manipulation; therefore, the shorter the time gaps in actions of cylinders and supports. In addition, all actions are regulated by the intelligent control of the master computer throughout the operations. The execution of actions is controlled by the hydraulic support electrohydraulic control system, thereby reducing the number of workers required at the working face and improving the overall efficiency. For the above reasons, the time of cyclic operation is the shortest for intelligent solid backfilling. The relationship between the time of cyclic operation and the intelligence index is plotted in Figure 11.

It can be deduced from Figure 11 that the time of cyclic operation in mechanized and intelligent solid backfilling technologies is irrelevant to the intelligence index. However, the time of cyclic operation in automated solid backfilling technology is inversely proportional to the intelligence index. At an intelligence index of 4, the times of cyclic operation for mechanized, automated, and intelligent solid backfilling technologies are 3.13, 2.22, and 1.92 h, respectively. Compared with mechanized filling, the backfilling efficiency of automated and intelligent operations is improved by 32% and 39%, respectively.

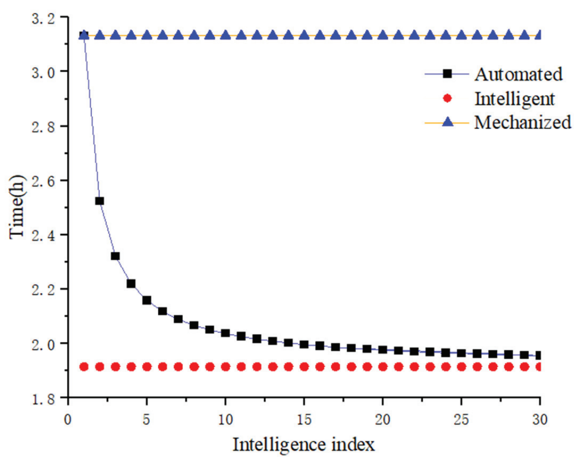

Figure 11. Relationship between the time of cyclic operation and the intelligence index.

6. Efficiency Analysis of Intelligent Solid Backfilling Mining

6.1. An Overview of the Case Study's Filling Working Face

A case study was performed for the #11233 filling working face of Xingdong Mine, China, operated by Jizhong Energy Resources Co., Ltd. In the case study, the average dip angle of the #2 coal seam under exploitation in the #11233 filling working face was 8° and the bulk density was 14.8 KN/m^3. The old roof was composed of fine sandstone with an average thickness of 6.8 m. The direct roof comprised sandy mudstone with an average thickness of 3.9 m. The direct floor was siltstone with an average thickness of 0.6 m. The working face was 58 m long, with a mining height of 4.4 m. The distance between support centers was 1.5 m. A total of 39 hydraulic supports were involved, and the step length of advance was 0.7 m. The time gap in cylinder actions was 5.0 s. A satisfactory filling effect was achieved with ten tampings, three supports used in parallel operation, and the intelligence index of 1.

6.2. Backfilling Efficiency Analysis and Optimization Plan

6.2.1. Efficiency Analysis

In Figure 12, the time of cyclic operation with ten tampings for mechanized solid backfilling was treated as the benchmark. Next, we studied the variations in backfilling efficiency for this working face under different numbers of tampings for different mining technologies. As the number of tampings increased, the backfilling efficiency dropped linearly for all three backfilling techniques.

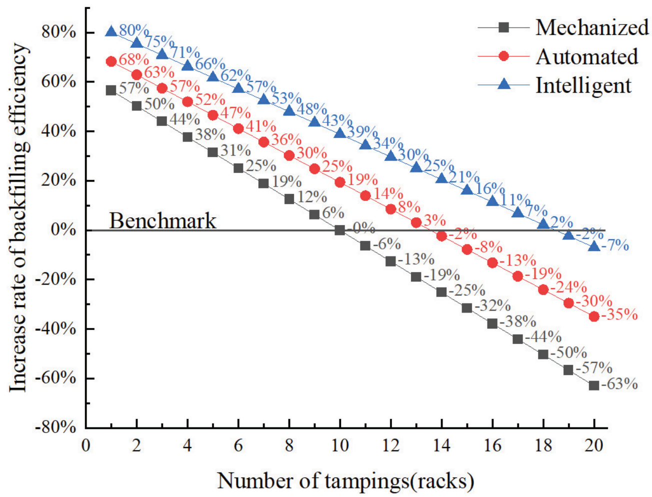

Figure 12. Variation of backfilling efficiency in the three mining technologies under different numbers of tamping.

Compared with mechanized solid backfilling, the backfilling efficiency of the intelligent and automated solid backfilling technologies with ten tampings increased by 39% and 19%, respectively, while those with three tampings increased by 71% and 57%, respectively. As seen in Figure 10, when the number of tampings was reduced from ten to three, the backfilling efficiency of mechanized solid backfilling increased by 44%.

The number of underground workers, time of cyclic operation for single support, time of cyclic operation for the whole face, and backfilling efficiency of the three solid backfilling technologies are compared and summarized in Table 2.

Table 2. Comparison of different parameters of the three technologies under study.

Type / Technology	Mechanized	Automated	Intelligent
Number of workers required for each shift (workers)	20–30	15–20	7–10
Time of cyclic operation for a single support (min)	20–35	10–20	5–10
Time of cyclic operation for the whole face (h)	3.5–5.0	2.0–3.5	1.0–2.0
Backfilling efficiency	Moderate	Improve efficiency by 20%	Improve efficiency by 40–80%
Interference and adjustment	Manual	Manual	Automated
Electrohydraulic control system	No	Yes	Yes
Intelligent system	No	No	Yes

6.2.2. Recommended Actions for Optimizing the Backfilling Efficiency

According to the performed analysis of Figure 11 and Table 2, reducing the number of tampings drastically improves the backfilling efficiency. The backfilling material used in working face #11233 is underground sorted gangue, which sources from various coal mining working faces. After sorting, its particle size becomes below 200 mm. The particle size gradation still needs to be optimized. We recommend the following measures to improve the backfilling efficiency: change the mix ratio of the backfill material, improve the material's cohesiveness, increase the natural angle of repose, and reduce the number of tampings.

The second direction is intelligent upgrade and transformation, which is underway in the case study site. Before the intelligence upgrade, workers were involved in many operation steps in the #11233 filling working face. The backfilling efficiency was greatly improved through intelligence upgrading and by increasing the number of supports in parallel while reducing the time gaps in the actions of cylinders and supports.

7. Conclusions

The results obtained in this study made it possible to draw the following conclusions:

(1) Based on the spatiotemporal linkage (SPL) of the mining and backfilling operations for single supports, the operations were divided into four processes involving cylinder actions for single support: support motion, support adjusting, dumping, and tamping. Theoretical formulas for calculating the actuation time of single support in the three solid backfilling technologies were derived and further validated via a case study.

(2) The SPL of different mining and backfilling processes in the whole face for intelligent parallel operations was studied. The intelligent solid backfilling operation for the whole face was subdivided into four distinct stages. We further presented the theoretical formula for estimating the time of cyclic operation for the whole face in the three mining technologies.

(3) The influence of key factors on the time of cyclic operation of three backfilling techniques was analyzed. It is concluded that the time of cyclic operation is positively correlated with the time gap between hydraulic cylinder actions and the number of tampings; it is hyperbolically correlated with the number of supports in parallel operation and the intelligence index. Moreover, reducing the number of tampings, increasing the number of supports in parallel operation, and the intelligence index can significantly improve the backfilling efficiency.

(4) A case study was performed for the #11233 filling working face of Xingdong Mine, China, operated by Jizhong Energy Resources Co., Ltd. Keeping other parameters unchanged, by adopting the optimized method of grain diameter grading of backfilling materials to reduce the number of tampings to 3 times and increasing the number of parallel supports to 4, with the intelligence index being 1, the backfilling efficiency can be increased by 39%. The improvement of backfilling efficiency is the most significant. It has great significance for improving production capacity, reducing staff, and improving efficiency and safety of the backfilling working face.

Author Contributions: Conceptualization and methodology, T.Z., G.Z. and Q.Z.; software and validation, Y.H., H.L. and J.C.; resources and data curation, K.Y., H.L. and Y.W.; writing—original draft preparation, T.Z.; writing review and editing, Q.Z., G.Z. and K.Y.; supervision and funding acquisition, Q.Z. All authors have read and agreed to the published version of the manuscript.

Funding: This work was supported by the National Natural Science Foundation of China (Grant No.52174134), the Fundamental Research Funds for the Central Universities (Project No. 2021GJZPY12), Funded by the Graduate Innovation Program of China University of Mining and Technology (Project No.2023WLJCRCZL036), Funded by the Postgraduate Research and Practice Innovation Program of Jiangsu Province (Project No. KYCX23_2807).

Institutional Review Board Statement: Not applicable.

Informed Consent Statement: Not applicable.

Data Availability Statement: The data presented in this study are available upon request from the corresponding author. The data are not publicly available. The key data used in this study represent field measurement statistics of a ZC5160/30/50-type solid backfilling mining hydraulic support from the Xingdong Coal Mine, and the related data are displayed in the text in Figure 5. The data contain detailed technical parameters of this type of support, and obtaining them again would infringe upon the rights and interests of Xingdong Mine and the factory that manufactures the hydraulic supports. In addition, the other data are all derived from the previously mentioned statistics and theoretical formulas.

Acknowledgments: Thanks to Henan Guoxing Technology Co., Ltd., and the Xingdong coal mine for the parameters of the backfilling hydraulic support.

Conflicts of Interest: Gaolei Zhu was employed by the Anhui RONDS Technology Co., Ltd. The remaining authors declare that the research was conducted in the absence of any commercial or financial relationships that could be construed as a potential conflict of interest.

References

1. Skrzypkowski, K. Comparative Analysis of the Mining Cribs Models Filled with Gangue. *Energies* **2020**, *13*, 5290. [CrossRef]
2. Skrzypkowski, K. Decreasing Mining Losses for the Room and Pillar Method by Replacing the Inter-Room Pillars by the Construction of Wooden Cribs Filled with Waste Rocks. *Energies* **2020**, *13*, 3564. [CrossRef]
3. Bo, L.; Yang, S.; Liu, Y.; Zhang, Z.; Wang, Y.; Wang, Y. Coal Mine Solid Waste Backfill Process in China: Current Status and Challenges. *Sustainability* **2023**, *15*, 13489. [CrossRef]
4. Hu, B.; Liu, P.; Cui, F.; Wang, H. Review and development status of backfill coal mining technology in China. *Coal Sci. Technol.* **2020**, *48*, 39–47. [CrossRef]
5. Chang, Q.; Chen, J.; Zhou, H.; Bai, J. Implementation of Paste Backfill Mining Technology in Chinese Coal Mines. *Sci. World J.* **2014**, *8*, 2014. [CrossRef]
6. Qing, D.; Wang, X. Study on rapid filling material and key technology of paste in coal mine. *Coal Chem. Ind.* **2015**, *38*, 6–8. [CrossRef]
7. Dong, P.; Kou, X.; Li, X.; Zhang, Y. Modification of Filling Automation System Based on PLC Control. *Min. Technol.* **2021**, *21*, 187–190. [CrossRef]
8. Shi, Y. Design of a Filling Automation System Based on DCS Control Technology. *Min. Technol.* **2021**, *21*, 150–154. [CrossRef]
9. Zhang, J.; Tu, S.; Cao, Y. Theory and technique of greening mining integrating mining, separating and backfilling in deep coal resources. *J. China Coal Soc.* **2018**, *43*, 377–389. [CrossRef]
10. Tu, S.; Hao, D.; Miao, K.; Liu, X.; Li, W. Research of synergetic mining for mining, dressing and backfilling integrated deep mines with complicated systems. *J. China Univ. Min. Technol.* **2021**, *50*, 431–441. [CrossRef]
11. Zhang, J.; Li, J.; An, T.; Huang, Y. Deformation characteristic of key stratum overburden by raw waste backfilling with fully-mechanized coal mining technology. *J. China Coal Soc.* **2010**, *35*, 357–360. [CrossRef]
12. Yao, B. Application of gangue filling process and the study of surface rock shift deformation. *Coal Chem. Ind.* **2021**, *44*, 31–33. [CrossRef]
13. Gao, W.; Zhang, M. Research on following automation technology of hydraulic support on fully-mechanized coal mining face. *J. Mine Autom.* **2018**, *44*, 14–17. [CrossRef]
14. Liu, Q.; Han, X.; Xu, L.; Qing, W. Cooperative control technology of shear and hydraulic support on fully-mechanized coal mining face. *J. Mine Autom.* **2020**, *46*, 43–48. [CrossRef]
15. Shi, Y.; Jiang, L.; Cui, Z.; Yan, X. Mathematical model of automatic following control in the middle of fully-mechanized mining face. *J. Mine Autom.* **2016**, *42*, 14–19. [CrossRef]
16. Liu, F.; Cao, W.; Zhang, J.M. Progress of scientific and technological innovation in my country's coal industry and the development direction of the "14th Five-Year Plan". *Coal J.* **2021**, *46*, 1–15. [CrossRef]
17. Liu, J.; Zhao, L.; Bi, J.; Xie, G. Research and application on automatic control of comprehensive mechanized solid backfill coal mining. *Coal Sci. Technol.* **2016**, *44*, 149–156. [CrossRef]
18. Wang, G.; Ren, H.; Peng, Y. Research and engineering progress of coal mine intelligent (primary stage) technology system. *Coal Sci. Technol.* **2020**, *48*, 1–27. [CrossRef]
19. Wang, G.; Du, Y.; Ren, H. Research and practice of top-level design of intelligent coal mines. *Chin. J. Coal* **2020**, *45*, 1909–1924. [CrossRef]
20. Huang, Z.; Wang, F.; Zhang, S. Research on the architecture and key technologies of intelligent coal mining system. *Chin. J. Coal* **2020**, *45*, 1959–1972. [CrossRef]
21. Present situation and prospect of coal gangue treatment technology. *J. Min. Saf. Eng.* **2020**, *37*, 136–146. [CrossRef]
22. Wang, Y.; Shi, Y.; Wang, Y.Y.; Qi, M.; Wang, H. Full pose measurement and virtual simulation of solid filling hydraulic support. *J. Mine Autom.* **2022**, *48*, 81–89. [CrossRef]
23. Zuo, X. Solid Intelligent Filling Method and Engineering Case Analysis in Coal Mine. Master's Thesis, China University of Mining & Technology, Xuzhou, China, 2021. [CrossRef]
24. Ren, H.; Li, S.; Zhao, G.; Zhang, K.; Du, M.; Zhou, J. Measurement method of support height and roof beam posture angles for working face hydraulic support based on depth vision. *J. Min. Saf. Eng.* **2022**, *39*, 72–81. [CrossRef]
25. Zhang, H. Autonomous Identification of Working Conditions and Forms of Key Equipment for Solid Intelligent Filling and Control Methods. Master's Thesis, China University of Mining & Technology, Xuzhou, China, 2022. [CrossRef]

26. Ralston, J.C.; Hargrave, C.O.; Dunn, M.T. Longwall automation: Trends, challenges and opportunities. *Int. J. Min. Sci. Technol.* **2017**, *27*, 733–739. [CrossRef]
27. Ralston, J.C.; Reid, D.C.; Dunn, M.T.; Hainsworth, D.W. Longwall automation: Delivering enabling technology to achieve safer and more productive underground mining. *Int. J. Min. Sci. Technol.* **2015**, *25*, 865–876. [CrossRef]
28. Guo, G.; Feng, W.; Zha, J.; Liu, Y.X.; Wang, Q. Subsidence control and farmland conservation by solid backfilling mining technology. *Trans. Nonferrous Met. Soc. China* **2011**, *21*, 665–669. [CrossRef]
29. Zhang, Q.; Zhang, J.; Guo, S.; Gao, R.; Li, W. Design and application of solid, dense backfill advanced mining technology with two pre-driving entries. *Int. J. Min. Sci. Technol.* **2015**, *1*, 127–132. [CrossRef]
30. Zong, T.; Zhang, Q.; Shi, P.; Wang, Y.; Li, F.; Chang, T. Critical characterization of solid-filled hydraulic support mechanism interference and autonomous demodulation method. *Coal Sci. Technol.* **2023**, *2051*, 260–270. [CrossRef]

applied sciences

Article

Autonomous Process Execution Control Algorithms of Solid Intelligent Backfilling Technology: Development and Numerical Testing

Tingcheng Zong [1,2], Fengming Li [1,2], Qiang Zhang [1,2,*], Zhongliang Sun [3] and Haonan Lv [1,2]

[1] School of Mines, China University of Mining & Technology, Xuzhou 221116, China; ts21020078a31@cumt.edu.cn (T.Z.); lifengming8005@163.com (F.L.); ts22020048a31@cumt.edu.cn (H.L.)
[2] State Key Laboratory of Coal Resources and Safe Mining, China University of Mining & Technology, Xuzhou 221116, China
[3] Chengdu Sense Time Technology Company Limited, Chengdu 610213, China; 18339167680@163.com
* Correspondence: leafkky@163.com

Abstract: This paper analyzes the typical technical problems arising from dumping and tamping collision interferences in the working faces of conventional mechanized solid backfilling mining (SBM). Additionally, the technical and consecutive characteristics of the solid intelligent backfilling (SIB) method, the execution device, and the corresponding process categories of the SIB process are analyzed. A design for an SIB process flow is presented. Critical algorithms, including automatic recognition and optimization planning based on the cost function and laying the algorithm foundation, are proposed to develop a backfilling process control system. A joint simulation test system is built on a MATLAB/Simulink simulation toolkit (MSST) to simulate and test the optimized algorithms. The results show that the optimized algorithm can realize the automatic optimization planning and automatic interference-recognition adjustment of the backfilling process under actual engineering conditions. In conclusion, this paper analyzes typical technical problems in the conventional backfilling process, designs the SIB process flow, and develops key algorithms to achieve the automatic control of the backfilling process.

Keywords: solid intelligent backfilling; joint simulation; interference recognition

Citation: Zong, T.; Li, F.; Zhang, Q.; Sun, Z.; Lv, H. Autonomous Process Execution Control Algorithms of Solid Intelligent Backfilling Technology: Development and Numerical Testing. *Appl. Sci.* **2023**, *13*, 11704. https://doi.org/10.3390/app132111704

Academic Editors: Jianhang Chen, Krzysztof Skrzypkowski, René Gómez, Fhatuwani Sengani, Derek B. Apel and Faham Tahmasebinia

Received: 19 September 2023
Revised: 19 October 2023
Accepted: 20 October 2023
Published: 26 October 2023

1. Introduction

With the state's active promotion of intelligent coal mine construction [1,2] and the development of intelligent mines [3,4], the intelligent advancement of backfilling mining technology was also in full swing [5,6], and intelligence was the prevalent direction of future backfilling mining development.

The existing backfilling methods, such as tailings and cemented backfilling, based on industrial pumps and the pipeline transportation of cementitious materials, achieved a significant development in intelligent research and initially achieved intelligent control of the backfilling material, key parameters, and core processes [7,8]. However, the SBM method was based on the collaborative control of backfilling hydraulic support and a perforated bottom discharge scraper conveyor, and the difficulty lay in the high number of key parameters and intricate core procedure. Despite the application of electrohydraulic control technology in mechanical devices, full autonomy in the mining and backfilling processes was yet to be achieved. Consequently, intelligent research currently mainly focuses on device and process improvements, and the degree of its intelligence is gradually increasing with the development of technology.

In the research of intelligent mining's internal logic and operation mode, the research team of Wang et al. [9–11] designed a set of coal mine top-level system frameworks based on integrating intelligent management and control. Huang [12] constructed a logical architecture centered on the "sensing, decision-making, execution and operation and maintenance" quadrants that could preliminarily realize the demand for intelligent and automatic mining. In the research on simulating intelligent mining devices, Liu et al. [13] proposed a method for establishing a digital twin model of equipment at a fully mechanized mining face. The study also conducted a simulation analysis of the fully mechanized mining process. Wang et al. [14] designed a virtual simulation system for solid backfilling hydraulic support (SBHS) based on Unity3D. The system utilized Unity3D to simulate the motion of the support. Yuan et al. [15] used MATLAB software (https://ww2.mathworks.cn/en/products/matlab.html (accessed on 10 October 2023)) to perform a kinematic simulation of a shielded hydraulic support. In terms of hydraulic support control algorithm development and testing, Tian et al. [16] combined BP neural network algorithms with PID control algorithms to achieve an online adjustment of PID parameters, improving the response speed and control accuracy of the hydraulic cylinders. Meng et al. [17] designed and built an emulsion/pure-water hydraulic cylinder precision push experiment platform that could complete eccentric loads, lateral loads, and other experiments on hydraulic cylinders, providing an experimental platform for the precise control of hydraulic cylinders and the coordinated control of hydraulic cylinder clusters.

The abovementioned literature mainly focuses on the automation and intelligence of fully mechanized mining equipment, while the research on the automation and intelligence of SBM technology is still limited and needs further investigation.

This paper analyzes the key links of the conventional mechanized backfilling process, clarifies the process organization requirements of the SIB working face, and designs the autonomous execution process of the coal mine SIB process flow. Based on the motion and positional constraint relationships between hydraulic support mechanisms, it develops algorithms for machine interference identification and tamping path planning to design an SIB process flow. It builds an SIB model simulation testing system to test and preliminarily validate the reliability of the algorithms.

2. Design for Solid Intelligent Backfilling Mining Process

2.1. Issues in the Execution of Dumping and Tamping Process

Backfilling technology can be divided into two stages: dumping and tamping. Firstly, the working face is filled to complete the front part of the coal cutting. The coal scraper conveyor is then pushed, followed by moving the frame and pushing the back part of the perforated bottom discharge scraper conveyor. The working face is filled straight at this point, and the backfilling technology can be executed. There are two typical kinds of pose interferences in the process [18]; one is dumping interference, which occurs when the tamping device is buried during the unloading of backfilling material from the middle slot of an open skylight in the dumping process, as shown in Figure 1.

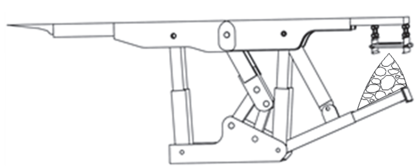

Figure 1. Dumping process interference.

The other one is collision interference, where the tamping device collides with the perforated bottom discharge scraper conveyor during the tamping process, as shown in Figure 2.

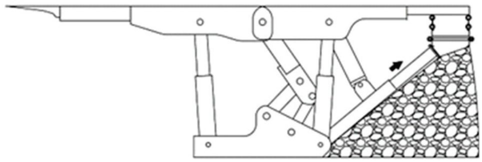

Figure 2. Tamping process interference.

2.2. The Solution for the Interference of Dumping and Tamping Processes

From the abovementioned analysis, it is evident that achieving the automatic control of fully mechanized coal mining solid backfilling technology is challenging due to the problems of dumping and collision interferences. Therefore, there is an urgent need to develop SIB technology with interference prediction and the automatic adjustment of the mechanism's movement. Before performing the tamping process, it must be ensured that there is a suitable dumping clearance distance between the tamping device of the SBHS and the perforated bottom discharge scraper conveyor to ensure that the backfilling materials fall into the backfilling space. During the tamping process, it must be ensured that the SBHS tamping device is properly positioned concerning the perforated bottom discharge scraper conveyor during the movement of the tamping device. Therefore, it is essential to develop an "interference-recognition algorithm" [19,20] to achieve the abovementioned function. By analyzing the relationship between the dumping and tamping processes, an SIB process flow without human intervention was designed, as shown in Figure 3.

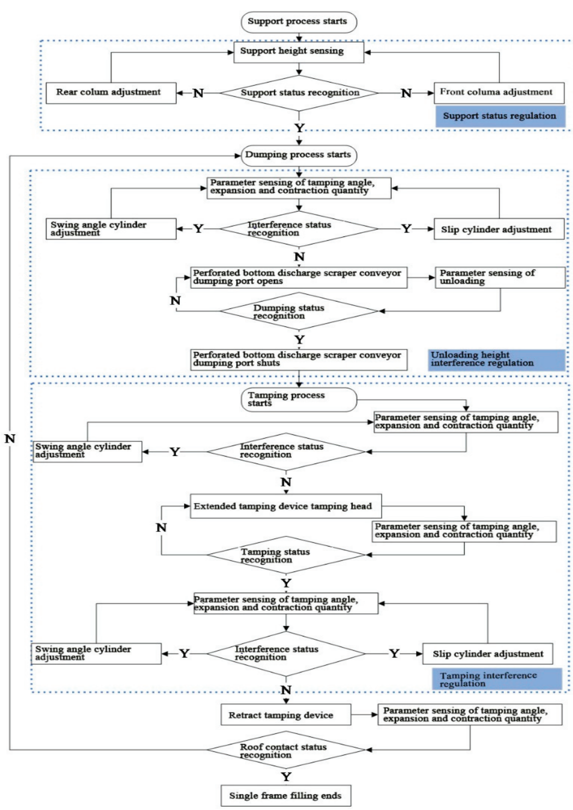

Figure 3. Solid intelligent backfilling process flow.

3. Interference Automatic Recognition and Tamping Path Planning

3.1. Interference Criticality Solving and Interference Automatic-Recognition Method

The SBHS tamping device is a two-degree-of-freedom structure [21], a rotating pair between the base and tamping device, and a moving pair between the primary and secondary tamping devices. A coordinate system was established to obtain the transformation relationship between the tamping device's head coordinates, tamping angle, and tamping path, as shown in Figure 4.

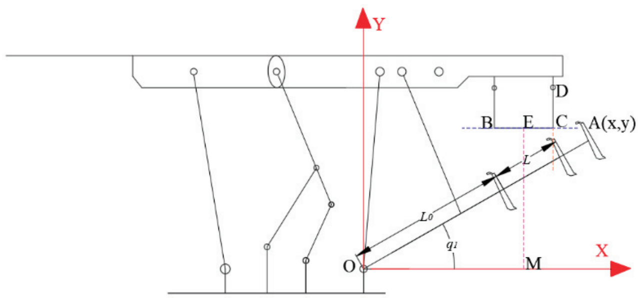

Figure 4. Interference critical analysis.

In Figure 4, BC and DC represent the bottom and rear boundaries of the perforated bottom discharge scraper conveyor, respectively; EM is the centerline of the dumping port of the perforated bottom discharge scraper conveyor [22,23]; L_0 is the unextruded length of the tamping device, mm; L is the tapping path, mm; q_1 is the tamping angle, °; $A(x,y)$ is the tamping head path function; x is the abscissa of the tamping head; y is the ordinate of the tamping head.

The kinematic equation establishment of the tamping device is as follows:

$$\begin{cases} x = L \cdot \cos(q_1) \\ y = L \cdot \sin(q_1) \\ L = L + L_0 \end{cases} \tag{1}$$

It is evident that to prevent any dumping interference in the dumping process, the tamping head coordinate must be positioned to the left of the EM straight-line portion before commencing the dumping. Therefore, the left side of the EM straight-line portion can be defined as the dumping non-interference area.

Similarly, during the execution of the tamping process, to prevent the collision interference between the tamping device and the bottom of the perforated bottom discharge scraper conveyor when the tamping device extends, it is only necessary to ensure that the tamping head coordinate is beneath the BC straight-line portion. When retracting the tamping device, it is necessary to ensure that the tamping head ordinate is smaller than the BC straight-line ordinate to avoid collision interference between the tamping device and the rear side of the multi-space perforated bottom discharge scraper conveyor, especially when the tamping head abscissa is higher than or close to the CD straight-line abscissa. For this reason, the area where the BC straight line rotates around point C to CD can be defined as the tamping non-interference area. Based on the abovementioned principles, an SIB process interference automatic recognition and regulation algorithm was designed, as shown in Figure 5.

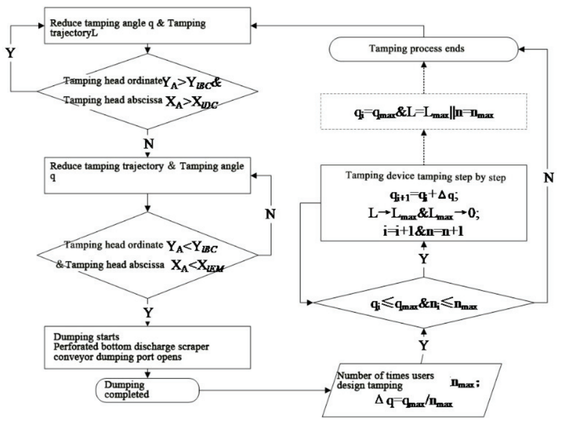

Figure 5. Automatic recognition and regulation algorithm of SIB process interference.

In Figure 5, L is the tamping path, mm; q is the tapping angle, °; Y_A is the ordinate value of the tamping head; X_A is the abscissa value of the tamping head; Y_{lBC} is the ordinate value of the BC straight-line portion; X_{lDC} is the abscissa value of the straight-line DC; X_{lEM} is the abscissa value of the EM straight-line portion; Δq is the increment of the cyclic tamping angle adjustment, °; L_{max} is the maximum tamping path, mm; $n_{\max}$ is the maximum number of cycles required for user-defined and designed tamping processes; and q_i is the tamping angle of the *i*-th tamping, °.

The left part of Figure 5 displays the automatic recognition and regulation algorithm of the dumping process, while the right part shows the automatic recognition and regulation algorithm of the tamping process. In the SIB process, the dumping and tamping processes form a loop.

In addition, it is necessary to calculate the conversion relationship between the tamping head coordinate A(x,y), tamping angle q_1, and tamping path L for the tamping device, which mainly involves a swing angle cylinder and tamping cylinder, and where the driving parameters are the tamping angle and tamping path, as shown below:

$$\begin{cases} q_1 = -2 \cdot \arctan\left(\frac{x-\sqrt{x^2+y^2}}{y}\right) \\ L_0 = \sqrt{x^2+y^2} - L \end{cases} \tag{2}$$

3.2. Automatic Control of the Tamping Device Hydraulic Cylinder

(1) Construction of the hydraulic drive physical model for the tamping device.

For example, a hydraulic drive physical model was established for the tamping device cylinder. As the main driving component, the hydraulic cylinder mainly involved hydraulic pressure F_y and its corresponding hydraulic pump station, relating to hydraulic pressure P. The hydraulic drive model ensured a stable hydraulic pressure provided by the hydraulic pump station and controlled the tamping angle and path, as well as the stability of its angular and linear velocities, through the internal oil pressure F_y of the cylinder. The analysis process is as follows:

$$F_y = m_y a_y + B v_y \tag{3}$$

where B is the damping coefficient; v_y is the velocity of the cylinder motion; a_y is the cylinder motion acceleration; m_y is the payload quality of the cylinder; and F_y is the internal liquid pressure of the cylinder.

$$\begin{aligned} \dot{x}_1 &= a_y \\ x_1 &= v_y \\ \dot{x}_2 &= x_1 \\ F_y &= U \end{aligned} \tag{4}$$

Therefore:

$$U = m\dot{x} + Bx \tag{5}$$

The equivalent equation has the following form:

$$\begin{aligned} \dot{x}_1 &= -\tfrac{B}{m}x_1 + \tfrac{U}{m} \\ \dot{x}_2 &= x_1 \end{aligned} \tag{6}$$

where x_1, x_2, and U are the conversion variables.

(2) Algorithm for automatic control of hydraulic cylinder position and motion.

To guarantee the stable and efficient navigation of the tamping device past obstacles towards its desired position, we used the common one (PID) control algorithm to build a PID closed-loop negative feedback controller for the position/motion control of the hydraulic cylinder, and the PID algorithm contained proportional, integral, and derivative parts. In the real control process, achieving the anticipated control effect involved continuous adjustments to the ratio coefficient K_p, integral time constant K_i, and differential time constant K_d parameters. The control principle diagram is shown in Figure 6 [24].

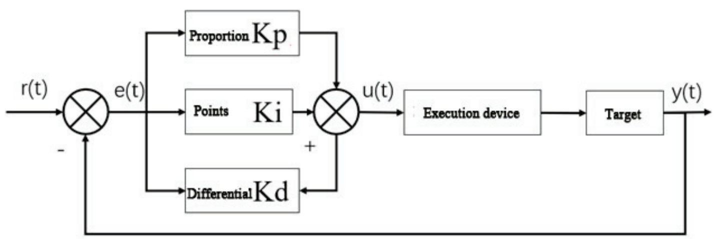

Figure 6. PID control system schematic diagram.

In Figure 6, $e(t)$ is the deviation between the input and output values, where $r(t)$ in $e(t) = y(t) - r(t)$ is the input value, $y(t)$ is the output value, t is the time interval between the start of the adjustment and the output of the current control quantity, and $y(t)$ is the input control signal at the moment when the PID starts adjusting. The adjustment process is a fixed value.

The hydraulic-cylinder-drive physical and PID control models were run using the MATLAB platform. Following a period of closed-loop control, the tamping angular velocity, angular acceleration, linear velocity, and linear acceleration of the tamping path of the tamping device all entered a stable state. The debugging results are shown in Figure 7.

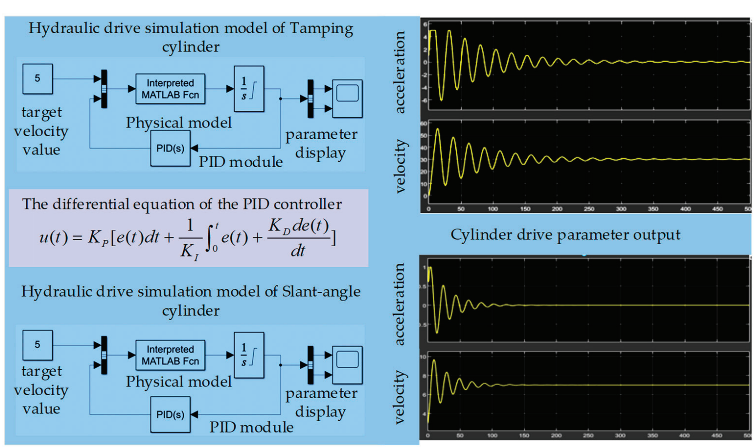

Figure 7. Hydraulic drive simulation model diagram.

3.3. Automatic Optimization Path Planning of the Tamping Device

During the movement of the tamping device, the tamping angle q_1 and tamping path L were functions of time t. By discretizing them, the point where the unit angle line intersected with the unit elongation line was determined as the movable position of the tamping device, and the path points within the movable range of the tamping device were obtained. The connection point between points was the movable path of the tamping device [25,26], forming the theoretical workspace lattice of the tamping device, as shown in Figure 8.

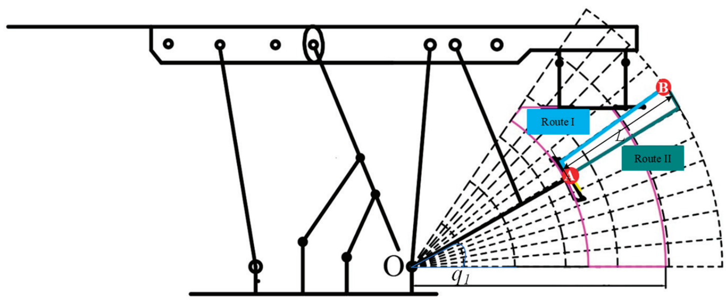

Figure 8. Movable path analysis diagram of the tamping device.

For a certain target location, the motion path of the tamping device included multiple paths. To achieve the automatic optimization planning of the tamping device path, the cost function was used to calculate the corresponding costs of multiple movable paths, and the optimal path selection was achieved by minimizing the cost. The cost function considers interference avoidance, angle adjustment, and elongation (path) adjustment.

$$F(i) = Z * \{w_q F(q) + w_L F(L)\} \tag{7}$$

where i is the alternative path label; $F(i)$ is the cost function; the Z value (0 or 1) indicates whether there are obstacles or not, respectively; $F(q)$ is the angle adjustment cost; $F(L)$ is the elongation (path) adjustment cost; w_q is the angle adjustment weight; and w_L is the path adjustment weight.

The value of Z was only 0 or 1, indicating whether there were obstacles or not. If there were obstacles, it was 0, indicating that the path cost was 0 and not selected. The weight was designed based on the actual impact of the working environment on the hydraulic adjustment. Due to the on-site data showing a higher cost of the angle adjustment, the angle adjustment weight exceeded the path adjustment weight.

For example, as shown in Figure 8, the tamping device has multiple paths to choose from, such as Paths I and II, from the current position A to the target position B in the movable paths set. From Equation (7), it is evident that both paths have the same costs as angle adjustments. Path I had a pose interference, Z = 0, and this path was discarded; Path II had no interference, Z = 1, and Path II was selected.

Based on the cost function principle, an automatic optimization planning of the tamping device motion path was achieved. Combined with the backfilling process interference automatic recognition and regulation algorithm previously constructed, as well as the control algorithm of the hydraulic cylinder, an intelligent control system of the backfilling operation movement was formed.

4. Establishment of the Simulation Test System and Design of Testing Methods

4.1. Design of the Simulation Test System Architecture

To guarantee the efficacy of simulation testing, the simulation test system was designed with three major functions: mechanical assembly and motion simulation, electrohydraulic control system simulation, and process action automatic-execution algorithm simulation. The system architecture is shown in Figure 9.

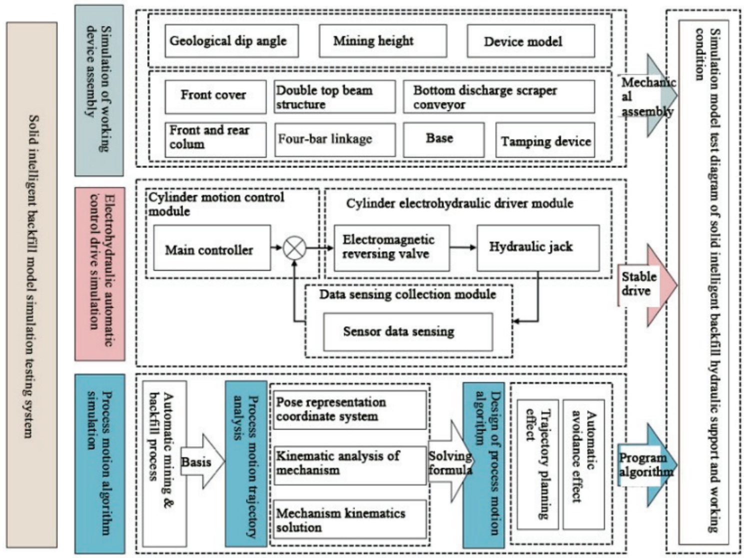

Figure 9. Architecture diagram of SIB process motion simulation testing system.

In Figure 9, the mechanical assembly and motion simulation function is achieved using SolidWorks to model, assemble, and provide a 3D motion simulation of the SBHS. It can perform a mechanical assembly and motion simulation of key mechanisms, which is the foundation of the entire simulation testing system. The simulation system of the hydraulic cylinder electrohydraulic control system was implemented through the MATLAB platform, which could analyze and simulate the driving process of the hydraulic cylinder, ensure the stability of the hydraulic cylinder speed, and ensure the effectiveness of the process action automatic-execution algorithm testing. The process action automatic-execution algorithm simulation function was implemented through the joint simulation of MSST and SolidWorks [27,28]. Based on the SIBPF, the process action automatic-execution algorithm was designed, mainly including the interference automatic-recognition and path automatic-planning algorithms.

4.2. Establishment of the Simulation Test System

(1) Three-dimensional model construction.

The SBHS model was assembled from key structures, such as a perforated bottom discharge scraper conveyor and tamping device, as shown in Figure 10.

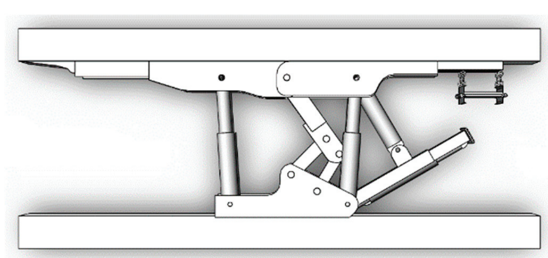

Figure 10. Assembly drawing of the support mechanical model.

The Simscape Multibody Link plugin can automatically convert the 3D geometric solid model established by SolidWorks into a SimMechanics model [29], as shown in Figure 11.

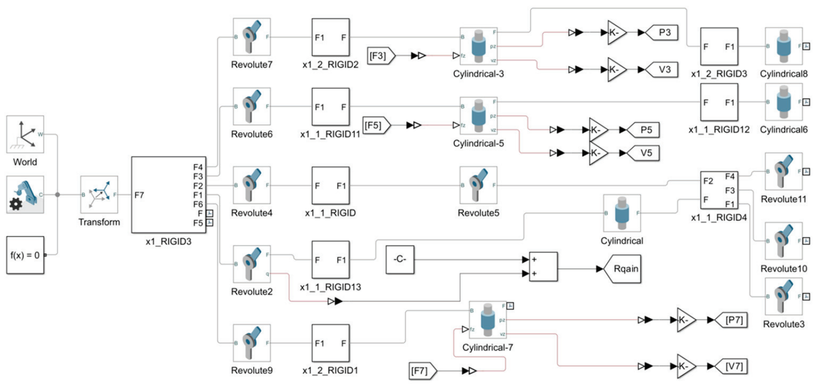

Figure 11. Backfilling hydraulic support SimMechanics model.

(2) Key parameter collection.

To achieve a simulation of the backfilling process, it was first necessary to implement the control of the backfilling hydraulic support model. Therefore, it was necessary to collect the paths of each hydraulic cylinder in the backfilling hydraulic support in real time. For example, the support process required obtaining the front and rear column paths to grasp the front top beam's support height and inclination angle. Key parameters, such as the expansion and contraction quantities of the perforated bottom discharge scraper conveyor, tamping path, tamping angle, and tamping pressure must be obtained in both the unloading and tamping processes. Correspondingly, the distance, angle, and pressure sensors were used, and those sensors were set in the model to monitor the positions [30], as shown in Table 1.

Table 1. Monitoring parameter settings and sensor arrangement for the backfilling hydraulic support model.

No.	Parameter Type	Sensor Type	Installation Position
1	Front column path ΔL_f	Range sensor	Front-column hinge joint A
2	Rear column path ΔL_h	Range sensor	Rear-column hinge joint B
3	Front top-beam height H_B	Range sensor	Front top-beam hinge joint C
4	Expansion and contraction quantities of perforated bottom discharge scraper conveyor ΔL_s	Range sensor	Scraper and jack hinge joint D
5	Tamping pressure F_N	Pressure sensor	Tamping head junction E
6	Tamping path L_0	Range sensor	Tamping head junction F
7	Tamping angle q_1	Angle sensor	Tamping-device hinge joint G

The installation location and model's data collected by the sensor on the model are illustrated in Figure 12.

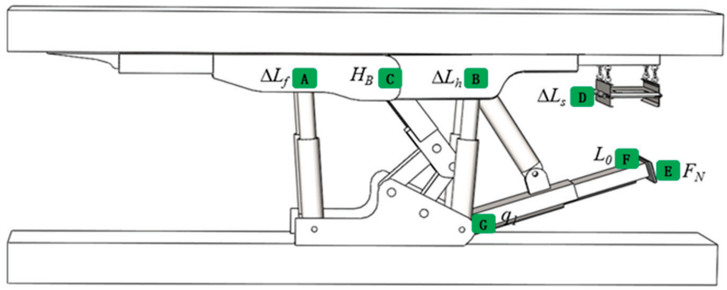

Figure 12. Installation design drawing of model sensor.

(3) Cylinder electrohydraulic drive function.

The expansion and contraction of each hydraulic cylinder in the backfilling hydraulic support were controlled by an electromagnetic directional valve. The electromagnetic directional valve belonged to a switch valve and its extension/retraction state corresponded to the extension and retraction states of the hydraulic cylinder. The opening time corresponded to a certain number of extension and retraction paths of the hydraulic cylinder. The reversing valve and corresponding cylinder settings in the model are shown in Figure 13.

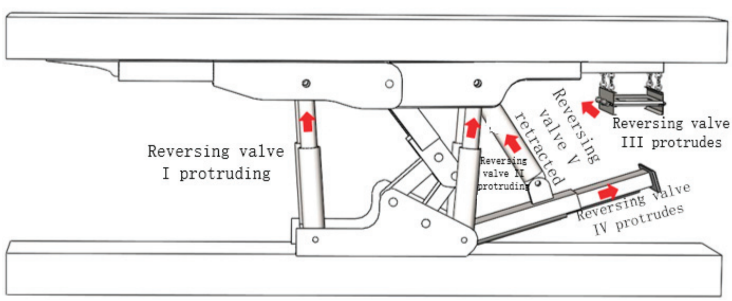

Figure 13. Model reversing-valve cylinder configuration design diagram.

Among them, the support process controlled the path of the front and rear columns by controlling the extension/contraction states of reversing valves I and II. The unloading process controlled the dumping cylinder of the perforated bottom discharge scraper conveyor by controlling the extension/contraction states of reversing valve III, thereby simulating the control of the unloading volume. The tamping process controlled the compaction and swing-angle cylinder paths by controlling the extension/contraction states of reversing valves IV and V, thereby achieving the control of the tamping head path, which was the main control object for the interference automatic-recognition and the path automatic-planning algorithms.

(4) Establishment of SolidWorks and (MSST) joint-simulation testing system.

The joint simulation testing system is shown in Figure 14. The key steps for the system setup are as follows:

(i) Build a PID hydraulic drive model for each hydraulic cylinder in the backfilling hydraulic support on the MSST and connect it to the motion joints in the SimMechanics model to serve as a controller for hydraulic cylinder actions.

(ii) Using the MSST, write the SIB process interference automatic recognition and regulation algorithm and the tamping path automatic-planning algorithm into the MATLAB-Function module and construct the process action automatic-execution algorithm module based on the SIBPF previously designed.

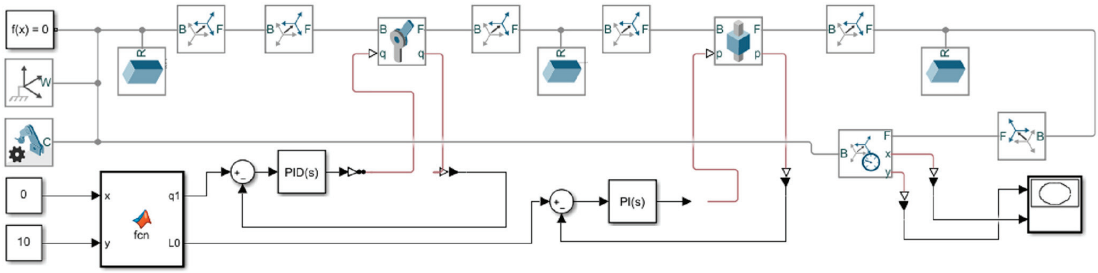

Figure 14. Joint-simulation testing system of SolidWorks and MATLAB/Simulink.

(iii) Use the constant module to set each hydraulic cylinder's target positions, i.e., operating parameters, in the backfilling hydraulic support. When executing the internal interference automatic-recognition and tamping path automatic-planning algorithms in the module, the tamping angle q1 and tamping path L obtained from the algorithm will be transmitted to the PID control module of the hydraulic drive simulation model, thereby controlling the movement of the tamping device.

(iv) Finally, the coordinate transformation sensor was used to output the motion path data of the tamping device, and the process motion path of the tamping head in the absolute coordinate system was displayed in the SBHS model built by SolidWorks.

4.3. Design of the Simulation Testing Plan and Process Simulation

Based on the simulation testing system previously established, different simulation testing schemes could be achieved by setting and adjusting the operating parameters, such as the support inclination angle and height; the initial states of driving parameters, such as the tamping angle, tamping path, and column path; as well as the target position of the tamping device motion.

This study simulated the support, dumping, and tamping processes using the column, swing-angle cylinder, and tamping cylinder path as the driving parameters. Before the start of the support process, the initial value of the support height was 2980 mm, the target position was 3550 mm, and the simulation path was A_1-A_2. Before starting the tamping process, the initial value of the tamping angle was 9° and the initial value of the tamping path was 600 mm. By setting the target position points of the tamping process to C_2 and C_5, the tamping device was controlled by the interface automatic-recognition and tamping path automatic-planning algorithm modules, also known as the process action automatic-execution algorithm module, and the simulation path was C_1-C_2-C_3-C_4-C_5. After the tamping process was completed, resetting the tamping device to the initial position before the dumping process started to prepare for the next dumping and tamping cycles was necessary. Before the dumping process started, the initial position of the tamping device was C_5, the target position point of the tamping device in the dumping process was C_8, and the simulation path was C_5-C_6-C_7-C_8. The abovementioned simulation results are shown in Figure 15.

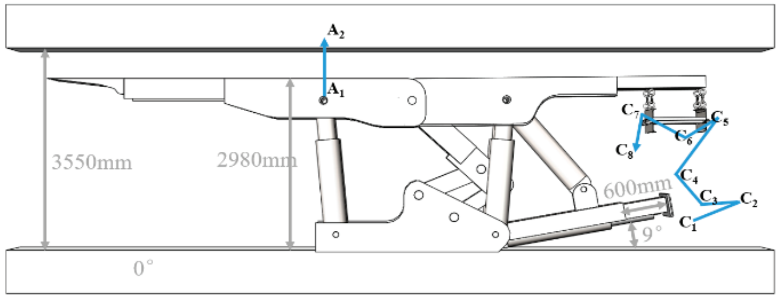

Figure 15. Simulation model test diagram of the SIB hydraulic support.

From Figure 15, it can be seen that the motion path of the tamping device does not reach the optimal path. During the movement process, there was a collision interference with the perforated bottom discharge scraper conveyor. For the C_5-C_6 and C_6-C_8 segments, the optimal action sequence should first reduce the tamping path and then increase the tamping angle to avoid collision interference. As shown in Figure 5, when the tamping angle reaches the maximum value, it needs to be further increased to trigger the tamping end process, which initiates the dumping interference-recognition part. This process might cause instability in the tamping device motion, leading to interference. Therefore, it was necessary to improve the process action automatic-execution algorithm module. The optimization of the algorithm is shown in the dashed box in Figure 5. The tamping device tamping angle and tamping path reaching the maximum value were used as discriminant markers for the end of the tamping, thus avoiding the abovementioned problems.

5. Engineering Cases

5.1. Overview of the Working Face and Process of the Solid Intelligent Backfilling

The SIB mining face of a particular coal mine in Xingtai taken as the case study was located in the first level-2# coal seams mining area, with an average thickness of 4.4 m and an average inclination angle of 8° for the coal seams. The old top was gray–white fine sandstone with a thickness of 5–8.5 m, and the direct top was dark-gray sandy mudstone with a 1.49–6 m thickness. The direct floor was black siltstone with a thickness of 0.40–1 m and the old bottom was gray, medium-grained sandstone with a 3–4.83 m thickness. The working face coal seams had a stable thickness and simple structure. The coal seams had a strike of 92–131°, a dip of 2–41°, an inclination angle of 3–12°, and a hardness coefficient of 0.62.

By analyzing the key geological parameters, such as the average thickness of the SIB mining-face coal seams, the average inclination angle of the coal seams, the mining length, and the recoverable reserves of the abovementioned mine in Xingtai, the respective parameters of the SIB mining working face were used, as listed in Table 2.

Table 2. SIB mining working face parameters.

Working Face Name	Working Face Length/m	Mining Distance/m	Mining Height/m	Average Inclination Angle/°	Recoverable Reserves/10,000 t
1#	58	633	4.4	8	21.6
2#	58	880	4.6	12	31.5
3#	58	730	4.5	11	25.5

The SIB mining face of the case study coal mine had abandoned the comprehensive mechanized backfilling technology of operating SBM devices with the staff as the core for full mining-height tamping.

The SIB technology of this working face comprised a sensing process, recognition process, pose adjustment and support processes, unloading process, and tamping process. The key SIB technology included operation movement, execution mechanism, and corresponding process categories, as shown in Table 3.

Table 3. Mining and backfilling process table for the SIB mining method.

No.	Device Name	Operation Movement	Execution Device	Process Category
1	Backfilling hydraulic support	Roof guard Moving frame, lifting frame Sensing of parameters, such as support height Pose interference recognition	Cylinder guard Cylinder bottom, column Sensing element Recognition module	Support process Support process Sensing process Recognition process
2	Tamping device	Tapping angle change Sensing of parameters, such as sampling angle Pose interference demodulation	Tamping cylinder Slant-angle cylinder Sensing element Tamping cylinder, slant-angle cylinder, etc.	Tamping process Tamping process Sensing process Pose adjustment process
3	Perforated bottom discharge conveyor	Material transportation Dumping port switch Body position slip Sensing parameters, such as dumping height Pose interference demodulation	Scraper chain Dumping cylinder Slip cylinder Sensing element Dumping cylinder, Slip cylinder	Unloading process Unloading process Unloading process Sensing process Pose adjustment process

After designing the SIB technology, various sensors were used to obtain the backfilling hydraulic support status and pose information. The optimized process action automatic-execution algorithm module controlled the execution of the support cyclone action. It controlled the electrohydraulic control system to execute the cylinder action without the need for coal-mining machine shutdown or human intervention, saving the continuation time of the cylinder action, reducing personnel, increasing efficiency, and ensuring a safe production.

5.2. Model Operating-Condition Parameter Setting and Simulation Testing Scheme Design

An SIB technology testing model was built based on the SIB model simulation testing system, combined with the mining geological conditions and filling equipment parameters of the SIB working face for the case-study coal mine. The pre- and post-improvement process action automatic-execution algorithm modules were used for the simulation testing to compare the improvement effect of the process action automatic-execution algorithm.

According to the test model design in Table 4, the SBHS's inclination angle was set at 8°, the mining height was set at 4400 mm, and the equipment model was a four-column backfilling hydraulic support. In the initial state, the device assembly simulation model had a sampling angle of 6°, a sampling path of 400 mm, and front and rear column paths of 620 mm were used as the carrier, while the front and rear columns, slant -angle cylinder, and tamping cylinder were used as the drivers. The A_1–A_2 path of the support process and C_1-C_2-C_3-C_4-C_5-C_6-C_7-C_8-C_9 of the tamping process were run for the simulation testing, as shown in Figure 16.

Table 4. SIB working-face test model design information.

Design Object		**Key Design Information**		
Assembly design	Working environment	Inclination angle/°	Mining height/mm	Device model
		8	4400	Four-column type
	Initial state	Tamping angle/°	Tamping path/mm	Column path/mm
		7	60	3000
Drive design	Drive cylinder	Front and rear columns		Slant-angle cylinder, tamping cylinder
	Key parameters	Front and rear column paths		Tamping angle, tamping path
Process plan	Process category	Support process		Tamping process
	Motion path	A_1-A_2		C_1-C_2-C_3-C_4-C_5-C_6-C_7-C_8-C_9

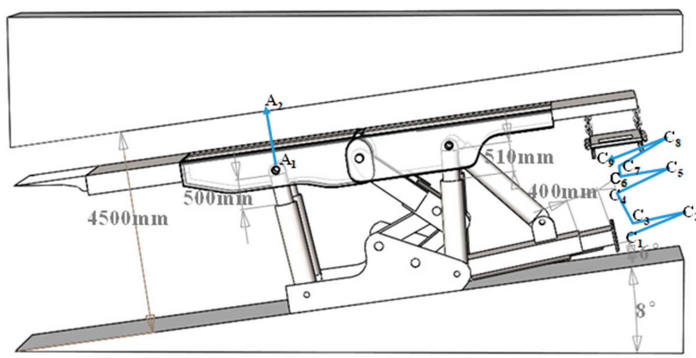

Figure 16. SIB process testing model diagram.

5.3. *Quantitative Analysis of the Test Results*

The motion path of the tamping device of the SBHS in the simulation testing model is shown in Figure 16. The model sensor module was used to output and analyze the path curve during the simulation process.

The variations of the tamping device of the SBHS tamping angle and path under the control of two algorithms during the process simulation are shown in Figure 17.

From Figure 17a,b, it can be seen that the response time of the old process action automatic-execution algorithm for controlling the tamping angle and tamping path is 32 s. The optimized process action automatic-execution algorithm for controlling the timing tamping angle and tamping path has a response time of 30 s, which improves the efficiency by 7%. In both cases, the tamping angle and path reach the target position C_1–C_9 with a small amplitude difference and do not result in pose interference.

The column path variations in the process simulation under the control of two algorithms are shown in Figure 18.

Figure 18 shows that, during the 2.0 s operation of the column, a pose interference g_1 occurs in the optimized process action automatic-execution algorithm. The optimized process action automatic-execution algorithm successfully conducts interference recognition s_1 and autonomously regulates b_1. The regulation is successful at around 3.2 s, and the columns overlap with the ideal state to achieve automatic avoidance. It reaches the target position A_2 of the process in 3.5 s.

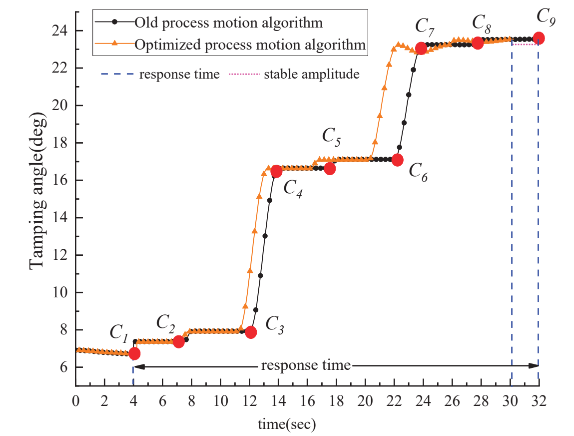

(**a**) Variation chart of tamping device tamping angle.

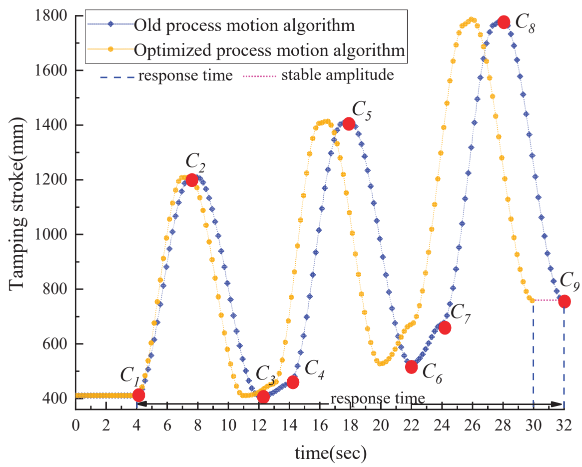

(**b**) Variation chart of tamping device tamping path.

Figure 17. Comparison of control effects of different algorithms on the tamping device.

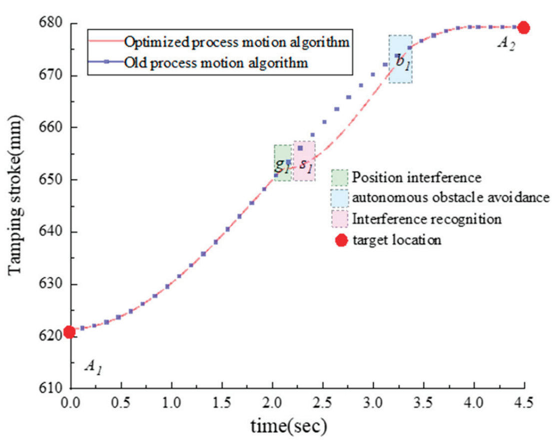

Figure 18. Comparison of control effects of different algorithms on the column.

The motion path of the tamping device under the control of two algorithms during the process simulation is shown in Figure 19.

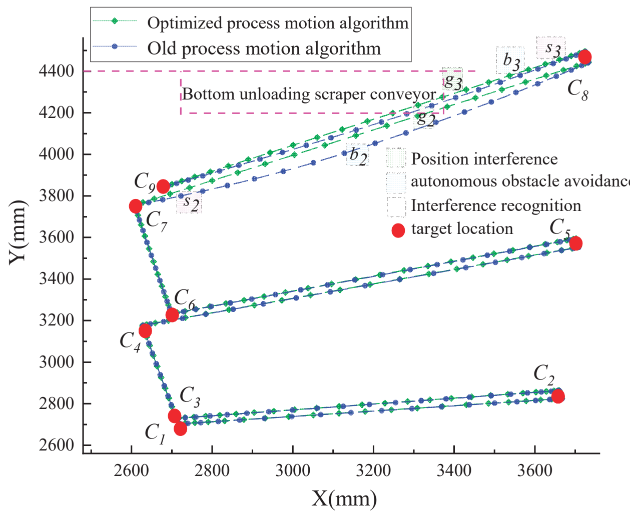

Figure 19. Motion path diagram under different algorithm controls.

Figure 19 shows no abnormalities in the C_1–C_7 process. In C_7–C_8 and C_8–C_9, the tamping device and the perforated bottom discharge scraper conveyor collide. The interference-recognition algorithm identifies s_2 and s_3 values, automatically avoiding b_2 and b_3. However, automatic avoidance b_3 still has a slight collision interference due to the low-accuracy control.

6. Conclusions

(1) This study investigated the dumping interference and tamping collision interference problems in a conventional mechanical solid backfilling working face. It designed the SIB process flow to mitigate these problems, providing a theoretical basis for realizing the intelligent control of the solid backfilling process.

(2) Crucial algorithms were proposed for the automatic interference recognition and planning the motion path of the tamping mechanism in an SIB process, including the interference automatic-recognition algorithm and automatic optimization planning algorithm based on the cost function, laying the algorithm foundation for the development of a backfilling process control system.

(3) A joint-simulation test system was built on the MSST to run and validate the optimized algorithms. The results show that the optimized algorithm can efficiently realize the automatic optimization planning and automatic interference-recognition adjustment of the backfilling process under actual engineering conditions.

Author Contributions: Conceptualization and methodology, T.Z. and Q.Z.; software and validation, T.Z., F.L. and Z.S.; formal analysis, H.L.; investigation, F.L.; resources, Z.S.; data curation, H.L. and F.L.; writing—original draft preparation, T.Z.; writing—review and editing, Q.Z.; visualization, Q.Z.; supervision, Q.Z.; project administration, T.Z.; funding acquisition, Q.Z. All authors have read and agreed to the published version of the manuscript.

Funding: The work was supported by the National Natural Science Foundation of China (Grant No. 52174134), the Fundamental Research Funds for the Central Universities (Project No. 2021GJZPY12), Funded by the Graduate Innovation Program of China University of Mining and Technology (Project No.2023WLJCRCZL036), Funded by the Postgraduate Research & Practice Innovation Program of Jiangsu Province (Project No. KYCX23_2807).

Institutional Review Board Statement: Not applicable.

Informed Consent Statement: Not applicable.

Data Availability Statement: The data presented in this study are available on request from the corresponding author.

Conflicts of Interest: The authors declare no conflict of interest.

References

1. He, M.; Wang, Q.; Wu, Q. The future of mining: Thinking about the construction of intelligent 5G N00 mines. *China Coal* **2020**, *46*, 1–9.
2. Wang, G.; Zhao, G.; Ren, H. Analysis on the key core technologies of smart coal mine and intelligent mining. *J. Coal* **2019**, *44*, 34–41. [CrossRef]
3. Fan, J.; Li, C.; Yan, Z. The overall architecture and core scenarios of intelligent coal mines integrating 5G technology ecology. *J. Coal Sci.* **2020**, *45*, 1949–1958. [CrossRef]
4. Zhang, F.; Ge, S.; Li, C. Research summary on digital twin technology for smart mines. *Coal Sci. Technol.* **2020**, *7*, 168–176. [CrossRef]
5. Zhang, Q.; Zhang, J.; Wu, Z.; Chen, Y. Overview of Solid Backfilling Technology Based on Coal-Waste Underground Separation in China. *Sustainability* **2019**, *11*, 2118. [CrossRef]
6. Bo, L.; Yang, S.; Liu, Y.; Zhang, Z.; Wang, Y.; Wang, Y. Coal Mine Solid Waste Backfill Process in China: Current Status and Challenges. *Sustainability* **2023**, *15*, 13489. [CrossRef]
7. Hu, Y.; Li, K.; Zhang, B.; Han, B. Strength Investigation and Prediction of Superfine Tailings Cemented Paste Backfill Based on Experiments and Intelligent Methods. *Materials* **2023**, *16*, 3995. [CrossRef] [PubMed]
8. Tran, V.Q. Using Artificial Intelligence Approach for Investigating and Predicting Yield Stress of Cemented Paste Backfill. *Sustainability* **2023**, *15*, 2892. [CrossRef]
9. Wang, G.; Ren, H.; Zhao, G.; Du, Y. Digital model and giant system coupling technology system of smart coal mine. *J. China Coal Soc.* **2022**, *47*, 61–74. [CrossRef]
10. Wang, G.; Ren, H.; Pang, Y.; Zhang, X. Research and engineering progress of coal mine intelligent (primary stage) technology system. *Coal Sci. Technol.* **2020**, *48*, 1–27.
11. Wang, G.; Du, Y.; Ren, H.; Fan, J.; Wu, Q. Research and practice of top-level design of intelligent coal mines. *Chin. J. Coal* **2020**, *45*, 1909–1924. [CrossRef]
12. Huang, Z. Exploration and research on transformation from intelligent single machine equipment to intelligent synergy in coal mine. *Coal Sci. Technol.* **2021**, *49*, 169–175. [CrossRef]
13. Liu, Q.; Zhang, L.; Li, T.; Du, P. A three machine digital twin and collaborative modeling method for fully mechanized working face. *J. Mine Au-Tomation* **2023**, *49*, 47–55. [CrossRef]
14. Wang, Y.; Shi, Y.; Wang, Y.Y.; Qi, P.L.; Wang, H.Q. Full pose measurement and virtual simulation of solid filling hydraulic support. *J. Mine Autom.* **2022**, *48*, 81–89. [CrossRef]
15. Yuan, X.; Gao, F.; Lian, Z. Kinematics Simulation and Experiment Investigation of Shield Powered Support Based on MATLAB. *Chin. Hydraul. Pneum.* **2021**, *45*, 25–31. [CrossRef]
16. Tian, J.; Li, Y.; Zhang, L.; Liu, Z. Adaptive control of temporary support force based on PSO-BP neural network. *J. Mine Autom.* **2023**, *49*, 67–74. [CrossRef]
17. Meng, L.; Zhou, R.; Guo, Z. Design and research of hydraulic cylinder precise control test system. *Coal Sci. Technol.* **2023**, *51*, 237–245. [CrossRef]
18. Zong, T.; Zhang, Q.; Shi, P. Critical characterization of solid-filled hydraulic support mechanism interference and autonomous demodulation method. *Coal Sci. Technol.* **2023**, *51*, 260–270.
19. Yang, Y.; Wang, Y.; Zhang, Q.; Cheng, G. Mechanism of interference discrimination and adjustment in the mechanical independent compaction process of intelligent solid backfilling method. *J. Min. Saf. Eng.* **2022**, *39*, 921–929.
20. Zhang, Q.; Wang, Y.; Zhang, J.; Zhang, Z. Research on intelligent filling mining method for coal mine solids. *J. Coal* **2022**, *47*, 2546–2556.
21. Ren, H.; Li, S.S.; Li, X.; Fu, Z. Simulation analysis of the position and posture control of hydraulic support roof beam. *Ind. Min. Autom.* **2019**, *45*, 11–16.
22. Zhang, Q.; Liu, Y.; Zhang, J.; Zhang, H.; Yin, W.; Wang, H. Influencing factors and control methods of mechanism interference in the autonomous compaction process of solid intelligent filling. *J. Coal* **2022**, *47*, 1043–1054. [CrossRef]
23. Shi, P.; Zhang, J.; Yan, H.; Zhang, Y.; Zhang, Q. Evaluation of Operating Performance of Backfilling Hydraulic Support Using Six Hybrid Machine Learning Models. *Minerals* **2022**, *12*, 1388. [CrossRef]
24. Gao, B.; Li, F. Posture Control of Hydraulic Proportional Drive Robot Arm Based on Inclination Sensor. *Mach. Tool Hydraul.* **2023**, *51*, 38–44.
25. Fang, X.; Liang, M.; Li, S.; Zhang, L. Key technologies for multi-parameter accurate perception and safety decision-making in intelligent working face. *J. Coal Sci.* **2020**, *45*, 493–508. [CrossRef]

26. Yang, Q.; Qu, D.; Xu, F. Path planning for mobile robots based on motion prediction of obstacles. *Comput. Eng. Des.* **2021**, *42*, 182–188. [CrossRef]
27. Zhu, Y. Application of SolidWorks in hydraulic support design. *Coal Min. Mach.* **2013**, *34*, 237–239. [CrossRef]
28. Huang, N.-B.; Kang, H.J. Observer-based dynamic parameter identification for wheeled mobile robots. *Int. J. Precis. Eng. Manuf.* **2015**, *16*, 1085–1093. [CrossRef]
29. Han, S.; Wang, H.; Tian, Y. Model-free based adaptive nonsingular fast terminal sliding mode control with time-delay estimation for a 12 DOF multi-functional lower limb exoskeleton. *Adv. Eng. Softw.* **2018**, *119*, 38–47. [CrossRef]
30. Cheng, J.; Zhu, M.; Wang, Y.H.; Yue, H.; Cui, W.X. Cascade construction of working face geological model for intelligent and precise coal mining and its key technologies. *J. Coal* **2019**, *44*, 2285–2295.

sustainability

MDPI

Article

Carbon Emission Prediction Model for the Underground Mining Stage of Metal Mines

Gaofeng Ren [1,2], Wei Wang [1,2,3], Wenbo Wu [1,2,*], Yong Hu [3] and Yang Liu [4]

[1] School of Resources and Environmental Engineering, Wuhan University of Technology, Wuhan 430074, China; rgfwhut@163.com (G.R.); 64810@whut.edu.cn (W.W.)
[2] Key Laboratory of Green Utilization of Key Non-Metallic Mineral Resources, Ministry of Education, Wuhan University of Technology, Wuhan 430074, China
[3] Hubei Sanxin Gold-Copper Co., Ltd., Daye 435100, China; whut12342021@163.com
[4] Hubei Carbon Emission Trading Center Co., Ltd., Wuhan 430070, China; liuyang@hbets.cn
* Correspondence: whut_wwb@outlook.com

Abstract: At present, the carbon emissions in China's metal mining industry can be calculated based on the amount of energy consumed in the mining process. However, it is still difficult to predict the carbon emissions before implementation of mining engineering. There are no effective approaches that could reasonably estimate the amount of carbon emissions before mining. To this end, based on the 'Top–down' carbon emission accounting method recommended by the Intergovernmental Panel on Climate Change (IPCC), this study proposes a model to predict the greenhouse gases emitted in seven carbon-intensive mining stages, namely, drilling, blasting, ventilation, drainage, air compression, transportation, and backfilling. The contribution of this model is to enable a prediction of the accumulation of greenhouse gases based on the mining preliminary design of mine, rather than on the consumption of energy and materials commonly used in recent research. It also establishes the amount of carbon emissions generated by mining per unit cubic meter of ore rock as the minimum calculation unit for carbon emissions, which allows for the cost and footprint of carbon emissions in the mining process to become clearer. Then, a gold–copper mine is involved as a case study, and the greenhouse gas emissions were predicted employing its preliminary design. Among all the predicted results, the carbon emissions from air compression and ventilation are larger than others, reaching 22.00 kg CO_2/m^3 and 10.10 kg CO_2/m^3, respectively. By contrast, the carbon emissions of rock drilling, drainage, and backfilling material pumping are 5.87 kg CO_2/m^3, 6.80 kg CO_2/m^3, and 7.79 kg CO_2/m^3, respectively. To validate the proposed model, the calculation results are compared with the actual energy consumption data of the mine. The estimated overall relative error is only 5.08%. The preliminary predictions of carbon emissions and carbon emission costs in mining before mineral investment were realized, thus helping mining companies to reduce their investment risk.

Keywords: mining carbon emissions; metal mines; carbon emission prediction model; cost of carbon emission; carbon emissions

Citation: Ren, G.; Wang, W.; Wu, W.; Hu, Y.; Liu, Y. Carbon Emission Prediction Model for the Underground Mining Stage of Metal Mines. *Sustainability* **2023**, *15*, 12738. https://doi.org/10.3390/su151712738

Academic Editors: Krzysztof Skrzypkowski, Faham Tahmasebinia, Jianhang Chen, René Gómez, Fhatuwani Sengani and Derek B. Apel

Received: 11 July 2023
Revised: 10 August 2023
Accepted: 21 August 2023
Published: 23 August 2023

1. Introduction

With the continuous emission of greenhouse gases, the frequency of extreme weather around the world has increased significantly, causing great economic losses and also posing a serious threat to human sustainable development [1–3]. Against the background of countries around the world having reached a consensus on the adjustment of the energy structure and control of greenhouse gas emissions, the impact of mining activities on climate change is often insufficiently considered. M. Azadi et al. [4] calculated a 130% increase in fuel consumption per unit of copper mined in Chile from 2001 to 2017 and a 32% increase in electricity consumption. Meanwhile, greenhouse gas emissions from metal and mineral production accounted for about 10% of global energy-related greenhouse gas emissions in 2018. Therefore, the large increase in energy consumption in the mining industry needs to be taken seriously, and regulators must consider greenhouse gas emissions more actively, accurately, and transparently to be able to implement effective mitigation strategies. According to the to the EU Green Deal fit for 55 packages [5], resource acquisition is also a strategic security issue in the process of realizing the Green New Deal. Therefore, accelerating the reduction of primary material production energy consumption caused by mining activities and ensuring the supply of sustainable raw materials are also prerequisites for achieving green transformation (EU 2018; Pelin and Mehmet 2022) [6,7]. At the same time, to further improve the initiative of enterprises in various industries to control greenhouse gas emissions, many countries and regions have successively formed their own carbon trading systems. China's carbon emission trading market was officially launched on December 19, 2017. In the long term, the carbon market will have a significant impact on the carbon emissions and investment decisions of various industries (X. Song et al., 2022) [8].

To date, numerous scholars have conducted extensive research on the problem of mining carbon emissions. With the goal of carbon emission reduction required in each production process of open-pit mines, Guoyu Wang et al. (2022) [9] used a multi-objective optimization algorithm to establish a multi-objective carbon emission distribution model for open-pit mines from the perspective of carbon quota allocation, and used this model to provide optimization suggestions for carbon emission quotas in each process link in the production process. Boyu Yang et al. (2021) [10] selected the Pingshuo open pit coal mine in Shanxi Province, China, as a case study object, analyzed the dynamic changes of carbon emissions based on the IPCC method, and used the IPAT equation to analyze the influencing factors of carbon emissions. It is concluded that the carbon emission sources of open-pit mines mainly include the use of fuel and explosives, methane escape from coal mines, spontaneous combustion of coal and gangue, power consumption, and other parts; at the same time, the carbon emissions caused by the open-pit coal mine increased year by year, with an average annual growth rate of 11.64%, of which the carbon emissions of fuel consumption and methane emissions accounted for 41.79% and 46.66%, respectively. This paper focuses on how to use the IPAT equation to analyze the influencing factors of carbon emissions in actual cases of mines. However, the dynamic change calculation of mine carbon emissions still uses the accounting model based on post-clearance provided by IPCC, and it is still difficult to solve the problem of how mining enterprises estimate the carbon emission intensity of mining before mining. Based on the life cycle concept, Benzheng Li et al. (2022) [11] established a carbon emission accounting model for each process link of a fully mechanized coal mine. And, according to the IPCC calculation method and the China Coal Production Enterprises Green Gas Emissions Accounting Methodology and Reporting Guide, producing the carbon emission model is feasible. However, the verification method of the model lacks the detailed data basis of real-time production statistics. Youshun Cui et al. (2015) [12] proposed a method for calculating the carbon emissions of diesel vehicles in underground mines using a geographic information system. The carbon emissions related to trucking work and were calculated by considering the carbon emission factors of the road and the distance as determined by the best-route analysis based on GIS. Lili Wei et al. (2021) [13] established a carbon emission estimation model to estimate the carbon emissions of the energy consumption of China's mining industry from 2000 to 2020, referring to the methods and parameters of the 2006 IPCC National Greenhouse Gas Inventory Guidelines. Then, using the extended Kaya identity and the LMDI model, analyzed the influencing factors of carbon emissions in the mining industry, including energy carbon emission intensity, energy structure, energy intensity, industrial structure, and output value. This paper analyzed the correlation between mining carbon emissions and economic output at the macro level, but ignored the significant differences in carbon emissions caused by different production processes among different types of mines.

Timothy Rijsdijk et al. (2022) [14] studied the impact of the change in carbon price on the mining economy of high-grade copper–cobalt mines in the Democratic Republic of Congo during mining and beneficiation processes. They came to the conclusion that the change in carbon price had little impact on the open-pit mining limit and cut-off grade. Yang Liu et al. (2022) [15] calculated the energy consumption of open-pit metal mines based on IPCC method and combined the traditional energy-saving supply curve analysis method with the open-pit mining boundary to evaluate the energy-saving potential and carbon emission costs caused by the application of energy-saving technologies. Sam Ulrich et al. (2022) [16] studied the interaction between greenhouse gas emissions from gold mining, abatement measures, and carbon prices. The impact of the carbon price varied markedly between countries, with a 100 USD/t CO_2-e price increasing gold production costs on average by 13 USD/oz in Finland and up to 275 USD/oz in South Africa. If the mine's primary energy source is replaced, the greenhouse gas emissions generated will be reduced by up to 46%. Further, by improving energy efficiency, the processes with the largest reductions in greenhouse gas emissions in underground mining are ventilation and cooling, going down by up to 24% (Sam Ulrich et al., 2022) [16]. From the perspective of carbon price, energy-saving technology application, and mining economy, the works above provide a reference for mineral development investors to make decisions by demonstrating the quantitative relationship between carbon emission costs and mining costs. However, mining is a huge and multi-process joint system. How to distinguish and clarify the carbon emission cost of various production processes is still a difficult problem.

In general, scholars have constructed a carbon emission accounting model for the whole life cycle of coal mine production, but research on carbon emission accounting models in the metal and non-metal mining stages is rare. At the same time, the current research in the mining field focuses on calculating carbon emissions based on the amount of energy consumed during the mining process, which is a method of post-liquidation. The disadvantage is that it can only passively calculate the carbon emissions generated after mining. If the prediction of mining carbon emissions can be realized before production, mining enterprises will be able to calculate the carbon emission cost in advance, thus reducing their investment risk. Table 1 shows the critical things such the parameter selection, modeling, analysis advantages, and limitations of existing literature. √ means the citation has used or studied the methods.

Table 1. Key information comparison table of existing literature.

Ref.	Coal Mine	Open-Pit Metal Mine	Underground Metal Mine	IPCC Method	Model Reliability Verification	Predicting Carbon Emissions
[9]		√			√	
[10]	√			√		
[11]	√			√	√	
[15]		√		√		

In China, where underground mines account for 90 per cent of the total number of metal mines, there has been no review of the technical strategy needed by Chinese metal mines to achieve the goals of "carbon peak and carbon neutrality" (Q.F. Guo et al., 2022) [17]. With China's carbon emission trading market and mechanism becoming more and more mature and perfect, a more detailed carbon emission estimation model has been established for underground mines. According to the geological survey and preliminary design data obtained before mining, the carbon emission prediction will be realized after the mine is put into operation. At the same time, if the mine is in the exploitation stage, the method can provide a more accurate assessment of carbon emissions and energy-saving technology applications generated by different processes in the mine. The above two points are of great significance to the current developers of mineral resources.

2. Carbon Emission Prediction Model for the Metal Mine Underground Mining Stage

To calculate the carbon emissions in the underground mining stage of metal mines, the calculation boundary first needs to be determined (R. Chambi-Legoas et al., 2021) [18]. All production processes in the actual mining stage fit into nine categories: drilling, blasting, supporting, ventilation, transportation, lifting, drainage, air compression, and backfilling. It is necessary to point out that the carbon emission of the underground support process mainly results from cement. Since almost all of the carbon emission of cement is from its production process, its carbon emission has been included in the cement production industry (T. Du et al., 2020) [19]. Since the lifting process involves the transport of ores, personnel, and all kinds of materials required for underground construction, the factors considered to affect the carbon emissions of this process include mining depth, personnel scheduling, underground production schedule, etc., making it difficult to model the energy consumption of different mines during the lifting process. Therefore, this study aimed to establish the seven production processes of rock drilling, blasting, ventilation, air compression, drainage, transportation, and backfilling as the calculation boundaries, and to construct the corresponding carbon emission models.

When metal mines are mined underground, there are differences in the types of energy and working methods used by equipment in various production processes. If the carbon emission calculation results of each process are not based on the same indicators, a comparison of the carbon emissions of different processes will be very inconsistent. Since the purpose of all mining work is to mine ore, in order to further quantify and compare the carbon emission value of each mining production process, this study opted to use 'per cubic meter rock mass' as the calculation unit for the process of mining carbon emissions.

2.1. Carbon Emission Accounting Method for Each Process in the Mining Stage

The most widely used carbon emission accounting method is the carbon emission coefficient method recommended by the Intergovernmental Panel on Climate Change (IPCC), which can be classified into two types of calculation methods: 'Top–down' and 'bottom–up'. The 'Top–down' method refers to the classification of energy used within the defined boundary, and the carbon emissions are obtained by multiplying the corresponding carbon emission coefficients after measuring the consumption. The 'bottom–up' method is used for the direct, on-site measurement of the carbon emissions of all equipment in order to calculate the total carbon emissions. Due to factors such as changing operating conditions, numerous sources of carbon emissions, and complex measurement environments in mines, it is almost impossible to use the 'bottom–up' method for the complete measurement of emission data for each source and component.

In this study, the 'Top–down' method was used to calculate the carbon emissions in the underground mining stage of metal mines (G.Y. Wang and J.S. Zhou, 2022) [9]. The calculation formula is as follows:

$$E = \sum_{\psi=1}^{\psi'} \Delta_\psi \cdot EF_\Delta \tag{1}$$

where E represents the carbon emission per cubic meter rock mass in the process, ψ represents the number of equipment types used, Δ_ψ represents the energy consumption per cubic meter rock mass, and EF_Δ represents the corresponding carbon emission factor of the energy type consumed by the ψ type of equipment. The subsequent model calculation formulas will be based on Formula (1).

In this study, when selecting the main types of carbon emission energy—which refers to the energy that is classified by carbon emission accounting according to the guidelines for the greenhouse gas emissions of national mining enterprises—two types of energy were selected: electricity and diesel. These two types of energy are the main sources of carbon emissions in the mining stage. In addition, because blasting is an important underground mining process, the explosive consumption in the blasting process is also measured. The following Figure 1 is shown as the boundary chart of carbon emission prediction in underground mining stage of metal mine.

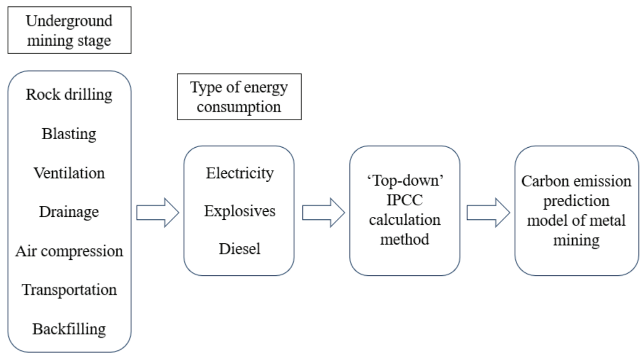

Figure 1. Carbon emission system boundary of the underground mining stage of a metals mine.

2.2. Carbon Emission Model in the Rock Drilling Process

The greenhouse gas emissions in the drilling process mainly result from the energy consumption of the drilling equipment. Underground drilling construction includes shaft and roadway excavation. The carbon emissions produced by different construction methods are not the same. To facilitate the calculation, it is assumed that drilling and blasting are used throughout the excavation of the mine, and, therefore, only the carbon emissions generated during the drilling process are considered. At present, the drilling tools used in underground mining are the pneumatic leg rock drill, tunneling trolley, and deep-hole trolley drilling. The pneumatic leg rock drill is used to drill shallow holes, and the tunneling and drilling trolleys are used to drill medium-depth and deep holes. Although the pneumatic leg rock drill is used for shallow-hole drilling work, its energy consumption is essentially different from the power and oil consumption of the tunneling and drilling trolleys. Its power results from the use of high-pressure air. The mine is equipped with several air compressors to supply compressed air to the underground pneumatic leg rock drill, air pick, and other rock drilling equipment by establishing a compressor station on the surface. Because the air compressor does not directly affect the rock drilling work, it is distinguished from the rock drilling work performed by the tunneling trolley drilling and deep-hole trolley drilling, and the carbon emissions from the shallow-hole drilling work of the pneumatic leg rock drill are calculated in the air pressure process.

The energy consumption of the drilling work carried out for medium-depth and deep holes depends on the rock breaking working time and the machine power of drilling tools. Machine power is usually a known quantity, and the time consumed by drilling work is related to factors such as drilling length, drilling number, and rock properties. The average drilling length, drilling number, and mechanical drilling efficiency required for mining are used to calculate the rock breaking working time per cubic meter rock mass of different drilling tools. Derived from Formula (1) above, when drilling medium-depth and deep holes, underground mines use the drilling and tunneling trolleys to drill different types of ore per cubic meter. The drilling carbon emissions per cubic meter rock mass are calculated as follows:

$$E_1^{dr} = \sum_{j=1}^{j'} P_1 \cdot \frac{a_j^1 \cdot b_j^1}{\eta_1} \cdot EF_{electricity} + \sum_{j=1}^{j'} P_2 \cdot \frac{a_j^2 \cdot b_j^2}{\eta_2} \cdot EF_{electricity} \quad (2)$$

where E_1^{dr} represents greenhouse gas emissions per cubic meter rock mass drilled by a rock drilling rig, t CO_2/m^3; j' represents the number of rock types with obvious differences in properties in the mine; P_1 and P_2 represent the rated power of the drilling trolley and deep-holetrolley at work, kW; a_j^1 and a_j^2 represent the average number of boreholes drilled by a drilling trolley and a deep-hole trolley in a certain type of rock mass; b_j^1 and b_j^2 represent the average borehole length per unit cube of a certain type of rock mass for the drilling and deep-hole trolleys, m/m^3; η_1 and η_2 represent the general drilling efficiency of tunneling drilling and deep-holetrolleys, m/h; $EF_{electricity}$ represents the greenhouse gas emission factor of electric energy, t CO_2/kWh.

2.3. Carbon Emission Model for the Blasting Process

The greenhouse gas emissions in blasting operations mainly result from the consumption of industrial explosives; the consumption of explosives is the product of unit explosive consumption and blasting volume. For underground metal mines, blasting work can be classified into excavation blasting, preparatory blasting, and stopping blasting. For excavation blasting and preparatory blasting, there is only one free surface, the blasting conditions are difficult, and the unit consumption of the explosives is generally higher than that in stopping blasting.

The average explosive unit consumption of various types of rocks commonly used in mine blasting work (distinguished here by the rock general coefficient) is measured. The calculation model for greenhouse gas emissions per cubic meter rock mass in different blasting processes is as follows:

$$E_2^{ex} = \sum_{j=1}^{j'} \frac{\left[K_j^1 \cdot \alpha + K_j^2 \cdot (1-\alpha)\right] \cdot EF_{explosive}}{1000} \tag{3}$$

where E_2^{ex} represents greenhouse gas emissions per cubic meter rock mass mined during blasting, t CO_2/m^3; j' represents the number of rock mass types with obvious differences in rock properties in the mines; K_j^1 and K_j^2 represent the unit consumption of explosives for the same type of rock mass for preparation blasting and ore blasting, respectively, kg/m^3; α represents the proportion of preparatory work in the whole underground mine; $EF_{explosive}$ represents the greenhouse gas emission factor for industrial explosives used in mines, t CO_2/t.

2.4. Carbon Emission Model in the Ventilation, Drainage, and Air Compression Processes

The carbon emission attributes of the ventilation, drainage, and compressed air systems in underground mines are similar, mainly in the following aspects: the carbon emissions of the three systems are all derived from power consumption; the number of fans, drainage pumps, and compressors required for the mine increases with the expansion of the mining area; during production, the main fan, drainage pump, and compressor are kept uninterrupted at work. The purposes of the ventilation, drainage, and compressed air systems are to ensure the safe production of mines, and they are not strongly related to the amount of ore being mined. Therefore, in order to convert the carbon emissions produced by ventilation, drainage, and air compression into unit cubic ore, the ratio of the daily power consumption of the ventilation and drainage systems to the sum of the daily ore and waste rock production in mines is considered to be able to determine the carbon emissions caused by ventilation and drainage technology when mining rock masses. By calculating the ratio of the daily power consumption of the compressed air system to the daily average amount of rock mass mined by the compressed air equipment in the mine, the carbon emission produced by air compression when mining the unit cubic rock mass is determined.

The carbon emissions of related equipment can be calculated using the following formula:

$$E_3^{v-w-c} = \frac{\left(\sum_{\imath=1}^{\imath'} P_{\imath}^{ve} \cdot n^{\imath} \cdot t_{\imath} + \sum_{g=1}^{g'} P_{g}^{wa} \cdot n^{g} \cdot t_{g}\right) \cdot \rho \cdot EF_{electricity}}{Q_{day} \cdot 1000} + \frac{\sum_{z=1}^{\mathcal{Z}'} P_{\mathcal{Z}}^{CO} \cdot n^{\mathcal{Z}} \cdot t_{z} \cdot \rho \cdot EF_{electricity}}{Q_{day}^1 \cdot 1000} \tag{4}$$

where E_3^{v-w-c} represents the greenhouse gas emissions from the ventilation, drainage, and pressurization processes when treating a unit cube of rock mass, t CO_2/m^3; $\imath$, g, and z

represent the number of types of ventilators, drainage pumps, and compressors; P_{i}^{ve}, P_{g}^{wa}, and P_{z}^{co} represent the respective working power of a certain type of fan, drain pump, and compressor, kW; n^{i}, n^{g}, and n^{z} represent the number of working units of ventilators, drainage pumps, and compressors of a certain type; t^{i}, t^{g}, and t^{z} represent the average daily working time of a certain type of ventilator, drainage pump, and compressor, h; ρ represents the average density of mine rock mass, kg/m^3; $EF_{electricity}$ represents greenhouse gas emission factor of electricity, t CO_2/kWh; Q_{day} represents the sum of daily ore and waste rock in the underground mine, t/day; Q_{day}^{1} represents the daily average amount of rock mass excavated in the underground mine using compressed air equipment, t/day.

2.5. Carbon Emission Model in the Transportation Process

The transportation process in underground mines can be divided into stope transportation and bottom-hole yard transportation. At present, the commonly used equipment for stope transportation includes the electric scraper, diesel scraper, loader, etc., and the bottom-hole yard transportation equipment generally involves the use of an electric locomotive. The carbon emission during the transportation process of the stope is the most complex, mainly due to the following aspects: the location and scope of the stope are constantly changing, and the distance covered by the transportation equipment is also constantly changing; the power consumed by the mining equipment varies under different transportation conditions, such as no-load, heavy load, uphill, downhill, and vehicle performance. In the process of mine production, there are usually multiple stopes at the same time, and the transportation distance and working conditions for the mining and loading equipment in each stope are not consistent. Therefore, in order to provide data statistics and facilitate calculation, the following assumptions are made on the transport process of the stope: without considering the transport distance of different stopes, the slope of the stope and the performance of the vehicle itself and their influence on the mining and loading equipment, the transport distance parameter is converted into the average round-trip time required for mining and loading; the load of the underground scraper is usually about 3 tons. The power ratio coefficient λ of the engine is defined when the mining vehicle is empty and heavy, and the value of λ could be taken as 0.91 (Z.Y. Zhang et al., 2014) [20]. Because the electric locomotive uses the method of rail transportation, its characteristics include having a large capacity and a small running friction resistance. The running power of the empty and heavy load is regarded as the rated power of the supporting motor.

Different from the electric scraper, the carbon emission of the diesel scraper is the result of diesel consumption. Therefore, it is necessary to convert the engine power of the diesel scraper into diesel consumption. The greenhouse gas emission model for transporting a unit cube of rock mass by diesel scraper is as follows:

$$E_{4}^{di} = \sum\nolimits_{\hbar=1}^{\hbar'} \frac{P_{di}^{\hbar}(1+\lambda)\cdot t_{sc}^{av}\cdot EF_{diesel}}{2\cdot \alpha_{di}\cdot V_{bucket}^{\hbar}\cdot k_{sc}} \tag{5}$$

where E_{4}^{di} represents carbon emissions per unit cube of rock mass for diesel scrapers, t CO_2/m^3; $\hbar'$ represents the number of diesel scraper types used in the mine; $P_{di}^{\hbar}$ represents the engine rated power of a certain type of diesel scraper, w; λ represents the power ratio coefficient of an engine under no-load and heavy load, λ = 0.91; t_{sc}^{av} represents the average round-trip time of the scraper, s; EF_{diesel} represents the carbon emission factor of diesel, t CO_2/J; α_{di} represents the diesel combustion conversion efficiency; $V_{bucket}^{\hbar}$ represents the bucket capacity corresponding to a certain type of diesel scraper used in the mine, m^3; k_{sc} represents the full bucket coefficient of the scraper.

Based on the above assumptions, the greenhouse gas emission models for electric scrapers and electric locomotives during underground mine transportation are as follows:

$$E_{5}^{el} = \sum\nolimits_{\hbar=1}^{\hbar'} \frac{P_{el}^{1}(1+\lambda)\cdot t_{sc}^{av}\cdot EF_{electricity}}{2\cdot V_{bucket}^{el-1}\cdot k_{sc}\cdot 3600} + \sum\nolimits_{\ell=1}^{\ell'} \frac{P_{el}^{2}\cdot t_{el}^{av}\cdot EF_{electricity}}{V_{bucket}^{el-2}\cdot n'\cdot k_{train}} \tag{6}$$

where E_5^{el} represents the carbon emissions per unit cube of rock mass shoveled by electric scrapers and electric locomotives in the mine, t CO_2/m^3; $\mathscr{k}'$ and ℓ' represent the number of types of electric scrapers and electric locomotives used in the underground mine; $P_{el}^{\mathscr{k}}$ and P_{el}^{ℓ} represent the respective rated power of a certain type of electric scraper and electric locomotive, kW; t_{el}^{av} represents the average round-trip time of electric locomotives, h; V_{bucket}^{el-1} and V_{bucket}^{el-2} represent the bucket volume of the electric scraper and the carriage volume of the electric locomotive, respectively, m^3; n' represents the number of carriages in the electric locomotives; k_{train} represents the full bucket coefficient of the electric locomotive.

2.6. Carbon Emission Model in the Backfilling Process

The carbon emission in the backfilling stage is the result of the large amount of electricity consumed during the preparation and transportation of the backfilling material. At present, there are many kinds of backfilling processes. Due to the different formation and geological conditions, the mineral processing technology used, and other factors, the backfilling process, backfilling material ratio, and backfilling material preparation equipment used in different mines are also different. The equipment utilized in the backfilling process includes filter presses, mixers, and pumps.

The carbon emission in the backfilling process is the sum of the preparation of the backfilling material and the hydraulic transportation. The source of carbon emissions during preparation is the equipment power consumption during the pressure filtration and mixing processes, while the carbon emissions in the hydraulic transportation process are the result of the equipment power consumption during the pumping process. Thus, the carbon emission accounting model for the backfilling unit cubic cavity process is obtained as follows:

$$EF_8^{fi} = \sum_{w=1}^{w'} \frac{P_{pr}^{w} \cdot t_{pr}^{av} \cdot n_{pr}^{w} \cdot EF_{electricity}}{V_{pr}^{av}} + \sum_{r=1}^{r'} \frac{P_{st}^{r} \cdot t_{st}^{av} \cdot n_{st}^{r} \cdot EF_{electricity}}{V_{st}^{av}} + \sum_{u=1}^{u'} \frac{P_{pu}^{u} \cdot t_{pu}^{av} \cdot n_{pu}^{u} \cdot EF_{electricity}}{V_{pu}^{av}} \quad (7)$$

where EF_8^{fi} represents the carbon emissions produced during the backfilling of each cubic cavity, t CO_2/m^3; w', r', and u' represent the types of filter presses, mixers, and pumps used in the processes of pressure filtration, mixing, and pumping, respectively; P_{pr}^{w}, P_{st}^{r}, and P_{pu}^{u} represent the rated power of each type of filter press, mixer, and pump, kW; t_{pr}^{av}, t_{st}^{av}, and t_{pu}^{av} represent the average working time of the filter press, mixer, and pump to complete a workflow, h; n_{pr}^{w}, n_{st}^{r}, and n_{pu}^{u} represent the number of presses, mixers, and pumps for each type, respectively; V_{pr}^{av}, V_{st}^{av}, and V_{pu}^{av} represent the treatment volume of the filter press, mixer, and pump in their respective single workflow time, m^3.

2.7. Summary of Section 2

In the Section 2, based on the IPCC 'Top–down' calculation method, we construct a carbon emission prediction model for different processes in the mining stage of underground metal mines. The calculation results of different processes are unified as the carbon emissions per cubic meter of ore, the core modeling idea is to decompose the mining process and divide the process into direct production processes and auxiliary production processes. The direct production processes include drilling, blasting, transportation, and filling process, their carbon emission models were constructed by calculating the energy consumption per unit cubic ore of direct production equipment. The auxiliary production processes include ventilation, drainage, and air pressing process, and their modeling method was to calculate the ratio of daily energy consumption of auxiliary production equipment to daily output of ore. The advantage of this modeling is that all input parameters in the model can be obtained in advance in the preliminary design, and it is easy to compare the differences in carbon emissions between different production processes. The disadvantage is that the model calculation results cannot be accurately adjusted according to the changes in the actual production plan of the mine, and when the production equipment is faced with changes in working capacity caused by migration and failure, it will lead to deviations in the model prediction results.

3. Case Study

This study selected an underground gold and copper mine located in Daye, Hubei Province, China (114°54′42″~114°55′45″ E, 30°04′45″~30°05′50″ N), and the total area is about 2.4 km^2. The underground mine is mined by the filling method. The main mineral products are gold copper ore, sulfur ore, and associated iron ore. At present, the mining depth has reached 500 m underground. Its actual production was investigated and measured, and the carbon emission accounting model designed above was utilized to calculate the carbon emission of each unit cube of ore body treated by each process flow. In calculating the carbon emissions of each process, the electric energy carbon emission factor used was 0.581 t CO_2/MWh, as given in the Enterprise Greenhouse Gas Emission Accounting Method and Reporting Guide Power Generation Facilities (Environmental Climate No. 111) (2022) [21], and the selected diesel carbon emission factor was 74.1 t CO_2/TJ, as given in the International Greenhouse Gas Emission Factor Guide provided by the IPCC in 2006 (IPCC, 2006) [22].

3.1. Carbon Emissions during Rock Drilling

The drilling parameters (drilling length and drilling number) for each unit cube of rock mass with different lithology were determined in this underground gold–copper mine, as shown in Table 2. The technical parameters of the excavation and drilling trolleys selected for the mine are shown in Table 3.

Table 2. Technical parameters of the drilling trolley under different rock masses.

Common Rock Mass Types in the Mine	Average Borehole Length (m/m^3)	Average Number of Boreholes
(Orebody) Skarn	0.83	5
(Orebody) Marble	0.83	5
(Wall-rock) Quartz diorite porphyrite	0.94	5
(Wall-rock) Diorite	0.94	5.4

Table 3. Technical parameters of the tunneling and drilling trolleys.

Drill Type	Model of Drill	Nominal Power (kW)	Rock Breaking Efficiency (m/h)	Equipment Size (m)	Equipment Weight (t)
Tunneling trolley	Huatai HT82	62	30	11 × 1.45 × 2.08	10
Deep-hole drilling	Huatai HT72	62	60	9.05 × 1.45 × 2.08	11.5

Substitute the data into Formula (2) to calculate:

When the tunneling trolley was used for rock drilling, the carbon emission of quartz diorite porphyrite was 5.64×10^{-3} t CO_2/m^3, and the carbon emission of diorite was 6.09×10^{-3} t CO_2/m^3.

When the deep-hole trolley was used for rock drilling, the general carbon emission of the ore rock with the lithology of skarn and marble was 2.49×10^{-3} t CO_2/m^3.

3.2. Carbon Emissions during Blasting

The explosive used in the mine production process is modified amine oil explosive, and its carbon emission factor is 0.2 t CO_2/t. The average density of skarn and marble is 2700 kg/m^3 and 2600 kg/m^3, respectively. The proportion of preparatory cutting work to the whole project is about 0.2. The average explosive unit consumption of various types of rocks in different blasting work of the mine (here, distinguished by the general coefficient of rock) is counted. The statistical results are shown in the Table 4.

Table 4. Explosive blasting parameters.

Rock Mass Types	Solid Coefficient of Rock (*f*)	Unit Explosive Consumption of Preparatory Cutting Work	Unit Explosive Consumption of Ore Blasting Work
Skarn	8~10	1.62~1.89 kg/m^3	1.49 kg/m^3
Marble	10~12	1.84~2.11 kg/m^3	1.58 kg/m^3

Substitute the data into Formula (2) to calculate:

When the rock is skarn, the carbon emission of blasting is about 3.03 $\times$ 10^{-4} t CO_2/m^3~3.14 $\times$ 10^{-4} t CO_2/m^3. When the rock is marble, the carbon emission of blasting is about 3.26 $\times$ 10^{-4} t CO_2/m^3~3.37 $\times$ 10^{-4} t CO_2/m^3.

3.3. Carbon Emissions during Ventilation, Drainage, and Air Compression

In the production process of the mine, the daily ore output was about 3000 t, the amount of waste rock was about 250 t per day, the average density of ore and rock was 3200 kg/m^3, and the proportion of the compressed air equipment used as power source to the mine ore accounts for about 70% of the total output of the mine. The mine made use of a frequency conversion fan, with the energy-saving effect reaching 40% (Z.X. Zeng et al., 2020) [23]; the fan was kept open for 24 h. The number of working tables with the same type of drainage pump was 2, and the rest were on standby. The average daily working time was 3 h. The working arrangement of the air compressor was as follows: 8:00–16:00 all open, 16:00–8:00 three open. This is because the working mechanism of the air compressor is meant to stop the air pressure when it reaches the required air pressure value, and when it is lower than this value, it is programmed to resume operation. Mine technicians found that the actual full-power working time of the air compressor in this gold–copper mine could be multiplied by the utilization coefficient of 0.8. The mine fan and drainage pump data are shown in Tables 5 and 6, while the surface air compressor data are shown in Table 7.

Table 5. Fan data.

Type of Fan	Operating Capacity (kW)	Number of Working Devices	Fan Air Volume (m^3/min)	Static Pressure (Pa)	Fan Speed (r/min)
K40-6-№14	30	1	984~2064	150~695	960
K45-6-№14	45	1	1434~2718	500~959	980
FCDZ-6-№22	370	3	2400~7600	750~2750	990
K40-4-№12	37	1	882~1926	242~1118	1450

Table 6. Drainage pump data.

Type of Pump	Operating Capacity (kW)	Number of Working Devices	Pumping Capacity (m^3/h)	Fan Speed (r/min)
200D43*6	300	1	280	1480
MD280-65*7	630	2	280	1480
MD280-43*5	250	2	280	1480
MD280-65*9	800	2	280	1480

Table 7. Air compressor data.

Type of Compressor	Operating Capacity (kW)	Number of Working Devices	Operating Time	Rated Exhaust Pressure (MPa)	Nominal Volume Flow (m^3/min)
TS325-400	300	8	8 h	0.7	41.8
TS325-400	300	3	16 h	0.7	61.7

Bring the above data into Formula (4), and the calculation results are as follows:

In the process of mine production, the carbon emission produced by the ventilation process is about 1.01×10^{-2} t CO_2/m^3, the carbon emission produced by the drainage process is about 6.80×10^{-3} t CO_2/m^3, and the carbon emission from the compressed air process is about 2.20×10^{-2} t CO_2/m^3.

3.4. Carbon Emissions during Transportation

The average round-trip time of the diesel scraper is 200 s; diesel engine efficiency is generally between 34% and 45%; here, 40% was used for the calculation. It is assumed that only one type of diesel scraper is used in the whole process of transporting the same rock mass. Data on diesel scrapers used in mines are shown in Table 8.

Table 8. Diesel scraper data.

Type of Diesel Scraper	Rated Power (kW)	Number of Working Devices	Bucket Capacity (m^3)	Full-Bucket Coefficient
WJ-1.5	63	8	1.5	1.12
WJ-0.75	58	4	0.75	1.09
WJ-1	58	7	1	1.10

Substitute the above diesel engine-related production data into Formula (5), and the calculation results are as follows:

When the WJ-1.5 diesel scraper was selected, the carbon emission produced by the process of scraping ore was about 1.33×10^{-4} t CO_2/m^3.

When the WJ-0.75 diesel scraper was used, the carbon emission produced by the process of scraping ore was about 2.51×10^{-4} t CO_2/m^3.

When the WJ-1 diesel scraper was used, the carbon emission produced by the process of scraping ore was about 1.87×10^{-4} t CO_2/m^3.

The average round-trip time of the electric scraper and the electric locomotive in the mine was 200 s and 600 s, respectively. Similarly, it is assumed that only one type of electric scraper and electric locomotive is used in the whole process of transporting the same rock mass. The electric scraper and electric locomotive equipment parameters are shown in Tables 9 and 10, respectively.

Table 9. Electric scraper data.

Types of Electric Scraper	Rated Power (kW)	Number of Working Devices	Bucket Capacity (m^3)	Full-Bucket Coefficient
WJD-1.5	55	20	1.5	1.12
WJD-1	45	13	1	1.10

Table 10. Electric locomotive production data.

Types of Electric Locomotive	Rated Power (kW)	Number of Working Devices	Number of Carriages and Capacity	Full-Bucket Coefficient
CJY5/6GB 250	15	16	96 (0.75 m^3)	0.91
CJK7/6GB 250	42	8	28 (1.2 m^3)	0.95
CTY5/6G	15	4	10 (1.2 m^3)	0.95

Substitute the above data into Formula (6), and the calculation results are as follows:

When the WJD-1.5 electric scraper was selected, the carbon emission produced by the process of scraping ore was about 1.01×10^{-3} t CO_2/m^3.

When the WJD-1 electric scraper was used, the carbon emission produced by the process of scraping ore was about 1.26×10^{-3} t CO_2/m^3.

In the transportation process of the CJY5/6GB 250 electric locomotive, the carbon emission produced by ore transportation was about 2.22×10^{-5} t CO_2/m^3.

In the CJY7/6GB 250 locomotive transport process, the carbon emissions produced by the ore handling process was about 1.27×10^{-4} t CO_2/m^3.

In the transportation process of the CTY5/6G electric locomotive, the carbon emission produced by ore transportation was about 1.27×10^{-4} t CO_2/m^3.

3.5. Carbon Emission during the Backfilling Process

In the process of mine production, the backfilling process is converted into 3000 T/day according to the ore, and to 800 m^3/day according to the backfilling amount. The specific parameters of the equipment involved in the backfilling process are shown in Table 11.

Table 11. Backfilling equipment parameter table.

Equipment	Number of Types	Number of Working Devices	Rated Power (kW)	Operating Time (h)
Filter press	KGZ600/2000-U	3	20.7	24
Mixer	φ2000*2200	1	30	16
	SJ6*6	2	30	16
	SJ6*8	1	30	16
Pump	100ZJ-I-A46	1	55	8
	100ZJ-I-A50	3	90	8
	100ZJ-I-A50	2	55	8
	150D30*3	1	75	8
	80ZBYL-450	7	90	8
	150ZJ-I-A70	1	200	8

Substitute the data into Formula (7), and the calculation results are as follows:

In the process of mine backfilling, the carbon emission produced by the pressure filtration process was about 1.08×10^{-3} t CO_2/m^3, the carbon emission produced by the agitation process was about 1.39×10^{-3} t CO_2/m^3, and the carbon emission produced by the pumping process was about 7.79×10^{-3} t CO_2/m^3.

3.6. Data Analysis

(1) Comparative analysis of the theoretical calculation and actual production

In the production process of the gold–copper mine in Hubei Province, the power consumption of the main departments of the mine is monitored and measured on a monthly basis. However, due to the relatively stable energy consumption, equipment operation positions, and working conditions in the mine's ventilation, drainage, compressed air, and backfilling departments, the energy consumption data for these departments were more accessible and accurate than those from other departments. Therefore, the monthly power consumption data of the ventilation, drainage, compressed air, and backfilling departments of the mine from January to June 2022 were averaged separately to eliminate the contingency of the monthly data. And the following Table 12 is the actual monthly energy consumption of the four departments of the mine.

Table 12. Actual monthly energy consumption data (January to June 2022).

Department	January (1.0×10^4 kwh)	February (1.0×10^4 kwh)	March (1.0×10^4 kwh)	April (1.0×10^4 kwh)	May (1.0×10^4 kwh)	June (1.0×10^4 kwh)	Average (1.0×10^4 kwh)
Ventilation	56.5684	52.7422	47.7846	51.5141	50.8204	51.7728	51.87
Drainage	28.8745	27.7241	22.0039	25.2564	24.3321	25.6627	25.64
Compressed air	83.7515	72.6625	74.2611	79.0424	83.2553	82.0065	79.16
Backfilling	44.6089	38.6525	39.6776	44.5871	39.0314	45.3569	41.99

The model calculates the carbon emission per cubic rock mass by calculating the ratio of the daily average carbon emission to the daily average production. The daily average carbon emission of each process is the product of the daily average energy consumption and the corresponding energy carbon emission factor in each process. Since the average daily output of the mine and the energy carbon emission factor can be regarded as fixed values, the reliability of the carbon emission model can be verified by ensuring that the theoretical energy consumption calculated by the model for each process is consistent with the actual energy consumption. Therefore, the theoretical monthly energy consumption of the above process is calculated and compared with the actual monthly energy consumption of the mine, as shown in Figure 2.

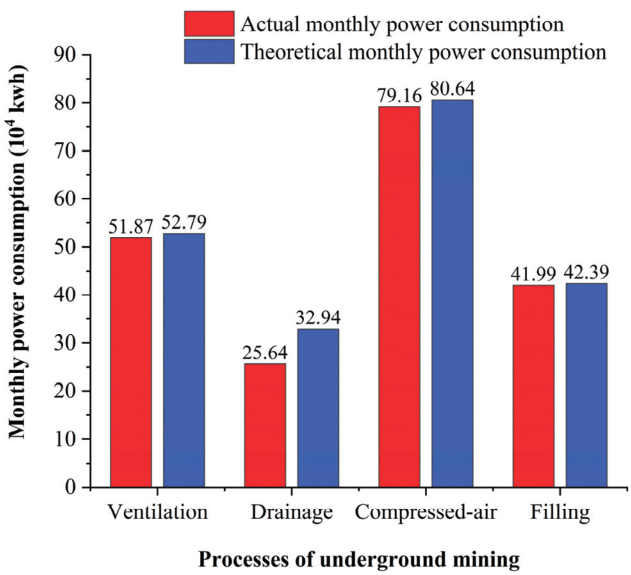

Figure 2. Comparison of the theoretical calculation and the actual energy consumption.

The analysis results show that the relative error between the overall calculation results of the model and the actual production statistics is 5.08%. For the ventilation process, the theoretically calculated power consumption of the model is 9200 kWh higher than the average monthly consumption of the mine, and the relative error is 1.77%. For the drainage process, the power consumption calculated by the model is 73,000 kWh higher than the average monthly consumption of the mine, and the relative error is 28.5%. For the air compression process, the power consumption calculated by the model is 14,800 kWh higher than the average monthly consumption of the mine, and the relative error is 1.87%. For the backfilling process, the power consumption calculated by the model is 4600 kWh higher than the average monthly consumption of the mine, and the relative error is 0.94%. It can be seen that the difference between the theoretical calculation and the actual consumption of the drainage process is the biggest. The main reason for this is that the mine drainage is affected by seasonal climate change. The precipitation is different for each month, resulting in different water inflows during the mine production process. The working time of the drainage pump is also different. In the theoretical model, this working time is a fixed value, and the statistical data in the previous paper were taken from the period of January–June, which is the dry season and when the rainfall is low; these produced a high relative error between the theoretical calculation and the actual energy consumption in the drainage process. In contrast, the relative errors between theory and practice in the ventilation, compressed air, and backfilling processes are less than 2%. Thus, the reliability of the model is well-verified, making it capable of conducting the accounting and estimation of the carbon emissions of each process in mine production.

(2) Analysis of carbon emission differences between different processes

The results of the calculation of carbon emissions for the different processes above are shown in Figure 3.

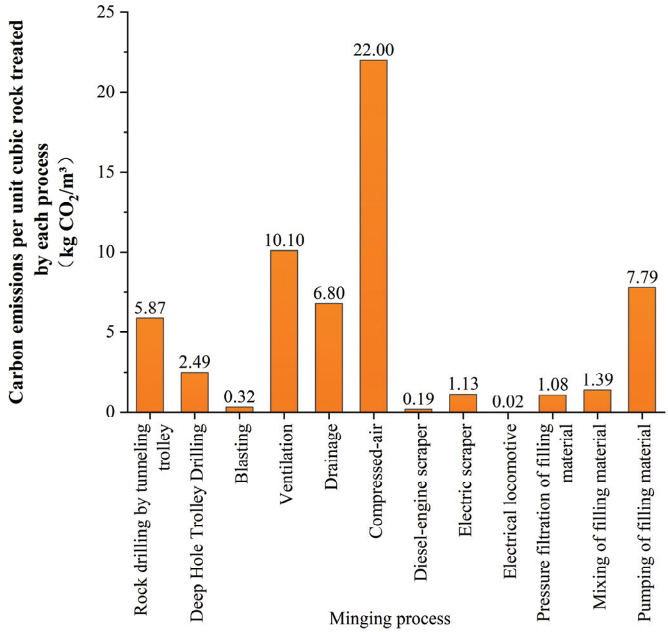

Figure 3. Carbon emission per unit cube of ore rock treated by each process.

In the diagram, it can be seen that there are obvious differences between the carbon emissions of different processes. The carbon emissions of the rock treated with compressed air and ventilation are the highest, reaching 22.00 kg CO_2/m^3 and 10.10 kg CO_2/m^3, respectively, and accounting for 54.24% of the whole process. The carbon emissions of rock drilling, drainage, and backfilling pumping of the heading trolley also reached 5.87 kg CO_2/m^3, 6.80 kg CO_2/m^3, and 7.79 kg CO_2/m^3, respectively; these are the key processes that need energy saving and carbon reduction. It is possible to start the energy-saving and carbon-reduction work of the compressed air process by reducing the use of the pneumatic leg rock drill and increasing the use of the tunneling trolley and the middle–deep-hole rock drilling trolley. The other processes can be applied based on economic rationality. New energy-saving and carbon-reducing technologies are used for equipment transformation.

For the underground transportation, although the direct carbon emission value of the rock from the diesel scraper is lower than that from the electric scraper, the use of the diesel scraper will increase the burden of the underground ventilation system, thus resulting in increased energy consumption. The indirect carbon emissions produced by this are not calculated, and other toxic and harmful gases produced by diesel combustion are not converted into CO_2 for the statistics. On the other hand, the carbon emission value of a unit cube of ore rock transported by the underground electric locomotive is only 0.02 kg CO_2/m^3, which is the lowest in the whole process. The large capacity of the underground electric locomotive fully reduces the carbon emission cost per cubic ore rock, which also demonstrates that the promotion and use of large-scale and intelligent equipment in underground mines indeed promotes a reduction in carbon emissions in production.

(3) Carbon emission cost calculation

The China Carbon Price Survey 2020 predicted the prices in the national carbon emission trading market and provided the following average expected price of carbon quotas: 49 CNY/t in 2020, 71 CNY/t in 2025, 93 CNY/t in 2030, and 167 CNY/t in 2050 (H. Shi, 2022) [24]. In the Carbon Emissions Trading Management Measures (Trial) issued by the Ministry of Ecology and Environment, the distribution of carbon quotas is mainly free in the early stage, while paid distribution is introduced in the later stage (B. Cox et al., 2022) [25]. The proportion of free carbon quotas has a great impact on the development of the industry. To compare the impact of different free quota ratios of carbon emission rights on the cost of carbon emissions per ton of ore mined, the gold–copper mine in Hubei Province is again used as an example. The total carbon emission per cubic ore and rock in underground mining is 59.18 kg CO_2/m^3, and the average density per ore and rock is 3200 kg/m^3. Different free quota ratios are set at 100%, 90%, 80%, 70%, 60%, and 50% of carbon emissions per ton of ore produced, and the cost of carbon emissions per ton of ore mined is calculated, as shown in Figure 4.

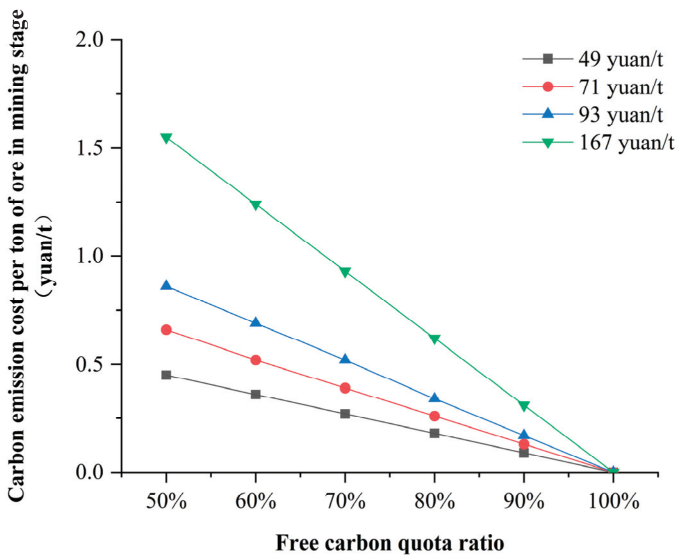

Figure 4. Carbon emission costs per ton of mining under different carbon quota ratios.

It can be seen in the figure that the carbon emission cost per ton of ore in the underground mining stage is positively correlated with the carbon price and negatively correlated with the free carbon quota ratio. When the ratio of the free carbon quota is 50%, according to the current carbon price forecast, the carbon emission cost interval of one ton of ore mined underground in this gold–copper mine is CNY 0.45–1.55. The gold grade of the ore is 1.74 g/t, and the carbon emission cost interval of one gram of gold mined underground is CNY 0.27–0.89. At the same time, after mining, it is necessary to crush and produce a concentration of the ore in the concentrator, and the energy consumption in this part is also huge. It is foreseeable that with the comprehensive improvement of China's carbon market and the continuous rise of the carbon price, mining enterprises will pay more and more attention to the cost increase caused by carbon emissions. Therefore, at this stage, mining enterprises should have the ability to make a preliminary estimate of the carbon emission cost in the mining production process before making an investment so as to reduce investment risk. For mines in the process of mining, an accounting of carbon emissions for various processes should also be carried out to provide a basis for decision making with respect to the application of energy-saving and carbon-reduction technology.

4. Conclusions

Based on the principle of the IPCC carbon emission calculation, this study utilized the carbon emission of a unit cube of rock mass as the calculation index; determined the drilling, blasting, ventilation, drainage, compressed air, transportation, and backfilling processes as the boundaries of carbon emission calculation; and established the carbon emission prediction model for each process. Taking a gold–copper mine in Hubei Province, China, as an example, the proposed model was verified. The following conclusions were drawn:

(1) The accuracy of the carbon emission accounting model was verified using the actual production energy consumption data from the ventilation, drainage, compressed air, and filling processes. The relative error between the overall calculation results of the model and the actual values was 5.08%, which verifies the practicability of the model and has a popularization value in underground mines using the same production processes. But among them, the prediction error of the drainage model is quite different from the actual one, reaching 28.5%. Although there are signs that this is due to the fact that the mine drainage situation is greatly affected by seasonal factors, it also shows that the model still has uncertainty in some aspects. Therefore, we still recommend that mining companies use models to predict and evaluate the average, and try to avoid the pursuit of accurate prediction at a certain stage;

(2) The existing post-liquidation method for calculating carbon emissions based on the amount of energy consumed in the mining industry was improved, and the preliminary prediction of carbon emissions and carbon emission costs in mining before mineral investment was realized;

(3) In the process of underground mining, the carbon emission per unit of cubic rock treated with compressed air and ventilation was the highest, reaching 22.00 kg CO_2/m^3 and 10.10 kg CO_2/m^3, respectively, accounting for 54.24% of the whole process. Our analysis showed that using the rock-drilling trolley instead of the pneumatic leg rock drill and increasing the proportion of the large transport equipment can effectively reduce carbon emissions.

Further Study

(1) Conduct a sensitivity analysis on the model's predictions, to study the influence of different input parameters on mining carbon emissions, so as to provide more clear decision-making suggestions for the subsequent application of energy saving and emission reduction technology in mines;

(2) Carbon emission prediction models still have many limitations, such as limited accounting boundaries, difficulty of making timely adjustments according to actual production plan changes of the mine, equipment production capacity, and working parameters not being immutable. Subsequent research should try to improve these defects, expanding the scope of research, considering cross-validation of different types of mines, and further improving the accuracy and generalization of the model.

Author Contributions: All authors contributed to the study concept and design. G.R. guided the topic selection and writing ideas of the article, W.W. (Wenbo Wu) proposed the prediction model and wrote this article, W.W. (Wei Wang) and Y.H. collected and proofread the actual mine data utilized in the article, W.W. (Wei Wang) completed the analysis of selected cases, and Y.L. provided help in the modeling process of the carbon emission prediction model in this article. All authors commented on previous versions of the manuscript. All authors have read and agreed to the published version of the manuscript.

Funding: This work was supported by the Department of Science and Technology of Hubei Province (grant number 2022BEC040). The project name is Research on Key Technologies for Optimal Mining and Carbon Emission Accounting of Close-Range Multi-Layer Phosphate Ore.

Institutional Review Board Statement: This study did not require ethics approval, thus this declaration is not applicable.

Informed Consent Statement: Not applicable.

Data Availability Statement: All data and materials used in this work have been permitted by all participants and published in the article.

Conflicts of Interest: The authors have no relevant financial or non-financial interests to disclose.

Abbreviations

The main notations comparison list is as follows:

Notations	Meaning	Unit
E_1^{dr}	greenhouse gas emissions per cubic meter rock mass drilled by a rock drilling rig	t CO_2/m^3
j'	the number of rock types with obvious differences in properties in the mine	
P_1	the rated power of the drilling trolley	kw
P_2	the rated power of the heading trolley	kw
a_j^1	the average number of boreholes drilled by a drilling trolley in a certain type of rock mass	
a_j^2	the average number of boreholes drilled by a heading trolley in a certain type of rock mass	
b_j^1	the average borehole length per unit cube of a certain type of rock mass for the drilling trolleys	m/m^3
b_j^2	the average borehole length per unit cube of a certain type of rock mass for the heading trolleys	m/m^3
η_1	the general drilling efficiency of drilling trolleys	m/h
η_2	the general drilling efficiency of heading trolleys	m/h
$EF_{electricity}$	greenhouse gas emission factor of electric energy	t CO_2/kwh
E_2^{ex}	greenhouse gas emissions per cubic meter rock mass mined during blasting	t CO_2/m^3
K_j^1	the unit consumption of explosives for the same type of rock mass for preparation blasting	kg/m^3
K_j^2	the unit consumption of explosives for the same type of rock mass for ore blasting	kg/m^3
$EF_{explosive}$	the greenhouse gas emission factor for industrial explosives used in mines	t CO_2/t
E_3^{v-w-c}	the greenhouse gas emissions from the ventilation, drainage, and pressurization processes when treating a unit cube of rock mass	t CO_2/m^3
$\imath$	the number of types of ventilators	kW
$\mathscr{g}$	the number of types of drainage pumps	kW
$\mathscr{z}$	the number of types of compressors	kW
$n^{\imath}$	the number of working units of ventilators of a certain type	
$n^{\mathscr{g}}$	the number of working units of drainage pumps of a certain type	
$n^{\mathscr{z}}$	the number of working units of compressors of a certain type	
$t^{\imath}$	the average daily working time of a certain type of ventilator	h
$t^{\mathscr{g}}$	the average daily working time of a certain type of drainage pump	h
$t^{\mathscr{z}}$	the average daily working time of a certain type of compressor	h
ρ	the average density of mine rock mass	kg/m^3
Q_{day}	the sum of daily ore and waste rock in the underground mine	t/day
Q_{day}^1	the daily average amount of rock mass excavated in the underground mine using compressed air equipment	t/day
E_4^{di}	carbon emissions per unit cube of rock mass for diesel scrapers	t CO_2/m^3
$\hbar$	the number of diesel scraper types used in the mine	
$P_{di}^{\hbar}$	the engine rated power of a certain type of diesel scraper	kw
λ	the power ratio coefficient of an engine under no-load and heavy load	
t_{sc}^{av}	the average round-trip time of the scraper	h
EF_{diesel}	the carbon emission factor of diesel	t CO_2/J
α_{di}	the diesel combustion conversion efficiency	
$V_{bucket}^{\hbar}$	the bucket capacity corresponding to a certain type of diesel scraper used in the mine	m^3
k_{sc}	the full bucket coefficient of the scraper	
E_5^{di}	carbon emissions per unit cube of rock mass shoveled by electric scrapers and electric locomotives in the mine	t CO_2/m^3

Notations	Meaning	Unit
$\mathscr{k}'$	the number of types of electric scrapers	
$\mathscr{l}'$	the number of types of electric locomotives	
$P_{el}^{\mathscr{k}}$	the respective rated power of a certain type of electric scraper	kw
$P_{el}^{\mathscr{l}}$	the respective rated power of a certain type of electric locomotive	kw
t_{el}^{av}	the average round-trip time of electric locomotives	h
V_{bucket}^{el-1}	the bucket volume of the electric scraper	m^3
V_{bucket}^{el-2}	the carriage volume of the electric locomotive	m^3
n	the number of carriages in the electric locomotive	
k_{train}	the full bucket coefficient of the electric locomotive	
EF_8^{fi}	the carbon emissions produced during the backfilling of each cubic cavity	t CO^2/m^3
$\mathscr{w}'$	the types of filter presses used in the processes of pressure filtration, mixing, and pumping	
$\mathscr{r}'$	the types of mixers used in the processes of pressure filtration, mixing, and pumping	
$\mathscr{u}'$	the types of pumps used in the processes of pressure filtration, mixing, and pumping	
$P_{pr}^{\mathscr{w}}$	the rated power of each type of filter press	kW
$P_{st}^{\mathscr{r}}$	the rated power of each type of mixers	kW
$P_{pu}^{\mathscr{u}}$	the rated power of each type of pumps	kW
t_{pr}^{av}	the average working time of the filter press to complete a workflow	
t_{st}^{av}	the average working time of the mixer to complete a workflow	
t_{pu}^{av}	the average working time of the pump to complete a workflow	
$n_{pr}^{\mathscr{w}}$	the number of presses for each type	
$n_{st}^{\mathscr{r}}$	the number of mixers for each type	
$n_{pu}^{\mathscr{u}}$	the number of pumps for each type	
V_{pr}^{av}	the treatment volume of the filter press in their respective single workflow time	m^3
V_{st}^{av}	the treatment volume of the mixer in their respective single workflow time	m^3
V_{pu}^{av}	the treatment volume of the pump in their respective single workflow time	m^3

References

1. Zhou, A.; Hu, J.; Wang, K. Carbon emission assessment and control measures for coal mining in China. *Environ. Earth Sci.* **2020**, *79*, 1–15. [CrossRef]
2. Yuan, Y.; Chuai, X.; Xiang, C.; Gao, R. Carbon emissions from land use in Jiangsu, China, and analysis of the regional interactions. *Environ. Sci. Pollut. Res.* **2022**, *29*, 44540. [CrossRef] [PubMed]
3. Clarke, B.J.; Otto, F.E.L.; Jones, R.G. Inventories of extreme weather events and impacts: Implications for loss and damage from and adaptation to climate extremes. *Clim. Risk Manag.* **2021**, *32*, 100285. [CrossRef]
4. Azadi, M.; Northey, S.A.; Ali, S.H.; Edraki, M. Transparency on greenhouse gas emissions from mining to enable climate change mitigation. *Nat. Geosci.* **2020**, *13*, 100–104. [CrossRef]
5. European (EU) Commission. *European Green Deal 2021 Fit for 55 Package: The EU's Fit for 55 Package—Key Takeaways from Bernstein Renewables, Chemical, Airlines & Energy Teams*; European (EU) Commission: Brussels, Belgium, 2021.
6. European (EU) Commission. *European Green Deal 2018 A Clean Planet for All*; European (EU) Commission: Brussels, Belgium, 2018; p. 773.
7. Yapıcıoğlu, P.; Yeşilnacar, M.I. Economic performance index assessment of an industrial wastewater treatment plant in terms of the European Green Deal: Effect of greenhouse gas emissions. *J. Water Clim. Chang.* **2022**, *13*, 3100–3118. [CrossRef]
8. Song, X.; Wang, D.; Zhang, X.; He, Y.; Wang, Y. A comparison of the operation of China's carbon trading market and energy market and their spillover effects. *Renew. Sustain. Energy Rev.* **2022**, *168*, 112864. [CrossRef]
9. Wang, G.; Zhou, J. Multiobjective Optimization of Carbon Emission Reduction Responsibility Allocation in the Open-Pit Mine Production Process against the Background of Peak Carbon Dioxide Emissions. *Sustainability* **2022**, *14*, 9514. [CrossRef]
10. Yang, B.Y.; Bai, Z.K.; Zhang, J.J. Environmental impact of mining-associated carbon emissions and analysis of cleaner production strategies in China. *Environ. Sci. Pollut. Res.* **2021**, *28*, 13659. [CrossRef]
11. Li, B.; Shi, Y.; Hao, J.; Ma, C.; Pang, C.; Yang, H. Research on a Carbon Emission Calculation Model and Method for an Underground Fully Mechanized Mining Process. *Energies* **2022**, *15*, 2871. [CrossRef]
12. Park, B.; Park, S.F.; Choi, Y.; Park, H.-S. Calculation of a Diesel Vehicle's Carbon Dioxide Emissions during Haulage Operations in an Underground Mine using GIS. *Tunn. Undergr. Space* **2015**, *25*, 373–382. [CrossRef]
13. Wei, L.; Feng, X.; Jia, G. Construction and Application Analysis of Carbon Emission Influence Factor Model of Energy Consumption in Mining Industry. *Adv. Civ. Eng.* **2021**, *2021*, 1–12. [CrossRef]
14. Rijsdijk, T.; Nehring, M. The effect of carbon pricing on cut-off grade and optimal pit limits in a high grade copper-cobalt deposit. *J. Clean. Prod.* **2022**, *356*, 131766. [CrossRef]

15. Liu, Y.; Zhang, C.; Xu, X.; Ge, Y.; Ren, G. Assessment of energy conservation potential and cost in open-pit metal mines: Bottom-up approach integrated energy conservation supply curve and ultimate pit limit. *Energy Policy* **2022**, *163*, 112809. [CrossRef]
16. Ulrich, S.; Trench, A.; Hagemann, S. Gold mining greenhouse gas emissions, abatement measures, and the impact of a carbon price. *J. Clean. Prod.* **2022**, *340*, 130851. [CrossRef]
17. Guo, Q.; Xi, X.; Yang, S.; Cai, M. Technology strategies to achieve carbon peak and carbon neutrality for China's metal mines. *Int. J. Miner. Metall. Mater.* **2022**, *29*, 626–634. [CrossRef]
18. Chambi-Legoas, R.; Ortega Rodriguez, D.R.; Figueiredo, M.D.; Pena Valdeiglesias, J.; Zevallos Pollito, P.A.; Marcelo-Pena, J.L.; Rother, D.C. Natural Regeneration After Gold Mining in the Peruvian Amazon: Implications for Restoration of Tropical Forests. *Front. For. Glob. Chang.* **2021**, *4*, 594627. [CrossRef]
19. Du, T.; Wang, J.; Wang, H.; Tian, X.; Yue, Q.; Tanikawa, H. CO^2 emissions from the Chinese cement sector: Analysis from both the supply and demand sides. *J. Ind. Ecol.* **2020**, *24*, 923–934. [CrossRef]
20. Zhang, Z.; Song, G.; Chen, J.; Zhai, Z.; Yu, L. Development of a Simplified Model of Speed-Specific Vehicle-Specific Power Distribution Based on Vehicle Weight for Fuel Consumption Estimates. *Transp. Res. Rec.* **2020**, *2674*, 52–67. [CrossRef]
21. Ministry of Ecology and Environement of the People's Republic of China. Enterprise Greenhouse Gas Emission Accounting Methods and Reporting Guidelines Power Generation Facilities (2022 Revision). Available online: https://www.mee.gov.cn/xxgk2018/xxgk/xxgk06/202203/W020220315357528424119.pdf (accessed on 20 March 2022). (In Chinese)
22. Intergovernmental Panel on Climate Change. *2006 IPCC Guidelines for National Greenhouse Gas Calculate Inventories*; IPCC: Geneva, Switzerland, 2006.
23. Zeng, Z.X.; Guo, J.M.; Wei, X.Y.; Lü, E.; Liu, Y. The Analysis of Cooling Time and Energy Consumption of VAV Fan-pad Evaporative Cooling Systems in a Greenhouse. *Hortscience* **2020**, *55*, 812–818. [CrossRef]
24. Shi, H. The value assessment of copper mining right from the perpective of carbon emission cost. *Sci. Technol. Ind.* **2022**, *22*, 198–203. (In Chinese)
25. Cox, B.; Innis, S.; Kunz, N.C.; Steen, J. The mining industry as a net beneficiary of a global tax on carbon emissions. *Commun. Earth Environ.* **2022**, *3*, 17. [CrossRef]

MDPI AG
Grosspeteranlage 5
4052 Basel
Switzerland
Tel.: +41 61 683 77 34

MDPI Books Editorial Office
E-mail: books@mdpi.com
www.mdpi.com/books

MDPI

Academic Open
Access Publishing

mdpi.com

ISBN 978-3-7258-3480-8